eurad

**European Joint Programme
on Radioactive Waste Management**

Deliverable 7.6:

Modelling report on the effect of temperature on

clay host rocks behaviour

Work Package 7

https://www.ejp-eurad.eu

Document information

Project Acronym	**EURAD**
Project Title	**European Joint Programme on Radioactive Waste Management**
Project Type	**Report**
EC grant agreement No.	**847593**
Project starting / end date	**01/06/2019–31/05/2024**
Work Package No.	**7**
Work Package Title	**Influence of temperature on clay-based material behaviour**
Work Package Acronym	**HITEC**
Deliverable No.	**7.6**
Deliverable Title	**Modelling report on the effect of temperature on clay host rocks behaviour**
Lead Beneficiary	**Andra**
Contractual Delivery Date	**31/05/2024**
Actual Delivery Date	**06/06/2024**
Type	**Report**
Dissemination level	**PU**
Authors	**Christophe de Lesquen (Andra), Minh-Ngoc Vu (Andra), Carlos Plua (Andra), Eric Simo (BGE), Alexandru Tatomir (BGE), Paola Léon Vargas (BGE), Pierre Bésuelle (CNRS-UGrenoble), Stefano Dal Pont (CNRS-UGrenoble), Alice di Donna (CNRS-UGrenoble), Nicolás Zalamea (CNRS-UGrenoble), Simon Raude (EDF), Ginger El Tabbal (EDF), Arnaud Dizier (EURIDICE), Suresh Seetharam (SCK CEN), Asta Narkuniene (LEI), Gintautas Poskas (LEI), Povilas Poskas (LEI), Frédéric Collin (ULiège), Hangbiao Song (ULiège), Abhishek Rawat (ULiège), Antonio Gens (UPC), Fei Song (UPC)**

To be cited as

Christophe de Lesquen (Andra), Minh-Ngoc Vu (Andra), Carlos Plua (Andra), Eric Simo (BGE), Alexandru Tatomir (BGE), Paola Léon Vargas (BGE), Pierre Bésuelle (CNRS-UGrenoble), Stefano Dal Pont (CNRS-UGrenoble), Alice di Donna (CNRS-UGrenoble), Nicolás Zalamea (CNRS-UGrenoble), Simon Raude (EDF), Ginger El Tabbal (EDF), Arnaud Dizier (EURIDICE), Suresh Seetharam (SCK CEN), Asta Narkuniene (LEI), Gintautas Poskas (LEI), Povilas Poskas (LEI), Frédéric Collin (ULiège), Hangbiao Song (ULiège), Abhishek Rawat (ULiège), Antonio Gens (UPC), Fei Song (UPC) (2024): Modelling report on the effect of temperature on clay host rocks behaviour. Final version as of 06/06/2024 of deliverable 7.6 of the HORIZON 2020 project EURAD. EC Grant agreement N˚ 847593.

Disclaimer

EURAD (Deliverable n˚ 7.6) – Modelling report on the effect of temperature on clay host rocks behaviour
Dissemination level: PU
Date of issue of this report: 06/06/2024

Page ii

Acknowledgement

EURAD (Deliverable n˚ 7.6) – Modelling report on the effect of temperature on clay host rocks behaviour
Dissemination level: PU
Date of issue of this report: 06/06/2024

Page iii

Status of deliverable			
		By	Date
Delivered (Lead beneficiary)		[Andra]	28 May 2024
Verified (WP Leader)		Markus Olin [VTT]	29 May 2024
Reviewed (Reviewers)		Steven Baxter	31 May 2024
Approved (PMO)		Bharti Reddy	05 June 2024
Submitted to EC (Coordinator)		[Andra]	06 June 2024

EURAD (Deliverable n˚ 7.6) – Modelling report on the effect of temperature on clay host rocks behaviour
Dissemination level: PU
Date of issue of this report: 06/06/2024

Page iv

Executive summary

The European Joint Programme on Radioactive Waste Management (EURAD) has been implemented as part of the EU Research and Innovation Programme Horizon 2020. The overall aim of the work package EURAD-WP7 HITEC ("Influence of temperature on clay-based material behaviour") is to improve the Thermo-Hydro-Mechanical (THM) description of the clay-based materials – host clay rock and bentonite buffer - at elevated temperatures.

Within this WP, Task 2 focused on the behaviour of the clay host rocks at temperatures of up to 120 °C. Laboratory experiments in subtasks 2.1 and 2.2 investigated the near-field and far-field effects of heating on the properties and behaviour of the host rocks. Subtask 2.3 focused on the development of THM models, their calibration with laboratory experiments and benchmarking to generic cases and in-situ experiments. Eight teams took part in the exercise and six numerical codes were tested.

The present report - D7.6 - Modelling report on the effect of temperature on clay host rocks behaviour - is the final deliverable for subtask 2.3. It summarises the results obtained by the different teams at the end of the project. The benchmarking exercise was divided in three steps, with firstly the modelling of near-field and far-field generic cases, then of some subtask 2.1 and 2.2 laboratory experiments, and finally of large scale in-situ heating experiments. The selection of benchmarking exercises is presented in details in the MS49 milestone document.

These exercises at three different scales showed that different numerical codes get consistent results when modelling the behaviour of clay rocks, both in the near-field and in the far-field. This outcome increases the confidence one can have in this type of model and shows the robustness of the modelling approach used to design some of the repositories.

Table of content

EURAD (Deliverable n° 7.6) – Modelling report on the effect of temperature on clay host rocks behaviour
Dissemination level: PU
Date of issue of this report: 06/06/2024

Page vii

EURAD (Deliverable n˚ 7.6) – Modelling report on the effect of temperature on clay host rocks behaviour
Dissemination level: PU
Date of issue of this report: 06/06/2024

Page viii

List of figures

EURAD (Deliverable n° 7.6) – Modelling report on the effect of temperature on clay host rocks behaviour
Dissemination level: PU
Date of issue of this report: 06/06/2024

Page x

EURAD (Deliverable n° 7.6) – Modelling report on the effect of temperature on clay host rocks behaviour
Dissemination level: PU
Date of issue of this report: 06/06/2024

Page xi

EURAD (Deliverable n˚ 7.6) – Modelling report on the effect of temperature on clay host rocks behaviour
Dissemination level: PU
Date of issue of this report: 06/06/2024

Page xii

EURAD (Deliverable n˚ 7.6) – Modelling report on the effect of temperature on clay host rocks behaviour
Dissemination level: PU
Date of issue of this report: 06/06/2024

Page xiii

EURAD (Deliverable n˚ 7.6) – Modelling report on the effect of temperature on clay host rocks behaviour
Dissemination level: PU
Date of issue of this report: 06/06/2024

Page xiv

EURAD (Deliverable n˚ 7.6) – Modelling report on the effect of temperature on clay host rocks behaviour
Dissemination level: PU
Date of issue of this report: 06/06/2024

Page xv

EURAD (Deliverable n˚ 7.6) – Modelling report on the effect of temperature on clay host rocks behaviour
Dissemination level: PU
Date of issue of this report: 06/06/2024

Page xvi

EURAD (Deliverable n˚ 7.6) – Modelling report on the effect of temperature on clay host rocks behaviour
Dissemination level: PU
Date of issue of this report: 06/06/2024

Page xvii

EURAD (Deliverable n˚ 7.6) – Modelling report on the effect of temperature on clay host rocks behaviour
Dissemination level: PU
Date of issue of this report: 06/06/2024

Page xviii

EURAD (Deliverable n˚ 7.6) – Modelling report on the effect of temperature on clay host rocks behaviour
Dissemination level: PU
Date of issue of this report: 06/06/2024

Page xix

List of tables

EURAD (Deliverable n° 7.6) – Modelling report on the effect of temperature on clay host rocks behaviour
Dissemination level: PU
Date of issue of this report: 06/06/2024

Page xxi

Acronyms

Organisations:

Andra	National Agency for Radioactive Waste Management (*Agence Nationale pour la Gestion des Déchets Radioactifs*) (France)
BGE	Federal Company for Radioactive Waste Disposal mbH (*Bundesgesellschaft für Endlagerung*) (Germany)
CNRS-U Grenoble	also CNRS-3SR: Institute of Earth Sciences (*Institut des sciences de la Terre – ISTerre*), depending on the University of Grenoble and CNRS(France)
EDF	Electricité de France (France)
EURIDICE	European Underground Research Infrastructure for Disposal of nuclear waste in Clay Environment (Belgium)
LEI	Lithuanian Energy Institute (Lithuania)
Nagra	National Cooperative for the Disposal of Radioactive Waste (*Nationale Genossenschaft für die Lagerung radioaktiver Abfälle*) (Switzerland)
ULg	University of Liège (Belgium)
UPC	Technical University of Catalonia (*Universitat Politècnica de Catalunya*) (Spain)

Other acronyms:

BC	Boom Clay
CMHM	Andra's research facility in Meuse and Haute-Marne, northeastern France (*Centre de Meuse/Haute-Marne*)
Cox	Callovo-Oxfordian Claystone
EDZ	Excavation damaged zone
HHGW	High Heat Generating Waste
HLW	High Level Waste
LTP	Linked third party
OPA	Opalinus Clay
PG	Praclay Gallery
PS	Plane Strain
SF	Spent Fuel
THM	Thermo-Hydro-Mechanical
UA	Argilaceous Unit in the Cox claystone (*Unité Argileuse*)
URL	Underground Research Laboratory
USC	Silty Carbonate Unit in the Cox claystone (*Unité Silto-Carbonatée*)
UT	Transition Unit between USC and UA in the Cox claystone (*Unité de Transition*)
WMO	Waste Management Organisation
WP	Work Package

1. Introduction

The WP7 "Influence of Temperature on Clay-based Material Behaviour" of the EURAD Project aimed to develop and document an improved thermo-hydro-mechanical (THM) understanding of clay-based materials (host rocks and buffers) exposed at high temperatures (>100°C) or having experienced high temperature transients for extended durations. The WP's raison d'être was to evaluate whether or not elevated temperature limits (of 100-150°C) are feasible for a variety of geological disposal concepts for high heat generating wastes (HHGW). HITEC planned to study clay host rock formations exposed at temperatures of up to 120°C, document and establish the possible extent of elevated temperature damage in the near- or far-field (e.g. from over-pressurisation) and also indicate the likely consequences of any such damage. The WP looked also at bentonite buffers and determined the temperature influence on buffer swelling pressure, hydraulic conductivity, erosion or transport properties and saw where the buffer safety functions started to be unacceptably impaired.

For the disposal of HHGW it is important to understand the consequences of the heat produced on the properties of the host rock and of the engineered clay barriers and on their long-term performance. Most safety cases for disposal concepts that involve clay currently consider a temperature limit of 90-100°C. Being able to tolerate higher temperature, whilst still ensuring an appropriate performance, would have significant advantages (e.g. shorter cooling times at surface, more efficient packaging, fewer disposal containers, fewer transport operations, smaller facility footprints, etc.).

Laboratory experiments in subtask 2.1 studied the effects of increased temperature in the near-field (fracturing and self-sealing in the excavated-damaged zone), while those performed in subtask 2.2 looked at the far-field effects, where thermal loading and the generation of overpressures may result in formation failure. Subtask 2.3 focused on the development of THM models, their calibration with laboratory experiments and benchmarking to generic cases and in-situ experiments. Eight teams took part in the exercise and six numerical codes were tested. Two sets of 2D models were first created to study the impact of temperature on the behaviour of the three clay host rocks (Boom Clay, Callovo-Oxfordian (Cox) claystone and Opalinus Clay) in the near-field and in the far-field. Some of the laboratory experiments were also simulated to improve the understanding of their THM behaviour. Three in-situ heating tests (PRACLAY in the Boom Clay, FE in the Opalinus Clay and ALC1605 in the Cox) were finally planned to be modelled, taking into account the results from the first two steps.

The initial D7.6 deliverable presented the codes used to model the THM behaviour of the three clay host rocks and the benchmarking exercises that have been selected. A second version presented the results of the first benchmarking exercise - 2D near-field / short-term generic model. This final report summarises the results obtained by the modelling teams during the project.

2. Benchmark description

ANDRA, EURIDICE and NAGRA selected the benchmarking exercises. They also provided data from their in-situ heating experiments.

The main objectives of the modelling exercises are:

- to compare the outputs from the different constitutive models and numerical codes,

- to get a better understanding of the THM behaviour of the host rocks, both in the near-field and in the far-field,

- to improve the existing models based on the new results from the Subtask 2.1 and 2.2 laboratory experiments,

- to compare the THM behaviour of the three host rocks.

In order to achieve these objectives, the subtask 2.3 is organised in four consecutive steps:

- 1. Creation of two 2D generic models to study the near-field and far-field effects of a temperature increase on the properties and behaviour of the clay host rocks

- 2. Modelling of Subtask 2.1 and 2.2 laboratory tests (triaxial compression and triaxial creep tests, thermal pressurisation tests).

- 3. Modelling of at least one of the in-situ heating experiments (PRACLAY, FE, ALC1605)

- 4. Models update if necessary, based on the laboratory tests results

This selection of benchmarking exercises is described in more details in the MS49 milestone document.

2.1. Generic case benchmarks

The objective of this step is to build two generic 2D models that will be used to simulate different host rocks. The first model will focus on the near-field effects of excavation and heating around the gallery, and the second one will be run over a longer period and will investigate the far-field effect of the thermal loading. The different model responses and the THM behaviour of the different host rocks will be compared.

In the NAGRA design, the gallery will be backfilled with bentonite, whereas the ANDRA concept leaves some room to facilitate a possible retrieval of the waste packages. In addition, the highly exothermic packages are separated by spacing buffers to reduce the thermal load. In order to focus on the host rocks and to be able to compare the models, the boundary condition around the gallery is set at the interface between the gallery and the host rock.

2.1.1. Near-field / short-term

The geometry of this model is a cross-section of a heating gallery and host rock perpendicular to the gallery axis. By considering the symmetric nature of the problem, only a quarter of the full cross-section is modelled, and the simulated region measures 100 m in both directions (Figure 2.1).
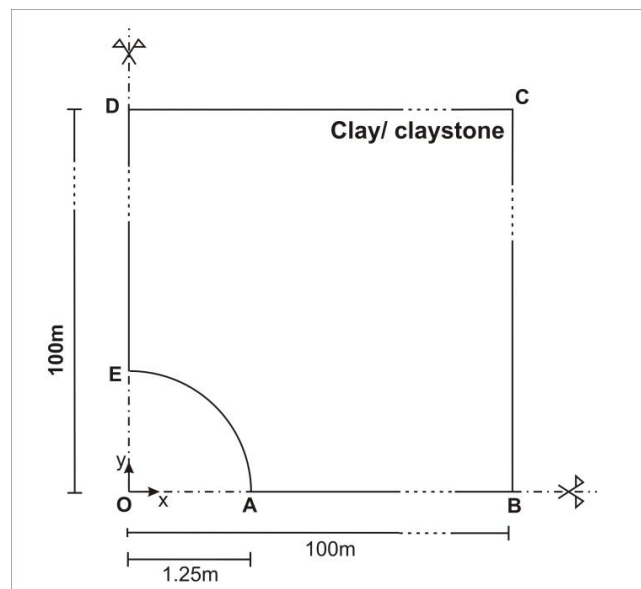
Figure 2.1: Model geometry for the near-field case

The teams were asked to run their model on at least two of the three host rocks (Boom Clay, OPA or Cox). Three subcases are proposed:

1. Isotropic stress conditions with isotropic elasticity and thermo-elasticity

2. Anisotropic stress conditions with cross-anisotropic elasticity and thermo-elasticity

3. Anisotropic stress conditions with elasto-plastic/damage model (the choice of the model is left free for the modelling team)

The goal with these subcases was first to compare the numerical codes on a fixed exercise (case 1 and 2) by imposing the boundary conditions and the mechanical constitutive laws and properties while the third case proposed to compare different approaches to reproduce the behaviour of the host rock formation and

EURAD (Deliverable n° 7.6) – Modelling report on the effect of temperature on clay host rocks behaviour
Dissemination level: PU
Date of issue of this report: 06/06/2024

Page 3

the development of the excavation damaged zone (EDZ). For this last case, the modelling teams could find relevant information in the state of the art of the project or could request additional data from ANDRA, EURIDICE or NAGRA.

2.1.1.1. Elastic isotropic case

As a first iteration, a simple elastic model was built with isotropic properties. The properties of the three host rocks are given in Table 2.1.

Table 2.1: Main physical, thermo-hydro-mechanical parameters for the three host rocks

			Boom Clay	Cox	OPA
Solid phase density	[kg/m^3]	ρ_s	2639	2690	2340
Bulk density	[kg/m^3]	ρ'	2000	2386	2030
Porosity		n	0.39	0.18	0.13
Isotropic intrinsic permeability	[m^2]	K	2.83E−19	2.3E−20	3.0E−20
Isotropic Young's modulus	[MPa]	E	300	7000	6000
Poisson's ratio	[–]	ν	0.125	0.3	0.3
Biot coefficient			1	0.8	0.6
Isotropic thermal conductivity	[W/m/K]	λ	1.47	1.67	1.85
Linear thermal expansion coefficient	[K^{-1}]	α_s	1E−5	1.25E−5	1.7E−5
Solid phase specific heat	[J/kg/K]	c_p	769	790	995

The following parameters were given for the water:

Table 2.2: Water properties

Density	1000 kg/m^3
Specific heat	4180 J/kg/K
Compressibility at 40 °C	4.5×10^{-4} MPa^{-1}
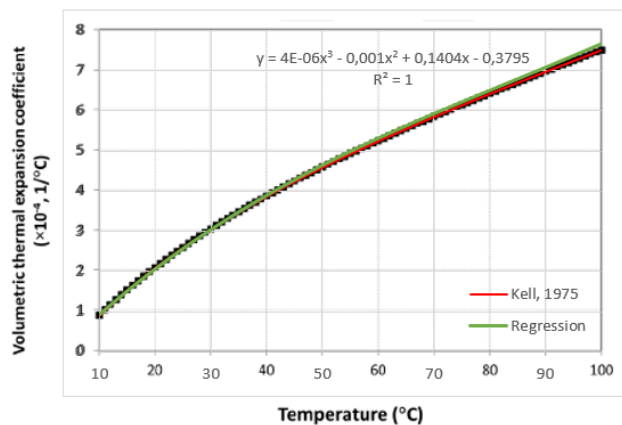
Figure 2.2: Evolution of the volumetric thermal expansion coefficient of water as a function of the temperature under atmospheric pressure (Kell, 1975).

The following power law for the volumetric thermal expansion coefficient of water (α_w) is proposed:

$$\alpha_w[10^{-4}\ 1/°C] = 4 \times 10^{-6}T^3 - 0.001\,T^2 + 0.1404\,T - 0.3795 \tag{2.1}$$

with T in °C.

EURAD (Deliverable n° 7.6) – Modelling report on the effect of temperature on clay host rocks behaviour
Dissemination level: PU
Date of issue of this report: 06/06/2024

Page 4

In the range of temperatures expected in the modelling, Vogel's formula gives a good approximation for the water viscosity (μ) and should be used:

$$\mu = e^{A + \frac{B}{C+T}} \qquad (2.2)$$

with T the temperature in K ($0\,^\circ$C = 273.15 K) and A = -3.719, B = 578.919, C = -137.546.
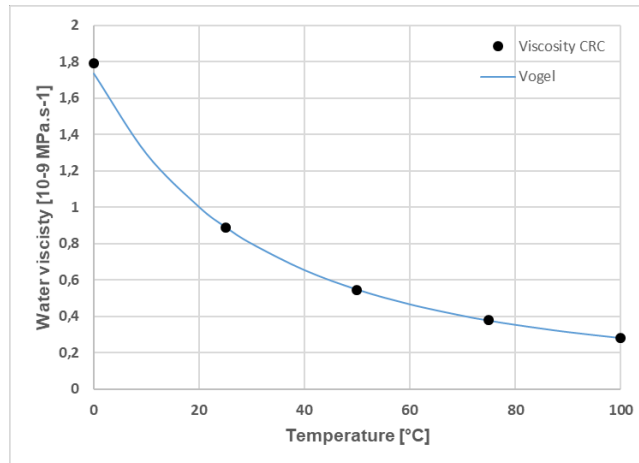
Figure 2.3: Evolution of water viscosity as a function of the temperature under atmospheric pressure (Rumble, 2019)

Initial and boundary conditions   For modelling purpose, the same in-situ stress and pressure conditions are given for the Cox and OPA cases.

Table 2.3: Initial conditions in the three host rocks

			Boom Clay	Cox/OPA
Total stress (isotropic)	[MPa]	σ_0 ($\sigma_{xx} = \sigma_{yy} = \sigma_{zz}$)	4.5	12.5
Pore pressure	[MPa]	P_0	2.25	4.7
Temperature	[$^\circ$C]	T_0	16.5	22

To model the excavation, the following boundary conditions are assumed:

Mechanical boundary conditions:

- A stress release technique is used and the pressure at the wall is decreased in 24 hours to 5% of the initial in-situ stress for Cox/OPA. For Boom Clay, it is proposed to reduce to 50% of the initial confining pressure as the clay is softer compared to Cox/OPA;
- The vertical and the horizontal displacements are respectively fixed in boundaries AB and DE;
- On boundaries DC and CB, impose a stress conditions equal to the in-situ stress conditions.

Hydraulic boundary conditions:

- the pore water pressure at the wall is reduced to atmospheric pressure (0.1 MPa) in 24 hours;
- the pore pressure at the boundaries DC and CB is constant (values in Table 2.3);
- the symmetric boundaries AB and DE are impervious (no flow).

EURAD (Deliverable n˚ 7.6) – Modelling report on the effect of temperature on clay host rocks behaviour
Dissemination level: PU
Date of issue of this report: 06/06/2024

Page 5

The boundary conditions during the waiting phase do not change, the pressure at the wall is maintained at 5% of the initial in-situ stress (50% for the Boom case) and the pore water pressure is fixed and equal to the atmospheric pressure at the wall. The waiting phase will last 6 months.

To model the heating phase, the boundary conditions change at the gallery wall; a heat flux of $200\,\mathrm{W/m}$ is applied. Heating is modelled over a period of 10 years. Constant stresses and pressure are maintained at DC and CB.

Table 2.4: Boundary conditions at the gallery wall

Period	Mechanical conditions	Hydraulic conditions	Thermal conditions
$T_0 - T_0 + 24$ hours: excavation	Stress reduction to 5% of the initial in-situ stress (Cox/OPA). Stress reduction to 50% of the initial in-situ stress for Boom Clay	Pore water pressure reduced to P atm (0.1 MPa) in 24 hours	No flow at the borehole wall
$T_0 + 24$ hours $- T_0 +$ 6 months: waiting	As above	$PP = P_{atm}$	As above
$T_0 + 6$ months $- T_0 +$ 10 years: heating	As above	No flow	Thermal flow at the borehole wall based on constant power ($200\,\mathrm{W/m}$)

Expected output   The following results are requested for comparison between modelling teams:

1. A description of the main characteristics of the THM model: geometrical model, spatial and temporal discretisation, potential simplifications, initial and boundary conditions

2. Presentation of the calculations carried out

3. Temperature, pressure, displacement and stress evolution at the points specified in Table 2.5 (1 tunnel radius (R), 1.5R, 2R, 5R, 50 m (OC/2) horizontally and vertically, C and E, plus 1R, 1.5R, 2R at 45 degrees). Horizontal profiles (at y = 0) and vertical profiles (at x = 0) should be given at the following timesteps: T_0, $T_0 + 12$ hours, $T_0 + 24$ hours, $T_0 + 3$ months, $T_0 + 6$ months, $T_0 + 1, 2, 4, 6, 8$ and 10 years

4. Information about the code: version, pre- and post-treatment, CPU time, computer performance...

EURAD (Deliverable n˚ 7.6) – Modelling report on the effect of temperature on clay host rocks behaviour
Dissemination level: PU
Date of issue of this report: 06/06/2024

Page 6

European Joint Programme on Radioactive Waste Management

Table 2.5: Control points for Step 2.1.1

Point	(x, y) coordinates	Parameter
P1	1.25, 0	T [°C], PP [MPa], σ_x, σ_y, σ_{xy} [MPa], DX, DY
P2	1.875, 0	T, PP, σ_x, σ_y, σ_{xy}, DX, DY
P3	2.5, 0	T, PP, σ_x, σ_y, σ_{xy}
P4	6.25, 0	T, PP, σ_x, σ_y, σ_{xy}
P5	50, 0	T, PP, σ_x, σ_y, σ_{xy}
P6	100, 0	T, PP, σ_x, σ_y, σ_{xy}
P7	0, 1.25	T, PP, σ_x, σ_y, σ_{xy}
P8	0, 1.875	T, PP, σ_x, σ_y, σ_{xy}
P9	0, 2.5	T, PP, σ_x, σ_y, σ_{xy}
P10	0, 6.25	T, PP, σ_x, σ_y, σ_{xy}
P11	0, 50	T, PP, σ_x, σ_y, σ_{xy}
P12	0, 100	T, PP, σ_x, σ_y, σ_{xy}
P13	0.884, 0.884	T, PP, σ_x, σ_y, σ_{xy}
P14	1.326, 1.326	T, PP, σ_x, σ_y, σ_{xy}
P15	1.768, 1.768	T, PP, σ_x, σ_y, σ_{xy}

2.1.1.2. Elastic anisotropic case

If their code allows it, the teams will include anisotropic stress conditions with cross-anisotropic elasticity and thermo-elasticity.

Mechanical anisotropy The anisotropic mechanical and thermal properties for the three host rocks are given in Table 2.6.

Table 2.6: Anisotropic thermo-hydro-mechanical parameters for the three host rocks

			Boom Clay	Cox	OPA
Intrinsic permeability parallel to bedding	[m^2]	$k_{\parallel}$	4E−19	3.9E−20	5E−20
Intrinsic permeability normal to bedding	[m^2]	$k_{\perp}$	2E−19	1.3E−20	1E−20
Young's modulus parallel to bedding	[MPa]	$E_{\parallel}$	400	8000	8000
Young's modulus normal to bedding	[MPa]	$E_{\perp}$	200	5000	4000
Poisson's ratio parallel to bedding	[–]	$\nu_{\parallel\parallel}$	0.125	0.21	0.35
Poisson's ratio normal to bedding	[–]	$\nu_{\parallel\perp}$	0.25	0.35	0.25
Shear modulus normal to bedding	[MPa]	$G_{\perp}$	80	2500	2300
Thermal conductivity parallel to bedding	[W/m/K]	$\lambda_{\parallel}$	1.65	1.88	2.4
Thermal conductivity normal to bedding	[W/m/K]	$\lambda_{\perp}$	1.31	1.25	1.3

Stress anisotropy A coefficient of earth pressure at rest of 0.7 is estimated at the HADES laboratory level in Mol. In the Meuse/Haute-Marne URL, a strike-slip to reverse faulting stress regime is proven in the Cox formation; however, for galleries drilled in the direction of the maximum horizontal stress, the stress is almost isotropic.

EURAD (Deliverable n˚ 7.6) – Modelling report on the effect of temperature on clay host rocks behaviour
Dissemination level: PU
Date of issue of this report: 06/06/2024

Page 7

Table 2.7: Initial conditions in the three host rocks

			Boom Clay	Cox	OPA
Total stress	[MPa]	σ_{xx}	3.825	12.4	2.2
		σ_{yy}	4.5	12.7	4.0
		σ_{zz}	3.825	16.4	6.5
Pore Pressure	[MPa]	P_0	2.25	4.7	2.1

Expected output   As in 2.1.1.1.

2.1.1.3. Modelling of the EDZ

The objective of this step is to model the development of the excavation damaged zone and its evolution under heating. The teams are free to choose their mechanical model.

As most results from the Subtask 2.2 laboratory tests were not available before 2021 or 2022 and in order to minimise the dispersion due to parameters calibration, a set of triaxial compression, extension and creep tests was provided by ANDRA, EURIDICE and NAGRA to help establish the constitutive models. Moreover, information on the mechanical behaviour of the clay/claystone could be found in the HITEC SotA (EURAD, 2020).

Expected output   As in 2.1.1.1, plus a description of the constitutive model chosen and a representation of the damaged zone. Particular attention should be given to the extension of the damaged zone during the heating phase.

2.1.2. Far-field / long-term

In this model, the heating period is extended to 1000 years. The model should therefore extend vertically to surface. The lateral extent is given by the symmetry axis through the HLW cell/tunnel and the half-distance between two adjacent SF/HLW tunnels.
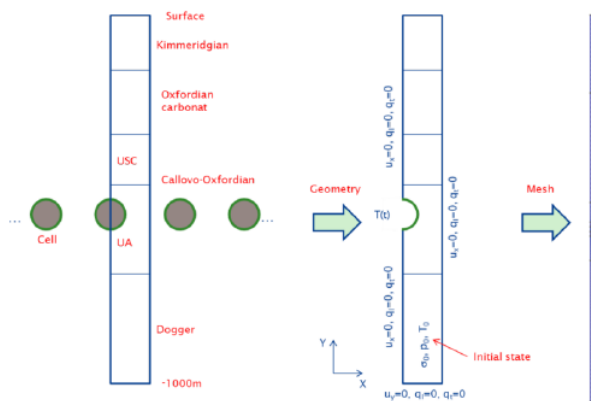
Figure 2.4: Model geometry for the far-field case (Cox case)

We assume that all the cells are filled at the same time. This hypothesis is valid if one considers the time needed to fill two adjacent cells (a few years at most) compared to the time required for the most exothermic waste to reach their thermal peak (several hundred years). Symmetrical loading by two adjacent cells implies that the zone located at half-distance between two parallel cells is subject to loads from both cells.

EURAD (Deliverable n° 7.6) – Modelling report on the effect of temperature on clay host rocks behaviour
Dissemination level: PU
Date of issue of this report: 06/06/2024

Page 8

The lateral symmetry conditions prevent any horizontal expansion (no displacement) and any pressure dissipation (no flow).

Two similar cases were proposed for modelling with Cox and Opalinus clay host rocks. However, only the Cox case was modelled finally and is described in detail here. The model extends from 0 to 1000 m depth, and the half cell-to-cell distance (lateral extent) is set equal to 25 m.

The following configuration is given:

- Depth: 480 m

- Excavated diameter: 1 m.

Table 2.8: Formation tops

		Depth (m)
Barrois Limestone / Kimmeridgian		0
Oxfordian		132.7
Callovo-Oxfordian	USC	406.8
	UT	436.4
	UA2-UA3	451.6
	UA1	514.9
Dogger		555.6
Alvéole		490

The thermo-poro-elastic properties are given in Table 2.10. An elasto-visco-plastic model can be applied to the clay-rich UA2 and UA3 subunits where the cell is located, while the other layers are poro-elastic.

Table 2.9: Over- and underburden parameters – Cox case

			Barrois limestone/ Kimmeridgian	Oxfordian	Dogger
Porosity	n	[%]	13	13	10
Bulk density	ρ	[kg/m^3]	2450	2470	2470
Biot coefficient	b		0.6	0.75	0.6
Mechanical properties					
Young modulus	E	[MPa]	3600	30000	30000
Poisson ratio	ν	[–]	0.3	0.3	0.3
Thermal expansion coefficient		[K^{-1}]	2.2×10^{-5}	4.5×10^{-6}	4.5×10^{-6}
Hydraulic and thermal properties					
Intrinsic Permeability	K	[m^2]	10^{-19}	10^{-16}	10^{-18}
Thermal conductivity	λ	[W/m/K]	$\lambda_\perp = 1.1$ $\lambda_\parallel = 1.4\lambda_\perp$	2.3	2.3
Specific heat	C	[J/kg/K]	1024	925	925

EURAD (Deliverable n˚ 7.6) – Modelling report on the effect of temperature on clay host rocks behaviour
Dissemination level: PU
Date of issue of this report: 06/06/2024

Page 9

Table 2.10: Cox THM parameters

Parameters		Subunit	Value
Thermal conductivity normal to bedding $\lambda_\perp$	[W/m/K]	USC	1.8
		UT	1.4
		UA2-UA3	1.25
		UA1	1.6
Thermal conductivity parallel to bedding $\lambda_\parallel$	[W/m/K]	USC	1.8
		UT & UA	$1.5 \times \lambda_\perp$
Solid phase specific heat Cs	[J/kg/K]		790
Bulk density	[kg/m^3]	USC	2480
		UT & UA	2386
Young's modulus normal to bedding $E_\perp$	[GPa]	USC	12.8
		UT	8.5
		UA2-UA3	7
		UA1	10
Young's modulus parallel to bedding $E_\parallel$	[GPa]	UA & UT	$1.5 \times E_\perp$
Poisson's ratio	[–]		0.3
Poisson's ratio anisotropy		UA & UT	$1.5 \, (\nu_\parallel = \nu_\perp/1.5)$
Shear modulus normal to bedding $G_\perp$	[GPa]	UT	3.8
		UA2-UA3	3.1
		UA1	4.4
Linear thermal expansion coefficient of skeleton	[K^{-1}]		1.28×10^{-5}
Intrinsic permeability parallel to bedding $k_\parallel$	[m^2]		3.9×10^{-20}
Intrinsic permeability normal to bedding $k_\perp$	[m^2]		1.3×10^{-20}
Biot coefficient	[–]		0.8
Porosity	[%]	USC	15
		UT & UA	18

The water properties are the same than in the near-field model.

2.1.2.1. Initial conditions and boundary conditions

Initial conditions The temperature follows the natural geothermal gradient. For the Cox case, a natural geothermal gradient of 0.025 °C/m is given in the overburden with a surface temperature of 10 °C, giving a temperature of 22 °C at 480 m (Figure 2.5).

EURAD (Deliverable n° 7.6) – Modelling report on the effect of temperature on clay host rocks behaviour
Dissemination level: PU
Date of issue of this report: 06/06/2024

Page 10
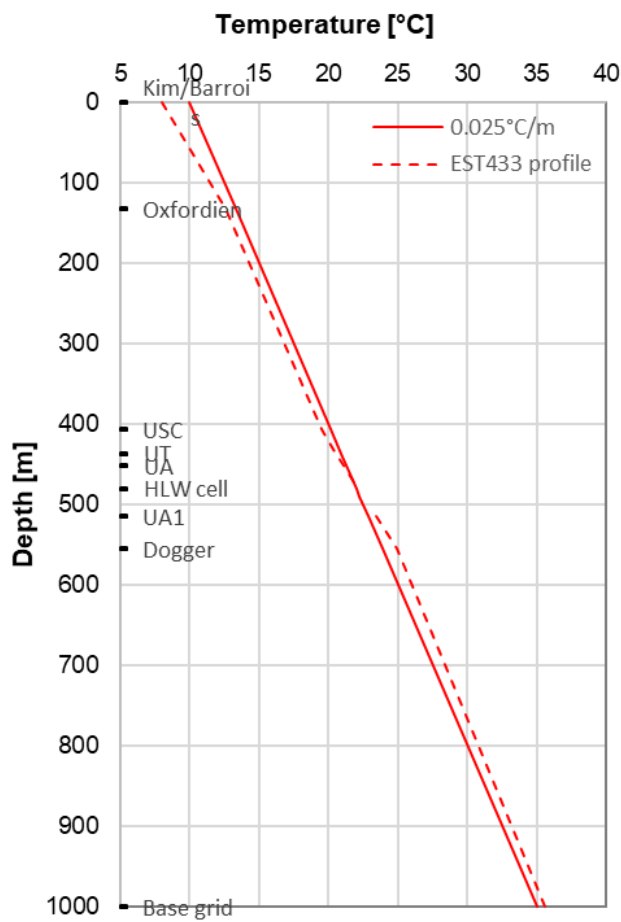
Figure 2.5: Temperature profile in the Cox case

In-situ stress state: At a given depth, the vertical stress corresponds to the weight of the overburden (for the Cox model, a mean overburden rock mass density of $2472 \, \text{kg}/\text{m}^3$ is used). The minimum horizontal stress (σ_h) is taken equal to the vertical stress. The maximum horizontal stress (σ_H) is equal to the vertical stress in the Kimmeridgian and $1.3 \times \sigma_h$ from top Cox. A linear interpolation is assumed in the Oxfordian carbonates (see Figure 2.6, left).

For the Cox case, a hydrostatic pore water pressure is assumed in the overburden and underburden, but an overpressure is observed in the Cox itself (Figure 2.6, right). This initial overpressure should be taken into account in the model.

Values and formulas for the stress, pressure and temperature profiles were given in a separate spreadsheet.

The hole is drilled in the direction of the maximum horizontal stress.

Boundary conditions The far-field boundary conditions are shown in Figure 2.7:

- Upper boundary: constant temperature ($10\,^{\circ}\text{C}$) and pressure ($1\,\text{atm}$), free displacement

- Lower boundary: constant temperature (based on geothermal gradient) and pressure (based on hydrostatic gradient), zero normal displacement

EURAD (Deliverable n° 7.6) – Modelling report on the effect of temperature on clay host rocks behaviour
Dissemination level: PU
Date of issue of this report: 06/06/2024

Page 11
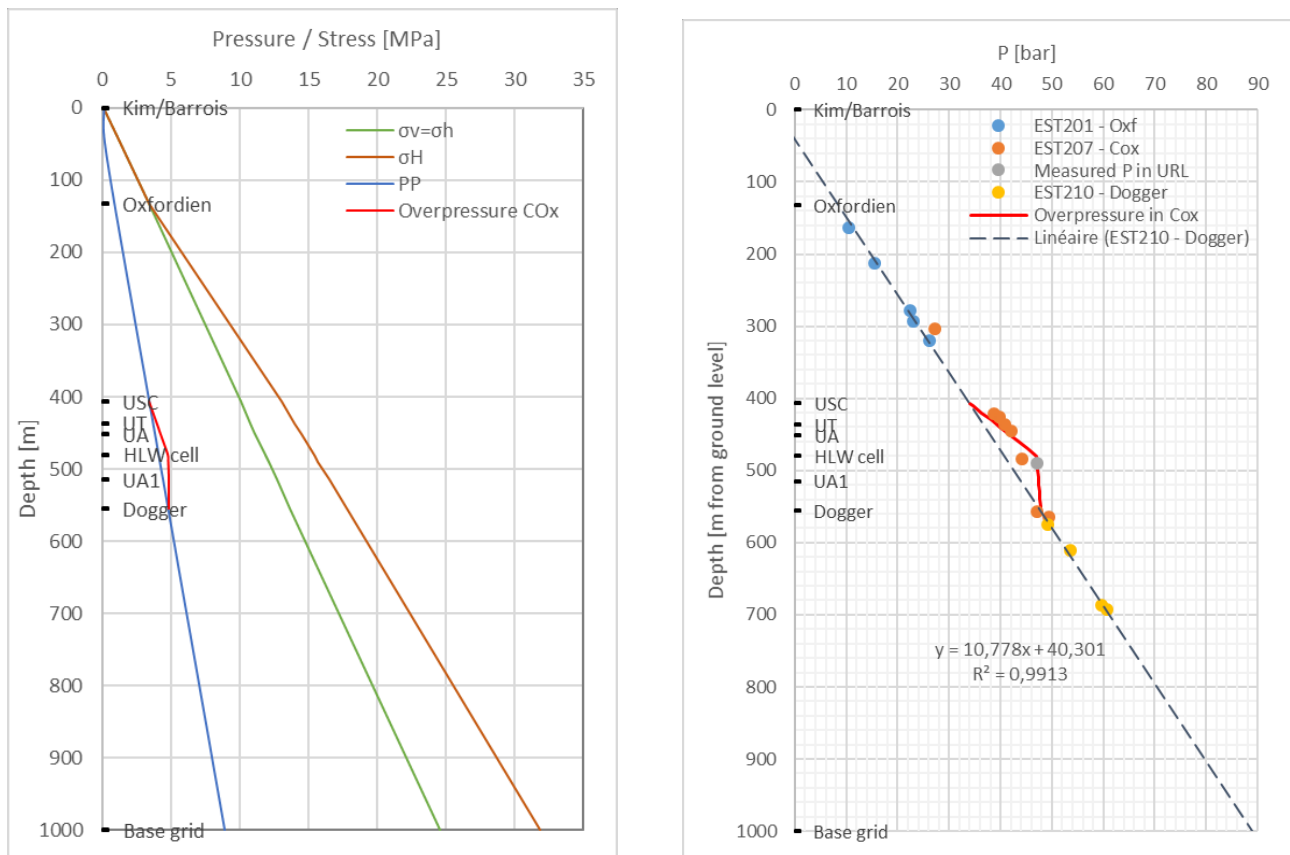
Figure 2.6: Cox stress profiles (left), and pore water pressure measurements and profile (right)

- Lateral boundaries: no flow, zero normal displacement

The boundary conditions at the excavated wall are given in Table 2.11 from T_0 = cell excavation.

Table 2.11: Boundary conditions at the borehole wall

Period	Mechanical conditions	Hydraulic conditions	Thermal conditions
$T_0 - T_0 + 24$ hours: Excavation	Stress reduction to 0% of the initial in-situ stress	Pore water pressure reduced linearly to Patm (0.1 MPa)	No flow at the borehole wall
$T_0 + 24$ hours $- T_0 +$ 2 years: Waiting	Linear stress increase from 0 to 3 MPa over the 2 years waiting period	No flow (undrained) at the borehole wall	No flow at the borehole wall
$T_0 + 2 - T_0 + 1000$ years: Heating	3 MPa constant pressure applied on the cell wall during the heating phase	No flow (undrained) at the borehole wall	Thermal flow based on applied power prediction at the borehole wall (Table 2.12)

The thermal history is based on a COG-800 package. In the ANDRA concept, 42 such packages will be stored in the 100 m long cell. From the moment they are installed in the cell, the thermal load will decrease progressively as shown on Table 2.12. Two cases should be modelled: in the first one, the packages are installed after having let them cool down for 85 years (initial load of 139 W/m). In the second one, they are

EURAD (Deliverable n° 7.6) – Modelling report on the effect of temperature on clay host rocks behaviour
Dissemination level: PU
Date of issue of this report: 06/06/2024

Page 12
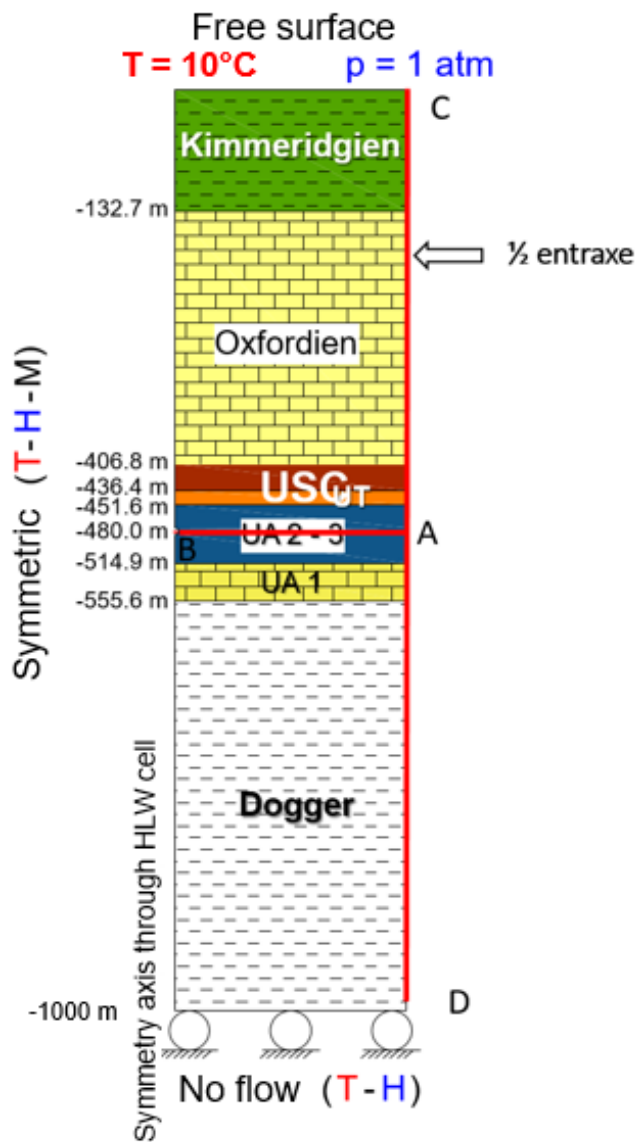
Figure 2.7: Far-field boundary conditions (with Cox stratigraphy)

installed after waiting only 55 years (initial load of $242\,\mathrm{W/m}$).

Expected output: stress, strain, temperature, pressure at the following points: at the borehole wall, 1, 2, 5 and 10 diameters and $25\,\mathrm{m}$ (far boundary, see Figure 2.8).

The teams are free to set the reference (y = 0) at surface or at the cell level.

EURAD (Deliverable n˚ 7.6) – Modelling report on the effect of temperature on clay host rocks behaviour
Dissemination level: PU
Date of issue of this report: 06/06/2024

Page 13

Table 2.12: Applied thermal load

Age (year)	Thermal load (W/m)	Age (year)	Thermal load (W/m)
55	242	200	45
60	219	210	43
65	199	220	41
70	181	230	40
75	165	240	39
80	151	250	38
85	139	260	37
90	128	270	36
95	118	280	35
100	110	290	35
110	95	300	34
120	84	400	29
130	75	500	24
140	67	600	21
150	61	700	18
160	57	800	16
170	53	900	13
180	50	1000	12
190	47	2000	3
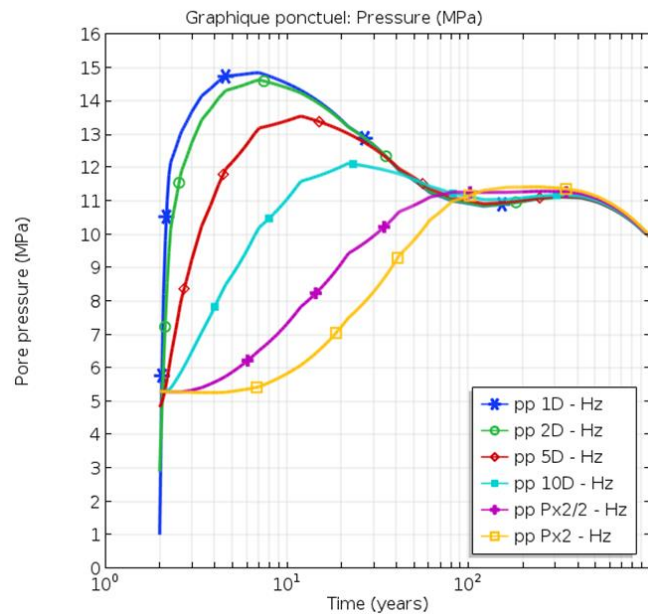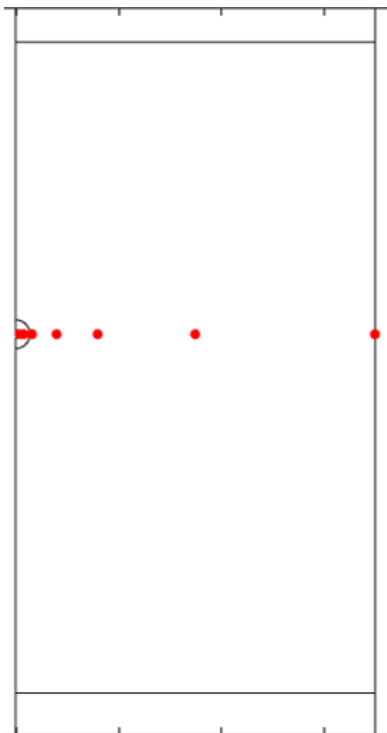
Figure 2.8: Example of control points distribution and output

EURAD (Deliverable n˚ 7.6) – Modelling report on the effect of temperature on clay host rocks behaviour
Dissemination level: PU
Date of issue of this report: 06/06/2024

Page 14

2.2. Laboratory experiments

In subtask 2.1 and 2.2, ULorraine performed some triaxial compression tests to study the THM behaviour of COx claystone subjected to different temperature conditions (from 20 to 150 °C).

The experimental program involved testing of groups of $20\,mm$ diameter and $40\,mm$ high samples cut in directions perpendicular ($\theta = 0°$) and parallel ($\theta = 90°$) to bedding planes, as shown in Figure 2.9. They were extracted from ANDRA's borehole cores. These samples were equipped with strain gauges and placed in a triaxial cell (Figure 2.10). Six strain gauges are glued for parallel orientation samples ($\theta = 90°$), while four strain gauges are installed for perpendicular orientation samples ($\theta = 0°$), as indicated in Figure 2.9.
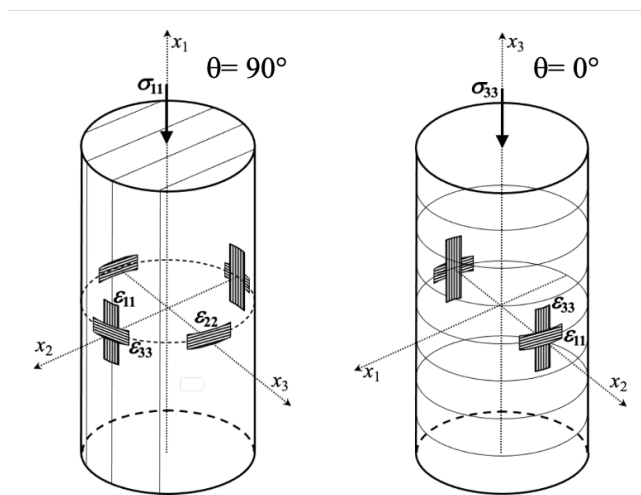
Figure 2.9: Definition of bedding orientations and locations of the strain gauges
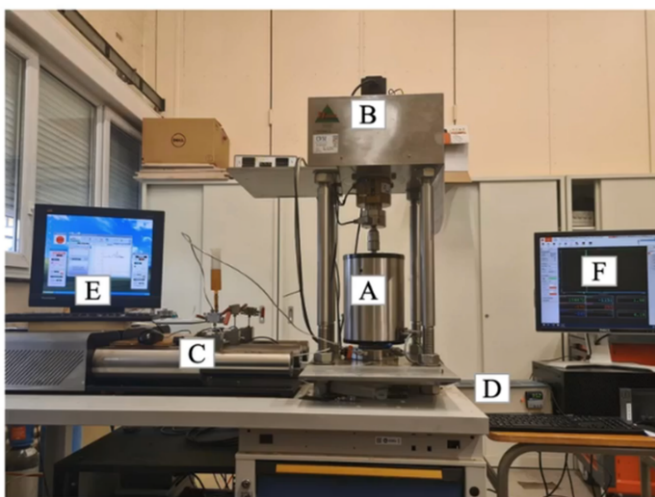
Photo of the experimental system

A: Triaxial cell equipped with heating collar

B: Mechanical press

C: Syringe pump

D: Thermal regulator

E: Press and pump controller

F: Acquisition system

Figure 2.10: Experimental system

Subsequently, all specimens were submitted to increasing cell pressure at a rate of $0.1\,MPa/min$, and then, the temperature was increased at a rate of 50 °C/hour. After 14 hours of the end of the temperature rise, deviatoric loading was applied at a controlled displacement rate of $12\,\mu m/min$. Two different hydraulic boundary conditions (B.C.) are considered: surface B.C. and point B.C. that will be described in the next section.

The applied confining pressure was 0 and 4 MPa for subtask 2.1 (short-term) tests and 12 MPa for long-

EURAD (Deliverable n° 7.6) – Modelling report on the effect of temperature on clay host rocks behaviour
Dissemination level: PU
Date of issue of this report: 06/06/2024

Page 15

term tests (subtask 2.2). More details on the test protocols and results may be found in the D7.5 deliverable.

The teams were encouraged to model the tests performed at 20 and 80 °C, with 4 and 12 MPa confining pressures and both orientations (parallel and perpendicular to bedding), giving eight cases in total. The main test features for these specimens are shown in Table 2.13 (θ is the plug orientation, 0° being perpendicular to bedding, s_l is the initial liquid saturation, n_t is the calculated total porosity and ρ_s is the solid matrix density). Experimental results in terms of stress-strain curves are also available, as described in the next section, and will be used to compare with numerical results. No measurement of pore pressure inside the sample was performed in the tests.

Table 2.13: Main test features.

Sample reference	θ (°)	S_l (%)	n_t (%)	Confining pressure (MPa)	T (°C)	Thermal loading rate (°C/h)	Peak deviatoric strength (MPa)	ρ_s (g/cm^3)	Time* (hour)
EST66760-14	0	94.6	16.83	4	20	50	25.00	2.66	14
EST66762-15	0	95.2	16.75	4	80	50	21.62	2.66	14
EST66764-14	0	95.5	16.43	12	20	50	28.60	2.65	14
EST66723-17	0	91.7	16.90	12	80	50	27.13	2.66	14
EST66420-4	90	90.2	16.62	4	20	50	28.03	2.69	14
EST66421-6	90	93.9	16.07	4	80	50	27.75	2.68	14
EST66723-1	90	91.7	16.90	12	20	50	49.48	2.66	14
EST66723-4	90	91.3	16.96	12	80	50	38.22	2.66	14

EURAD (Deliverable n˚ 7.6) – Modelling report on the effect of temperature on clay host rocks behaviour
Dissemination level: PU
Date of issue of this report: 06/06/2024

Page 16

2.3. In-situ heating experiments

The last step consisted of modelling an in-situ heating experiment. Three cases were initially proposed: the Praclay experiment in the Boom clay, the ALC1605 experiment in the Callovo-Oxfordian claystone, and the FE experiment in the Opalinus clay. Because of the workload and the necessity to have enough modelling teams on each case for comparison, only the first two were modelled. Detailed descriptions of the Praclay and ALC1605 experiments and of the proposed modelling activities are given in sections 7.1 and 7.2

EURAD (Deliverable n˚ 7.6) – Modelling report on the effect of temperature on clay host rocks behaviour
Dissemination level: PU
Date of issue of this report: 06/06/2024

Page 17

3. Process model descriptions

3.1. Code_Aster

The THM model implemented in Code_Aster (EDF, 2022) is based on the theory of porous media as developed by (Coussy, 2004). The constitutive relations are obtained from a thermodynamic point of view with homogenization arguments taken into consideration.

The considered porous medium is a volume made up of a homogeneous solid matrix with pores. It is assumed that the pores can be occupied by at most two constituents: water and air. Each of them can co-exist in two phases: a liquid (lq) or/and a gaseous phase (gz). In a general way, water can be present as liquid water (w) or water vapour (vp) and the air can be present as dissolved air (ad) or dry air (dra). In the context of the current study, the material is considered saturated with a liquid water (w) phase.

The general assumptions made in the THM model correspond to those made usually in a classical poromechanical framework as in (Coussy, 2004) and are the following:

- small displacements,

- reversible thermodynamic processes,

- gases are perfect gases,

- ideal mixture of perfect gases (total pressure = sum of partial pressures)

- thermodynamic equilibrium between the phases of the same component

While x and t are respectively the geometrical and time variables, the general thermodynamic variables in the THM model are the temperature of the environment $T(x, t)$ and the partial pressure of each j constituent $p_j(x, t)$. The latter pressures are not completely independent: for an unsaturated medium, a capillary pressure could be considered with

$$p_c = p_{gz} - p_{lq} = p_{gz} - p_w - p_{ad} \text{ and } p_{gz} = p_{ad} + p_{dra}$$

For a saturated medium, as in the context of this study, the only pressure considered is that of the liquid water p_w.

The balance equations to be resolved in the THM model, for a saturated medium, are:

- the equilibrium equation for mechanics:

$$\frac{\partial \sigma_{ij}}{\partial x_j} + \rho F_i = 0$$

where σ_{ij} is the total stress, ρ is the homogenized density of the medium and F_i the external mass force (such as the gravity).

- the liquid water mass balance equation for hydraulics, where in the absence of a volumetric source term, we can write:

$$\frac{\partial m_w}{\partial t} + \frac{\partial M_{w,i}}{\partial x_i} = 0$$

m_w is the liquid water mass content and $M_{w,i}$ is the liquid water mass flow vector. The fluid velocity in the medium is described using Darcy's law, relating the liquid water mass flow and the liquid water pressure as follows:

$$\frac{M_{w,i}}{\rho_w} = -\frac{k_{ij}}{\mu_w}\left(\frac{\partial p_w}{\partial x_i} - \rho_w F_i\right)$$

where ρ_w is the liquid water density, k is the intrinsic permeability and μ_w is the dynamic viscosity of liquid water.

- the conservation of energy for heat:

$$h_w\frac{\partial m_w}{\partial t} + \frac{\partial Q'}{\partial t} + \frac{\partial(h_w M_{w,i})}{\partial x_i} + \frac{\partial q_i}{\partial x_i} = M_{w,i}F_i + \theta_i$$

where h_w is the mass enthalpy of liquid water, Q' is the non-convective heat received by the medium outside enthalpic contributions (equation 3.2.4.3-1 in the Code_aster reference (R7.01.10, 2014)), q is the heat flow rate described by Fourier's law and θ is the external source of heat.

The writing of these equations for the general case of an unsaturated medium is given in (R7.01.10, 2014). The main unknowns in those equations are 2 or 3 (depending on the dimension of space) displacements $u_x(x,t)$, $u_y(x,t)$, $u_z(x,t)$, the temperature $T(x,t)$, the capillary and the gas pressures for an unsaturated media and the filling fluid pressure for a saturated one (p_w in the current context).

Regarding the coupled hydromechanical formulation used to describe the saturated porous medium in this study, it relies on the classical framework of (Biot, 1973). The total stress σ_{ij}, the effective stress σ'_{ij} and the pore fluid pressure p_w are related by the equation:

$$\sigma_{ij} = \sigma'_{ij} + p_w\beta\delta_{ij}$$

where β is the Biot's coefficient, defined as $\beta = 1 - K_0/K_s$ with K_0 is the drained bulk modulus of the porous medium and K_s the bulk modulus of the solid matrix.

The variation of the medium porosity for the saturated medium is defined by the following equation:

$$d\varphi = \beta d\varepsilon - \varphi d\varepsilon_v - 3\alpha_\varphi dT + dp_w/M_\varphi$$

where ε is the total strain, φ is the Eulerian porosity defined as the porosity occupied by the voids in the current configuration Ω and is linked to the Lagrangian porosity (that corresponds to the initial configuration Ω_0) by $\phi = (1+\varepsilon_v)\varphi$ with ε_v the volumetric strain. α_φ is the thermal expansion coefficient of the pore volume and $1/M_\varphi$ is a Biot modulus depending on the Biot coefficient, the Eulerian porosity, the Young modulus and the Poisson ratio of the solid matrix. The expression of $1/M_\varphi$ as well as additional FE implementation details are given in the official documentation of Code_Aster (R7.01.10, 2014).

EURAD (Deliverable n˚ 7.6) – Modelling report on the effect of temperature on clay host rocks behaviour
Dissemination level: PU
Date of issue of this report: 06/06/2024

Page 19

3.2. CODE_BRIGHT

From a modelling perspective, unsaturated geomaterials are assumed as an equivalent porous medium. The multi-phases and multi-species approach is used to build the THM formulations in CODE_BRIGHT (Gens et al., 2007; Olivella et al., 1995; Song et al., 2022, 2021b). Three phases are considered: solid phase (s), liquid phase (l) and gas phase (g). Meanwhile, three species are considered: solid (-): the mineral is coincident with the solid phase, water (w): as liquid or vapour in the gas phase, and air (a): dry air, as gas or dissolved in the liquid phase.

The analysis of coupled THM problems involving saturated materials is based on the simultaneous solution of the following balance equations:

The mass balance of the solid phase in the medium is:

$$\frac{\partial}{\partial t}\left[\rho_S(1-\phi)\right] + j_{i,i}^S = 0$$

where ρ_s represents the mass of solid per unit volume of solid; ϕ is porosity; j_i^s represents the mass flux of the solid with respect to a fixed reference system.

The total mass balance of water in the liquid:

$$\frac{\partial}{\partial t}\left[\omega_l^w \rho_l S_l \phi + \omega_g^w \rho_g S_g \phi\right] + \left(j_{i,i}^{l,w} + j_{i,i}^{g,w}\right) = f^w$$

where ω_l^w and ω_g^w represent the mass of the component (water) with respect to the total mass of the liquid phase and gas phase, respectively. S_l and S_g are the degree of saturation of liquid and gas phases, i.e., the fraction of pore volume occupied by each phase. ρ_l and ρ_g represent the liquid density and gas density, respectively. $j_i^{l,w}$ represent the mass flux of liquid in the water, and $j_i^{g,w}$ represent the mass flux of gas in the water. f^w represents an external supply of water.

The balance of internal energy for the medium:

$$\frac{\partial}{\partial t}\left[E_S \rho_S(1-\phi) + E_l \rho_l S_l \phi + E_g \rho_g S_g \phi\right] + \left(i_i^c + j_j^{Es} + j_j^{El} + j_j^{Eg}\right)_{i,i} = f^Q$$

where i_i^c is energy flux due to conduction through the porous medium; f^Q is internal or external energy supply; j_i^E represents the advective fluxes of energy due to mass motions; E is specific internal energy.

The equilibrium equation:

$$\sigma_{ij,j} + b_i = 0$$

where σ_{ij} is the component of stress, b_i represents body force.

In order to better reproduce the thermal pressurisation process, the thermal expansion coefficient of water α_w and water viscosity μ_L are set dependent on temperature. Water viscosity is assumed to vary exponentially with temperature as follows:

$$\mu_L = Ae^{\left(\frac{B}{273.15+T}\right)}$$

with A = 2.12×10^{-12} MPa s, B = 1808.5 K, T is temperature [°C].

The water thermal expansion coefficient (α_w) in CODE_BRIGHT is expressed as:

$$\rho_l = \rho_{l0}\left[1 + \beta_w(P_l - P_{l0}) + A(T)\right]$$

$$A(T) = -\frac{(T + 288.9414)(T - 3.9863)^2}{(508929.2(T + 68.12963))}$$

EURAD (Deliverable n° 7.6) – Modelling report on the effect of temperature on clay host rocks behaviour
Dissemination level: PU
Date of issue of this report: 06/06/2024

Page 20

where ρ_l is liquid density, ρ_{l0} = 1000 kg m^{-3}, β_w is the water compressibility. p_{l0} is a reference liquid pressure. The water thermal expansion coefficient is then computed as $\alpha_w = \frac{1}{\rho_l}\frac{\partial \rho_l}{\partial T}$.

Figures 3.1 (a) and (b) show the comparisons of the water thermal expansion coefficient and water viscosity between the specified and CODE_BRIGHT expressions, respectively. A good agreement is observed between both results, verifying that the current approach to represent water properties is correct.
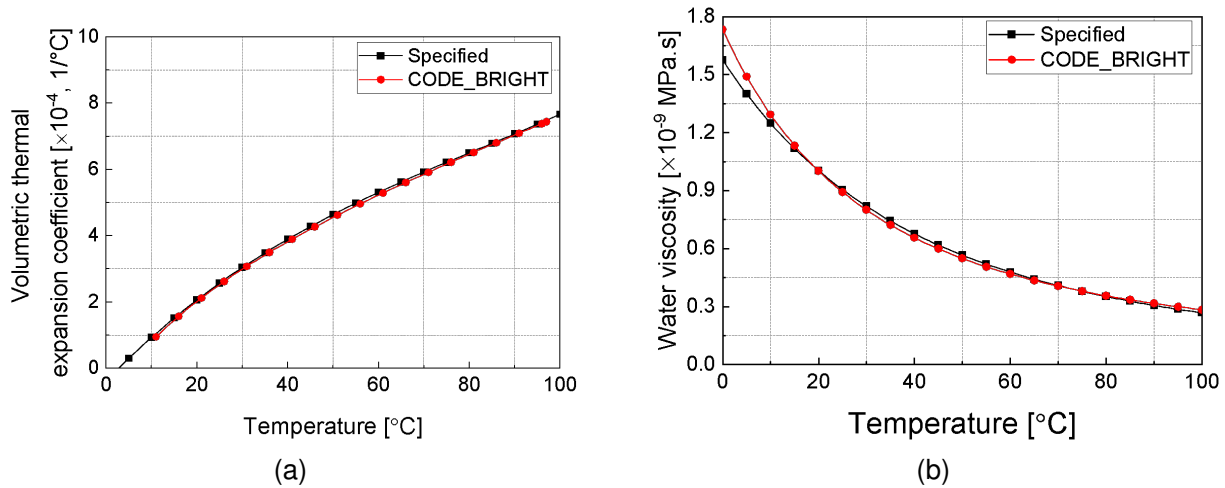
Figure 3.1: (a) Variation of thermal expansion coefficient of water with temperature according to CODE_BRIGHT and the specified law, and (b) variation of water viscosity with temperature according to CODE_BRIGHT and the specified law.

In a micromechanical analysis, the solid and fluid contents, and the pores can be explicitly modelled. The solid grain is assumed to be homogeneous and isotropic at the microscopic (pore) scale. The mean stress on the solid phase (p_s) can be expressed in terms of the total mean stress (p), the porosity (ϕ) and the liquid pressure (p_l) (Vu et al., 2020):

$$p_s = \frac{(p + \phi p_l)}{1 - \phi}$$

The coupled THM formulation described above was implemented in the Finite Element Method (FEM) software CODE_BRIGHT (Olivella et al., 2022). CODE_BRIGHT is a FEM code designed to solve thermo-hydro-mechanical problems in geological media. Unknowns (state variables) are associated with each of the final balance equations. The vector of unknowns is obtained by solving the system of PDEs (Partial Differential Equations) numerically in a coupled monolithic way.

The numerical approach can be viewed as divided in two parts: spatial and temporal discretization. Galerkin's finite element method is used for spatial discretization, while finite differences are used for temporal discretization. The discretization in time is linear and an implicit scheme is used for the solution. Finally, since the problems tackled are generally non-linear, the Newton-Raphson method is adopted as the iterative scheme.

A feature of the numerical approach is that it can use a wide library of elements including segments, triangles, quadrilaterals, tetrahedrons, triangular prisms and quadrilateral prisms. Linear interpolation functions and, for some elements, quadratic interpolation functions are adopted. Analytical or numerical integration is used depending on the element type. For the mechanical problem, selective integration is used for quadrilateral plane elements and quadrilateral prisms where the volumetric part is integrated at a single point with a reduced integration scheme.

The code has a procedure for the automatic discretization of time. Reduction of time increment may be caused by excessive variation of unknowns per iteration, by the excessive number of iterations to

EURAD (Deliverable n° 7.6) – Modelling report on the effect of temperature on clay host rocks behaviour
Dissemination level: PU
Date of issue of this report: 06/06/2024

Page 21

reach convergence or if the correction is larger than in the previous iteration. Convergence criteria are established in terms of forces or flows and state variables. Regarding the boundary conditions of the mechanical problem, forces and displacement rate can be enforced in any spatial direction and at any node. In the hydraulic problem, the mass flow rate of water and dry gas or liquid/gas pressure can be also prescribed at any node. Finally, regarding the thermal problem, heat flow and temperature can be enforced at any node of the mesh. More details on the finite element formulations employed in CODE_BRIGHT can be found in (Olivella et al., 2022, 1995), including the weak forms of the governing equations and the explicit definitions of the resulting matrices and vectors.

EURAD (Deliverable n˚ 7.6) – Modelling report on the effect of temperature on clay host rocks behaviour
Dissemination level: PU
Date of issue of this report: 06/06/2024

Page 22

3.3. COMSOL Multiphysics

COMSOL Multiphysics is a general-purpose finite element software. In this work, the built-in modules, viz. heat transfer in solid, Darcy's law and solid mechanics are used to model the near-field case.

Heat transfer in porous media is described by the following governing equation, where conduction is seen as the predominant mechanism and convection is not needed for the benchmark exercises:

$$(\rho C_p)_{\text{eff}}\frac{\partial T}{\partial t} + \nabla \cdot (-\lambda_{ij}\nabla T) = Q_T$$

where T: temperature in K, ρ_w: density of water in kg m^{-3}, Q_T: heat source in W m^{-3}.

The effective thermal conductivity (λ) and equivalent volumetric heat capacity (($\rho C_p)_{\text{eff}}$) are defined as follows:

$$(\rho C_p)_{\text{eff}} = (1 - \phi)\rho_s c_p + \phi\rho_w C_{p,w}$$
$$\lambda_{ij} = (1 - \phi)\lambda_{ij}^s + \phi\lambda_w$$

where ϕ: porosity, ρ_s: solid density (kg m^{-3}), c_p: heat capacity of solid ($\text{J kg}^{-1}\text{ K}^{-1}$), $C_{p,w}$: specific heat capacity of water ($\text{J kg}^{-1}\text{ K}^{-1}$), λ_{ij}^s: thermal conductivity of solid ($\text{W m}^{-1}\text{ K}^{-1}$), λ_w: thermal conductivity of water ($\text{W m}^{-1}\text{ K}$).

Soil deformation is described by the standard equation of motion, however, expressed in terms of effective stress (σ_{ij}') following Biot poroelasticity:

$$\nabla \cdot \sigma_{ij}' = 0; \ \sigma_{ij}' = \sigma_{ij}^t + \beta_{ij}p_f$$

where σ_{ij}^t: total stress, p_f: excess pore pressure, β_{ij}: components of the Biot coefficient tensor,

Excess pore pressure is defined via:

$$p_f = p_A - p_{ref} \tag{3.1}$$

where p_A: absolute water pressure (Pa), p_{ref}: reference pressure, usually set as equal to atmospheric pressure (0.1 MPa).

The water mass (m_w (kg m^{-3})) balance equation includes additional water source terms to take into account the different coupling processes (HM, TH and TM) and is expressed as follows:

$$\frac{\partial m_w}{\partial t} + \nabla \cdot (\rho_w \mathbf{u}) = Q_{HM} + Q_{TH} + Q_{TM}$$

where Q_{HM}, Q_{TH} and Q_{TM} are water source terms ($\text{kg m}^{-3}\text{ s}^{-1}$), $\mathbf{u}$ is displacement vector.

The groundwater flow in clay medium is described following Darcy's law:

$$q_i = -\frac{k_{ij}}{\mu}\nabla p$$

EURAD (Deliverable n˚ 7.6) – Modelling report on the effect of temperature on clay host rocks behaviour
Dissemination level: PU
Date of issue of this report: 06/06/2024

Page 23

where q_i: Darcy's velocity (m s^{-1}), k_{ij}: intrinsic permeability tensor (m^2), μ: viscosity of water (Pa s, p: porewater pressure (Pa).

The development of the water mass variation as a function of the pressure and temperature leads to the following equation:

$$\frac{\partial m_w}{\partial t} = \rho_w \left(\phi C_w + \frac{(\beta - \phi)}{K_s} \right) \frac{\partial p}{\partial t}$$
$$+ \rho_w \, \beta \frac{de_v}{dt} + \rho_w \left(-\phi \alpha_w \right) \frac{\partial T}{\partial t} + \rho_w \left((1 - \beta)\alpha_{TD} - (1 - \phi)\alpha_s \right) \frac{\partial T}{\partial t}$$

where C_w: water compressibility (Pa^{-1}), α_w: volumetric water thermal expansion coefficient ($^\circ$C^{-1}), α_{TD}: volumetric thermal expansion coefficient of porous medium ($^\circ$C) α_s: volumetric thermal expansion coefficient of solid grains ($^\circ$C^{-1}).

By rearranging the water mass balance equation, the flow governing equation can be expressed as:

$$\rho_w S \frac{\partial p}{\partial t} + \nabla \cdot (\rho_w q_i) = Q_{HM} + Q_{TH} + Q_{TM}$$

where S, the storage coefficient is expressed as:

$$S = \left(\phi C_w + \frac{\beta - \phi}{K_s} \right)$$

with K_s the solid or grain bulk modulus (Pa).

The hydro-mechanical coupling source term (variation of the porosity with the deformation) is defined by:

$$Q_{HM} = -\rho_w \beta \frac{d\varepsilon_v}{dt}$$

where ε_v is the volumetric strain. The thermo-hydraulic coupling source term includes the thermal expansion of the water, which can be written as:

$$Q_{TH} = \rho_w \phi \alpha_w \frac{\partial T}{\partial t}$$

And the thermo-mechanical coupling that considers the thermal expansion of the solid phase is defined by:

$$Q_{TM} = -\rho_w \left[(1 - \beta)\alpha_{TD} - (1 - \phi)\alpha_s \right] \frac{\partial T}{\partial t} = \rho_w \alpha_s (\beta - \phi) \frac{\partial T}{\partial t}$$

Temperature-induced elastic strains are defined as:

$$\varepsilon_{th} = \alpha_T (T - T_0)$$

where α_T is the (secant) linear thermal expansion coefficient of clay and T_0 is the initial temperature in clay.

EURAD (Deliverable n° 7.6) – Modelling report on the effect of temperature on clay host rocks behaviour
Dissemination level: PU
Date of issue of this report: 06/06/2024

Page 24

3.4. FLAC3D

Unlike most codes used in HITEC for benchmark activities that are based on the finite element method, FLAC3D uses the finite difference method with an explicit Lagrangian solution scheme. Implicit time-stepping is optionally available for heat and fluid flow calculations.

The equations describing the fluid-thermal-mechanical response of a porous material to heat transport through conduction within the material in FLAC3D are described below (Itasca, 2019).

The fluid transport is described by Darcy's law:

$$q_i = -k_{il}\,\hat{k}(s)\left[p - \rho_f x_j g_j\right]_{,l}$$

where q_i is the specific discharge vector, p is fluid pore pressure, k is the tensor of absolute mobility coefficients (FLAC3D permeability tensor) of the medium, $\hat{k}(s)$ is the relative mobility coefficient, which is a function of fluid saturation, s, ρ_f is the fluid density, and $g_i, i = 1, 3$ are the three coordinates of the gravity vector.

Heat flow by conduction is described by Fourier's law of heat transport:

$$q_i^T = -\lambda_{ij}^T T_{,j}$$

where q_i^T is the heat flux vector, T is temperature and λ^T is the thermal conductivity tensor. In the FLAC3D formulation, temperature, flux, convective, and adiabatic boundary conditions are all taken into account.

The following equation describes the fluid mass balance for small deformations:

$$-q_{i,i} + q_v = \frac{\partial \zeta}{\partial t}$$

The volumetric fluid source intensity, q_v in s^{-1}, represents the rate at which fluid is added to or removed from the porous material, while ζ represents the change in fluid content due to diffusive mass transport. This concept was first introduced by Biot (1956).

The thermal energy balance is expressed as

$$-q_{i,i}^T + q_v^T = \frac{\partial \zeta^T}{\partial t}$$

where ζ^T is the heat stored per unit volume of porous material, and q_v^T is the volumetric heat source intensity.

The balance of momentum has the form

$$\sigma_{ij,j} + \rho g_i = \rho \frac{dv_i}{dt}$$

where $\rho = \rho_d + \phi s \rho_w$ is the bulk density, and ρ_d and ρ_w are the densities of the dry matrix and the fluid, respectively, ϕ is porosity, and s is saturation. σ_{ij} is the stress tensor, g_i and $\frac{dv_i}{dt}$ are respectively the gravity and acceleration vector at the i-th direction.

EURAD (Deliverable n° 7.6) – Modelling report on the effect of temperature on clay host rocks behaviour
Dissemination level: PU
Date of issue of this report: 06/06/2024

Page 25

The fluid content, or volume of fluid within a porous material, may vary due to changes in factors such as pore pressure p, saturation s, mechanical volumetric strains ϵ and temperature T. This variation can be described using the response equation:

$$\frac{1}{M}\frac{\partial p}{\partial t} + \frac{\phi}{s}\frac{\partial s}{\partial t} = \frac{1}{s}\frac{\partial \zeta}{\partial t} - \beta\frac{\partial \epsilon}{\partial t} + \alpha\frac{\partial T}{\partial t}$$

where M is Biot modulus [N m^{-2}], β is Biot coefficient and α is the undrained thermal coefficient [$^\circ$C^{-1}]. The undrained thermal coefficient takes into account the fluid and grain thermal expansions.

EURAD (Deliverable n˚ 7.6) – Modelling report on the effect of temperature on clay host rocks behaviour
Dissemination level: PU
Date of issue of this report: 06/06/2024

Page 26

3.5. Lagamine

In the previous European projects (BEACON (Gramegna et al., 2022), TIMODAZ (François et al., 2014), etc), Lagamine has shown good performance in predicting the multiphasic coupled behaviour in geomaterials. The modelling activity in HITEC is a good opportunity to test the reliability of the code. The governing equations for the classical porous medium in the saturated case are recalled here, and a weak form is used for the finite element formulation. The balance equations are written in the current deformed configuration denoted Ω^t.

The momentum balance equation of the solid and liquid mixture is obtained by considering the equality between internal and external virtual works:

$$\int_{\Omega^t} \sigma_{ij}^t \frac{\partial u_i^*}{\partial x_j^t} d\Omega^t = \int_{\Omega^t} \rho^t g_i u_i^* d\Omega^t + \int_{\Gamma_\sigma^t} \bar{t}_i^t u_i^* d\Gamma^t$$

where σ_{ij}^t is the Cauchy stress field, $\frac{\partial u_i^*}{\partial x_j^t}$ is the virtual macrodeformation gradient, ρ^t is the density of the porous mixture, g_i is the gravitational acceleration. $\bar{t}_i^t$ is the classical external traction force per unit area, applied on a part of external surface Γ_σ^t of the boundary of Ω^t.

The density of the porous mixture is given by:

$$\rho^t = \rho_s^t(1 - \phi^t) + \rho_w^t \phi^t$$

where ρ_s^t and ρ_w^t are the density of the solid and fluid phases respectively, ϕ^t is the porosity.

The effective stress is defined using Biot poroelasticity theory:

$$\sigma_{ij}'^t = \sigma_{ij}^t + \beta_{ij} p_w^t$$

where β_{ij} is Biot coefficient tensor.

The fluid mass balance equation is expressed in a weak form for any admissible virtual pore pressure field p_w^*:

$$\int_{\Omega^t} \left(\dot{M}_w^t p_w^* - f_{w,i}^t \frac{\partial p_w^*}{\partial x_i^t} \right) d\Omega^t = \int_{\Omega^t} Q_w^t p_w^* d\Omega^t - \int_{\Gamma_{q_w}^t} \bar{q}_w^t p_w^* d\Gamma^t$$

where $f_{w,i}^t$ is the mass flow, Q_w^t is a fluid sink term and $\Gamma_{q_w}^t$ is the part of the boundary where the input fluid mass per unit area $\bar{q}_w^t$ is prescribed. The time derivative of fluid mass $\dot{M}_w^t$ is defined as:

$$\dot{M}_w^t = \rho_w^t \left[(\frac{\dot{p}_w^t}{\chi_w} - \alpha_w \dot{T}^t)\phi^t + \frac{\dot{p}_w^t}{K_s}(b - \phi^t) + b\frac{\dot{\Omega}^t}{\Omega^t} \right]$$

where χ_w is the fluid bulk modulus, K_s is the bulk modulus of the solid grains, and α_w is the thermal expansion coefficient of fluid which is dependent on the temperature evolution. According to (Kell, 1975), the thermal expansion coefficient of fluid is computed by the derivative of water density with respect to temperature.

EURAD (Deliverable n° 7.6) – Modelling report on the effect of temperature on clay host rocks behaviour
Dissemination level: PU
Date of issue of this report: 06/06/2024

Page 27

The fluid flow is defined by Darcy's law:

$$f_{w,i} = -\rho_w^t \frac{k_{ij}}{\mu_w} \left(\frac{\partial p_w^t}{\partial x_j^t} + \rho_w^t g_j \right)$$

where the k_{ij} is the intrinsic permeability tensor. μ_w is the water viscosity depending on the temperature evolution (Rumble, 2019).

The energy balance equation is derived in a weak form for any allowed virtual temperature field T^*:

$$\int_{\Omega^t} \left(\dot{S}_T^t T^* - f_{T,i}^t \frac{\partial T^*}{\partial x_i^t} \right) d\Omega^t = \int_{\Omega^t} Q_T^t T^* d\Omega^t - \int_{\Gamma_{q_T}^t} \bar{q}_T^t T^* d\Gamma^t$$

where $\dot{S}_T^t$ is the enthalpy evolution of the porous medium, $f_{T,i}^t$ is the heat flow, Q_T^t is a heat sink term and $\Gamma_{q_T}^t$ is the part of the boundary where the input heat flux per unit area $\bar{q}_T^t$ is prescribed.

The enthalpy of the porous mixture is characterised by the sum of the enthalpy of each phase:

$$S_T^t = \left[\phi^t \rho_w^t c_{p,w} + (1 - \phi^t) \rho_s^t c_{p,s} \right] (T^t - T_0)$$

where $c_{p,w}$ and $c_{p,s}$ are the specific heat of the fluid and solid phases respectively, T_0 is the initial temperature in the reference configuration.

The heat flow is presented by thermal conduction and convection:

$$f_{T,i} = -\lambda_{ij}^t \frac{\partial T^t}{\partial x_j^t} + c_{p,w} f_{w,i} (T^t - T_0)$$

where λ_{ij}^t is the thermal conductivity tensor for the mixture.

The large strains and large rotation effects are taken into account under the framework of Lagrange actualised formulation (Collin et al., 2002), therefore the solid convection effect is implicitly considered in the Lagamine code.

EURAD (Deliverable n˚ 7.6) – Modelling report on the effect of temperature on clay host rocks behaviour
Dissemination level: PU
Date of issue of this report: 06/06/2024

Page 28

3.6. OpenGeoSys

Two process models in OpenGeoSys have been used in the scope of this benchmarking initiative:

- a non-isothermal Richards flow model coupled with mechanics.

- a TH model with thermo-mechanical storage coefficients Buchwald et al. (2021)

3.6.1. Non-isothermal Richards flow model coupled with mechanics

The first model assumes a monolithic approach, in which the process couplings between the hydraulic and mechanical models are derived from the three-dimensional approach of effective stresses. We neglect the effects of vapour diffusion in the description due to the present benchmark assumptions. The governing equations for this model are described as follows:

The energy balance equation is given by

$$(\rho c_p)^{\text{eff}} \dot{T} - \left(\lambda_{ij}^{\text{T}} T_{,j} \right)_{,i} + \rho^{\text{l}} c_p^{\text{l}} T_{,i} v_i^{\text{l}} = Q_T$$

with T the temperature, $(\rho c_p)^{\text{eff}}$ the effective volumetric heat capacity, λ_{ij}^{T} the effective thermal conductivity, ρ^{l} the density of liquid, c_p^{l} the specific heat capacity of liquid, v_i^{l} the Darcy velocity, and Q_T the point heat source. The effective volumetric heat can be considered as a composite of the contributions of the solid phase and the liquid phase as

$$(\rho c_p)^{\text{eff}} = (1 - \phi)\rho^{\text{s}} c_p^{\text{s}} + S^{\text{l}} \phi \rho^{\text{l}} c_p^{\text{l}}$$

with ϕ the porosity, S^{l} the liquid saturation, ρ^{s} the solid density, and c_p^{s} the specific heat capacity of solid. Similarly, the effective thermal conductivity is given by

$$\lambda_{ij}^{\text{T}} = (1 - \phi)\lambda_{sij}^{T} + S^{\text{l}} \phi \lambda_{\text{l}}^{T} \delta_{ij}$$

where λ_{sij}^{T} is the thermal conductivity tensor of solid, $\lambda_{\text{l}}^{\text{T}}$ is the thermal conductivity of liquid.

The mass balance equation is given by

$$\left(S^{\text{l}}\Omega - \phi \frac{\partial S}{\partial p_c} \right) \rho^{\text{l}}\dot{p} - S \left(-\frac{\partial \rho^{\text{l}}}{\partial T} + 3\rho^{\text{l}}(\beta - \phi)\alpha_{\text{T}}^{\text{s}} \right) \dot{T}$$
$$+ \left(\rho^{\text{l}} v_i^{\text{l}} \right)_{,i} + S\beta\rho^{\text{l}}\dot{u}_{i,i} = Q_H$$

where p is the pore pressure, p_c is the capillary pressure, which is $-p$ under the single phase assumption. Ω is a composite coefficient of the liquid compressibility and solid compressibility, β is the Biot's constant, $\alpha_{\text{T}}^{\text{s}}$ is the linear thermal expansivity of solid, Q_H is the point source of sink term, u_i is the displacement. The liquid velocity v_i^{l} is the described by the Darcy's law as

$$v_i^{\text{l}} = -\frac{k_{ij}k_{\text{rel}}}{\mu}(p_{,j} - \rho^{\text{l}}g_j)$$

EURAD (Deliverable n˚ 7.6) – Modelling report on the effect of temperature on clay host rocks behaviour
Dissemination level: PU
Date of issue of this report: 06/06/2024

Page 29

with k_{ij} the intrinsic permeability, k_{rel} the relative permeability, g_j the gravitational acceleration and μ the liquid viscosity coefficient.

The momentum balance equation takes the form of

$$(\sigma'_{ij} - b(S)\beta p^l \delta_{ij})_{,j} + f_i = \mathbf{0}$$

with σ' the effective stress tensor, $b(S)$ the Bishop model, f_i the body force, and δ the Kronecker delta. The primary unknowns of the momentum balance equation are the displacement u_i, which is associated with the stress by the generalized Hook's law as

$$\dot{\sigma}'_{ij} = c_{ijkl}\dot{\epsilon}^e_{ij} = c_{ijkl}\left(\dot{\epsilon}_{ij} - \dot{\epsilon}_{ij}{}^T - \dot{\epsilon}_{ij}{}^{vp} - \dot{\epsilon}_{ij}{}^{sw}\right)$$

c_{ijkl} is the fourth-order stiffness tensor, $\dot{\epsilon}_{ij}$ the total strain rate, $\dot{\epsilon}^e_{ij}$ the elastic strain rate, $\dot{\epsilon}^T_{ij}$ the thermal strain rate, $\dot{\epsilon}^{vp}_{ij}$ the visco-plastic strain rate, $\dot{\epsilon}^{sw}_{ij}$ the swelling strain rate.

The strain tensor is given as the symmetric part of the displacement gradient, $\epsilon = \frac{1}{2}\left(u_{i,j} + u_{j,i}\right)$.

More details on THM formulations in OGS can be found in Chaudhry et al. (2019); Grunwald et al. (2022).

3.6.2. TH model with thermo-mechanical storage coefficients

The second model implicitly considers the mechanical behaviour in the mass balance equation of the thermo-hydraulic process by means of simplifying assumptions using thermo-mechanical storage coefficients. The model assumes uniaxial strain conditions ($\epsilon_{xx} = \epsilon_{yy} = 0$) and constant vertical normal stress σ_{zz}. It takes also thermal stresses into account, originating from the constrained thermal expansion in the transverse directions:

$$\dot{u}_{i,i} := \dot{u}_{z,z} \,,$$
$$\dot{\sigma}_{zz} := 0 = \dot{\sigma}'_{zz} - \beta\dot{p} = \underbrace{(\lambda + 2G)}_{E^S_s}\left(\dot{u}_{i,i} - \alpha^S_T\dot{T}\right) - 2\alpha^S_T\lambda\dot{T} - \beta\dot{p} \,,$$

with the uniaxial aggregate modulus E^S_s. We obtain a simplified expression for the mass balance:

$$\dot{u}_{z,z} = \frac{\beta}{E^S_s}\dot{p} + \alpha^S_T\left(1 + 2\frac{\lambda}{E^S_s}\right)\dot{T} \,,$$
$$0 = \left(S_{THM} + \frac{\beta^2}{E^S_s}\right)\dot{p} - \left[\alpha^{eff}_T - \beta\alpha^S_T\left(1 + 2\frac{\lambda}{E^S_s}\right)\right]\dot{T} + (w_L)_{i,i} \,,$$
$$E^S_s = \frac{E(1-\nu)}{(1+\nu)(1-2\nu)} \,, \quad \lambda = \frac{E\nu}{(1+\nu)(1-2\nu)} \,,$$
$$0 = \left(S_{THM} + \frac{\beta^2}{E^S_s}\right)\dot{p} - \left[\alpha^{eff}_T - \beta\alpha^S_T\frac{1+\nu}{1-\nu}\right]\dot{T} + (w_L)_{i,i} \,.$$

λ and μ are the Lamé elastic parameters. G is the shear modulus. S is the THM storage term. (w_L) is the fluid velocity vector.

One refers to Buchwald et al. (2021) for further elaborations of the balance equations as well as the extension to orthotropic materials can be found in Buchwald et al. (2021).

EURAD (Deliverable n˚ 7.6) – Modelling report on the effect of temperature on clay host rocks behaviour
Dissemination level: PU
Date of issue of this report: 06/06/2024

Page 30

4. Constitutive model development

4.1. ANDRA

As part of an ongoing scientific collaboration with Andra to develop advanced constitutive models for the Cox claystone behaviour, Ineris developed a regularized anisotropic elastoplastic and damage model including both non-linear short- and long-term responses (Souley et al., 2023b). The influence of damage and fracturing on the transport and viscous properties is also considered. The proposed model was implemented with a regularization scheme based on the non-local implicit gradient in COMSOL Multiphysics®. This model was further developed to take into account the small decrease in strength observed in the subtask 2.1 and 2.2 short-term compression tests performed by ULorraine (Gbewade et al. (2023) and D7.5 deliverable)

4.1.1. Main characteristics of the model

The constitutive model is expressed in terms of the three stress invariants (p,q,θ), where the stresses geometry is defined by the Lode angle θ. The following features are considered:

- Elasticity: linear anisotropic

- Plasticity: anisotropic strain hardening/softening (γ, plastic distorsion) with tensile cut-off

- Plastic yield and potential functions: based on Hoek and Brown criterion and a non-associated flow rule (Drucker-Prager)

- Residual strength and stage (perfectly plastic): bilinear Mohr-Coulomb criterion

- Transition from brittle to ductile behaviour as the confining pressure increases

In addition, several laboratory tests performed on Cox samples show a slight strength anisotropy, the lowest compressive strength is measured on samples oriented at about 30-45° to the bedding plane while the maximum strengths are reached in the directions parallel and perpendicular to bedding. The strength anisotropy is introduced using the microstructure tensor (Pietruszczak et al., 2002) for the strength parameters **p** (initiation, peak and residual):

$$p_{ani} = p_0 \left(1 + A_{ij}l_il_j + a_1(A_{ij}l_il_j)^2 + a_2(A_{ij}l_il_j) \right)^3 \tag{4.1}$$

with a_1 and a_2 : anisotropic parameters related to the material microstructure, the anisotropy parameter $A_{ij}l_il_j$ represents the projection of the microstructure tensor on the loading direction.

The damage occurring in post-peak before the residual stage is assumed to be isotropic and based on the continuum damage mechanics. The damage criterion f_d (Mazars 1986) is defined by the conjugate thermodynamic force Y_d:

$$f_d(Y_d, d) = d_{res}\{1 - exp[-B_d(Y_d - Y_0)]\} - d \leq 0 \tag{4.2}$$

with Y_d the extensional strain: $Y_d = \sqrt{\langle\epsilon\rangle : \langle\epsilon\rangle}$

An associated flow rule is assumed

$$\dot{d} = \dot{\lambda}_d \frac{\partial f_d}{\partial Y_d} \tag{4.3}$$

The transition from brittle behaviour under low confining pressure (σ_3) to ductile failure with the increase of σ_3 is given through $\mathbf{B_d}$

$$B_d = \begin{cases} B_{d0}\left(\frac{\sigma_3^{bd} - |\sigma_3|}{\sigma_3^{bd}}\right), & \text{if } |\sigma_3| < \sigma_3^{bd} \\ 0, & \text{if } |\sigma_3| \geq \sigma_3^{bd} \end{cases} \tag{4.4}$$

$$\tag{4.5}$$

The other key characteristic of the Cox claystone is its long-term behaviour (creep deformations, Armand et al. (2017)). The time-dependent strains are based on laboratory tests and observations in the underground laboratory:

- $\epsilon^{\mathbf{vp}}$ increases non linearly with the deviatoric stress $\mathbf{q}$

- $\dot{\epsilon}^{\mathbf{vp}}$ varies non linearly with $\epsilon^{\mathbf{vp}}$

- Temperature $\mathbf{T}$ impacts $\epsilon^{\mathbf{vp}}$

- Finally, the Lemaitre creep model correctly reproduces the deferred behavior of the Cox claystone

$$\frac{\partial \underline{\underline{\epsilon}}^{vp}}{\partial t} = A(d, T) \left\langle \frac{q - q_0}{\sigma_{ref}} \right\rangle^n (\epsilon^{vp})^m \frac{3\underline{\underline{s}}}{2q} \tag{4.6}$$

with $\mathbf{A}$ the viscosity, $\mathbf{q_0}$ the creep threshold, σ_0 the reference stress, $\mathbf{n}$ the deviatoric stress exponent and $\mathbf{m}$ the exponent of hardening work

The variations of permeability and creep strain induced by damage and shear failure are based on laboratory and in-situ observations around the MHM URL drifts. The damage rate d_{rat}^* (d/d_{res}, with d_{res} the maximum damage, reached at the beginning of the residual phase) and the fracturing rate γ_{sf}^* related to shear failure are introduced:

- permeability:

$$\underline{\underline{k}} = \underline{\underline{k}} h_d(d^*) h_{sf}(\gamma_{sf}^*) \tag{4.7}$$

- creep strain (viscosity and hardening exponent change) based on Souley et al. (2017):

$$\mathbf{A} = f(A_0, A_1); \mathbf{m} = f(m_0, m_1) \tag{4.8}$$

where (A_0, m_0) refer to the intact material, (A_1, m_1) to the damaged material.

The model was implemented with a regularization scheme based on the non-local implicit gradient in Comsol for both damage and equivalent shear plastic strain.

EURAD (Deliverable n˚ 7.6) – Modelling report on the effect of temperature on clay host rocks behaviour
Dissemination level: PU
Date of issue of this report: 06/06/2024

Page 32

4.1.2. Validation and applications

The model was validated by simulating several triaxial compression tests at σ_3 = 2MPa with different loading direction compared to bedding and some creep tests at different deviatoric stresses. As shown on Figure 4.1 and Figure 4.2, the simulation compared successfully to theoretical curves.

(a)   (b)
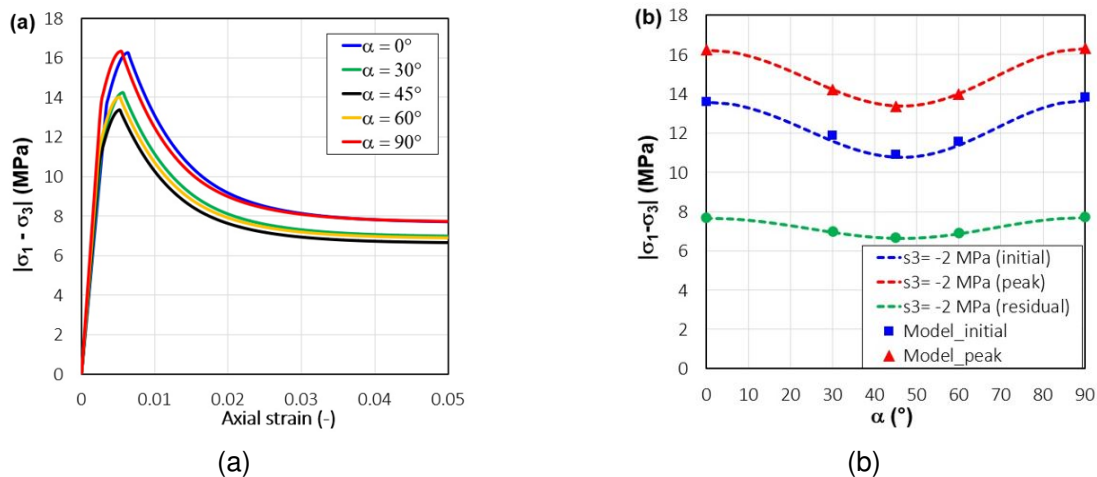
Figure 4.1: Triaxial tests: effect of load direction with respect to bedding
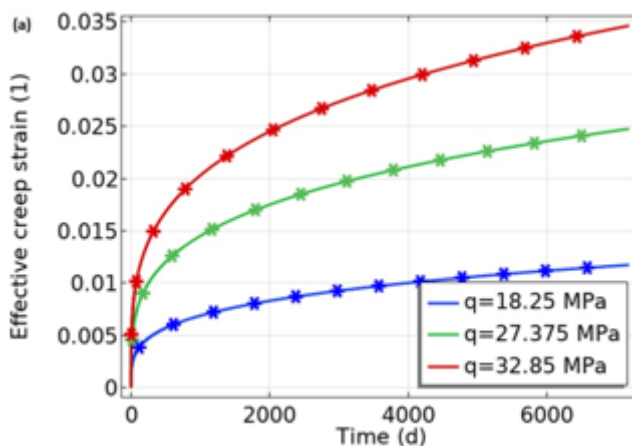
Figure 4.2: Triaxial creep test at Pc=12 MPa: theoretical (cont.) vs. numerical (star)

This model was then tested successfully by modelling the convergence around a drift drilled in the direction of the maximum horizontal stress in the MHM URL (Souley et al., 2023a). The second application on the last case of the near-field benchmark is developed in 5.1.4.1.

EURAD (Deliverable n° 7.6) – Modelling report on the effect of temperature on clay host rocks behaviour
Dissemination level: PU
Date of issue of this report: 06/06/2024

Page 33

4.2. BGE

BGE initiated a collaborative research project alongside EURAD, aimed at supporting its efforts within the HITEC project. The project consisted of developing and implementing a new material model for claystone which incorporates its mechanical, thermal, and hydraulic behaviour. Together with the Institute of Engineering UNAM (IINGEN), the implementation of the constitutive model developed by Mánica (2018) within the open-source computer code OpenGeoSys (OGS) has been carried out. The model incorporates a number of characteristic features of indurated clayey materials including mechanical anisotropy and time-dependent deformations. The model also accounts for the objective simulation of localised deformations through a nonlocal regularisation. The final objective is the simulation of the thermo-hydro-mechanical behaviour of stiff argillaceous formations in the context of deep geological disposal of nuclear waste within the OGS modelling platform.

The implementation of the model into OGS is performed through MFront, which is an open-source code generator that simplifies the development of material models, particularly by handling the algorithm for the integration of the constitutive equations and allowing to write those equations in a form very close to the actual mathematical description of the model.

The implementation of the model was divided into three tasks to be executed by IINGEN; a brief summary of each task is given below:

- **Task 1.** This task involves the implementation of the local version of the model, i.e. without the nonlocal regularisation.

- **Task 2.** The model originally assumes isothermal conditions and does not include any dependence of the stiffness and strength with temperature. Therefore, this task involves the incorporation of thermal effects in the local version of the model according to recent approaches in the literature.

- **Task 3.** Finally, this task involves the incorporation of the nonlocal regularisation for the objective simulation of localised deformations.

The material model to be implemented to characterise the mechanical, thermal, and hydraulic behaviour of claystone was developed by Mánica (2018). It falls within the frameworks of the elasto-viscoplasticity theory (Perzyna, 1966) and the plasticity-creep partition approach (Chaboche, 2008), and it incorporates a number of features that are considered relevant for the satisfactory description of indurated clays such as:

- a nonlinear yield criterion,
- strength and stiffness anisotropy,
- a non-associated flow rule,
- rate-dependency,
- strain hardening/softening,
- nonlocal regularisation,
- creep deformations, and
- permeability increase with damage (plastic strains).

The model has been described in detail in a number of publications (Mánica, 2018; Mánica et al., 2018, 2020, 2022a,b). Mánica et al. (2022a) showed its ability to reproduce the hydromechanical response

EURAD (Deliverable n˚ 7.6) – Modelling report on the effect of temperature on clay host rocks behaviour
Dissemination level: PU
Date of issue of this report: 06/06/2024

Page 34

of underground excavations in the Meuse/Haute-Marne Underground Research Laboratory, in France, excavated in the Callovo-Oxfordian argillite (Cox). A description of the complete mechanism underlying the observed overpressures around the excavation was provided by including the relevant behavioural features of the Cox claystone.

A summary of the constitutive equations is given in Table 4.1. As already mentioned above, this version of the model assumes isothermal conditions and does not include any dependence of the stiffness and strength with temperature. The summary in Table 4.1 also includes the adopted nonlocal regularisation technique and the evolution law of permeability with the accumulation of plastic strains.

EURAD (Deliverable n˚ 7.6) – Modelling report on the effect of temperature on clay host rocks behaviour
Dissemination level: PU
Date of issue of this report: 06/06/2024

Page 35

Table 4.1: Material model for the behaviour of claystone (Mánica, 2018).

Description	Equation	Parameters
Strain decomposition	$\mathrm{d}\boldsymbol{\epsilon} = \mathrm{d}\boldsymbol{\epsilon}^{\mathrm{e}} + \mathrm{d}\boldsymbol{\epsilon}^{\mathrm{vp}} + \mathrm{d}\boldsymbol{\epsilon}^{\mathrm{c}}$	-
Elastic behaviour	$\mathrm{d}\boldsymbol{\sigma} = \hat{\mathbf{D}}^{\mathrm{e}}\,\mathrm{d}\boldsymbol{\epsilon}^{\mathrm{e}}$ $\hat{\mathbf{D}}^{\mathrm{e}} = \mathbf{T}^{\mathrm{T}}\mathbf{D}^{\mathrm{e}}\mathbf{T}$	E_1, E_2, G_2, ν_1, ν_2, α^{rot}, β^{rot}
Yield criterion	$F = \sqrt{\frac{J_2}{f_{\mathrm{d}}(\theta)} + (c^* + p_t \tan\phi^*)^2} - (c^* + p' \tan\phi^*)$ $f_{\mathrm{d}}(\theta) = \alpha_{\mathrm{d}}(1 + B_{\mathrm{d}}\sin 3\theta)^{n_{\mathrm{d}}}$	α_{d}
Strength anisotropy	$c^* = \Omega(\delta)c_0^*$ $p_t = \Omega(\delta)p_{t0}$ $\Omega = \frac{Ae^{(\delta_{\mathrm{m}}-\delta)n}}{[1+e^{(\delta_{\mathrm{m}}-\delta)n}]^2} + \frac{B}{1+e^{(\delta_{\mathrm{m}}-\delta)n}} + C$ $A = \frac{2(e_1+1)(e_2+1)(e_1-e_2+\Omega_{90}+e_1 e_2+e_1\Omega_{90}-e_2\Omega_{90}-2e_1\Omega_{\mathrm{m}}+2e_2\Omega_{\mathrm{m}}-e_1 e_2\Omega_{90}-1)}{(e_1-e_2)(e_1-1)(e_2-1)}$ $B = \dfrac{\Omega_{90}-\dfrac{Ae_1}{(e_1+1)^2}+\dfrac{Ae_2}{(e_2+1)^2}-1}{\dfrac{1}{e_1+1}-\dfrac{1}{e_2+1}}$ $C = 1 - \frac{Ae_2}{(e_2+1)^2} - \frac{B}{e_2+1}$ $e_1 = e^{n(\delta_{\mathrm{m}}-90)}$ $e_2 = e^{n\delta_{\mathrm{m}}}$	Ω_{90}, Ω_{m}, δ_{m}, n
Hardening law	$\tan\phi^* = \tan\phi_{\mathrm{ini}}^* + \dfrac{\epsilon_{\mathrm{eq}}^{\mathrm{p}}}{a_{\mathrm{hard}} + \epsilon_{\mathrm{eq}}^{\mathrm{p}}\left(\frac{\xi}{\tan\phi_{\mathrm{peak}}^*-\tan\phi_{\mathrm{ini}}^*}-a_{\mathrm{hard}}\right)}$	ϕ_{ini}^*, ϕ_{peak}^*, ξ, a_{hard}
Softening laws	$\tan\phi^* = \tan\phi_{\mathrm{peak}}^* - \left(\tan\phi_{\mathrm{peak}}^* - \tan\phi_{\mathrm{res}}^*\right)\left[1 - e^{-b_{\mathrm{res}}(\epsilon_{\mathrm{eq}}^{\mathrm{P}}-\xi)}\right]$ $c_0^* = \left(c_{0\,\mathrm{peak}}^* - c_{0\,\mathrm{post}}^*\right)e^{-b_{\mathrm{post}}(\epsilon_{\mathrm{eq}}^{\mathrm{P}}-\xi)} + c_{0\,\mathrm{post}}^* e^{-b_{\mathrm{res}}(\epsilon_{\mathrm{eq}}^{\mathrm{P}}-\xi)}$ $p_{t0} = \left(p_{t0\,\mathrm{peak}} - p_{t0\,\mathrm{post}}\right)e^{-b_{\mathrm{post}}(\epsilon_{\mathrm{eq}}^{\mathrm{P}}-\xi)} + p_{t0\,\mathrm{post}}e^{-b_{\mathrm{res}}(\epsilon_{\mathrm{eq}}^{\mathrm{P}}-\xi)}$ $\epsilon_{\mathrm{eq}}^{\mathrm{p}} = (\boldsymbol{\epsilon}^{\mathrm{P}} : \boldsymbol{\epsilon}^{\mathrm{P}})^{1/2}$ $\boldsymbol{\epsilon}^{\mathrm{P}} = \boldsymbol{\epsilon}^{\mathrm{vp}} + \boldsymbol{\epsilon}^{\mathrm{c}}$ $r_{\mathrm{post}} = \frac{c_{0\,\mathrm{post}}^*}{c_{0\,\mathrm{peak}}^*} = \frac{p_{t0\,\mathrm{post}}}{p_{t0\,\mathrm{peak}}}$	ϕ_{res}^*, $c_{0\,\mathrm{peak}}^*$, $p_{t\,\mathrm{peak}}$, r_{post}, b_{post}, b_{res}
Plastic potential	$\frac{\partial G}{\partial \boldsymbol{\sigma}'} = \Omega\frac{\partial F}{\partial p}\frac{\partial p}{\partial \boldsymbol{\sigma}'} + \frac{\partial F}{\partial J_2}\frac{\partial J_2}{\partial \boldsymbol{\sigma}'} + \frac{\partial F}{\partial \theta}\frac{\partial \theta}{\partial \boldsymbol{\sigma}'}$	Ω
Visco-plasticity	$\mathrm{d}\boldsymbol{\epsilon}^{\mathrm{vp}} = \frac{\langle\Phi(F)\rangle}{\eta}\frac{\partial G}{\partial \boldsymbol{\sigma}'}\,\mathrm{dt}$ $\Phi(F) = \left(\frac{F}{p_{\mathrm{atm}}}\right)^N$	N, η
Creep deformations	$\mathrm{d}\boldsymbol{\epsilon}^{\mathrm{c}} = \dot{\boldsymbol{\epsilon}}^{\mathrm{c}}\mathrm{dt}$ $\dot{\boldsymbol{\epsilon}}^{\mathrm{c}} = \begin{cases} \mathbf{0} & \text{if } \epsilon_{\mathrm{eq}}^{\mathrm{p}} \leq \epsilon_{\mathrm{thr}} \\ \gamma e^{(-m\epsilon_{\mathrm{eq}}^{\mathrm{c}})}\left(\mathbf{s} + \mu p'\mathbf{I}\right) & \text{if } \epsilon_{\mathrm{eq}}^{\mathrm{p}} > \epsilon_{\mathrm{thr}} \end{cases}$ $\epsilon_{\mathrm{eq}}^{\mathrm{c}} = (\boldsymbol{\epsilon}^{\mathrm{c}} : \boldsymbol{\epsilon}^{\mathrm{c}})^{1/2}$	γ, μ, m, ϵ_{thr}
Nonlocal regularisation	$\bar{\epsilon}_{\mathrm{eq}}^{\mathrm{p}}(\mathbf{x}) = \int_V w(\mathbf{x},\boldsymbol{\xi})\,\epsilon_{\mathrm{eq}}^{\mathrm{p}}(\boldsymbol{\xi})\,\mathrm{d}\boldsymbol{\xi}$ $w(\mathbf{x},\boldsymbol{\xi}) = \frac{w_0(\|\mathbf{x}-\boldsymbol{\xi}\|)}{\int_V w_0(\|\mathbf{x}-\boldsymbol{\zeta}\|)\mathrm{d}\boldsymbol{\zeta}}$ $w_0 = \frac{\|\mathbf{x}-\boldsymbol{\xi}\|}{l_{\mathrm{s}}}e^{-\left(\frac{\|\mathbf{x}-\boldsymbol{\xi}\|}{l_{\mathrm{s}}}\right)^2}$	l_{s}
Hydro-mechanical coupling	$\boldsymbol{\sigma}' = \boldsymbol{\sigma} + S_{\mathrm{e}}s\mathbf{B}\mathbf{I}$ $S_{\mathrm{e}} = \frac{S_{\mathrm{l}}-S_{\mathrm{lr}}}{S_{\mathrm{ls}}-S_{\mathrm{lr}}} = \left[1 + \left(\frac{s}{P}\right)^{\frac{1}{1-\lambda}}\right]^{-\lambda}$ $\mathbf{K} = \frac{\mathbf{k}k_{\mathrm{r}}}{\mu_{\mathrm{w}}}$ $k_{\mathrm{r}} = S_{\mathrm{e}}^{\frac{1}{2}}\left[1 - \left(1 - S_{\mathrm{e}}^{\frac{1}{\lambda}}\right)^{\lambda}\right]^2$ $\mathbf{k} = \mathbf{k}_0\left[1 + \beta\left(\epsilon_{\mathrm{eq}}^{\mathrm{p}}\right)^3\right]$	B, λ, P, β, k_{h}, k_{v}

EURAD (Deliverable n˚ 7.6) – Modelling report on the effect of temperature on clay host rocks behaviour
Dissemination level: PU
Date of issue of this report: 06/06/2024

Page 36

4.2.1. Task 1: Implementation and validation of the local version of the model in MFront

The implementation of the model was carried out using the numerical tool MFront. MFront is a code generator that translates a set of closely related domain-specific languages into plain C++. Those languages cover three kinds of material knowledge: (1) material properties, (2) mechanical behaviours and (3) simple point-wise models. For the implementation of the model summarised in Table 4.1, we refer here to the mechanical behaviour kind. The latter supplies the infrastructure for the integration of the constitutive equations of the model. Particularly, it provides several general-purpose domain-specific languages for the implementation. Here, we used the `Implicit` domain-specific language, which allows the user to perform the integration using an implicit scheme (Helfer et al., 2020). The communication between the generated C++ code by MFront and the finite element code OGS is provided by the `MFrontGenericInterfaceSupport` project (Helfer et al., 2020), which facilitates cross-software integration. OGS is already capable of recognising the interface as an available material model (Nagel et al., 2019).

An important part of the work is the validation of the implementation. Special attention was paid to this aspect and a number of simulations were performed for testing. Due to the modular character of the material model, many of its features were assessed independently. These features were verified through numerical simulations, using the implemented model, and compared to theoretical values or to the original implementation in the finite element code Plaxis.

Simulations were performed with the MTest tool, which allows the description of a single material point for a model implemented in MFront. This is particularly useful since the MTest tool can be manipulated with `python` code. Therefore, performed simulations were organised into `jupyter notebooks`. Since Plaxis has a similar tool to MTest (SoilTest) (Bentley Systems, 2020), which can also be manipulated with `python` code, a direct comparison between the legacy and the new implementation was possible for different simulation cases. A description of the simulations performed, contained in the `jupyter notebooks`, is given below. Many of the parameters adopted in the validation examples correspond to those in Mánica et al. (2022a).

For the sake of brevity only three verification examples will be illustrated in this report. The first example consists of verifying the non-linear hardening/softening law. A strain-controlled triaxial test was performed with parameters selected to obtain a non-linear pre-peak hardening and post-peak softening behaviour. Results were compared with the original implementation in Plaxis. They are shown in Figure 4.3, where an excellent agreement between both implementations can be noticed.

EURAD (Deliverable n˚ 7.6) – Modelling report on the effect of temperature on clay host rocks behaviour
Dissemination level: PU
Date of issue of this report: 06/06/2024

Page 37
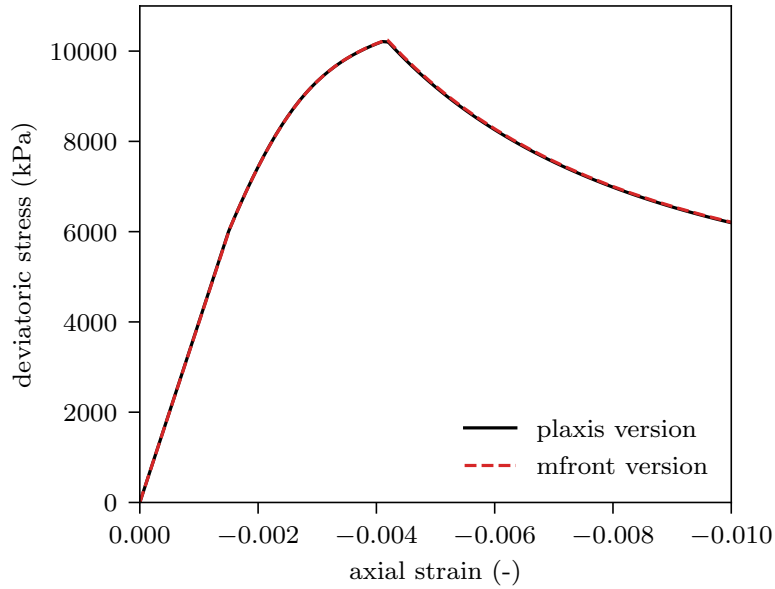
Figure 4.3: Verification of the non-linear hardening/softening law.

The second verification example involves simulations aiming at verifying the non-associated flow rule. The same strain-controlled triaxial test in Figure 4.3 was repeated, but with different values of the non-associativity constant ω. Results were compared with the original implementation in Plaxis. They are shown in Figure 4.4, where an excellent agreement between both implementations can be noticed.
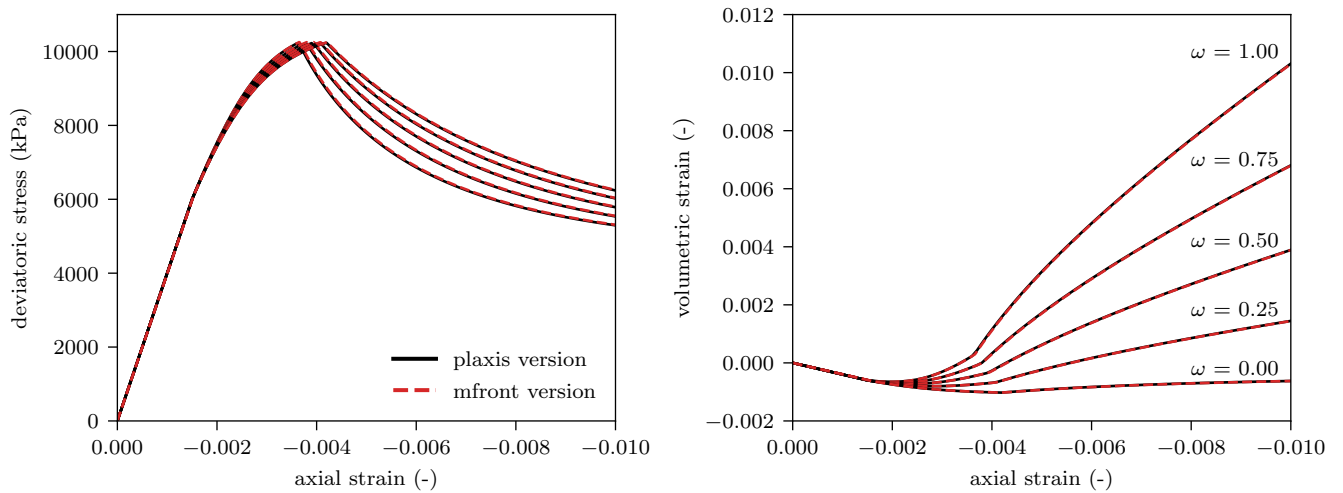
Figure 4.4: Verification of the non-associated flow rule.

The last verification example aims at verifying viscous effects incorporated through the overstress theory of Perzyna (1966). The same strain-controlled triaxial tests of Figure 4.3 was repeated, but considering the viscous parameters N and η (see Table 4.1) and three different strain rates. Results were compared with the original implementation in Plaxis. They are shown in Figure 4.5, where it can be noticed how the apparent peak strength increases by increasing the applied strain rate. An excellent agreement between both implementations can be noticed.

EURAD (Deliverable n˚ 7.6) – Modelling report on the effect of temperature on clay host rocks behaviour
Dissemination level: PU
Date of issue of this report: 06/06/2024

Page 38
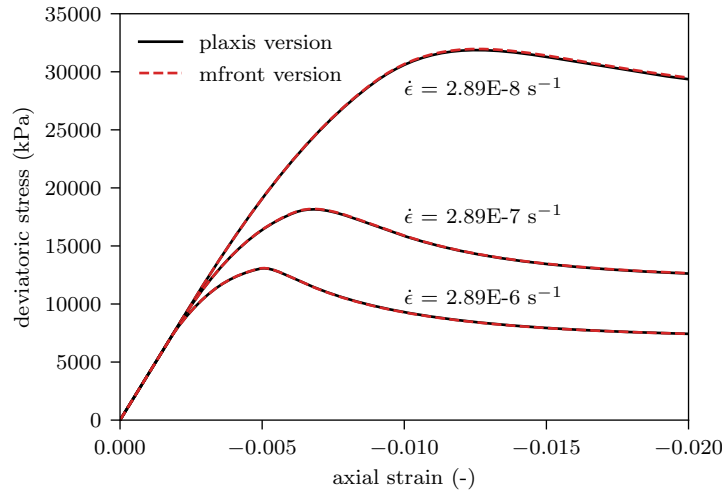
Figure 4.5: Verification of viscous effects.

4.2.2. Task 2: Incorporation of thermal effects in the local version of the model

4.2.2.1. Volumetric yield function

The two main features for the incorporation of thermal effects into the constitutive model being implemented are the thermal expansion of the solid and liquid phases and the dependence of the yield surface with temperature. However, the former is already integrated into the balance equations of the adopted coupled THM formulation, i.e. in the finite element code OGS. Therefore, thermal effects are accounted for only by a dependence of the yield function with temperature. However, so far the implemented model only considers a deviatoric yielding mechanism, characterised by a hyperbolic approximation of the Mohr-Coulomb criterion (see Ovando and Mánica, 2021). Dependence of temperature into this yield function would allow us to reproduce the observed decrease of strength with temperature. Although the latter might be the most relevant characteristic in the context of the behaviour of underground excavations subjected to thermal loading (Tourchi et al., 2023), it would not allow us to reproduce thermal phenomena associated with the volumetric yielding mechanism, such as the elastic expansion-plastic compression transition. Therefore, an additional volumetric yield function was incorporated into the constitutive model within the framework of multi-surface plasticity. The latter is achieved through the generalisation of its components, such as the elastic domain, the yield function, the definition of plastic strains and the loading/unloading conditions in the following way:

$$\mathcal{E} = \left\{ \boldsymbol{\sigma} \mid F_i\left(\boldsymbol{\sigma}, \ \boldsymbol{\alpha}_i\right) < 0, \ i = 1, ..., n \right\} \tag{4.9}$$

$$F_i\left(\boldsymbol{\sigma}, \boldsymbol{\alpha}_i\right) = 0 \tag{4.10}$$

$$\Delta \epsilon^{\mathrm{p}} = \sum_{i=1}^{n} \Delta \lambda_i \frac{\partial g_i}{\partial \boldsymbol{\sigma}} \tag{4.11}$$

$$F_i \leq 0, \quad \Delta \lambda_i \geq 0, \quad F_i \Delta \lambda_i = 0 \tag{4.12}$$

where $\mathcal{E}$ is the elastic domain, $\boldsymbol{\sigma}$ is the effective stress tensor, F is the yield surface, $\boldsymbol{\alpha}$ is the vector of state variables, ϵ^{p} is the plastic strain tensor, λ is the plastic multiplier, g is the plastic potential function, i refers to a given yield surface, and n is the total number of surfaces adopted (see further details in de Souza Neto et al., 2008; Simo et al., 1988).

Of course, integration only has to be performed on the actual active yield mechanisms. The latter results in

EURAD (Deliverable n˚ 7.6) – Modelling report on the effect of temperature on clay host rocks behaviour
Dissemination level: PU
Date of issue of this report: 06/06/2024

Page 39

different systems of equations being solved for different situations. With the incorporation of the volumetric cap, the following five different situations can occur in the model:

- a purely elastic behaviour,

- activation of the deviatoric yield surface,

- activation of the volumetric yield surface,

- simultaneous activation of the deviatoric and volumetric yield surfaces, and

- only activation of the creep deformation mechanism.

The specific function to characterise the volumetric yield function corresponds to that proposed in Resende and Martin (1985), defined by the following expression:

$$F_2 = R^2 J^2 + p_c - p \tag{4.13}$$

where J is the square root of the second invariant of the deviatoric stress tensor $\mathbf{s} = \boldsymbol{\sigma} - p\mathbf{I}$, p is the mean effective stress, p_c is the isotropic yield pressure, i.e. the state variable controlling the position of the yield surface, and R is a parameter controlling the curvature of the function. The yield function was selected mainly due to its simplicity and due to the fact that, for realistic values of R, the function unambiguously defines its activation in combination with the adopted deviatoric yield mechanism.

Figure 4.6 shows the volumetric yield surface in the J-p space, for different values of R, along with the deviatoric yield surface. For very low values of R, the function results in a vertical line in the J-p space. Nevertheless, as R is increased, it is possible to approximate the shape of volumetric yielding observed in these indurated clayey materials. However, it is important to notice that R has units of *stress*$^{-0.5}$. The latter is inconvenient and unnecessary since R is a material constant. Therefore, the actual yield function implemented reads

$$F_2 = \frac{J^2}{R} + p_c - p \tag{4.14}$$

so that R has units of *stress*.
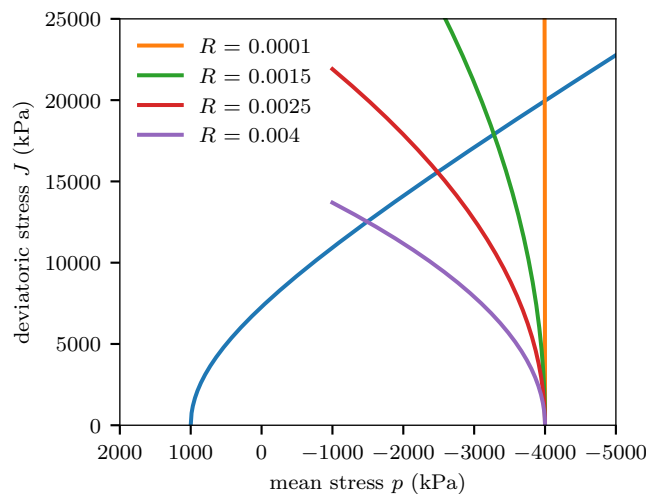
Figure 4.6: Deviatoric yield function and volumetric yield function for different values of R.

EURAD (Deliverable n˚ 7.6) – Modelling report on the effect of temperature on clay host rocks behaviour
Dissemination level: PU
Date of issue of this report: 06/06/2024

Page 40

The other important aspect of the volumetric yield function is how it evolves with the accumulation of plastic deformation, i.e. its hardening law. Originally, a similar hardening law to the Modified Cam Clay was explored, i.e. a constant elastoplastic slope in a semi-logarithmic plot. However, since a stress-independent linear cross-anisotropic elasticity is being employed in the model, this can very easily lead to inconsistencies when the elastoplastic stiffness becomes higher than the elastic one. Therefore, a linear hardening law was adopted instead, which reads:

$$\frac{\partial p_c}{\partial \epsilon_v^p} = \frac{K^{ep} K^e}{K^{ep} - K^e} \tag{4.15}$$

where ϵ_v^p is the volumetric plastic strain and K^e and K^{ep} are the elastic and elastoplastic bulk modulus respectively. Therefore, K^{ep} is an additional parameter controlling the mobilisation of the cap during plastic straining. Figure 4.7 shows the definition of K^e and K^{ep} under isotropic loading. It is important to notice that Figure 4.7 implies that the definition is only approximate, due to the fact that there is not an exact definition for the elastic bulk modulus for the case of cross-anisotropic elasticity. Here, we adopted the Voigt average bulk modulus to characterise K^e , which reads

$$K^e = \frac{1}{9} [D_{11} + D_{22} + D_{33} + 2 (D_{12} + D_{23} + D_{13})] \tag{4.16}$$

where D_{ij} are the components of the cross-anisotropic stiffness tensor **D**.
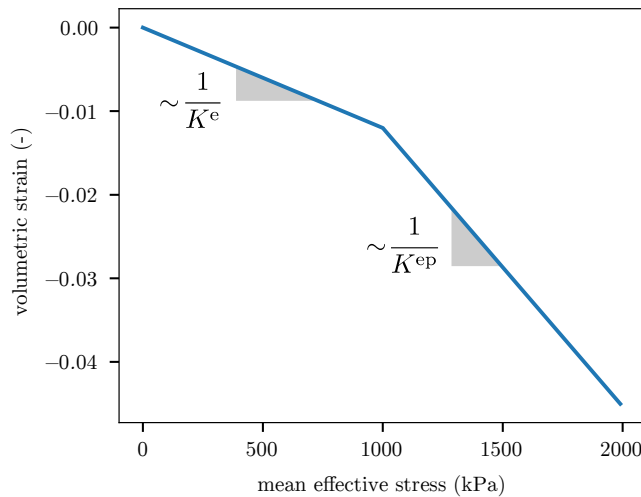
Figure 4.7: Elastic and elastoplastic response under isotropic loading.

4.2.2.2. Temperature dependence of the deviatoric yield surface

Temperature increases cause a monotonic reduction of the shear strength in indurated clayey materials. Therefore, this behaviour can be incorporated by assuming that the deviatoric yield function depends on temperature. Following Tourchi et al. (2023), this dependence can be incorporated by assuming that the strength parameters, i.e. the friction angle ϕ, the cohesion c, and the tensile strength p_t, depend on temperature. The same logarithmic function as in Tourchi et al. (2023) was adopted here, so that input strength parameters are defined as:

$$\phi_{ini}^*(T) = \phi_{ini}^*(T_0) \left[1 - \mu_\phi \ln \left(T/T_0 \right) \right] \tag{4.17}$$

$$\phi_{peak}^*(T) = \phi_{peak}^*(T_0) \left[1 - \mu_\phi \ln \left(T/T_0 \right) \right] \tag{4.18}$$

$$\phi_{res}^*(T) = \phi_{res}^*(T_0) \left[1 - \mu_\phi \ln \left(T/T_0 \right) \right] \tag{4.19}$$

EURAD (Deliverable n° 7.6) – Modelling report on the effect of temperature on clay host rocks behaviour
Dissemination level: PU
Date of issue of this report: 06/06/2024

Page 41

$$c^*_{0\,\text{peak}}(T) = c^*_{0\,\text{peak}}(T_0)\left[1 - \mu_c \ln\left(T/T_0\right)\right] \tag{4.20}$$

$$p_{t0\,\text{peak}}(T) = p_{t0\,\text{peak}}(T_0)\left[1 - \mu_c \ln\left(T/T_0\right)\right] \tag{4.21}$$

where T is the temperature, T_0 is a reference temperature, and μ_ϕ and μ_c are parameters controlling the reduction of the friction angle and the cohesion (and tensile strength) as a function of temperature. The specific definition of the strength parameters appearing in Equations (4.17) to (4.21) are explained more in detail in Mánica et al. (2022a). It is important to notice that parameters in Equations (4.17) to (4.21) are not directly used in the yield function, and actual mobilised values are computed from them and from the state variable accounting for the amount of accumulated plastic strain (i.e. strain hardening/softening). In this way, strength degradation can occur due to both mechanical loading and heating.

Although the constitutive model is implemented following an implicit integration scheme, the dependence of strength parameters on temperature was incorporated in an explicit manner, where temperature-dependent strength parameters are computed at the beginning of the step. The latter is a reasonable approach since temperature changes are generally much slower compared to mechanical loading.

4.2.2.3. Temperature dependence of the volumetric yield surface

The volumetric yielding mechanism also depends on temperature. Similar to the deviatoric mechanism (Section 4.2.2.2), this effect can be incorporated by assuming that the position of the yield function depends on temperature. In this case, to preserve the definition of p_c as a state variable that depends only on volumetric plastic deformations, temperature effects were directly incorporated into the yield function as follows:

$$F_2 = \frac{J^2}{R} + p_c - p_{c0}(T_0)\left[1 - \mu_{p_c} \ln\left(T/T_0\right)\right] - p \tag{4.22}$$

where $p_{c0}(T_0)$ is the yield pressure at the reference temperature T_0, which is a material parameter and μ_{p_c} is a parameter controlling the effect of temperature on the position of the volumetric yield function. The yield pressure p_c is initialised at the beginning of the simulation as $p_c = p_{c0}(T_0)$.

As shown in Section 4.2.2.4, this modification results in constant elastoplastic compressibility, independent of temperature; only the yield pressure is affected by temperature changes. The latter is consistent with experimental results (Campanella and Mitchell, 1968; Tidfors and Sällfors, 1989).

4.2.2.4. Verification examples

A number of simulations were performed to demonstrate the new features implemented in the constitutive model. They were performed from a constitutive standpoint, using the MTest tool, which allows the description of a single material point for a model implemented in MFront (CEA and EDF, 2023). In addition, MTest can be manipulated through a `Python API` and, therefore, performed simulations were organised into `Jupyter Notebooks`. In the following, validation examples are briefly described.

- **Verification 1**. These simulations are intended to demonstrate the dependence of the deviatoric yield function with temperature, to reproduce the reduction of the strength observed in these indurated clayey materials when heated. They correspond to a triaxial test, where only the deviatoric mechanism is mobilised. However, simulations are performed assuming different temperatures, and with $\mu_\phi = \mu_c = 0.2$. Obtained results are shown in Figure 4.8 in terms of the (a) deviatoric stress vs. axial strain and (b) in terms of the peak deviatoric stress vs. temperature. The formulation results in a monotonic reduction of the strength with temperature, as observed for these materials in the laboratory.

EURAD (Deliverable n° 7.6) – Modelling report on the effect of temperature on clay host rocks behaviour
Dissemination level: PU
Date of issue of this report: 06/06/2024

Page 42
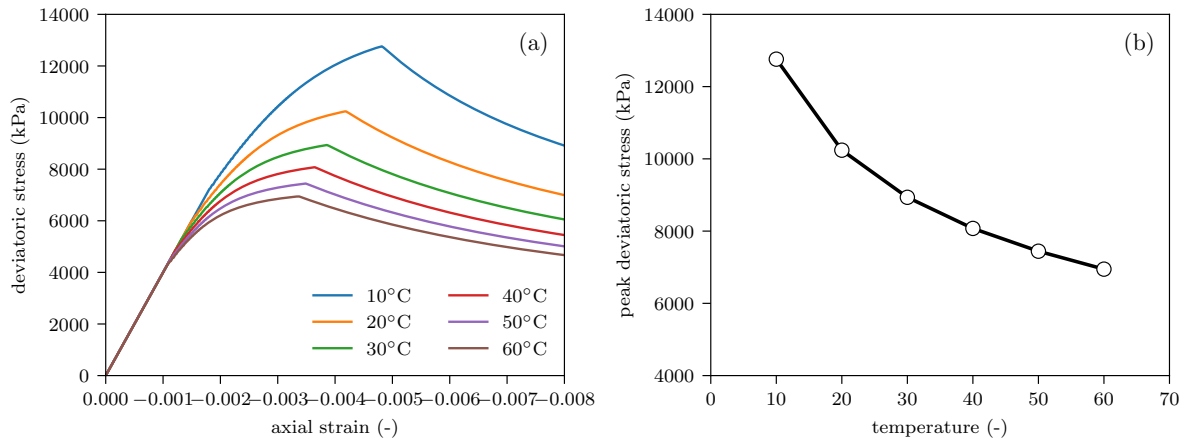
Figure 4.8: Simulation of strain-controlled triaxial tests under different temperatures.

- **Verification 2**. These simulations are intended to demonstrate the dependence of the volumetric yield function on temperature. They correspond to a oedometric test, where only the volumetric mechanism was mobilised. However, simulations were performed here assuming different temperatures and $\mu_{pc} = 0.3$. Obtained results are shown in Figure 4.9 in terms of (a) volumetric strain vs. mean effective stress and in terms of (b) the yield pressure vs. temperature. As for the deviatoric function, the yield pressure decreases monotonically with temperature, reaching yielding earlier as the temperature is increased. However, compressibility is constant, independent of temperature, characterised by K^{ep}.
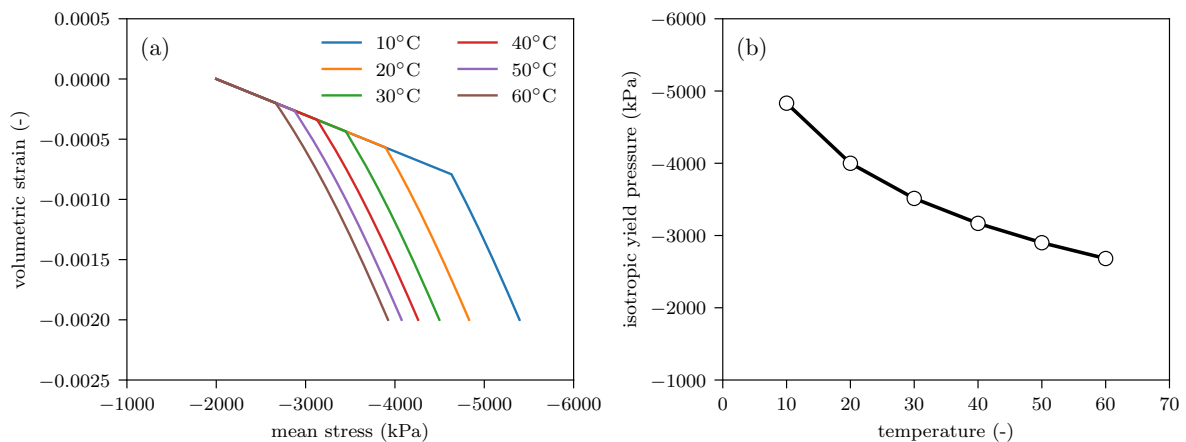
Figure 4.9: Simulation of strain-controlled oedometric tests under different temperatures.

4.2.3. Task 3: Incorporation of the nonlocal regularisation

The last task related to the constitutive model development involves the incorporation of a nonlocal regularisation for the objective simulation of localised deformations. In a general sense, a nonlocal constitutive model is one where the behaviour at a Gauss point depends not only on its state but also on the state of neighbouring points. This is accomplished by replacing a given state variable with its nonlocal counterpart, the latter computed as a weighted average of the local state variables of neighbouring points. Particularly, the approach followed by Mánica et al. (2018), implemented in the finite element code PLAXIS, is considered here, where the assumed nonlocal variable is the one controlling the softening process. This ap-

EURAD (Deliverable n˚ 7.6) – Modelling report on the effect of temperature on clay host rocks behaviour
Dissemination level: PU
Date of issue of this report: 06/06/2024

Page 43

proach is based on the alternative weighting function proposed by Galavi and Schweiger (2010), which has shown very good results in terms of consistency and mesh independence (see e.g. Galavi and Schweiger, 2010; Summersgill et al., 2017; Mánica et al., 2018, 2022b).

Although a rigorous implementation of the nonlocal approach involves the simultaneous solution of all Gauss points in the domain, due to the interdependence between them, it has been shown that an explicit approach, where the nonlocal variable at each Gauss point is assumed constant during a given global iteration, provides objective and mesh independent results (see Mánica, 2018, for further details). Consequently, stress integration can be performed in a standard way, independently in each Gauss point.

For the implementation of the mentioned approach, the constitutive model requires access to the location of all Gauss points for the identification of neighbouring points and the computation of the corresponding weights. Presently, OpenGeoSys lacks this capability in the THM process class. Therefore, further development of OpenGeoSys is required to enable the use of this nonlocal regularisation. Ongoing efforts are already underway to address this issue.

EURAD (Deliverable n˚ 7.6) – Modelling report on the effect of temperature on clay host rocks behaviour
Dissemination level: PU
Date of issue of this report: 06/06/2024

Page 44

4.3. CNRS[UGrenoble]

4.3.1. Introduction

The model is developed by CNRS[UGrenoble] within the framework of double-scale models by homogenisation of the FE^2 type. The constitutive law at the macroscopic scale, required to solve a boundary values problem, results itself from the homogeneised computational response of a mesoscale boundary value problem. Whenever necessary, at each Gauss point, the macroscopic-scale problem calls on the mesoscopic-scale problem, which is associated with a mesostructure. After solving the latter, the incremental response of the mesostructure is returned to the macro problem, which can then iterate. In our case, the two problems at both scales are addressed using the finite element method (Fig. 4.10). The multiphysics couplings are considered at the mesocopic scale, at the level of a representative elementary volume (REV). Such an approach has been developed previously for clayey rocks for hydro-mechanical couplings, making it possible to take into account the effect of deformation and damage on the flow properties of the pore fluid (Frey et al., 2013; Van den Eijnden et al., 2016; Van den Eijnden et al., 2017). The model developed in this work has been extended to incorporate thermo-hydro-mechanical coupling and has been implemented in the finite element code LAGAMINE.

With respect of thermo-mechanical coupled FE^2 models, important work has been developed by Özdemir et al. (2008), nevertheless thermally induced damage was not introduced. This work proposes a micromechanical description of the clayrock microstructure as well as its interstitial fluid flow and heat transfer mechanisms, as an extension of the model proposed by Van den Eijnden et al. (2016) with the incorporation of the thermal components and its respective couplings. The resulting interactions at the microscale will control the macroscopic behavior, e.g. the effect of the fluid in the propagation of micro-cracks leads, at a macroscopic level, to a description of the evolution of the water and heat transfer processes under mechanical solicitations.
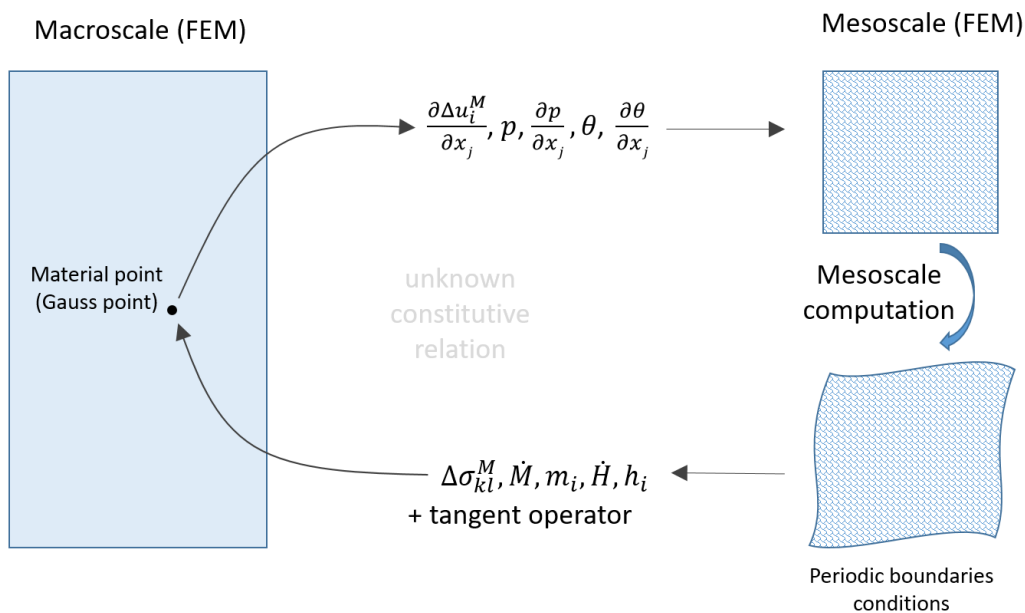
Figure 4.10: Scheme of the computational FE^2 double scale model.

4.3.2. Macroscale field equations

Field equation needs to satisfy the moment, mass and energy balance equations and can be expressed in a weak form:

EURAD (Deliverable n° 7.6) – Modelling report on the effect of temperature on clay host rocks behaviour
Dissemination level: PU
Date of issue of this report: 06/06/2024

Page 45

$$\int_\Omega \sigma_{ij} \frac{\partial u_i^*}{\partial x_j} - \int_\Omega \rho g_i u_i^* d\Omega - \int_\Gamma t_i u_i^* d\Gamma = 0, \tag{4.23}$$

$$\int_\Omega \left(\dot{M} p^* - m_i \frac{\partial p^*}{\partial x_i} \right) d\Omega + \int_\Gamma q_i^w n_i p^* d\Gamma = 0, \tag{4.24}$$

$$\int_\Omega \left(\dot{H} \theta^* - h_i \frac{\partial \theta^*}{\partial x_i} \right) d\Omega + \int_\Gamma q_i^h n_i \theta^* d\Gamma = 0, \tag{4.25}$$

where u, p and θ are, respectively, the displacement, pressure and temperature fields, the * super index denotes virtual quantities. σ is the Cauchy stress tensor, M the fluid storage, H the internal energy (H = $c_p \rho \theta$) of the system, m the water flow and h the heat flow, where Ω, Γ are the domain and the domain boundary respectively; t, q^w and q^h are the traction force at the boundary (t = σn), the water flux at the boundary (m = q_wn) and the heat flux at the boundary (h = q_hn); where n is the external unit vector normal to the boundary.

In order to regularise the problem in the presence of strain localisation, by adding internal length, the formalism of second gradient developed by Chambon et al. (1998) is adopted. The equaltion 4.23 in then replaced by:

$$\int_\Omega \left(\sigma_{ij} \frac{\partial u_i^*}{\partial x_j} + \Sigma_{ijk} \frac{\partial^2 u_i^*}{\partial x_j \partial x_k} \right) d\Omega - \int_\Omega \rho g_i u_i^* d\Omega - \int_\Gamma \left(t_i u_i^* + T_{ij} \frac{\partial u_i^*}{\partial x_j} \right) d\Gamma = 0, \tag{4.26}$$

where $\boldsymbol{\Sigma}$ and T are, respectively, the double stress and the double traction force on the boundary.

The finite element for second gradient with hydro-mechanical coupling, developped by Collin et al. (2006), has been extended for this work to take into account thermo-hydro-mechanical couplings. The degree of freedom for temperature has been added and the stiffness matrix has been reworked.

4.3.3. Macro-meso scale bridging

Local periodicity of the mesostructure is assumed, providing a straightforward formulation of the REV boundary conditions for mesoscale degrees of freedom u_i^m (displacement), p_m (fluid pressure) and θ^m (temperature) in relation with the local macroscale kinematics u_i^M, p^M and θ^M:

$$u_i^m(x^+) - u_i^m(x^-) = \frac{\partial u_i^M}{\partial X_j}(x_j^+ - x_j^-), \tag{4.27}$$

$$p^m(x^+) - p^m(x^-) = \frac{\partial p^M}{\partial X_j}(x_j^+ - x_j^-), \tag{4.28}$$

$$\theta^m(x^+) - \theta^m(x^-) = \frac{\partial \theta^M}{\partial X_j}(x_j^+ - x_j^-), \tag{4.29}$$

with x^+ and x^- the homologous couples of coordinates on the periodic REV boundary. The average pressure and temperature over the REV is prescribed by the local macroscale quantities:

$$p^M = \frac{1}{\Omega} \int_\Omega p^m d\Omega, \tag{4.30}$$

$$\theta^M = \frac{1}{\Omega} \int_\Omega \theta^m d\Omega. \tag{4.31}$$

After solving the REV boundary value problem by means of the finite element method, the homogenised macroscale response of total stress σ_{ij}^M, fluid mass flux m_i^M, heat flow h_i^M, the fluid mass storage $\dot{M}^M$

EURAD (Deliverable n˚ 7.6) – Modelling report on the effect of temperature on clay host rocks behaviour
Dissemination level: PU
Date of issue of this report: 06/06/2024

Page 46

and the internal energy $\dot{H}^M$ is derived from the equilibrated REV based on Hills condition for macro homogeneity. This condition prescribes equal (virtual) work at both scales. From this relation, the homogenized response of the REV to prescribe macroscale kinematics is derived:

$$\sigma_{ij}^M = \frac{1}{\Omega} \int_\Gamma t_i^+(x_j^+ - x_j^-)d\Gamma, \tag{4.32}$$

$$m_i^M = \frac{1}{\Omega} \int_\Gamma q_i^{w+}(x_j^+ - x_j^-)d\Gamma, \tag{4.33}$$

$$h_i^M = \frac{1}{\Omega} \int_\Gamma q_i^{h+}(x_j^+ - x_j^-)d\Gamma, \tag{4.34}$$

$$\dot{M}^M = \frac{M^t - M^{t-\Delta t}}{\Delta t}, \quad M^t = \frac{1}{\Omega} \int_{\Omega^w} \rho^w d\Omega, \tag{4.35}$$

$$\dot{H}^M = \frac{H^t - H^{t-\Delta t}}{\Delta t}, \quad H^t = \frac{1}{\Omega} \left(\int_{\Omega^s} c_p{}^s \rho^s \theta^s d\Omega + \int_{\Omega^w} c_p{}^w \rho^w \theta^w d\Omega \right), \tag{4.36}$$

with t_i^+ the REV boundary traction force and q_i^+, the boundary fluxes on REV boundary Γ^+. These terms are antiperiodic with respect to t_i^- and q_i^- on boundary Γ^-, the homologous counterpart of Γ^+.

The macroscale consistent tangent stiffness matrix is derived by static condensation from the mesoscale consistent tangent stiffness matrix, in the spirit of Van den Eijnden et al. (2016), extended here for thermal coupling.

4.3.4. Mesoscale model

The numerical model at the mesoscale is constructed on a Representative Elementary Volume (REV) and solved with the Finite Elements Method with periodic boundaries. The mechanical description of the REV in the model is constituted by polygonal grains with a distribution representative of the mineralogy observed in Cox samples. The interfaces between the grains constitute a fluid flow network. By doing so the heterogeneity and mesoscopic structure of the material is taken into account.

The formulation of the balance equations at the mesoscale are formulated considering steady state using the weak formulation:

$$\int_\Omega \frac{\partial u_i^*}{\partial x_j} \sigma_{ij} d\Omega - \int_\Gamma u^* \tilde{t} d\Gamma = 0, \tag{4.37}$$

$$\int_\Omega \frac{\partial p^*}{\partial x_i} m_i d\Omega - \int_\Gamma p^* q_w d\Gamma = 0, \tag{4.38}$$

$$\int_\Omega \frac{\partial \theta^*}{\partial x_i} h_i d\Omega - \int_\Gamma \theta^* q_h d\Gamma = 0. \tag{4.39}$$

At the mesoscale, constitutive equations need to be formulated to describe the behaviour of each constituent.

4.3.4.1. Solid materials

The solid constituents are constituted by the clay matrix particles and the mineral inclusions and a description of their thermo-hydro-mechanical behaviour is expressed through the constitutive equations as follow.

EURAD (Deliverable n° 7.6) – Modelling report on the effect of temperature on clay host rocks behaviour
Dissemination level: PU
Date of issue of this report: 06/06/2024

Page 47

Mechanics. The solid grains are considered to have thermo-elastic behaviour as follows:

$$\delta\sigma_{ij} = C_{ijkl}\left(\delta\varepsilon_{kl} - \alpha_{kl}\,\delta\theta\right), \tag{4.40}$$

where C_{ijkl} is the forth order stiffness tensor, α_{kl} is the thermal expansion tensor.

Hydraulics. The diffusive water flux through clay grains has been considered in Van den Eijnden et al. (2017), but due to the very low permeability of the intact clay matrix it can be neglected and is not considered in the current model.

Thermal. Heat conduction in a solid is a diffusive process that is described by Fourier's law:

$$h_i = -\Lambda_{ij}\frac{\partial\theta}{\partial x_j}, \tag{4.41}$$

where the thermal conductivity is defined as Λ_{ij}.

4.3.4.2. Interfaces

The interfaces are considered as uni-dimensional elements going along the contacts of the grains forming a fluid flow network across the REV.

Mechanics. The interfaces are considered to have normal and tangential cohesion with a damage threshold and linear degradation of the cohesion.

$$\delta T_t = C_t^I \delta\Delta u_t, \tag{4.42}$$

$$\delta T_n = C_n^I \delta\Delta u_n, \tag{4.43}$$

where Δu_t and Δu_n are the tangential and normal relative displacement. Additionally, strength thresholds are defined and a degradation of the stiffness of the interfaces (Frey et al., 2013; Van den Eijnden et al., 2017), see Figure 4.11.
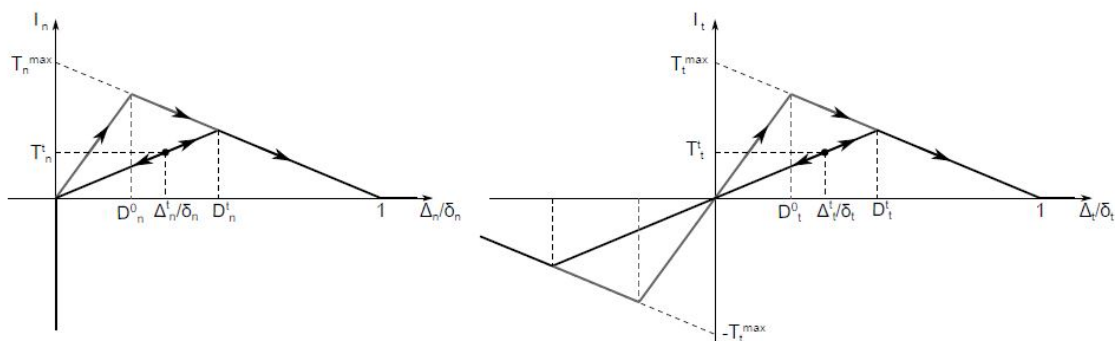
Figure 4.11: Scheme of the mechanical behaviour of the interfaces (from Van den Eijnden et al., 2017), (left) for the normal aperture and (right) for the tangential shearing.

EURAD (Deliverable n˚ 7.6) – Modelling report on the effect of temperature on clay host rocks behaviour
Dissemination level: PU
Date of issue of this report: 06/06/2024

Page 48

Hydraulics. The interfaces constitute a connected flow network where the hydraulic conductivity of an interface is obtained considering laminar water flow in parallel plates leading to the so-called Cubic law:

$$\vec{m} = \rho_w \frac{\Delta u_h{}^3}{12\eta} \frac{dp}{ds},$$ (4.44)

where η is the dynamic viscosity of the fluid, ρ_w is the density of the fluid, $\frac{dp}{ds}$ is the pressure gradient along the direction of the interface (s) and u_h is the effective hydraulic aperture, that depends on the mechanical aperture (Eq. 4.45) but takes into account the roughness of the interface as well as a minimum value that reproduces the permeability of the intact material.

$$\Delta u_h = \begin{cases} \Delta u_{min} & \text{if } a \cdot \Delta u_n < \Delta u_{min} \\ a \cdot \Delta u_n & \text{if } a \cdot \Delta u_n \geq \Delta u_{min} \end{cases}$$ (4.45)
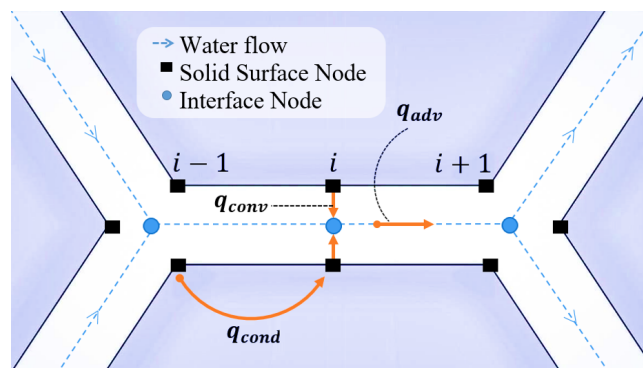
Figure 4.12: Heat transfer mechanisms at the interface level

Thermal. For heat transfers in the interfaces, they are modelled as parallel plates. Under such conditions, three main heat transfer phenomenons take place: conduction, advection and convection (see Fig. 4.12). In the case of conduction along the fluid phase, the heat is transferred as a diffusive phenomenon. On the other hand, for the advective and convective heat transfers, relative motion of particles is required. To study those heat transfer mechanism, the boundary layer theory is applied (Bergman et al., 2011). The temperature profile is considered to be completely developed and the systems (both hydraulic and thermal) are already in steady state equilibrium. For the advection, the displacement of particles with different internal kinetic energy leads to macroscopic heat flow at the interface scale expressed as follows:

$$q_{adv} = \vec{m} c_p \frac{\partial \theta^i}{\partial s},$$ (4.46)

where c_p is the water heat capacity and θ^i is the average temperature of the cross section of interface defined as:

$$\theta^i = \frac{1}{\vec{m} c_p} \int_A \rho v_s c_p \theta dA,$$ (4.47)

where A is the cross-section area and v_s is the fluid velocity.
Finally, the conduction at the solid-fluid contact induces convective heat exchange between solid and fluid. The flow can be obtained as follows:

$$q_{conv} = h(\theta^s - \theta^i),$$ (4.48)

where θ_s is the temperature of the surface of the grains and h is the convection coefficient. This coefficient is defined as the temperature gradient perpendicular to the flow at the point of contact, usually is associated

EURAD (Deliverable n° 7.6) – Modelling report on the effect of temperature on clay host rocks behaviour
Dissemination level: PU
Date of issue of this report: 06/06/2024

Page 49

with the Nusselt number. This adimensional number is defined as the ratio between the convective and conductive flow (see Bergman et al., 2011).

4.3.4.3. Multiscale porosity

Studying the pore size distribution in the Callovo-Oxfordian claystone (Menaceur et al., 2016), it can be observed that there is a double porosity: a mesoporosity with a 12 μm average size accounting for roughly 10% of the total porosity and a microporosity < 1 μm. The proposal is to take into consideration the effect of mesoporosity in the microstructure, as shown in Fig. 4.13 and to be able to reflect the pore compression. The behavior of the pores is implemented as follows:
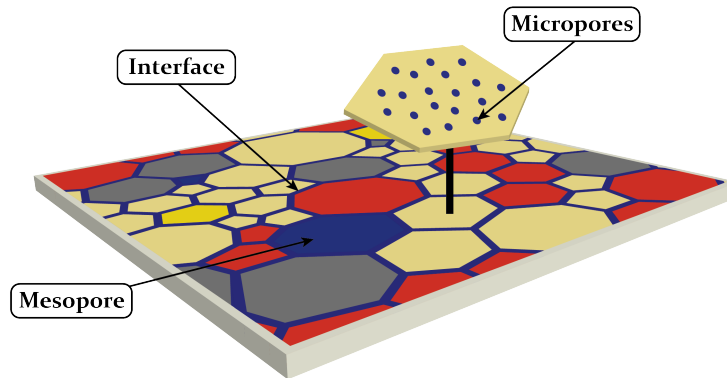
Figure 4.13: Schematic of the microstructure and the different components of the pore spaces: porosity in the interfaces, in the mesoporosity (equant pores) and microporosity in the clay phase (yellow).

Mesoporosity. From the mechanical point of view, a mesopore applies the macroscopic pressure normal to the surrounding grains. Pressure gradients as well as water velocities inside a mesopore are considered negligible. The pore volume of the pores is computed in the final configuration enabling the computation of the fluid storage variation due to pore deformation. The thermal behaviour of pores is considered purely conductive inside the pore and as water velocity inside the pore can be neglected, convective flux between solid grains and mesopore is replaced with conductive heat at the contact. Heat capacity of the pore is already taken into account with the heat capacity of the fluid phase.

Microporosity. An additional implementation for the microscale is to account for the 90% of remaining porosity that is in the clay matrix. With this intent porous material constitutive laws are implemented for the microscale clay phase components.

For the mechanical constitutive behaviour of the clay phase, the Terzaghi effective stress definition is used.

$$\sigma_{ij} = C_{ijkl}(\varepsilon_{kl} - \alpha_{kl}(\theta - \theta_0)) + (p - p_0), \tag{4.49}$$

where the pressure p and θ are the uniform pressure and temperature field equal to the macroscopic pressure and temperature, respectively. θ_0 is the reference temperature and C_{ijkl} and α_{kl} are the stiffness tensor and the thermal dilation tensor and are material parameters.

Fluxes inside the clay matrix are sufficiently small that diffusive flow remains neglected in the current formulation and water fluxes are considered only in the interfaces.

EURAD (Deliverable n˚ 7.6) – Modelling report on the effect of temperature on clay host rocks behaviour
Dissemination level: PU
Date of issue of this report: 06/06/2024

Page 50

In relation of the water storage variation, the volumetric variation of the pore space needs to be computed. One of the hypothesis is that the stiffness of the solid constituents is great enough that the volumetric deformation of the material can be considered to be pore space reduction (i.e. $\delta V_\phi = \delta V$). Staying under the finite strain framework, the deformation of the pore space can be computed as follows:

$$\frac{\delta V_\phi}{V} = \varepsilon_{ii} - \alpha_{ii}(\theta - \theta_0). \tag{4.50}$$

The thermal behaviour of pores is considered purely conductive as water flux is neglected. For the sake of simplicity in calibrating, the parameter taken is the conductivity of the clay matrix (i.e., its independent of the porosity).

4.3.4.4. Mesoscale solution scheme
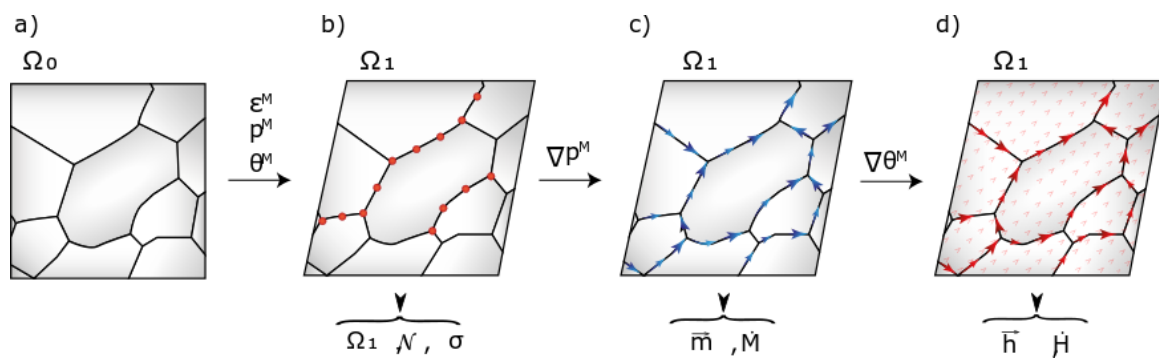
Figure 4.14: Solution scheme of the REV. a) REV at initial configuration, b) REV after mechanical calculation, c) REV after hydraulic solution, d) REV after thermal solution.

The mechanic, hydraulic and thermal systems are solved separately and the solution procedure is shown in Fig. 4.14. First, the mechanical system is solved under uniform pressure and temperature fields equal to the macroscopic pressure and temperature, respectively. Its boundary conditions are specified by applying displacement to the REV boundaries that corresponds to the macroscopic strain. Solving the mechanical system leads to a new configuration of the microstructure, the state of the interfaces and the homogenized stress. Then, a pressure gradient is applied and the hydraulic system is solved by formulating the mass balance at the interface nodes, the hydraulic conductivity is calculated from the current configuration with the temperature field is still considered uniform and equal to the macroscopic temperature. The pressure fluctuations field with respect to the macroscopic pressure are considered to be sufficiently small that its effect on the configuration and the homogenized stress is negligible. For the solution of the thermal system, an equivalent thermal resistance model is formulated. The thermal resistance matrix is obtained from the current configuration and the advection resulting from the calculated water flux. The temperature fluctuation field is considered to be small with respect of the macroscopic temperature and its effect very limited on the mechanical and hydraulic systems. The resulting solution scheme proves efficient as the only iterative procedure is the solution of the mechanical system and it has to be solved only once per macroscale iteration.

4.3.5. Validation numerical versus analytical solutions

A set of validation case is run in order to verify the code, selecting a very simple mesostructure for which analytical solutions can be derived. The mesostucture is one grain with one horizontal interface, the height and width of the REV are 1 mm each and its made of homogeneous clay. Material properties and water properties used in this validation are listed in Table 4.2.

EURAD (Deliverable n° 7.6) – Modelling report on the effect of temperature on clay host rocks behaviour
Dissemination level: PU
Date of issue of this report: 06/06/2024

Page 51

Property	Magnitude	Units
Water		
ρ_0	10^{-3}	g/mm^3
η_0	10^{-9}	MPa/s
K	$2.2\,10^{+3}$	MPa
α_v	$2.1\,10^{-4}$	1/K
Λ	$0.598\,10^{-3}$	J/mm.s.K
c_p	4.19	J/g.K
Clay Matrix		
ρ_0	$2.7\,10^{-3}$	g/mm^3
K	$2.0\,10^{+2}$	Mpa
α	$3.4\,10^{-5}$	1/K
Λ	$1.2\,10^{-3}$	J/mm.s.K
c_p	0.878	J/g.K

Table 4.2: Material properties for the simulations, for pressure = 0 MPa and temperature = 20 ℃

4.3.5.1. Thermal conduction - without water flow

Heat flow Parallel to interface. A horizontal temperature gradient is applied to the REV at constant and uniform pressure. Analytical solutions of the thermal system can be found as only conduction in the solid grain is considered (conduction along the interface is neglected). Comparison of the numerical simulation versus the analytical solution is shown in Fig. 4.15 (case 1).

Heat flow Perpendicular to interface. A vertical temperature gradient is applied to the REV at constant and uniform pressure. In this case, the conduction is perpendicular to the interface, therefore the convective heat flow throught the interface has to be considered. The system can be described as a 1D in series heat conduction where there is a conduction through half of the height then convection and finally conduction through the remaining half of the solid grain.

4.3.5.2. Thermal conduction - with water flow

Here, pressure gradients are going to be added, adding the advective heat transfer component to the model. The horizontal pressure and temperature gradients are applied, so that they flow parallel to the interface. Analytically, the solution is given by adding the heat transfers of the conduction on the solid and the advective heat flow of the interfaces (case 3 in Fig. 4.15).

EURAD (Deliverable n˚ 7.6) – Modelling report on the effect of temperature on clay host rocks behaviour
Dissemination level: PU
Date of issue of this report: 06/06/2024

Page 52
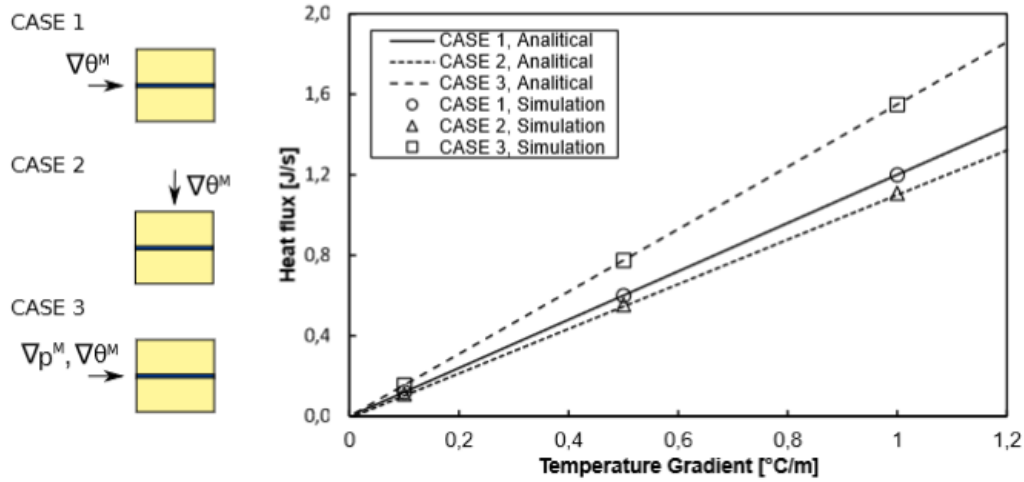
Figure 4.15: Validation analytical vs. numerical of the thermal conduction of the REV for different cases, flux parallel to the interface and perpendicular to the interface and finally parallel to the interface with a pressure gradient of 0.01MPa/m

4.3.5.3. Water flux

The water flux of one interface is obtained with the cubic law,

$$m = \frac{\rho}{12\eta} u_h^3 \nabla p \tag{4.51}$$

where ρ and η are the density and the dynamic viscosity respectively. These properties depend on the temperature and pressure, described by the following relation:

$$\rho = \rho_0 e^{\frac{p-p_0}{K}} e^{\alpha(\theta_0 - \theta)} \tag{4.52}$$

$$\tag{4.53}$$

where K and α are the volumetric modulus and the volumetric thermal expansion coefficient of the fluid.

The expression for the dynamic viscosity is obtained from the Vogel-Fulcher-Tammann equations:

$$\eta = A \, exp \left(\frac{B}{\theta - C} \right) \tag{4.54}$$

where A, B and C are material dependent parameters, in the case of water:

Parameter	Value	Units
A	0.02939	$MPa\,s^{-1} MPa \cdot s$
B	507.88	K
C	149.3	K

The comparison with the numerical simulation is shown in Fig. 4.16.

EURAD (Deliverable n° 7.6) – Modelling report on the effect of temperature on clay host rocks behaviour
Dissemination level: PU
Date of issue of this report: 06/06/2024

Page 53
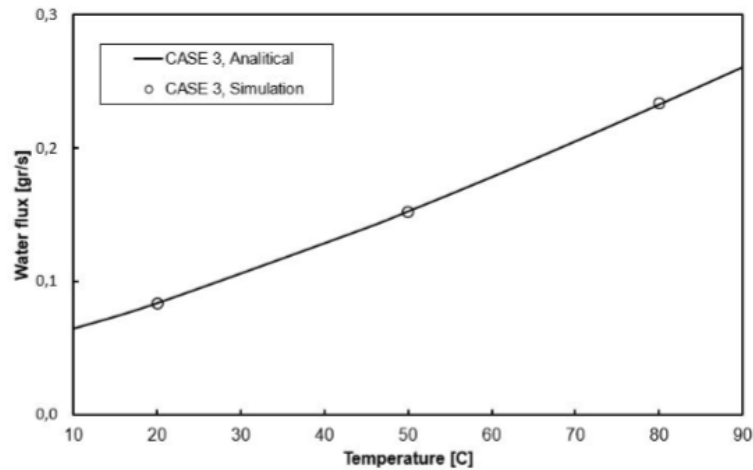
Figure 4.16: Validation of the hydraulic conduction of the REV for a pressure gradient of 0.01 MPa/m at different temperatures

4.3.5.4. Model calibration

Experimental observations and characterisations of the rock microstructure (Yven et al., 2007; Robinet et al., 2012; Cosenza et al., 2015a,b, 2019; Desbois et al., 2017) are considered to define the material in a realistic manner. In order to not obiterate the computation time, the mesostructure should be limited in term of complexity and is generated in an artificial way, to remain both simple (easy to mesh with few elements) and respect a certain realism. The focus is mainly on the description of mineralogical constituents, grain morphology (i.e., geometrical characteristics), and microstructural patterns. The analysis methods on micro- to meso-structures include SEM, X-ray micro-CT, and image analysis with segmentation techniques. Measurements lead to the determination of mineral groups, spatial distributions, mineral area fractions, as well as size, shape, and orientation of mineral inclusions.

A specific Voronoi tessellation has been developed to mimic the morphology of the mesostructure, in term of mineralogy distribution, grain size distribution, specific elongation and orientation distribution (Pardoen et al., 2020).

The mesostructure selected here contains about 50 grains (Fig. 4.17) with a clay content of 48%, which corresponds to the clay unit of the median depth of the Cox layer (-490m) at URL Meuse-Haute Marne.
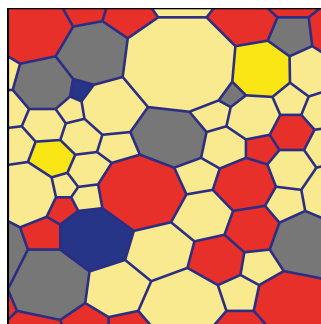
Figure 4.17: Mesostructure of the model, each colours of grains correspond to a mineralogical phase; yellow for clay (48%), red for carbonates (33%), grey for quartz (16%) and blue for pyrite (3%).

The model calibration consist to determine the constitutive parameters of the mesoscale. Some of the parameters (e.g., bulk moduli of the mineral phases, thermal conduction, etc...), have been determined

EURAD (Deliverable n° 7.6) – Modelling report on the effect of temperature on clay host rocks behaviour
Dissemination level: PU
Date of issue of this report: 06/06/2024

Page 54

from the litterature (Table 4.3). Other parameters, like the interface constitutive moduli or strength have been determined to fit the response of the mesostructure on the experimental results (Table 4.4).

Property	Units	COx [1]	Clay	Calcite	Quartz	Pyrite	Pore
Composition[2]	[-]	100%	50%	30%	18%	2%	-
Bulk density	[kg/m^3]	2450	-	-	-	-	
Porosity	[-]	18%	16%	0	0	0	2%
Intrinsic permeability	[m^2]	$2.3\ 10^{-20}$	0	0	0	0	-
Young's Modulus [2]	[MPa]	7000	2300	84000	95000	305000	-
Poisson's Ratio [2]	[-]	0.3	0.11	0.317	0.074	0.154	-
Thermal conductivity [3]	[W/mK]	1.67	1.2	3.4	6.0	4.0	-
Thermal expansion coef. [4]	[1/K]	$1.25\ 10^{-5}$	$8.3\ 10^{-6}$	$5.0\ 10^{-6}$	$1.1\ 10^{-5}$	$4.0\ 10^{-6}$	-
Specific heat [4]	[J/kgK]	978	878	710	1100	748	-

Table 4.3: Cox properties and mineral properties.
[1] *Values taken from Robinet et al. (2012),* [2] *From Pardoen et al. (2020),* [3] *From Horai (1971),* [4] *From Braun (2019a)*

Property	Units	value
$D_{t,crit}$	[-]	0.05
$D_{n,crit}$	[-]	0.05
$D_{t,0}$	[-]	0.001
$D_{n,0}$	[-]	0.001
$T_{t,max}$	[MPa]	5.5
$T_{n,max}$	[MPa]	2
Δu_{min}	[-]	$1.4\ 10^{-5}$
Δu_{trans}	[-]	$-1.4\ 10^{-5}$

Table 4.4: Interface constitutive parameters.

4.3.6. Doublescale modelling

Several double-scale modelling runs were carried out. Some were carried out to validate the method, in order to model simple cases. They are not presented here. The most advanced boundary condition problem that we perform with in this study was the modelling of a parallelepiped of the laboratory sample type, to which we applied boundary conditions close to those of the near-field case. The boundary conditions were slightly modified in order to show that, in addition to the multi-physical coupling aspects, the numerical model could be used to model the strain localisation thanks to the second gradient regularisation.

Several steps were therefore carried out, firstly an anisotropic mechanical loading with a horizontal stress of 12.5 MPa and a vertical stress of 50 MPa on the parallelepipedic sample of dimension 0.5 x 1 m^2. Next, thermal loading was applied to the base of the sample, imposing a heat flux of $25\,\mathrm{Wm^{-1}}$, with perfectly insulated surfaces on the lateral sides, and a convective control condition at the top (temperature set at $24\,°C$ a few metres from the surface, with a modulus of $0.0167\,\mathrm{Wm^{-2}K^{-1}}$).

EURAD (Deliverable n˚ 7.6) – Modelling report on the effect of temperature on clay host rocks behaviour
Dissemination level: PU
Date of issue of this report: 06/06/2024

Page 55
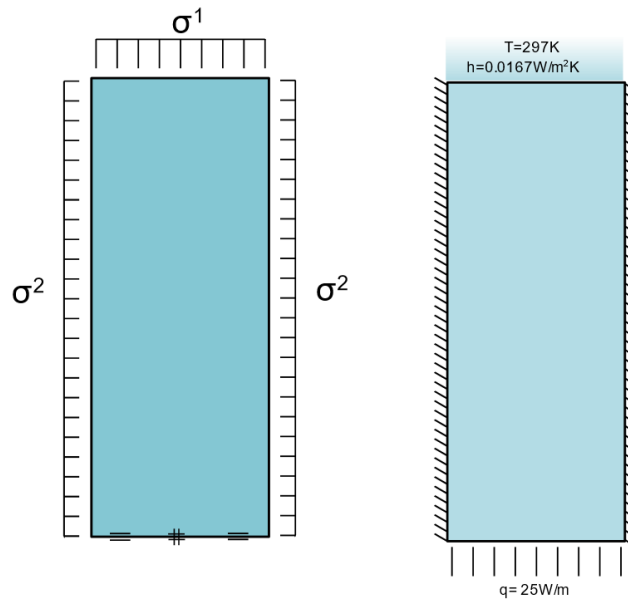
Figure 4.18: Mechanical and thermal boundary conditions applied on the specimen which is undrained.

The increase in temperature caused by the heating resulted in an increase in pore pressure due to the thermal expansion of the water. This increase led to damage at the interfaces of the mesostructure (Fig. 4.19b). This damage was then localised in bands across the macrosotructure (Fig. 4.19a). This in turn induced a localised dilation of the material and, in the same time, an increase in the flow properties (which can be interpreted as permeability) of the mesostructure within the bands. As a result, there is a temporary difference in pressure between the top and bottom of the sample (Fig. 4.19c).

This example shows that the model can describe the strain localisation triggered by thermal loading that induce interface damage at the level of the mesostructure.

4.3.7. Conclusions

The model developed allows the material's mesostructure to be explicitly taken into account within the framework of computational homogenisation. The thermal aspect has been added to an existing model. This coupling takes into account various components of heat transport by advection, convection and conduction at the interfaces of the interstitial fluid flows and the solid grains. The model naturally describes the thermal overpressurisation induced by the expansion of the water when the temperature rises. It can also describe the mechanical damage potentially induced by overpresurisation when this reaches levels comparable to the total stresses applied to the medium, as well as the increase in permeability that may result.

The calibration of the model is based both on known properties of the different mineralogical phases of the rock, and on a calibration of the interface parameters so that the homogenised response of the microstructure can be identified with the laboratory experimental results. The morphology of the mesostructure is chosen so as to match the accessible experimental data, such as the size of inclusions per mineral family and their preferred shape and orientation. The choice of mesostructure also allows the anisotropy of the material to be taken into account. Finally, thanks to the regularisation introduced in the second-gradient medium framework, the model allows objective modelling of the strain localisation, whether it is initiated by mechanical or thermal stresses.

As part of this work, the model was validated by a series of tests. We have also demonstrated its ability

EURAD (Deliverable n˚ 7.6) – Modelling report on the effect of temperature on clay host rocks behaviour
Dissemination level: PU
Date of issue of this report: 06/06/2024

Page 56
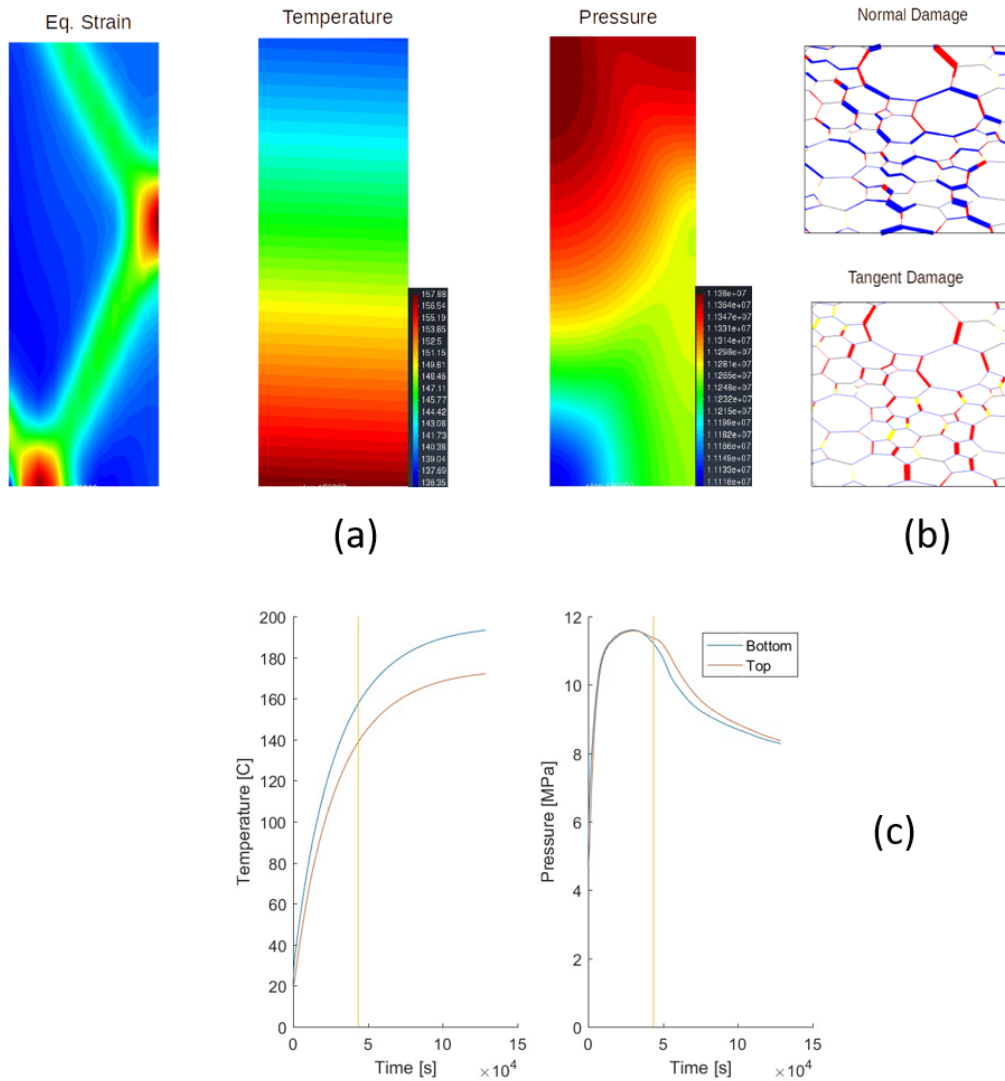
Figure 4.19: (a) equivalent strain field, temperature and pressure fields at 4.10^4 s, respectively ; (b) illustration of the interfaces' damage in the normal and tangeantial directions in a mesoscruture inside the shear band ; (c) evolution of the bottom and top temperatures and pore pressures with time.

to model a problem with boundary conditions close to those that may exist in the near field of a gallery. This development work has been substantial, both conceptually and in terms of its implementation in the Lagamine finite element code. It represents an innovative modelling approach, but it took longer than initially expected and did not allow us to tackle the benchmark exercises in more detail.

EURAD (Deliverable n° 7.6) – Modelling report on the effect of temperature on clay host rocks behaviour
Dissemination level: PU
Date of issue of this report: 06/06/2024

Page 57

4.4. EDF

For the modelling of the EDZ in the near-field case, EDF refered to a visco-elasto-plastic model (LKR model) based on the works of ((Laigle, 2004), (Kleine, 2007), (Raude, 2015)) and used previously by EDF for the modeling of non linear behavior of soils/rocks (ex: Cox galleries). This model describes two physical mechanisms : the first mechanism, describes the instantaneous deviatoric behavior of geomaterials, the second one, the viscoplastic mechanism, reflects the effect of time on the deviatoric behavior of geomaterials.

The instantaneous deviatoric behavior is characterized by extension and unconfined compression triaxial tests. The conceptual framework retained for the development of the elasto-plastic mechanism is mainly based on the analysis of behaviour in triaxial compression. The response of geomaterials to this kind of request breaks up into two phases: for relatively weak deformations, the resistance of a sample increases with its axial deformation. This phase, qualified as pre-peak, ends when the material reaches its maximum resistance. Beyond this peak, resistance decreases until reaching a residual value. The evolution of a material between its resistances of peak and residual is described as post-peak. The effect of time on the deviatoric behavior is characterized by triaxial compression or creep tests at various loading rates.

The conceptual framework retained for the development of the visco-plastic mechanism is mainly based on the analysis of the behaviour during a creep test.

Further detailed descriptions of this model are given in the code_aster reference (EDF, 2017).

The LKR model depends on a large number of parameters that are usually determined from triaxial compression tests and creep tests at different temperatures and confining pressures. As a first approach, the near-field modelling of the Cox is done while using parameters determined in previous THM works of EDF on the Cox host rock. Those parameters should be further updated with the calibration works on the experimental results of HITEC-Subtask 2.2. However, due to the delayed delivery of the latter results, those updates will not be presented in this report. Table 4.5 presents the LKR parameters used as a first approach in this exercise :

EURAD (Deliverable n˚ 7.6) – Modelling report on the effect of temperature on clay host rocks behaviour
Dissemination level: PU
Date of issue of this report: 06/06/2024

Page 58

Parameter	Name	Value	Unit
β, γ	Shape parameters of the plasticity criterion in the deviatoric plane	1.5, 0.85	-
$\hat{\sigma_c}$	Mean compressive strength	12.5	MPa
A_{11}, b	Strength anisotropy parameters	0.17,4.2	-
$m_{[0]}^0$	Slope of the initial elasticity threshold	0.1	-
$m_{[1]}^0$	Slope of the maximal strength threshold	8	-
v_1	Parameter for the pre-peak strain-hardening kinetic	1.89	-
$\xi_{[1]}^0$	Value of the strain-hardening variable on the maximal strength threshold	$6.3 \ 10^{-3}$	-
$r_{[1]}^x, r^s, r^m$	Temperature dependance parameters	0,0,0	-
v_2	Parameter for the post-peak strain-hardening kinetic	1.85	-
$\xi_{[2]}^0$	Value of the strain-hardening variable on the intermediate threshold	$2. \ 10^{-2}$	-
$a_{[2]}$	Curvature of the intermediate threshold	0.7	-
q_i^0	Intersection of maximal strength, intermediate and residual thresholds	59.5	-
r^q	Temperature evolution of the residual threshold	0	-
$r_{[2]}^x$	Axial strain-stress relation at different temperatures and confining pressures	0	-
A_v, η_v	Parameters for the creep kinetic	$9.34 \ 10^{-14}$, 1.86	s^{-1},-
f_p	Creep parameter	0.1	-
$\xi_{[s]}^0$	Parameter for the amplitude of delayed strains	$2.71 \ 10^{-3}$	-
ρ_1, ρ_2, ρ_3	Parameters for the amplitude of volumetric strains	1, 0.14, 1.1	-
Z	Parameter for creep in temperature	0	-

Table 4.5: The LKR model parameters

EURAD (Deliverable n˚ 7.6) – Modelling report on the effect of temperature on clay host rocks behaviour
Dissemination level: PU
Date of issue of this report: 06/06/2024

Page 59

4.5. LEI

During HITEC project LEI revised and developed their constitutive model based on thermo-poroelasticity and thermo-elastoplasticity. Subsequently models were implemented in COMSOL Multiphysics for the modelling of near field effects in generic 2D system under isotropic and anisotropic stress conditions and material properties.

4.5.1. Thermo-poroelastic model

For modelling of THM response of clay-rock in the near-field, water mass balance in porous media was revised and related key thermo-hydro-mechanical couplings were identified. Missing thermo-mechanical coupling was implemented in COMSOL Multiphysics.

Water properties such as water viscosity, volumetric thermal expansion coefficient were set as a function of temperature according to benchmark specification in [EURAD (Milestone n° 49), 2020]. Anisotropic mechanical properties of the rock were described as transverse anisotropy with isotropic properties in the plane parallel to bedding.

4.5.2. Thermo-elastoplastic model

Development of the elastoplastic model was based on Drucker-Prager soil plasticity model with non-local regularisation (Zreid, 2016). Following (Zreid, 2016) the Drucker-Prager yield function was modified replacing model parameter k with $(1 - w(\overline{\epsilon_{pm}}))\sigma_y(\epsilon_p)$:

$$F_y = \sqrt{J_2} + \alpha_{DP}I_1 - (1 - w(\overline{\epsilon_{pm}}))\sigma_y(\epsilon_p) \leq 0 \qquad (4.55)$$

Here I_1, J_2 - stress tensor invariants, α_{DP}, k - Drucker-Prager model parameters related to friction angle and cohesion, $\sigma_y(\epsilon_p)$ – yield stress, $w(\overline{\epsilon_{pm}})$ – damage variable.

In this model formulation hardening is described by a hardening law and controlled via the hardening parameter h, which is always positive:

$$\sigma_y(\epsilon_p) = (\sigma_{y0} + h\epsilon_p), h > 0 \qquad (4.56)$$

The damage variable (which can have a value between 0 and 1) is used to represent material softening by multiplying the yield stress with it:

$$w(\overline{\epsilon_{pm}} = \alpha_p[1 - exp(-\beta\overline{\epsilon_{pm}})] \qquad (4.57)$$

Here $\overline{\epsilon_{pm}}$ is the equivalent plastic strain, α_p, β - material parameters. The material parameter β controls the shape of the softening curve, and α_p controls the maximum degradation of the yield stress. The value of α_p typically ranges from 0.96 to 1.0.

Within softening (due to various microcracks, defects etc.) material a strain localisation could occur. This could lead to mesh dependent model results obtained from the finite element code. To avoid model results' dependency on mesh the regularisation methods are usually applied. In the work of (Zreid, 2016) a

EURAD (Deliverable n˚ 7.6) – Modelling report on the effect of temperature on clay host rocks behaviour
Dissemination level: PU
Date of issue of this report: 06/06/2024

Page 60

non-local regularisation method (implicit gradient enhanced method) was introduced. Variable ($\overline{\epsilon_{pm}}$) is a maximum equivalent plastic strain $\overline{\epsilon_{pm}}$ over simulation time.

$$\overline{\epsilon_{pm}}(t) = max\{\overline{\epsilon_p}(\tau)|0 \leq \tau \leq t\} \tag{4.58}$$

The non-local variable $\overline{\epsilon_p}$ is derived simultaneously solving Helmholtz type equation and takes into account the plastic strains in the neighbour points within certain distance called internal length:

$$\begin{cases} \nabla \cdot \boldsymbol{\sigma} + \tilde{f} = 0 \\ \overline{\epsilon_p} - l_{int}^2 \nabla^2 \overline{\epsilon_p} = \overline{\epsilon_p} \end{cases} \tag{4.59}$$

Drucker-Prager model parameter α_{DP} is a function of friction angle:

$$\alpha_{DP} = tan\phi/(\sqrt{(9 + 12.(tan\phi)^2)} \tag{4.60}$$

In current model formulation coefficient α_{DP} is function of friction angle, which varies according to (Mánica et al., 2018):

$$\tan \phi = \begin{cases} \tan \phi_{ini} + \dfrac{\epsilon_{eq}^p}{a_\phi + \frac{\epsilon_{eq}^p}{\delta}}, \Delta = \dfrac{\chi}{\frac{\chi}{\tan \phi_{peak} - \tan \phi_{ini}} - a_\phi} & (\epsilon_{eq}^p \leq \chi) \\ \tan \phi_{peak} - (\tan \phi_{peak} - \tan \phi_{res})\left[1 - e^{-b_\phi(\epsilon_{eq}^p - \chi)}\right] & (\epsilon_{eq}^p > \chi) \end{cases} \tag{4.61}$$

Where $\phi_{ini}, \phi_{peak}, \phi_{res}$ - initial, peak and residual friction angle, χ – strain threshold when friction angle decrease starts, a_ϕ, b_ϕ – hardening and softening parameters, ϵ_{eq}^p is defined as scalar:

$\epsilon_{eq}^p = (\epsilon^p : \epsilon^p)^{1/2}, \epsilon^p$ is the plastic strain tensor.

Developed plastic strains will affect clay-rock permeability (Nguyen T.S., 2015):

$$k = k_{ii}.\exp(a\epsilon_v).\exp(b\epsilon_{eq}^p) \tag{4.62}$$

where a and b are material parameters, ϵ_v is volumetric strain, ϵ_p is equivalent plastic strain.

The model formulation was enhanced with linear temperature dependence of model parameters (initial yielding stress, hardening parameter) derived from laboratory experiment modelling. This modification allows the representation of a decrease of strength with increasing temperature for saturated Cox clayrock.

EURAD (Deliverable n° 7.6) – Modelling report on the effect of temperature on clay host rocks behaviour
Dissemination level: PU
Date of issue of this report: 06/06/2024

Page 61

4.6. ULg

ULg participated to the different benchmark activities of the subtask 2.3: Near field and far field Benchmark, Laboratory test modelling, PRACLAY and ALC1605 in situ heater tests. The classical mechanical law and the second gradient constitutive model are presented in this section.

4.6.1. First gradient mechanical law

An elastoplastic model with cross-anisotropy and horizontal isotropic bedding planes is considered for the host rock. The elastoplastic relation for the stress-strain relationship is expressed in rate (incremental) form as follows:

$$\widetilde{\sigma}'_{ij} = C_{ijkl}\dot{\varepsilon}_{kl} \tag{4.63}$$

where $\dot{\varepsilon}_{kl}$ is the strain rate, C_{ijkl} is the stiffness tensor, and $\widetilde{\sigma}'_{ij}$ is the Jaumann objective effective stress rate. Due to the unsaturated condition of the samples in the laboratory test, the pore fluid pressure effect on the Cauchy total stress field σ_{ij} herein is characterized by taking into account the anisotropy of Biot's coefficients and the partial saturation effect. Apart from the modelling of laboratory tests, the saturation degree of the material should be equal to 1 for other benchmark modellings. The Biot's stress definition for unsaturated and anisotropic materials yields:

$$\sigma_{ij} = \sigma'_{ij} + b_{ij}S_{r,w}p_w \tag{4.64}$$

where σ_{ij} is the effective stress field, $S_{r,w}$ is the degree of water saturation, p_w is the pore water pressure, and b_{ij} is the Biot's anisotropic tensor. Therefore the total strain rate $\dot{\varepsilon}_{ij}$ comprises an elastic component $\dot{\varepsilon}_{ij}^e$ and a plastic component $\dot{\varepsilon}_{ij}^p$:

$$\dot{\varepsilon}_{ij} = \dot{\varepsilon}_{ij}^e + \dot{\varepsilon}_{ij}^p \tag{4.65}$$

The elastic and plastic behaviours are defined in the following for anisotropic materials, which means that the elastoplastic properties depend on the coordinate axes to which the properties are referred and therefore depend on the orientation.

Elastic component

The linear elastic behaviour of the rock is based on the classical Hooke's law linking the stress rate $\dot{\sigma}_{ij}^e$ to the reversible strain rate component $\dot{\varepsilon}_{kl}^e$:

$$\dot{\sigma}_{ij}^e = C_{ijkl}^e\,\dot{\varepsilon}_{kl}^e \iff \dot{\varepsilon}_{ij}^e = D_{ijkl}^e\,\dot{\sigma}_{kl}^e \tag{4.66}$$

Where C_{ijkl}^e is the elastic stiffness tensor and D_{ijkl}^e is the elastic compliance tensor corresponding to the inverse of the matrix C_{ijkl}^e.

For an isotropic material, the elastic compliance tensor is expressed as a function of only two parameters which can be the Poisson's ratio ν and the Young modulus E, or the shear modulus G and the bulk modulus

EURAD (Deliverable n˚ 7.6) – Modelling report on the effect of temperature on clay host rocks behaviour
Dissemination level: PU
Date of issue of this report: 06/06/2024

Page 62

K. Switching to a material with anisotropic elasticity increases the total number of required independent parameters. However, anisotropic geomaterials often exhibit limited forms of anisotropy such as orthotropy or cross-anisotropy Lekhnitskii et al. (1964). In such materials with axes of symmetry, the number of parameters is reduced. In orthotropic materials where the anisotropy is induced by three mutually orthogonal symmetry planes, the elastic matrix is defined with 9 parameters:

$$
D^e_{ijkl} =
\begin{bmatrix}
\frac{1}{E_1} & -\frac{\nu_{21}}{E_2} & -\frac{\nu_{31}}{E_3} & 0 & 0 & 0 \\
-\frac{\nu_{12}}{E_1} & \frac{1}{E_2} & -\frac{\nu_{32}}{E_3} & 0 & 0 & 0 \\
-\frac{\nu_{13}}{E_1} & -\frac{\nu_{23}}{E_2} & \frac{1}{E_3} & 0 & 0 & 0 \\
0 & 0 & 0 & \frac{1}{2G_{12}} & 0 & 0 \\
0 & 0 & 0 & 0 & \frac{1}{2G_{13}} & 0 \\
0 & 0 & 0 & 0 & 0 & \frac{1}{2G_{23}}
\end{bmatrix}
\tag{4.67}
$$

The symmetry of the stiffness matrix imposes that:

$$
\frac{\nu_{21}}{E_2} = \frac{\nu_{12}}{E_1}, \qquad \frac{\nu_{31}}{E_3} = \frac{\nu_{13}}{E_1}, \qquad \frac{\nu_{23}}{E_2} = \frac{\nu_{32}}{E_3}
\tag{4.68}
$$

In cross-anisotropic materials, such as the Boom Clay and Callovo-Oxfordian formation, the behaviour remains isotropic in the parallel bedding planes which requires only 5 independent parameters Amadei (2012):

$$
\begin{cases}
E_1 = E_3 = E_\parallel \\
E_2 = E_\perp \\
\nu_{13} = \nu_{31} = \nu_{\parallel\parallel} \\
\nu_{12} = \nu_{32} = \nu_{\parallel\perp} \\
\nu_{21} = \nu_{23} = \nu_{\perp\parallel} \\
G_{12} = G_{32} = G_{\parallel\perp} \\
G_{13} = \frac{E_\parallel}{2(1+\nu_{\parallel\parallel})} = G_{\parallel\parallel}
\end{cases}
\tag{4.69}
$$

Where the subscripts $\parallel$ and $\perp$ refer respectively to the direction parallel to the isotropic bedding plane (directions 1 and 3 here) and perpendicular to the bedding (direction 2).

The compliance tensor is then defined as:

$$
D^e_{ijkl} =
\begin{bmatrix}
\frac{1}{E_\parallel} & -\frac{\nu_{\perp\parallel}}{E_\perp} & -\frac{\nu_{\parallel\parallel}}{E_\parallel} & 0 & 0 & 0 \\
-\frac{\nu_{\parallel\perp}}{E_\perp} & \frac{1}{E_\perp} & -\frac{\nu_{\parallel\perp}}{E_\parallel} & 0 & 0 & 0 \\
-\frac{\nu_{\parallel\parallel}}{E_\parallel} & -\frac{\nu_{\perp\parallel}}{E_\perp} & \frac{1}{E_\parallel} & 0 & 0 & 0 \\
0 & 0 & 0 & \frac{1}{2G_{\parallel\perp}} & 0 & 0 \\
0 & 0 & 0 & 0 & \frac{1}{2G_{\parallel\parallel}} & 0 \\
0 & 0 & 0 & 0 & 0 & \frac{1}{2G_{\perp\parallel}}
\end{bmatrix}
\tag{4.70}
$$

Another important aspect of the anisotropic elasticity is the compressibility of the solid grains. It is expressed through Biot's symmetric tensor which is defined for anisotropic material as follows ((Cheng, 1997)):

EURAD (Deliverable n˚ 7.6) – Modelling report on the effect of temperature on clay host rocks behaviour
Dissemination level: PU
Date of issue of this report: 06/06/2024

Page 63

$$b_{ij} = \delta_{ij} - \frac{D^e_{ijkk}}{3K_s} \tag{4.71}$$

where δ_{ij} is the Kronecker symbol and K_s is the bulk modulus of the solid phase. This expression adopts the micro-homogeneity and micro-isotropy assumptions ((Cheng, 1997)) for which K_s is homogeneous and isotropic at grain scale. The generalised Biot's coefficient reads:

$$b = \frac{b_{ii}}{3} = 1 - \frac{K}{K_s} \tag{4.72}$$

Where K is the generalised drained bulk modulus of the poroelastic material:

$$K = \frac{D^e_{iijj}}{9} \tag{4.73}$$

Following the Biot's tensor definition of Eq. 4.71, the Biot's coefficients for cross-anisotropic materials with isotropic planes oriented parallel to (e1,e3) can be expressed as:

$$b_{\parallel} = 1 - \frac{2D^e_{\parallel\parallel\parallel\parallel} + D^e_{\parallel\parallel\perp\perp}}{3K_s} = 1 - \frac{1 + \nu_{\parallel\parallel} + \nu_{\parallel\parallel}\nu_{\perp\parallel} + \nu_{\perp\parallel}}{3E_{\parallel}E_{\perp}\gamma K_s} \tag{4.74}$$

$$b_{\perp} = 1 - \frac{2D^e_{\perp\perp\parallel\parallel} + D^e_{\perp\perp\perp\perp}}{3K_s} = 1 - \frac{1 - \nu^2_{\parallel\parallel} + 2\nu_{\parallel\perp} + 2\nu_{\parallel\perp}\nu_{\parallel\parallel}}{3E_{\parallel}E_{\perp}\gamma K_s} \tag{4.75}$$

$$\gamma = \frac{1 - \nu^2_{\parallel\parallel} - 2\nu_{\perp\parallel}\nu_{\parallel\perp}(1 + \nu_{\parallel\parallel})}{E^2_{\parallel}E_{\perp}} \tag{4.76}$$

For isotropic materials, the Biot's coefficients reduce to:

$$b = 1 - \frac{K}{K_s} \tag{4.77}$$

$$K = \frac{E}{3(1 - 2\nu)} \tag{4.78}$$

Plastic component

The classical mechanical law ORTHOPLA in LAGAMINE is used in the HITEC project, which is a non-associated elastoplastic model with linear elasticity and a Van Eekelen criterion (VE). It consists of a smoothing of the Mohr Coulomb plasticity surface (Figure 4.20). The yield formulation (Van Eekelen, 1980) reads:

$$II_{\hat{\sigma}} + m\left(I_{\sigma} - \frac{3c}{\tan\phi_c}\right) = 0 \tag{4.79}$$

where I_{σ} is the first stress invariant, $II_{\hat{\sigma}}$ is the second deviatoric stress invariant, c is the cohesion, ϕ_c is the friction angle in compression, m is a parameter of the yield surface defined as follow:

$$m = a(1 + bsin3\beta)^{\eta} \tag{4.80}$$

EURAD (Deliverable n° 7.6) – Modelling report on the effect of temperature on clay host rocks behaviour
Dissemination level: PU
Date of issue of this report: 06/06/2024

Page 64

(a)   (b)
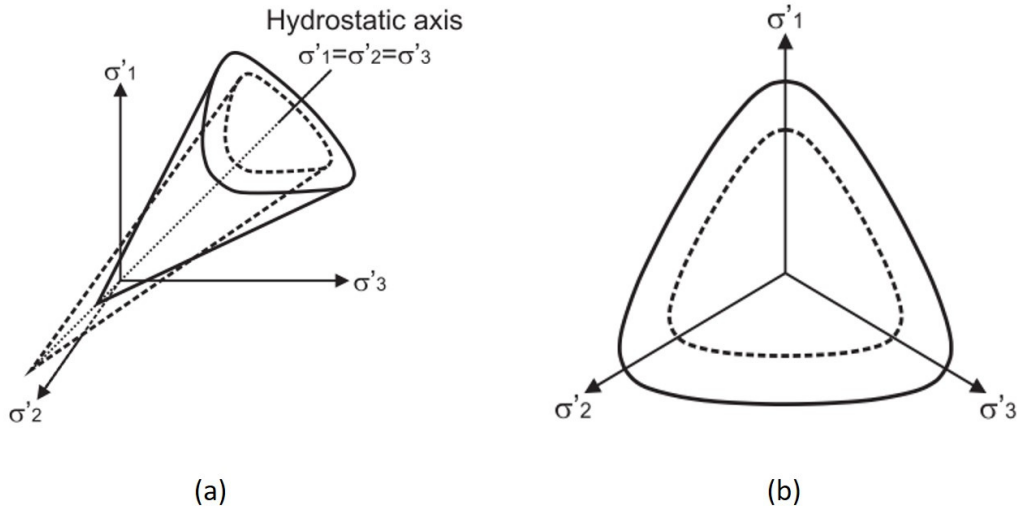
Figure 4.20: Van Eekelen yield surface: (a) in the principal effective stress space, (b) in the deviatoric plane.

where β is the Lode angle given by:

$$\sin(3\beta) = -\frac{3\sqrt{3}}{2}\frac{III_{\hat{\sigma}}}{II_{\hat{\sigma}}^3} \tag{4.81}$$

where $III_{\hat{\sigma}}$ is the third deviatoric stress invariant, a and b are the internal parameters related to the friction angles in compression and in extension, and the default value $\eta = -0.229$ is generally chosen to control the yield surface convexity. The isotropic hardening and/or softening of friction angle and cohesion are considered as a function of Von Mises' equivalent plastic strain ϵ_{eq}^p which is defined as follow:

$$\epsilon_{eq}^p = \sqrt{\frac{2}{3}\hat{\epsilon}_{ij}^p\hat{\epsilon}_{ij}^p} \tag{4.82}$$

where $\hat{\epsilon}_{ij}^p$ is the deviatoric strain tensor determined by the plastic strain tensor ϵ_{ij}^p:

$$\hat{\epsilon}_{ij}^p = \epsilon_{ij}^p - \frac{\epsilon_{ii}^p}{3}\delta_{ij} \tag{4.83}$$

The functions of hardening/softening are introduced by an hyperbolic variation of the internal variables (Barnichon, 1998):

$$\phi_c = \phi_{c,0} + \frac{(\phi_{c,f} - \phi_{c,0})\epsilon_{eq}^p}{B_\phi + \epsilon_{eq}^p} \tag{4.84}$$

$$\phi_E = \phi_{E,0} + \frac{(\phi_{E,f} - \phi_{E,0})\epsilon_{eq}^p}{B_\phi + \epsilon_{eq}^p} \tag{4.85}$$

$$c = c_0 + \frac{(c_f - c_0)\epsilon_{eq}^p}{B_c + \epsilon_{eq}^p} \tag{4.86}$$

where c_0 and c_f are the initial and final cohesions, $\phi_{c,0}$ and $\phi_{c,f}$ are the initial and final compression friction angles, $\phi_{E,0}$ and $\phi_{E,f}$ are the initial and final extension friction angles, and the coefficients B_ϕ and B_c are the values of the equivalent plastic strain where half of the hardening/softening of friction angles and cohesion are reached (Figure 4.21). In this benchmark, the selected host rock exhibits strong cross-anisotropic material behaviour. Figure 4.22 describes the material (orthotropic) axes e_1, e_2, and e_3, which may be not consistent with the global axes x, y, and z. The cross-anisotropic material displays a certain type of symmetry with a symmetry axis (e_2) and an isotropic plane called bedding plane (e_1e_3) normal to the axis (Abelev and Lade, 2004; Lade, 2007). As a result, five independent parameters

EURAD (Deliverable n° 7.6) – Modelling report on the effect of temperature on clay host rocks behaviour
Dissemination level: PU
Date of issue of this report: 06/06/2024

Page 65
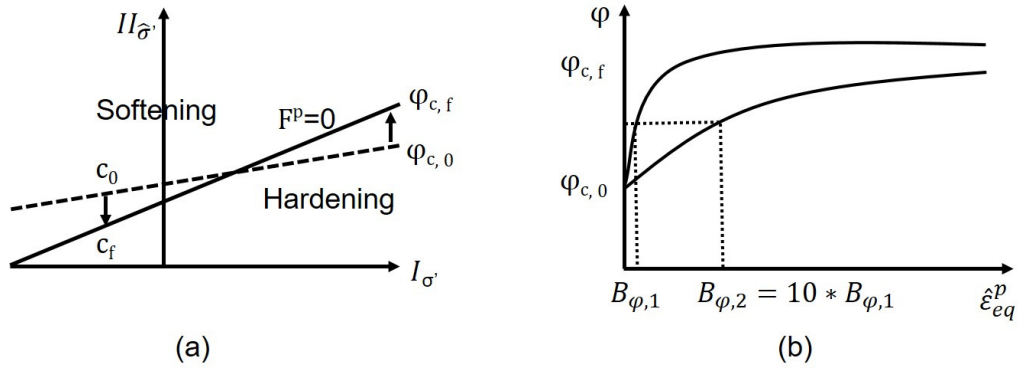
Figure 4.21: Van Eekelen yield surface with hardening/softening: (a) in the stress invariant plane, (b) hyperbolic relation for two values of coefficient B_ϕ.
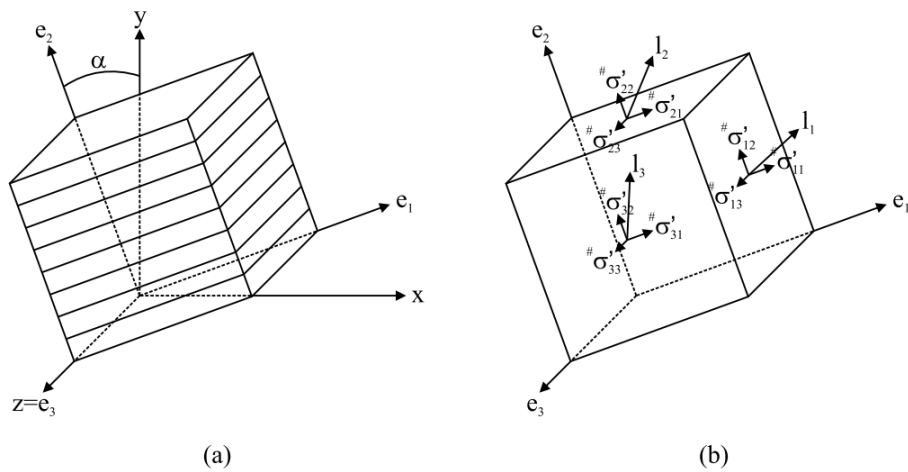
Figure 4.22: Principal axes for cross-anisotropy material: (a) rotation of the bedding plane, (b) stress state in the material axes configuration and loading vectors.

EURAD (Deliverable n° 7.6) – Modelling report on the effect of temperature on clay host rocks behaviour
Dissemination level: PU
Date of issue of this report: 06/06/2024

Page 66

$(E_\parallel, E_\perp, \nu_{\parallel\parallel}, \nu_{\parallel\perp}$ and $G_{\parallel\perp})$ are requested to describe the cross-anisotropic elastic behaviour, and the compressibility of solid grains skeleton is introduced by anisotropic Biot coefficients ($b_\parallel$ and $b_\perp$), where the subscripts $\parallel$ and $\perp$ indicate the directions parallel and normal to the bedding planes respectively. Additionally, plastic behaviour can be also anisotropic and be subjected to loading and material structure orientations. Numerous studies on yield surface variation for anisotropic materials have already been carried out (Lade, 2007; Jaeger, 1960; Hoek and Brown, 1980). Here cohesion anisotropy expressed by the fabric tensor concept is considered. A second order microstructure fabric tensor a_{ij} draws the spatial distribution of cohesion, where the subscripts i, j are corresponding to the principal material microstructure axes (e_1, e_2, and e_3). The cohesion is defined as the projection of the tensor on a unit loading vector l_i which denotes the loading direction relative to the principal material axes (Pietruszczak and Mroz, 2000, 2001; Chen et al., 2010). The component of l_i is determined by the stress resultant imposed on facets of normal axis e_i and reads:

$$l_i = \sqrt{\frac{{}^\sharp\sigma'^2_{i1} + {}^\sharp\sigma'^2_{i2} + {}^\sharp\sigma'^2_{i3}}{{}^\sharp\sigma'_{jk}{}^\sharp\sigma'_{jk}}} \tag{4.87}$$

where ${}^\sharp\sigma'_{jk}$ is given within the reference of material axes. The cohesion hence describes the effect of loading direction relative to material axes (Pietruszczak et al., 2002; Pietruszczak, 2010)):

$$c_0 = a_{ij}l_il_j \tag{4.88}$$

By adopting the deviatoric part of microstructure tensor (Ken-Ichi, 1984):

$$c_0 = \bar{c}(1 + A_{ij}l_il_j) \tag{4.89}$$

$$A_{ij} = \frac{\hat{a}_{ij}}{\bar{c}} = \frac{a_{ij}}{\bar{c}} - \delta_{ij} \tag{4.90}$$

$$\bar{c} = \frac{a_{ii}}{3} \tag{4.91}$$

where $\bar{c}$ is a microstructure parameter, A_{ij} is a traceless symmetric tensor, $A_{ii} = 0$, and $\hat{a}_{ij} = a_{ij} - \frac{a_{kk}}{3}\delta_{ij}$ is the deviatoric part of the microstructure tensor. The higher order tensors are taken into account within Eq. 4.89:

$$c_0 = \bar{c}\left(1 + A_{ij}l_il_j + b_1(A_{ij}l_il_j)^2 + b_2(A_{ij}l_il_j)^3 + \cdots\right) \tag{4.92}$$

where b_1, b_2,... are constants. Within the material axes, $A_{ij} = 0$ for $i \neq j$ with $A_{ii} = A_{11} + A_{22} + A_{33} = 0$ is denoted, and the projection of A_{ij} on the loading vector reads:

$$A_{ij}l_il_j = A_{11}l_1^2 + A_{22}l_2^2 + A_{33}l_3^2 \tag{4.93}$$

Assuming that an isotropic stress state is applied, where $l_1 = l_2 = l_3 = \sqrt{1/3}$ by Eq. 4.87 leads to $A_{ij}l_il_j = A_{ii}/3 = 0$ by Eq. 4.90 and 4.93, and to $c_0 = \bar{c}$ by Eq. 4.89, hereafter $\bar{c}$ is the cohesion under isotropic loading. For cross-anisotropy, $A_{11} = A_{33} = A_\parallel$ and $A_{22} = -2A_{11} = -2A_\parallel$ are implied if the bedding planes are parallel to (e_1, e_3), where $A_\parallel$ is the component of microstructure tensor A_{ij} in the bedding planes. Accordingly:

$$A_{ij}l_il_j = A_\parallel(1 - 3l_2^2) \tag{4.94}$$

where l_2 is the component of l_i acting on the facet parallel to the bedding planes. The Eq. 4.92 can be rewritten as:

$$c_0 = \bar{c}\left(1 + A_\parallel(1 - 3l_2^2) + b_1A_\parallel^2(1 - 3l_2^2)^2 + b_2 1A_\parallel^3(1 - 3l_2^2)^3 + \cdots\right) \tag{4.95}$$

The constants $\bar{c}$, $A_\parallel$, b_1, b_2, ... can be acquired from experimental data. It is worth mentioning that the evolution of cohesion is both dependent on the material fabric and to the loading, hence it is more convenient to define a final cohesion c_f using $c_f = \xi c_0$, where ξ is the ratio of cohesion softening.

EURAD (Deliverable n˚ 7.6) – Modelling report on the effect of temperature on clay host rocks behaviour
Dissemination level: PU
Date of issue of this report: 06/06/2024

Page 67

4.6.2. Second gradient mechanical law

The second gradient model is introduced to define the constitutive relation between double stress and microkinematics. Assuming the microkinematic gradient is only relevant to mechanical part, the second gradient law can be decoupled with classical mechanic law appropriately. A linear isotropic relationship is derived for simplicity from Mindlin (1965):

$$
\begin{bmatrix}
\tilde{\Sigma}_{111} \\
\tilde{\Sigma}_{112} \\
\tilde{\Sigma}_{121} \\
\tilde{\Sigma}_{122} \\
\tilde{\Sigma}_{211} \\
\tilde{\Sigma}_{212} \\
\tilde{\Sigma}_{221} \\
\tilde{\Sigma}_{222}
\end{bmatrix}
= D
\begin{bmatrix}
1 & 0 & 0 & 0 & 0 & \frac{1}{2} & \frac{1}{2} & 0 \\
0 & \frac{1}{2} & \frac{1}{2} & 0 & -\frac{1}{2} & 0 & 0 & \frac{1}{2} \\
0 & \frac{1}{2} & \frac{1}{2} & 0 & -\frac{1}{2} & 0 & 0 & \frac{1}{2} \\
0 & 0 & 0 & 1 & 0 & -\frac{1}{2} & -\frac{1}{2} & 0 \\
0 & -\frac{1}{2} & -\frac{1}{2} & 0 & 1 & 0 & 0 & 0 \\
\frac{1}{2} & 0 & 0 & -\frac{1}{2} & 0 & \frac{1}{2} & \frac{1}{2} & 0 \\
\frac{1}{2} & 0 & 0 & -\frac{1}{2} & 0 & \frac{1}{2} & \frac{1}{2} & 0 \\
0 & \frac{1}{2} & \frac{1}{2} & 0 & 0 & 0 & 0 & 0
\end{bmatrix}
\begin{bmatrix}
\frac{\partial \dot{v}_{11}}{\partial x_1} \\
\frac{\partial \dot{v}_{11}}{\partial x_2} \\
\frac{\partial \dot{v}_{12}}{\partial x_1} \\
\frac{\partial \dot{v}_{12}}{\partial x_2} \\
\frac{\partial \dot{v}_{21}}{\partial x_1} \\
\frac{\partial \dot{v}_{21}}{\partial x_2} \\
\frac{\partial \dot{v}_{22}}{\partial x_1} \\
\frac{\partial \dot{v}_{22}}{\partial x_2}
\end{bmatrix}
\tag{4.96}
$$

where D is the constitutive elastic modulus, representing the physical microstructure and characterising the internal length scale for the width of shear band (Chambon et al., 1998), $\dot{v}_{ij}$ is the time derivative of v_{ij}, and $\tilde{\Sigma}_{ijk}$ is the Jaumann double stress rate (Collin et al., 2006):

$$
\tilde{\Sigma}_{ijk} = D_{ijklmn}\frac{\partial \dot{v}_{lm}}{\partial x_n} = \dot{\Sigma}_{ijk} + \Sigma_{ljk}\omega_{li} + \Sigma_{imk}\omega_{mj} + \Sigma_{ijp}\omega_{pk}
\tag{4.97}
$$

where $\dot{\Sigma}_{ijk}$ is the time derivative of Σ_{ijk}, and ω_{ij} is the spin tensor.

EURAD (Deliverable n˚ 7.6) – Modelling report on the effect of temperature on clay host rocks behaviour
Dissemination level: PU
Date of issue of this report: 06/06/2024

Page 68

4.7. UPC

In this section, the Thermo-Hydro-Mechanical (THM) constitutive model for argillaceous rocks is described. Fourier's law and generalized Darcy's law have been utilized to represent heat conduction and advective water flow, respectively. In adition, an advanced advanced Hyperbolic Mohr-Coulomb (HMC) model has been used to represent the mechanical behaviour of argillaceous rocks.

4.7.1. Thermal flow

Heat conduction is governed by Fourier's law:

$$\mathbf{i}_c = \lambda \cdot \nabla T = \begin{bmatrix} \lambda_1 & 0 & 0 \\ 0 & \lambda_2 & 0 \\ 0 & 0 & \lambda_3 \end{bmatrix} \cdot \nabla T \tag{4.98}$$

where $\mathbf{i}_c$ is the conductive flux, and λ_i is the thermal conductivity in the i-th principal direction. Generally, for cross-anisotropic geomaterials, $\lambda_1 = \lambda_2$ and λ_3 respectively represent the thermal conductivity parallel and perpendicular to the bedding plane.

4.7.2. Hydraulic model

Advective water flow is controlled by the generalized Darcy's law expressed by:

$$q_1 = -\frac{\mathbf{k} k_{rl}}{\mu_1} (\nabla p_1 - \rho_1 g) \tag{4.99}$$

$$\mathbf{k} = \mathbf{k}_0 \frac{\phi^3}{(1-\phi)^2} \frac{(1-\phi_0)^2}{\phi_0^3} \tag{4.100}$$

$$\mathbf{k}_0 = \begin{bmatrix} (\mathbf{k}_0)_1 & 0 & 0 \\ 0 & (\mathbf{k}_0)_2 & 0 \\ 0 & 0 & (\mathbf{k}_0)_3 \end{bmatrix} \tag{4.101}$$

$\mathbf{k}$ is the intrinsic permeability tensor, depending on porosity and direction. k_{rl} is the relative permeability. $\mathbf{k}_0$ is the intrinsic permeability at the reference porosity (ϕ_0), and $(\mathbf{k}_0)_i$ represents the value of $\mathbf{k}_0$ in the i-th principal direction. $\mathbf{g}$ is the gravity forces vector.

Note that, in this study, Eq. (4.99) works only for the elastic case. Instead, when involving the elastoplastic constitutive model, to account for the observed permeability increase due to damage evolution, the intrinsic permeability varies as the accumulated plastic deformation (ε_{eq}^p) increases:

$$\mathbf{k} = \mathbf{k}_0 \left[1 + \beta^k (\varepsilon_{eq}^p)^3 \right]$$

β^k is the hydro-mechanical coupling parameter. The well-known Van-Genuchten model is adopted for the relative permeability law:

$$k_{rl} = \sqrt{S_e} \left[1 - \left(1 - S_e^{1/\lambda} \right) \lambda \right]^2 \tag{4.102}$$

$$S_e = \frac{S_l - S_{lr}}{S_{ls} - S_{lr}} = \left[1 + \left(\frac{S_u}{P} \right)^{\frac{1}{1-\lambda}} \right]^{-\lambda} \tag{4.103}$$

S_e is the effective liquid saturation. S_l is the degree of saturation; S_{lr} is the residual degree of saturation; S_{ls} is the degree of saturation in saturated conditions; P and λ are model parameters.

EURAD (Deliverable n° 7.6) – Modelling report on the effect of temperature on clay host rocks behaviour
Dissemination level: PU
Date of issue of this report: 06/06/2024

Page 69

4.7.3. Mechanical constitutive model

In this study, the advanced Hyperbolic Mohr-Coulomb (HMC) constitutive model with hardening-softening and nonlocal formulation is employed. The mechanical constitutive model is formulated within the framework of elastic-viscoplasticity, which considers non-linearity and hardening-softening properties, anisotropy of stiffness and strength, as well as permeability variation due to damage. In addition, the mechanical properties are coupled with thermal loading and accumulated plastic strains. In addition, the adopted nonlocal and viscoplastic approaches enhance numerical efficiency, providing the possibility to simulate localization phenomena.

The effective stress can be calculated by:

$$\boldsymbol{\sigma}' = \boldsymbol{\sigma} - \mathrm{p_l}\mathbf{B} \tag{4.104}$$

$$\mathbf{B} = \begin{bmatrix} \mathrm{b_1} & 0 & 0 \\ 0 & \mathrm{b_2} & 0 \\ 0 & 0 & \mathrm{b_3} \end{bmatrix} \tag{4.105}$$

with $\boldsymbol{\sigma}'$ = effective stress tensor, $\boldsymbol{\sigma}$ = total stress tensor, $\mathrm{p_l}$ = pore water pressure, $\mathbf{B}$ = Biot's coefficient tensor. The cross-anisotropic Biot's coefficients can be expressed as (Pardoen et al., 2015b; Tan and Konietzky, 2014; Vu et al., 2020):

$$\begin{cases} \mathrm{b_1} = 1 - \dfrac{\mathrm{D_{11} + D_{12} + D_{13}}}{3\mathrm{K_S}} \\[2mm] \mathrm{b_2} = 1 - \dfrac{\mathrm{D_{21} + D_{22} + D_{23}}}{3\mathrm{K_S}} \\[2mm] \mathrm{b_3} = 1 - \dfrac{\mathrm{D_{31} + D_{32} + D_{33}}}{3\mathrm{K_S}} \end{cases} \tag{4.106}$$

$\mathrm{D_{ij}}$ is the ij-th competent in the drained stiffness matrix $\mathbf{D}_e$. $\mathrm{b_i}$ (i = 1, 2, 3) represents the coefficients in the i-th principal direction. Specifically, for cross-anisotropic material, $\mathrm{b_1} = \mathrm{b_2}$ represent the Biot's coefficients in the bedding plane, while $\mathrm{b_3}$ represents the Biot's coefficient in the direction perpendicular to the isotropic plane.

The total strain rate, $\frac{\mathrm{d}\varepsilon}{\mathrm{d}t}$, can be decomposed into instantaneous elastic strain rate ($\frac{\mathrm{d}\varepsilon_e}{\mathrm{d}t}$), time-dependent viscoplastic strain rate ($\frac{\mathrm{d}\varepsilon_{vp}}{\mathrm{d}t}$) and thermal-induced strain rate ($\frac{\mathrm{d}\varepsilon_T}{\mathrm{d}t}$):

$$\frac{\mathrm{d}\varepsilon}{\mathrm{d}t} = \frac{\mathrm{d}\varepsilon_e}{\mathrm{d}t} + \frac{\mathrm{d}\varepsilon_{vp}}{\mathrm{d}t} + \frac{\mathrm{d}\varepsilon_T}{\mathrm{d}t}$$

The elastic strain can be expressed by:

$$\frac{\mathrm{d}\varepsilon_e}{\mathrm{d}t} = \mathbf{C}_e \frac{\mathrm{d}\boldsymbol{\sigma}'}{\mathrm{d}t}$$

where $\mathbf{C}_e$ is the compliance matrix and is characterised by a cross-anisotropic form of Hooke's law. In the local coordinate system, the compliance matrix can be expressed by:

$$\mathbf{C}_e \begin{bmatrix} 1/E_1 & -\nu_1/E_1 & -\nu_2/E_2 & 0 & 0 & 0 \\ -\nu_1/E_1 & 1/E_1 & -\nu_2/E_2 & 0 & 0 & 0 \\ -\nu_2/E_2 & -\nu_2/E_2 & 1/E_2 & 0 & 0 & 0 \\ 0 & 0 & 0 & 2(1+\nu_1)/E_1 & 0 & 0 \\ 0 & 0 & 0 & 0 & 1/G_2 & 0 \\ 0 & 0 & 0 & 0 & 0 & 1/G_2 \end{bmatrix}$$

In addition, the anisotropic stiffness matrix ($\mathbf{D}_e$) is the inverse of the compliance matrix ($\mathbf{C}_e$), i.e., $\mathbf{D}_e =$

EURAD (Deliverable n˚ 7.6) – Modelling report on the effect of temperature on clay host rocks behaviour
Dissemination level: PU
Date of issue of this report: 06/06/2024

Page 70

$[\mathbf{C}_e]^{-1}$, which can be expressed in:

$$
\mathbf{D}_e \begin{bmatrix}
E_1 \dfrac{1 - \bar{n}\nu_2^2}{(1 + \nu_1)\bar{m}} & E_1 \dfrac{\nu_1 + \bar{n}\nu_2^2}{(1 + \nu_1)\bar{m}} & E_1 \dfrac{\nu_2}{\bar{m}} & 0 & 0 & 0 \\[3mm]
E_1 \dfrac{\nu_1 + \bar{n}\nu_2^2}{(1 + \nu_1)\bar{m}} & E_1 \dfrac{1 - \bar{n}\nu_2^2}{(1 + \nu_1)\bar{m}} & E_1 \dfrac{\nu_2}{\bar{m}} & 0 & 0 & 0 \\[3mm]
E_1 \dfrac{\nu_2}{\bar{m}} & E_1 \dfrac{\nu_2}{\bar{m}} & E_2 \dfrac{1 - \nu_1}{\bar{m}} & 0 & 0 & 0 \\[3mm]
0 & 0 & 0 & \dfrac{E_1}{2(1 + \nu_1)} & 0 & 0 \\[3mm]
0 & 0 & 0 & 0 & G_2 & 0 \\[3mm]
0 & 0 & 0 & 0 & 0 & G_2
\end{bmatrix}
$$

where $\bar{n} = E_1/E_2$ and $\bar{m} = \left(1 - v_1 - 2\bar{n}v_2^2\right)$. Table 4.6 shows the definition of elastic constants for cross-anisotropic materials.

The transformation matrix, $\mathbf{T}$, is needed to express the relationship of stiffness matrices between the global and the local coordinate systems. In CODE_BRIGHT, the global coordinate system (x, y, z) first rotates around the z-axis for $\alpha°$, and then around the x-axis for $\beta°$, to obtain the local coordinate system $(1, 2, 3)$ (see Figure 4.23). Thus, the cross-anisotropic stiffness in the global coordinate system $(\hat{\mathbf{D}}_e)$ can be expressed in terms of the stiffness matrix in the local coordinate system $(\mathbf{D}_e)$ and the transformation matrix $(\mathbf{T})$:

$$
\hat{\mathbf{D}} = [\mathbf{T}]^{\mathsf{T}} \mathbf{D}_e [\mathbf{T}] \tag{4.107}
$$

$$
\mathbf{T} = \begin{bmatrix}
l_1^2 & m_1^2 & n_1^2 & l_1 m_1 & m_1 n_1 & l_1 n_1 \\
l_2^2 & m_2^2 & n_2^2 & l_2 m_2 & m_2 n_2 & l_2 n_2 \\
l_3^2 & m_3^2 & n_3^2 & l_3 m_3 & m_3 n_3 & l_3 n_3 \\
2l_1 l_2 & 2m_1 m_2 & 2n_1 n_2 & l_1 m_2 + l_2 m_1 & m_1 n_2 + m_2 n_1 & l_2 n_2 + l_2 n_1 \\
2l_2 l_3 & 2m_2 m_3 & 2n_2 n_3 & l_2 m_3 + l_3 m_2 & m_2 n_3 + m_3 n_2 & l_2 n_3 + l_3 n_2 \\
2l_3 l_1 & 2m_3 m_1 & 2n_1 n_3 & l_3 m_1 + l_1 m_3 & m_3 n_1 + m_1 n_3 & l_3 n_1 + l_1 n_3
\end{bmatrix} \tag{4.108}
$$

where $l_1 = \cos\alpha$, $l_2 = -\sin\alpha\cos\beta$, $l_3 = \sin\alpha\sin\beta$, $m_1 = \sin\alpha$, $m_2 = \cos\alpha\cos\beta$, $m_3 = -\cos\alpha\sin\beta$, $n_1 = 0$, $n_2 = \sin\beta$, $n_3 = \cos\beta$.

Regarding the plastic part, Perzyna's viscoplastic model is used and, therefore, the strain rates can be expressed as:
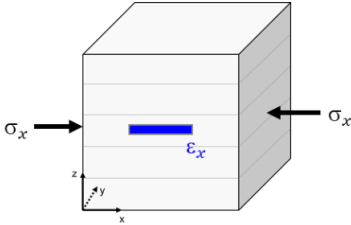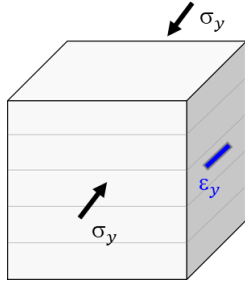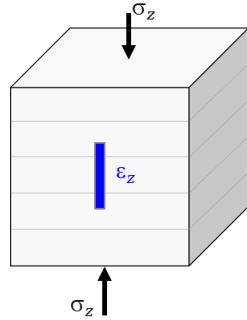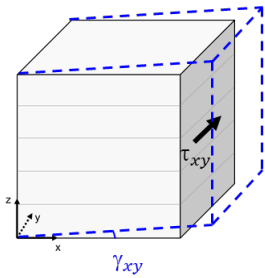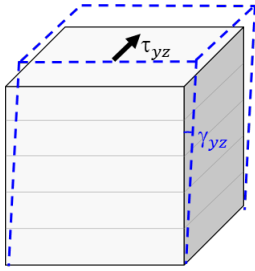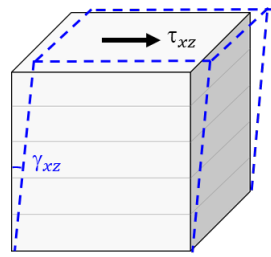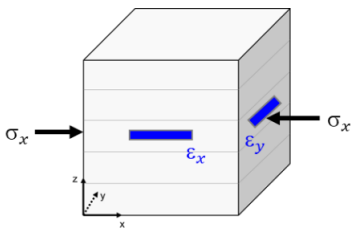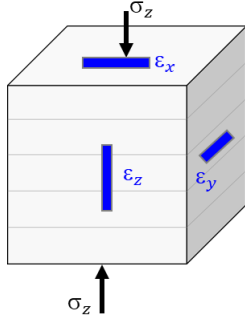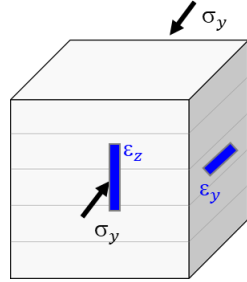
$$
\frac{d\varepsilon_{vp}}{dt} = \frac{1}{\eta_{vp}} \langle \Phi(F) \rangle \frac{\partial G}{\partial \boldsymbol{\sigma}'} \tag{4.109}
$$

$$
\langle \Phi(F) \rangle = \begin{cases} \Phi(F), & \text{if } \Phi(F) \geq 0 \\ 0, & \text{if } (F) < 0 \end{cases} \tag{4.110}
$$

$$
\Phi(F) = F^m \qquad (m \geq 1) \tag{4.111}
$$

η_{vp} is the viscosity of Perzyna's viscoplastic model; F and G represent the overstress function and the viscoplastic potential, respectively, of Perzyna's viscoplastic model, 'm' is the stress power.

EURAD (Deliverable n˚ 7.6) – Modelling report on the effect of temperature on clay host rocks behaviour
Dissemination level: PU
Date of issue of this report: 06/06/2024

Page 71

Table 4.6: Definitions of elastic constants for cross-anisotropic materials.

$$E_1 = \frac{\sigma_x}{\varepsilon_x} \qquad\qquad E_2 = \frac{\sigma_z}{\sigma_z}$$

$$G_1 = \frac{\tau_{xy}}{\gamma_{xy}} \text{ (dependent)} \qquad\qquad G_2 = \frac{\tau_{yz}}{\gamma_{yz}}$$

$$\nu_1 = -\frac{\varepsilon_y}{\varepsilon_x} \qquad \nu_2 = -\frac{\varepsilon_x}{\varepsilon_z} = -\frac{\varepsilon_y}{\varepsilon_z} \qquad \nu_3 = -\frac{\varepsilon_z}{\varepsilon_y} = \frac{E_1}{E_2}\nu_2 \text{ (dependent)}$$

The yield surface and flow rule of the utilized HMC model can be expressed as shown in:

$$F = \sqrt{\frac{J_2}{f_d(\theta)} + (c^* + p_t \tan \varphi^*)^2} - (c^* + p' \tan \varphi^*) \tag{4.112}$$

$$\frac{\partial G}{\partial \boldsymbol{\sigma}'} = \omega \frac{\partial F}{\partial p'}\frac{\partial p'}{\partial \boldsymbol{\sigma}'} + \frac{\partial F}{\partial J_2}\frac{\partial J_2}{\partial \boldsymbol{\sigma}'} + \frac{\partial F}{\partial \theta}\frac{\partial \theta}{\partial \boldsymbol{\sigma}'} \tag{4.113}$$

p' represents Biot's mean effective stress; J_2 is the second invariant of the deviatoric stress tensor; and is the Lode's angle. The term $f_d(\theta)$ defines the shape of the yield surface in the deviatoric plane by $f_d(\theta) = \alpha_d(1 + B_d \sin 3\theta)^{n_d}$. In this study, $\alpha_d = 0.972$, $B_d = 0.838$ and $n_d = -0.229$. Representations of the yield surface in the $p' - J_2$ and in the octahedral plane are shown in Figure 4.24.

$c^*\left(T, \varepsilon_{eq}^p, \delta\right)$ is the asymptotic cohesion, $p_t\left(T, \varepsilon_{eq}^p, \delta\right)$ is the tensile strength, and $\varphi^*\left(\varepsilon_{eq}^p\right)$ is the asymptotic friction angle. Note that the cohesion and tensile strength depend on temperature (T), accumulated

EURAD (Deliverable n˚ 7.6) – Modelling report on the effect of temperature on clay host rocks behaviour
Dissemination level: PU
Date of issue of this report: 06/06/2024

Page 72

(a)   (b)
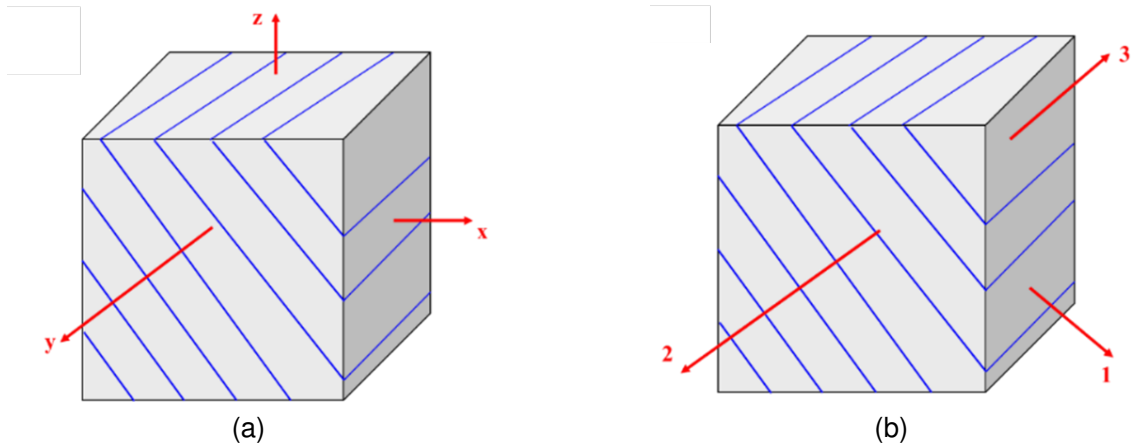
Figure 4.23: (a) Global coordinate system (x, y, z), and (b) local coordinate system $(1, 2, 3)$.

(a)   (b)
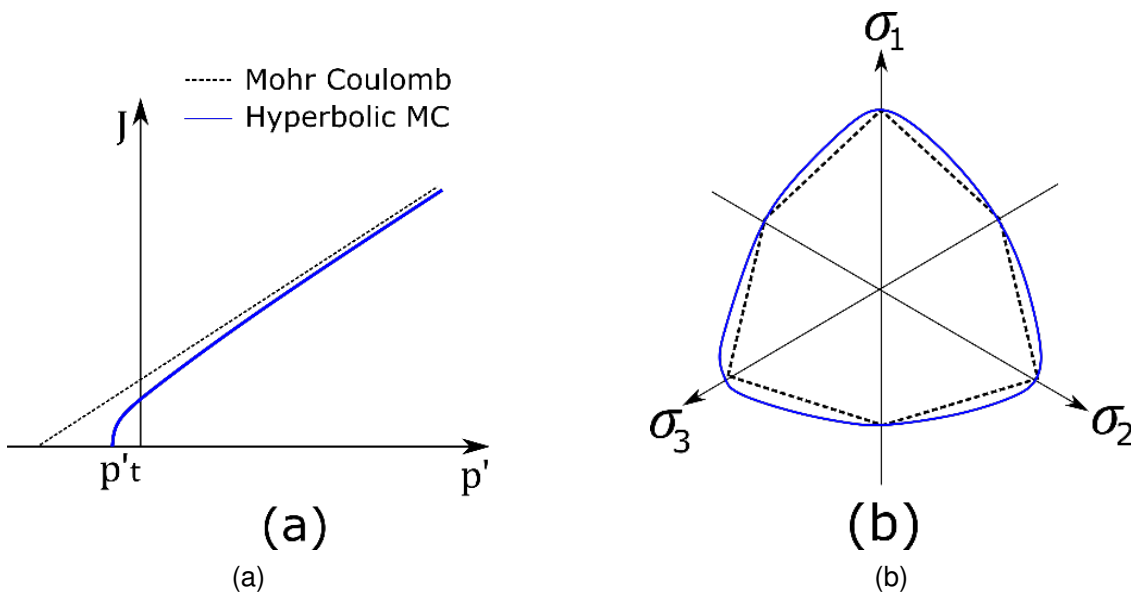
Figure 4.24: Representation of the yield surface in (a) $p - J$ plane, and (b) octahedral plane.

equivalent plastic strains (ε^P_{eq}), and loading direction (δ). In contrast, the friction angle only depends on the accumulated plastic strains (ε^P_{eq}). The evolutions of cohesion and tensile strength with temperature can be expressed as:

$$c^*_{0peak}(T) = c^*_{0peak}(T_0) + c^*_{0peak}(T_0)E_e \{1 - \exp[E_f(T - T_0)]\} \tag{4.114}$$

$$p_{t0peak}(T) = p_{t0peak}(T_0) + p_{t0peak}(T_0)E_g \{1 - \exp[E_h(T - T_0)]\} \tag{4.115}$$

where T is the current temperature, T_0 is the reference temperature, and E_e, E_f, E_g, E_h are coefficients that need to be calibrated based on experimental data.

Furthermore, a hardening-softening model is adopted and an isotropic non-linear hardening-softening law

EURAD (Deliverable n˚ 7.6) – Modelling report on the effect of temperature on clay host rocks behaviour
Dissemination level: PU
Date of issue of this report: 06/06/2024

Page 73

is considered to reproduce the strength evolution:

$$\tan \varphi^* = \begin{cases} \tan \varphi_{ini}^* + \dfrac{\varepsilon_{eq}^p}{a_{hard} + \dfrac{\varepsilon_{eq}^p}{\triangle}}, \triangle = \dfrac{\xi}{\dfrac{\xi}{\tan \varphi_{peak}^* - \tan \varphi_{ini}^*} - a_{hard}}, \varepsilon_{eq}^p \leq \xi \\ \tan \varphi_{peak}^* - \left(\tan \varphi_{peak}^* - \tan \varphi_{res}^*\right) \left[1 - e^{-b_{res}\left(\varepsilon_{eq}^p - \xi\right)}\right], \varepsilon_{eq}^p > \xi \end{cases} \quad (4.116)$$

$$c_0^* = \begin{cases} c_{0peak}^*, \varepsilon_{eq}^p \leq \xi \\ \left(c_{0peak}^* - c_{0post}^*\right) e^{-b_{post}\left(\varepsilon_{eq}^p - \xi\right)} + c_{0post}^* e^{-b_{res}\left(\varepsilon_{eq}^p - \xi\right)}, \varepsilon_{eq}^p > \xi \end{cases} \quad (4.117)$$

$$p_{t0} = \begin{cases} p_{t0peak}, \varepsilon_{eq}^p \leq \xi \\ \left(p_{t0peak} - p_{t0post}\right) e^{-b_{post}\left(\varepsilon_{eq}^p - \xi\right)} + p_{t0post} e^{-b_{res}\left(\varepsilon_{eq}^p - \xi\right)}, \varepsilon_{eq}^p > \xi \end{cases} \quad (4.118)$$

where ε_{eq}^p is a scalar state variable defined by $\varepsilon_{eq}^p = (\varepsilon^p : \varepsilon^p)^{1/2}$, where ε^p is the plastic strain tensor.

The initial position of the yield surface is defined by φ_{ini}^*, c_{peak}^* and p_{tpeak}. It is assumed that plastic deformations before peak strength can occur, so after reaching the yield-limit hardening takes place. During the hardening phase, the cohesion and tensile strength are assumed to remain constant, while, the friction angle evolves from φ_{ini} to φ_{peak}. Peak strength is achieved at $\varepsilon_{eq}^p = \xi$, i.e., ξ is the value of the state variable separating the hardening and softening regimens.

After that, softening occurs, characterised by an exponential decay function; b_{post} and b_{res} are the softening rates related to the post-rupture and residual strengths, respectively. The post-rupture parameters are a function of the peak parameters, as shown in:

$$r_{post} = \frac{c_{0post}^*}{c_{0peak}^*} = \frac{p_{t0post}}{p_{t0peak}}$$

Strength anisotropy is characterised by assuming that c^* and p_t depend on the loading direction. The asymptotic cohesion and tensile strength are defined as:

$$c^* = \Omega(\delta)c_0^* \quad (4.119)$$

$$p_t = \Omega(\delta)p_{t0} \quad (4.120)$$

$\Omega(\delta)$ is a function defining the variation of strength with δ, which is expressed in as:

$$\Omega(\delta) = \frac{Ae^{(\delta_m - \delta)n}}{\left[1 + e^{(\delta_m - \delta)n}\right]^2} + \frac{B}{1 + e^{(\delta_m - \delta)n}} + C \quad (4.121)$$

$$\delta = \cos^{-1} \frac{\mathbf{n} \cdot \mathbf{v}}{|\mathbf{n}| \cdot |\mathbf{v}|} \quad (4.122)$$

where:

$$A = \frac{2(e_1 + 1)(e_2 + 1)(e_1 - e_2 + \Omega_{90} + e_1 e_2 + e_1 \Omega_{90} - e_2 \Omega_{90} - 2e_1 \Omega_m + 2e_2 \Omega_m - e_1 e_2 \Omega_{90} - 1)}{(e_1 - e_2)(e_1 - 1)(e_2 - 1)}$$

$$B = \frac{\Omega_{90} - \dfrac{Ae_1}{(e_1+1)^2} + \dfrac{Ae_2}{(e_2+1)^2} - 1}{\dfrac{1}{e_1+1} - \dfrac{1}{e_2+1}}$$

$$C = 1 - \frac{Ae_2}{(e_2 + 1)^2} - \frac{B}{e_2 + 1}$$

$e_1 = e^{n(\delta_m - 90)}$, $e_2 = e^{n\delta_m}$; $\mathbf{n}$ is the vector normal to the bedding plane, and $\mathbf{v}$ is the direction of the major principle effective stress. Ω_{90}, Ω_m, δ_m and n are material parameters characterizing the strength anisotropy.

EURAD (Deliverable n˚ 7.6) – Modelling report on the effect of temperature on clay host rocks behaviour
Dissemination level: PU
Date of issue of this report: 06/06/2024

Page 74

Nonetheless, instability may occur because softening concentrates on isolated elements, while other elements in their vicinity experience stress relaxation. To solve this problem, the nonlocal approach is used in the presented constitutive model, which means that the behaviour at a Gauss point depends not only on its state but also on the state of neighbouring points, as shown in Figure 4.25(a). The nonlocal approach can eliminate mesh dependency and improve numerical efficiency.

In addition, the viscoplastic approach has been used in this constitutive model (see Figure 4.25(b)), which can be able of homogenizing the spatial distribution of softening strain. Therefore, both the nonlocal approach and viscoplastic approach can benefit the control of the size of the localized zone and, thus, avoid pathological mesh dependency (Günther et al., 2015; Mánica, 2018; Song, 2021).

(a)   (b)
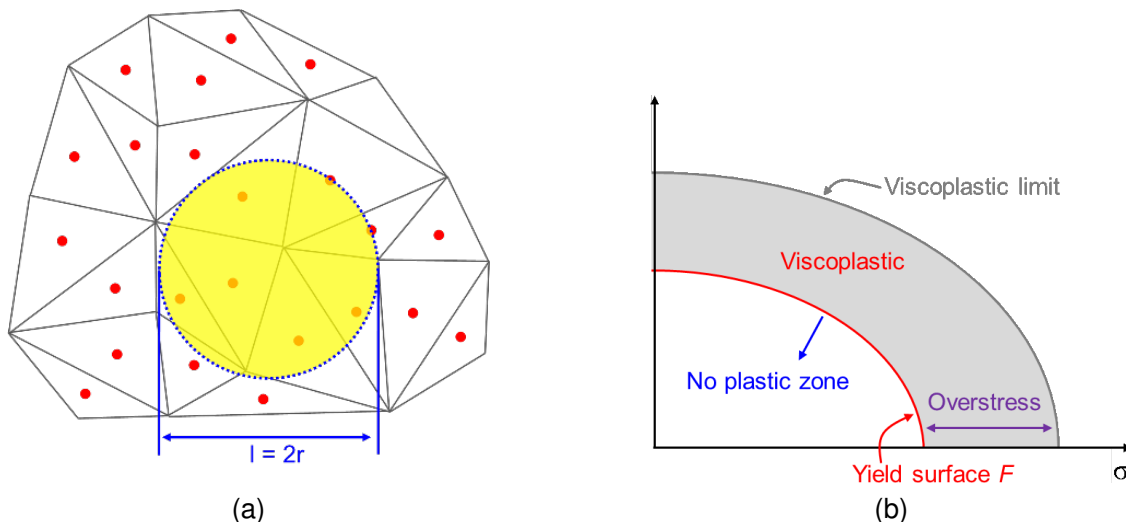
Figure 4.25: Conceptual models of (a) nonlocal approach, and (b) overstress theory of the viscoplastic model.

Finally, the volumetric thermally-induced strain is expressed by:

$$d\varepsilon_T = -\alpha_s\, dT$$

where ε_T is the thermal-induced strain. The anisotropy of thermal expansion coefficients has been implemented in CODE_BRIGHT.

EURAD (Deliverable n˚ 7.6) – Modelling report on the effect of temperature on clay host rocks behaviour
Dissemination level: PU
Date of issue of this report: 06/06/2024

Page 75

5. Generic cases modelling benchmark

5.1. Near-field generic cases

5.1.1. Modelling approaches

5.1.1.1. ANDRA

Andra ran the near-field cases on the Callovo-Oxfordian claystone, and built two grids in Code_Aster and in Comsol for comparison. Both the isotropic and anisotropic cases were run on the Code_Aster model, the Comsol model was run for verification in the isotropic case only. With both codes, the mesh is refined around the tunnel boundary (see Figure 5.1).
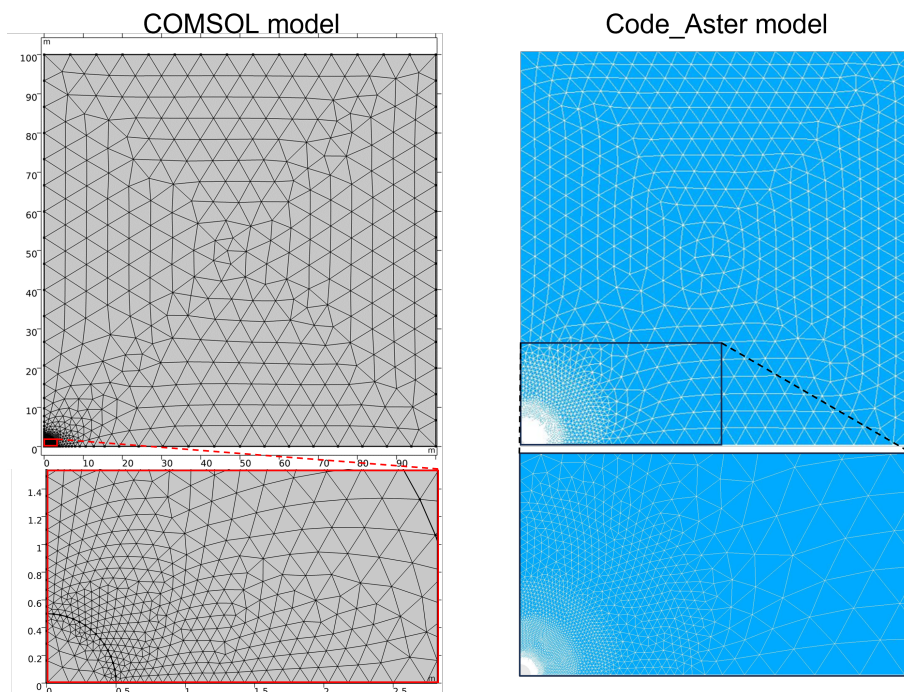
Figure 5.1: Comsol and Code_Aster meshes built by Andra for the near-field cases

Table 5.1: Mesh size

	Mesh type	Number of elements	Computation time (isotropic case)
Code_Aster	Triangular	6594	3 min
Comsol	Triangular	1828	4 min 24 s

5.1.1.2. BGE

BGE performed the modelling of the benchmark exercises for the near field cases in Boom, Opalinus and Callovo-Oxfordian clay. A comprehensive overview and intricate details pertaining to the benchmark simulations are thoroughly outlined in Chapter 2.

As mentioned in Chapter 2, the 2D analyses described in the present report were performed using the finite

element code OpenGeoSys and the finite difference code FLAC3D. They were conducted by assuming plane strain conditions. The domain of analysis is 100 m high and 100 m wide, see Figure 5.2. Due to symmetry, only one quarter of the gallery was simulated. The domain was discretised in 46025 6-noded triangular finite elements with second-order interpolation in OpenGeoSys. The mesh is highly refined around the excavation, where high gradients of pore pressure and stresses are expected. FLAC3D as a 3D finite difference code requires hexahedral meshes. Thus a numerical model consisting of 4040 linear zones have been developed for the analyses of the near field benchmark exercises in FLAC3D.

The initial isotropic stress state determined, shown in Table 2.3, was specified as the initial conditions for the numerical model depending on the host rock. Null horizontal displacements were prescribed at the lateral left boundary corresponding to the symmetry axis, and null vertical displacements were prescribed at the bottom boundary. On the other hand, at the top and right boundaries, the corresponding total stresses were applied. The corresponding liquid pressure, according to the prescribed isotropic conditions, was applied as the initial condition in the domain and as a boundary condition at the top and right boundaries. At the symmetry axis, null fluxes were prescribed. All boundaries except at the gallery wall are thermally adiabatic.
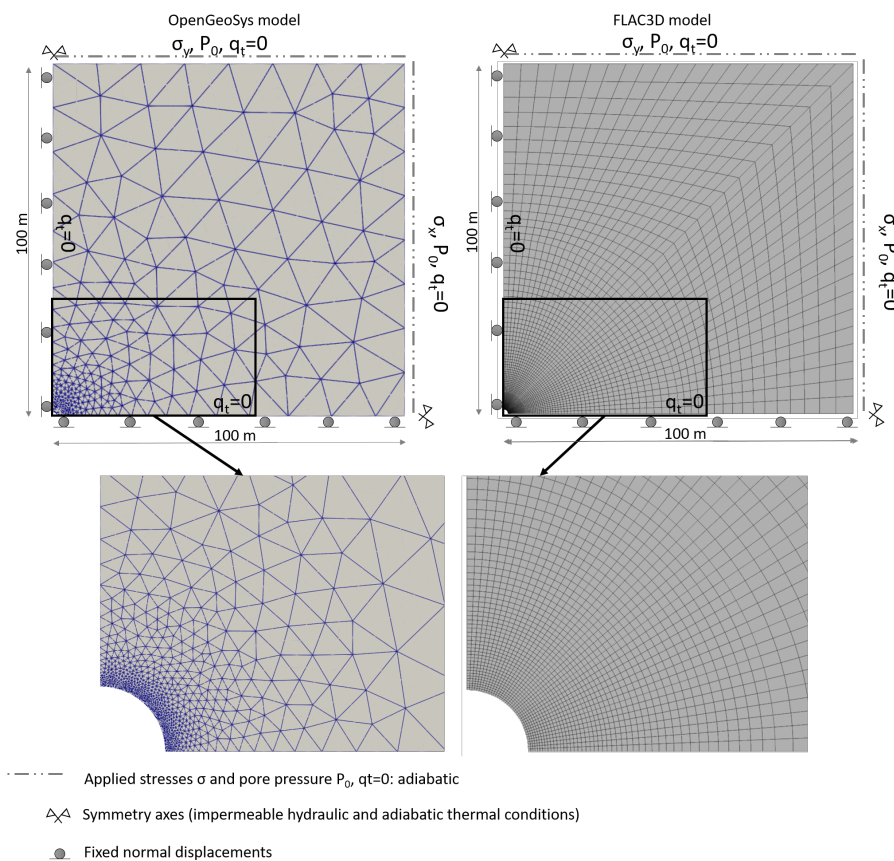
Figure 5.2: Developed numerical models for the near-field cases studied by BGE

5.1.1.3. EDF

The subtask 2.3 of the WP7 focuses on modelling the effects of increased temperature in the near field, where damage could be caused by the excavation of the galleries and by the effects of thermal pressurization and on the effects of increased temperature in the far field led by a risk of tensile and shear failure. For this subtask, two sets (near-field and far-field) of 2D models are created to study the impact of temperature on the behaviour of clay host rocks. For the near-field set, the participants were asked to model two types of host rocks to be chosen between a Callovo-Oxfordian (Cox) claystone, an Opalinus Clay host rock

EURAD (Deliverable n° 7.6) – Modelling report on the effect of temperature on clay host rocks behaviour
Dissemination level: PU
Date of issue of this report: 06/06/2024

Page 77

(OPa) and a Boom Clay host rock. EDF has chosen to model the behaviour of the Callovo-Oxfordian (Cox) claystone as it is one of the most studied rocks in the previous research works of EDF and the Opalinus Clay for comparison. The numerical code used for the latter computations is Code_Aster.

For each of the modelled host rocks, two types of symmetries will be tested for the near-field case: an isotropic symmetry case and an anisotropic symmetry case. Moreover, for the Cox , two types of mechanical constitutive models will be used: an elastic model and a visco-elasto-plastic model developed and used at EDF to model the non-linear behavior of soils and rocks: the LKR (Laigle (2004), Kleine (2007), Raude (2015)) model (see section 4.4). For the time being, the LKR model is only used for the modelling of the Cox host rock due to the unavailability of the Subtask 2.2 experimental results for the Opalinus Clay, that are necessary for the calibration of the later model parameters. The different near-field modelling sub-cases are summarized in figure 5.3:

Geometry	Geomaterial	Mech. Const. model	Symmetry
Near Field	COx. argillite	Elasticity	Isotropy
			Transverse isotropy
		LKR	Transverse isotropy
	Opalinus clay	Elasticity	Isotropy
			Transverse isotropy

Figure 5.3: Near field cases studied by EDF

The geometry of the near-field model is a cross-section of a heating gallery. By considering the symmetric nature of the problem, only a quarter of the full cross-section is modelled and the simulated region measures 100 m in both directions. The mesh of this geometry is presented in the figure below and is done while using quadrangular meshes in the EDZ and triangular meshes elsewhere (refer to section 5.4). This mesh is used to model the two host rocks (OPa and Cox) and contains 28666 mesh elements.
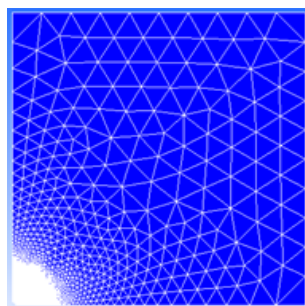
Figure 5.4: Near field mesh considered by EDF - 28666 elements

The boundary conditions applied for the near-field modelling case and the material properties are according to those defined in the MS49 Hitec report.

5.1.1.4. LEI

A model domain of 100 m x 100 m was defined in 2D geometry. The symmetry was taken into account and ¼ of full cross-section was modelled with tunnel radius of R=1.25 m (Figure 5.5). Initial and boundary conditions were set according to specification [EURAD (Milestone n° 49), 2020]. For Cox claystone in-situ total stresses were defined: $\sigma_{xx} = \sigma_{yy} = \sigma_{zz} = 12.5$MPa (for isotropic stress conditions); $\sigma_{xx} = 12.4$MPa, $\sigma_{yy} = 12.7$MPa, $\sigma_{zz} = 16.4$MPa (for anisotropic stress conditions). Absolute pore pressure was

EURAD (Deliverable n˚ 7.6) – Modelling report on the effect of temperature on clay host rocks behaviour
Dissemination level: PU
Date of issue of this report: 06/06/2024

Page 78

set as 4.7 MPa in both analyzed cases. 22 °C was accepted as the initial temperature in both analyzed cases.

The boundary conditions for the model boundaries (except tunnel) were assumed:

- The vertical and the horizontal displacements are respectively fixed at bottom and left boundaries;

- On the top and right boundaries the load was imposed equal to the in-situ stress conditions (vertical stress and horizontal stress, respectively);

- the pore pressure at the top and right model boundaries was set constant (4.7 MPa);

- temperature at the top and right model boundaries was constant (22°C);

- the symmetric boundaries (bottom and left) are impervious (no water and heat flow).

For representation of tunnel excavation, the effective stresses acting on the tunnel wall were described as boundary load. This boundary load was set equal to in-situ stress and was reduced by multiplication by a linear function. This linear function gets values from 1 to 0.05 over 1 day period and helps to represent the stress decrease to 5 percent of initial in-situ stress. The pore water pressure at the tunnel wall (4.7 MPa) was reduced linearly to the atmospheric pressure (0.1 MPa) over 1 day. This was realized by multiplying the initial porewater pressure by a linear function getting values from 1 to 0 over 1 day. The waiting phase (6 months) was simulated by keeping these reduced values. The heating phase was represented by prescribed heat flux of 200 W/m over the tunnel boundary starting after the waiting phase and keeping Dirichlet boundary condition (drained conditions) or switching Dirichlet boundary condition to no flow boundary condition for pore water pressure (undrained conditions).

For the elastic cases, modelling domain was discretized into 3461 triangular mesh elements (Figure 5.5) in thermo-poroelastic model. Timestep size was determined by the solver.

a)   b)
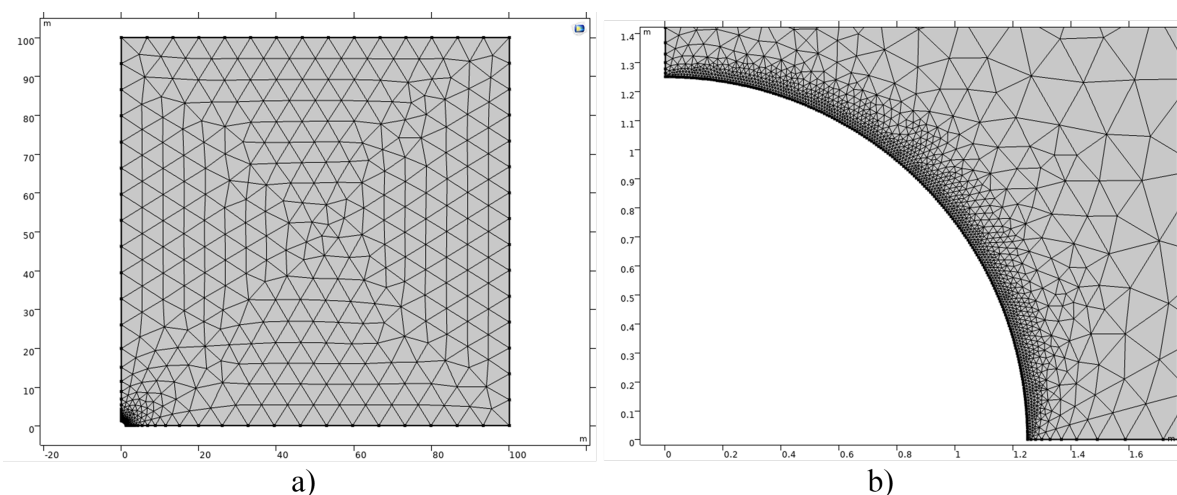
Figure 5.5: Mesh of a) whole model domain, b) mesh close to tunnel boundary

The simulations were performed with COMSOL Mutiphysics (v5.6). All the pre-treatment and post- treatment has been performed within a single platform (COMSOL Mutiphysics). The code run on a standalone personal computer. For isotropic stress conditions and isotropic properties of Cox claystone, the computation time was 4 minutes 39 seconds, number of elements was 3461 triangular elements, type of solver was fully coupled direct solver MUMPS. For anisotropic stress conditions and anisotropic properties of

EURAD (Deliverable n˚ 7.6) – Modelling report on the effect of temperature on clay host rocks behaviour
Dissemination level: PU
Date of issue of this report: 06/06/2024

Page 79

Cox claystone, the computation time was 4 minutes 31 seconds, number of elements was 3461 triangular elements, type of solver was fully coupled direct solver MUMPS.

For modelling of THM response under anisotropic stress and material conditions of Cox with thermo-elastoplastic model, COMSOL Mutiphysics (v6) was used. A finer mesh was used (15077 triangular elements, Figure 5.6) with enhanced discretization close to the tunnel wall. The simulation run 52 minutes 2 seconds; type of solver was fully coupled direct solver MUMPS.

a)   b)
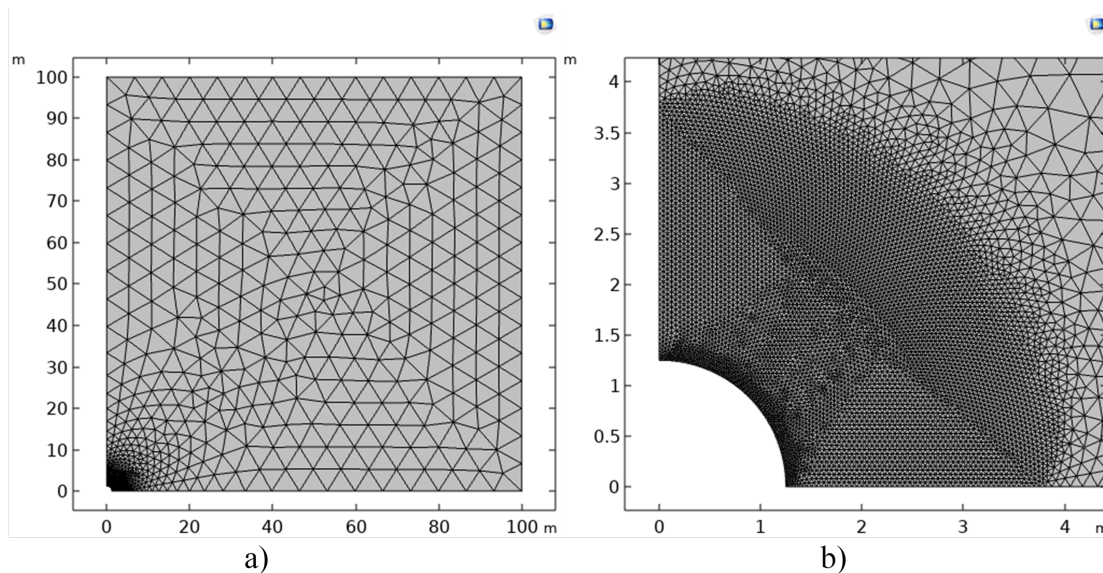
Figure 5.6: Mesh of a) whole model domain, b) mesh close to tunnel boundary

5.1.1.5. ULg

Within the Benchmark organized in WP HITEC, ULg participates in Subtask 2.3 with the modelling of the generic 2D models. A 2D plane strain model considering thermo-hydro-mechanical coupling effects is run on two different kinds of argillaceous rocks, i.e. Boom clay and Callovo-Oxfordian claystone (Cox). The geometry of this model is a cross-section of a heating drift in the host rock. Only a quarter of the full drift is modelled thanks to the symmetry of the problem and the boundary conditions. The radius of the drift wall is 1.25 m with an extension of 100 m to the external boundary.

For elastic cases, the constitutive model used is linear elastic model with isotropy/anisotropy. The mesh consists of 6181 nodes and 2120 elements, and a refinement of the mesh is also included in the zone of interest by getting closer to the gallery's outer face (Figure 5.7). The length and width of the element at the gallery wall are about 10cm and 5 cm respectively. In this case, no support is defined inside the drift wall.

For the modelling of EDZ (only for Cox), the elastoplastic constitutive law is employed. The THM parameters are defined in Table 5.2. The strain localisation in the mode of shear bands is expected to reproduce the thermal effects on the thermo-hydro-mechanical behavior of host rock. However, classical finite element methods suffer the mesh-dependency problem, both of mesh size and orientation, as illustrated by Pietruszczak and Mroz (1981), Zervos et al. (2001a), Collin et al. (2009), and Wu and Wang (2010). This dependency problem can be addressed by introducing the second gradient mechanical law in the numerical computation. The discretisation is performed with 22923 nodes and 5760 elements. The mesh is well refined close to the drift wall to get a better reproduction of rock behaviour in the EDZ. A steel liner is modelled to avoid large deformation of the drift wall. The gap between the drift wall and the liner is defined as 4.6 mm. The gap value is in accordance with the numerical prediction of the average deformation of the drift wall at the end of excavation, when there is no liner imposed. The numerical application is

EURAD (Deliverable n˚ 7.6) – Modelling report on the effect of temperature on clay host rocks behaviour
Dissemination level: PU
Date of issue of this report: 06/06/2024
Page 80

performed with the finite element code Lagamine developed at University of Liège. It is worth mentioning that, the radius of 1.25 m is not the size of French high-level waste (HLW) concept, but only a proposed benchmark in the EURAD Hitec project. The steel liner in the simulation is simply modelled by an infinitely rigid element in the code.

Table 5.2: THM parameters for the Callovo-Oxfordian claystone

	Symbol	Name	Value	Unit
Elastic	ρ_s	Solid phase density	2690	kg/m^3
	$E_\parallel$	Young's modulus parallel to bedding	8000	MPa
	$E_\perp$	Young's modulus normal to bedding	5000	MPa
	$\nu_{\parallel\parallel}$	Poisson's ratio parallel to bedding	0.21	-
	$\nu_{\parallel\perp}$	Poisson's ratio normal to bedding	0.35	-
	$G_\perp$	Shear modulus normal to bedding	2500	MPa
	$b_\parallel$	Parallel Biot's coefficient	0.83	-
	$b_\perp$	Perpendicular Biot's coefficient	0.87	-
Plastic	η	Van Eekelen yield surface convexity parameter	-0.229	-
	$\psi_c = \psi_E$	Dilatancy angles	0.5	°
	$\phi_{c,0}$	Initial compression friction angle	10	°
	$\phi_{c,f}$	Final compression friction angle	23	°
	$\phi_{E,0}$	Initial extension friction angle	7	°
	$\phi_{E,f}$	Final extension friction angle	23	°
	B_ϕ	Friction angle hardening coefficient	0.001	-
	B_c	Cohesion softening coefficient	0.003	-
	$\bar{c}$	Cohesion for isotropic loading	4.1	MPa
	$A_\parallel$	Cohesion parameter	0.117	-
	b_1	Cohesion parameter	14.24	-
Hydraulic	$k_\parallel$	Intrinsic permeability parallel to bedding	$3.9E^{-20}$	m^2
	$k_\perp$	Intrinsic permeability normal to bedding	$1.3E^{-20}$	m^2
	ϕ	Porosity	0.18	-
	χ_w^{-1}	Water compressibility	$4.5E^{-4}$	MPa^{-1}
	ρ_w	Water density	1000	kg/m^3
Thermal	c_s	Solid phase specific heat	790	J/kg/K
	α_s	Linear thermal expansion coefficient	$1.25E^{-5}$	K^{-1}
	c_w	Water specific heat	4180	J/kg/K
	$\lambda_\parallel$	Thermal conductivity parallel to bedding	1.88	W/m/K
	$\lambda_\perp$	Thermal conductivity normal to bedding	1.25	W/m/K

Considering the symmetry conditions, the normal displacements are constrained along the symmetry axes, where an impervious and an adiabatic boundary are defined to avoid the water flow and thermal flow. Additional kinematics boundary conditions with the case of 2nd gradient model are also considered for symmmetry (Zervos et al., 2001b). It requires the radial displacement u_r should keep symmetric on both sides of symmetry axes, which means the normal derivative of u_r with respect to tangential direction θ has to cancel (Figure 5.8). The definition of the second gradient boundary aims to reproduce the evolution of strain localisation similar to the full-drift results, also for the reason of simulation simplicity. (Pardoen et al., 2015a).

To well reproduce the strain localisation, proper definition of internal length scale of second gradient law

EURAD (Deliverable n˚ 7.6) – Modelling report on the effect of temperature on clay host rocks behaviour
Dissemination level: PU
Date of issue of this report: 06/06/2024

Page 81
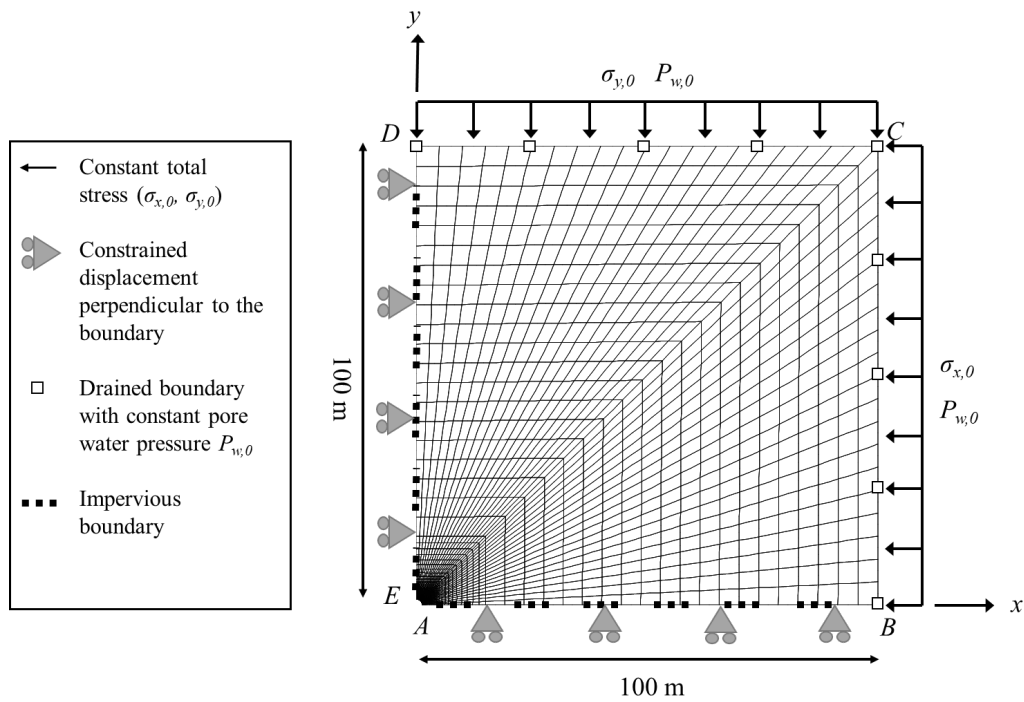
Figure 5.7: Model geometry of the 2D plane strain model for the near-field case in elasticity
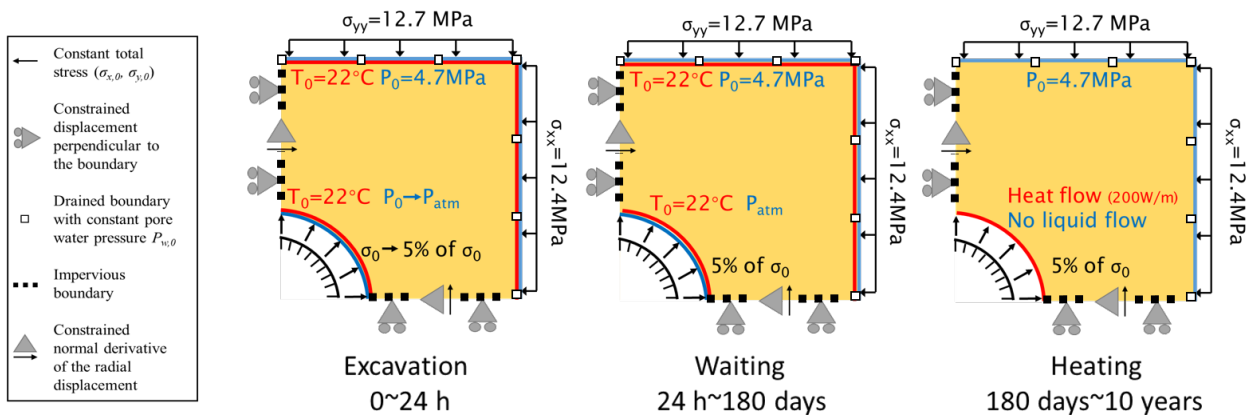
Figure 5.8: Adjusting boundary conditions at the drift wall in modelling EDZ

EURAD (Deliverable n° 7.6) – Modelling report on the effect of temperature on clay host rocks behaviour
Dissemination level: PU
Date of issue of this report: 06/06/2024

Page 82

is of paramount importance. The internal length scale is charaterised with the D value of second gradient law, which is mesh independent (Collin et al., 2006). The value of D = 15000N is applied in the following modelling.

5.1.1.6. UPC

In accordance with specifications, Thermo-Hydro-Mechanical (THM) modelling for three subcases in the near-field/short-term conditions has been carried out:

- Subcase 1: Elastic isotropic case Cox/OPA. Isotropic stress conditions with isotropic elasticity and thermo-elasticity.

- Subcase 2: Elastic anisotropic case Cox/OPA. Anisotropic stress conditions with cross-anisotropic elasticity and thermo-elasticity.

- Subcase 3: Plastic anisotropic case Cox. Anisotropic stress conditions with elastoplastic/damage model. Both unsupported and supported tunnels heve been considered.

The goal of these subcases is first to compare the numerical codes on the fixed exercise (subcases 1 and 2) by prescribing the same boundary conditions and mechanical constitutive laws and properties, while subcase 3 intends to compare different approaches to reproduce the behaviour of the host rock and the development of the Excavation Damaged Zone (EDZ). This section reports the modelling approaches and analyses relative to subcases 1 and 2 for Callovo-Oxfordian claystone (Cox) and Opalinus clay (OPA) together with the modelling approaches and analyses relative to subcase 3 for Cox. As specified, in subcase 1 (isotropic elastic case Cox/OPA) and subcase 2 (anisotropic elastic case Cox/OPA), numerical models of the unsupported tunnel are carried out. In subcase 3 (anisotropic plastic case Cox), both models of unsupported and supported tunnels are considered.

(a). The main physical and thermo-hydro-mechanical properties Subcase 1 refers to a simple elastic isotropic case, considering isotropic mechanical, hydraulic and thermal properties. Subcase 2 is the elastic anisotropic case with principal directions oriented parallel and perpendicular to the bedding plane, which coincides with the horizontal and vertical directions of both Cox and OPA cases. Anisotropy of mechanical, hydraulic and thermal properties is then considered. Along the principal vertical direction, both host rocks exhibit lower intrinsic permeability, elastic modulus and thermal conductivity. Table 5.3 contains the mechanical parameters for isotropic and anisotropic elastic cases used in subcase 1 and subcase 2, while Table 5.4 and Table 5.5 list the parameters concerning the main physical and liquid properties, respectively.

Subcase 3 refers to the plastic anisotropic Cox case, considering the elastoplastic behaviour of the host rock and anisotropy of mechanical, hydraulic, and thermal properties. The main physical and liquid properties used in subcase 3 are the same as the elastic anisotropic Cox case in subcase 2, following Table 5.4 and Table 5.5. Input parameters of the mechanical properties, the retention curves and the hydromechancial coupling parameter β^k are shown in Table 5.6.

EURAD (Deliverable n˚ 7.6) – Modelling report on the effect of temperature on clay host rocks behaviour
Dissemination level: PU
Date of issue of this report: 06/06/2024

Page 83

Table 5.3: *Mechanical parameters for Callovo-Oxfordian claystone (Cox) and Opalinus clay (OPA). Elastic isotropic and anisotropic cases. Iso represents isotropic, while, Ani represents anisotropic.*

			Iso-Cox	Iso-OPA	Ani-Cox	Ani-OPA
Young's modulus	$E_{\parallel}$	[MPa]	7000	6000	8000	8000
	$E_{\perp}$	[MPa]	7000	6000	5000	4000
Poisson's ratio	$\nu_{\parallel\parallel}$	[–]	0.3	0.3	0.21	0.35
	$\nu_{\parallel\perp}$	[–]	0.3	0.3	0.35	0.25
Shear modulus	$G_{\perp}$	[MPa]	$E/2/(1+\nu)$	$E/2/(1+\nu)$	2500	2300

Table 5.4: *Main physical parameters for Callovo-Oxfordian claystone (Cox) and Opalinus clay (OPA). Iso represents isotropic, while, Ani represents anisotropic.*

			Iso-Cox	Iso-OPA	Ani-Cox	Ani-OPA
Intrinsic permeability	$K_{\parallel}$	[m^2]	2.30×10^{-20}	3.0×10^{-20}	3.9×10^{-20}	5×10^{-20}
	$K_{\perp}$	[m^2]	2.30×10^{-20}	3.0×10^{-20}	1.3×10^{-20}	1×10^{-20}
Thermal conductivity	$\lambda_{\parallel}$	[W/m/K]	1.67	1.85	1.88	2.4
	$\lambda_{\perp}$	[W/m/K]	1.67	1.85	1.25	1.3
Solid phase density	ρ_s	[kg/m^3]	2690	2340	2690	2340
Bulk density	ρ_b	[kg/m^3]	2386	2030	2386	2030
Porosity	ϕ	[–]	0.18	0.13	0.18	0.13
Biot coefficient	B	[–]	0.8	0.6	0.8	0.6
Thermal expansion coefficient	α_s	[K^{-1}]	1.25×10^{-5}	1.7×10^{-5}	1.25×10^{-5}	1.7×10^{-5}
Solid phase specific heat	c_s	[J/kg/K]	790	995	790	995
The inverse of solid compressibility	$1/\beta_s$	[MPa^{-1}]	3.43×10^{-5}	8×10^{-5}	2.3×10^{-5}	5.41×10^{-5}

Table 5.5: *Liquid properties.*

Density	ρ_l	[kg/m^3]	1000
Specific heat	c_w	[J/kg/K]	4180
Compressibility [40 °C]	β_w	[MPa^{-1}]	4.5×10^{-4}

EURAD (Deliverable n˚ 7.6) – Modelling report on the effect of temperature on clay host rocks behaviour
Dissemination level: PU
Date of issue of this report: 06/06/2024

Page 84

Table 5.6: Input parameters of the host rock for the plastic anisotropic Cox case, based on the work of Mánica (2018).

Elastic	Young's modulus	$E_{\parallel}$	[MPa]	8000
		$E_{\perp}$	[MPa]	4000
	Poisson's ratio	$\nu_{\parallel\parallel}$	[–]	0.25
		$\nu_{\parallel\perp}$	[–]	0.3
	Shear modulus	$G_{\perp}$	[MPa]	2010
Plastic	Peak strength	$\varphi^*_{ini} = \varphi^*_{peak}$	[°]	20
		c^*_{0peak}	[MPa]	4
		p_{t0peak}	[MPa]	1.5
	Residual strength	r_{post}	[–]	0.3
		φ^*_{res}	[°]	16
	Post-rupture	b_{post}	[–]	160
		b_{res}	[–]	2
	Associativity	ω	[–]	0.2
	Threshold	ξ	[–]	0, i.e., no hardening
Viscoplastic	Viscosity	η_{vp}	[MPa s]	1.3×10^7
	Stress power	m	[–]	1
Strength anisotropy	$\Omega_{90} = 1.3$, $\Omega_m = 0.819$, $\delta_m = 49.7°$, n = 0.1			
Hydraulic	$\beta^k = 4 \times 10^7$, $\lambda^r = 0.32$, P = 17.6 MPa			
Thermal-Mechanical coupling	$E_e = E_g = E_f = E_h = 0$			

EURAD (Deliverable n˚ 7.6) – Modelling report on the effect of temperature on clay host rocks behaviour
Dissemination level: PU
Date of issue of this report: 06/06/2024

Page 85

(b). Modelling of elastic problems (subcases 1 and 2) The model consists of a cross-section of a heating gallery and the host rock perpendicular to the gallery axis. The numerical model developed using CODE_BRIGHT is calculated under plane-strain conditions. Only a quarter of the gallery cross-section is modelled in the numerical model, because of the double symmetry of the geometry and the boundary conditions at both x- and y- axes. The simulated region measures 100 m in both x- and y- directions. In addition, the normal displacements along the bottom (y = 0) and the left (x = 0) boundaries are restrained.

A representation of the domain is shown in Figure 5.9(a) together with the specified study points. Figure 5.9(b) shows the mesh of the numerical model in subcase 1 and subcase 2. A mesh of 4792 quadrilateral elements is adopted, with smaller elements near the excavation. The generalised selective integration procedure implemented in CODE_BRIGHT is able to suppress element locking and hour glassing issues of linear quadrilateral elements.

(a)   (b)
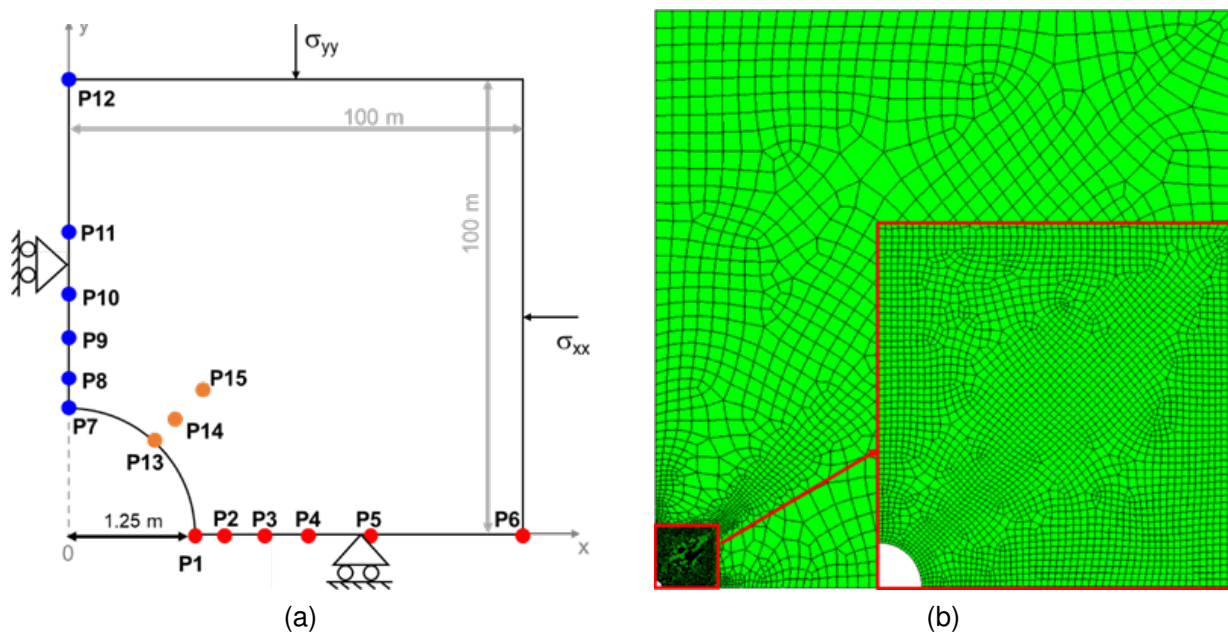
Figure 5.9: (a) Basic features of the two-dimensional plain-strain numerical model for unsupported tunnel and study points (conceptual model), and (b) finite element mesh (4792 quadrilateral elements).

Initial total stress, pore pressure and temperature are considered within the whole domain of the numerical model, as listed in Table 5.7. Depending on the different subcases investigated, different stresses are applied in horizontal, vertical and out of the plane direction. Different pore pressures are also applied in different cases, while a constant temperature of $22\,°C$ is considered for all these subcases.

Table 5.7: Initial conditions of total stresses, pore pressure and temperature. Subcase 1 and subcase 2 in the near-field/short-term analyses. Iso represents isotropic, while, Ani represents anisotropic.

			Iso-Cox	Iso-OPA	Ani-Cox	Ani-OPA
Total stresses	ρ_{xx}	[MPa]	12.5	12.5	12.4	2.2
	ρ_{yy}	[MPa]	12.5	12.5	12.7	4.0
	ρ_{zz}	[MPa]	12.5	12.5	16.4	6.5
Pore pressure	P_0	[MPa]	4.7	4.7	4.7	2.1
Temperature	T	[°C]	22	22	22	22

Boundary conditions along the gallery wall are reported in Table 5.8.

EURAD (Deliverable n˚ 7.6) – Modelling report on the effect of temperature on clay host rocks behaviour
Dissemination level: PU
Date of issue of this report: 06/06/2024

Page 86

Table 5.8: Summary of the boundary conditions applied on the gallery wall. Unsupported tunnel in the near-field/short-term part.

Period	Mechanical conditions	Hydraulic conditions	Thermal conditions
$T_0 - T_0 + 24$ hours: excavation	$\sigma_0 \to 5\%$ of σ_0	$P_0 \to P_{atm}(0.1\,\text{MPa})$	No thermal flow
$T_0 + 24$ hours $- T_0 + 6$ months: waiting	5% of σ_0	$P_l = P_{atm}(0.1\,\text{MPa})$	No thermal flow
$T_0 + 6$ months $- T_0 + 10$ years: heating	5% of σ_0	No liquid flow	Constant thermal flow (200 W/m)

According to specifications, the modelling stages of the unsupported tunnel are represented by three main steps:

- **Excavation stage** (Figure 5.10a): which extends from T_0 to $T_0 + 24$ hours. The pore pressure at the gallery wall is linearly reduced in 24h from its initial value to 0.1 MPa, while on boundaries BC and CD a constant pore pressure is prescribed. Impervious boundaries are assigned on AB and DE. No thermal flux is applied at this stage.

- **Waiting stage** (Figure 5.10b): which extends from $T_0 + 24$ hours to $T_0 + 6$ months. The total stress at the gallery boundary is maintained at 5% of the initial in-situ stress, and constant stress is applied to BC and CD. The pore pressure is fixed and equal to the atmospheric one (0.1 MPa), allowing water to drain towards the tunnel while a constant pore pressure is applied on BC and CD. No thermal flux is applied at this stage.

- **Heating stage** (Figure 5.10c): which extends from $T_0 + 6$ months to $T_0 + 10$ years. Constant stress is applied to BC and CD. Impervious hydraulic boundaries are assigned to the borehole wall, while a constant pore pressure is applied on BC and CD. A heat flux of 200 W/m is applied to the gallery wall over ten years.

(a) Excavation (0 → 1 day) (b) Waiting (1 day → 180 days) (c) Heating (180 days → 10 years)
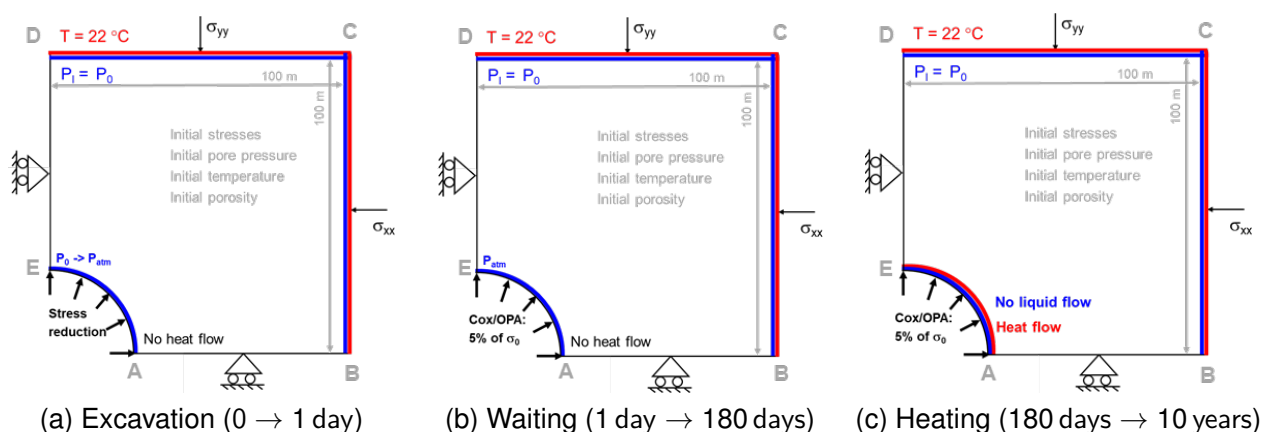
Figure 5.10: Boundary conditions for the unsupported tunnel in different modelling stages: (a) excavation stage, (b) waiting stage, and (c) heating stage.

(c). Modelling of plastic problems (subcase 3)   As specified, both unsupported and supported tunnels are considered in subcase 3. In terms of the unsupported tunnel, the geometry, initial and boundary

EURAD (Deliverable n˚ 7.6) – Modelling report on the effect of temperature on clay host rocks behaviour
Dissemination level: PU
Date of issue of this report: 06/06/2024

Page 87

conditions and modelling stages are the same as those for the elastic anisotropic Cox case. Table 5.4 and Table 5.5 list the main physical and liquid properties, and Table 5.6 contains the input parameters of the elastoplastic model. The internal length for the nonlocal formulation (l_s) is adopted as 0.1 m. A mesh of 47 933 quadrilateral elements is adopted, with smaller elements near the excavation, as shown in Figure 5.11.
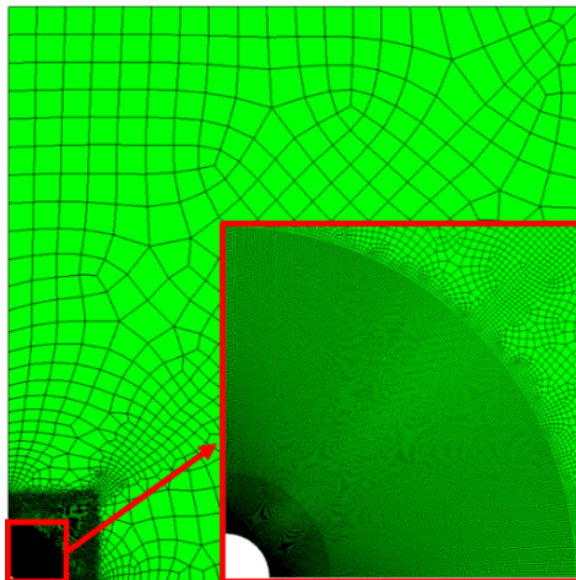
Figure 5.11: Finite element mesh (47 933 quadrilateral elements). Unsupported tunnel in the plastic anisotropic Cox case.

As specified for the supported tunnel defined by Task 2.3, a 2.5 cm-thick steel liner (the external diameter being equal to the excavated diameter) is set at the start of the heating phase (i.e., t = 6 months). Figure 5.12(a) shows the basic features of the numerical model for the supported tunnel, while Figure 5.12(b) gives the mesh in the numerical simulations. A mesh of 28 205 quadrilateral elements is adopted.

(a)

(b)
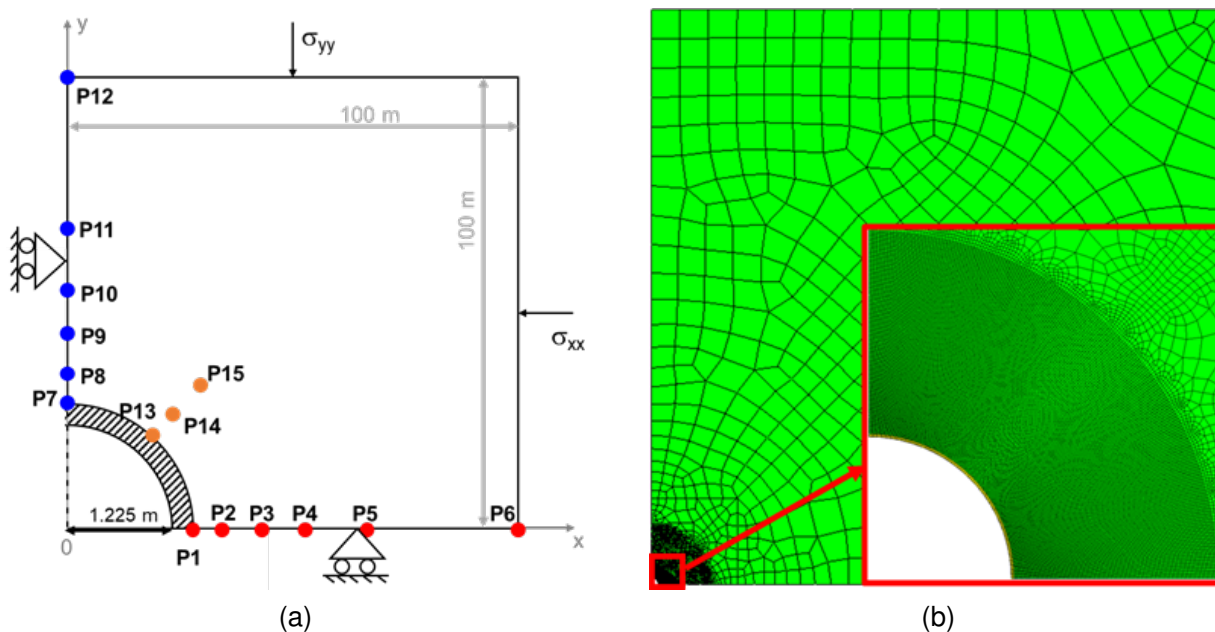
Figure 5.12: (a) Basic features of the two-dimensional plain-strain numerical model for supported tunnel and study points (conceptual model), and (b) finite element mesh (28 205 quadrilateral elements).

The mechanical, hydraulic and thermal properties of the host rock are the same as those used in the

EURAD (Deliverable n˚ 7.6) – Modelling report on the effect of temperature on clay host rocks behaviour
Dissemination level: PU
Date of issue of this report: 06/06/2024

Page 88

numerical model of the unsupported tunnel, except for the internal length for the nonlocal formulation (l_s) that is adopted as $0.07 \, \text{m}$. Table 5.9 lists the material parameters of the steel liner.

Table 5.9: Input parameters of the steel liner.

Young's modulus	E	[MPa]	1.8×10^5
Poisson's ratio	ν	[–]	0.3
Porosity	n	[–]	0.01
Biot coefficient	B	[–]	1.0
Intrinsic permeability	K_x	[m^2]	1×10^{-30}
	K_y	[m^2]	1×10^{-30}
Thermal conductivity	ρ_{dry}	[W/m/K]	80
	ρ_{sat}	[W/m/K]	80
Solid phase specific heat	c_p	[J/kg/K]	550
Solid phase density	ρ_s	[kg/m^3]	7900
Thermal expansion coefficient	α_s	[K^{-1}]	1.4×10^{-5}

According to specifications, the modelling of the supported tunnel is reproduced in three main stages:

- **Excavation stage**: the same as plastic anisotropic Cox case for unsupported tunnel.

- **Waiting stage**: the same as plastic anisotropic Cox case for unsupported tunnel.

- **Heating stage**: which extends from $T_0 + 6 \, \text{months}$ to $T_0 + 10 \, \text{years}$. The steel liner is suddenly installed at the moment of $t = 6 \, \text{months}$, while, at the same time, the applied support forces are removed and the support forces are only provided by the support-rock interaction. Constant stress and pore pressure are applied on BC and CD. A heat flux ($200 \, \text{W/m}$) and a constant pore pressure ($0.1 \, \text{MPa}$) are applied at the inner boundary of the steel liner over ten years.

(a) Excavation (0 → 1 day) (b) Waiting (1 day → 180 days) (c) Heating (180 days → 10 years)
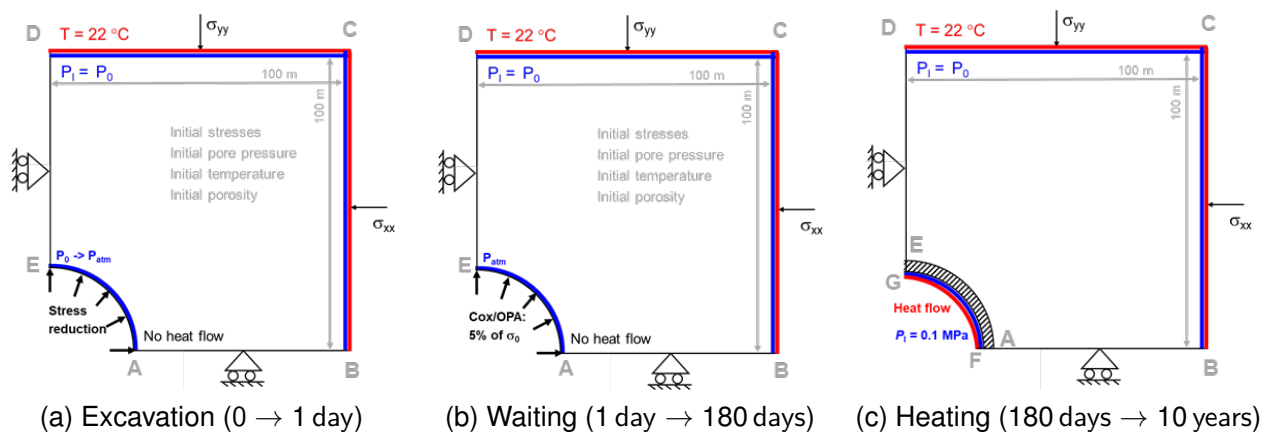
Figure 5.13: Boundary conditions of the supported tunnel at different modelling stages: (a) excavation stage, (b) waiting stage, and (c) heating stage.

EURAD (Deliverable n˚ 7.6) – Modelling report on the effect of temperature on clay host rocks behaviour
Dissemination level: PU
Date of issue of this report: 06/06/2024

Page 89

5.1.2. Modelling results for the elastic isotropic case

Seven modelling teams took part in the near-field benchmarking exercise. Three teams modelled the Boom clay and Opalinus clay cases and six teams worked on the Callovo-Oxfordian case (Table 5.10).

Table 5.10: Choice of near-field cases

	ANDRA	BGE	EDF	EUR	LEI	ULg	UPC
Boom Clay		x		x		x	
Callovo-Oxfordian	x	x	x	x	x	x	x
Opalinus Clay		x	x				x

All the teams got matching results in the elastic isotropic case (Figure 5.14, Figure 5.15, and Figure 5.16). The codes give very consistent results on the temperature evolution in the three host rocks, predicting a maximum temperature after 10 years of heating of 75 °C in the Boom Clay, 76 °C in the Callovo-Oxfordian claystone, and 74 °C in the Opalinus Clay.

During the excavation stage, the pore pressure linearly decreases in the gallery. The applied drained boundary condition allows pore pressure to be reduced during the waiting phase until the heating stage begins. In the heating stage, an undrained boundary condition is applied to the gallery wall, and a fast pore pressure increase is observed. This type of thermal pressurization is caused by the difference between the thermal expansion coefficients of the pore water and the solid skeleton. The obtained maximum pore pressure is around 3 MPa in Boom Clay, 11 MPa in the Callovo-Oxfordian and 9 MPa in the Opalinus Clay.

The radial displacements are also very consistent for all the codes. During the excavation stage, the host rock converges towards the tunnel wall (positive displacement). In the waiting stage, the convergence continues due to water drainage. Finally, the host rock starts to dilate during the heating stage, except at points located at the gallery wall where the host rock keeps a constant convergence. The final displacement after 10 years of heating is larger in the more plastic Boom Clay (ca. 5 mm at the P4 point, 5 radii away from the gallery wall) than in more consolidated Callovo-Oxfordian and Opalinus clays (ca. 3 mm in both cases).

All codes match well also on the stress evolution, however in the Boom clay case, the stress calculation at points P3 and P4 differs a bit with FLAC3D (Figure 5.14) in the waiting and heating stages. In the Cox case, a smooth stress reduction function was applied during excavation (between 0 and 1 day) in the Andra Comsol model instead of a linear one. It explains why the stress evolution is different, with a slower start (Figure 5.15). However, this does not impact the results at the end of excavation and during the heating phase.

For all the codes and in all three host rocks, the excess pore pressure generated due to thermal pressurisation seems to induce tensile (positive) effective horizontal stresses at the gallery wall (point P1). This effect is very local as no failure is shown at point P2. However, in-situ observations show that this area is already fractured after excavation (development of the excavation-damaged zone, EDZ). This simple elastic approach cannot model properly the behaviour of the formation there.

EURAD (Deliverable n° 7.6) – Modelling report on the effect of temperature on clay host rocks behaviour
Dissemination level: PU
Date of issue of this report: 06/06/2024

Page 90
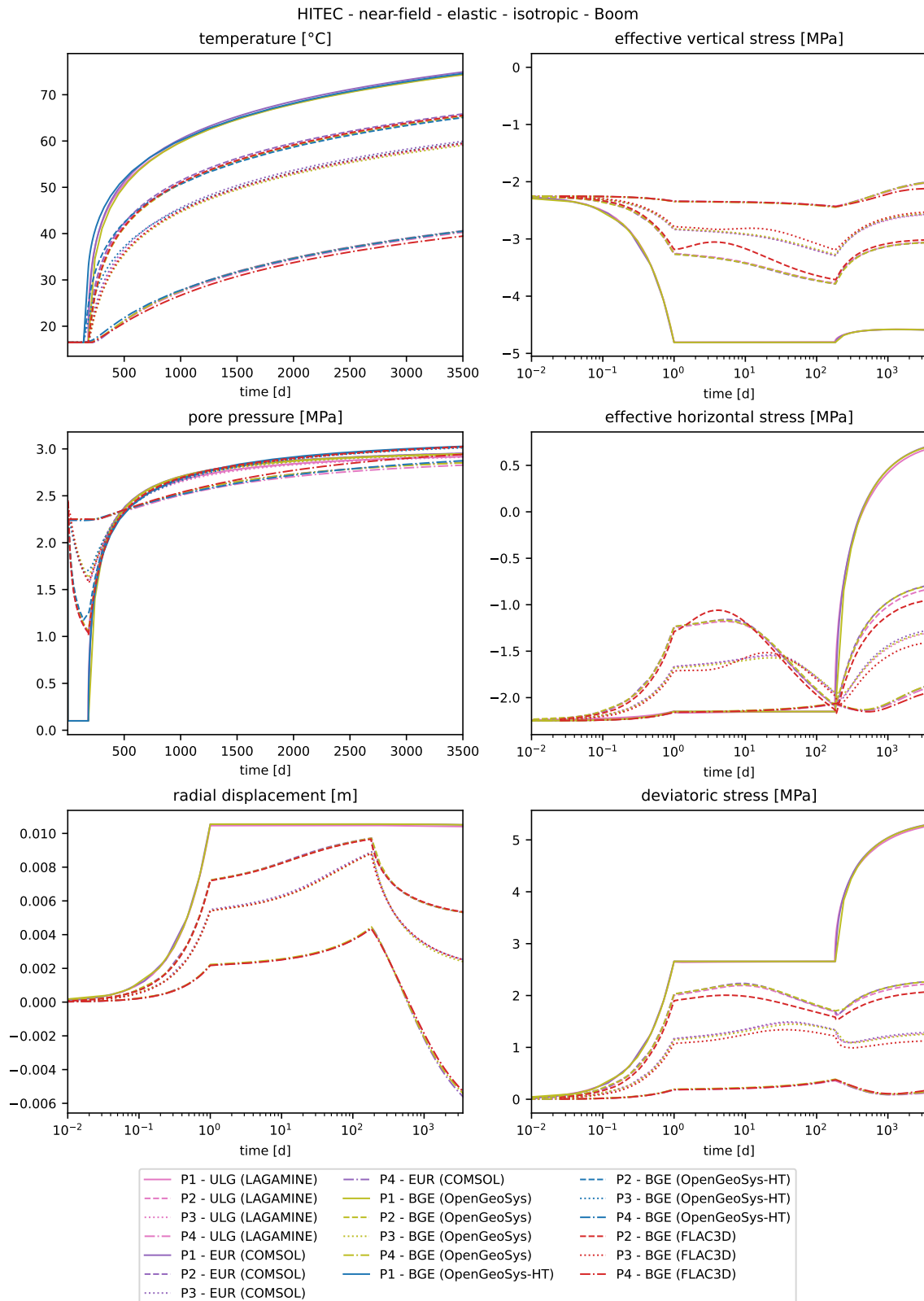
Figure 5.14: Evolution of temperature, pore pressure, radial displacement and stresses for Boom clay - isotropic case

EURAD (Deliverable n˚ 7.6) – Modelling report on the effect of temperature on clay host rocks behaviour
Dissemination level: PU
Date of issue of this report: 06/06/2024

Page 91
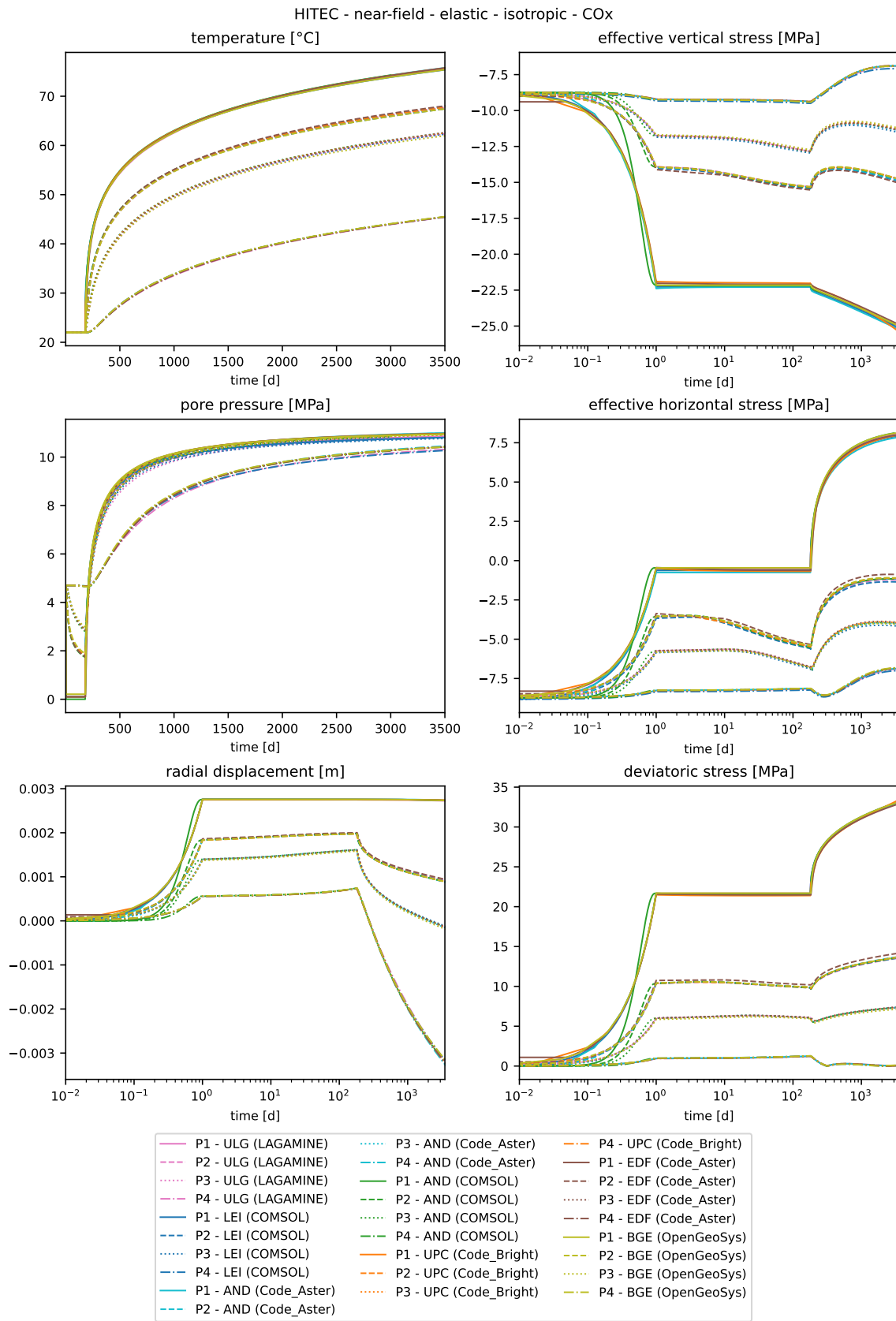
Figure 5.15: Evolution of temperature, pore pressure, radial displacement and stresses for the Callovo-Oxfordian clay - isotropic case

EURAD (Deliverable n° 7.6) – Modelling report on the effect of temperature on clay host rocks behaviour
Dissemination level: PU
Date of issue of this report: 06/06/2024

Page 92
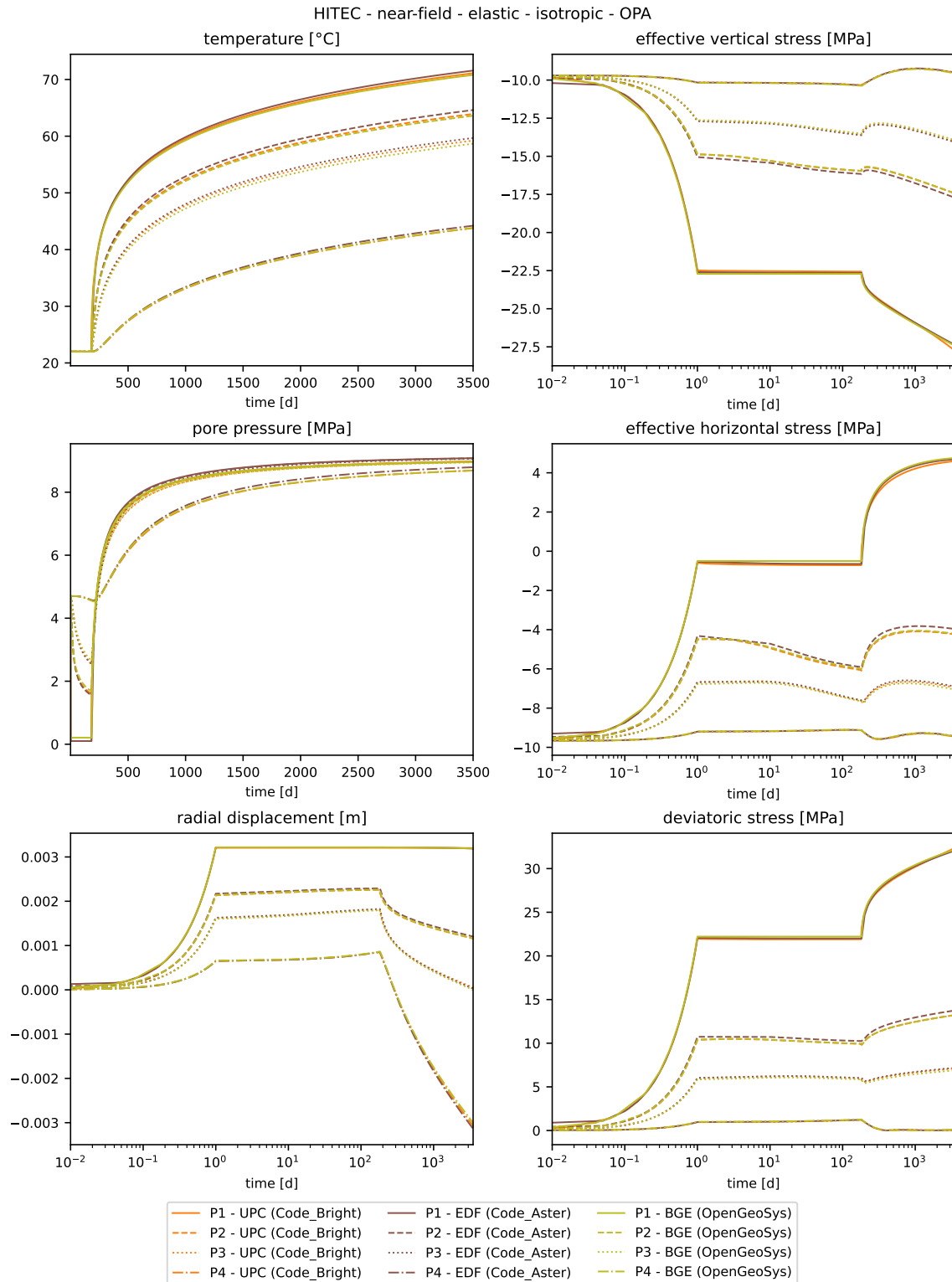
Figure 5.16: Evolution of temperature, pore pressure, radial displacement and stresses for Opalinus clay - isotropic case

EURAD (Deliverable n˚ 7.6) – Modelling report on the effect of temperature on clay host rocks behaviour
Dissemination level: PU
Date of issue of this report: 06/06/2024

Page 93

5.1.3. Modelling results for the elastic anisotropic case

Three teams have been modelling the anisotropic case on the Boom clay: BGE, Euridice (Comsol) and ULiège (Lagamine). BGE ran the case with two process models on OpenGeoSys (OGS), hydrothermal (HT) and THM. All the codes get very consistent results, except on the pore pressure (Figure 5.17). The hydrothermal model in OGS overestimates the pressure increase during the heating phase. This discrepancy is still being investigated at the time of writing.

The seven participating teams have been modelling the Cox anisotropic case: Andra, BGE, EDF, Euridice, LEI, ULg and UPC. Overall the codes agree well on the temperature, displacements and stress evolution (Figure 5.18). Some discrepancies are however observed once again on the pore pressure prediction: most teams predict a maximum pressure of 11.4-11.5 MPa at the tunnel wall, but BGE and EDF get lower estimates at 11.1 and 10.5 MPa respectively. As both Andra and EDF used Code_Aster (but different versions of the code), these differences may be due to the way the teams set up their model (mesh, time step, convergence criteria, etc.). At the beginning of the exercise, the initial results were actually very scattered because of ambiguities on some input parameters and especially on the anisotropic Poisson's ratios. More consistent results were obtained after some iterations, thanks to a good communication between the modelling teams and the WMOs.

The Opalinus clay case was modelled by BGE, EDF and UPC. There again, BGE and EDF predict a lower pore pressure than UPC, but the three teams agree on the general behaviour of the host rock (Figure 5.19). Compared to the Cox, a much lower maximum pore pressure is predicted with the anisotropic properties (around 6 MPa vs. 9 MPa with the isotropic parameters).

For all three host rocks, the anisotropy results in higher temperatures and pressures parallel to bedding than perpendicular for points located at the same distance from the tunnel wall. As for the isotropic case, all the codes predict tensile effective horizontal stresses at the tunnel wall for all three host rocks. More advanced models are needed to take into account the formation and the presence of the EDZ, this was the purpose of the last step of the near-field exercise (5.1.4).

EURAD (Deliverable n° 7.6) – Modelling report on the effect of temperature on clay host rocks behaviour
Dissemination level: PU
Date of issue of this report: 06/06/2024

Page 94
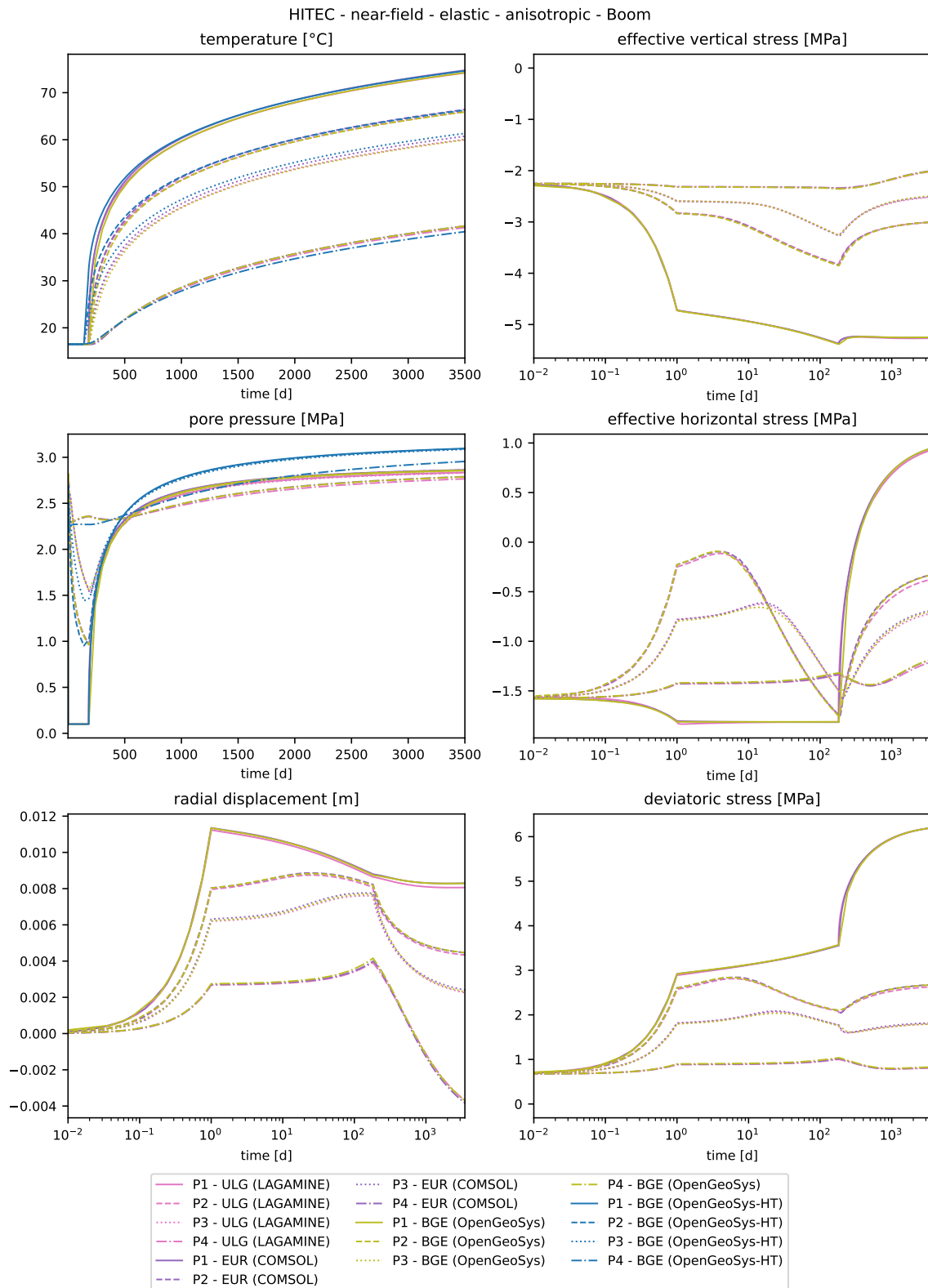
Figure 5.17: Evolution of temperature, pore pressure, radial displacement and stresses for Boom clay - elastic anisotropic case

EURAD (Deliverable n° 7.6) – Modelling report on the effect of temperature on clay host rocks behaviour
Dissemination level: PU
Date of issue of this report: 06/06/2024

Page 95
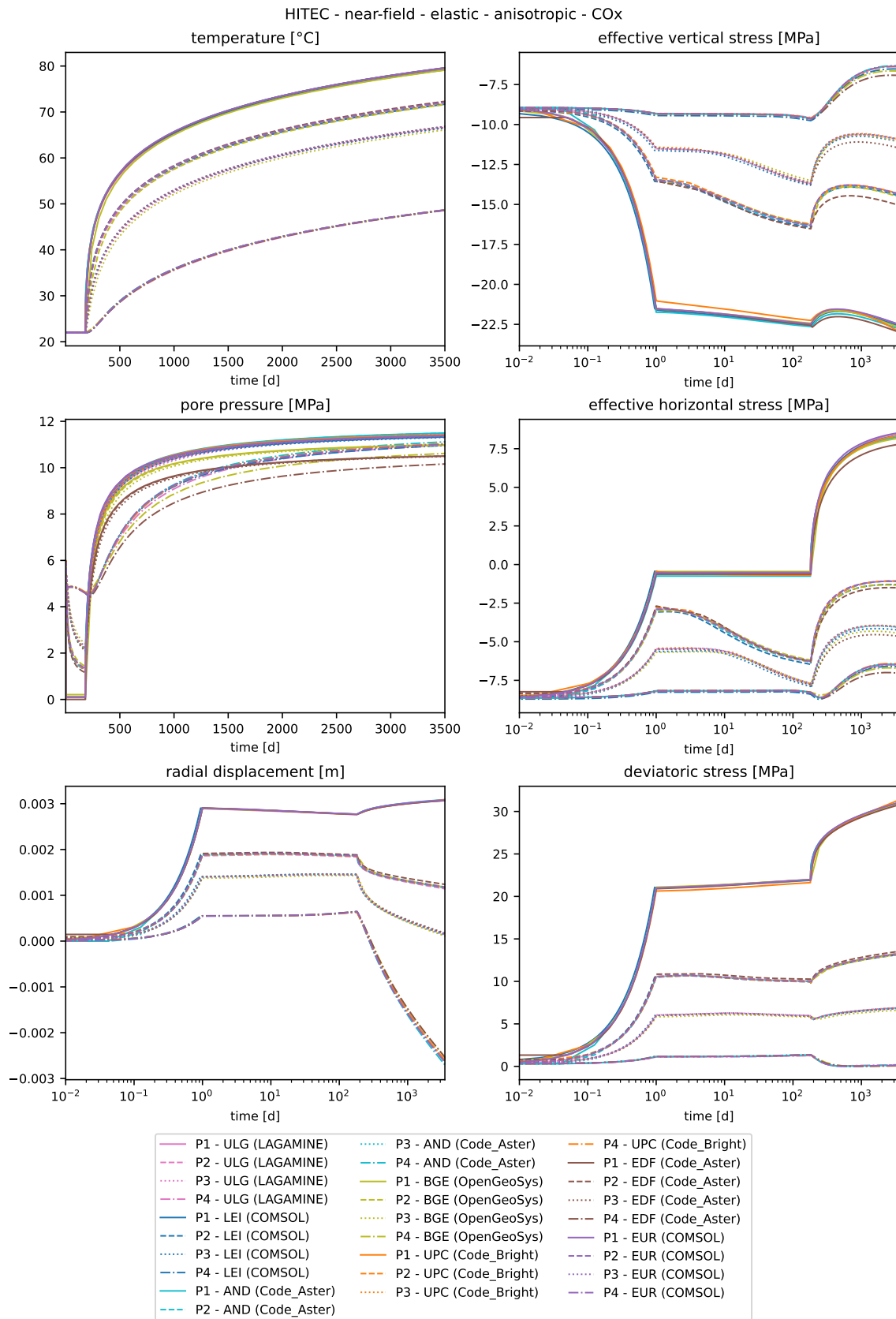
Figure 5.18: Evolution of temperature, pore pressure, radial displacement and stresses for Cox claystone - elastic anisotropic case

EURAD (Deliverable n° 7.6) – Modelling report on the effect of temperature on clay host rocks behaviour
Dissemination level: PU
Date of issue of this report: 06/06/2024

Page 96
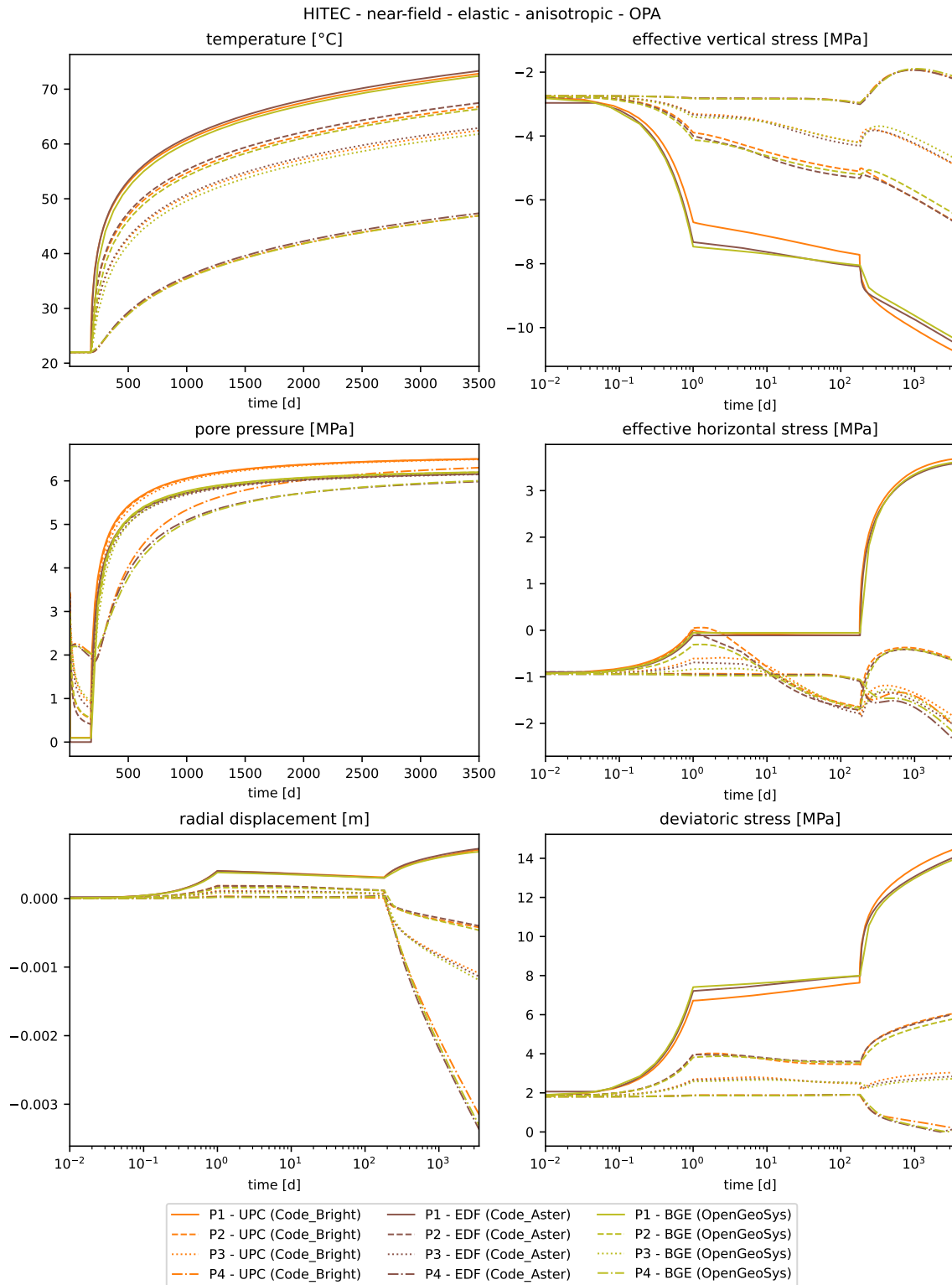
Figure 5.19: Evolution of temperature, pore pressure, radial displacement and stresses for Opalinus clay - elastic anisotropic case

EURAD (Deliverable n° 7.6) – Modelling report on the effect of temperature on clay host rocks behaviour
Dissemination level: PU
Date of issue of this report: 06/06/2024

Page 97

5.1.4. Modelling of the EDZ

5.1.4.1. Andra

In the framework of an ongoing collaborative scientific research agreement, Ineris developed for Andra an anisotropic elastoplastic, damage and viscoplastic model for the Cox claystone. This model is described in more details in section 4.1. This new model was tested on the last subtask of the near-field benchmarking exercise to model the development of the EDZ after excavating the gallery and after heating.

Three numerical simulations are performed: thermo-poro-elasticity (using the proposed model with infinite strengths and creep deactived) aimed to check the proposed model with several physics, thermo-poro-elasto-plasticity (proposed model with true strengths and without creep) and thermo-poro-elasto-visco-plasticity (full proposed model). In the thermo-poro-elasto-plastic case, the evolutions between the ends of excavation (1 d) and heating (10 y) of the EDZ extension, the damage rate and the equivalent shear plastic strain are shown in Figure 5.20. The extensions of the damaged and residual plastic zones (ZD) after the peak strength or plastic zones in pre-peak (hardening) do not progress after ten days of drainage (t = 11 d) in the entire drainage and heating phases. On the other hand, the magnitudes of damage and plastic strains are still increasing in these two phases. As an indication, the plastic strain is 65% higher between the end of excavation and drainage and 10% higher after 10 days of heating.
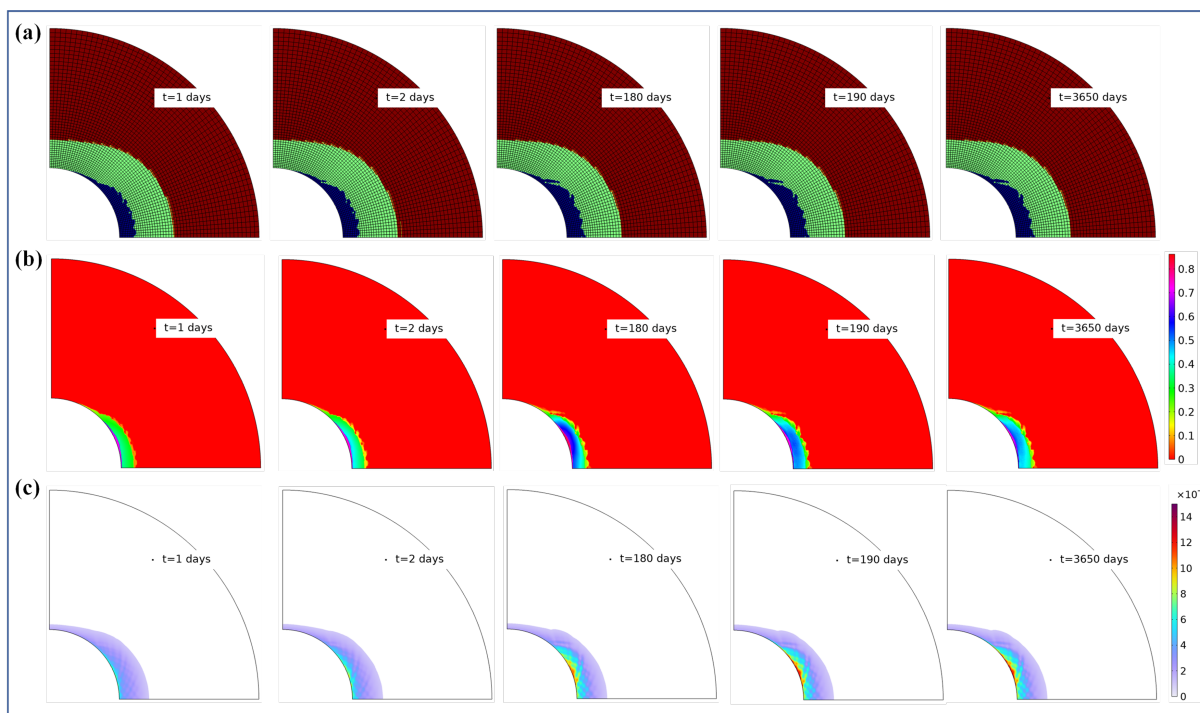
Figure 5.20: Extent of numerical EDZ (a), damage rate (b) and shear plastic strain (c) at the end of excavation (1 d); 2 d; end of drainage (180 d); 10 days of heating (190 d) and 10 y (thermo-poro-elasto-plastic case)

5.1.4.2. BGE

To investigate the behaviour of the EDZ under the effect of temperature in the course of the THM evolution of the repository system, the constitutive model developed by BGE (see section 4.2) was used to carry out the near field benchmark exercise for Cox. As already mentioned, this model takes into account the effect of temperatures on clay rocks and has already been calibrated for Cox. The parameters adopted for this simulation are summarised in Table 5.11. The 3D mesh developed for this is the one that has

EURAD (Deliverable n° 7.6) – Modelling report on the effect of temperature on clay host rocks behaviour
Dissemination level: PU
Date of issue of this report: 06/06/2024

Page 98

been previously used for the simulations of the elastic near field benchmark with FLAC3D, see Figure 5.2. The simulation was performed in OpenGeoSys. The initial and boundary conditions used for the elastic benchmark cases for Cox were also assumed for this analysis, see Table 2.3. The only difference in this case is that the pore pressure at the end of the waiting phase remains fixed to a value equal to the atmospheric pressure during the heating phase.

Table 5.11: Parameters adopted for the constitutive model.

Parameter	Value	Units
(Transverse-isotropy)		
Young modulus, E_1	2500	MPa
Young modulus, E_2	1250	MPa
Poisson ratio, ν_1	0.25	-
Poisson ratio, ν_2	0.30	-
Shear modulus, G_2	628.2	MPa
Strength		
Initial friction angle, ϕ_{ini}^*	10	°
Peak friction angle, ϕ_{peak}^*	30	°
Residual friction angle, ϕ_{res}^*	16	°
Initial cohesion, $c_{0\,\mathrm{peak}}^*$	3	MPa
Initial tensile strength, $p_{t0\,\mathrm{peak}}$	1	MPa
Post-rupture ratio, r_{post}	0.01	-
Hardening parameter, χ	0.003	-
Hardening parameter, a_{hard}	0.001	-
Softening parameter, b_{post}	200	-
Softening parameter, b_{res}	2	-
Plastic potential		
Non-associativity constant, ω	0.05	-
Viscoplasticity		
Order of Perzyna's formulation, N	2	-
Viscosity parameter, η	10	day
Strength anisotropy		
Strength anisotropy parameter, Ω_{90}	1.3	-
Strength anisotropy parameter, Ω_{m}	0.819	-
Strength anisotropy parameter, δ_{m}	49.7	°
Strength anisotropy parameter, n	0.1	-
Creep		
Parameter in the creep law, γ	7.4e-7	MPa^{-1} day^{-1}
Parameter in the creep law, μ	0.3	-
Parameter in the creep law, m	50	-
Parameter in the creep law, ϵ_{thr}	5e-3	-
Temperature		
Reference temperature, T_{ref}	20	°C
Parameter for the evolution of strength with temperature, μ_ϕ	0.0	-
Parameter for the evolution of strength with temperature, μ_{coh}	0.35	-

The results of the simulation are presented in Figure 5.21. The figure presents the equivalent plastic strains and the pore pressure distribution at the end of the excavation, waiting and heating phase. During the excavation, plastic strains develop around the gallery due to the stress redistribution. The extent of the plastic strains shows the zone of influence where damages in the rock is to be expected. This zone usually called excavation damaged zone (EDZ) changes little at the end of waiting time, six month later. During the heating phase, the plastic strains increase close to the gallery wall but the extent of the EDZ remains the same. In the heating phase, some induced damage occurs in the rock but they are limited to the region where the EDZ was already formed. The results suggest that the temperature increase has a limited effect on the formation and evolution of the EDZ.

The pore pressure evolution at the end of the excavation shows a similar pattern as the plastic strains at the

EURAD (Deliverable n˚ 7.6) – Modelling report on the effect of temperature on clay host rocks behaviour
Dissemination level: PU
Date of issue of this report: 06/06/2024

Page 99

same observation time leading to the assumption that both variables are driven by the same mechanism. A zone of high pore pressure is observed in the horizontal direction near the gallery wall. In the vertical direction, a zone with low pore pressure up to high suction is observed. This phenomenon has been denoted by Mánica et al. (2022a) as "anisotropic deconfinement". According to Mánica et al. (2022a), horizontal stresses decrease and vertical stresses increase in the horizontal direction near the gallery wall during the excavation. This results in a volume reduction (contractancy) at the sidewall especially in anisotropic materials with higher stiffness in the horizontal bedding plane as it is the case for Cox. In the crown, a dilatancy behaviour occurs. There, the vertical stresses decrease leading to extension whereas the horizontal stresses increase resulting in a compression. Because the stiffness is higher in the horizontal direction, the extension vertical component is higher than the compressive horizontal one leading to dilatancy. Compressive and dilatant regions are clearly observed respectively in horizontal and in vertical direction in the plastic strain distribution plot at the end of the excavation phase. In low permeability media, where pore water is almost trapped in the pores, the dilatancy behaviour leads to a decrease of pore pressure whereas contractancy is accompanied by an increase in pore pressure. During the waiting and the heating phase, the system tends to a steady state that is conditioned by the applied boundary conditions at the limits of the investigated domain. The assumed draining conditions at the gallery wall limit significantly the build up of overpressure so that the initial state is recovered rapidly. The actual state of the model does not take into account a coupling between the plastic deformations and the resulting increase of permeability as it is observed in in situ experiments, see (Seyedi et al., 2017). Assuming such a coupling will change the pore pressure distribution permanently by allowing a high water flow in the EDZ.
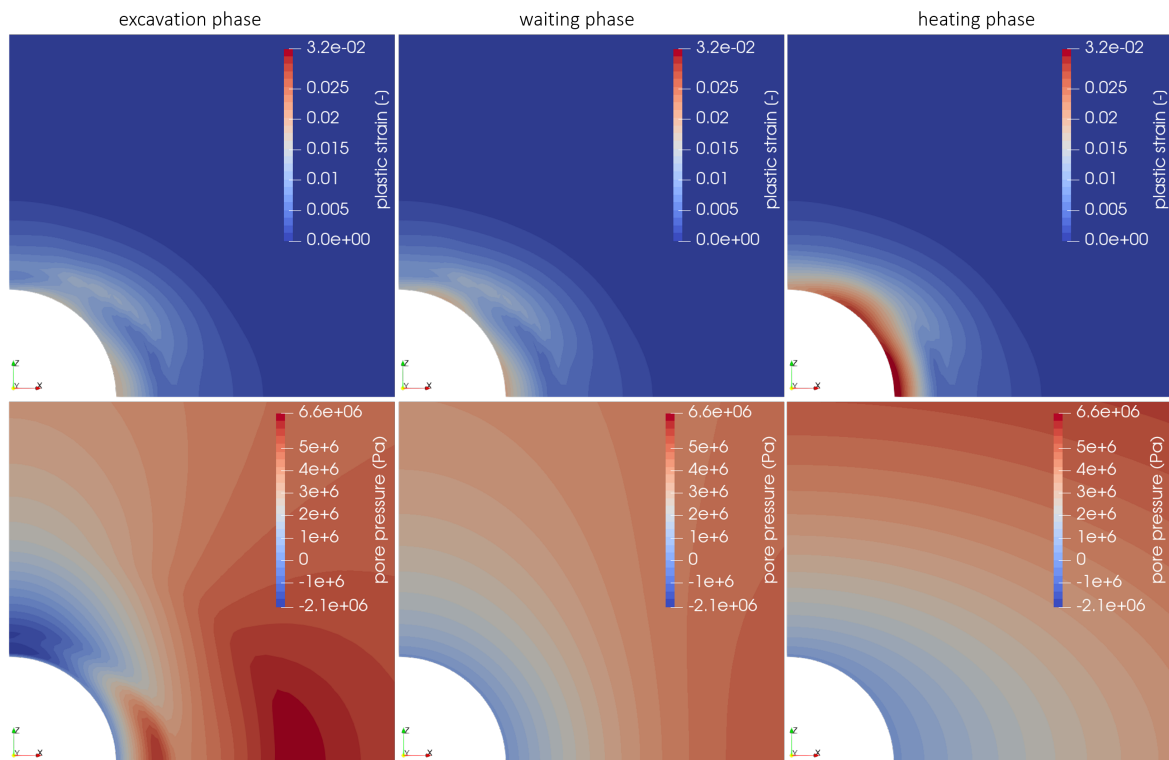
Figure 5.21: equivalent plastic strain and pore pressure evolution in the clay rock during due to THM loadings

EURAD (Deliverable n° 7.6) – Modelling report on the effect of temperature on clay host rocks behaviour
Dissemination level: PU
Date of issue of this report: 06/06/2024

Page 100

5.1.4.3. EDF

For the modelling of the EDZ in the near-field case, EDF refered to a visco-elasto-plastic model (LKR model) based on the works of (Laigle (2004), Kleine (2007), Raude (2015)) and used previously by EDF for the modeling of non linear behavior of soils/rocks (ex: Cox galleries). Further detailed descriptions of this model are given in section 4.4.

Figure 5.22 presents an overview of the obtained results for each of the previously cited modelling sub-cases for the Cox host rock. An additional modelling sub-case was suggested by the subtask 2.3 host to prevent possible occurring numerical convergence issues while using a plastic model. This sub-case consists of using the LKR model while supporting the excavation wall by a steel liner.

According to the results presented in figure 5.22:

- A maximum temperature of about 76°C (in the elastic isotropic subcase) to 80°C (for the other subcases) is observed during the heating phase.

- Anisotropy results in differences of displacements, an increase of pore pressure during the excavation and waiting phases and a decrease of the pore pressure during the heating phase.

- A maximum pore pressure varying between 5.5 MPa (with the elastic anisotropic model) to 6.8 MPa (anisotropic LKR model) during the excavation and waiting phases is observed. A maximum pore pressure of about 9 MPa to 11 MPa is observed during the heating phase.

- Compared to the anisotropic elastic model, the use of the LKR visco-elasto-plastic model with anisotropy results in smaller modelled pore pressures and bigger displacements during the heating phase.

- Supporting the excavation wall with a steel liner when using the LKR model results in bigger pore pressures and different displacements (smaller negative displacements and bigger positive displacements) to when the LKR model is used with no steel liner applied.

Model	Symmetry	Excavation + waiting phase				Heating phase			
		u_x (mm)	u_y (mm)	P_w (MPa)	T (°C)	u_x (mm)	u_y (mm)	P_w (MPa)	T (°C)
Elastic	Isotropy	- 2.8 : 0.0	- 2.8 : 0.0	0.1 : 4.7	22:22	-2.8 : 6.1	-2.8 : 6.1	0.1 : 11	22 : 76.2
Elastic	Anisotropy	-2.55 : 0.0	-3.6 : 0.0	0.1 : 5.5	22:22	-3.1: 4.7	-3.6 : 6.9	0.1 : 10.5	22 : 80
LKR	Anisotropy	-5.4 : 0.0	-6.35 : 0.0	0.1 : 5.8	22:22	-21.5 : 5.6	-16.8: 6.5	0.1 : 8.92	22 : 80
LKR + Steel liner**	Anisotropy	-5.4 : 0.0	-6.35 : 0.0	0.1 : 5.8	22:22	-7.4 : 6.0	-6.4: 7.3	0.1 : 9.76	22 : 80

Figure 5.22: Maximum and minimum values for the Cox modelling subcases - u_x and u_y are the displacements along x and y respectively, P_w is the pore water pressure and T is the temperature

The evolution of the pore water pressure is presented in the figure 5.23 colormaps for the anisotropic LKR modelling of the Cox (without a liner) and for different times: after 0.5 years, 1 year, 2, 4, 6, 8 and 10 years. It is clearly observed that the water pressure value is increasing in time and is more important near the excavation wall than from far of it.

EURAD (Deliverable n˚ 7.6) – Modelling report on the effect of temperature on clay host rocks behaviour
Dissemination level: PU
Date of issue of this report: 06/06/2024

Page 101
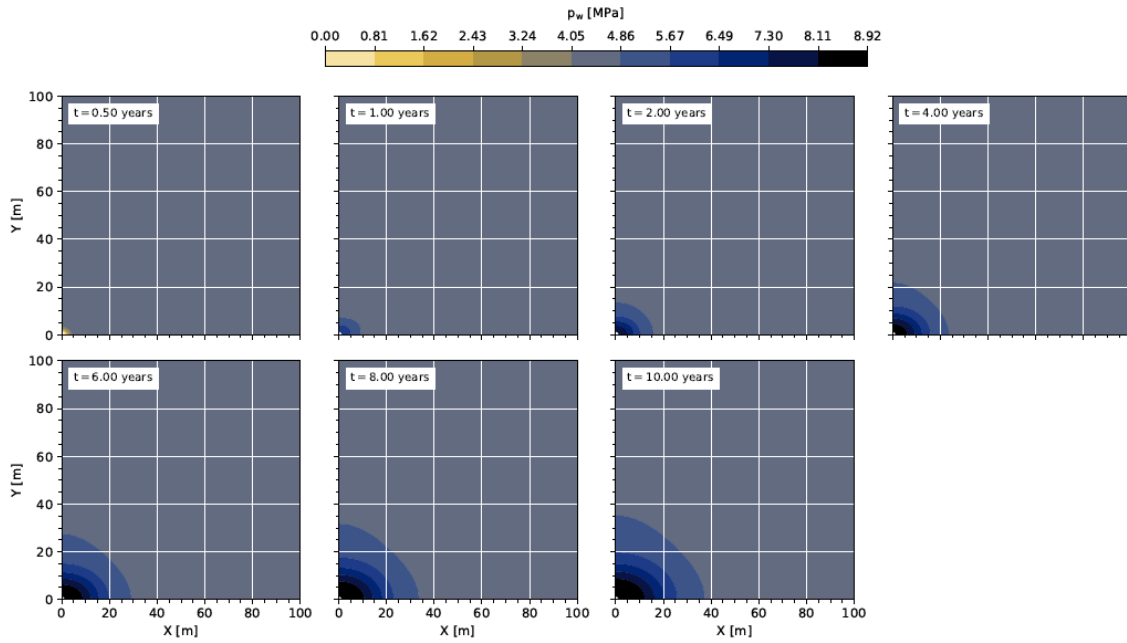
Figure 5.23: Pore water pressure evolution for the anisotropic LKR modelling of the Cox

In Figure 5.24 an indicator of plasticity in the zone near the excavation of the Cox is shown: in red, the surface that is already plasticized at the end of the heating phase is given (thermal flow of 200 W/m for 10 years) whilst in blue, the surface that is still in the elasticity region of the material is shown. In total, the plasticized region has reached an extent of approximately 3.5R from the center of the excavation.

Figure 5.24: Plasticized zone near the excavation of the Cox, at the end of the heating phase

EURAD (Deliverable n˚ 7.6) – Modelling report on the effect of temperature on clay host rocks behaviour
Dissemination level: PU
Date of issue of this report: 06/06/2024

Page 102

5.1.4.4. LEI

The main thermo-elastoplastic model parameters are presented in Table 5.12

Table 5.12: Main parameters and data for LEI thermo-elastoplastic model

Parameter	Value	Units
For transverse-isotropy		
Young modulus, E_1	8000	MPa
Young modulus, E_2	5000	MPa
Poisson ratio, ν_1	0.21	-
Poisson ratio, ν_2	0.35	-
Shear modulus, G_2	2500	MPa
For strength		
Initial friction angle, ϕ_{ini}	19.9	°
Peak friction angle, ϕ_{peak}	20	°
Residual friction angle, ϕ_{res}	16	°
b_ϕ	2	-
a_ϕ	1	-
Plastic strain threshold for softening, χ	0	-
Tensile strength	1.5	MPa
Hardening parameter, h	1E9	Pa
Initial yield stress, σ_{y0}	9.8E5	Pa
For regularisation		
Material parameter, α_{p}	0.998	-
Material parameter, β	45	-
Internal length, l_{int}	0.1	m
For permeability		
Intrinsic permeability, K_{xx}	3.9e-20	m^2
Intrinsic permeability, K_{xx}	3.9e-20	m^2
a	240	-
b	450	-

The results of the simulation are presented in Figure 5.25. Extension of the excavation disturbed zone (EDZ) is assumed to be related to the distribution of the equivalent plastic strains developed around the tunnel. The plots present strains at the end of the excavation, waiting, after 10 and 1000 days of heating. During the excavation, plastic strains develop around the gallery due to release of stress on the tunnel boundary. In this region the rock would be affected most and could be damaged (fractured). The distribution of plastic strains is not isotropic, it was pronounced more in the horizontal direction. By the end of the waiting phase the extent of the plastic strain zone remained similar to that after the excavation, but with higher magnitude. Meanwhile during the heating phase, model results showed an increase in the magnitude of plastic strain with a larger distribution around the tunnel. Results presented were derived by model without calibration for Cox clayrock and without consideration of strength dependence on temperature or strength anisotropy.

Figure 5.26 presents the pore pressure distribution around the tunnel after 10 years of constant heating. Similarly, to the results obtained with thermo-poroelastic model, the pore water distribution was anisotropic, but maximum pressure was observed to be lower by 2 MPa. Due to plastic strains the permeability tends to increase and allow easier dissipation of heat induced overpressure.

EURAD (Deliverable n˚ 7.6) – Modelling report on the effect of temperature on clay host rocks behaviour
Dissemination level: PU
Date of issue of this report: 06/06/2024

Page 103
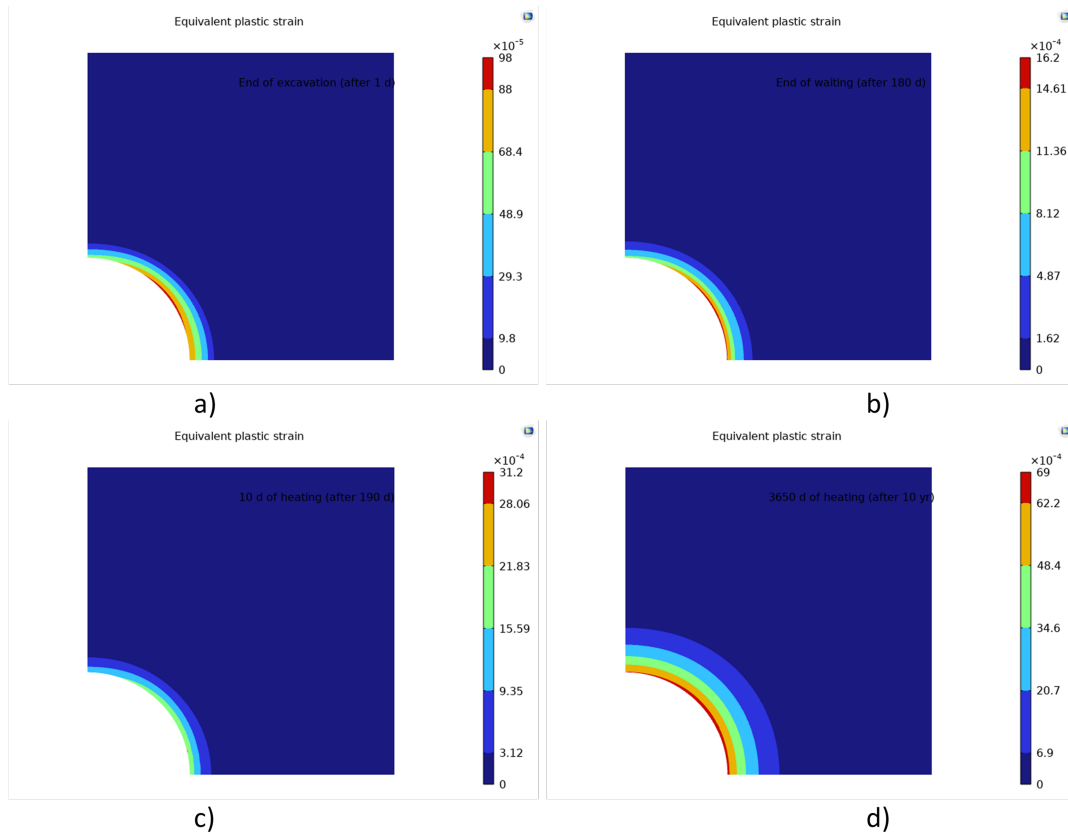
Figure 5.25: Distribution of plastic strains a) after 1 day (by the end of excavation), b) after 180 days (by the end of waiting phase), c) after 10 days of heating, d) after 3650 days of heating
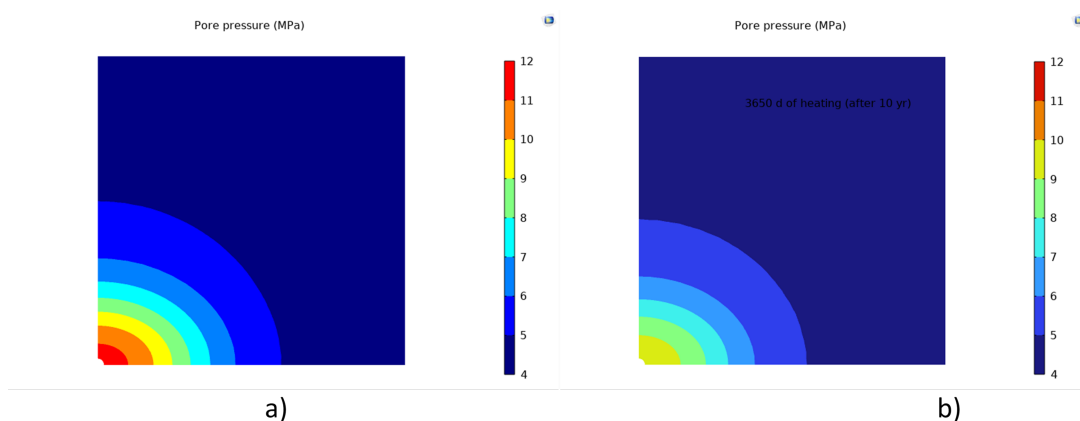
Figure 5.26: Distribution of pore pressure after 10 yr of heating a) without consideration of plastic strains and change on permeability, b) taking into consideration the development of plastic strains and change of permeability

EURAD (Deliverable n˚ 7.6) – Modelling report on the effect of temperature on clay host rocks behaviour
Dissemination level: PU
Date of issue of this report: 06/06/2024

Page 104

5.1.4.5. ULg

The numerical results of temperature, pore pressure and convergence are presented at the points 1.25 m, 1.9 m, 2.5 m, 6.25 m, 50 m, and 100 m horizontally and vertically, plus 1.25 m, 1.9 m, 2.5 m at 45 degrees (OB, OD and OC directions in Figure 2.1). The evolution of temperature, pore pressure and convergence are presented in Figure 5.27, Figure 5.28, Figure 5.29.

During excavation and waiting steps, the temperature keeps constant as no thermal flow is imposed. The pore pressure at the drift wall decreases as defined with boundary condition during excavation, from 4.7 MPa to atmospheric pressure. The overpressure in the horizontal direction is observed at the end of excavation, while the pore pressure in the vertical direction continues to decrease in this stage. This discrepancy is due to the hydro-mechanical behaviour induced by anisotropic properties. The stabilisation of pore pressure is noticed during waiting. The host rock close to the wall experiences an increase of radial displacement during excavation, and the first contact between the wall and the liner is located at 45 degrees direction. The second contact is also reached during waiting in the vertical direction.

When the heating starts, the temperature increase is observed in the near field, and the excess pore pressure is highly pronounced due to the thermal pressurization. The maximum of temperature is located at the drift wall with about $80°C$ after 10 years. Inside the rock structure, the different distribution of temperature is evidenced due to the anisotropy of thermal conductivity. The higher temperature values are observed in the horizontal direction with a higher thermal conductivity. This difference also leads to the variation of pore pressure. The pore pressure at 6.25 m in the horizontal direction is slightly higher than that in the vertical direction, while the pore pressure at the wall is the same due to the same amount of received thermal power. The full contact between the wall and the liner is obtained rapidly around the wall after the start of heating. The radial displacement decreases due to the thermal dilation of the host rock close to the wall, and the thermal expansion is more pronounced vertically than horizontally. For the location far from the wall, the temperature and pore pressure changes are not observed, and the modification of radial displacement is related to the accumulation of the thermal dilation from the nearfield rock.

Since the material anisotropy is one of the principal features in the benchmark of THM coupling problem, Figure 5.30 (in $5m \times 5m$ scale) shows the distribution of horizontal displacement, vertical displacement, and pore pressure at the end of excavation and heating. In the vertical direction after 24h, the displacements are observed deeper into the rock mass with respect to the horizontal direction. At the drift wall, the rigid liner imposes the same displacement in both directions. At the end of the heating, vertical extension due to thermal dilation is more evidenced than in the horizontal direction. Negative pore pressure is predicted close to the drift wall due to hydro-mechanical couplings at the end of excavation. An overpressure peak is clearly evidenced in the horizontal direction at the end of excavation, due to the anisotropy. At the end
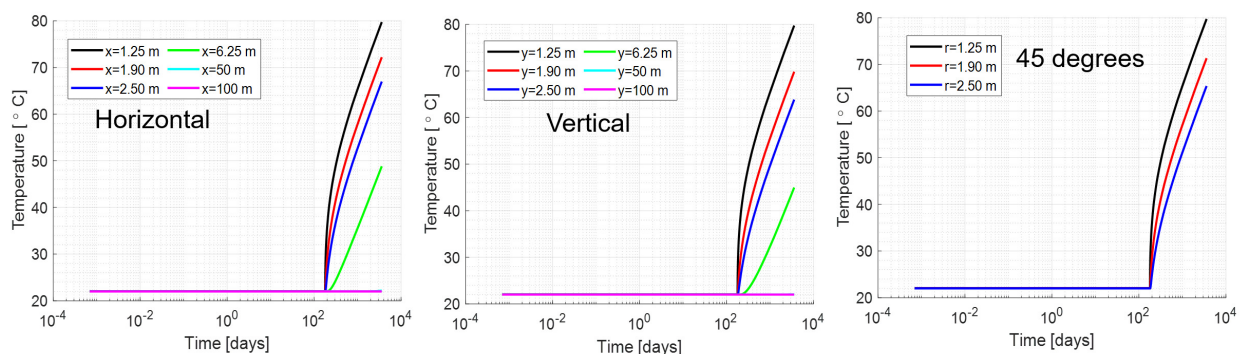
Figure 5.27: Evolution of temperature at different locations

EURAD (Deliverable n˚ 7.6) – Modelling report on the effect of temperature on clay host rocks behaviour
Dissemination level: PU
Date of issue of this report: 06/06/2024

Page 105
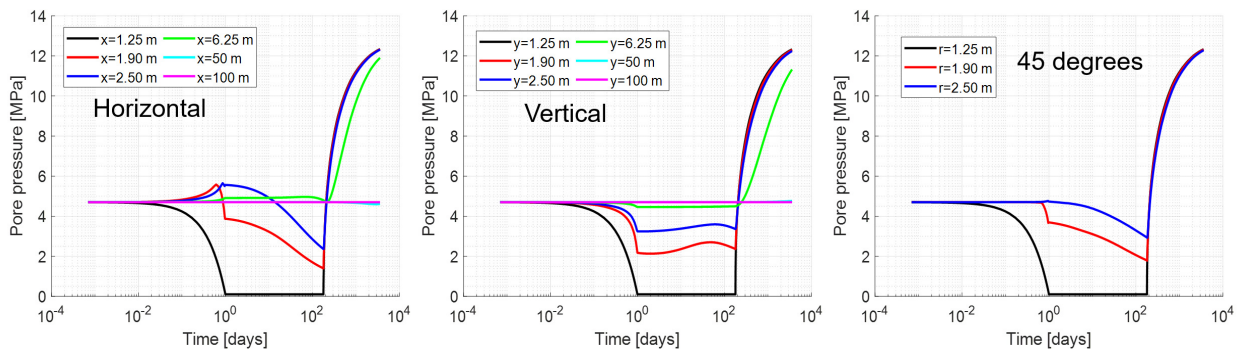
Figure 5.28: Evolution of pore pressure at different locations
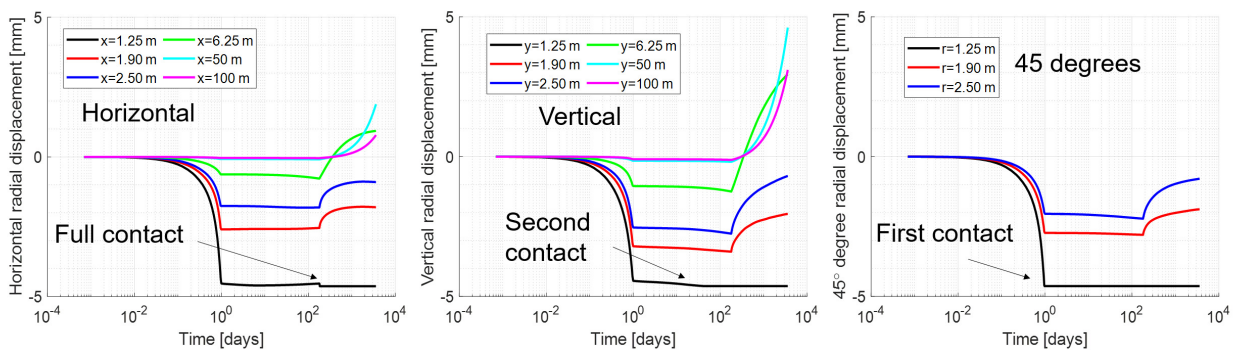
Figure 5.29: Evolution of radial displacement at different locations
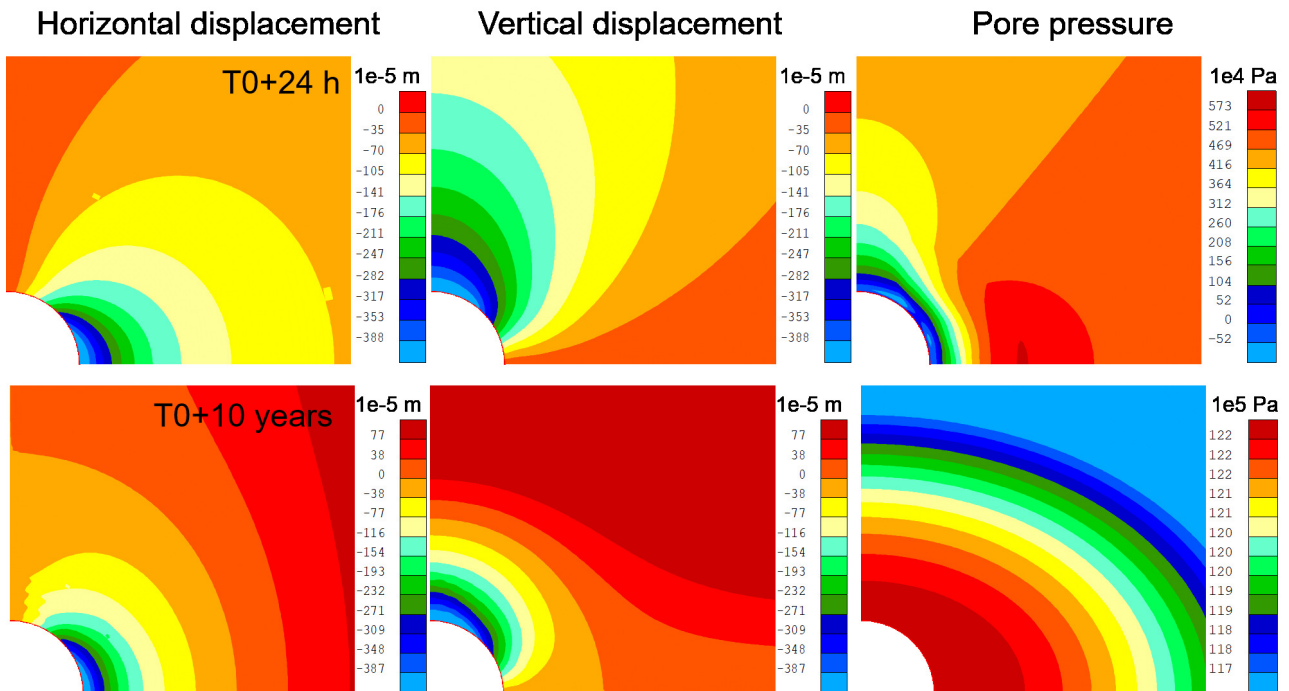
Figure 5.30: Distribution of horizontal displacement, vertical displacement, and pore pressure at the end of excavation and heating

EURAD (Deliverable n° 7.6) – Modelling report on the effect of temperature on clay host rocks behaviour
Dissemination level: PU
Date of issue of this report: 06/06/2024

Page 106

of heating, the overpressure is more pronounced horizontally due to a higher thermal conductivity in this direction.

The evolution of shear strain localisation process is described in 3m × 3m scale in Figure 5.31, and the numerical results are plastic points, the deviatoric strain increment and the total deviatoric strain. The host rock in 45 degrees direction gets the first contact with the liner, where the deformation is limited. Meanwhile, the horizontal and vertical convergence continues to develop, leading to an elastic zone located at the 45 degrees of the drift wall at the end of the excavation. The deviatoric strain increment also evidences the existence of the elastic zone. An elastic unloading process is predicted due to the continuous drainage during the waiting phase. The strain localisation process is less active during this phase, and the total deviatoric strain keeps constant as well.

Once the heating phase is activated, the rock behaviour in EDZ comes to plasticity rapidly, and the shear bands are more pronounced than during excavation. The competition between different emerging shear bands is witnessed at the initial heating stage, and the bands are slightly more oriented along the minor horizontal principal stress direction, which is in agreement with the *in-situ* observation of localisation induced by the excavation process (Armand et al., 2014). It is worth mentioning that the initiation of the new shear bands does not follow the existing previous bands generated during the excavation. It illustrates that thermal effects strongly dominate the development of shear bands, neglecting the previous existing bands from excavation.

At the end of the heating phase, the competition between different emerging shear bands ends up with the domination of horizontal shear bands. The vertical shear bands are also visible in the total deviatoric strain, but they are not much developed as in the horizontal ones. In addition, the effect of strain localisation process on the rock behaviour in EDZ is also evidenced in Figure 5.31. When a shear band initiates, the stress state inside the band is purely localised in plasticity, the rock structure outside the band undergoes an elastic unloading process. At 360 days, the shear bands development is more observed horizontally in the upper half area, thus the stress state of the rock at the upper half wall consist of both elasticity (outside the bands) and plasticity (inside the bands). At 4 years, due to the initiation of a vertical shear band, the stress state at the upper half wall is almost in elasticity. At 10 years, the shear bands are developed horizontally due to thermal loading, hence some locations at the wall are back to plasticity again. With the initiation and disappearance of shear bands, the rock behaviour can be switched between plasticity and elasticity during heating.

In real *in-situ* construction, a liner is usually constructed to limit the convergence of the drift wall. Figure 5.31 shows that the liner can affect the development of the localisation pattern in the EDZ. In order to better understand the gap effect on the EDZ development during the heating phase, three gap values are considered in the numerical investigations: 4.6 mm, 5.8 mm and infinite gap (no liner). 5.8 mm is actually the average predicted displacement of the drift wall at the end of waiting phase, when no liner is imposed.

Figure 5.32 shows the evolution of the plastic points, deviatoric strain increment and total deviatoric strain at 237 days in 3m × 3m scale. With an increasing gap, the plastic area becomes larger, and the strain localisation is gradually more pronounced. When the gap is equal to 4.6mm, there are not many shear bands initiated from the drift wall. With a gap of 5.8mm, the horizontal shear bands close to the wall are clearly observed. When there is no liner, the localised horizontal shear bands are highly pronounced. Such kind of phenomenon can be also observed in the evolution of total deviatoric strain. When the gap is infinite, the magnitude of total deviatoric strain is ten times higher than that of gap= 4.6mm, and the shear bands are more localised with the increase of gap.

The gap effect on the rock behaviour can be explained through the contact situation between the wall and the liner. Figure 5.33 (in 3m × 3m scale) describes the different contact situation between the wall and liner

EURAD (Deliverable n˚ 7.6) – Modelling report on the effect of temperature on clay host rocks behaviour
Dissemination level: PU
Date of issue of this report: 06/06/2024

Page 107
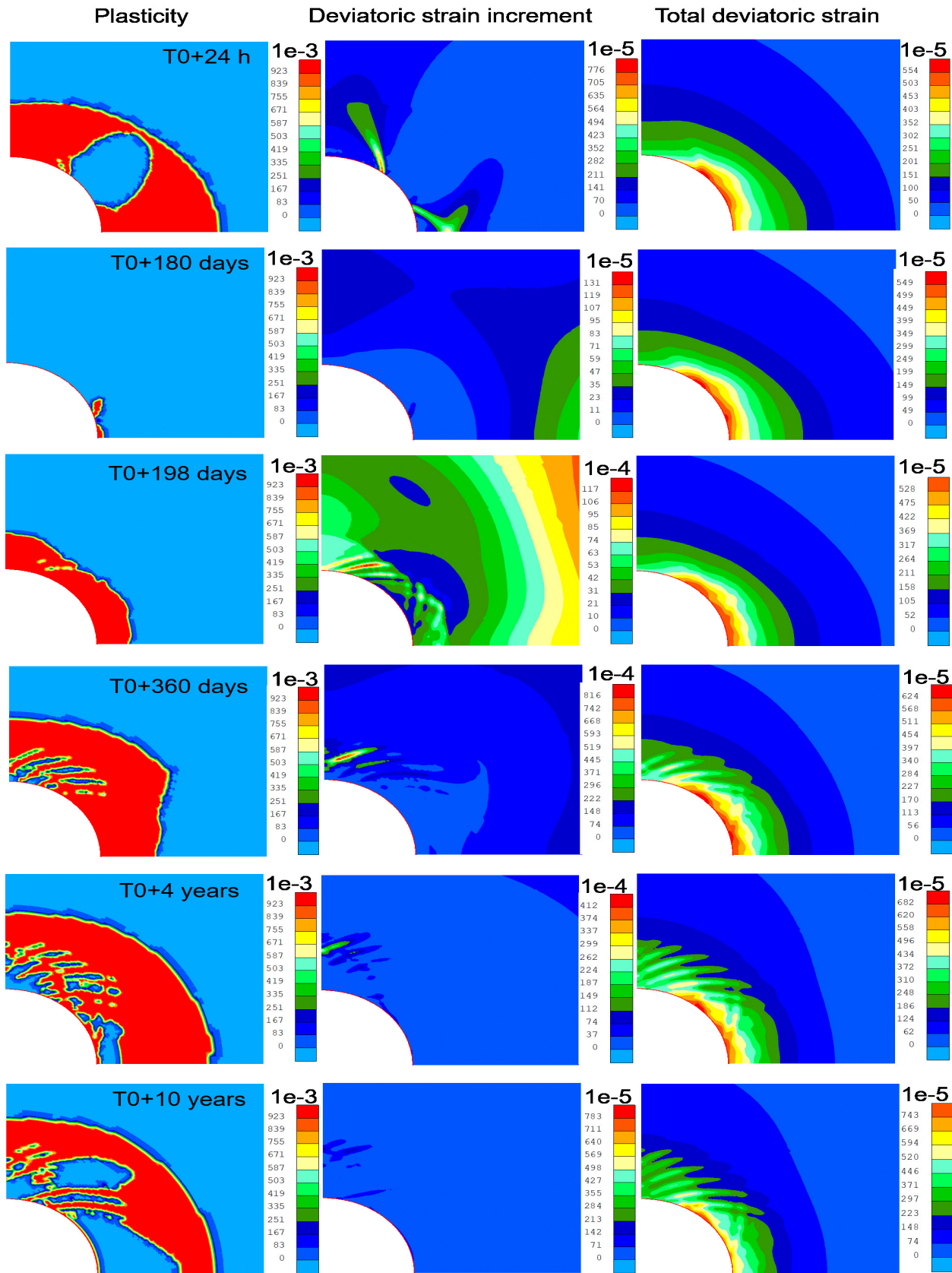
Figure 5.31: Evolution of plastic points, deviatoric strain increment and total deviatoric strain around the EDZ (Gap=4.6 mm)

EURAD (Deliverable n° 7.6) – Modelling report on the effect of temperature on clay host rocks behaviour
Dissemination level: PU
Date of issue of this report: 06/06/2024

Page 108
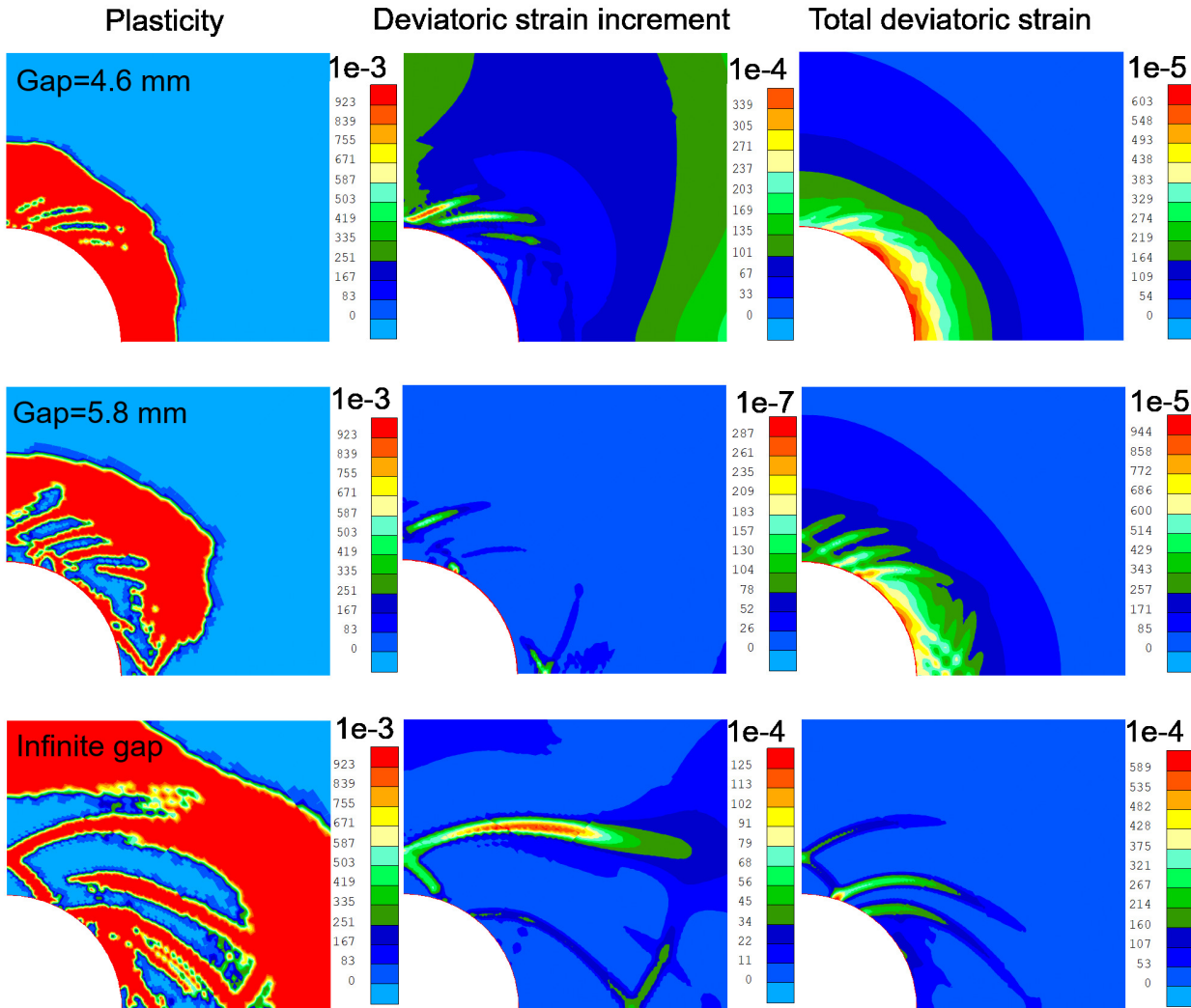
Figure 5.32: Evolution of plastic points, deviatoric strain increment and total deviatoric strain at 237 days for different gap values.

for a gap respectively of 4.6mm and 5.8mm, where the red diagram is the contact pressure. The contact process for gap= 4.6mm is consistent with the evolution of radial displacement. However, for the gap equal to 5.8mm, only few elements in 45 degrees direction get contact with the liner at the end of waiting phase. No full contact is reached yet after 237 days, and the contact is not homogeneously distributed along the wall. Compared to Figure 5.32, the strain localisation is less developed when the full contact is reached. Nonetheless, the shear bands are preferable to develop when the contact situation is poor. The shear bands are more pronounced in upper half area where no contact is obtained, which also evidences the mechanism. Considering the case without liner, the strain localisation can develop without any restriction, hence the shear bands are much more localised.

EURAD (Deliverable n° 7.6) – Modelling report on the effect of temperature on clay host rocks behaviour
Dissemination level: PU
Date of issue of this report: 06/06/2024

Page 109
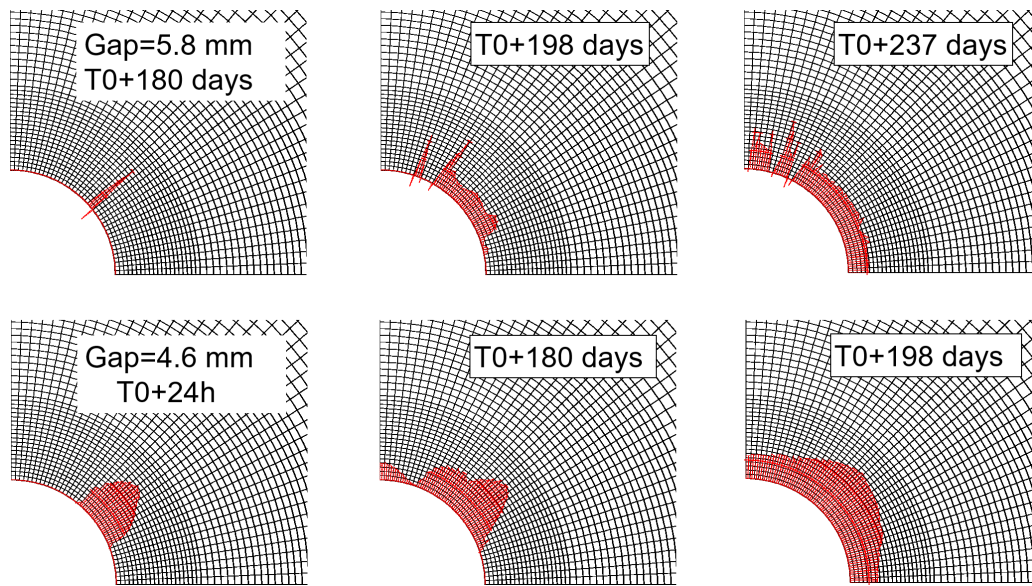
Figure 5.33: Contact situation between the drift wall and liner for different gap values (Red diagram represents the contact pressure between the liner and the wall).

5.1.4.6. UPC

Modelling of the EDZ has been carried out in this section, for the plastic anisotropic Cox case (subcase 3). The elastoplastic model with damage and nonlocal formulation is used in the numerical simulation. As specified by Task 2.3, both unsupported and supported tunnels are carried out.

(a). Unsupported tunnel   As observed in Figure 5.34(a), a maximum temperature of around $80\,°C$ has been obtained on the gallery wall, while the temperature decreases as the distance from the gallery increases. The evolution of the temperature is the same as the one in the elastic anisotropic Cox case, because the same thermal properties are considered in both models. As shown in Figure 5.34(b), during the excavation stage, positive excess pore pressure is generated along the x-direction. Meanwhile, the pore pressure linearly decreases at the gallery wall during the waiting stage, because of the applied drained boundary condition. Note that, lower pore pressures are observed in the heating stage compared to the elastic cases, since large plastic deformations and large volumetric strains occur.

Moreover, there are significant differences between the elastic and plastic cases, in terms of displacements and effective stresses. The displacements continuously increase during the excavation and waiting stages, and a very significant increase can be observed in the heating stage. The maximum displacements in the x- and y- directions are around 147 mm (at P_1) and 156 mm (at P_{13}), respectively. Such large deformations can be attributed to the evolution of damage.

Contours of plastic shear strains can be employed to observe the configuration of localised plastic deformations and to assess the extension of the excavation damage zone (EDZ). Figure 5.35 presents the evolution of the plastic shear strain contours. It can be observed that no obvious shear bands develop in the excavation stage, and the shear bands just start to be developed during the waiting stage. In the heating stage (from 180 to 3650 days), more obvious shear bands can be identified. Shear bands extend from the gallery wall (r = 1.25 m) in the horizontal direction up to around 5.8 m into the host rock.

Considering the evolution of permeability with damage is necessary to properly capture the pore water pressure response (Mánica, 2018). In this study, the increase of permeability with the evolution of damage

EURAD (Deliverable n° 7.6) – Modelling report on the effect of temperature on clay host rocks behaviour
Dissemination level: PU
Date of issue of this report: 06/06/2024

Page 110
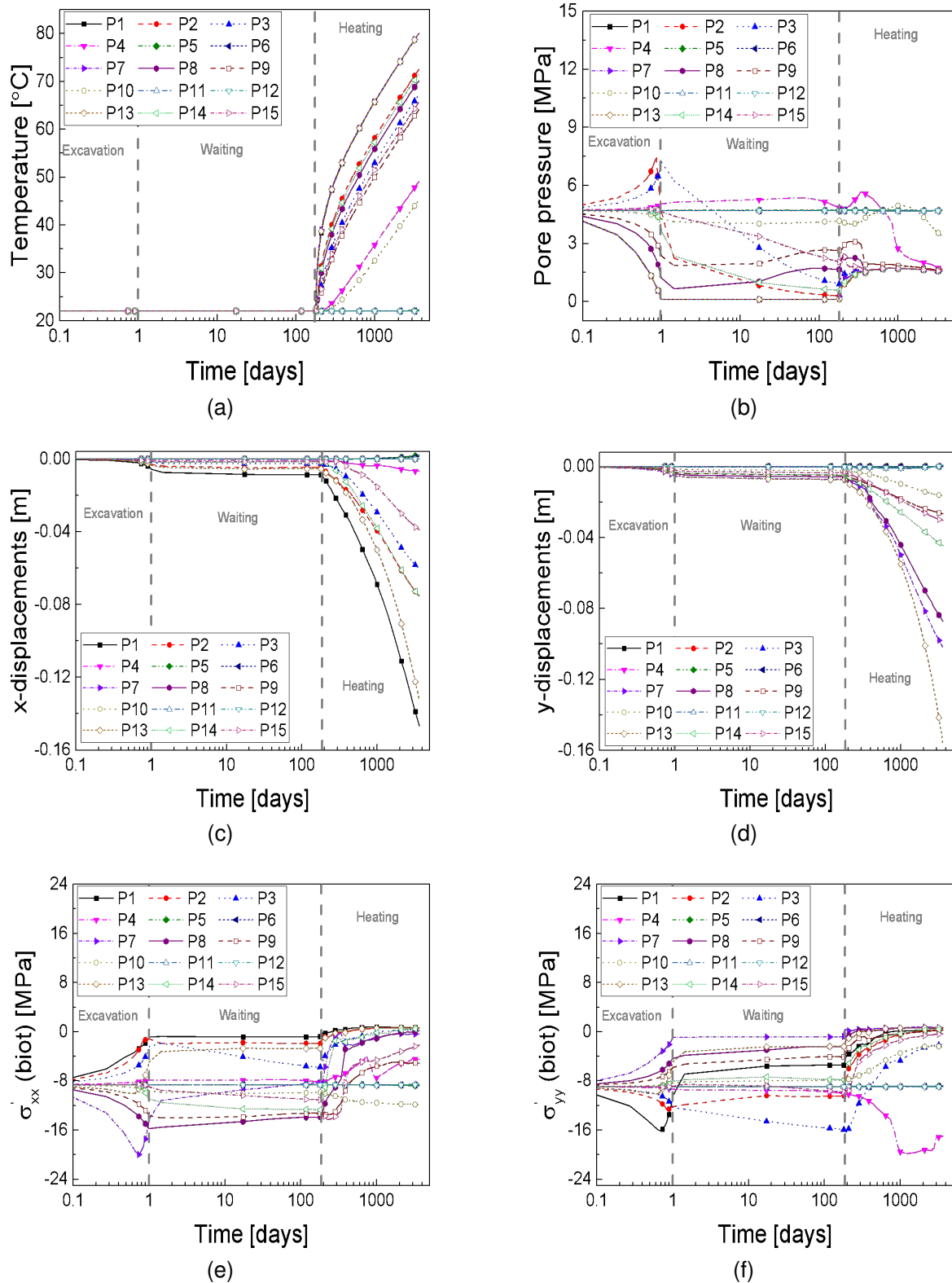
Figure 5.34: Evolution of (a) temperature, (b) pore pressure, (c) x-displacements, (d) y-displacements, (e) Biot effective stresses in the x-direction, and (f) Biot effective stresses in the y-direction, for the unsupported tunnel in the plastic anisotropic Cox case.

EURAD (Deliverable n˚ 7.6) – Modelling report on the effect of temperature on clay host rocks behaviour
Dissemination level: PU
Date of issue of this report: 06/06/2024

Page 111

is considered, as described in Section 3.2.8. Therefore, the preferential pathways for the water flux occur in the localised zones due to the increase in permeability. The increase of permeability concentrates within the shear bands where close to the gallery wall, because the plastic deformations concentrate there. Figure 5.36 shows the groundwater flux at time $t = 3650$ days, where the preferential pathways and the localized can be observed.
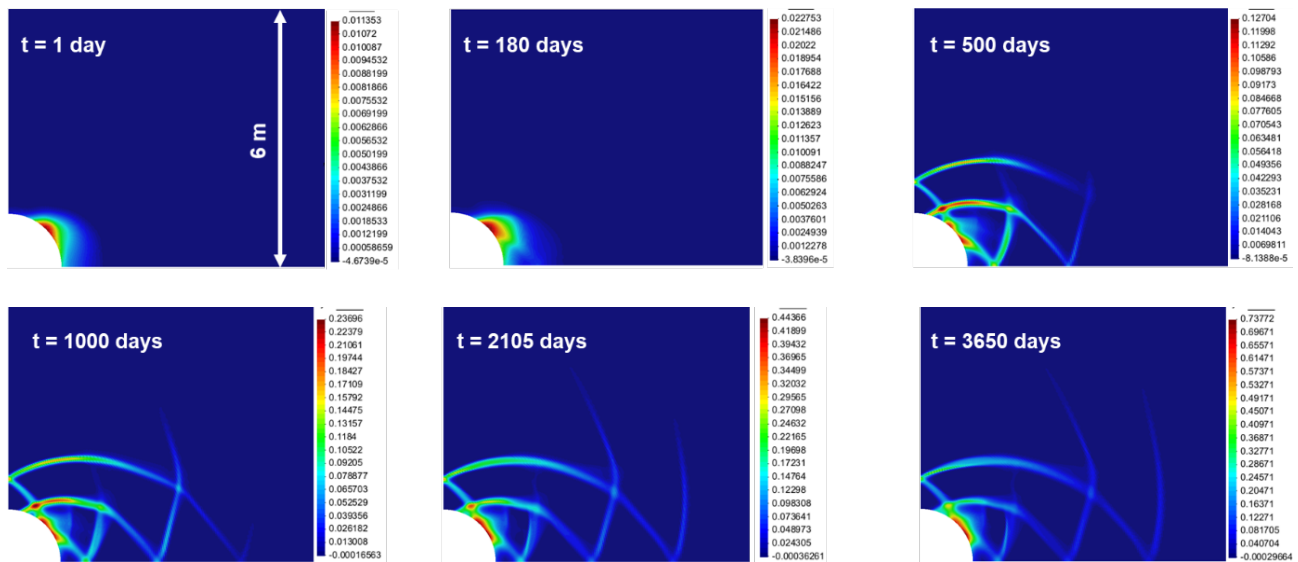
Figure 5.35: Evolution of the plastic shear strains, for the plastic anisotropic case Cox. Unsupported tunnel.

(a)   (b)   (c)
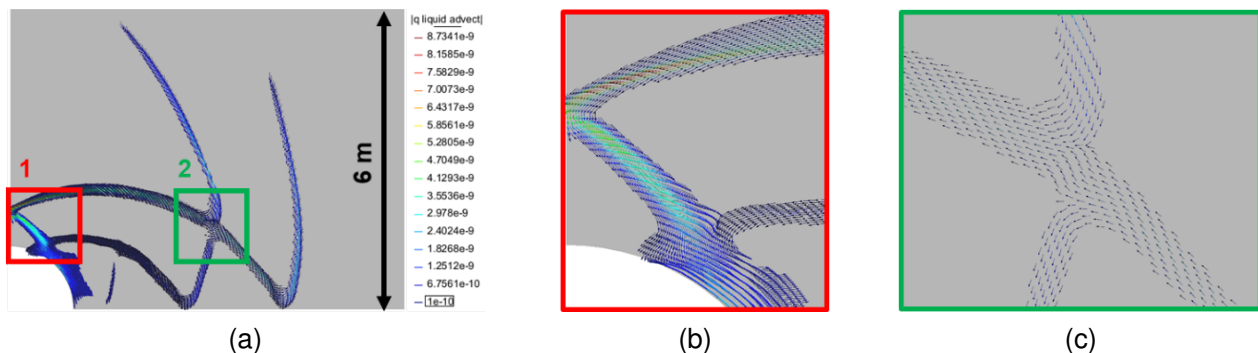
Figure 5.36: (a) Groundwater flux at time $t = 3650$ days. (b) and (c) show the zoom-in results of zone 1 and zone 2 in Figure 5.36(a). Plastic anisotropic case Cox, unsupported tunnel.

(b). Supported tunnel   Evolutions of temperature, pore pressure, displacements and effective stresses for the supported tunnel are shown in Figure 5.37. The evolution of temperature is reported in Figure 5.37(a), and a maximum value of around $78.8\,°C$ has been obtained at the gallery, around $1.2\,°C$ lower than the one obtained in the unsupported tunnel. Such difference can be mainly attributed to the boundary conditions of the heat flow: the heat flow is applied at the gallery wall ($r = 1.25\,m$) in the unsupported tunnel, while it is applied at the inner boundary of the steel liner ($r = 1.225\,m$) in the supported tunnel.

Figure 5.37(b) presents the evolution of pore pressure. During the excavation stage and waiting stage, there is no big difference in the pore pressure between unsupported and supported tunnels. However, during the heating stage, there is a big difference in pore pressures between both models. A fast pore pressure increase is observed up to a maximum value of around $10.5\,MPa$ for the supported tunnel, and the pore pressures are much bigger than the ones obtained from the unsupported tunnel.

EURAD (Deliverable n° 7.6) – Modelling report on the effect of temperature on clay host rocks behaviour
Dissemination level: PU
Date of issue of this report: 06/06/2024

Page 112

The evolution of displacements and Biot effective stresses are reported in Figure 5.37(c), Figure 5.37(d) and Figure 5.37(e), Figure 5.37(f), respectively. The maximum displacements in the x- and y- directions are 12 mm (P_1) and 10 mm (P_{13}), respectively. By comparing the displacements obtained from unsupported and supported tunnels, it can be concluded that the installation of the steel liner can significantly limit the deformations, and therefore, increase the safety of the host rocks.

Figure 5.38 shows the evolution of plastic shear strain contours for the supported tunnel. During the heating stage, shear bands extend in the horizontal direction up to around 2.3 m into the host rock. Compared with the obtained shear bands of the unsupported tunnel, it can be observed that the steel liner can significantly reduce the development of the shear bands. Additionally, a more diffuse zone of shear bands can be observed very close to the gallery wall.

EURAD (Deliverable n° 7.6) – Modelling report on the effect of temperature on clay host rocks behaviour
Dissemination level: PU
Date of issue of this report: 06/06/2024

Page 113
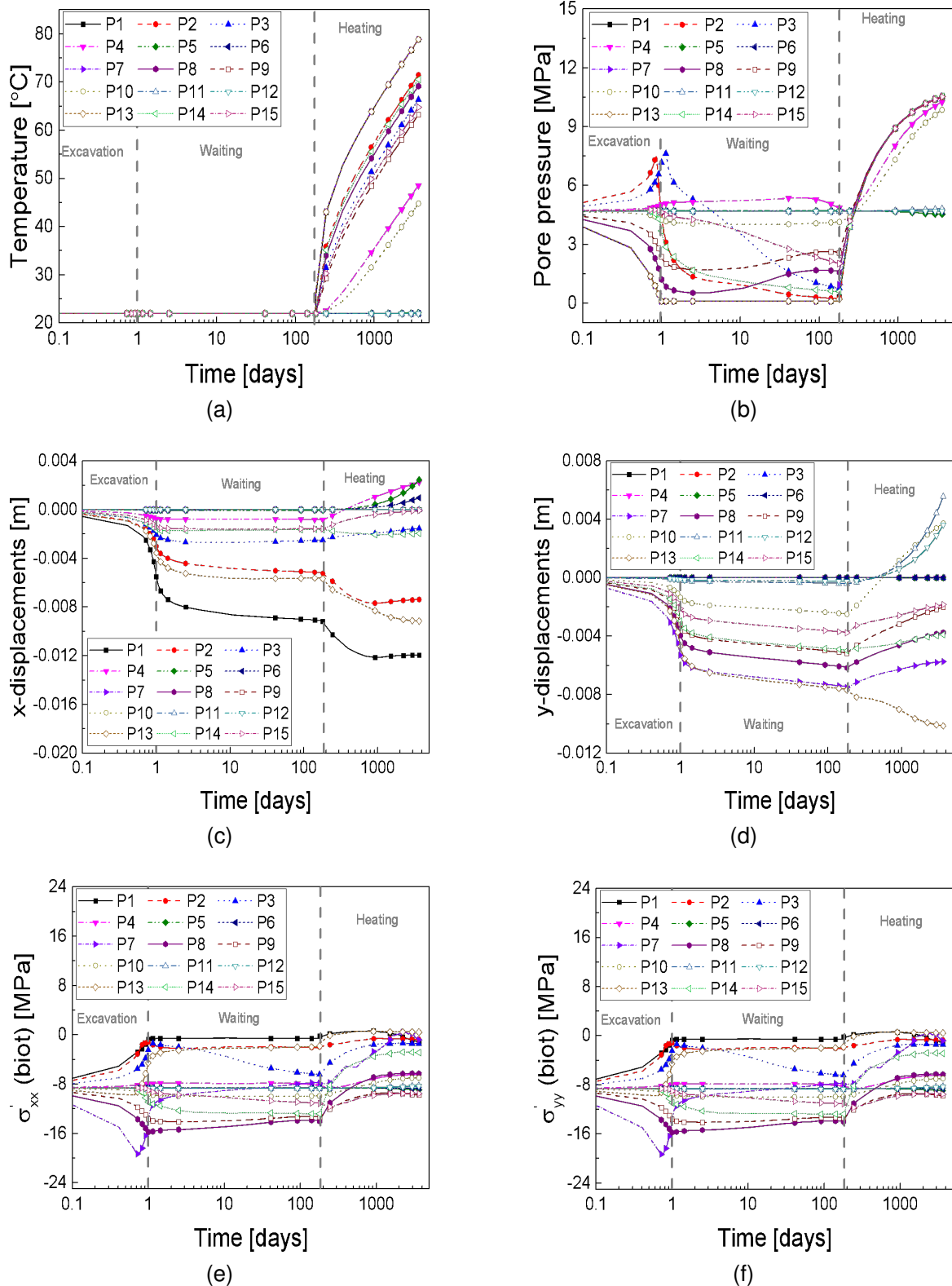
Figure 5.37: Evolution of (a) temperature, (b) pore pressure, (c) x-displacements, (d) y-displacements, (e) Biot effective stresses in the x-direction, and (f) Biot effective stresses in the y-direction, for the supported tunnel in the plastic anisotropic Cox case.

EURAD (Deliverable n° 7.6) – Modelling report on the effect of temperature on clay host rocks behaviour
Dissemination level: PU
Date of issue of this report: 06/06/2024

Page 114
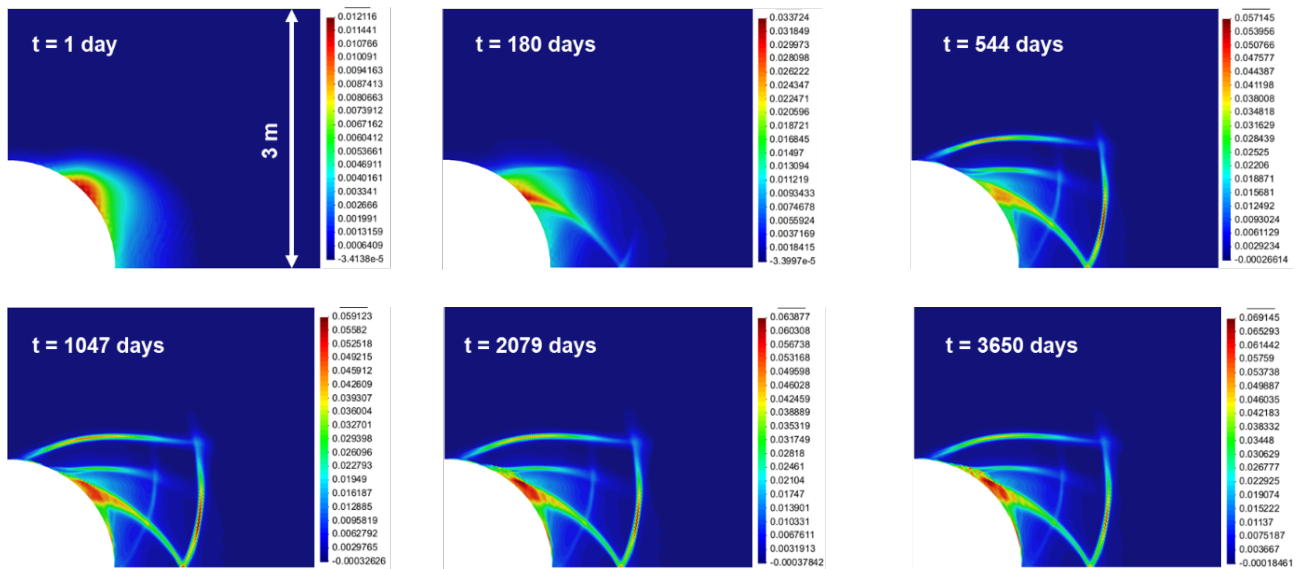
Figure 5.38: Evolution of the plastic shear strains, for the supported tunnel in the plastic anisotropic Cox case.

EURAD (Deliverable n˚ 7.6) – Modelling report on the effect of temperature on clay host rocks behaviour
Dissemination level: PU
Date of issue of this report: 06/06/2024

Page 115

5.2. Far-field generic case

5.2.1. Modelling approaches

5.2.1.1. ANDRA

(a). Elastic model Andra ran an anisotropic elastic model in Comsol. The mesh displayed on Figure 5.39 consists of 5228 elements.
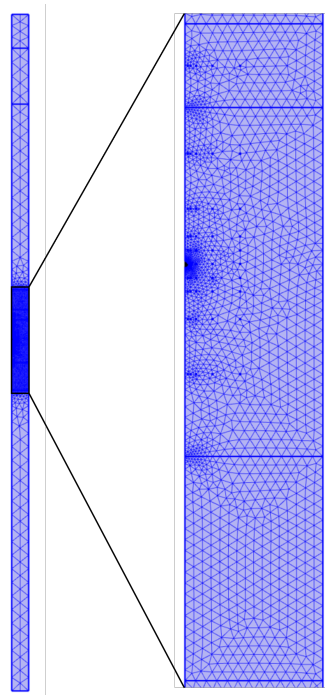
Figure 5.39: Far-field mesh and zoom on the Callovo-Oxfordian layer

The results and comparisons with the other teams' are presented in section 5.2.2.

(b). Phase field model LamCube's phase field model was also run to investigate the impact of the EDZ and the long-term behaviour on the temperature and pore pressure responses in the far-field. This model was developed as part of the DECOVALEX-2023 project and is described in detail in Yu et al., 2023.

Two subcases were run: an elastic damage model and an elasto-visco-plastic damage model. The excavation induces mainly some shear damage on the side of the tunnel but heating induces some tensile damage on the whole periphery (Figure 5.40).

This effect is however very local: no tensile damage is modelled two diameters away from the tunnel (Figure 5.41).

EURAD (Deliverable n˚ 7.6) – Modelling report on the effect of temperature on clay host rocks behaviour
Dissemination level: PU
Date of issue of this report: 06/06/2024

Page 116
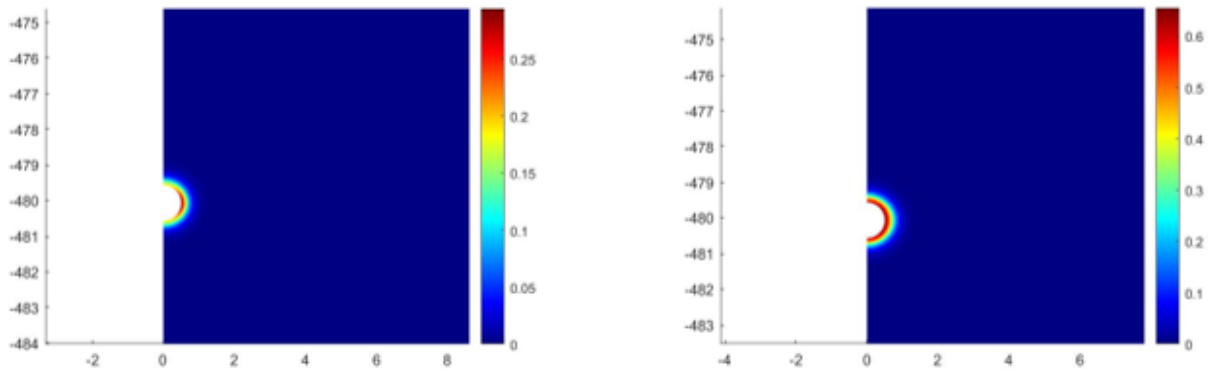
Figure 5.40: Shear damage induced by excavation (left) and tensile damage induced by heating (right)
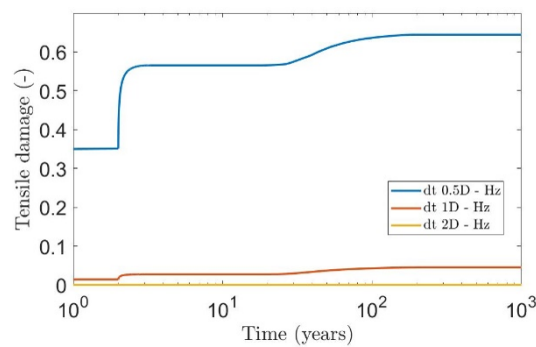
Figure 5.41: Tensile damage evolution with time at 0.5D, 1D and 2D (85 years case)

5.2.1.2. BGE

The model used by BGE for the far-field benchmark simulation assumes two vertical symmetric boundaries positioned equidistantly between two parallel cells, one to the left and one to the right of the cell under investigation. The developed model consists of 41.975 quadrilateral elements with quadratic shape function. The model goes from 0 to 1000 m depth and covers the geological layers Kimmeridian (from 0 m to -132.7 m), Oxfordian (from -123.7 m to -406.8 m), USC (from -406.8 m to 436.4 m), UT (from -436.4 m to -451.6 m), UA (from -451.6 m to -555.6 m and subdivided in three sublayers UA1, UA2 and UA3) and Dogger (from -555.6 m to -1000 m). Material parameters for these units were already specified in section 2.1.2. The simulation has been carried out in OpenGeoSys.

At the left, right and bottom boundary of the model, adiabatic and no flow boundary conditions are assumed. The normal displacements to those three boundaries are also fixed. These assumptions imply that an infinite number of cells are being investigated simultaneously. This case is the most conservative in regard to the THM loading at the disposal level and corresponds to a sufficiently large disposal area with high number of cells.

EURAD (Deliverable n˚ 7.6) – Modelling report on the effect of temperature on clay host rocks behaviour
Dissemination level: PU
Date of issue of this report: 06/06/2024

Page 117
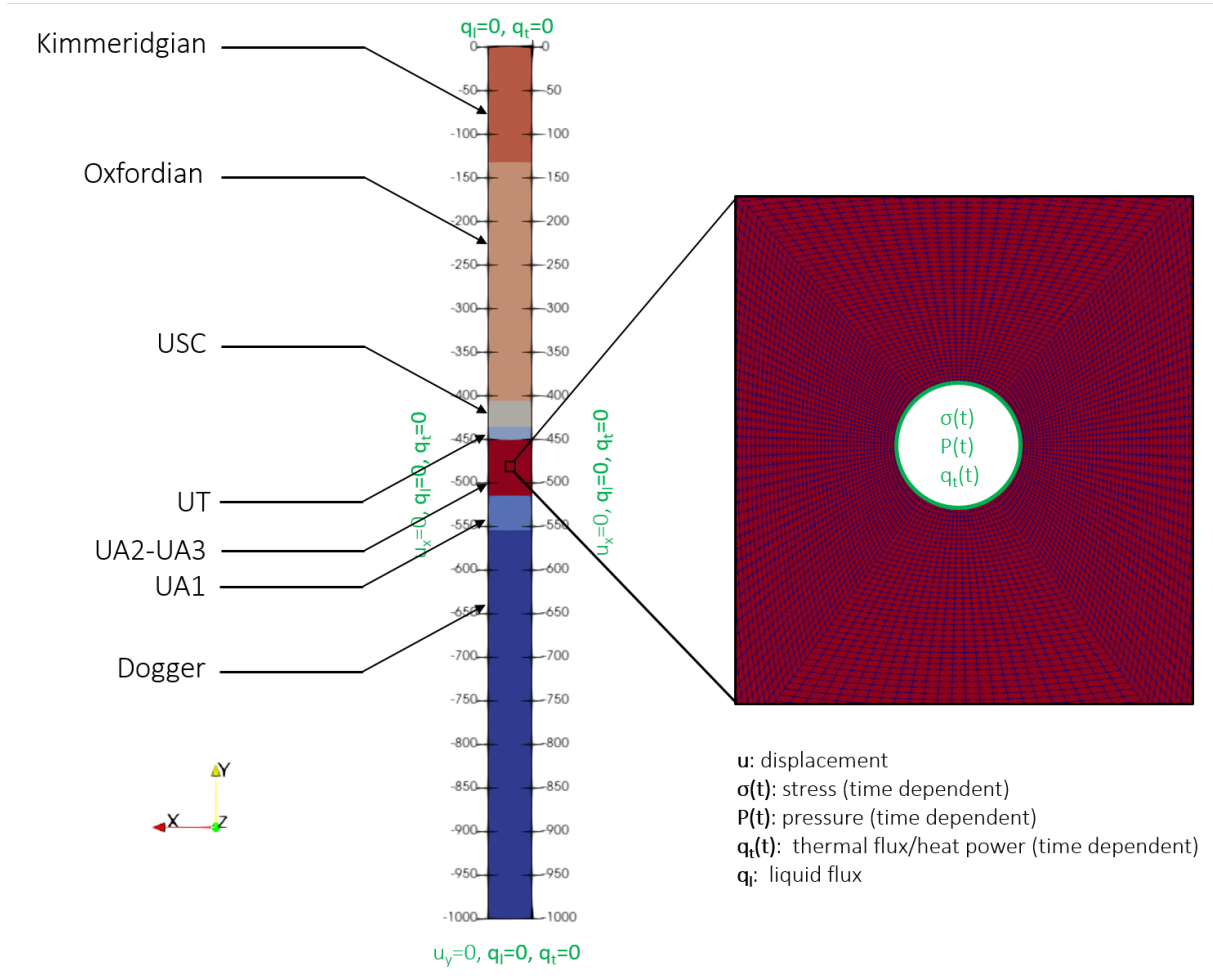
Figure 5.42: Numerical model for the far-field cases studied by BGE

In the cell, thermal, hydraulic and mechanical loads are applied as function of time. The stresses at the boundary of the tunnel are completely deconfined within 24 hours. It follows an isotropic pressure build-up up to 3 MPa mimicking the effect of swelling pressure of bentonite. This pressure remains till the end of the simulation up to 2000 years. In the absence of dedicated function in OpenGeoSys, a new one has been implemented that allows the deconfinement under anisotropic stress conditions and as a function of time and depth. During the excavation phase that goes till 24 hours, the pore water pressure is linearly decreased to atmospheric pressure. After that, undrained conditions are assumed at the borehole wall till the end of the simulation. The system remains isothermal up to two years. Two years after the excavation, a thermal flow is applied at the borehole wall corresponding to the thermal load defined in Table 2.12. Two simulation cases were defined by assuming two interim storage times of 85 years and 55 years corresponding respectively to an initial load of $139\,\mathrm{W\,m^{-1}}$ and $242\,\mathrm{W\,m^{-1}}$.

The initial conditions in the model were set up according to the prescriptions given in Figure 2.6 for Cox. Because OpenGeoSys expects as input the effective stresses according to the Biot effective stress concept, the effective stress profiles needed were first computed taking into account the biot coefficient in each geological layer and the overpressure observed in the Cox layer. A python routine was developed in this context to facilitate the initialisation of stresses and pore pressure in the model. The resulting effective stresses and pore pressure initialised in the model were extracted from the model and are plotted against the computed values for control in Figure 5.43.

EURAD (Deliverable n° 7.6) – Modelling report on the effect of temperature on clay host rocks behaviour
Dissemination level: PU
Date of issue of this report: 06/06/2024

Page 118
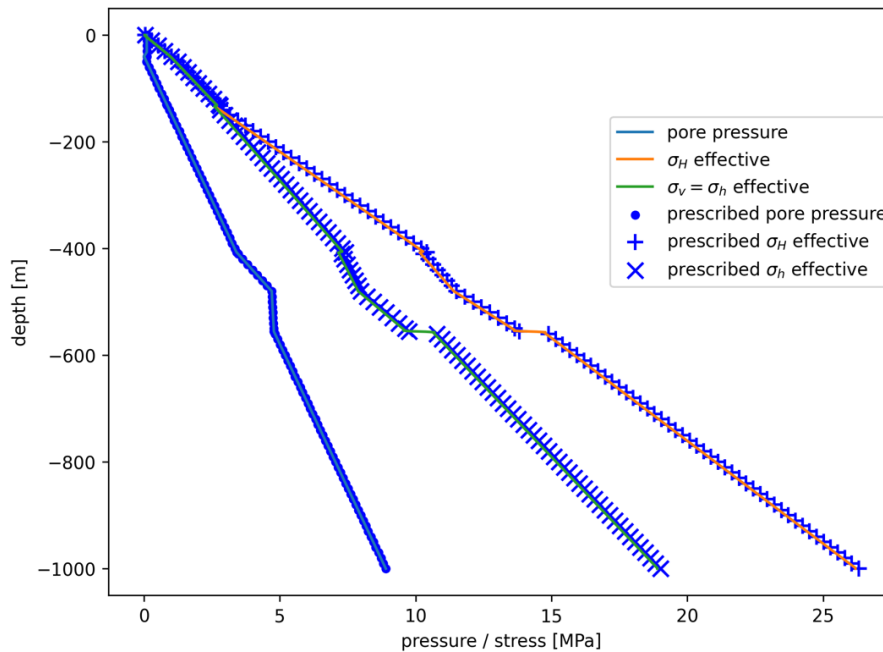
Figure 5.43: Prescribed and intialiased initial pore pressure and effective stresses in the numerical model

5.2.1.3. EDF

For the far-field set, the participants were also asked to model two types of host rocks to be chosen between a Callovo-Oxfordian (Cox) claystone, an Opalinus Clay host rock and a Boom Clay host rock. As in the the near-field case, EDF has chosen to model the behaviour of the Callovo-Oxfordian (Cox) claystone and the Opalinus Clay (OPa). For each of the modelled host rocks, an anisotropic elastic model was used.

The geometry of the far-field model is a vertical cross section presented by a symmetry axis passing through the HLW cell/tunnel and a half-distance between two adjacent tunnels. This geometry was given by the MS49 Hitec report:

- Two similar general geometry are proposed for modelling the Cox and the Opalinus clay host rocks. For both cases, the model will extend from 0 to 1000 m depth, and the half cell-to-cell distance (lateral extent) is set equal to 25 m.

- For the Cox, the excavation diameter is of 1m and the excavation is situated at 480m of depth from the top surface.

- For the Opalinus clay, the excavation diameter is of 1m and the excavation is situated at 600m of depth from the top surface.

Due to the unavailability and imprecision of some material input parameters for the Opalinus far field case, we represent in this report only the results for the far-field modelling case of the Cox. However, it should be noted that the Opalinus far field case has been modelled while making a certain number of hypothesis for the material properties and has shown comparable orders of magnitudes of displacements, stresses, pressures and temperatures to those obtained for the Cox far field case.

The mesh of the far field geometry is presented in the figure below and is done while using triangular

EURAD (Deliverable n˚ 7.6) – Modelling report on the effect of temperature on clay host rocks behaviour
Dissemination level: PU
Date of issue of this report: 06/06/2024

Page 119

meshes in the Cox layer near the excavation and triangular meshes elsewhere (in the other layers). This mesh presents a total of 27194 elements.
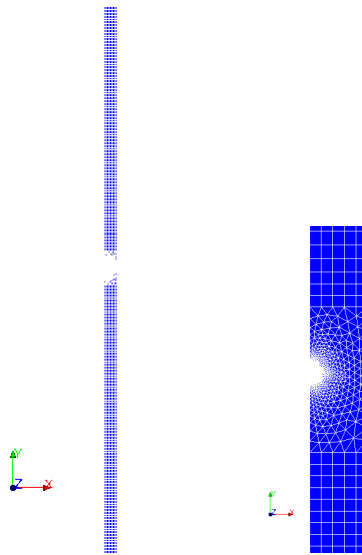
Figure 5.44: Vertical cross section on the Far field mesh (left) Zoom on the mesh near the excavation (right) - Total of 27194 elements

The boundary conditions applied for this modelling case and the material propreties are according to those defined in the MS49 Hitec report.

5.2.1.4. LEI

During the HITEC project, LEI participated in benchmark activities for the Cox THM response analysis in the far-field. The previously developed thermo-poroelastic model implemented in COMSOL Multiphysics was applied. For this model, THM related material properties of 7 geological layers were defined according to the specification (EURAD (Milestone n° 49), 2020). Model domain of 25 m x 1000 m was defined in 2D geometry considering symmetry in vertical direction. Tunnel radius of R=0.5 m was set.

For Cox claystone in-situ total stresses, pore pressure varying with depth were imported from the specification. Temperature distribution was prescribed in the model considering the natural geothermal gradient of 0.025 °C/m and surface temperature of 10 °C, resulting in a temperature of 22 °C at repository level (-480 m).

The boundary conditions for the model boundaries (except tunnel) were assumed:

- Temperature was fixed on top and bottom model boundaries, no heat flow through vertical boundaries;

- Pore water pressure was fixed on top and bottom model boundaries, no water flow through vertical boundaries;

- The zero horizontal displacements were respectively fixed at vertical boundaries, zero vertical displacement was prescribed on model bottom boundary;

- On model top boundary a constant load was imposed equal to the in-situ stress conditions.

THM boundary conditions applicable for tunnel were set according to specification (EURAD (Milestone

EURAD (Deliverable n˚ 7.6) – Modelling report on the effect of temperature on clay host rocks behaviour
Dissemination level: PU
Date of issue of this report: 06/06/2024

Page 120

n° 49), 2020). For representation of tunnel excavation, the initial effective stresses acting on the tunnel wall were described as boundary load multiplied by linear function getting values [1, 0] over 1 day period to represent stress decrease to 0 percent of initial in-situ stress. During period 1 day-2 years (waiting phase) the stress was increased from 0 to 3 MPa and kept fixed during heating phase. The pore water pressure at the tunnel wall (4.7 MPa) was reduced to the atmospheric pressure (0.1 MPa) by multiplication by linear function getting values [1, 0] over 1 day. Dirichlet boundary condition was switched to no flow boundary condition for pore water pressure after excavation phase. The heating phase was represented by prescribed heat flux of two different time dependent thermal load (in W/m) over the tunnel boundary starting after the waiting phase. Evolution of hydro-mechanical boundary conditions for tunnel is presented in Figure 5.45.
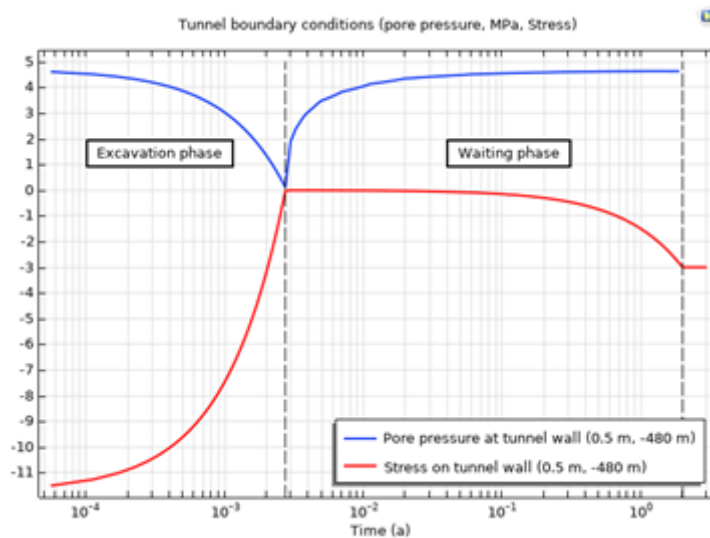
Figure 5.45: Hydro-mechanical boundary conditions for tunnel

Modelling domain was discretized into 2696 triangular and quadratic mesh elements (Figure 5.46) in thermo-poroelastic model. Timestep size was determined by the solver.

The simulations were performed with COMSOL Mutiphysics (v. 5.6). All the pre-treatment and post- treatment has been performed within a single platform (COMSOL Mutiphysics). The code run on a standalone personal computer. For THM response of Cox claystone in the far field, the computation time was 57 seconds, type of solver was fully coupled direct solver MUMPS.

EURAD (Deliverable n˚ 7.6) – Modelling report on the effect of temperature on clay host rocks behaviour
Dissemination level: PU
Date of issue of this report: 06/06/2024

Page 121

a)   b)
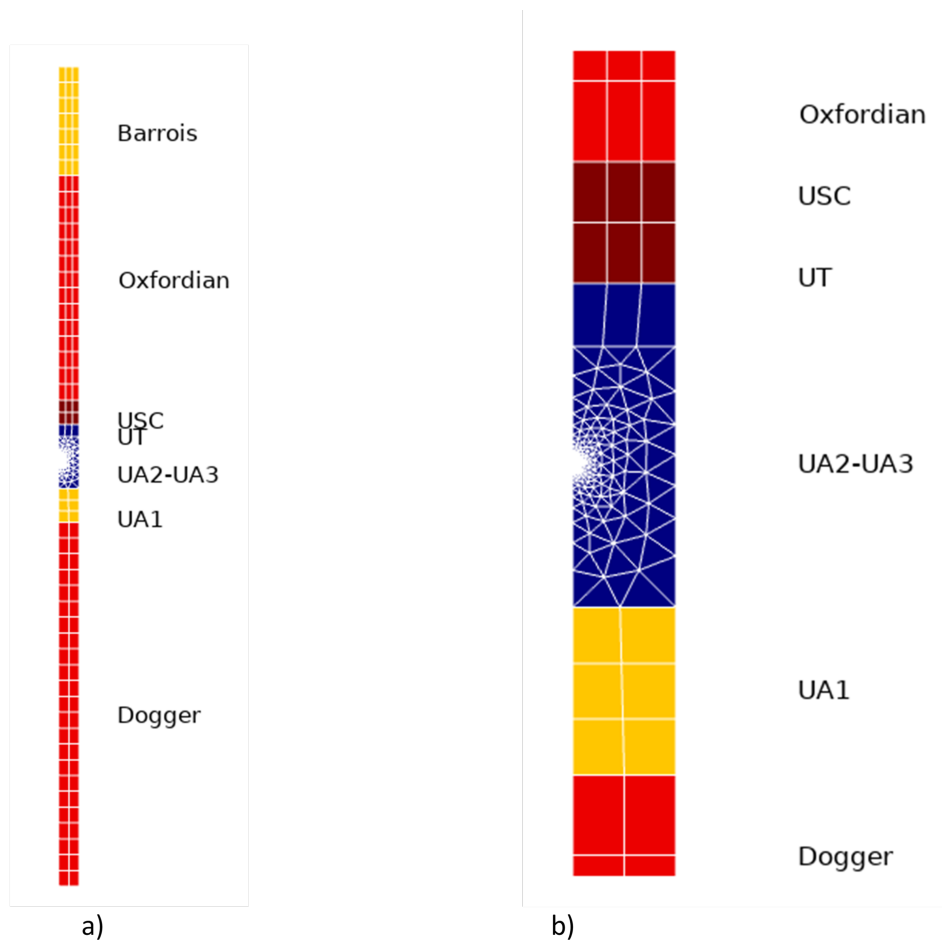
Figure 5.46: Mesh of a) whole model domain, b) mesh close to tunnel boundary (model domain representing units UA2-UA3 (Cox) discretized more)

5.2.1.5. ULg

The following section presents the key features of numerical simulation campaign which was performed in WP 7: sub-task 2.3. The report also discusses the main contributions from University of Liege. Following the mandate of sub-task 2.3, the prime objective was to examine the temperature-induced artifacts in a generic repository in Callovo-Oxfordian (Cox) formation. Two different scenarios were simulated based on the given technical guidelines, in Case 1 the waste canisters are supposed to be disposed after a cooling of 85 years, while the Case 2 represents a cooling period of 55 years.

Features of numerical simulation

Two-dimensional (2D) plane strain finite element analysis was performed using the in-house software LAGAMINE. The geometric features of 2D model were in accordance with the given specifications (see Figure 5.47). The overall depth in Y-direction was 1000m and width in X-direction was 25m. The lithological profile for Cox along with the initial temperature, pore water and stress distribution along the Y-axis were implemented based on the provided field data (see Figure 5.48).

After setting up the 2D model, a finite element mesh was created using an isoparametric quadrilateral element (MWAT) with 8 nodes Collin et al. (2002). The element for 2D case has five degrees of freedom at each node: two displacements (X, Y) of the soil skeleton, a liquid water pressure (P_w), a gas (dry air + vapor) pressure (P_g) and temperature (T). Figure 5.49 shows the finite element mesh used for the

EURAD (Deliverable n˚ 7.6) – Modelling report on the effect of temperature on clay host rocks behaviour
Dissemination level: PU
Date of issue of this report: 06/06/2024

Page 122

analysis. The total number of elements was 4575.
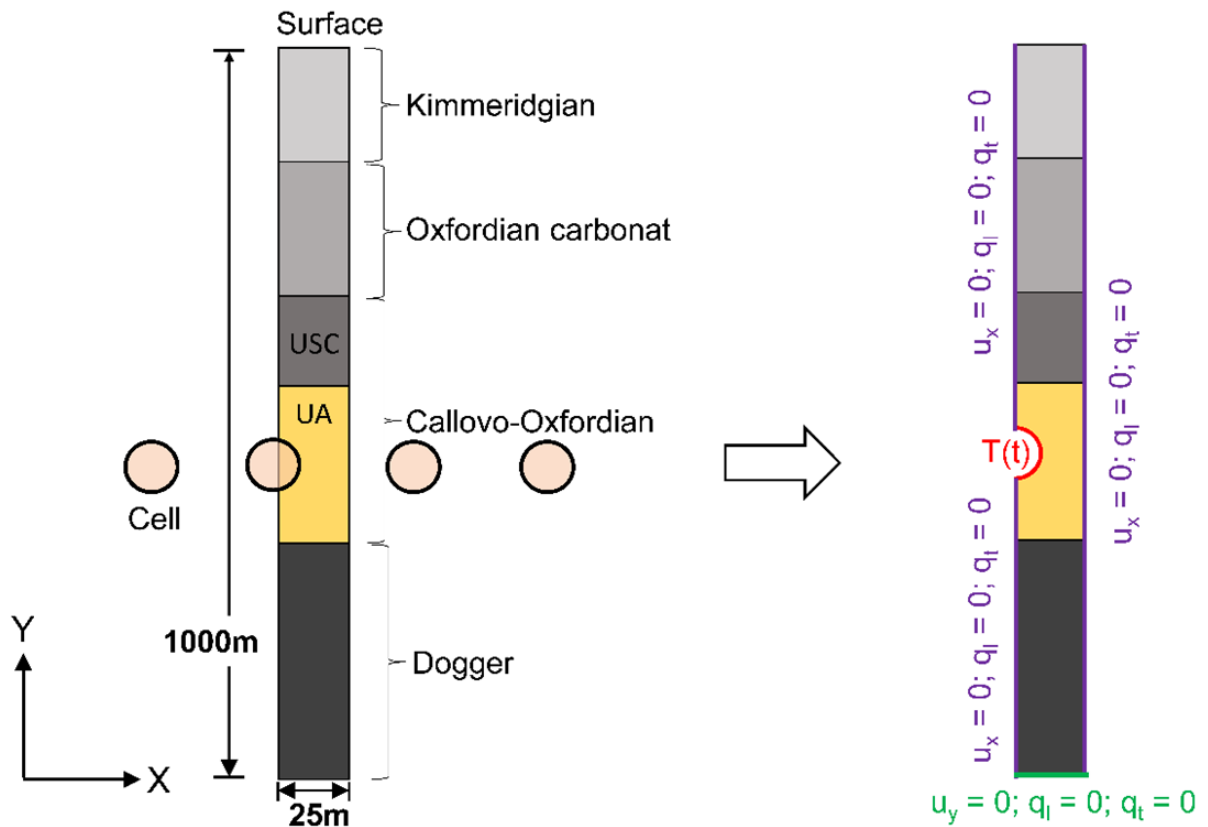
Figure 5.47: ULg 2D PS simulation: model geometry for the far-field case for Cox clay stone.

EURAD (Deliverable n˚ 7.6) – Modelling report on the effect of temperature on clay host rocks behaviour
Dissemination level: PU
Date of issue of this report: 06/06/2024

Page 123
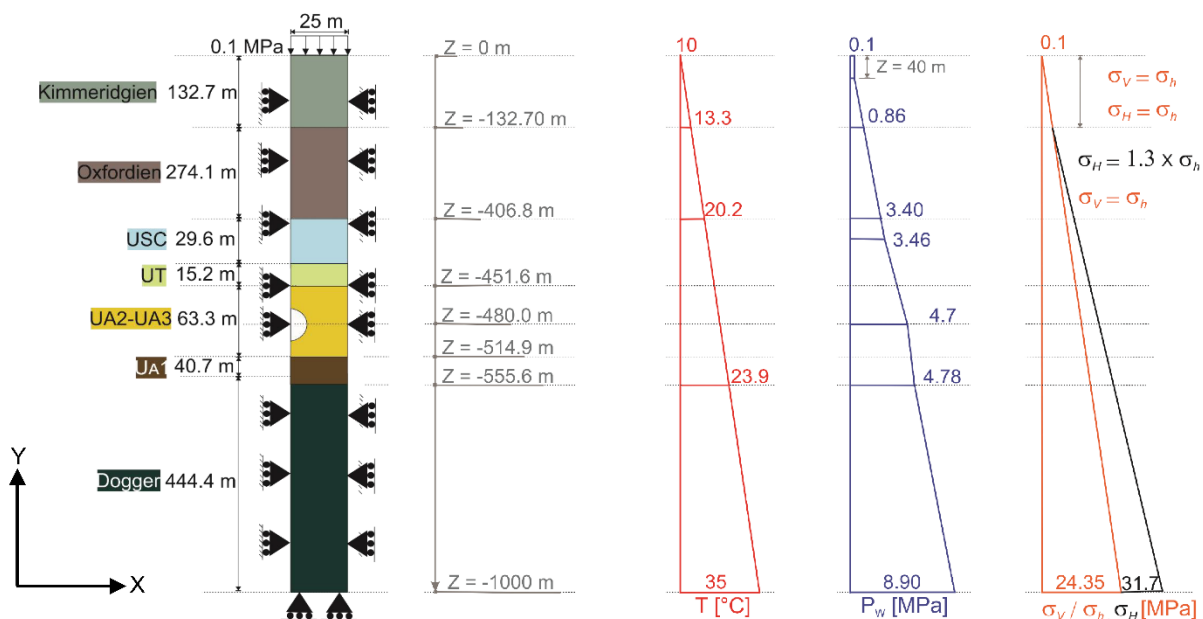
Figure 5.48: ULg 2D PS simulation: Initial conditions (Z = depth; T = temperature; P_w = pore water pressure; $\sigma_v/\sigma_h/\sigma_H$ = vertical/horizontal/max. horizontal total stress).
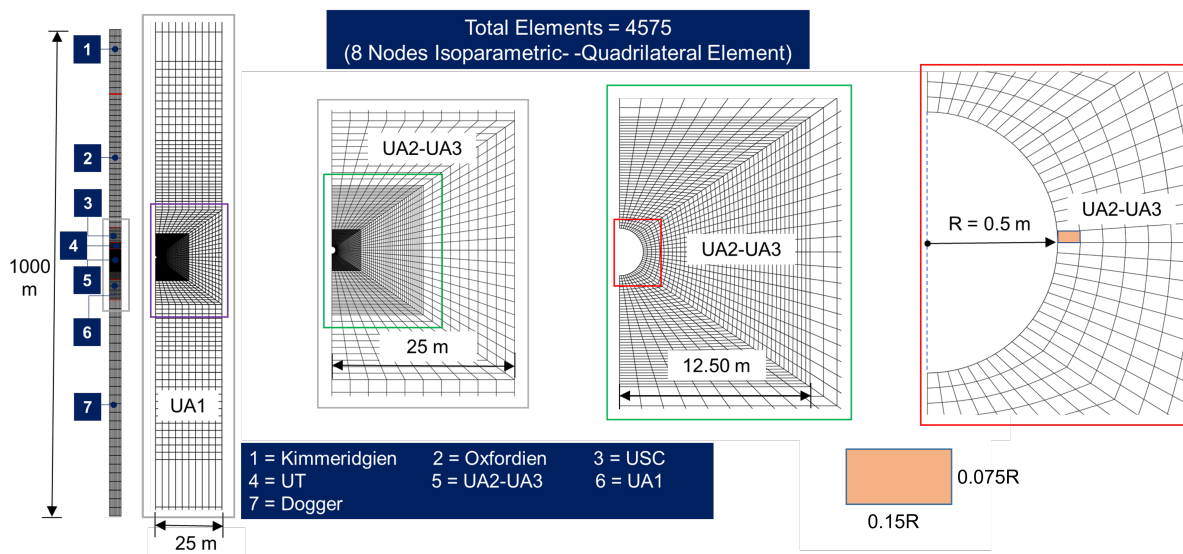
Figure 5.49: ULg 2D PS simulation: Finite element mesh along with the geometrical features (e.g., size of an element in X direction = 0.075m (0.15R) and in Y-direction = 0.0375m (0.075R)).

Time varying boundary conditions

Time varying boundary conditions in the far-field benchmark exercise evolve in three phases (see Table 5.13). In the initial phase (T < 0), the repository is not present, which signifies the activation of in-situ stresses (σ_v and σ_h), hydro-static pressure (P_w) and natural geothermal field (T) in the model as depicted in Figure 5.50.

EURAD (Deliverable n° 7.6) – Modelling report on the effect of temperature on clay host rocks behaviour
Dissemination level: PU
Date of issue of this report: 06/06/2024

Page 124

Table 5.13: ULg 2D PS analysis: Features of time-varying boundary conditions at the borehole wall.

Phase	Mechanical conditions	Hydraulic conditions	Thermal conditions
P1: Excavation (0 to 24 hrs.)	Initial vertical stress reduce to zero	Drained	No flow
P2: Waiting (24 hrs. to 2 yrs.)	Increase vertical stress (0 to 3 MPa) linearly over 2 years	Undrained	No flow
P3: Heating (2 to 1000 yrs.)	Constant vertical stress (3MPa)	Undrained	Based on Case1 / Case2 scenario
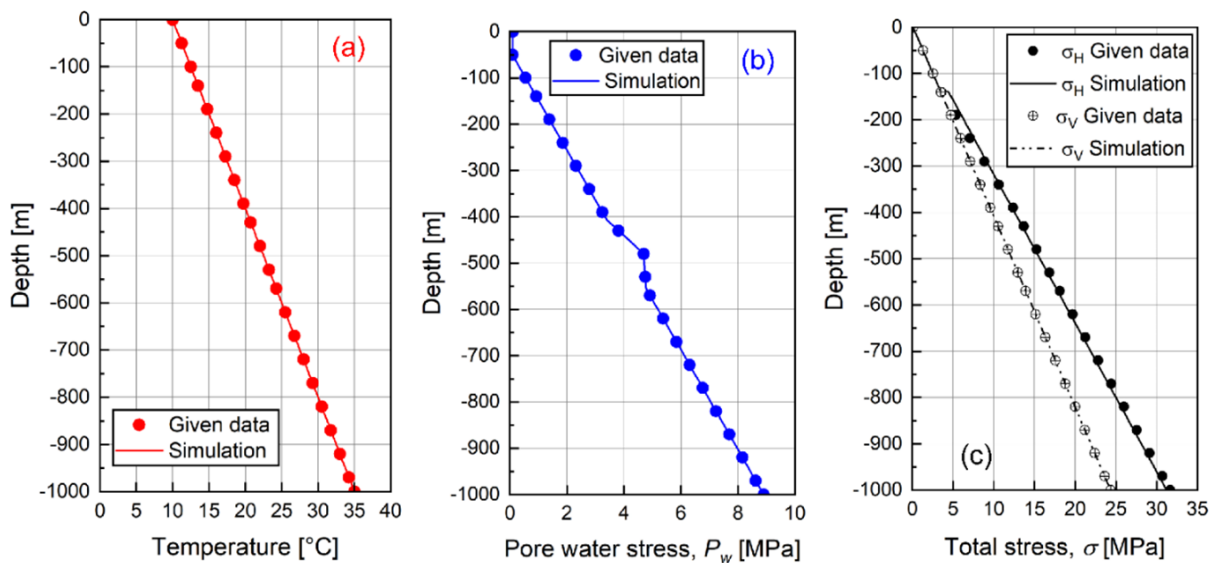
Figure 5.50: ULg 2D PS simulation: Setting-up of initial conditions in terms of (a) temperature, (b) pore water pressure, and (c) in-situ stress state along the depth in Y-direction.

In the excavation phase (P1: 0 to 24 hours), the initial vertical stress at the borehole wall was reduced to 0 under drained conditions. The excavation phase is followed by waiting phase (P2: 24 hours to 2 years). In the waiting phase, the vertical stress at the borehole wall was increased linearly from 0 to 3 MPa over a span of two years. During the waiting period, no water and heat flow took place at the borehole wall. Phase3 is the heating phase which was initiated immediately once Phase2 was over. The applied vertical stress at the cell/borehole wall in heating phase was kept constant at 3 MPa under undrained conditions, while the heat was injected along the borehole wall as per the specified scenarios of 85/55 years cooling-period.

As a first step, initial conditions were setup in the model as depicted in Figure 5.50. The excavation process was mimicked using the stress-reduction method as shown in Figure 5.51 along with the flow conditions. In Phase3, the equivalent heat flux was imposed along the cell/borehole wall. The calculation of heat flux was based on the given thermal load data and the consideration of two different cooling period scenarios as shown in Figure 5.52.

EURAD (Deliverable n° 7.6) – Modelling report on the effect of temperature on clay host rocks behaviour
Dissemination level: PU
Date of issue of this report: 06/06/2024

Page 125
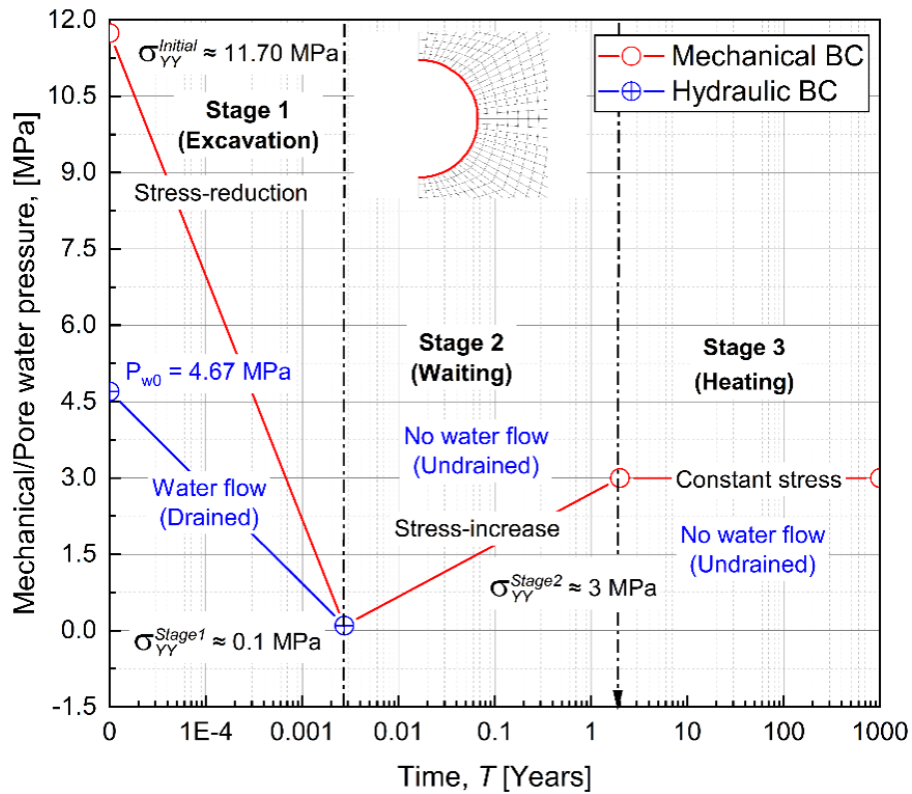
Figure 5.51: ULg 2D PS simulation: Implementation of time varying boundary conditions at the borehole wall during excavation, waiting and heating phase.
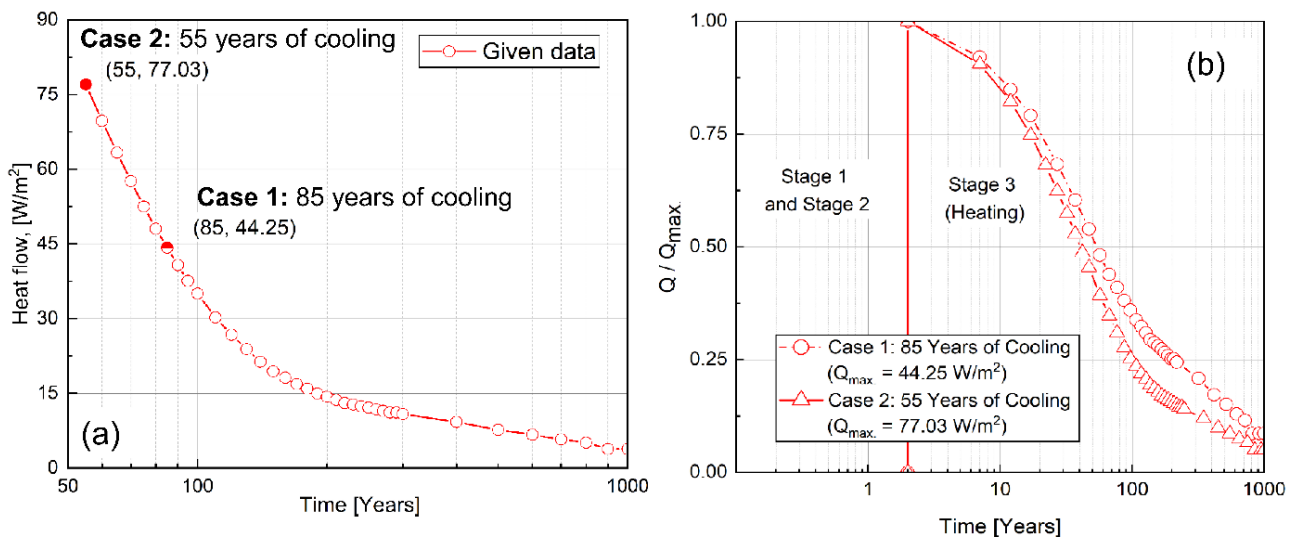
Figure 5.52: ULg 2D PS simulation: Calculation of heat flux at the borehole wall during the heating phase, (a) given thermal source term in the specification with two different options of cooling period, and (b) scaling of given thermal flux during the numerical simulation.

EURAD (Deliverable n˚ 7.6) – Modelling report on the effect of temperature on clay host rocks behaviour
Dissemination level: PU
Date of issue of this report: 06/06/2024

Page 126

Constitutive laws and material properties

Concerning the mechanical constitutive laws, isotropic linear elastic model was adopted for Limestone, Oxfordian, Dogger, and for Cox sub unit USC. Whereas anisotropic linear elastic model was used for the Cox sub units UT, UA2-UA3, and UA1 as outlined in Table 5.14.

Table 5.14: ULg 2D PS analysis: Constitutive model for mechanical behaviour of different geomaterials used in the analysis.

Depth	Material	Mechanical law
0 to 132.7m	Barrois Limestone	Isotropic linear elasticity
132.7 to 406.8m	Oxfordian	Isotropic linear elasticity
406.8 to 436.4m	Cox: USC	Isotropic linear elasticity
436.4 to 451.6m	Cox: UT	Anisotropic linear elasticity
451.6 to 514.9m	Cox: UA2-UA3	Anisotropic linear elasticity
514.9 to 555.6m	Cox: UA1	Anisotropic linear elasticity
555.6 to 1000 m	Dogger	Isotropic linear elasticity

As per the given specifications, Table 5.15 summarize the nature of material properties i.e., isotropic or anisotropic which were used for the numerical analysis.

Table 5.15: ULg 2D PS analysis: Nature of given material properties (Iso. = Isotropic; Aniso. = Anisotropic; E = Young's modulus; ν = Poisson's ratio; G = Shear modulus; b = Biot's coefficient; $K_{sat.}$ = Saturated permeability; λ = Thermal conductivity)

Material	E	ν	G	b	$K_{sat.}$	λ
Barrois Limestone	Iso.	Iso.	Iso.	Iso.	Iso.	Aniso.
Oxfordian	Iso.	Iso.	Iso.	Iso.	Iso.	Iso.
Cox: USC	Iso.	Iso.	Iso.	Iso.	Aniso.	Iso.
Cox: UT	Aniso.	Aniso.	Aniso.	Aniso.	Aniso.	Aniso.
Cox: UA2-UA3	Aniso.	Aniso.	Aniso.	Aniso.	Aniso.	Aniso.
Cox: UA1	Aniso.	Aniso.	Aniso.	Aniso.	Aniso.	Aniso.
Dogger	Iso.	Iso.	Iso.	Iso.	Iso.	Iso.

Detailed material properties related with the mechanical and hydraulic constitutive laws are summarized in Table 5.16 for Cox and in 5.17 for over- and underlying materials. Table 5.18 shows the fluid i.e., water and air properties used during the simulation.

The volumetric thermal expansion coefficient of water depends on the ambient temperature as per the relationship proposed by Kell (1975) as depicted in Figure 5.53. Also, the water viscosity is also dependent on the temperature as per the relationship proposed by Rumble (2019).

Simulation results

The required output such as temperature and pore water pressure evolution along with the Biot's effective stress distribution were plotted and compared with the other teams (see Figure 5.60 and 5.62). Additionally, the temperature, pore water pressure and stress profiles were also plotted along the depth of repository (0 to 1000 m). As per the given initial conditions, the temperature at the surface (d = 0m) and far-field (d = 1000m) were kept constant at $10°C$ and $35°C$, respectively. Temperature changes during the

EURAD (Deliverable n˚ 7.6) – Modelling report on the effect of temperature on clay host rocks behaviour
Dissemination level: PU
Date of issue of this report: 06/06/2024

Page 127

Table 5.16: ULg 2D PS analysis: Material parameters for Callovo-Oxfordian claystone (Cox)

Material property	Material	Value
Thermal conductivity normal to bedding, $\lambda_\perp$ [W/m/K]	USC UT UA2-UA3 UA1	1.8 1.4 1.25 1.6
Thermal conductivity parallel to bedding, $\lambda_\parallel$ [W/m/K]	USC UT and UA	1.8 $1.5 \times \lambda_\perp$
Solid phase specific heat, C_s [J/kg/K]		790
Bulk density [kg/m3]	USC UT and UA	2480 2386
Young's modulus normal to bedding, $E_\perp$ [GPa]	USC UT UA2-UA3 UA1	12.8 8.5 7 10
Young's modulus parallel to bedding, $E_\parallel$ [GPa]	UA and UT	$1.5 \times E_\perp$
Poisson's ratio, (USC: Isotropic) [-]	USC	0.3
Poisson's ratio (UA and UT), $\nu_\perp$ [-]	UA and UT	0.3
Poisson's ratio (UA and UT), $\nu_\parallel$ [-]	UA and UT	0.2
Shear modulus normal to bedding, $G_\perp$ [GPa]	UT UA2-UA3 UA1	3.8 3.1 4.4
Linear thermal expansion coefficient of skeleton, [K^{-1}]		1.28×10^{-5}
Intrinsic permeability parallel to bedding, $K_\parallel$ [m^2]		3.9×10^{-20}
Intrinsic permeability normal to bedding, $K_\perp$ [m^2]		1.3×10^{-20}
Biot coefficient, (USC: Isotropic) [-]	USC	0.8
Biot coefficient, (UT: Anisotropic) [-]	UT	b1 = 0.742857 b2 = 0.80 b3 = 0.742857
Biot coefficient, (UA2-UA3: Anisotropic) [-]	UA2-UA3	b1 = 0.788235 b2 = 0.835294 b3 = 0.788235
Biot coefficient, (UA1: Anisotropic) [-]	UA1	b1 = 0.697479 b2 = 0.764706 b3 = 0.697479
Porosity [-]	USC UT and UA	0.15 0.18

heating phase mainly occurred in the Cox layer (-406.8 to -555.6m) along with the overlaying (Oxfordian), and underlying (Dogger) layers (see Figure 5.54).

The pore water pressure isochrones along the depth (0 to 1000m) for both the cases are shown in Figure

EURAD (Deliverable n˚ 7.6) – Modelling report on the effect of temperature on clay host rocks behaviour
Dissemination level: PU
Date of issue of this report: 06/06/2024

Page 128

Table 5.17: ULg 2D PS analysis: Material parameters for over- and underburden parameters for Cox case

Material property	Material	Value
Porosity, n [-]	Barrois limestone	0.13
	Oxfordian	0.13
	Dogger	0.10
Bulk density, ρ [kg/m^3]	Barrois limestone	2450
	Oxfordian	2470
	Dogger	2470
Biot coefficient, b [-]	Barrois limestone	0.60
	Oxfordian	0.75
	Dogger	0.60
Young's modulus, E [GPa]	Barrois limestone	3.6
	Oxfordian	30
	Dogger	30
Poisson ratio, ν [-]	Barrois limestone	0.30
	Oxfordian	0.30
	Dogger	0.30
Thermal expansion coefficient, [K^{-1}]	Barrois limestone	2.2×10^{-5}
	Oxfordian	4.5×10^{-6}
	Dogger	4.85×10^{-6}
Intrinsic permeability, K [m^2]	Barrois limestone	1×10^{-19}
	Oxfordian	1×10^{-16}
	Dogger	1×10^{-18}
Thermal conductivity, λ [W/m/K]	Barrois limestone	$\lambda_\perp = 1.1$; $\lambda_\parallel = 1.5 \times \lambda_\perp$
	Oxfordian	2.3
	Dogger	2.3
Specific heat, C [J/kg/K]	Barrois limestone	1024
	Oxfordian	925
	Dogger	925

Table 5.18: ULg 2D PS analysis: Fluid properties for water and air used in the simulation

Fluid	Parameter	Value
Water	Density, ρ_{w0} [kg/m^3]	1000
	Compressibility at 40°, $\frac{1}{\chi_w}$ [Pa^{-1}]	4.5×10^{-10}
	Thermal conductivity, λ_w [W/m/K]	0.528
	Specific heat, c_{pw} [J/kg/K]	4180
Air	Density, ρ_a [kg/m^3]	1.205
	Dynamic viscosity, μ_a [Pa.s]	1.80×10^{-5}
	Thermal conductivity, λ_a [W/m/K]	0.025
	Specific heat, c_{pa} [J/kg/K]	1000

5.55 along with the saturated permeability values for different layers. The pore water pressure at the surface (d = 0m) and far-field (d = 1000m) were kept constant to 0.1 MPa and 8.9 MPa, respectively. From the

EURAD (Deliverable n˚ 7.6) – Modelling report on the effect of temperature on clay host rocks behaviour
Dissemination level: PU
Date of issue of this report: 06/06/2024

Page 129
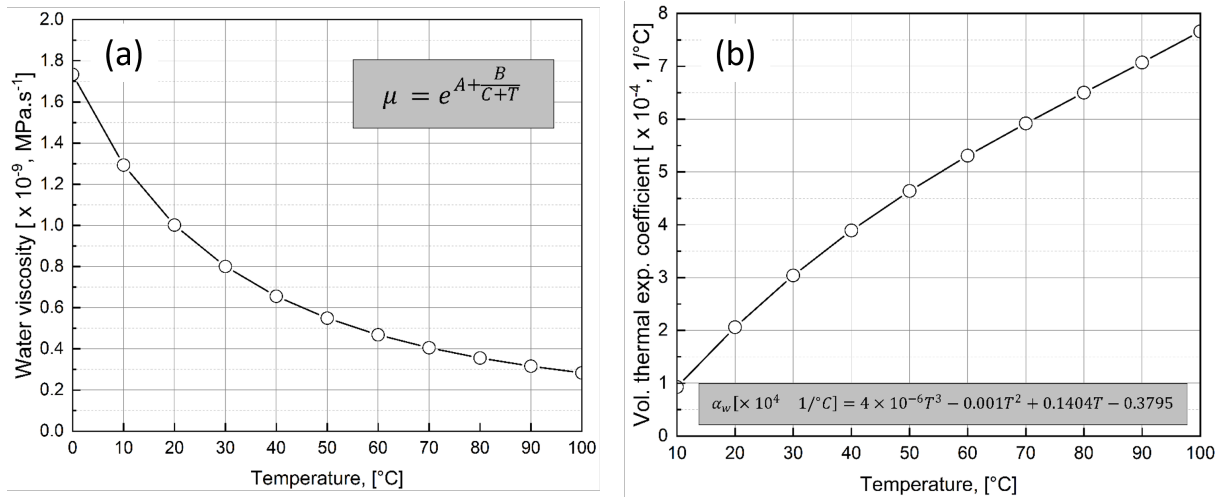
Figure 5.53: ULg 2D PS simulation: temperature dependent properties of water, (a) volumetric thermal expansion coefficient under atmospheric pressure, and (b) viscosity under atmospheric pressure.
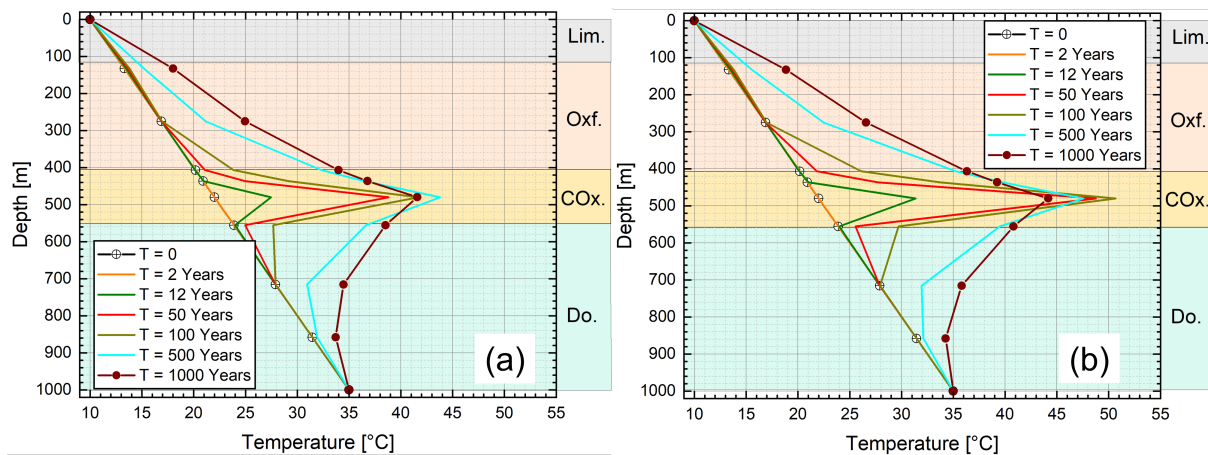
Figure 5.54: ULg simulation results: temperature isochrones at 25m (25D) along the depth (a) Case 1, and (b) Case 2.

figure, the temperature induced excess pore water pressure generates mainly in the Cox layer which has the lowest intrinsic permeability value ($10^{-20}\,m^2$). These isochrones highlight the role of available hydraulic gradient along with the intrinsic permeability values of different layers in the pore water pressure distribution along the depth during the heating phase. In both the cases, the temperature-induced pore water pressure variations are more dominant in the Oxfordian layer which has the highest intrinsic permeability ($10^{-16}\,m^2$) value among the other over/under laying layers.

The effective stress in Y-direction isochrones is plotted along the depth (0 to 1000m) and shown in Figure 5.56. These isochrones reveal the far-field effects of imposed mechanical and hydraulic boundary conditions at the borehole wall during excavation, waiting and heating phase. Stress redistribution takes place in different layers along the depth. These changes in the stress state are more pronounced in the Cox layer. The saturated permeability plays a key role in the stress distribution along the depth.

EURAD (Deliverable n° 7.6) – Modelling report on the effect of temperature on clay host rocks behaviour
Dissemination level: PU
Date of issue of this report: 06/06/2024

Page 130
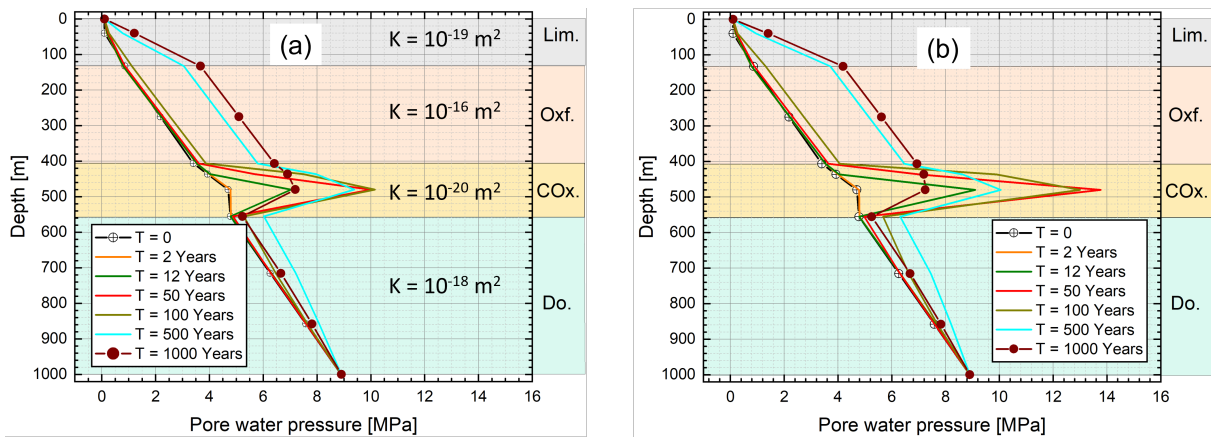
Figure 5.55: ULg simulation results, pore water pressure isochrones at 25m (25D) along the depth, (a) Case 1, and (b) Case 2.
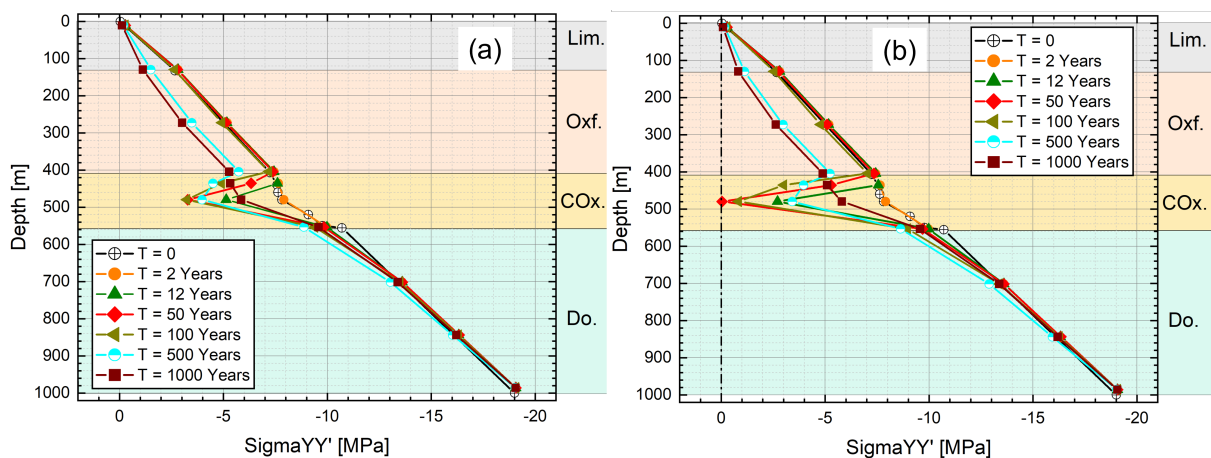
Figure 5.56: ULg simulation results: effective stress isochrones at 25m (25D) along the depth (a) Case 1, and (b) Case 2.

5.2.1.6. UPC

In accordance with specifications, Thermo-Hydro-Mechanical (THM) modelling of the Cox host rock under the far-field/long-term conditions has been carried out in this section. The simulations are performed over a long period, investigating the effect of the thermal loading on the far-field/long-term case. In the numerical model, the heating period is extended to 1000 years. The modelling domain is extended vertically to the surface. The lateral extent is defined by the symmetry axis through the High-Level Waste (HLW) cell/tunnel and the half-distance between two adjacent SF/HLW tunnels.

In the simulations, all the cells are assumed to be filled at the same time. This hypothesis is valid if one considers the time needed to fill two adjacent cells (a few years at most) compared to the time required for the most exothermic waste to reach their thermal peak (several hundred years). Symmetrical loading by two adjacent cells implies that the zone located at half-distance between two parallel cells is subject to loads from both cells. The lateral symmetry conditions prevent any horizontal expansion (no displacement) and any pressure dissipation (no flow).

(a). Geometry and material properties   Based on the geometry configuration given, a two-dimensional plane strain condition is assumed, where only one cell is modelled in the geometry model and the interac-

EURAD (Deliverable n° 7.6) – Modelling report on the effect of temperature on clay host rocks behaviour
Dissemination level: PU
Date of issue of this report: 06/06/2024

Page 131

tion between cells is provided by the symmetry condition. As shown in Figure 5.57, a model representing the geological formations from the surface to 1000 m deep is considered. The excavated diameter of the cell is 1 m. Table 5.19 lists the input material parameters for the different rock layers. As specified, all the formations except the Cox claystone are assumed to behave isotropically elastically whereas the Cox materials are considered to be anisotropic elastic. A mesh of 13 310 nodes and 12 863 quadrilateral elements is adopted, with smaller elements near the gallery. Note that the generalised selective integration procedure, implemented in CODE_BRIGHT, can suppress element locking and hourglassing issues in linear quadrilateral elements (Olivella et al., 1995).
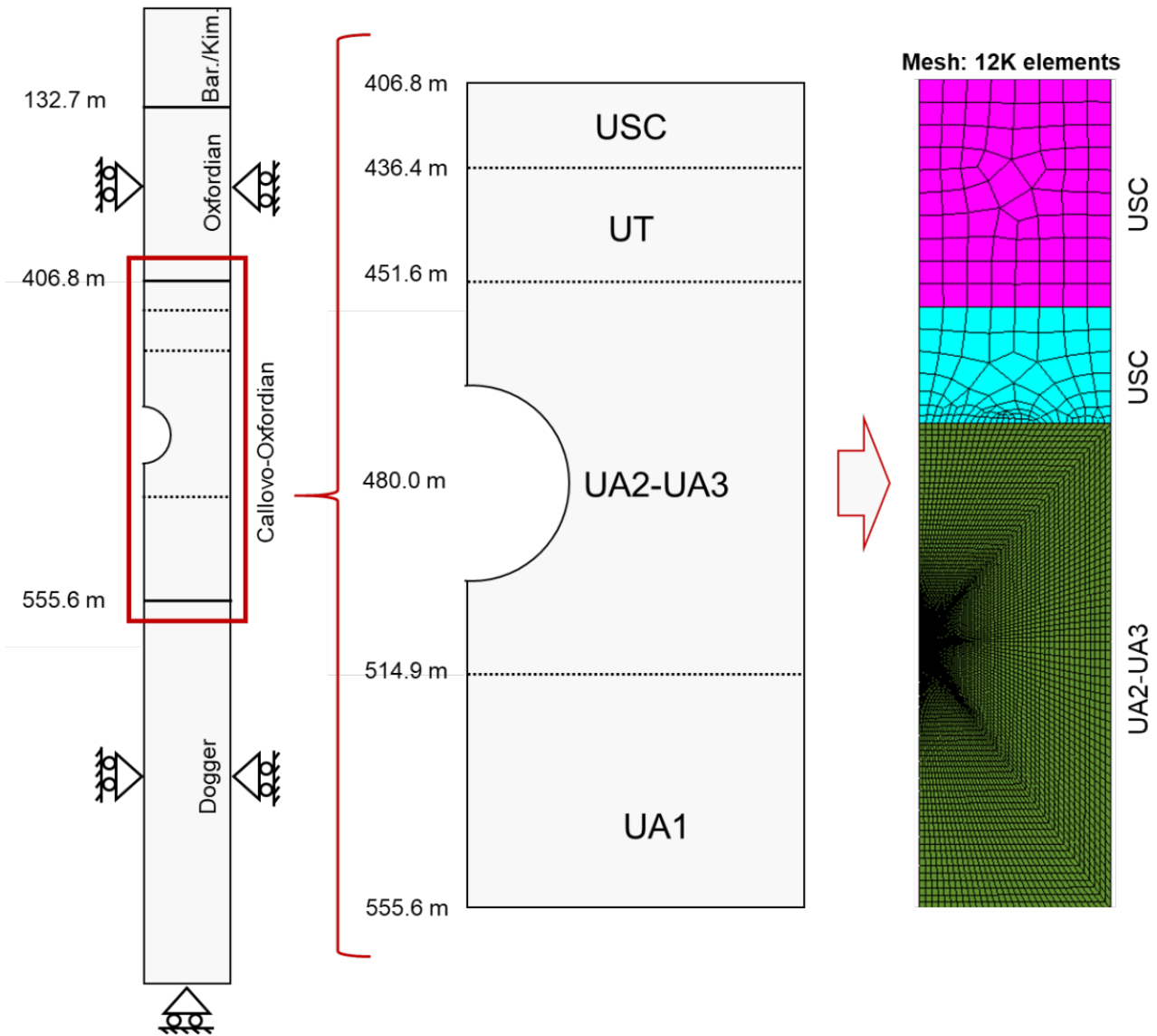
Figure 5.57: Geometry, boundary conditions and mesh size of the numerical model.

(b). Initial conditions The temperature and pore pressure at the upper surface is assumed as $10\,°C$ and $0.1\,MPa$, respectively. The temperature follows the natural geothermal gradient of $0.025\,°C/m$ (see Figure 5.58(a)). A hydrostatic pore water pressure is assumed in the overburden and underburden, but an overpressure is observed in the Cox layer and has been taken into account in the model, as shown in Figure 5.58(b). This type of overpressure is simulated by a linear increase up to cell centreline depth and it then decreases to recover the hydrostatic pressure.

EURAD (Deliverable n° 7.6) – Modelling report on the effect of temperature on clay host rocks behaviour
Dissemination level: PU
Date of issue of this report: 06/06/2024

Page 132

Table 5.19: Input parameters of different layers.

Parameters	Notation		Bar./Kim.	Oxf.	USC	UT	UA2-UA3	UA1	Dog.
Young's moduli	E_1	[MPa]	3600	30 000	12 800	12 750	10 500	15 000	30 000
	E_2	[MPa]	3600	30 000	12 800	8500	7000	10 000	30 000
Poisson's ratios	ρ_1	[–]	0.3	0.3	0.3	0.2	0.2	0.2	0.3
	ρ_2	[–]	0.3	0.3	0.3	0.3	0.3	0.3	0.3
Shear modulus	G_2	[MPa]	1384	11 538	4923	3800	3100	4400	11 538
Thermal conductivities	λ_x	[W/m/K]	1.54	2.30	1.80	2.10	1.875	2.40	2.30
	λ_y	[W/m/K]	1.10	2.30	1.80	1.40	1.25	1.60	2.30
Intrinsic permeabilities	K_x	[m^2]	1×10^{-19}	1×10^{-16}	3.9×10^{-20}	3.9×10^{-20}	3.9×10^{-20}	3.9×10^{-20}	1×10^{-18}
	K_y	[m^2]	1×10^{-19}	1×10^{-16}	1.3×10^{-20}	1.3×10^{-20}	1.3×10^{-20}	1.3×10^{-20}	1×10^{-18}
Solid phase density	ρs	[kg/m^3]	2667	2690	2741	2690	2690	2690	2633
Porosity	ϕ	[–]	0.13	0.13	0.15	0.18	0.18	0.18	0.10
Anisotropic Biot coefficients	$b_1 = b_2$	[–]	0.6	0.75	0.8	0.791	0.791	0.791	0.6
	b_3	[–]	0.6	0.75	0.8	0.818	0.818	0.818	0.6
Thermal expansion coefficient	α_s	[°C^{-1}]	2.21×10^{-5}	4.51×10^{-6}	1.28×10^{-5}	1.28×10^{-5}	1.28×10^{-5}	1.28×10^{-5}	4.51×10^{-6}
Solid phase specific heat	c_p	[J/kg/K]	1024	925	790	790	790	790	925
Computed solid compressibility	β_s	[MPa^{-1}]	1.33×10^{-4}	1×10^{-5}	1.88×10^{-5}	2×10^{-5}	2.43×10^{-5}	1.7×10^{-5}	1.6×10^{-5}

Bar.: Barrois limestone; Kim.: Kimmeridgian; Oxf: Carbonated Oxfordian; USC: Callovo-Oxfordian USC; UT: Callovo-Oxfordian UT; UA23: Callovo-Oxfordian UA2-UA3; UA1: Callovo-Oxfordian UA1; DOG: Dogger.

The vertical stress corresponds to the weight of the overburden (in this study, the overburden rock mass density of $2472\,\mathrm{kg/m^3}$ is used) and the minimum (σ_h) horizontal stress is taken equal to vertical stress. The minimum (σ_H) horizontal stress is equal to the vertical stress in the Kimmeridgian and 1.3 times of σ_h from the top Cox. A linear interpolation is assumed in the Oxfordian carbonates. Figure 5.58(c) shows the in-situ stress state. Specifically, a good agreement between numerical results (at the end of the initial generation after running the model for 1 year) and field test results are presented in Figure 5.58(a), Figure 5.58(b) and Figure 5.58(c).

(a)   (b)   (c)
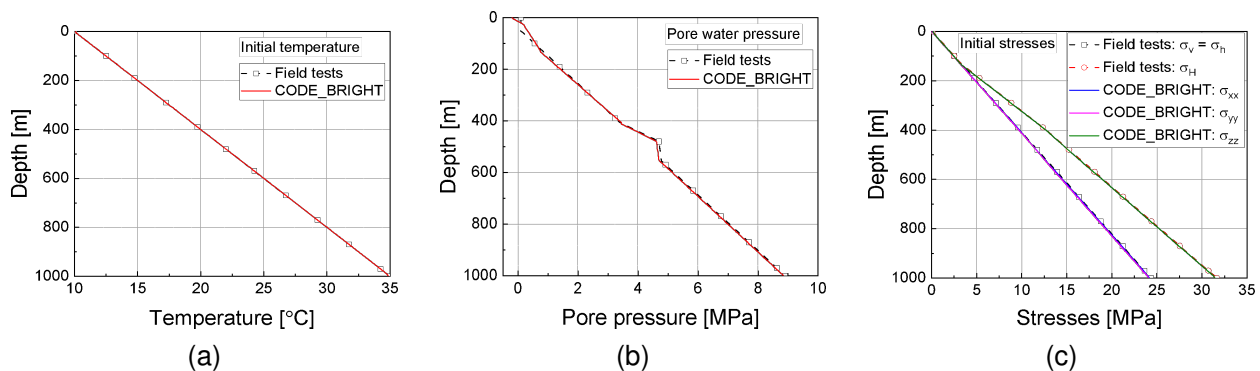
Figure 5.58: Comparisons of initial conditions between the field tests and CODE_BRIGHT simulations (at time t = 0*, i.e., after the initial balance calculation) in terms of (a) initial temperature, (b) initial pore pressure, and (c) initial stresses.*

(c). Modelling stages and boundary conditions The far-field boundary conditions are kept constant in all modelling stages. On the upper boundary, the constant temperature is set as $10\,°\mathrm{C}$ and the constant pore pressure is set as $0.1\,\mathrm{MPa}$. Meanwhile, a free displacement boundary condition is considered at the upper surface. Furthermore, on the bottom surface, the constant temperature is set as $35\,°\mathrm{C}$ and pore pressure is set as $8.9\,\mathrm{MPa}$, and zero normal displacements are considered. No flow and zero normal displacements are applied to the lateral boundaries.

Four modelling stages have been considered and the corresponding boundary conditions at the gallery

EURAD (Deliverable n˚ 7.6) – Modelling report on the effect of temperature on clay host rocks behaviour
Dissemination level: PU
Date of issue of this report: 06/06/2024

Page 133

wall are:

- **Initial generation (-1 year to 0).** As specified, numerical simulations are performed to get the initial conditions before excavation.

- **Excavation stage (0 to 24 hours).** No thermal flow was applied at the gallery wall; pore water pressure linearly decrease from its initial value to 0.1 MPa; applied stresses reduced from 100% to 0% of the initial in-situ stress by using the smoothed excavation method implemented in CODE_BRIGHT (Song et al., 2021a).

- **Waiting stage (24 hours to 2 years).** No-thermal flow and no-hydraulic flow boundary conditions are applied at the gallery wall; along the gallery wall, the applied stresses linearly increase from 0 to 3 MPa over 2 years during the waiting stage.

- **Heating stage (2 years to 1000 years).** The applied thermal flow based on applied power prediction is applied at the borehole wall; non-hydraulic flow boundary condition is applied at the gallery wall; 3 MPa constant pressure is applied on the gallery wall during the heating phase. The thermal history is based on a COG-800 package, as shown in Figure 5.59. Two different cases have been simulated: (1) The waste packages are installed after having let them cool down for 85 years and the initial thermal load is 139 W/m (see Figure 5.59(a)), and (2) The waste packages are installed after waiting only 55 years and the initial thermal load is 242 W/m (see Figure 5.59(b)).

EURAD (Deliverable n˚ 7.6) – Modelling report on the effect of temperature on clay host rocks behaviour
Dissemination level: PU
Date of issue of this report: 06/06/2024

Page 134

(a)

(b)
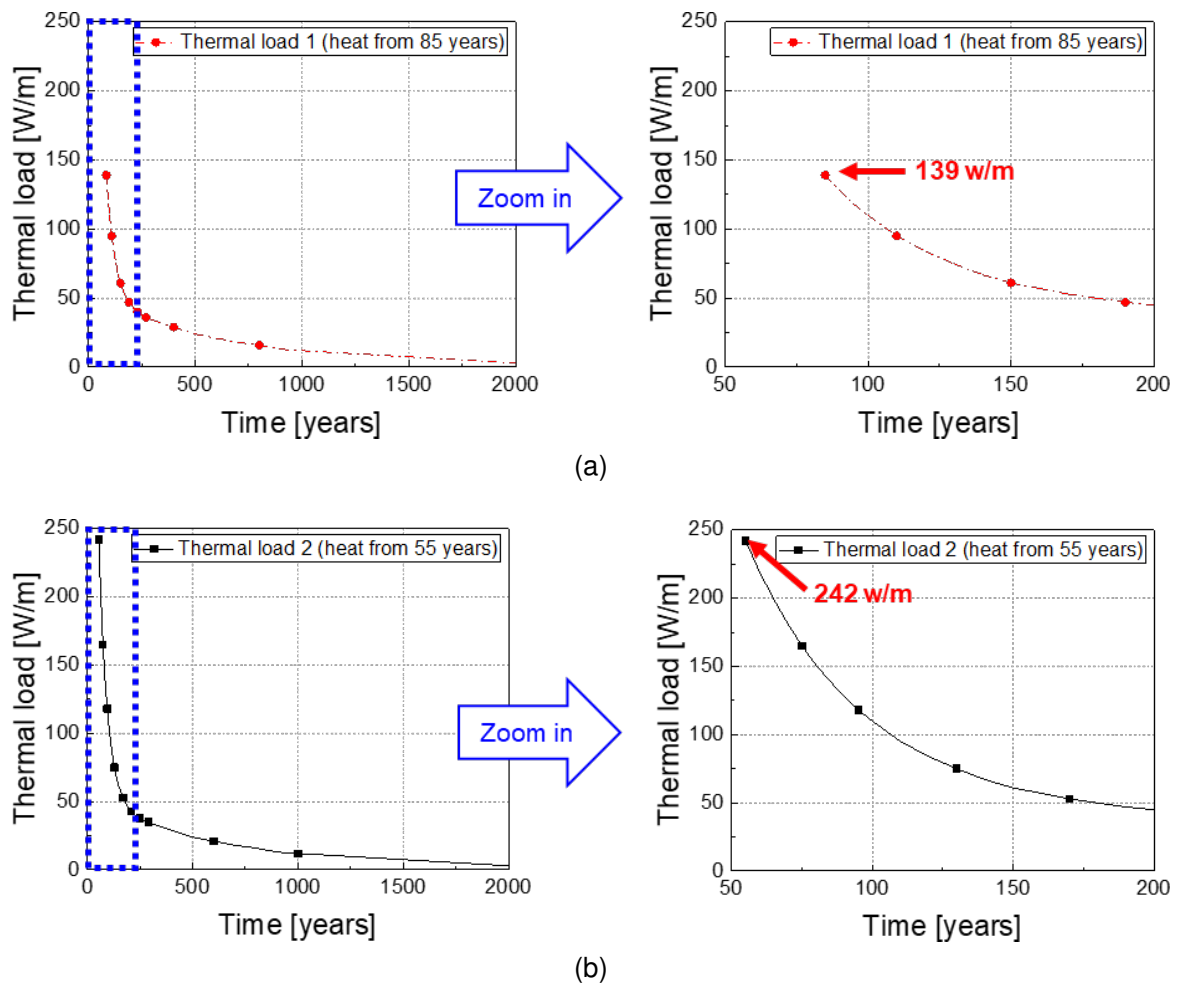
Figure 5.59: Applied thermal loads for (a) the first case (heat from 85 years, starting from 139 W/m), and (b) the second case (heat from 55 years, starting from 242 W/m).

5.2.2. Modelling results for the far-field generic case

Six teams took part in the far-field exercise: Andra, BGE, EDF, LEI, ULg and UPC. Both Andra and LEI ran the case on Comsol. Because of some issues with the Opalinus Clay parameters, only the Callovo-Oxfordian case was finalised.

For this model, all the teams used an anisotropic thermo-poro-elastic approach. This method was indeed found in a previous benchmark to predict reliably the THM response in the far-field (Seyedi et al., 2021).

The evolution of temperature, pressure and Terzaghi effective stresses at two points located 5 diameters away from the tunnel (P4) and at mid-distance between two tunnels (P6) for the first heating case are displayed on Figure 5.60. For these points located far enough from the tunnels, very consistent results are obtained on the temperature, pore pressure and effective vertical stress evolution. When most teams used an isotropic Biot coefficient equal to 0.8, ULg took into account the anisotropy, as shown in Table 5.16. This parameter does not appear to have any large impact on the far-field calculations. However, the discrepancy observed during the heating phase on the effective horizontal stress (bottom right plot) illustrates the impact of the anisotropic Poisson's ratio: all teams used the same $\nu_{\|\|} = 0.2$ but Andra took $\nu_{\perp\|} = 0.35$ instead of 0.30. In addition Andra used a different initial horizontal stress value.

EURAD (Deliverable n˚ 7.6) – Modelling report on the effect of temperature on clay host rocks behaviour
Dissemination level: PU
Date of issue of this report: 06/06/2024

Page 135
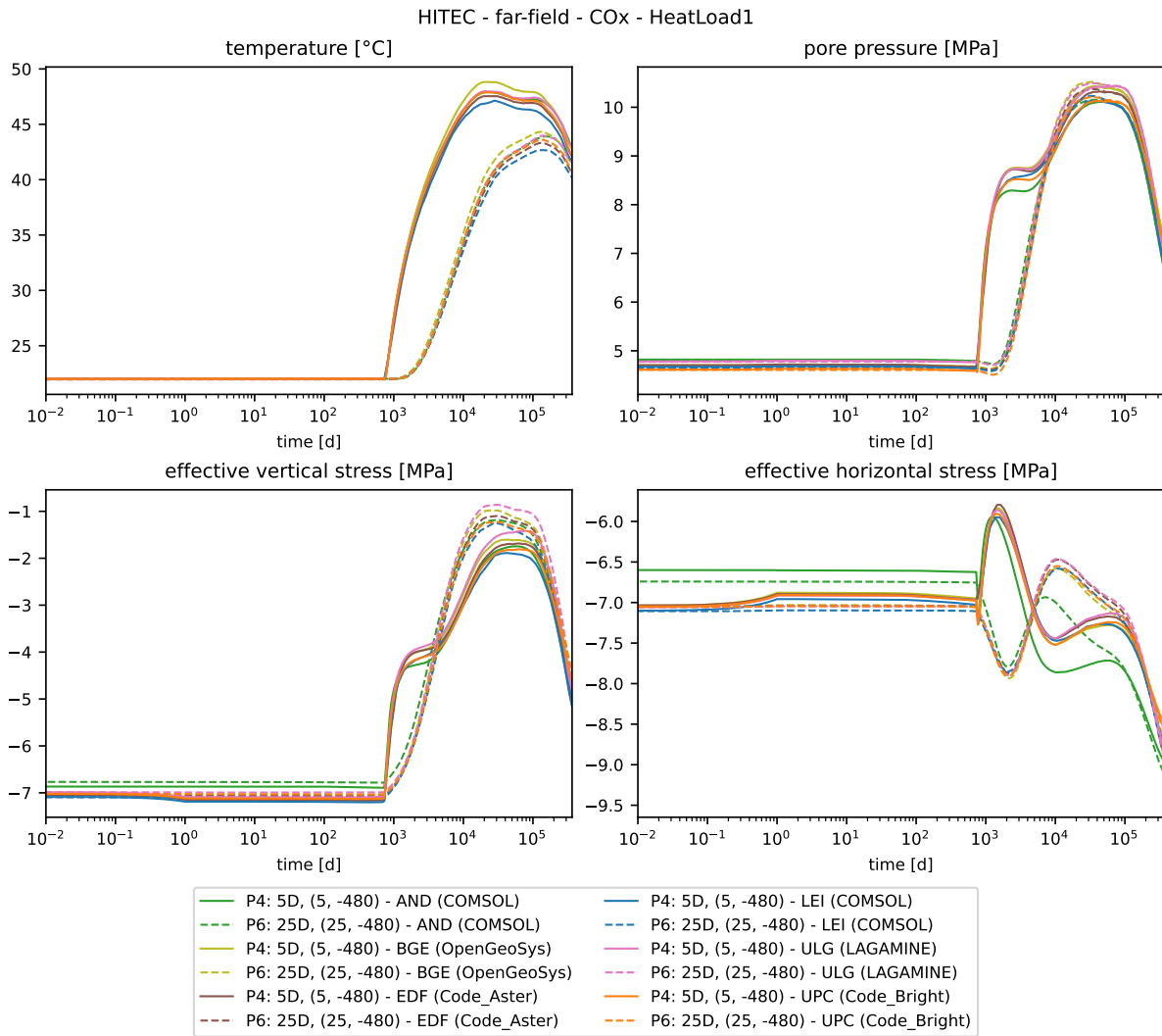
Figure 5.60: Evolution of temperature, pore pressure and Terzaghi effective stresses for the Cox far-field case

With simultaneous thermal loading in two neighbouring cells, lateral symmetry conditions will apply at mid-distance. Even though the maximum temperature is expected at the tunnel wall ($69 \pm 1°C$, point P1), all models concur to predict that the induced pore pressure will be maximum at mid-distance between two neighbouring cells (point P6), Figure 5.61. The lateral symmetry condition prevents indeed any horizontal strain and any horizontal dissipation of the pore pressure at this point.

EURAD (Deliverable n° 7.6) – Modelling report on the effect of temperature on clay host rocks behaviour
Dissemination level: PU
Date of issue of this report: 06/06/2024

Page 136
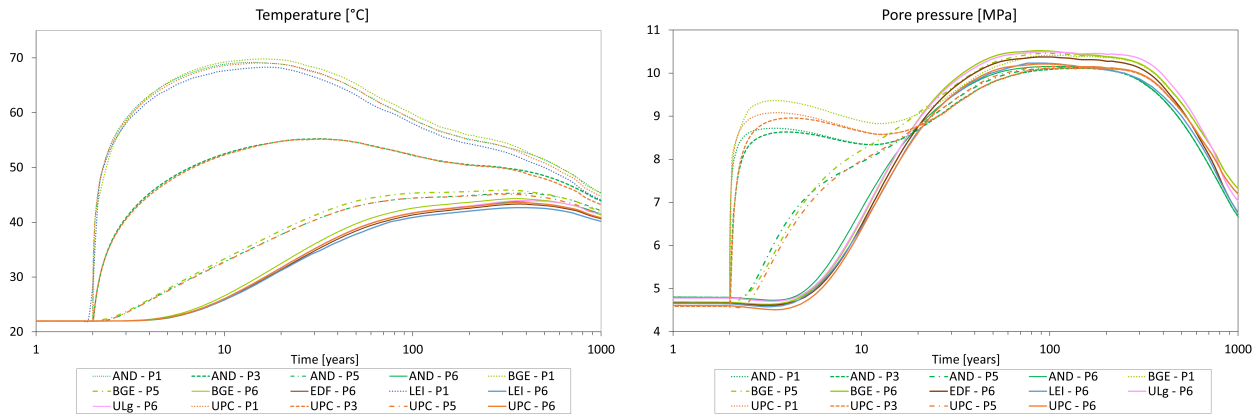
Figure 5.61: Evolution of temperature and pore pressure at different distances from the tunnel wall for the Cox far-field heat load 1 case

Two economical optimisation options may be studied with this type of model:

- Shortening the spacing between two contiguous cells (shorter access drifts, less civil works);

- Reducing the cooling time at surface.

The second option was studied in this exercise: as recalled in 2.1.2, two heating scenarios were proposed. In the base case, the waste packages are cooling down for 85 years at surface, providing an initial thermal load of 139 W/m. In a second case, the waiting time is reduced to 55 years, resulting in a initial load of 242 W/m. A comparison between these two heating scenarios is displayed on Figure 5.62. One can see that in the later case, the Terzaghi effective vertical stress becomes positive and some damage or tensile failure may develop at point P6 that is located at mid-distance between two cells.

EURAD (Deliverable n˚ 7.6) – Modelling report on the effect of temperature on clay host rocks behaviour
Dissemination level: PU
Date of issue of this report: 06/06/2024

Page 137
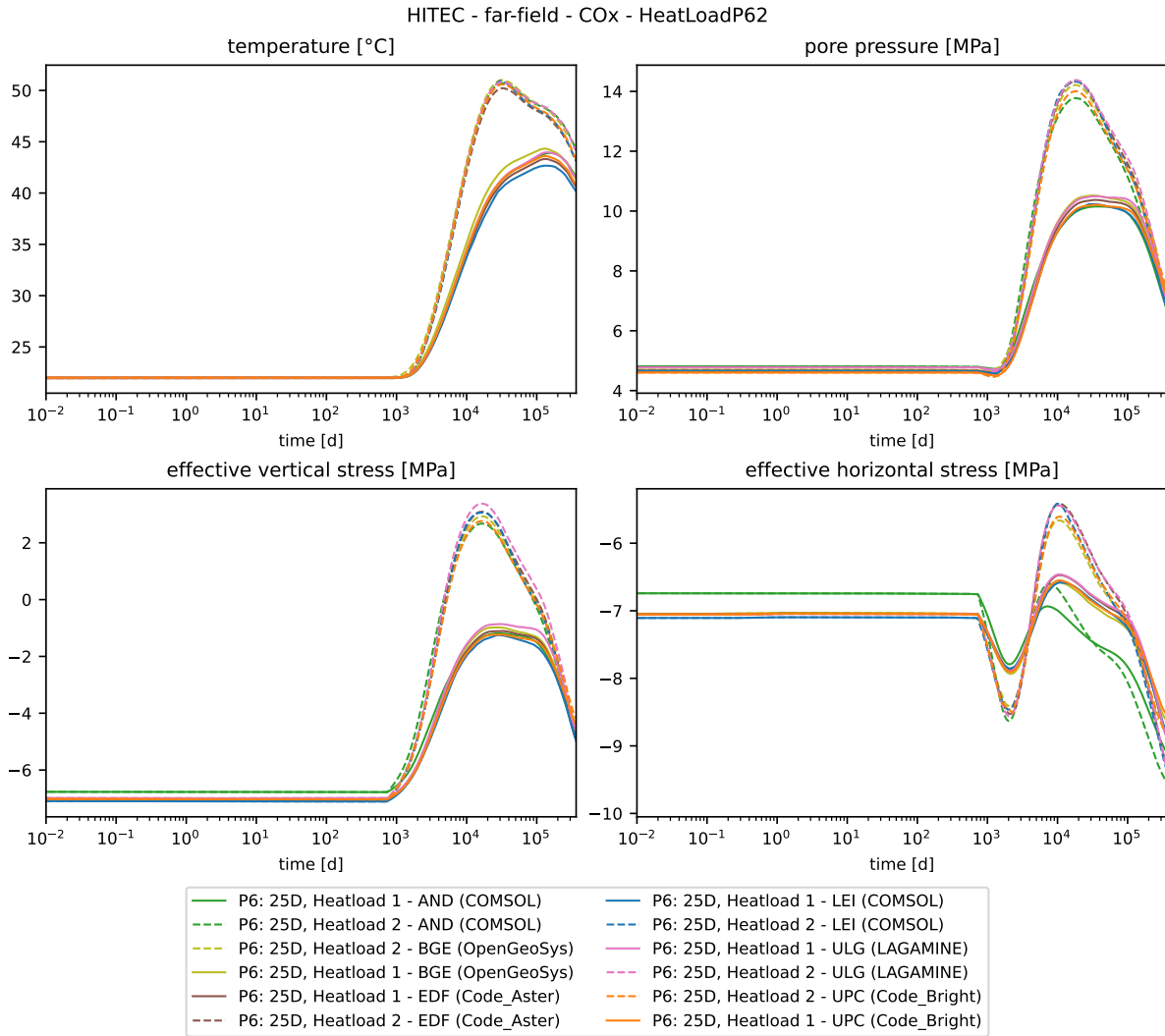
Figure 5.62: Comparison of temperature, pore pressure and Terzaghi effective stresses for the two heating cases at point P6

One can see on Figure 5.63 the importance of the failure criterion used: with the proposed 25m spacing between two neighbouring cells, tensile failure would be reached using the Terzaghi effective stress. On the other hand, the Biot effective stress stays negative or barely exceeds 0 in both heating scenarios.
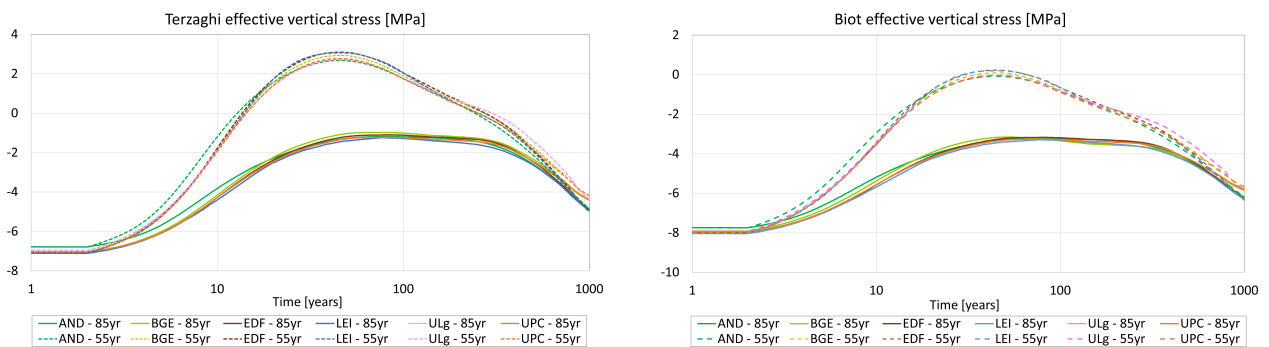
Figure 5.63: Terzaghi (left) vs Biot (right) effective vertical stress at point P6 in the two heating scenarios

Taking into account the tensile strength of the rock in this criterion may also add a safety margin.

EURAD (Deliverable n° 7.6) – Modelling report on the effect of temperature on clay host rocks behaviour
Dissemination level: PU
Date of issue of this report: 06/06/2024

Page 138

6. Modelling of Lab experiments

6.1. Andra

In the framework of its collaboration with Andra, Ineris modelled the Subtask 2.1 and 2.2 triaxial compression tests performed by ULorraine. Ineris has recently developed an anisotropic elastoplastic, viscoplastic and damage model for the hydromechanical behaviour of claystones ((Souley et al., 2023a)) and briefly presented in paragraph 5.1.4.1. This model is implemented in the finite element software Comsol Multiphysics (version 6.0) with an implicit gradient-based regularization scheme. Herein this rheological model is extended to include the influence of temperature on the thermo-hydro-mechanical behaviour of claystone on the basis of laboratory characterisations.

6.1.1. Modelling approach

THM laboratory tests at a confining pressure of Pc and a temperature T are simulated according four steps of THM loadings in relation to the experimental protocol. The waiting phase to dissipate the thermal-induced pore overpressure is set to 4.2 h (less than experimentally), but sufficient to numerically dissipate the pore pressure.

Table 6.1: Modelling steps

	Process	Value [Units]
Step 1	Hydrostatic phase up to Pc (cylindrical sample boundaries)	0.1 [MPa/min]
Step 2	Thermal loading up to Tf (heating collar)	50 [°C/hour]
Step 3	Waiting phase (overpressure dissipation)	4.2 [h]
Step 4	Deviatoric phase (mechanical press on top)	0.2e-6 [m/s]

Drainage in this case is assumed along the lateral surface of the sample and over the full top and bottom steel plates. Thanks to symmetry conditions, only one eighth of the sample was modelled.

The triaxial compression tests performed by Gbewade et al. (2023) indicated a reduction of strength with temperature. Trends on the moduli and Poisson's ratio were however more uncertain. The evolution of mechanical properties with T in the range [20, 80 °C] was implemented in Comsol Multiphysics by the mean of factor tables. Finally, the choice to implement the influence of temperature on short- and long-term mechanical properties is based more on the evolution of parameters as tabulation that can be updated with new advances.

Despite unclear trends on some parameters, the following properties were made dependent on the temperature:

- Uniaxial compressive strength, σ_c, assuming the same table for elastic limit σ_{ci} and residual cohesion C_{res}

- Elastic modules (E_1, E_3, G_{13})

- Initial and maximum dilatancy (volumetric plastic strain) (β_0, β_m)

For example, Figure 6.1 below shows the reduction that is implemented for the peak strength. The ratio $\sigma_{c\parallel}/\sigma_{c\perp}$ of 1.2 from Gbewade's tests is identical to what Mánica et al. (2022a) proposed.
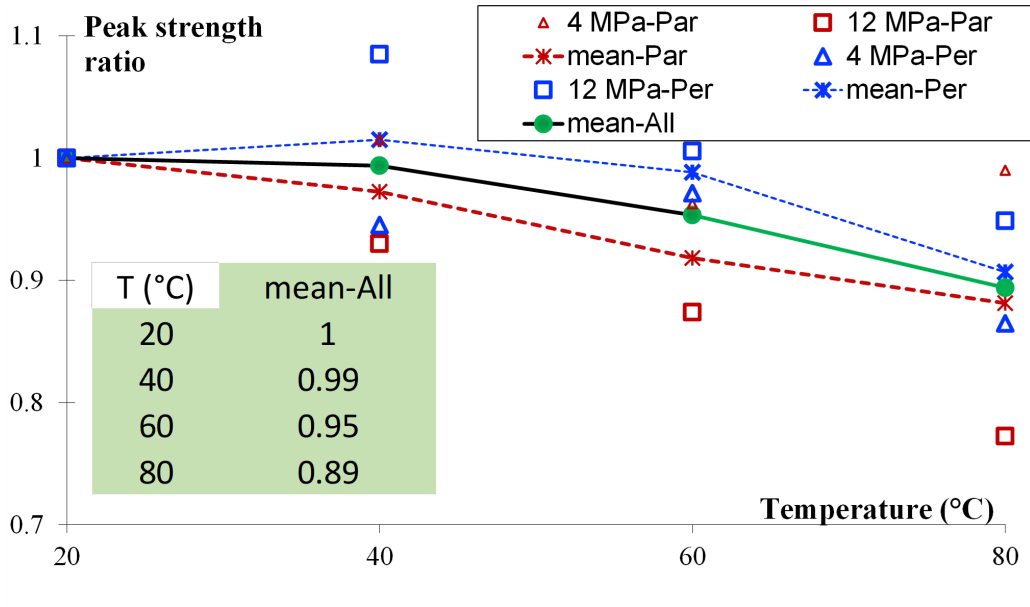
Figure 6.1: Variation of σ_c with T

6.1.2. Modelling results

The temperature and pressure evolution for the 40 °C heating case with a confining pressure of 12 MPa are shown in Figure 6.2 and Figure 6.3. The heat being applied on the periphery by heating collars, the target temperature is reached last at the core of the sample; on the other hand, and because of the draining conditions, the overpressure induced by the thermal loading is highest there. Both the temperature and pressure are predicted to remain constant during the last two steps (waiting phase and deviatoric loading).
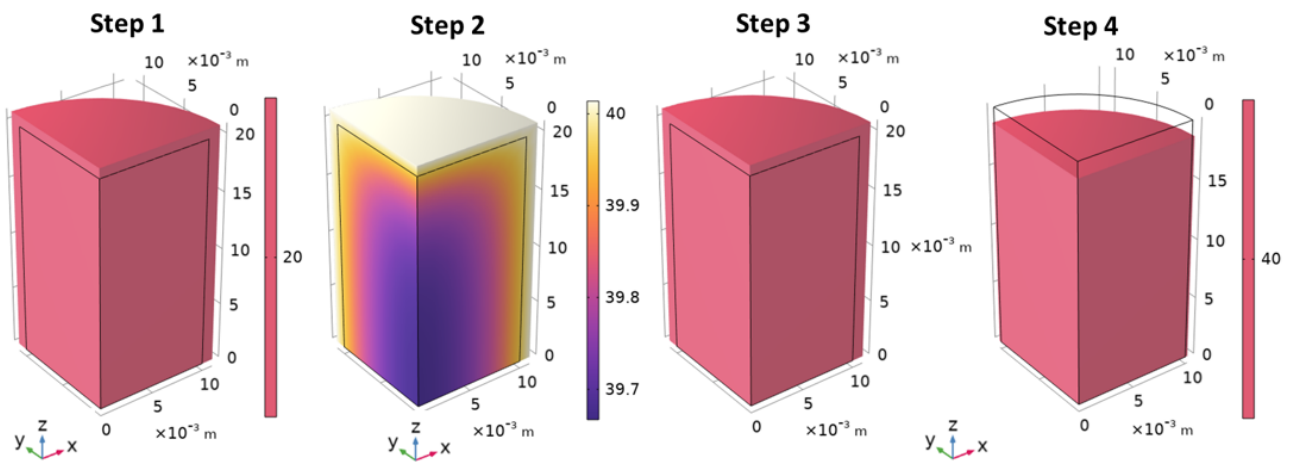
Figure 6.2: Temperature evolution for the case Pc=12 MPa and Tf=40 °C

EURAD (Deliverable n° 7.6) – Modelling report on the effect of temperature on clay host rocks behaviour
Dissemination level: PU
Date of issue of this report: 06/06/2024

Page 140
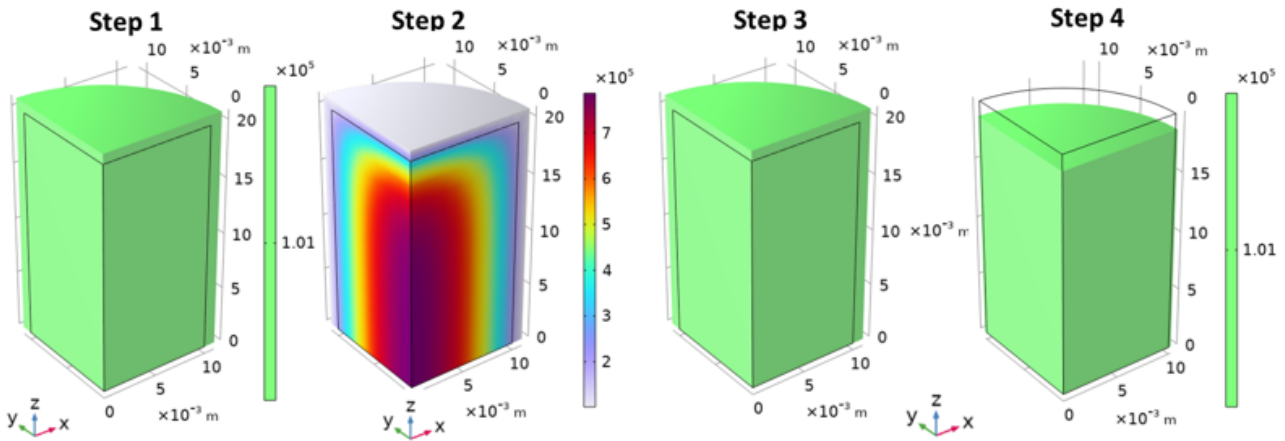
Figure 6.3: Pressure evolution for the case Pc=12 MPa and Tf=40 ℃

The pressure and temperature evolutions at three points located at three different locations from the middle of the plug (P1) and close to the end (P3). For this relatively small temperature increase to 40℃, and with these large drainage conditions, a maximum overpressure of 0.75 MPa is predicted at the centre of the sample.
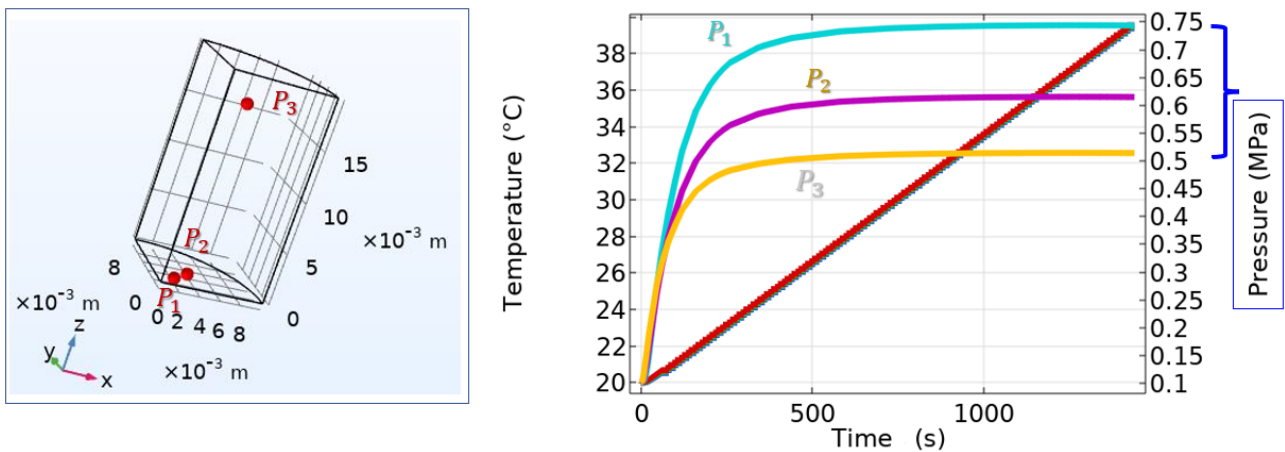
Figure 6.4: Pressure and temperature evolution at three different points for the case Pc=12 MPa and Tf=40 ℃

The speed of dissipation of the overpressure for the sample heated to 80℃ at 12 MPa confining pressure is illustrated on Figure 6.5.
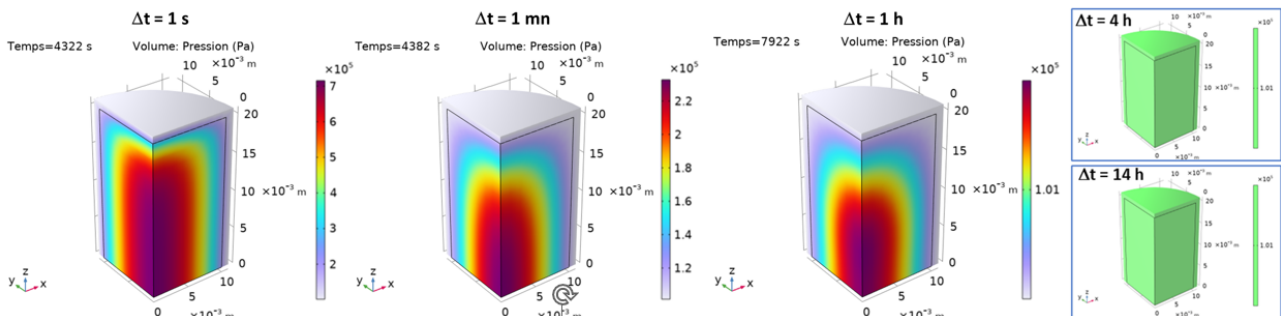
Figure 6.5: Pressure evolution over time during the waiting phase (step 3) for the case Pc=12 MPa and Tf=80 ℃

EURAD (Deliverable n˚ 7.6) – Modelling report on the effect of temperature on clay host rocks behaviour
Dissemination level: PU
Date of issue of this report: 06/06/2024

Page 141

We see that with these draining boundary conditions, stationary regime is already reached after 4 hours. In addition, the overpressure induced when heating to 80 °C does not appear to be much larger than that modelled in the 40 °C heating case.

To illustrate the new performances of the rheological model, the stress vs. strain curves for two tests at Pc=12 MPa and Tf=40 and 80 °C are displayed on Figure 6.6. They show that a relatively good agreement is achieved.
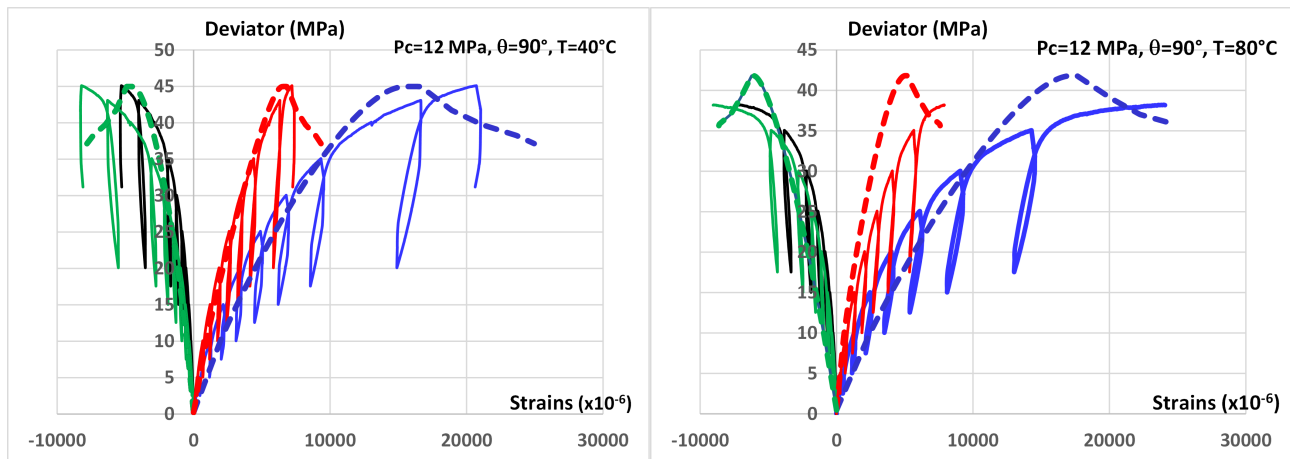
Figure 6.6: Numerical (dashed) vs. lab stress-strain curves for the tests at Pc=12 MPa and Tf=40 and 80 °C

In these numerical simulation results, it is important to emphasise that all the short-term mechanical behaviour parameters at ambient temperature result from the values referenced in Andra's database and Souley et al. (2023a). No other identification apart from the influence of temperature has been made here. The same approach has been adopted for the long-term behaviour of the viscosity with respect to temperature by implementing a tabulation, deduced for the moment from Arrhenus' law.

Sensitivity studies are now planned especially on the boundary conditions, with an impermeable top surface of the sample and with drainage only through a small borehole. The effect of temperature on the long-term behaviour of the Cox claystone will also be taken into account and will be implemented in the model when the results from the UL creep tests are made available. Finally, the reduction of properties with temperature will also be applied on large scale applications to evaluate its impact on the behaviour of the Cox in the near- and far-field.

EURAD (Deliverable n° 7.6) – Modelling report on the effect of temperature on clay host rocks behaviour
Dissemination level: PU
Date of issue of this report: 06/06/2024

Page 142

6.2. BGE

This section describes the thermo-hydro-mechanical (THM) simulation of a series of temperature-controlled triaxial compression tests performed on Callovo-Oxfordian argillite (Cox) samples. The constitutive description adopted to characterise the THM behaviour of the Cox corresponds to the model mentioned in Section 4.2, which has been employed in the past to reproduce the behaviour of an experimental excavation in Cox at the Meuse/Haute-Marne (MHM) underground research laboratory (URL) (Mánica et al., 2022a). The main objective of the simulations is to demonstrate the recent implementation of the model in the finite element code OpenGeoSys, through the MFront platform, including its enhancement to account for the effect of temperature, described in Section 4.2.2.

6.2.1. Description of the tests

Tests were performed on cylindrical Cox samples, with a radius and height of approximately 0.01 and 0.04 m, respectively. They were performed under nominally drained conditions, i.e. drainage is allowed at the top and bottom ends of the sample, although full drainage cannot be guaranteed due to the low permeability of the material. The samples are not initially fully saturated, with a degree of saturation of about 92.9%. The tests comprise four main stages:

- application of the confinement pressure at a rate of 0.1 MPa/min,

- temperature increase at a rate of 50 K/hour,

- stabilisation of the sample for 14 hours after reaching the target temperature, and

- application of the deviatoric loading, under displacement control, at a rate of 12 μm/min.

The samples were instrumented with a number of strain gauges to measure axial and radial strains during the application of the deviatoric loading. The vertical displacement of the equipment's loading platen was also monitored. Due to the brittle behaviour of the Cox, the samples will generally tend to exhibit a localised deformation pattern, particularly after reaching the peak deviatoric stress, with the initiation and propagation of fractures, affecting local strain measurements. In the context of this modelling exercise, results of the tests were interpreted in terms of nominal strains, computed from the displacement of the loading platen. Figure 6.7 shows an example of a deviatoric stress vs. nominal axial strain curve from the raw laboratory data. An initial behaviour with a low stiffness can be identified, typical of uniaxial and triaxial testing in rock specimens. This is generally attributed to the closure of preexisting micro-cracks and/or to adjustments between the loading platen and the sample's end, and it is generally not considered to be part of the actual behaviour of the material. Therefore, the raw data was adjusted by inferring the actual initial stiffness and subtracting the corresponding deformation, as shown in Figure 6.7. The resulting stress-strain curves were used for comparison with numerical results.

6.2.2. Initial effective stress state

As already mentioned, the samples were not saturated, with an initial degree of saturation of about 92.9%, which in these clayey materials can be related to a significant suction and, therefore, affect the observed mechanical parameters. To estimate the latter, the water retention curve shown in Figure 6.8 was employed, derived by adjusting the van Genuchten (1980) model (Equation 6.1) to represent an average of several experimental characterisations of the water retention behaviour of the Cox claystone (Armand et al., 2017).

$$S_e = \left[1 + \left(\frac{s}{P} \right)^{1/(1-\lambda)} \right]^{-\lambda} \tag{6.1}$$

EURAD (Deliverable n˚ 7.6) – Modelling report on the effect of temperature on clay host rocks behaviour
Dissemination level: PU
Date of issue of this report: 06/06/2024

Page 143
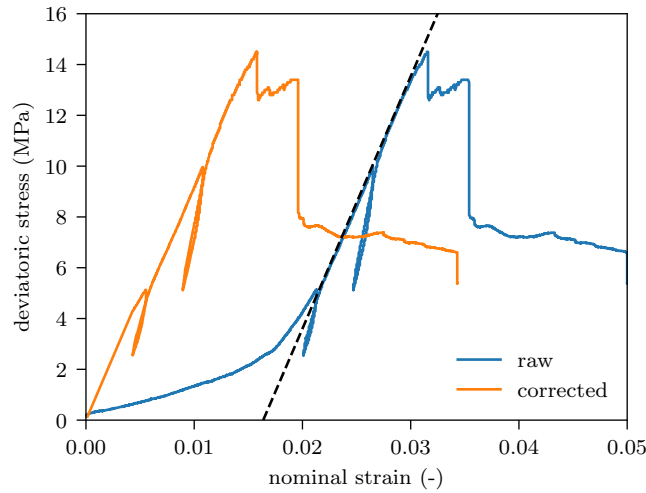
Figure 6.7: Raw and corrected deviatoric stress vs. nominal strain curve from the test EST66762-11.

where S_e is the effective degree of saturation, s is the suction, and P and λ are model parameters, the former related to the air entry pressure and the latter to the shape of the function. Particularly, values of P = 17.6 MPa and λ = 0.32 were used here, resulting in an initial suction of 7.02 MPa for the assumed degree of saturation of 92.9%.
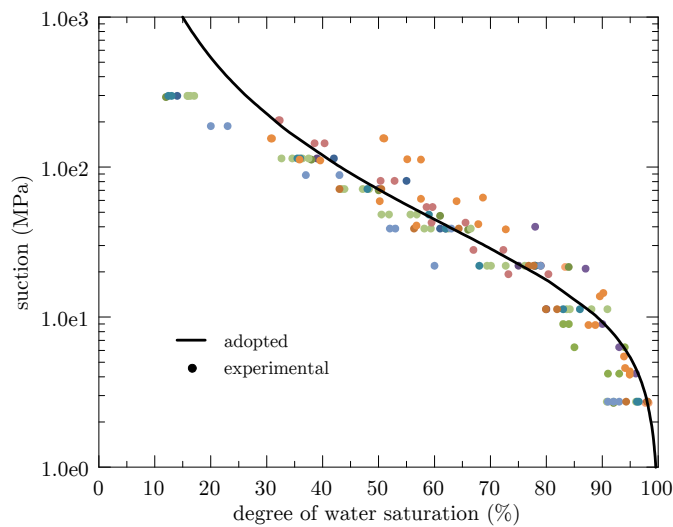
Figure 6.8: Water retention curve adopted and experimental data of Cox claystone (Armand et al., 2017).

With the computed suction value, the initial stress state of the samples was estimated by adopting the following definition of effective stresses, which was also considered in the numerical analyses:

$$\sigma' = \sigma + S_e s B \mathbf{I} \tag{6.2}$$

where σ' and σ are the effective and total stress tensors, B is the Biot's coefficient, and $\mathbf{I}$ is the identity tensor. Assuming B = 0.6, which is a frequently employed value in numerical simulations involving the Cox claystone (Mánica et al., 2022a), a mean effective stress of -3.91 MPa was estimated as the initial condition for the samples.

EURAD (Deliverable n° 7.6) – Modelling report on the effect of temperature on clay host rocks behaviour
Dissemination level: PU
Date of issue of this report: 06/06/2024

Page 144

6.2.3. Main features of the analyses

Tests were simulated by means of coupled THM analyses in the finite element code OpenGeoSys. Particularly, the non-isothermal Richards flow process coupled with mechanics was adopted here. The tests simulated correspond to the samples with horizontal bedding, for confinement stresses of 0 and 4 MPa and temperatures of 20, 40, 60, 80, and 100°C. Figure 6.9 shows the geometry, boundary conditions, and finite element mesh used for analyses. Due to symmetry, only an eighth of the sample's geometry was considered, as shown in Figure 6.9a. The resulting mesh (Figure 6.9b) comprises 1093 finite elements. Normal displacements were constrained on the face boundaries perpendicular to each of the Cartesian directions. On those faces, null liquid and heat fluxes were also prescribed. On the external face of the sample, the corresponding confinement pressure and temperature were applied, with a value depending on the particular tests and simulation time. On the top end, the confining pressure is applied during thermal loading and stabilisation, while vertical displacements were prescribed during deviatoric loading. The corresponding liquid pressure and temperature were also prescribed on this boundary.
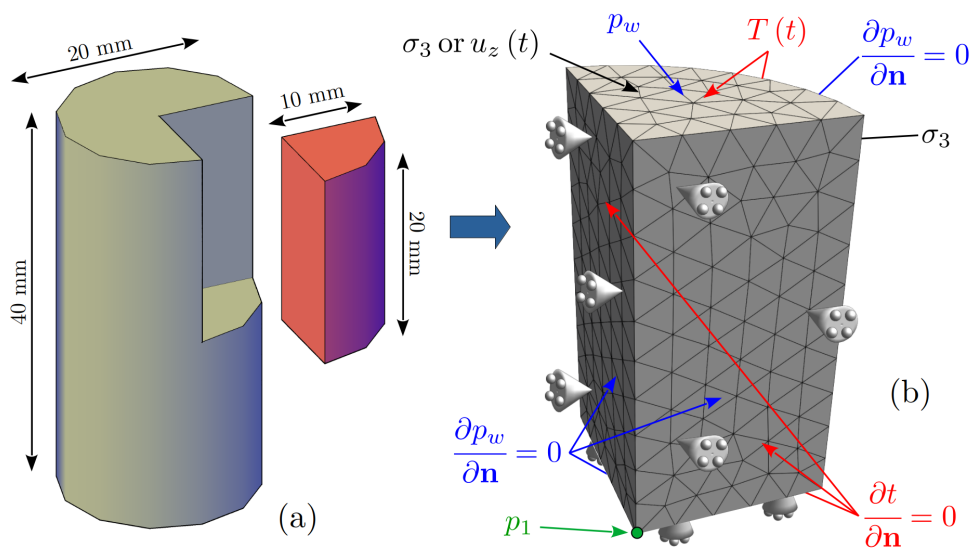
Figure 6.9: Geometry, boundary conditions, and finite element mesh adopted.

The gradual application of the confinement pressure was not simulated and the corresponding initial and boundary stresses were prescribed. For confining pressures of 0 and 4 MPa, mean effective pressures of -3.91 and -7.91 MPa were initially assigned at all integration points, respectively, as well as a liquid pressure of -7.02 MPa (initial suction), which was also prescribed as a boundary condition at the top end. This initial stress state is in equilibrium with the external confinement according to the adopted effective stress definition (Equation 6.2), and takes into account the initial suction of the partially saturated samples. The liquid pressure at the top end was maintained during the whole simulation assuming that the initial state of the sample is in equilibrium with the drainage line.

An initial simulation phase was considered, where the temperature was linearly increased, at a rate of 50°C/hour, up to reaching the target temperature at a constant external confinement pressure. Then, the temperature is maintained and stabilisation is permitted for 14 hours. Afterwards, a simulation phase is defined where a displacement increment is prescribed at the top end at a rate of 12 μm/min.

Adopted parameters for the constitutive model are summarised in Table 5.11. In general, they were calibrated to achieve a good agreement with the experimental results. Parameters for strength anisotropy and creep deformations were taken from Mánica et al. (2022a), although they do not play a significant role in the simulations performed. Regarding temperature dependence, only the evolution of the deviatoric

EURAD (Deliverable n˚ 7.6) – Modelling report on the effect of temperature on clay host rocks behaviour
Dissemination level: PU
Date of issue of this report: 06/06/2024

Page 145

yield function was considered in the simulations and, therefore, the volumetric yield pressure was set very high in order not to activate this yielding mechanism (see Section 4.2.2.3). The observed evolution of the strength as a function of temperature was reasonably captured by assuming that only the cohesion and tensile strength evolve with temperature and, therefore, μ_ϕ was set to zero. Other physical properties used in the simulation are summarised in Table 7.7.

Table 6.2: Cox properties used in the simulation.

Parameter	Value	Units
Liquid phase		
Viscosity	temperature dependent function	Pa s
Density	temperature dependent function	kg m^{-3}
Specific heat capacity	temperature dependent function	J kg^{-1} K^{-1}
Thermal conductivity	temperature dependent function	W m^{-1} K^{-1}
Thermal expansion coefficient	2.0e-4	K^{-1}
Solid phase		
Density	2270	kg m^{-3}
Specific heat capacity	800	J kg^{-1} K^{-1}
Thermal conductivity normal to bedding	1.33	W m^{-1} K^{-1}
Thermal conductivity parallel to bedding	2.05	W m^{-1} K^{-1}
Thermal expansion coefficient	1.4e-5	K^{-1}
Medium		
Relative permeability	van Genuchten (1980)	-
Degree of saturation	van Genuchten (1980)	-
Biot's coefficient	0.6	-
Intrinsic permeability normal to bedding	2.5e-20	m^2
Intrinsic permeability parallel to bedding	5.0e-20	m^2
Porosity	0.18	-

6.2.4. Obtained results

Figure 6.10 shows the evolution of temperature and liquid pressure at the centre of the sample, i.e. in the location indicated as p_1 in Figure 6.9. The curve for 20°C was omitted since this was the assumed initial temperature for all samples and, therefore, no temperature change is applied in this case. It can be observed that the liquid pressure increases (suction is reduced) with temperature; up to 1.2 MPa for the tests where the temperature is increased to 100°C. The latter occurs mainly due to the differential thermal expansion of the liquid and solid phases, leading to thermal pressurisation (see e.g. Delage et al., 2000). After thermal loading, during stabilisation, liquid pressure decreases (suction increase) towards the initial value, since this is being applied as a boundary condition at the top end of the sample. By the end of the stabilisation phase, the pressure is close to the initial value in all tests, even though the considered observation point is at the centre of the sample.

EURAD (Deliverable n° 7.6) – Modelling report on the effect of temperature on clay host rocks behaviour
Dissemination level: PU
Date of issue of this report: 06/06/2024

Page 146
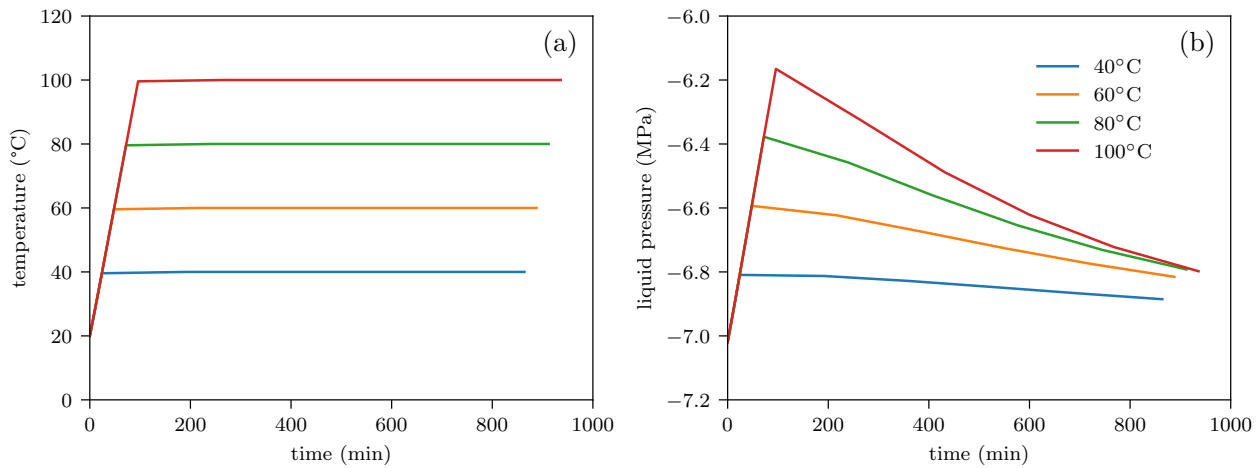
Figure 6.10: Evolution of (a) temperature and (b) liquid pressure during thermal loading and stabilisation.

As previously described, after stabilisation a new simulation phase is considered where a displacement increment is prescribed at the top end. Obtained results were interpreted analogously to the laboratory results. The deviatoric stress was computed from the total vertical reaction, by adding the resulting vertical forces of all nodes at the top end, where the vertical displacement was prescribed. Likewise, the axial nominal strain was directly computed from the prescribed vertical displacement. Figure 6.11 shows the resulting deviatoric stress vs. axial nominal strain curves compared with the test results. Although the laboratory data shows significant scatter, especially after the peak deviatoric stress, the simulations were able to reasonably capture the behaviour of the tests. For instance, a higher strength loss was obtained for the unconfined simulations (i.e. σ_3 = 0 MPa), as it occurs in the laboratory. The highest peak deviatoric stress is attained for the lowest temperature (20°C), and it reduces as the temperature is increased up to 100°C. The evolution of the strength with temperature was nicely captured by the numerical analyses. The latter can be more clearly identified in Figure 6.12, summarising the peak deviatoric stress from all simulations as a function of temperature compared to the laboratory data. A very good agreement can be identified, demonstrating the capability of the model in reproducing the effect of temperature on the strength of the Cox claystone.

EURAD (Deliverable n˚ 7.6) – Modelling report on the effect of temperature on clay host rocks behaviour
Dissemination level: PU
Date of issue of this report: 06/06/2024

Page 147
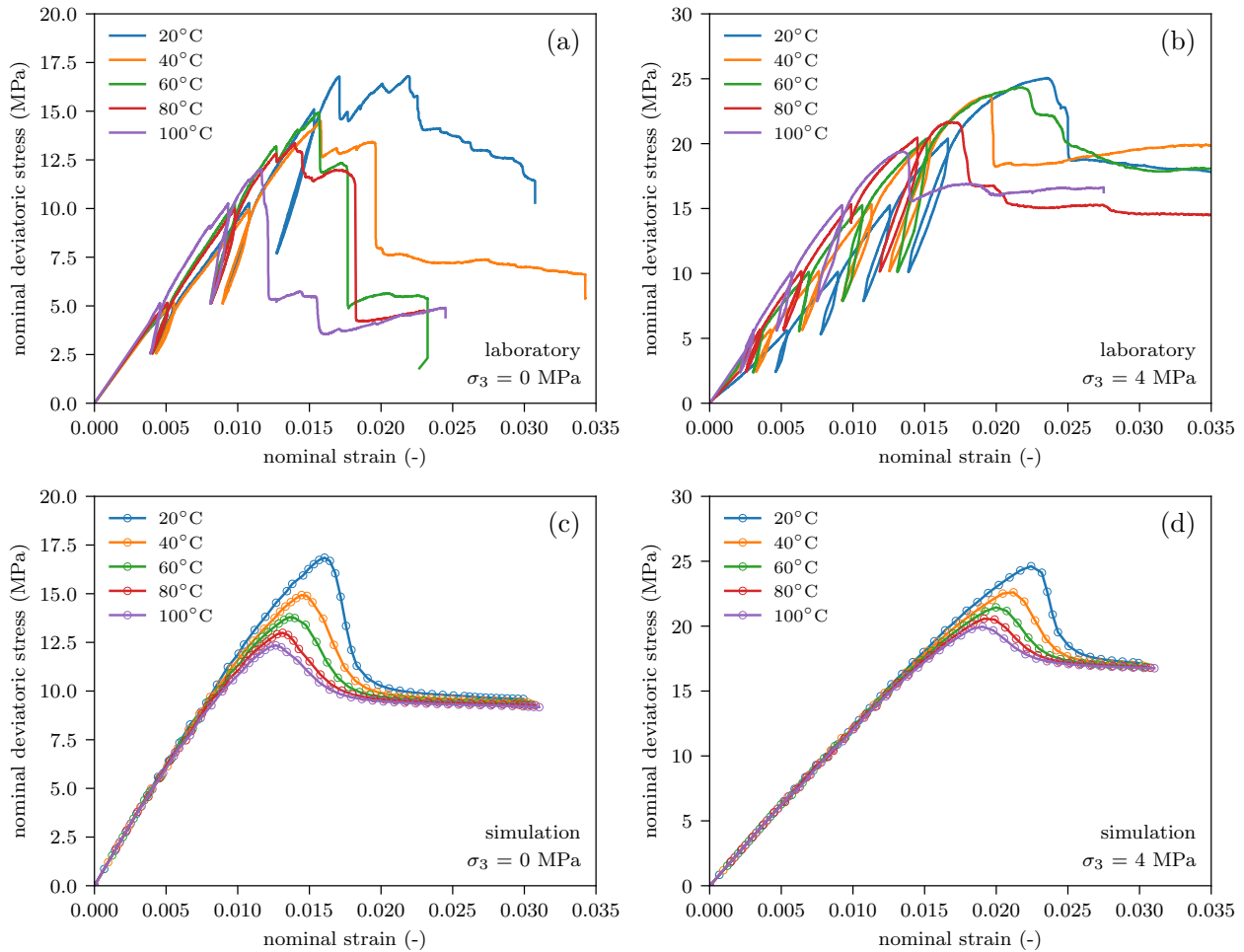
Figure 6.11: Deviatoric stress vs. axial nominal strain (a,b) from laboratory data and (c,d) from simulation results.
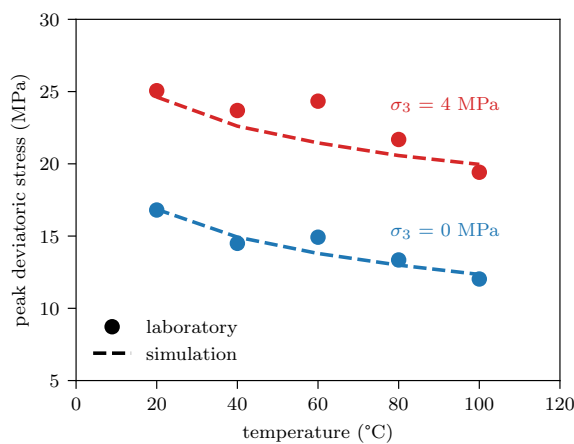
Figure 6.12: Peak deviatoric stress vs. temperature from the simulations and the laboratory data.

EURAD (Deliverable n˚ 7.6) – Modelling report on the effect of temperature on clay host rocks behaviour
Dissemination level: PU
Date of issue of this report: 06/06/2024

Page 148

6.3. LEI

This section describes the modelling of a series of temperature-controlled triaxial compression tests performed on Callovo-Oxfordian argillite (Cox) samples. The main objective of the modeling of laboratory experiments was to estimate the parameters' values of the elastoplasticity model so that the response function gives similar results to the experimental ones. Also, to estimate which of these parameters depend on the temperature. Fitted parameters to be used to model the in-situ experiment ALC1605.

6.3.1. Description of the laboratory experiments

Laboratory experiments were done by CNRS (ULorraine) by performing triaxial tests of Cox material at different temperatures (20 °C, 40 °C, 60 °C and 80 °C) and at different confining pressures (0 MPa, 4 MPa and 12 MPa). In the experiments, the samples were loaded mechanically in two directions: when the direction of the applied load is parallel to the bedding direction and when it is perpendicular to the bedding direction in the sample. The purpose of the experiments was to determine the compressive strength of the material at different temperatures when the sample is saturated with water. The temperature of the sample was raised at a certain rate, it was allowed to settle, and the induced increase of water pressure dissipated (flowed out) and thus the influence of the pore water in the sample was eliminated (water did not change the effective stresses in materials). The load increase was also carried out at a controlled rate so that the increase in water pressure caused by compression could dissipate. Such experiment procedure corresponds to the drained triaxial test conditions.

6.3.2. Modelling methodology

Since compression and temperature caused increase in pore pressure was allowed to dissipate, heat and water flow was not modelled. For description of material mechanical behaviour a numerical 2D axisymmetric models in COMSOL Multiphysics were used. In the model applied load was calculated from the displacements in the vertical direction at the top of the specimen. Obtained stress-strain relationships were compared to experimental ones. Numerical models did not take into account loading/unloading cycles done during the experiment.

The important input parameters required for the numerical model are Young's modulus, determined from experimental curves from strain gauges. Young's modulus was taken as the average of three experimental values determined from experimental stress-strain curves at deviatoric stresses: q = 5 MPa, 10 MPa and 15 MPa. Then these values were plotted for different confining pressures (0 MPa, 4 MPa and 12 MPa) at different temperatures.

EURAD (Deliverable n˚ 7.6) – Modelling report on the effect of temperature on clay host rocks behaviour
Dissemination level: PU
Date of issue of this report: 06/06/2024

Page 149
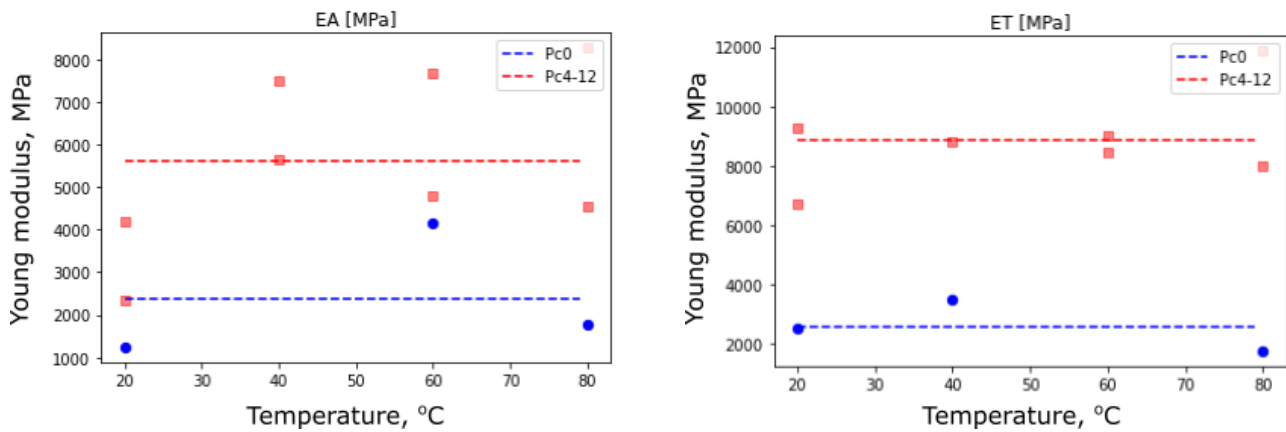
Figure 6.13: Young's modulus (EA – perpendicular to bedding, ET – parallel to bedding) for cases when confining pressure is 0 MPa and when confining pressure is between 4-12 MPa derived from experimental results at different temperature °C

As there were no clear tendency against temperature, the constant average values (one for case when confining pressure is 0 MPa and one when confining pressure is between 4-12 MPa) were chosen for the model.

The purpose of modelling laboratory experiments was to estimate (fit) the values of the model parameters such as initial yield stress - sigma0y, hardening modulus – h used in developed elastoplastic model based on Drucker-Prager soil plasticity model so that the modelled stress-strain curves give similar results to the experimental ones, i.e., peak shear strength. Also, to estimate whether these parameters depend on the temperature.
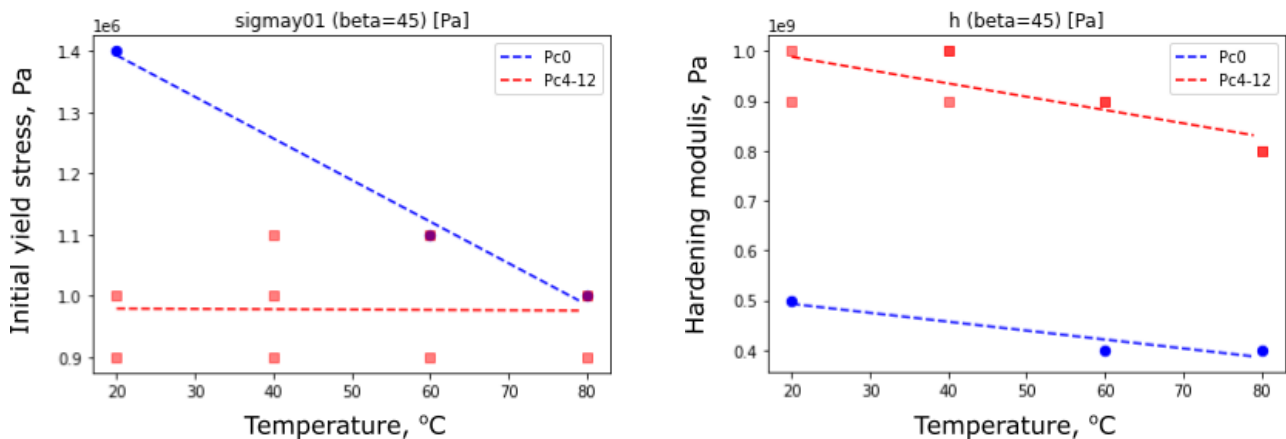
Figure 6.14: Fitted initial yield stress (sigma0y) and hardening modulus (h) against temperature °C

6.3.3. Results

Using fitted parameters, the Cox specimen was modelled and compared to experimental results (Figure 6.15 - 0 MPa confining pressure, Figure 6.16 – 4 MPa confining pressure, Figure 6.17 – 12 MPa confining pressure), with the maximum load direction perpendicular to the bedding.

EURAD (Deliverable n° 7.6) – Modelling report on the effect of temperature on clay host rocks behaviour
Dissemination level: PU
Date of issue of this report: 06/06/2024

Page 150
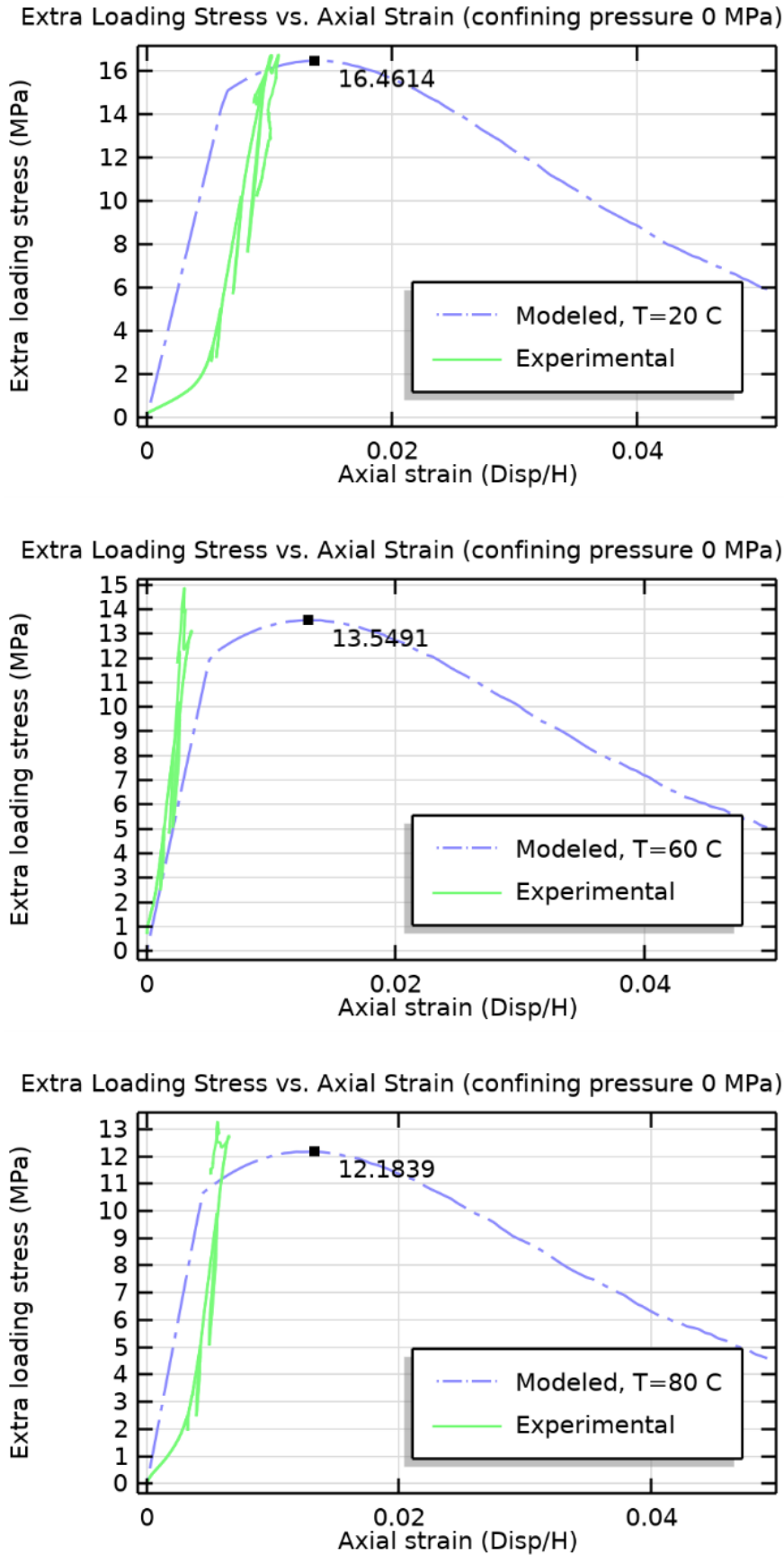
Figure 6.15: Comparison of experimental and modeled extra loading stress vs axial strain for 0 MPa confining pressure

EURAD (Deliverable n˚ 7.6) – Modelling report on the effect of temperature on clay host rocks behaviour
Dissemination level: PU
Date of issue of this report: 06/06/2024

Page 151
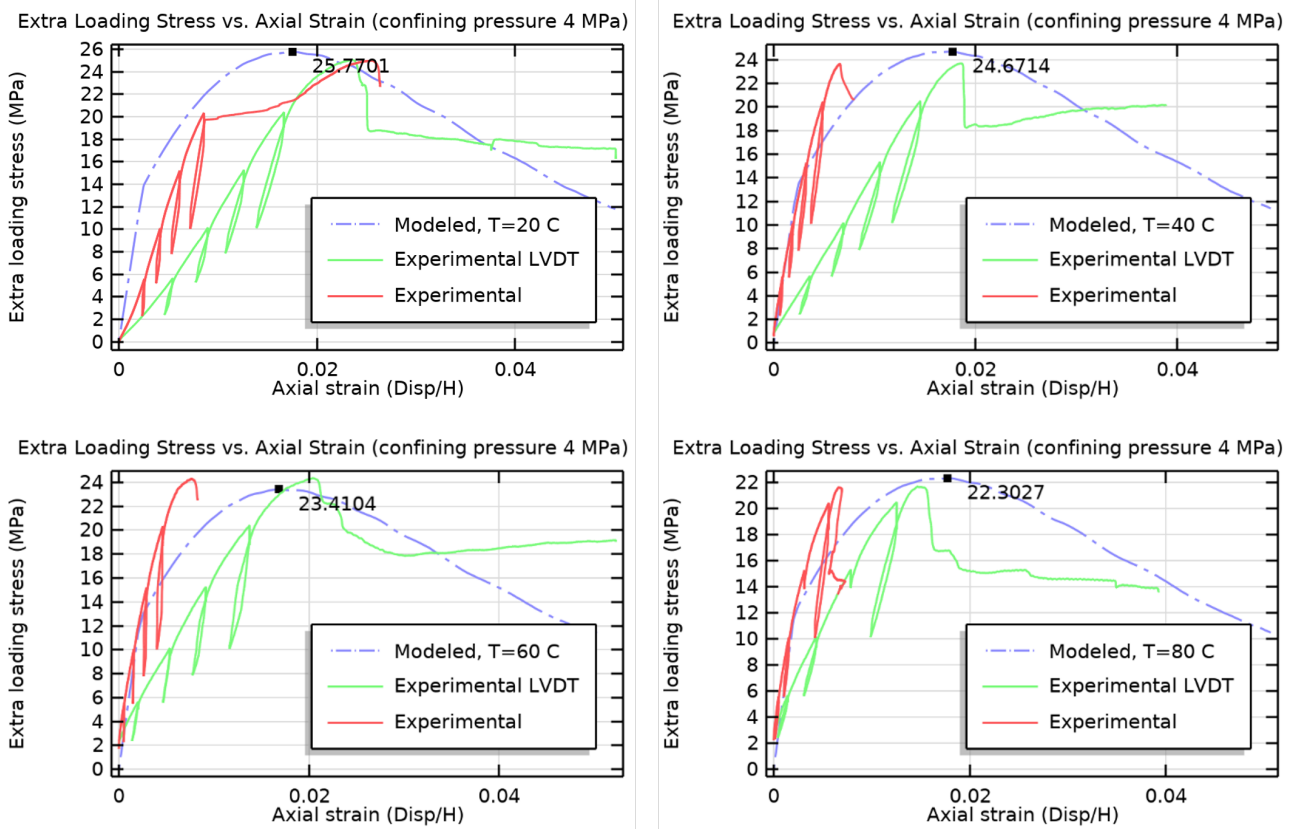
Figure 6.16: Comparison of experimental and modelled extra loading stress vs axial strain for 4 MPa confining pressure

EURAD (Deliverable n˚ 7.6) – Modelling report on the effect of temperature on clay host rocks behaviour
Dissemination level: PU
Date of issue of this report: 06/06/2024

Page 152
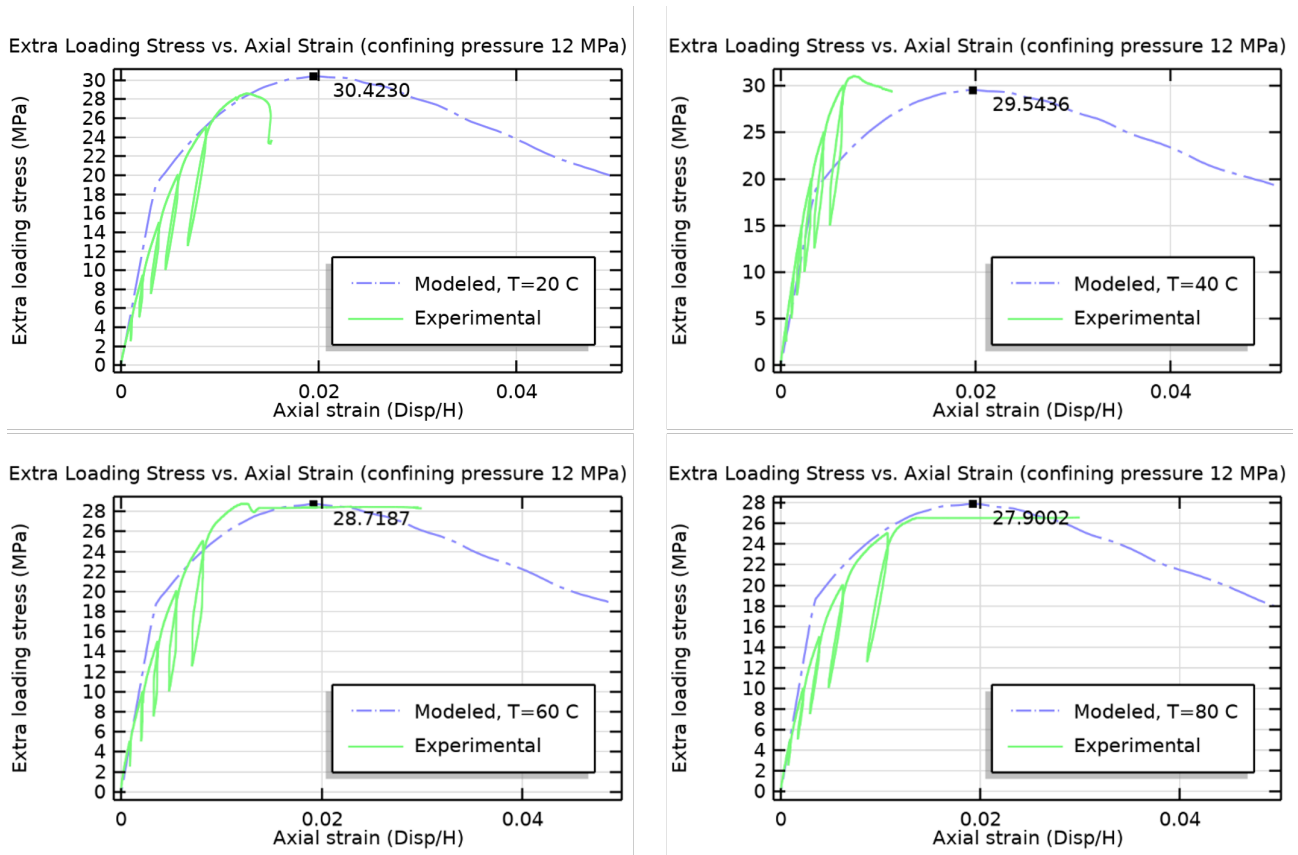
Figure 6.17: Comparison of experimental and modelled extra loading stress vs axial strain for 12 MPa confining pressure

EURAD (Deliverable n˚ 7.6) – Modelling report on the effect of temperature on clay host rocks behaviour
Dissemination level: PU
Date of issue of this report: 06/06/2024

Page 153

The highest peak stress was for the lowest temperature (20 °C) for all modelled results and almost for all experiments (except for confining pressure of 12 MPa at 20 °C), and it reduces as the temperature increased. Also, the higher the confining pressure the higher the peak stresses. This can be clearly seen in Figure 6.18, summarizing the peak strength from all simulations. A good agreement can be identified, demonstrating the capability of the model in reproducing the effect of temperature on the strength of the Cox claystone.
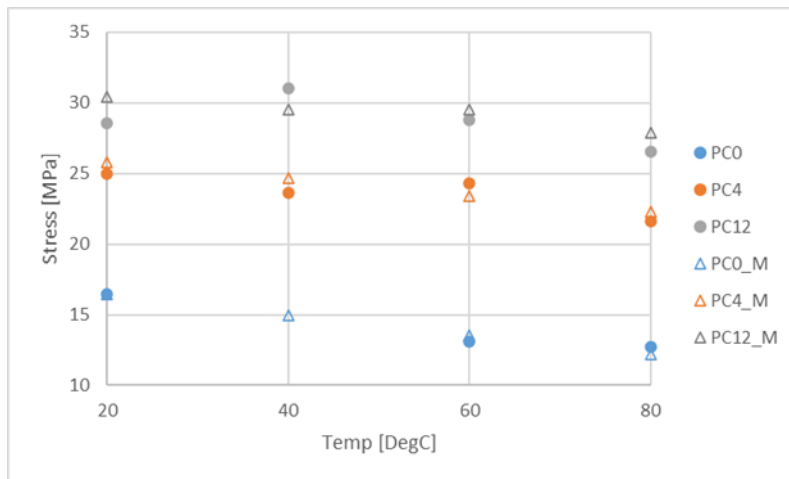
Figure 6.18: Comparison of experimental (PC0, PC4, PC12) and modeled peak stress data (PC0_M, PC4_M, PC12_M)

The set of parameters for elastoplastic model was compiled to be used for modelling of THM response of Cox in-situ experiment ALC1605.

EURAD (Deliverable n° 7.6) – Modelling report on the effect of temperature on clay host rocks behaviour
Dissemination level: PU
Date of issue of this report: 06/06/2024

Page 154

6.4. ULg

A 2D axisymmetric model was introduced as a primary model for the prediction of the THM response of the triaxial compression tests. The geometry of the model was generated by rotation around the central axis of the test samples in the longitudinal direction. The simulated region measures 0.01 m in the radial direction, and 0.04 m in the axial direction. The model was discretized by eight-node quadrilateral elements. The mesh comprises 1301 modes and 450 elements.

6.4.1. Modelling approach

The triaxial compression tests were represented in a two-dimensional axisymmetric coupled THM model. The lateral displacement was constrained along the axis and the bottom of the test samples. The drained system was located at the top and bottom of the samples, while at the surface of the cylinder, the undrained boundary was imposed. The undrained boundary was also put along the axis due to the symmetric condition. There were two steps composed of the numerical modelling illustrated in Figure 6.19: isotropic consolidation and deviatoric loading. In the first step, an increase of the isotropic confining pressure was applied in the horizontal and vertical directions. The temperature of the samples increased homogeneously. The pore pressure dissipation was allowed during the consolidation process. The second step of the numerical modelling was to represent the shear behaviour of the test samples. The confining pressure in the bedding and the temperature of the sample were kept constant. The deviatoric loading was imposed by controlling the deformation of the top of the samples. The Callovo-Oxfordian claystone is a sedimentary material that exhibits horizontal or quasi-horizontal bedding planes, and the main orientations of anisotropy are located in the horizontal isotropic planes and along the vertical direction. In this study, the cross-anisotropic THM behaviour of the host rock was considered between the bedding plane (x direction) and its normal direction (y direction) in Figure 6.19. Due to 2D problem, the samples loaded perpendicular to the bedding were modelled with confining pressure of $0\,\mathrm{MPa}$, $4\,\mathrm{MPa}$ and $12\,\mathrm{MPa}$ at $20\,^\circ\mathrm{C}$, $40\,^\circ\mathrm{C}$, $60\,^\circ\mathrm{C}$, $80\,^\circ\mathrm{C}$, and $100\,^\circ\mathrm{C}$. The experimental results at $150\,^\circ\mathrm{C}$ with different confining stresses are not considered due to the potential water evaporation process of the samples, causing the increase of the peak strength.

Step 1: Consolidation   Step 2: Deviatoric loading
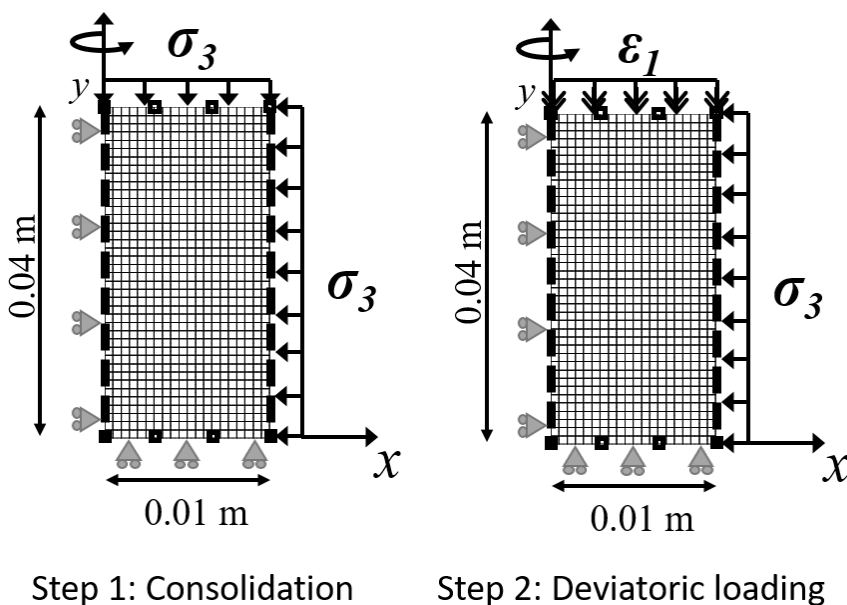
Figure 6.19: Geometry and mesh of the numeric model for the consolidation and deviatoric loading

The main THM parameters used in the numerical modelling are from Table 5.2. However, the numerical

EURAD (Deliverable n° 7.6) – Modelling report on the effect of temperature on clay host rocks behaviour
Dissemination level: PU
Date of issue of this report: 06/06/2024

Page 155

prediction was unable to capture the stress path and peak strength of the experimental results using the cohesion and B_ϕ in the table. The cohesion of the samples is considered a function of temperatures. A general tendency of decrease in peak strength with the increase of temperature is observed from the experimental results, thus the dependency of cohesion on the temperature is taken into account in the modelling. The friction angle is considered independent of temperature, while B_ϕ is believed to be related to the confining pressure. The cohesion of the samples was back computed by using the Mohr-Coulomb criterion, where the deviatoric stress q is a function of mean effective stress p′ (Eq. 6.3). The cohesion values at different temperatures are summarized in Table 6.3 and shown in Figure 6.20. It is worth mentioning that the experimental samples were in unsaturated conditions before the experimental tests, thus the negative pore pressures were defined by the retention curve in the modelling.

$$f = q - M\left(p' + \frac{c}{\tan\phi}\right) \tag{6.3}$$

where

$$M = \frac{6\sin\phi}{3 - \sin\phi} \tag{6.4}$$

$$p' = \frac{\sigma_1 + \sigma_2 + \sigma_3}{3} \tag{6.5}$$

$$q = \sigma_1 - \sigma_3 \tag{6.6}$$

Table 6.3: Cohesion values dependent on different temperatures.

Temperature /°C	cohesion/MPa
20	4.27
40	4.06
60	3.74
80	3.15
100	2.29
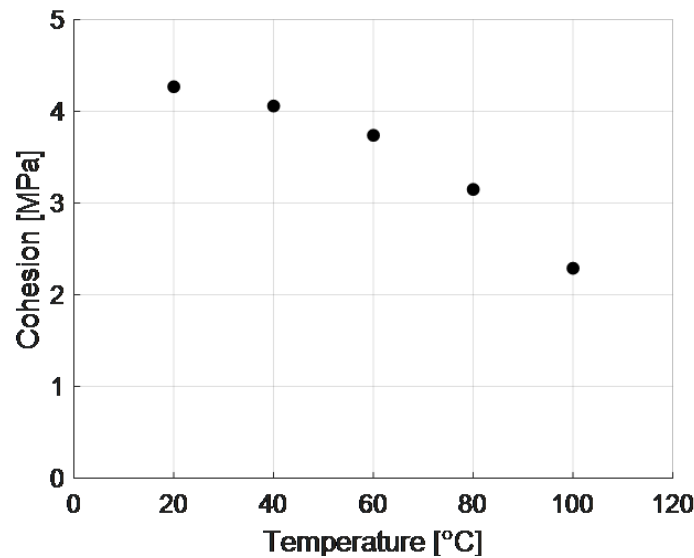
Figure 6.20: The evolution of cohesion with the temperatures

EURAD (Deliverable n˚ 7.6) – Modelling report on the effect of temperature on clay host rocks behaviour
Dissemination level: PU
Date of issue of this report: 06/06/2024

Page 156

6.4.2. Modelling results

The cohesion values corresponding to different temperatures were introduced in the modelling of triaxial compression tests. Figure 6.21,Figure 6.22 and Figure 6.23 show the stress-strain curve at different temperatures with confining stress of 0MPa, 4MPa and 12MPa. The radial strain components ϵ_{xx} and ϵ_{zz} are the same due to the axisymmetric problem, and the ϵ_{yy} is the axial strain component. Globally, the peak strengths decrease with the rise of temperatures. The numerical prediction underestimates the peak strength with the confining stress of 0MPa, which may be due to the potential damage during the loading procedure. The model is able to reproduce the stress-strain path, and the peak strengths are well triggered with the confining stress of 4MPa. Except when the sample is heated to $100\,^\circ$C, higher peak strength is observed experimentally. The numerical prediction obtained a good agreement with the experimental results with confining stress of 12MPa at different temperatures. In general, a clear increase in the peak strength of the samples is evidenced due to the increase in the confining stress.

In this study, the experimental results were modelled by adapting the values of cohesion. However, the relation between the parameter B_ϕ (hardening parameter) also plays an important role in the stress-strain path. In future studies, the temperature-dependent formulation of cohesion and the confining stress-dependent relation will be investigated based on the current results.

EURAD (Deliverable n˚ 7.6) – Modelling report on the effect of temperature on clay host rocks behaviour
Dissemination level: PU
Date of issue of this report: 06/06/2024

Page 157
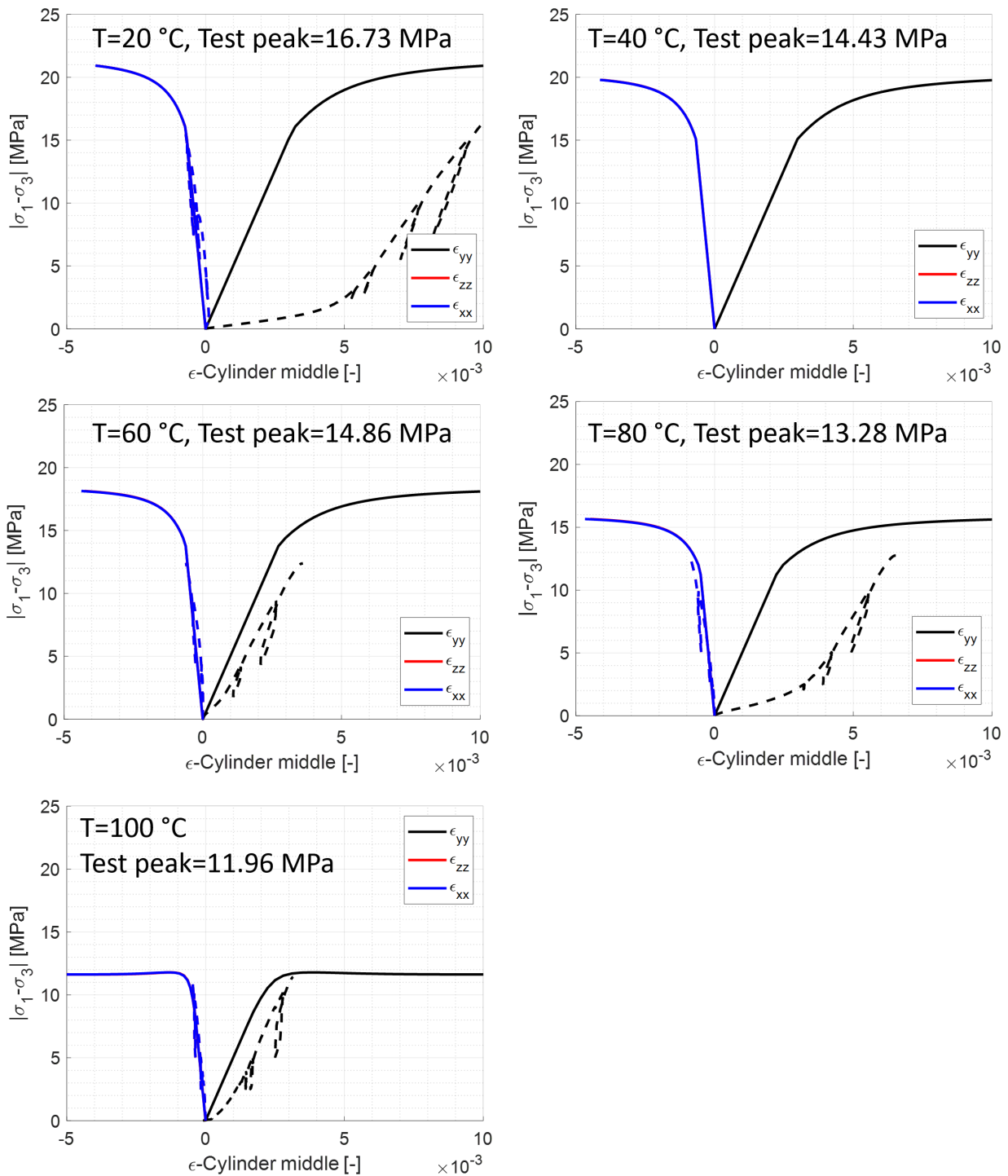
Figure 6.21: Stress strain curve with $0\,\mathrm{MPa}$ at different temperatures (Solid lines: Numerical; Dash lines: Experimental)

EURAD (Deliverable n° 7.6) – Modelling report on the effect of temperature on clay host rocks behaviour
Dissemination level: PU
Date of issue of this report: 06/06/2024

Page 158
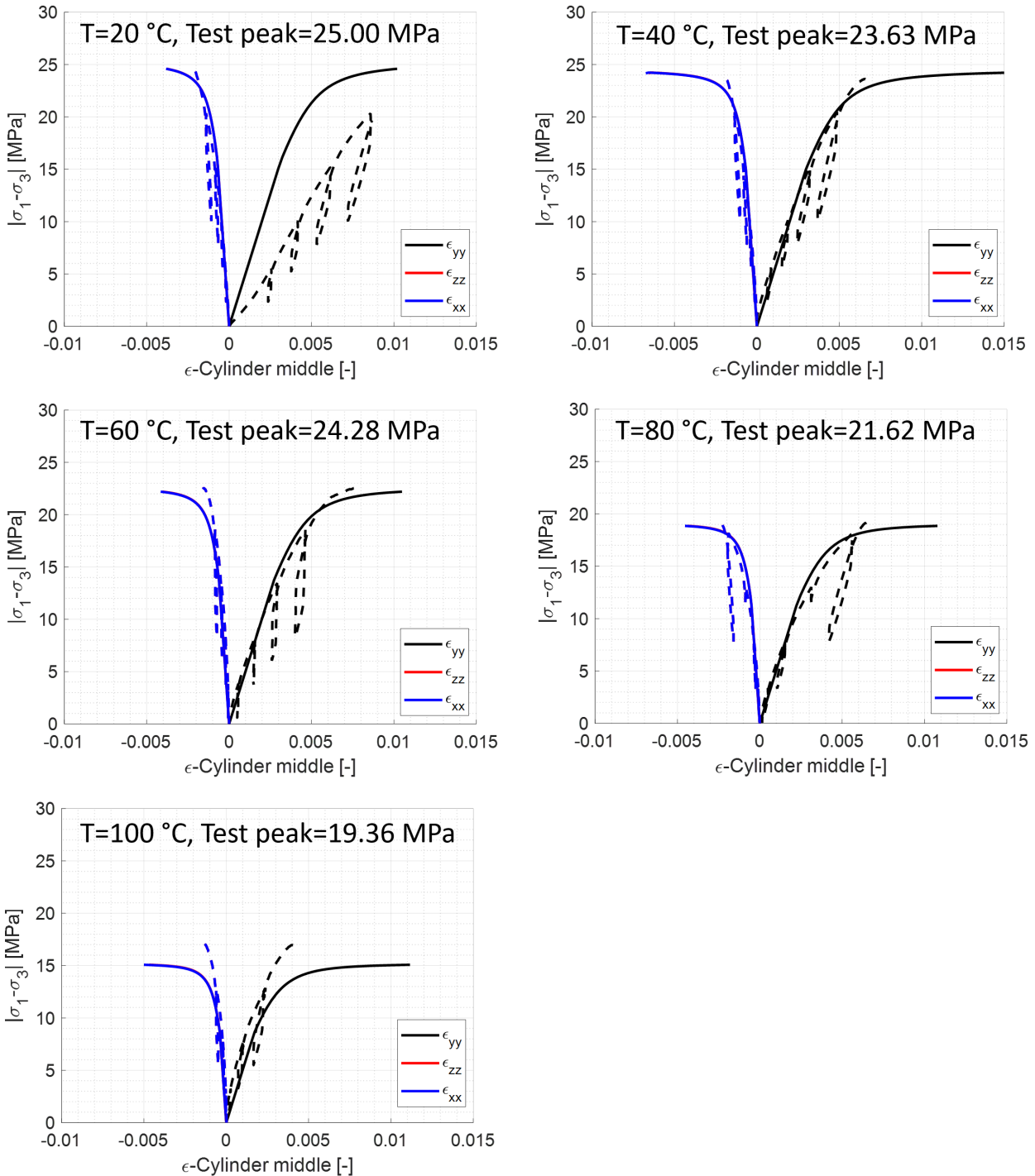
Figure 6.22: Stress strain curve with 4 MPa *at different temperatures (Solid lines: Numerical; Dash lines: Experimental)*

EURAD (Deliverable n° 7.6) – Modelling report on the effect of temperature on clay host rocks behaviour
Dissemination level: PU
Date of issue of this report: 06/06/2024

Page 159
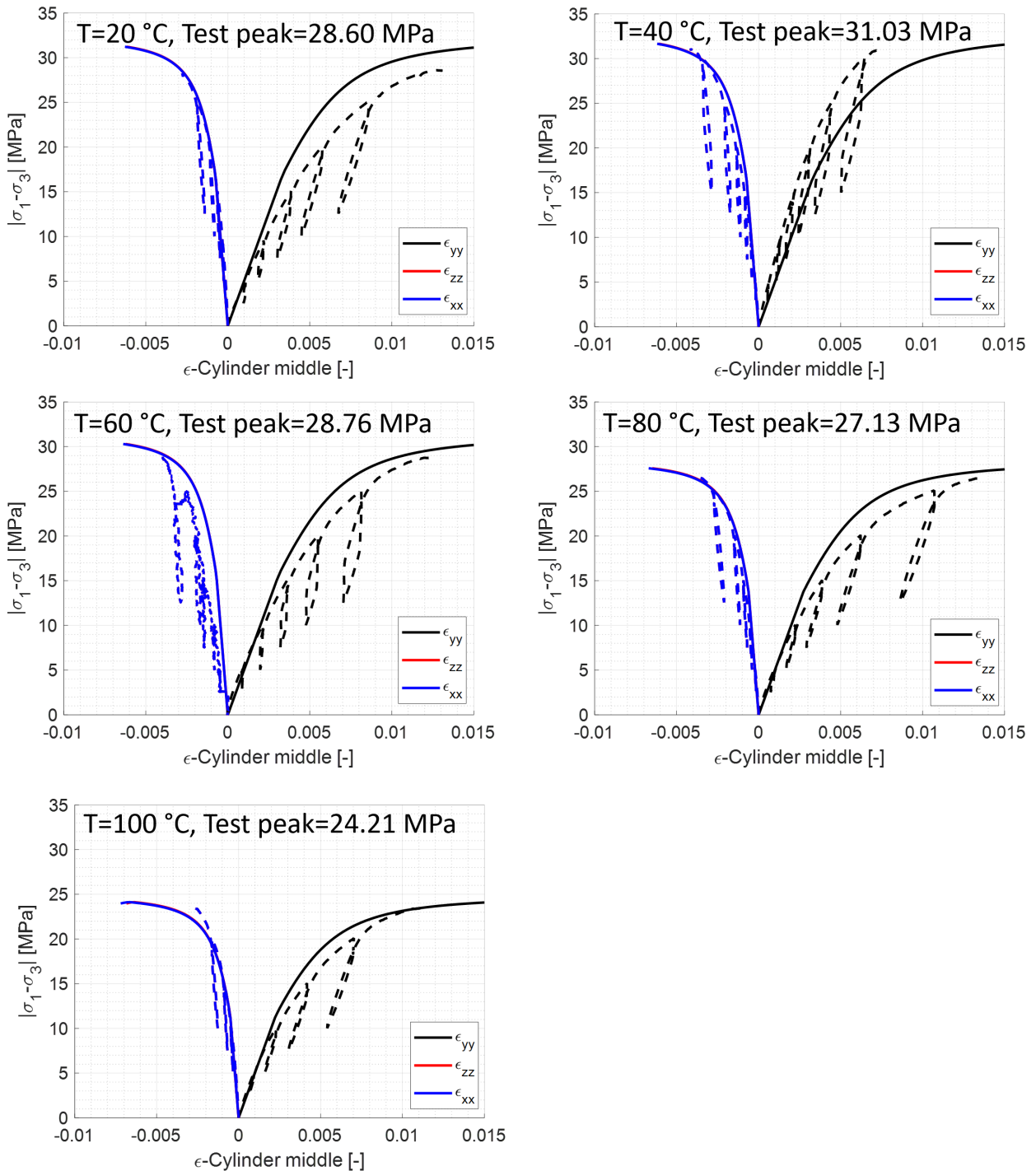
Figure 6.23: Stress strain curve with 12 MPa *at different temperatures (Solid lines: Numerical; Dash lines: Experimental)*

EURAD (Deliverable n˚ 7.6) – Modelling report on the effect of temperature on clay host rocks behaviour
Dissemination level: PU
Date of issue of this report: 06/06/2024

Page 160

6.5. UPC

6.5.1. Numerical model

The numerical model used in this study is a three-dimensional (3D) cylindrical model with a diameter of 20 mm and a height of 40 mm, as shown in Figure 6.24(a). Two hydraulic boundary conditions (B.C.), are considered: (1) surface B.C.: atmospheric boundary condition (0.1 MPa) is applied to the whole of the upper and bottom surfaces, and (2) point B.C.: atmospheric boundary condition (0.1 MPa) is applied only at a zone at the centre of the top and bottom surfaces. Note that this zone is a small square surface with a side length of 0.3 mm. The point B.C represents more accurately the real drainage conditions of the tests. During the experimental tests, the drain system is opened and the vapour can flow through the tube at the upper and bottom surfaces. For the surface B.C. and point B.C. models, meshes with 15 075 and 15 994 tetrahedra elements are respectively considered (see Figure 6.24(b) and Figure 6.24(c)), sufficiently accurate and resulting in an acceptable computation time.

(a) (b) (c)
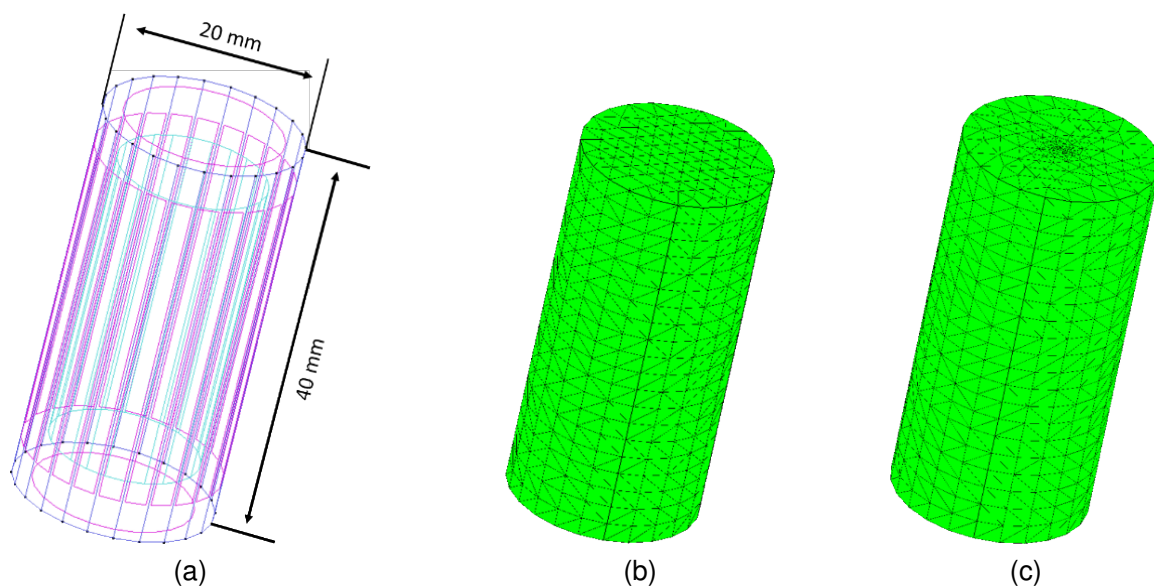
Figure 6.24: (a) Geometry of the numerical model, (b) mesh for the 'surface boundary condition' model, and (c) mesh for the 'point boundary condition' model.

At the start, the initial conditions in terms of temperature ($20\,°C$), porosity (0.166) and suction ($10.4\,MPa$) are applied in the whole numerical model. The initial porosity value of 0.166, and the initial saturation value of 92.6% are the average values of the experimental observations in all specimens. The initial suction is calculated from the initial saturation and the water retention curve. Input parameters for Cox are listed in Table 6.4. Four different modelling stages are considered (as shown in Table 6.5):

- Increase of the cell pressure. The applied stress increase at a rate of $0.1\,MPa/min$.

- Increase of the applied temperature. The temperature increases at a rate of $50\,°C/hour$.

- Waiting stage. After the temperature rise, a 14 hours waiting period is enforced to let liquid pressure dissipate.

- Deviatoric loading stage. A displacement rate of $12\,\mu m/min$ is applied at the top surface.

In all modelling stages, the normal displacements at the bottom surface are restrained.

EURAD (Deliverable n˚ 7.6) – Modelling report on the effect of temperature on clay host rocks behaviour
Dissemination level: PU
Date of issue of this report: 06/06/2024

Page 161

Table 6.4: Input parameters of Cox.

Elastic	Elastic moduli	$E_1 = 6000$ MPa, $E_2 = 4000$ MPa
	Poisson's ratio	$\nu_1 = 0.3$, $\nu_2 = 0.3$
	Shear modulus	$G_2 = 1700$ MPa
Plastic	Peak strength	$\varphi^*_{ini} = \varphi^*_{peak} = 25°$, $c^*_{0peak}(T_0) = 8.5$ MPa, $p_{t0peak}(T_0) = 2.5$ MPa
	Post-rupture	$b_{post} = 60$, $b_{res} = 2$
	Residual strength	$r_{post} = 0.3$, $\phi_{res} = 15°$
	Thermal-Mechanical coupling	$E_e = E_g = -0.8$, $E_f = E_h = -2.2 \times 10^{-2}$
	Flow rule	$\omega = 0.4$
	Threshold	$\xi = 0.0$
Viscoplastic	η_{vp}	3×10^6 MPa s
	Stress power	1
Strength anisotropy	$\Omega_{90} = 1.3$, $\Omega_m = 0.82$, $\delta_m = 49.7$ deg, $n = 0.1$	
Internal length	l_s	0.05 m
Solid phase density	ρ_s	2673 kg/m^3
Biot Coefficient	Biot	0.8
Thermal expansion coefficient	α_s	1.25×10^{-5} K^{-1}
Solid phase specific heat	c_p	790 J/kg/K
Intrinsic permeability	$K_\parallel = 5 \times 10^{-20}$ m^2, $K_\perp = 2.5 \times 10^{-20}$ m^2, $\beta = 4 \times 10^7$	
Thermal conductivity	$\rho_\parallel = 1.88$ W/m/K, $\rho_\perp = 1.25$ W/m/K	
Water retention curve	$\lambda^r = 0.32$, $P = 17.6$ MPa	

6.5.2. Numerical results

Numerical simulations are carried out for the elastic and plastic cases. The objective of performing elastic cases is to investigate the evolution of pore pressures and stress paths, to better understand the effect of temperature variation and bedding orientations on the THM responses. Afterwards, numerical studies are carried out for plastic cases, considering both perfectly-plastic and strain-softening behaviour models. Additionally, parametric analyses are carried out to identify the influence of the hydraulic B.C. on the evolution of pore pressure and strength.

(a). Numerical analyses for the elastic case In the preliminary analyses, numerical simulations are carried out for elastic cases; the cell pressure considered is 4 MPa. Two different temperatures (20 °C, 100 °C) and two different bedding orientations (0°, 90°) are considered. In addition, two different hydraulic boundary conditions are utilized, i.e. the surface B.C. and the point B.C.

As shown in Figure 6.25, in the heating stage, the pore pressure increases due to thermal pressurization: the pore pressures obtained with point B.C. are much higher than the ones obtained using surface B.C.,

EURAD (Deliverable n˚ 7.6) – Modelling report on the effect of temperature on clay host rocks behaviour
Dissemination level: PU
Date of issue of this report: 06/06/2024

Page 162

Table 6.5: Boundary conditions at different modelling stages, for both surface B.C. and point B.C. models.
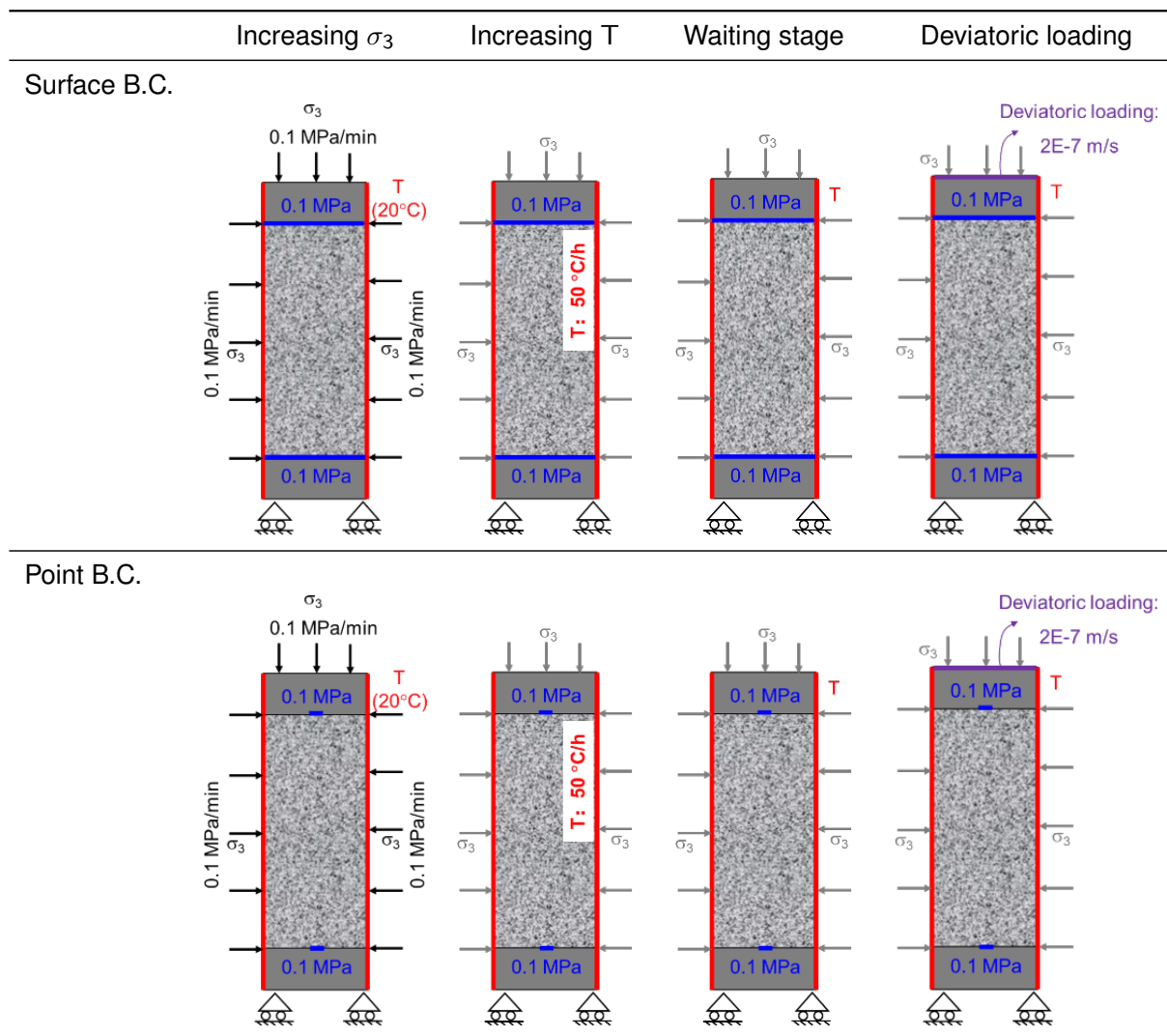
because faster liquid dissipation occurs when using surface B.C. As can be observed in Figure 6.25(b), the pore pressure in the heating stage can reach values up to around $30\,\mathrm{MPa}$; in turn, this overpressure may contribute to yielding when using the strain-softening model. Another significant conclusion is that the waiting stage of 14 hours is enough for liquid pressure dissipation for both hydraulic B.C. cases: it can be observed that at the beginning of the deviatoric loading stage, the liquid pressure in the study point is close to the atmospheric pressure ($0.1\,\mathrm{MPa}$).

In the deviatoric loading stage, when using surface B.C., the pore pressures first increase, and then achieve an approximately stable value. The samples tested at higher temperatures result in lower stable pore pressure values, due to the faster liquid dissipation associated with lower water viscosity. When using point B.C., the pore pressures of samples tested at higher temperatures are lower than the ones tested at lower temperatures; whereas the pore pressures of samples with $\theta = 90°$ are significantly lower than the ones of samples with $\theta = 0°$. The difference of pore pressure obtained between samples with $\theta = 0°$ and with $\theta = 90°$, is mainly caused by anisotropy of the intrinsic permeability and stiffness.

Figure 6.26 shows the stress paths of Biot $p' - \sqrt{J_2}$ at point $(0, 0, 0.02\,\mathrm{m})$, at the centre of the specimen. By comparing Figure 6.26(a) and Figure 6.26(b), the difference behaviour between different temperatures is more evident when using the surface B.C. It can also be observed that stress will likely encounter the yield surface in the tests. Based on these preliminary analyses, we can conclude that introducing the

EURAD (Deliverable n˚ 7.6) – Modelling report on the effect of temperature on clay host rocks behaviour
Dissemination level: PU
Date of issue of this report: 06/06/2024

Page 163

thermal-mechanical coupled constitutive model might be of benefit to better characterise the experimental observations, i.e. to consider the coupling between material behaviour and thermal loading history.

(a)   (b)
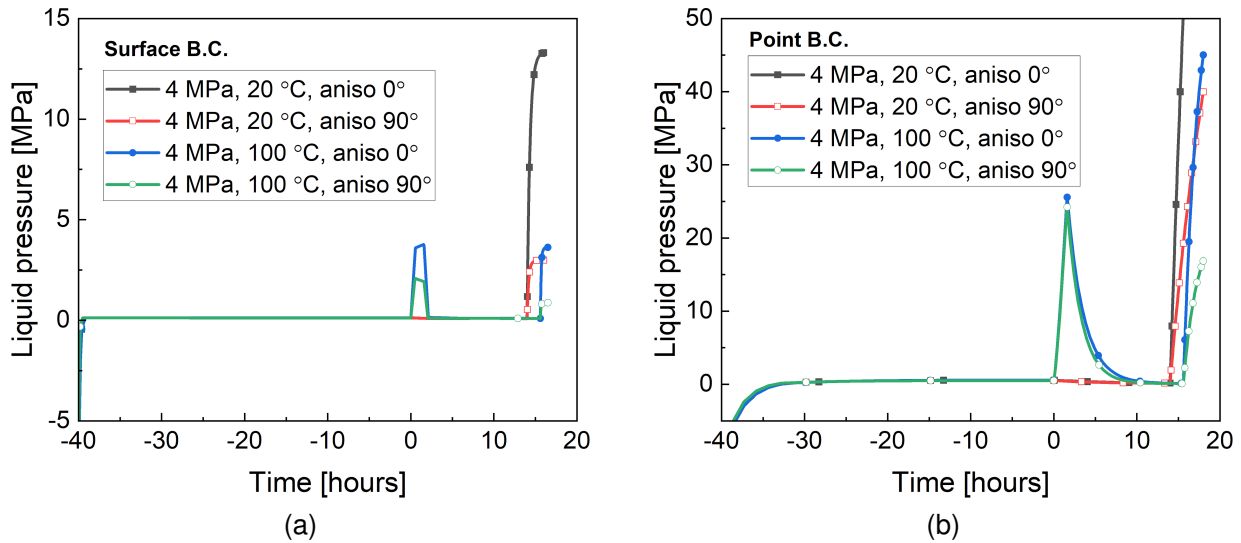
Figure 6.25: Evolutions of pore pressure at the centre of the specimen for (a) surface B.C., and (b) point B.C. cases. The cell pressure is 4 MPa*. Time zero corresponds to the start of heating. Both temperatures (*20 °C*,* 100 °C*) and both bedding orientations (*0°*,* 90°*) are plotted.*

(a)   (b)
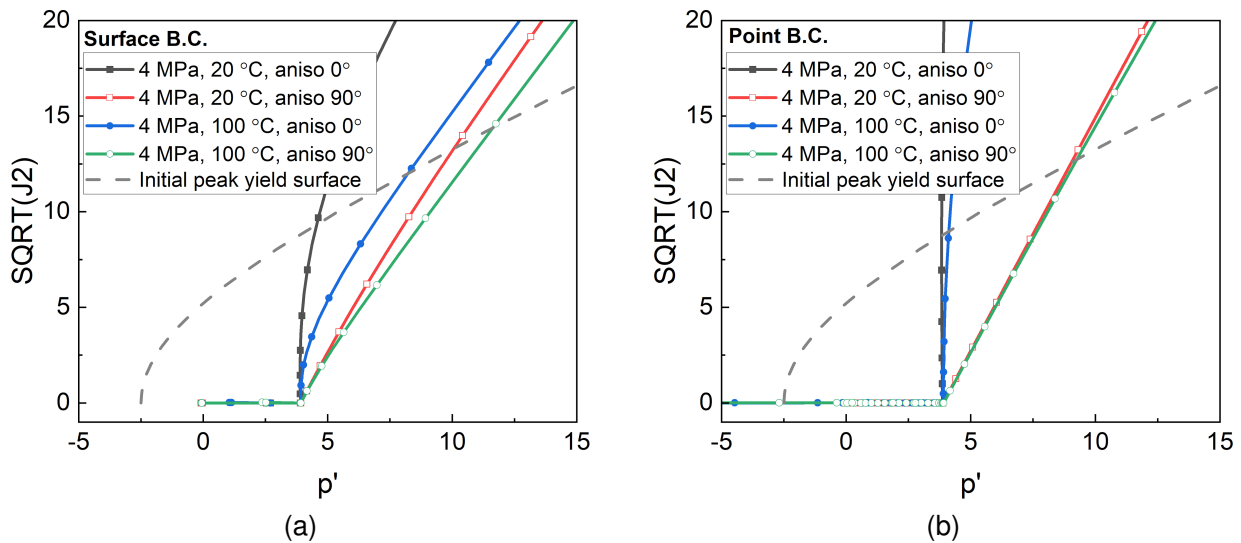
Figure 6.26: Stress paths of Biot $p' - \sqrt{J_2}$ *at the centre of the specimen for (a) surface B.C., and (b) point B.C. cases. The cell pressure is* 4 MPa*. Time zero corresponds to the start of heating. Both temperatures (*20 °C*,* 100 °C*) and both bedding orientations (*0°*,* 90°*) are plotted. The initial yleld surface for the material is also plotted for reference.*

To further identify the reason for the differences in pore pressures and stress paths for samples with different bedding orientations, numerical simulations are carried out using isotropic elastic stiffness while all other parameters are the same as those listed in Table 6.4, i.e., anisotropy in both hydraulic and thermal conductivities is maintained. As shown in Figure 6.27(a) and Figure 6.27(c), for models with surface B.C.: the pore pressure of samples with $\theta = 0°$ is significantly higher than the ones of samples with $\theta = 90°$, whereas higher testing temperature result in lower pore pressures. However, in Figure 6.27(b) and Figure 6.27(d), for models with point B.C., there is only a slight difference in pore pressures and stress paths for different bedding orientations. It means that when using the surface B.C., the anisotropy of HM responses is mainly contributed by the anisotropic hydraulic conductivity; however, for models with point

EURAD (Deliverable n° 7.6) – Modelling report on the effect of temperature on clay host rocks behaviour
Dissemination level: PU
Date of issue of this report: 06/06/2024

Page 164

B.C., the anisotropic HM behaviour is mainly caused by the anisotropy of stiffness but not anisotropy of intrinsic permeability.
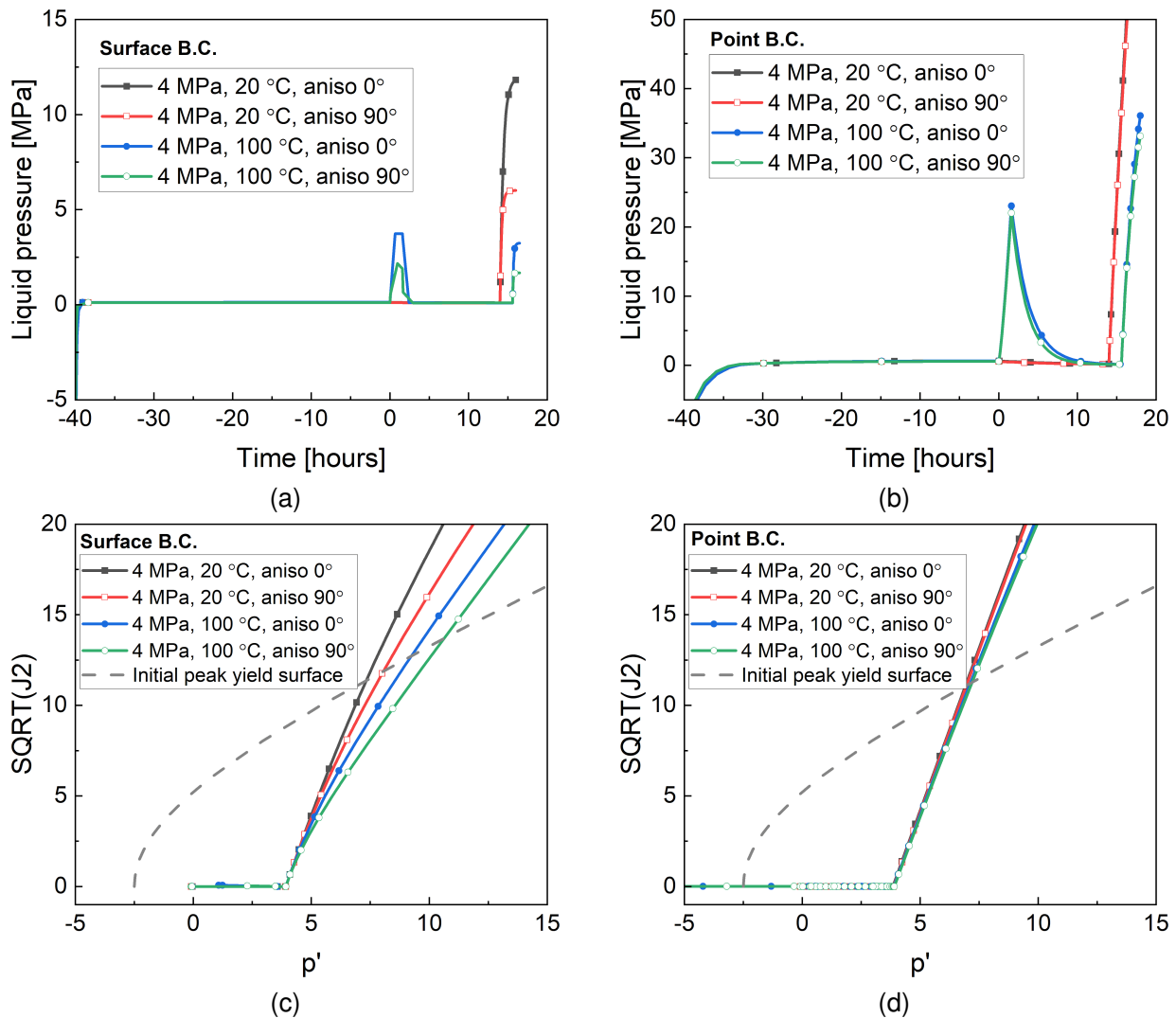
Figure 6.27: Evolutions of pore pressure at the centre of the specimen for (a) surface B.C., and (b) point B.C. cases and stress paths of Biot $p' - \sqrt{J_2}$ at the centre of the specimen for (c) surface B.C., and (d) point B.C. cases. The cell pressure is $4\,\text{MPa}$. Both temperatures ($20\,°\text{C}$, $100\,°\text{C}$) and both bedding orientations ($0°$, $90°$) are considered. Isotropic elastic stiffness is considered. The initial yIeld surface for the material is also plotted for reference.

(b). Numerical analyses for the plastic case   For the plastic simulations, two different hydraulic boundary conditions (surface B.C. and point B.C.) and two different post-failure behaviour models (perfectly-plastic and strain-softening) have been considered. Figure 6.28 shows the comparison of peak deviatoric strengths for Cox between numerical predictions (plotted as lines) and experimental observations (plotted as points). The dash and the solid lines represent the numerical results for the strain-softening (SS) and perfectly-plastic (PP) cases, respectively.

For samples with bedding orientation with $\theta = 0°$ (Figure 6.28(a) and Figure 6.28(c)), , the numerical results obtained by using the perfectly-plastic (PP) models overestimate experimental observations, especially for cases of $12\,\text{MPa}$ cell pressure. However, when using the strain-softening (SS) model and point B.C., numerical results match better the experimental data, as shown in Figure 6.28(c).

EURAD (Deliverable n˚ 7.6) – Modelling report on the effect of temperature on clay host rocks behaviour
Dissemination level: PU
Date of issue of this report: 06/06/2024

Page 165

As shown in Figure 6.29 and Table 6.6, there is a significant difference in pore pressure between surface B.C. and point B.C. analyses due to different liquid dissipations. When using the strain-softening model, overpressure developed in the heating stage causes the stress path to reach the yield surface which, in turn, leads to lower strengths in the deviatoric loading stage. The different pore pressures obtained by point B.C. and by surface B.C. result in different stress paths, as shown in Figure 6.29(b) and Figure 6.29(d).

Figure 6.30, Figure 6.31, and Figure 6.32 respectively show the comparisons of stress-strain curves between numerical and experimental results for three different cell pressures (0 MPa, 4 MPa and 12 MPa) for specimens with bedding orientation $\theta = 0°$. In addition, Figure 6.33, Figure 6.34 and Figure 6.35 show the same comparison for samples with bedding orientation $\theta = 90°$. In general, a good agreement of stress-strain curves between numerical predictions and experimental data obtained from laboratory tests can be observed, showing that the numerical predictions can reasonably represent the THM behaviour of Cox.

6.5.3. Discussion and conclusions

Thermo-Hydro-Mechanical (THM) laboratory tests have been carried out on Cox samples. The tests included four different stages: increase of cell pressure, heating stage, waiting stage and deviatoric loading stage. In the thermal phase the Cox specimens are subjected to different temperature increases (20 °C, 40 °C, 60 °C, 80 °C, 100 °C). Additionally, three different cell pressures were applied: 0 MPa, 4 MPa and 12 MPa. Experimental data in terms of stress-strain curves and peak deviatoric strengths are available.

In this study, coupled THM modelling has been carried out using a fully coupled THM constitutive model for clay rocks under unsaturated and saturated conditions. The constitutive model is formulated within the framework of elastic-viscoplasticity, which considers non-linearity and softening after peak strength, anisotropy of stiffness and strength, as well as permeability variation due to damage. In addition, the mechanical properties are coupled with thermal loading history.

The proposed constitutive model has been validated against experimental data from the laboratory tests; the Callovo-Oxfordian (Cox) claystone samples that are initially unsaturated under suction. Two different hydraulic boundary conditions (surface B.C. and point B.C.) and two different behaviour models (perfectly plastic and strain-softening) have been used in the analyses. The numerical predictions of pore pressures when using point B.C. are much higher than the ones obtained when using surface B.C., due to different liquid dissipations. This, in turn, affects the stress paths and peak strengths.

EURAD (Deliverable n˚ 7.6) – Modelling report on the effect of temperature on clay host rocks behaviour
Dissemination level: PU
Date of issue of this report: 06/06/2024

Page 166

Table 6.6: Evolution of pore pressure contours, for both surface B.C. and point B.C. Cell pressure is 12 MPa*, temperature* 100 °C *and anisotropy angle* $\theta = 0°$*.*

Surface B.C.	Point B.C.
3D view at t = 1.6 hours (the end of the heating stage)	

t = 0 (at the beginning of the heating stage)	

t = 1.6 hours (at the end of heating stage)	

t = 15.6 hours (at the end of waiting stage)	

t = 15.92 hours (during the deviatoric loading stage)	

EURAD (Deliverable n° 7.6) – Modelling report on the effect of temperature on clay host rocks behaviour
Dissemination level: PU
Date of issue of this report: 06/06/2024

Page 167

Figure 6.28: *Comparison of peak strengths between experimental data (points) and numerical results (lines) for: (a) anisotropy angle θ = 0° samples, with surface B.C., (b) (a) anisotropy angle θ = 90° samples, with surface B.C., (c) anisotropy angle θ = 0° samples, with point B.C., and (d) anisotropy angle θ = 90° samples, with point B.C. Dash lines represent the results obtained by the perfectly-plastic (PP) model, while solid lines are the results obtained by the strain-softening (SS) model. Three different cell pressures are considered (Pc = 0 MPa, 4 MPa and 12 MPa).*

EURAD (Deliverable n° 7.6) – Modelling report on the effect of temperature on clay host rocks behaviour
Dissemination level: PU
Date of issue of this report: 06/06/2024

Page 168
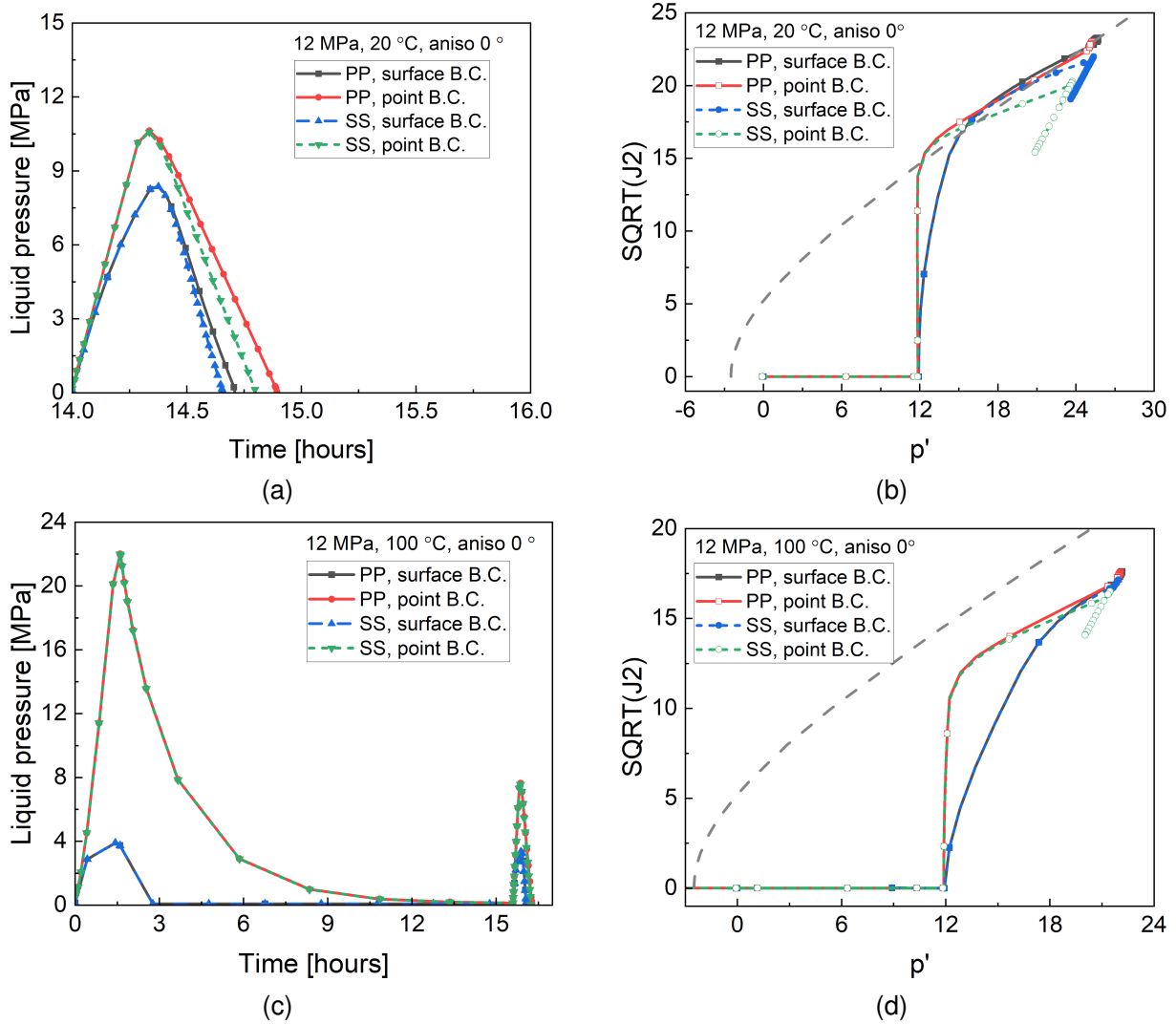
Figure 6.29: Evolutions of (a) pore pressure for samples with T = 20 °C, *(b) stress paths for samples with* T = 20 °C, *(c) pore pressure for samples with* T = 100 °C, *(d) stress paths for samples with* T = 100 °C. *Cell pressure is* 12 MPa *and anisotropy angle* θ = 0°.

EURAD (Deliverable n° 7.6) – Modelling report on the effect of temperature on clay host rocks behaviour
Dissemination level: PU
Date of issue of this report: 06/06/2024

Page 169
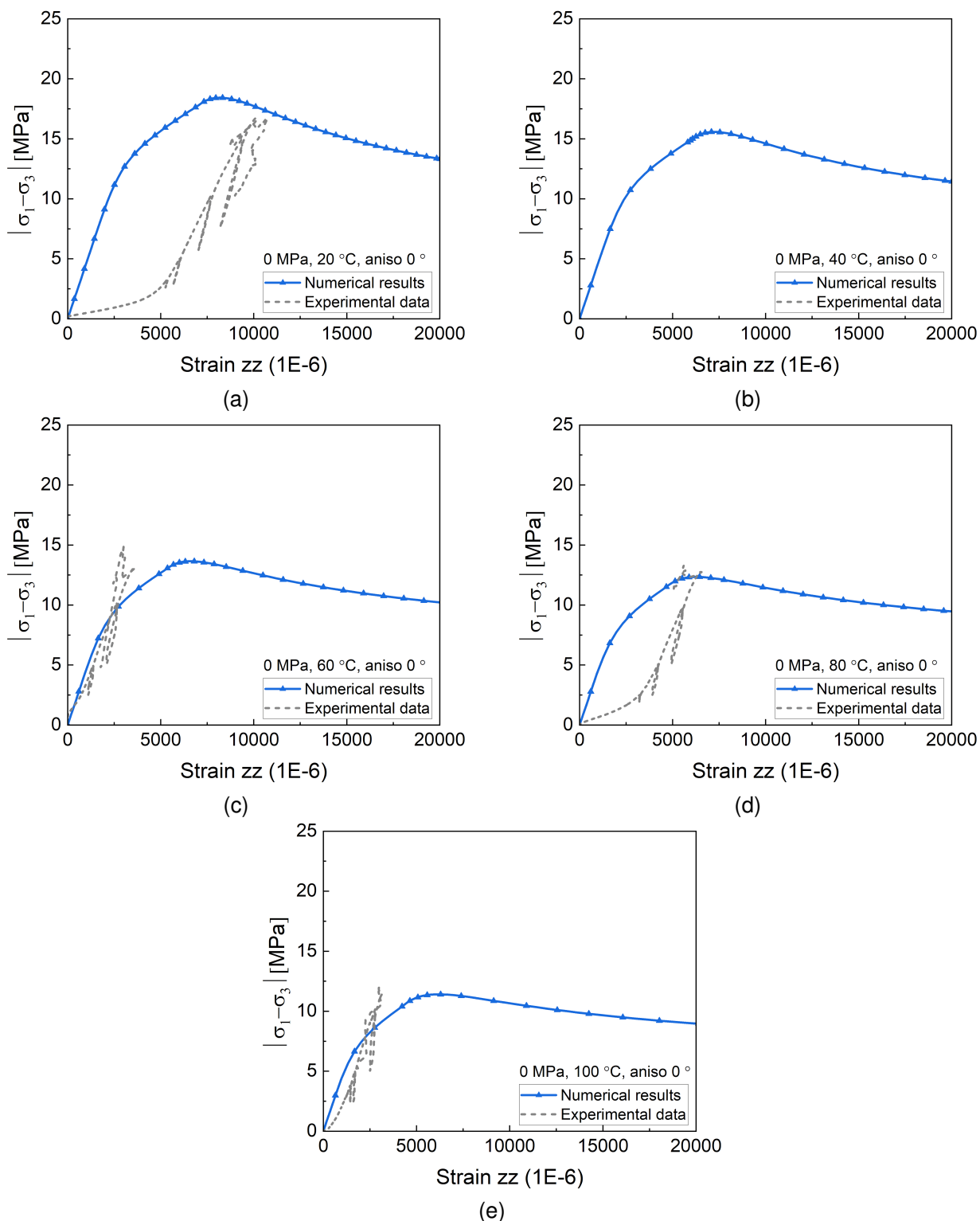
Figure 6.30: Comparison of the stress-strain curves between experimental data (dash lines) and numerical results (solid lines) for: (a) T = 20 °C, (b) T = 40 °C, (c) T = 60 °C, (d) T = 80 °C, and (e) T = 100 °C. Cell pressure is 0 MPa and anisotropy angle θ = 0°.

EURAD (Deliverable n° 7.6) – Modelling report on the effect of temperature on clay host rocks behaviour
Dissemination level: PU
Date of issue of this report: 06/06/2024

Page 170
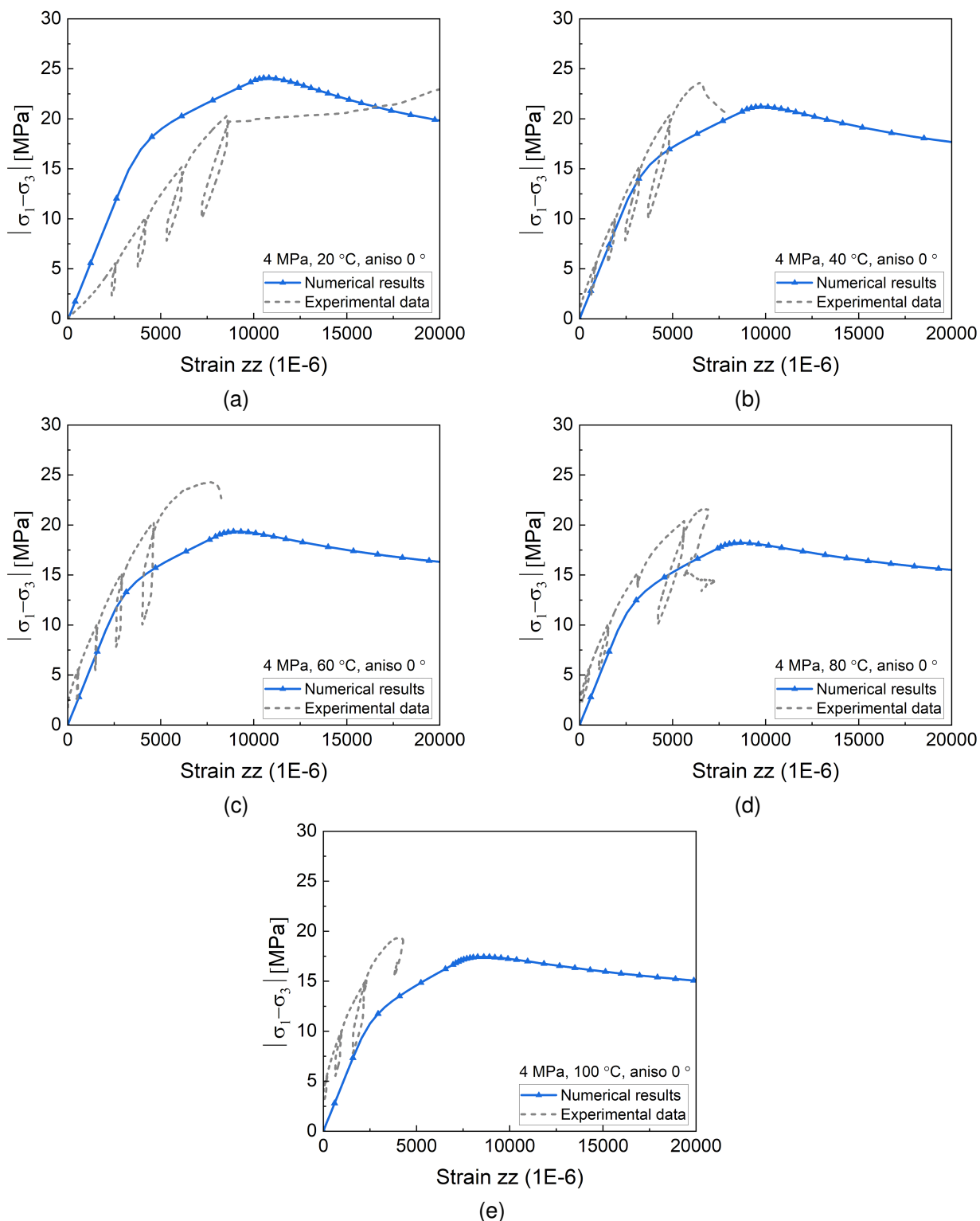
Figure 6.31: Comparison of the stress-strain curves between experimental data (dash lines) and numerical results (solid lines) for: (a) T = 20 °C, (b) T = 40 °C, (c) T = 60 °C, (d) T = 80 °C, and (e) T = 100 °C. Cell pressure is 4 MPa and anisotropy angle θ = 0°.

EURAD (Deliverable n˚ 7.6) – Modelling report on the effect of temperature on clay host rocks behaviour
Dissemination level: PU
Date of issue of this report: 06/06/2024

Page 171
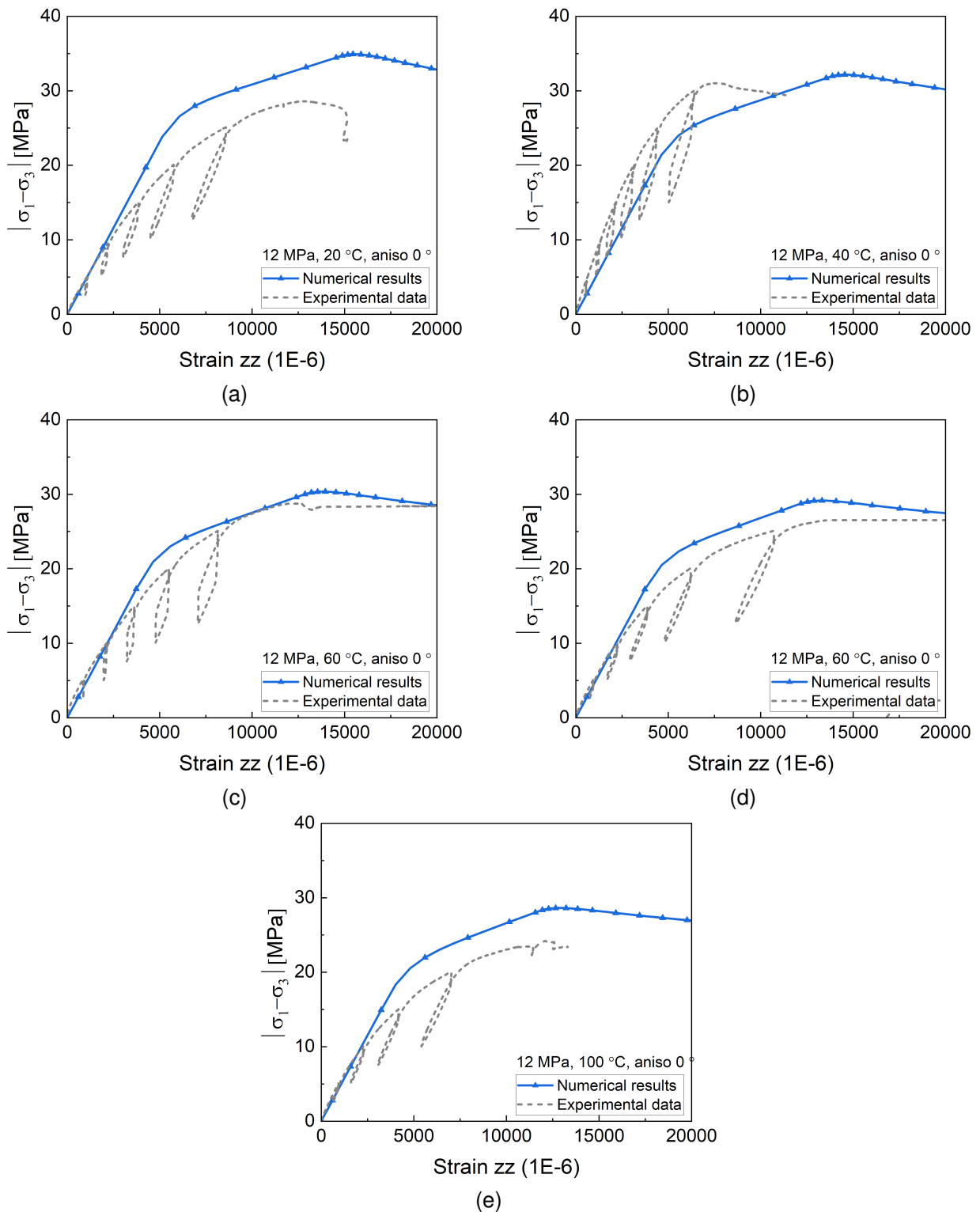
Figure 6.32: Comparison of the stress-strain curves between experimental data (dash lines) and numerical results (solid lines) for: (a) T = 20 °C, (b) T = 40 °C, (c) T = 60 °C, (d) T = 80 °C, and (e) T = 100 °C. Cell pressure is 12 MPa and anisotropy angle θ = 0°.

EURAD (Deliverable n° 7.6) – Modelling report on the effect of temperature on clay host rocks behaviour
Dissemination level: PU
Date of issue of this report: 06/06/2024

Page 172
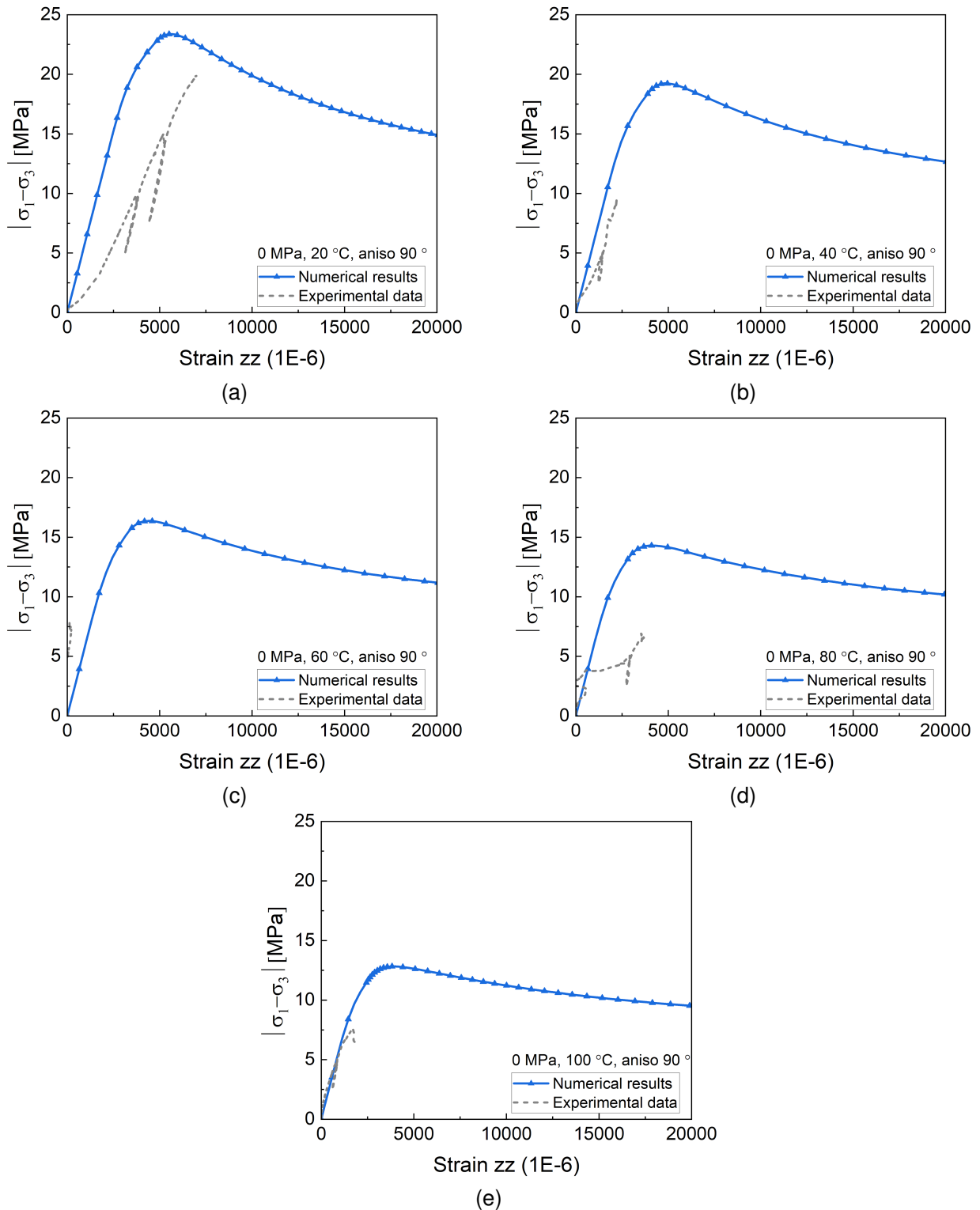
Figure 6.33: Comparison of the stress-strain curves between experimental data (dash lines) and numerical results (solid lines) for: (a) T = 20 °C, (b) T = 40 °C, (c) T = 60 °C, (d) T = 80 °C, and (e) T = 100 °C. Cell pressure is 0 MPa and anisotropy angle θ = 90°.

EURAD (Deliverable n° 7.6) – Modelling report on the effect of temperature on clay host rocks behaviour
Dissemination level: PU
Date of issue of this report: 06/06/2024

Page 173
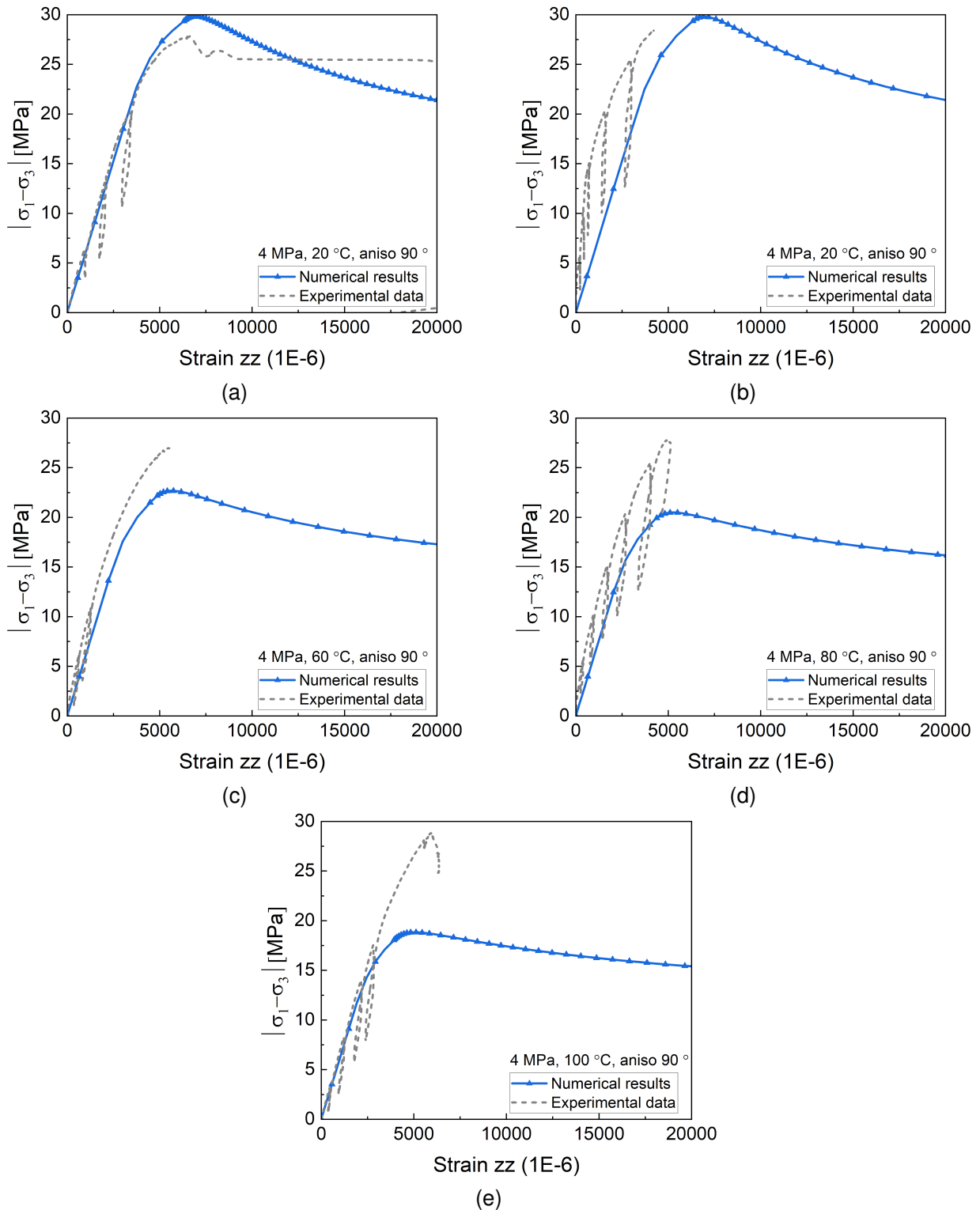
Figure 6.34: Comparison of the stress-strain curves between experimental data (dash lines) and numerical results (solid lines) for: (a) T = 20 °C, (b) T = 40 °C, (c) T = 60 °C, (d) T = 80 °C, and (e) T = 100 °C. Cell pressure is 4 MPa and anisotropy angle θ = 90°.

EURAD (Deliverable n˚ 7.6) – Modelling report on the effect of temperature on clay host rocks behaviour
Dissemination level: PU
Date of issue of this report: 06/06/2024

Page 174
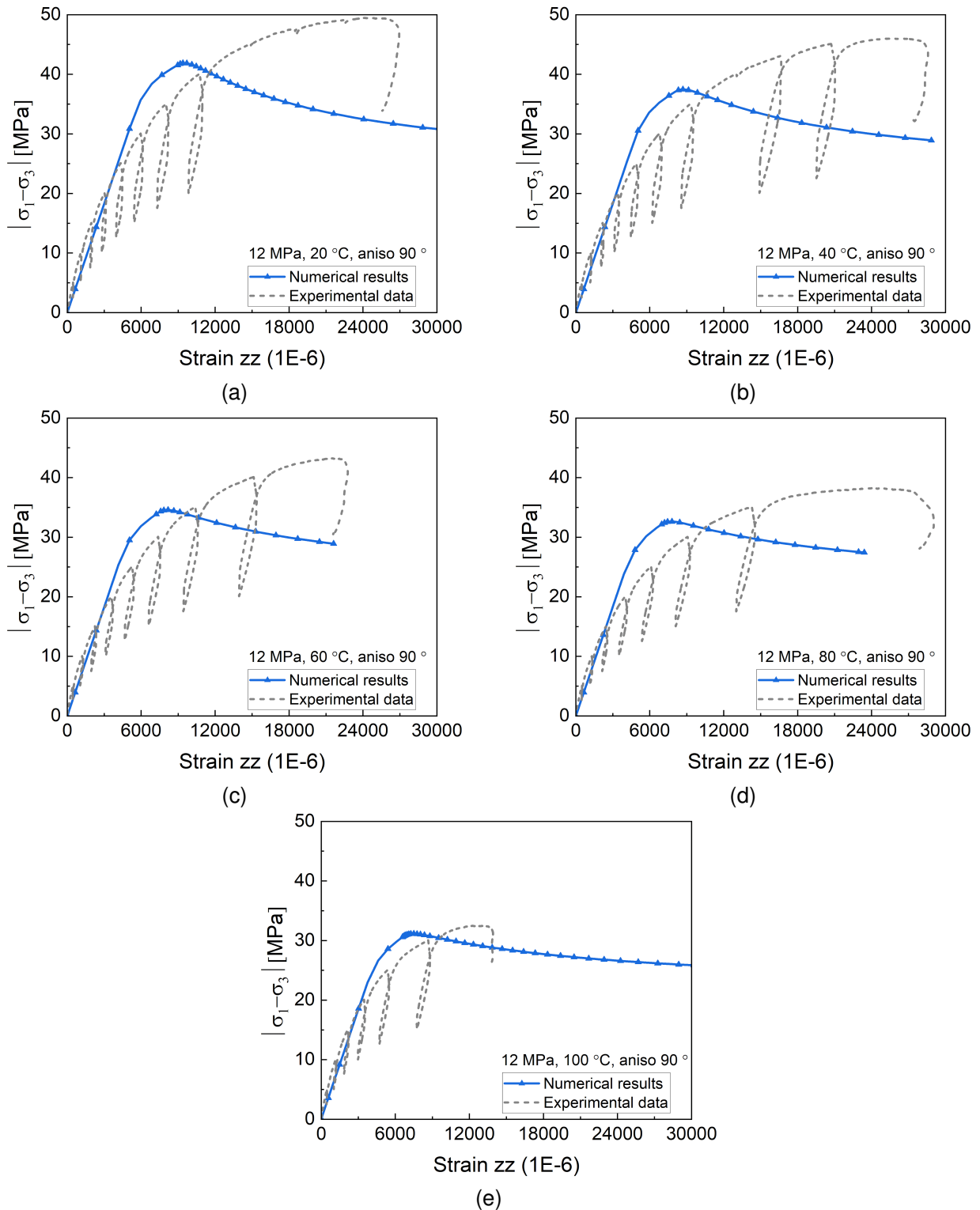
Figure 6.35: Comparison of the stress-strain curves between experimental data (dash lines) and numerical results (solid lines) for (a) T = 20 °C, (b) T = 40 °C, (c) T = 60 °C, (d) T = 80 °C, and (e) T = 100 °C. Cell pressure is 12 MPa and anisotropy angle θ = 90°.

EURAD (Deliverable n° 7.6) – Modelling report on the effect of temperature on clay host rocks behaviour
Dissemination level: PU
Date of issue of this report: 06/06/2024

Page 175

7. Modelling of in-situ experiments

7.1. ALC1605

7.1.1. Presentation of the ALC1605 in-situ experiment

As last step of the HITEC modelling benchmark, Andra proposed to model the ongoing ALC1605 in-situ heating experiment. The experiment is a full-scale representation of a single high-level waste (HLW) cell in the Callovo-Oxfordian (Cox) claystone. Here, we refer to a HLW cell as a sub-horizontal steel-cased micro-tunnel in which the wastes will be emplaced. Reference is made to the initial SotA (Villar et al., 2020, chapter 2.1) for a description of the French concept for the disposal of the HLW.

The general objective of the ALC1605 experiment is to study the behaviour of a 2015 concept HLW cell (with filled annulus between the steel casing and the clay host rock) under thermal load. The detailed objectives of the experiment are to:

- Study the impact of a thermal load on the TM behaviour of the liner when the annulus is filled with an MREA (*Materiau de remplissage de l'Extrados des Alvéoles*) cement. The MREA is injected in the annulus to reduce the corrosion rate of the casing by: (i) neutralising the acidic drainage produced by pyrite oxidation, (ii) reducing the amount of oxygen coming from the drift

- Study the impact of a thermal load on the THM behaviour of the Cox claystone in the near-field (but beyond the EDZ) and in the far-field (beyond a few cell diameters) with a filled annulus. The temperature and pressure evolution are monitored around the cell and at different offset from the drift. A comparison with the measurements made during the previous ALC1604 experiment will help identify a potential impact of the filling material on the kinetics and the amplitude of the thermal pressuring in the near-field, and possibly the far-field.

This exercise focused on the second objective and was divided into two phases. Step 3a consisted in a predictive modelling of the ALC1605 experiment, using for the rock mass parameters the reference values provided from step 1 and step 2, or from previous work done on the ALC1604 experiment. The discrepancies between the results of the different models obtained for this prediction were analyzed. Step3b consisted in an interpretative modelling of the ALC experiment. At this time the teams had the in-situ measurements from the experiment and the models were improved from step3a if necessary. The head part and the steel insert of a HLW cell are not reproduced in this experiment. The ability of the insert to absorb the eventual axial thermal dilation of the casing was evaluated in the ALC1604 experiment.

The ALC1605 experiment is located in the CMHM underground lab. It was drilled from the GAN drift (Figure 7.1) with a slight upwards inclination and is oriented parallel to σ_H (N155°).
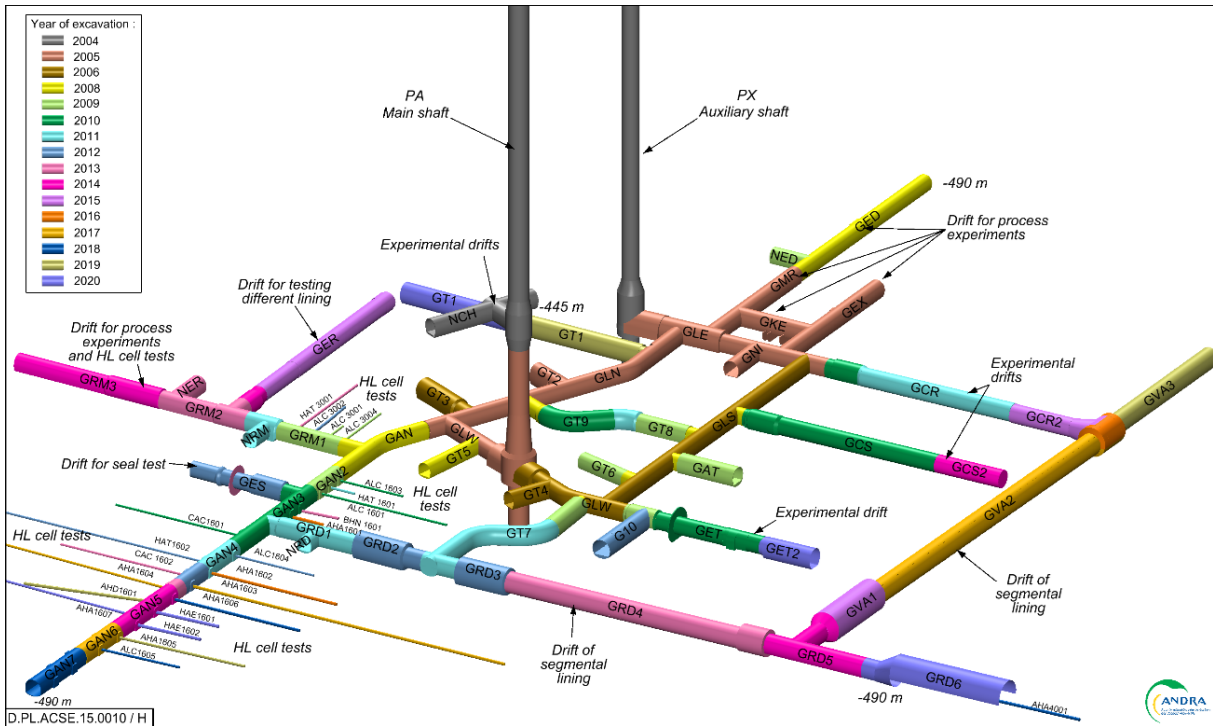
Figure 7.1: Location of the ALC1605 experiment in the GAN6 drift

7.1.1.1. Description of the ALC1605 micro-tunnel

The micro-tunnel (Figure 7.2) was drilled with the following sequences:

- Drill the micro-tunnel;

- Pull out of hole with the boring machine, the front shield is left in place at the end of the micro-tunnel;

- Run in hole with the 30" casing;

- Inject MREA into the annulus.
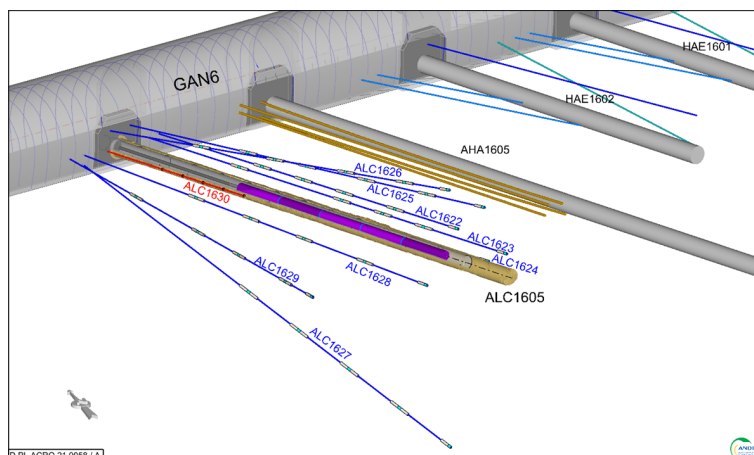
Figure 7.2: 3D schematic of the ALC1605 cell with peripheral boreholes

The characteristics of the casing are:

EURAD (Deliverable n˚ 7.6) – Modelling report on the effect of temperature on clay host rocks behaviour
Dissemination level: PU
Date of issue of this report: 06/06/2024

Page 177

- API 5L X65 « sour service » steel;

- Outer diameter: 762 mm;

- Thickness : 25,4 mm ;

- The casing joints are fit together, the connections are tight for an external water pressure of 10 bar;

- Length of the casing elements: 2 m.

The casing is centralised in the micro-tunnel (Figure 7.3, left), as per the recent evolution of the reference concept. Centralisers are installed to ensure a minimal thickness of MREA over the whole circumference and avoid any direct contact between the casing and the formation. These centralisers are not continuous and are not included in all the casing elements (Figure 7.3, right).
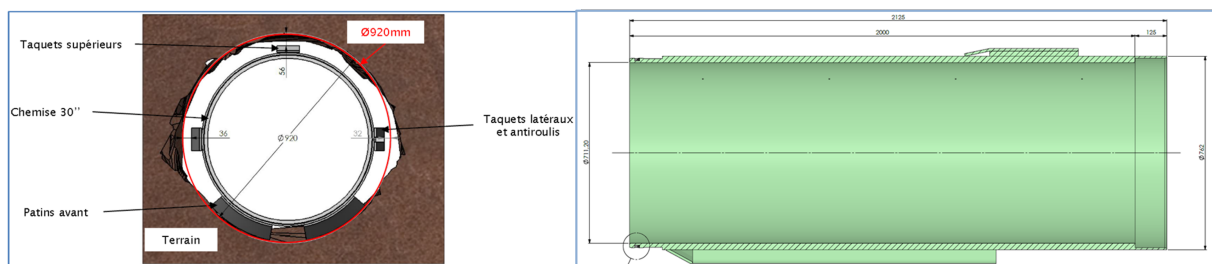
Figure 7.3: Cross-section of the ALC1605 cell and longitudinal section of a casing element with centralisers

The micro-tunnel has the following characteristics:

- diameter : 920 mm (160 mm annular space) ;

- 25.5 m usable length corresponding to the distance between the drift and the plate welded half way in the head joint, total excavation depth: 28.5 m ;

- inclination : 2% upward, tolerance ± 1 % everywhere in the micro-tunnel (no counterslope):

- azimuth: axis of the cell N335° (// σ_H), tolerance ± 1 % of the length everywhere in the micro-tunnel.

The heated section is located between 10 and 25 m and is made up of five heating elements. Each element is 3 meters long and has an outer diameter of 559 mm. Figure 7.4 shows the exact location of the heating elements in the cell
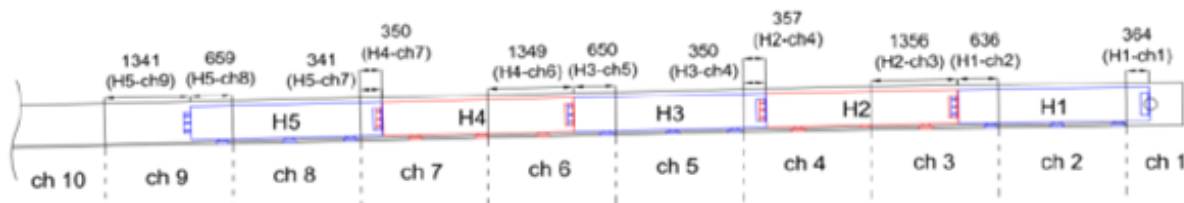
Figure 7.4: Location of the heating elements in the cell

Peripheral instrumentation The peripheral instrumentation aimed at measuring the THM impact of heating on the host rock comprises eight boreholes equipped with a multipacker system and drilled from the GAN drift (Figure 7.5 and Figure 7.6). It supplements the characterisation achieved in ALC1604 and provide pore pressure and temperature measurements in the near-field and in the semi-far field:

EURAD (Deliverable n˚ 7.6) – Modelling report on the effect of temperature on clay host rocks behaviour
Dissemination level: PU
Date of issue of this report: 06/06/2024

Page 178

- 3 boreholes, diverging from the cell in a vertical plane with 5 measuring chambers and at least three of them in the heated zone ;

- 4 boreholes in an horizontal plane on each side of the cell (2 of them diverging and 2 parallel to the cell) with 5 measuring chambers and at least three of them in the heated zone ;

- 1 borehole parallel to the cell in a horizontal plane with 3 measuring chambers

These boreholes also help monitor the evolution of permeability in the formation and detect potential thermal damage.

A last borehole called ALC1630, with five temperature sensors, was drilled parallel to the ALC1605 cell.
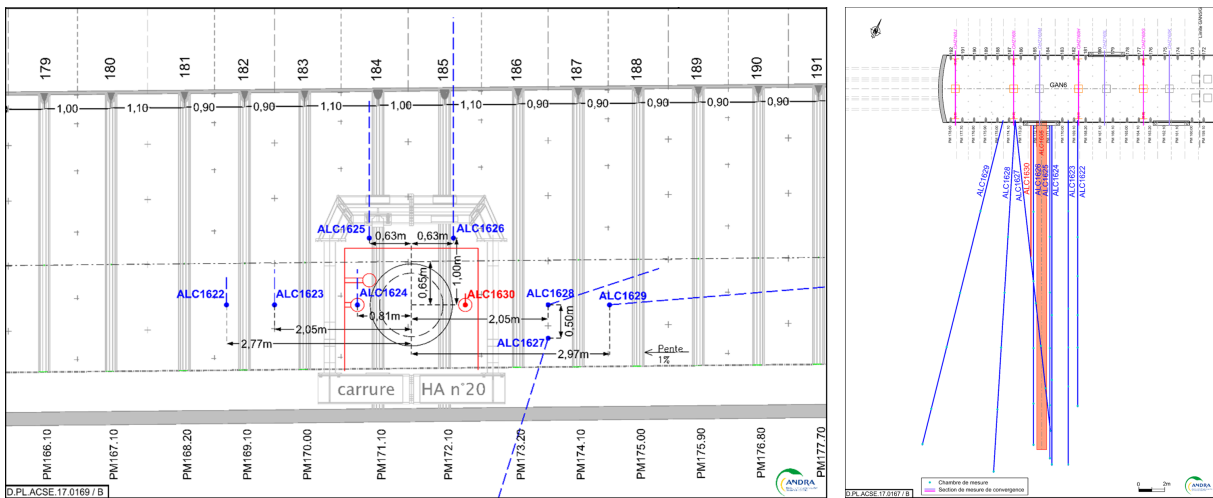
Figure 7.5: Front and top view of the monitoring boreholes around the ALC1605 cell
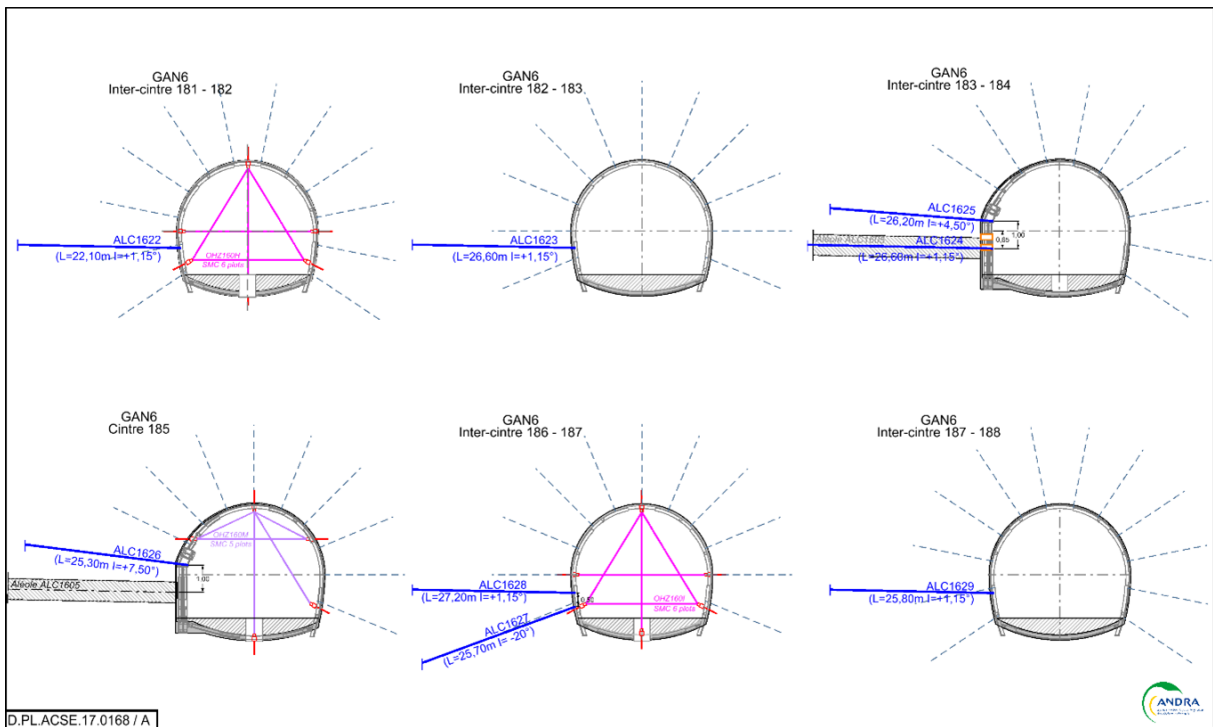
Figure 7.6: Side view of the monitoring boreholes around the ALC1605 cell

EURAD (Deliverable n° 7.6) – Modelling report on the effect of temperature on clay host rocks behaviour
Dissemination level: PU
Date of issue of this report: 06/06/2024

Page 179

Timeline of the ALC1605 experiment   The sequence of events related to the experiment, starting from the excavation of section 5 of the GAN drift, is detailed in Table 7.1. All the pressure monitoring boreholes were drilled and completed by the end of 2017 / beginning 2018 to let the pressure increase and stabilise before heating started. The drilling dates for the ALC1605 cell are given, as those for the neighbouring AHA1605 (22.65 m long) and HAE1602 (81.95 m long) cells. These two 920 mm diameter micro-tunnels were drilled and completed with the same design as ALC1605: they have the same 2% upward slope, are cased and the annulus is filled with MREA. Four monitoring boreholes were drilled parallel to the AHA1605 cell and filled with a cement and bentonite mixture. These boreholes will not be taken into account here.

Table 7.1: Sequence of events for the ALC1605 experiment

Events	Start	End	Comments
GAN5	09/12/2013	23/04/2014	Between 125 and 159.1 m
GAN6	12/07/2017	21/09/2017	Between 159.1 m and 178.6 m.
			The ALC1605 axis meets the GAN axis at 171.613 m
GAN7	10/04/2018	19/06/2018	Between 178.6 m and 203.75 m
Drilling of monitoring boreholes	11/12/2017	17/01/2018	ALC1622 to ALC1629 boreholes
ALC1605 drilling	14/11/2018	15/11/2018	
Injection of MREA	26/11/2018	26/11/2018	
Drilling of ALC1630	28/05/2019	29/05/2019	
Drilling of AHA1605	01/07/2019	04/07/2019	
Heating test (low power)	25/02/2020	12/03/2020	Heating test at 33 W/m
Main heating stage	08/06/2020	-	Heating in one step at 220 W/m
Drilling of HAE1602 cell	28/09/2020	29/09/2020	
Setting the head plate	24/02/2021	24/02/2021	Set a closing plate at cell head to reduce convection phenomena

The heating is applied continuously over 15 m, between 10 and 25 m from the drift wall. The heating history from ALC1604 experiment was replicated to help comparing the two concepts (with and without filled annulus): a heating test at low power (33 W/m) was first conducted, starting on May 28th, 2020. The main heating stage (220 W/m) started on June 8th 2020 and is currently ongoing. A steel plate was installed at the head of ALC1605 on February 24th, 2021 in order to reduce the thermal convection inside the casing towards the access drift. (Figure 7.7).

Figure 7.7: Closing plate at the head of the ALC1605 cell

During the main heating stage, the recording of the thermal power evolution was occasionally interrupted because of some issues with the data acquisition system, the longest period being between September 27th and October 1st, 2021. The temperature in the rock was not impacted by these events.

EURAD (Deliverable n° 7.6) – Modelling report on the effect of temperature on clay host rocks behaviour
Dissemination level: PU
Date of issue of this report: 06/06/2024

Page 180

7.1.1.2. Modelling of the ALC1605 experiment

Geometry of the model The teams are required to propose a two- or tri-dimensional realistic THM numerical model that takes into account the experimental set-up of the ALC experiment. The models should include the GAN drift (radius = 2.6 m) and the ALC1605 cell. The neighbouring cells AHA1605 and HAE1602 will require a sensitivity analysis to evaluate their impact in the experiment due to their relative proximity. The x-axis is parallel to the longitudinal direction of the cell, and the y-axis is parallel to the longitudinal direction of the GAN drift. The origin of the local system is the 0 metric point of ALC1605 cell, located on the front face of the cell flange, at 171.613 m on the theoretical axis of the GAN drift. It is worth mentioning that the drift wall and the head of ALC1605 may not coincide since the micro-tunnel is not directly excavated from the drift wall but from a concrete structure as illustrated in Figure 7.2. The coordinates of the end of the micro-tunnel are thus (-28.76, 0.01, 0.61), and the end of the cased section is at (-25.40, 0.00, 0.54). For the 3D case, the proposed geometry for the ALC1605 model is shown on Figure 7.8. The model will represent only half of the GAN drift, extend to 60 m in the x direction and 50 m in the y and z directions. This geometry is considered large enough regarding the diameter of the ALC1605 cell (each boundary is located beyond 30 diameters of the cell).
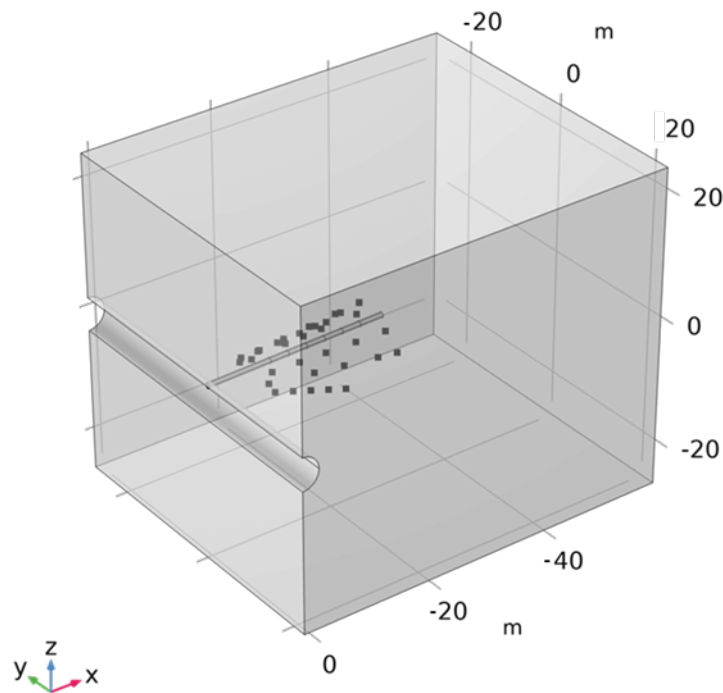
Figure 7.8: Proposed geometry for the ALC1605 3D model (neighbouring cells missing)

The 2D model is a transversal section located at the mid-plane of the heated zone, the centre of the cell is at (-17.26, 0.01, 0.36) in the local coordinate system. It should extend over 50m in the y and z directions (see Figure 7.9).

EURAD (Deliverable n˚ 7.6) – Modelling report on the effect of temperature on clay host rocks behaviour
Dissemination level: PU
Date of issue of this report: 06/06/2024

Page 181
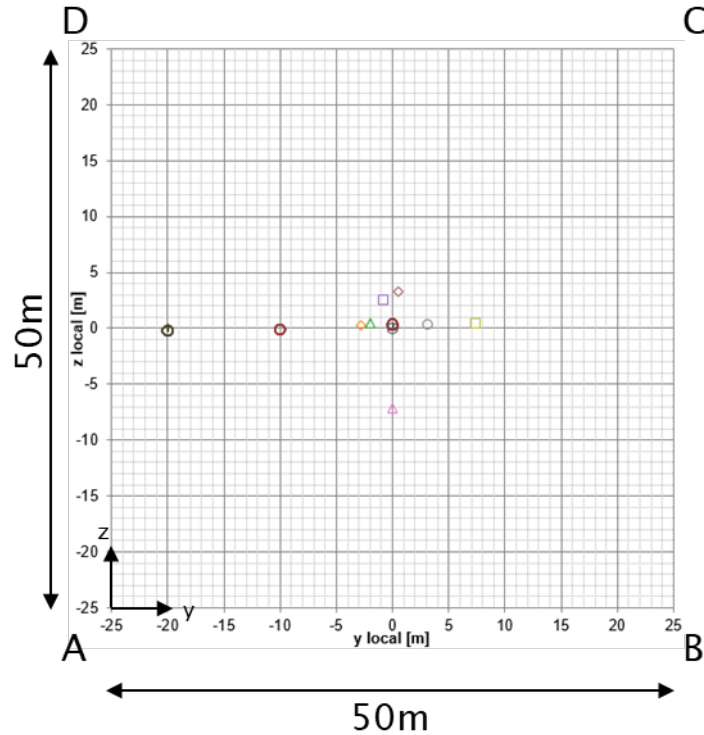
Figure 7.9: 2D model extent

THM parameters For step 3a (predictive modelling), the teams will use the Cox parameters given for the elastic anisotropic generic case (Table 2.6).

The casing is made of API 5L X65 « sour service » steel with the following properties:

- E = 210 000 MPa

- ν = 0.3

- λ = 54 W/m/K (at 20 °C)

- ρ = 7850 kg/m^3

- C_p = 480 J/kg/K (at 20 °C)

- α = 1e-5 1/K

Annular space: The thermal properties of the MREA filling under different conditions are given in Table 7.2.

EURAD (Deliverable n˚ 7.6) – Modelling report on the effect of temperature on clay host rocks behaviour
Dissemination level: PU
Date of issue of this report: 06/06/2024

Page 182

Table 7.2: Thermal Properties of MREA

Condition	Thermal Conductivity (λ) [mW/m/K]	Density (ρ) [kg/m^3]	Specific Heat Capacity (C$_p$) [J/g/K]
Water at 20 ℃	595	1142	2.64
Water at 50 ℃	730	1154	2.67
Water at 80 ℃	890	1160	2.56
Air at 20 ℃, 70% RH	89	375	1.01
Air at 50 ℃, 70% RH	81	369	1.46
Air at 80 ℃, 70% RH	77	358	1.80
Drying 50 ℃	73	357	0.98
Drying 80 ℃	70	338	1.29

In order to determine its mechanical properties, MREA samples (5.5 cm diameter and 8-11 cm height) were cast and stored in their mold (endogenous) or under water at different temperatures and tested after 6 to 12 months. The results are shown in Table 7.3. A similar behaviour is observed at 20 and 50 ℃, but mechanical properties are significantly improved at 80 ℃, most likely due to a complete hydration of the cement.

Table 7.3: Evolution of MREA mechanical properties with time

State	Setting time [days]	Temp [℃]	Rc [MPa]	E [MPa]
	7		0.14	29
	104	25	0.49	37
	180		0.55	47.5
	285		0.67	60
Endogenous	180	50	0.79	63.5
	368		0.83	58.5
	180	80	1.46	89
	368		1.71	93.5
	104		0.47	37.5
	180	25	0.58	52
	285		0.60	52
Under water	180	50	0.67	42
	360		0.70	42
	180	80	1.00	72.5
	360		1.00	67.5

Other samples were stored for 4 years at room temperature and then heated to 50 or 80 ℃. At 20 and 50 ℃, the strength and Young modulus are very similar: Rc=0.78 $\pm$ 0.04 MPa and E=122 $\pm$ 2 MPa. On the other hand at 80 ℃, much higher values were obtained, Rc=1.12 MPa and E=189 MPa at 80 ℃. It confirms that the setting process is triggered by temperature.

Because of its formulation with 75 % water in mass, fresh MREA has a very high porosity (86-87 % at 20 ℃, dropping to 82-83 % after setting at 80 ℃) and is very permeable, in the order of 10^{-15}m^2. It is however very compressible. When loaded at 8 MPa, the total volume of the samples is reduced by 45 to 55%, and the pore volume of a dried sample is divided by 6 (Figure 7.10). The water permeability is then reduced to 10^{-18}m^2 (Figure 7.11).

EURAD (Deliverable n˚ 7.6) – Modelling report on the effect of temperature on clay host rocks behaviour
Dissemination level: PU
Date of issue of this report: 06/06/2024

Page 183
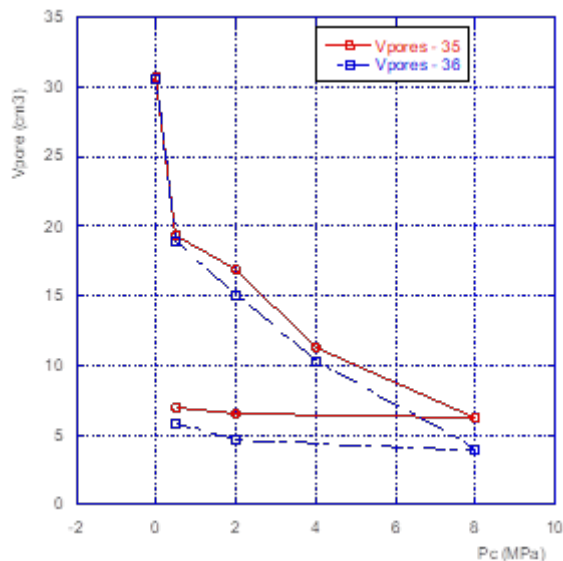
Figure 7.10: Evolution of pore volume under hydrostatic loading
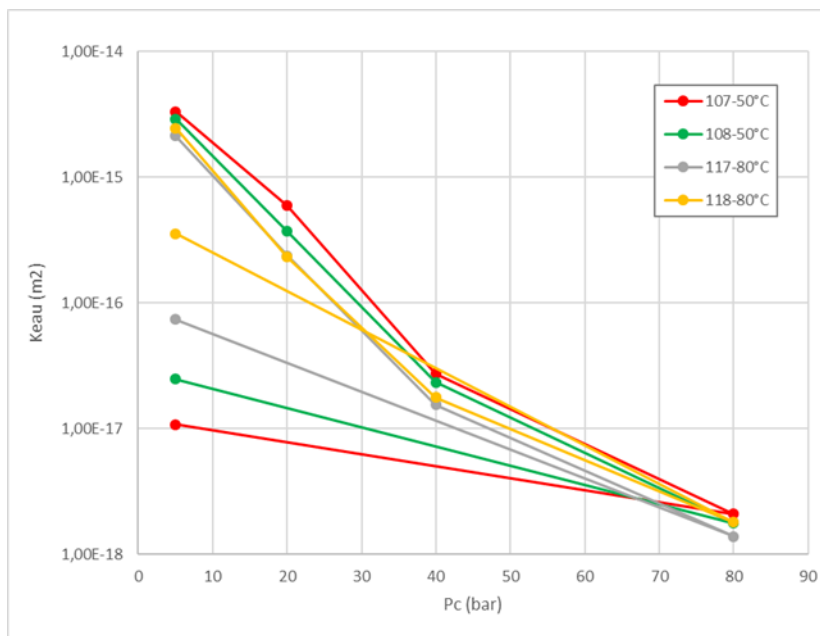
Figure 7.11: Evolution of water permeability as a function of confining pressure and temperature

Boundary conditions

3D case: The different THM boundary conditions for the 3D model are summarised in Table 7.4 below (the front face being along the GAN drift, on the left-hand side on Figure 7.8, and looking towards the end of the cell).

EURAD (Deliverable n° 7.6) – Modelling report on the effect of temperature on clay host rocks behaviour
Dissemination level: PU
Date of issue of this report: 06/06/2024

Page 184

Table 7.4: THM boundary conditions for the ALC1605 experiment modelling (3D case)

Boundary	Thermal condition	Hydraulic condition	Mechanical condition
Left and front faces	No heat flux	No water flux	No normal displacements
Right face	No heat flux	No water flux	Minimum horizontal stress σ_h = 12.4 MPa
Back face	No heat flux	No water flux	Maximum horizontal stress σ_H = 16.0 MPa
Top (depth = 465 m, z = 25 m)	In situ temperature T = 21 °C	4.7 MPa	Vertical geostatic stress σ_v = 12.1 MPa *
Bottom (depth = 515 m, z = -25 m)	In situ temperature T = 23 °C	4.7 MPa	No normal displacements No normal displacements
GAN drift wall	Temperature meas. in the GAN drift	Draining condition atmospheric pressure	Radial stress of 0.3 MPa (shotcrete lining)
AHA1605 and HAE1602 cells	No heat flux	Draining condition: No water flux**	No normal displacements No normal displacements

* Calculated from the vertical stress Sv at 490 m that is estimated at 12.7 MPa, and a bulk density of 2.386 g/cc. SH and Sh are assumed constant over the considered interval.
** As a first approximation

2D case: The boundary conditions for the 2D case are described in Table 7.5 and Figure 7.9.

Table 7.5: THM boundary conditions for the ALC1605 experiment modelling (2D case)

Boundary	Thermal condition	Hydraulic condition	Mechanical condition
Left face (AD)	No heat flux	No water flux	No normal displacements
Right face (BC)	No heat flux	No water flux	Minimum horizontal stress σ_h = 12.4 MPa
Top (DC) (depth = 465 m)	In situ temperature T = 21 °C	4.7 MPa	Vertical geostatic stress σ_v = 12.1 MPa *
Bottom (AB) (depth = 515 m)	In situ temperature T = 23 °C	4.7 MPa	No normal displacements

* Calculated from the vertical stress Sv at 490 m that is estimated at 12.7 MPa, and a bulk density of 2.386 g/cc. SH and Sh are assumed constant over the considered interval.

All the monitoring boreholes can be considered watertight but the neighbouring cells (AHA1605 and HAE1602) may be draining. They may be modelled in two ways:

- Equivalent porous medium inside the cell (permeability to be calibrated by the teams)

- Modelling of the cemented casing

A sensitivity analysis may be performed with or without these cells to check their influence on the pore pressure evolution.

Boundary conditions for ALC1605 The teams may adapt the boundary conditions around the ALC1605 cell depending on the level of detail of their model (modelling of the MREA, casing, heating elements . . .). The initial pressure field around the ALC cell is mainly controlled by its excavation and the presence of the GAN drift. An accurate and detailed HM modelling of the drift's excavations can however represent a time-consuming task. For the modelling purposes, it can be assumed for this step that the pressure and stress field is not so much affected by the presence of the damaged zone around GAN given that the heating part of the cell is located far from the drift wall (10-25m). A simplification may consist in reproducing the hydraulic gradient towards the GAN by approximating the pressure profile given in Figure 7.12.

EURAD (Deliverable n˚ 7.6) – Modelling report on the effect of temperature on clay host rocks behaviour
Dissemination level: PU
Date of issue of this report: 06/06/2024

Page 185
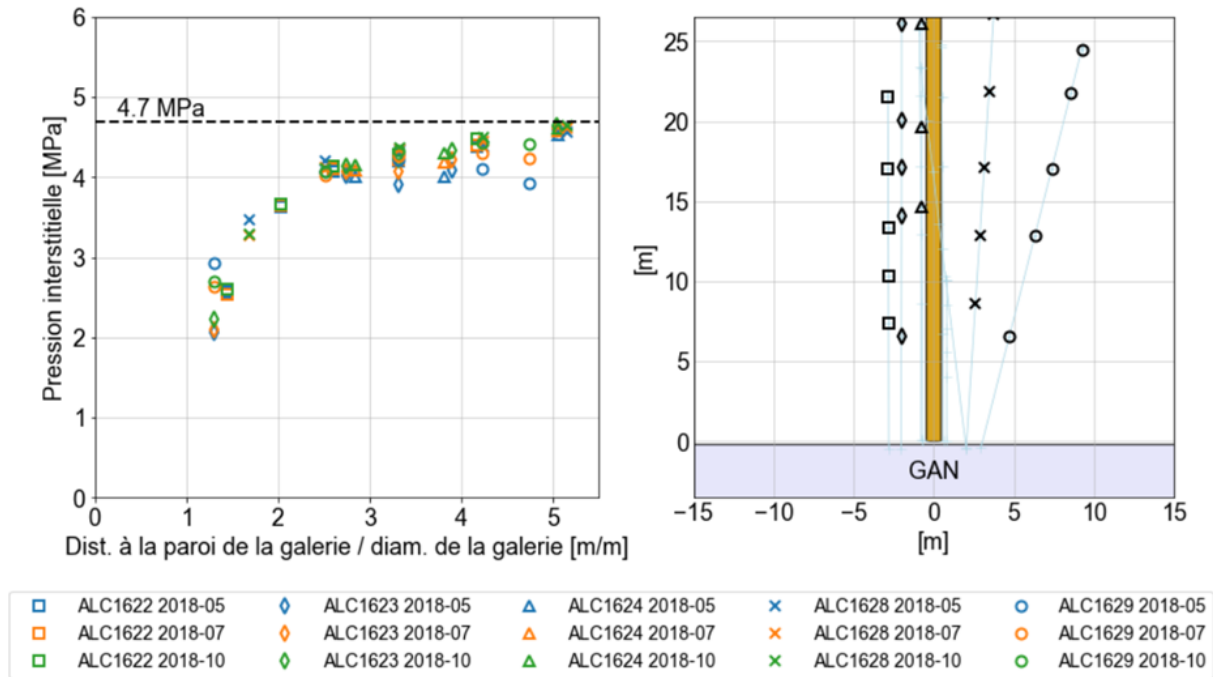
Figure 7.12: Pore pressure profile around the GAN drift before the excavation of ALC1605

On the other hand, the excavation of the ALC1605 cell should be modelled properly as the pressure measurements in the monitoring boreholes clearly show the anisotropic behaviour of the Cox claystone. In the horizontal plane and parallel to bedding (Figure 7.13, left), the excavation of ALC1605 cell in November 2018 resulted in an increase in pore pressure, whereas it triggered a pore pressure drop in the vertical direction (Figure 7.13, right). This anisotropic response was already described in the ALC1604 experiment (Bumbieler et al., 2020).
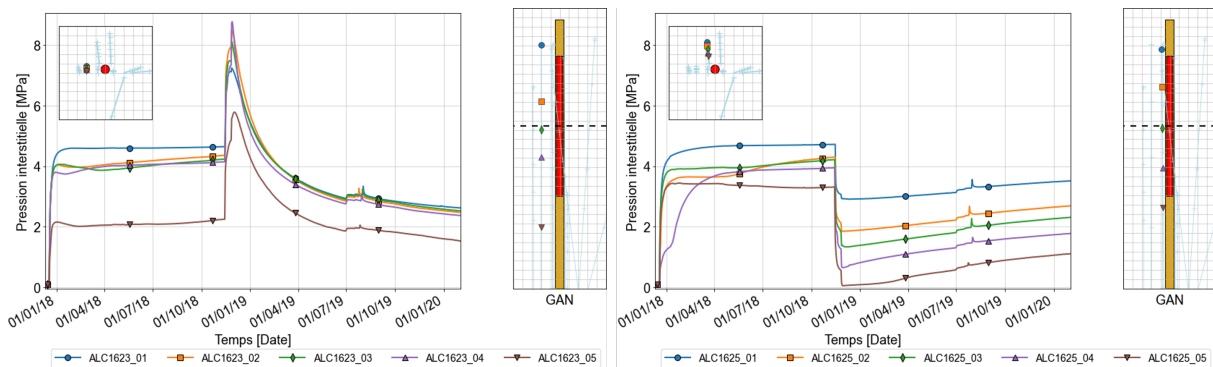
Figure 7.13: Pore pressure change caused by the excavation of ALC1605, parallel to bedding (left) and perpendicular to bedding (right).

A draining condition (atmospheric pressure) must be considered at the wall. As in previous in situ experiments, a correction factor of 95 % was applied to account for power losses.

7.1.2. ANDRA

7.1.2.1. Modelling concept

Based on previous experience modelling the TED and ALC1604 in-situ heating experiments (Seyedi et al., 2017), (Plúa et al., 2021), Andra used a thermo-poro-elastic approach accounting for transversely isotropic

EURAD (Deliverable n˚ 7.6) – Modelling report on the effect of temperature on clay host rocks behaviour
Dissemination level: PU
Date of issue of this report: 06/06/2024

Page 186

behaviour. A 3D mesh with approximately 100,000 second-order finite elements was built in Comsol. The total number of degrees of freedom was 700,000.

As per the specifications, the model domain was 60 m long in the axial direction of the ALC1605 micro-tunnel with a cross-sectional section of 50 m x 50 m (Figure 7.14).
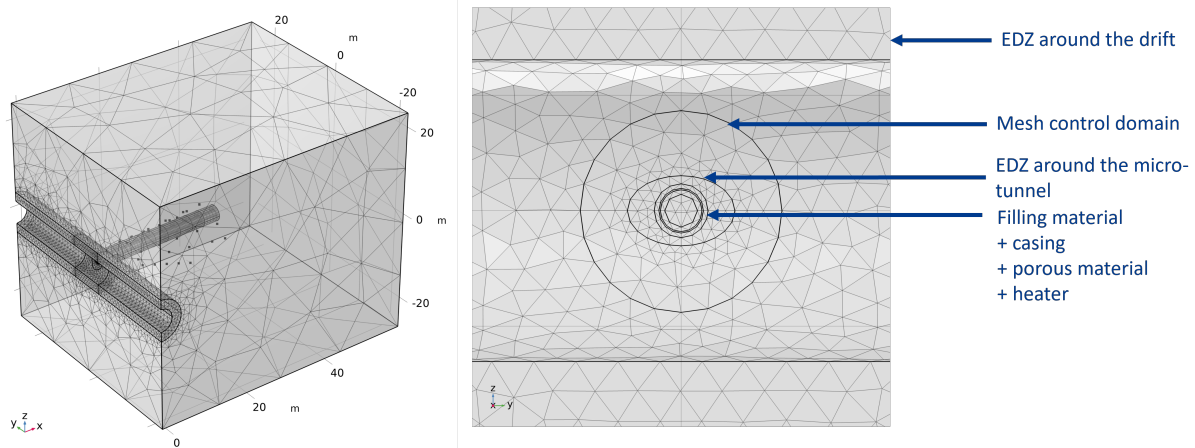
Figure 7.14: Andra model for ALC1605 experiment and zoom from the front of the HLW cell

The model domain considered the ALC1605 micro-tunnel, the GAN drift and their respective EDZ. The extension of the EDZ around the micro-tunnel was based on observations in the MHM URL (Armand et al., 2014). The EDZ was represented by an ellipse with minor and major axes equal to 2.0 and 1.3 times the micro-tunnel radius, respectively. On the contrary, the EDZ around the GAN drift was represented in a simpler manner with a cylinder with a radius 1.8 larger than the GAN drift radius.

The ALC1605 cell considered the annular gap filled with MREA, the casing, and the outer heater's surface, represented by a hollow cylinder of 559 mm. The volume space between the casing and the heater was modelled as a rigid porous medium. The rigid medium had a high conductivity with the following characteristics:

- $E_{poro} = 5 \times E_v$

- $k_{poro} = 10^3 \times k_v$

- $\lambda_{poro} = 10^2 \times \lambda_v$

The heat power is applied on the outer heater's surface. Based on the modelling of the previous ALC1604 experiment (Bumbieler et al., 2020), Andra applied a reduction of 10% of the total heat power.

7.1.2.2. Predictive modelling

Compared to the parameters used in the near-field benchmark, the following values were used:

EURAD (Deliverable n˚ 7.6) – Modelling report on the effect of temperature on clay host rocks behaviour
Dissemination level: PU
Date of issue of this report: 06/06/2024

Page 187

Table 7.6: Specific Cox and EDZ properties used in this simulation.

Parameter	Value
Cox	
Young's modulus E_v	6.0 GPa
Anisotropy	$E_h = 1.5E_v$
Vertical permeability k_v	$1e - 20m^2$
Anisotropy	$k_h = 3k_v$
EDZ	
E_{EDZ}	6.0 GPa
k_{EDZ}	$1e - 17m^2$

The simulation consisted in three stages: GAN drift excavation, ALC1605 micro-tunnel excavation, and heating test. The heating test at low power was not considered. Both excavations were assumed to be instantaneous, followed by a waiting phase of 5 years in the case of the drift and 550 days in the case of the micro-tunnel. Figure 7.15 shows the pore pressure field at the end of the waiting phase of the GAN drift excavation and the pore pressure profile around the drift. The latter is compared against the measurements recorded before the ALC1605 micro-tunnel excavation. The numerical results show a slight over-prediction of pore pressure of less than 0.5 MPa.
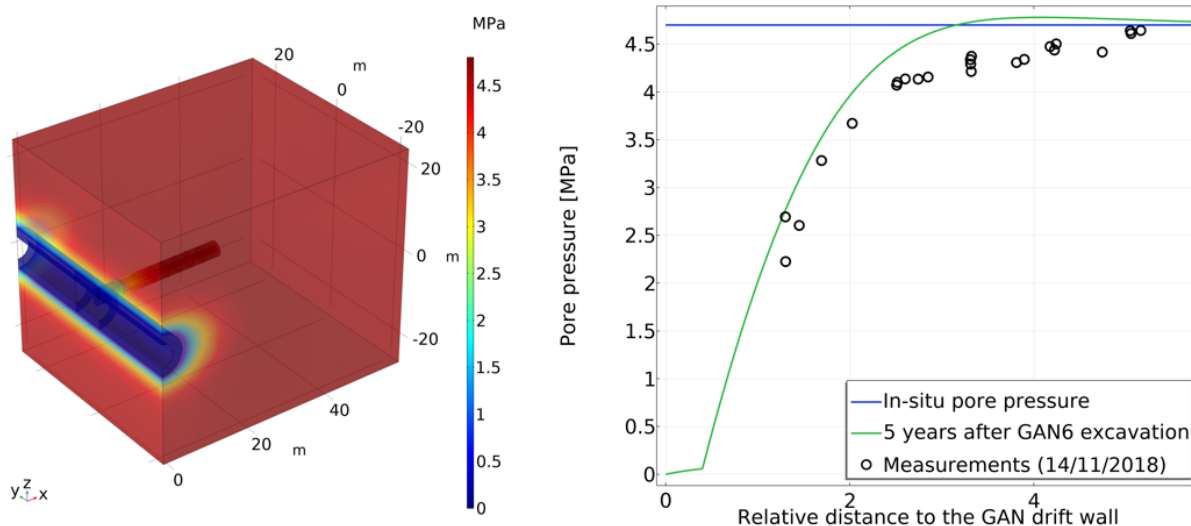
Figure 7.15: Simulated pore pressure before the beginning of the ALC1605 micro-tunnel excavation. (Left) Pore pressure field. (Right) Pore pressure profile.

Temperature is consistently reproduced in both directions of anisotropy. On the other hand, the modelled anisotropic pore pressure response has discrepancies with measurements during the excavation and this influences the thermal pressurisation results (Figure 7.16).

EURAD (Deliverable n˚ 7.6) – Modelling report on the effect of temperature on clay host rocks behaviour
Dissemination level: PU
Date of issue of this report: 06/06/2024

Page 188
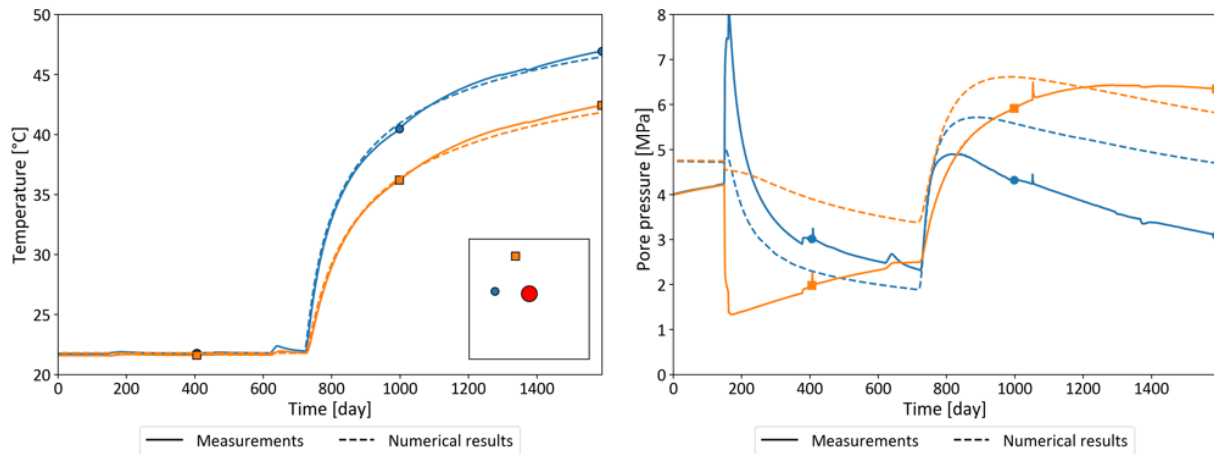
Figure 7.16: Predictive modelling - temperature and pore pressure prediction vs. measurements

7.1.2.3. Interpretative modelling

In order to get a better match with the actual data, a parameter analysis on the Young's modulus and permeability was carried out. The following parameters were changed:

Table 7.7: Specific Cox and EDZ properties used in the interpretative modelling phase

Parameter	Value
Cox	
Young's modulus E_v	4.0 GPa
Anisotropy	$E_h = 2.0E_v$
Vertical permeability k_v	$7e-21m^2$
Anisotropy	$k_h = 3k_v$
EDZ	
E_{EDZ}	3.0 GPa
k_{EDZ}	$5e-17m^2$

On the one hand, the major changes consisted in increasing the anisotropy ratio of the Young's modulus to improve the anisotropic response during the excavation phase of the micro-tunnel. On the other hand, the permeability was reduced to delay the pore pressure dissipation in the vertical direction as observed in the measurements. The second modification implied a longer waiting phase after the GAN drift excavation: from 5 years to 8 years. This longer waiting phase was chosen to match the pore pressure measurements before the micro-tunnel excavation, as shown in Figure 7.16.

The model matches well the temperature evolution in both directions since no changes were made. The modelling of the excavation consisted in removing the elements within the micro-tunnel and the EDZ to improve the anisotropic pore pressure response. The numerical results match better the thermally-induced pore pressure response in the horizontal direction. However, the pore pressure in the vertical direction dissipates faster than the measurements. This discrepancy is related to the kinetics induced by the excavation leading to a recovery phase in the vertical direction that the model is not capable to reproduce. (Figure 7.17).

EURAD (Deliverable n˚ 7.6) – Modelling report on the effect of temperature on clay host rocks behaviour
Dissemination level: PU
Date of issue of this report: 06/06/2024

Page 189
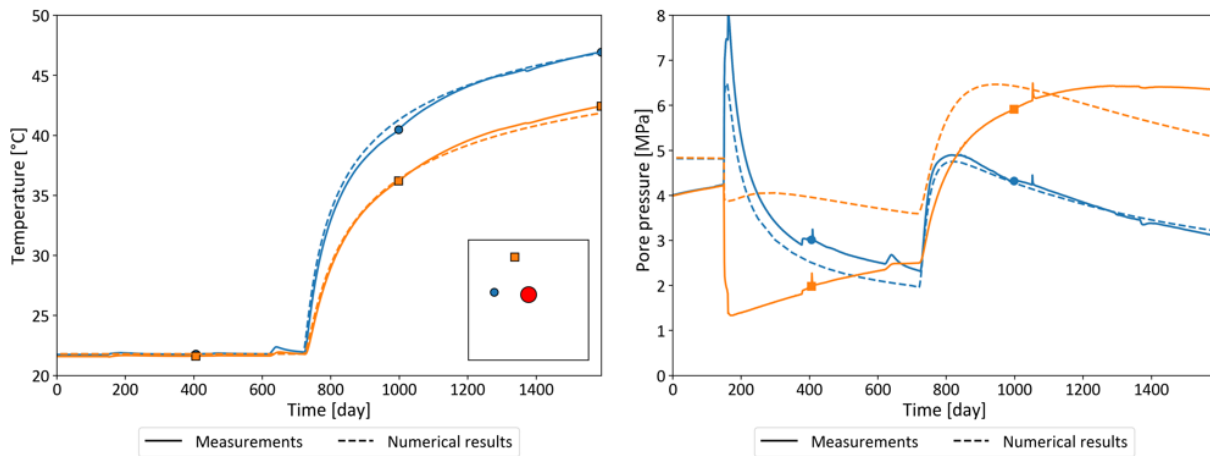
Figure 7.17: Interpretative modelling - temperature and pore pressure prediction vs. measurements

Similar results can be observed for the rest of study points located at the mid-plane of the ALC1605 micro-tunnel (Figure 7.18). The temperature is well reproduced in all study points, while pore pressure shows a similar response in those sensors in the direction parallel to the bedding: ALC1622_02 and ALC1628_03. Sensor ALC1629_03 is also located in the horizontal direction, but it is not well reproduced as it dissipates faster in the model. This could be explained by the fact that the GAN7 is not explicitly reproduced in the model. Consequently, the overpressure generated during its excavation is not taken into account in the numerical results.
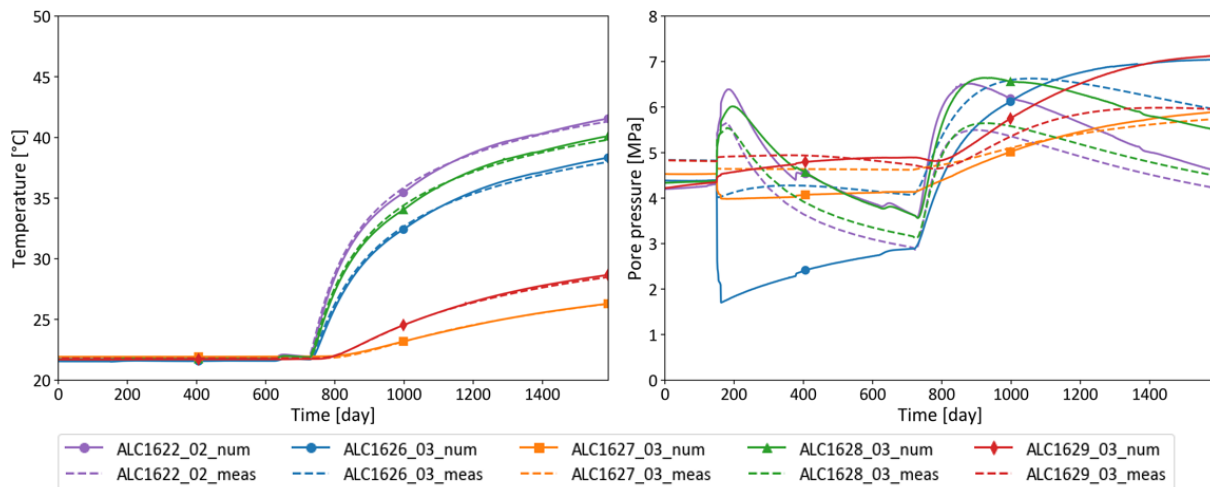
Figure 7.18: Temperature and pore pressure prediction vs. measurements at the mid plane

The anisotropy response during the excavation plays an important role on the heating test. Additional work must be done to better reproduce the pore pressure in the direction perpendicular to the bedding. Nevertheless, the thermo-poro-elastic approach can reasonably well reproduce the THM response of the Cox.

7.1.3. BGE

7.1.3.1. Modelling concept

BGE undertook the modelling of the ALC1605 in-situ heating experiment using a three-dimensional approach to achieve a very detailed representation of the actual experiment. The devised 3D model meticulously accounts for all materials placed in the borehole. Specifically, it encompasses the host rock for-

EURAD (Deliverable n˚ 7.6) – Modelling report on the effect of temperature on clay host rocks behaviour
Dissemination level: PU
Date of issue of this report: 06/06/2024

Page 190

mation, within which the access drift, termed the GAN drift, is excavated. Branching from the GAN drift is the ALC1605 borehole, whose inclination is faithfully represented in the model. Inside this borehole, the model includes a steel casing surrounded by MREA cement injection. Steel heaters are situated within the casing, and any remaining void in the borehole is also treated as a distinct material. Importantly, the model employs the exact coordinate system used in the experimental design, ensuring consistency in numerical modelling. As a result, the in-situ sensor positions in the host rock match those in the model, as depicted in Figure 7.19.
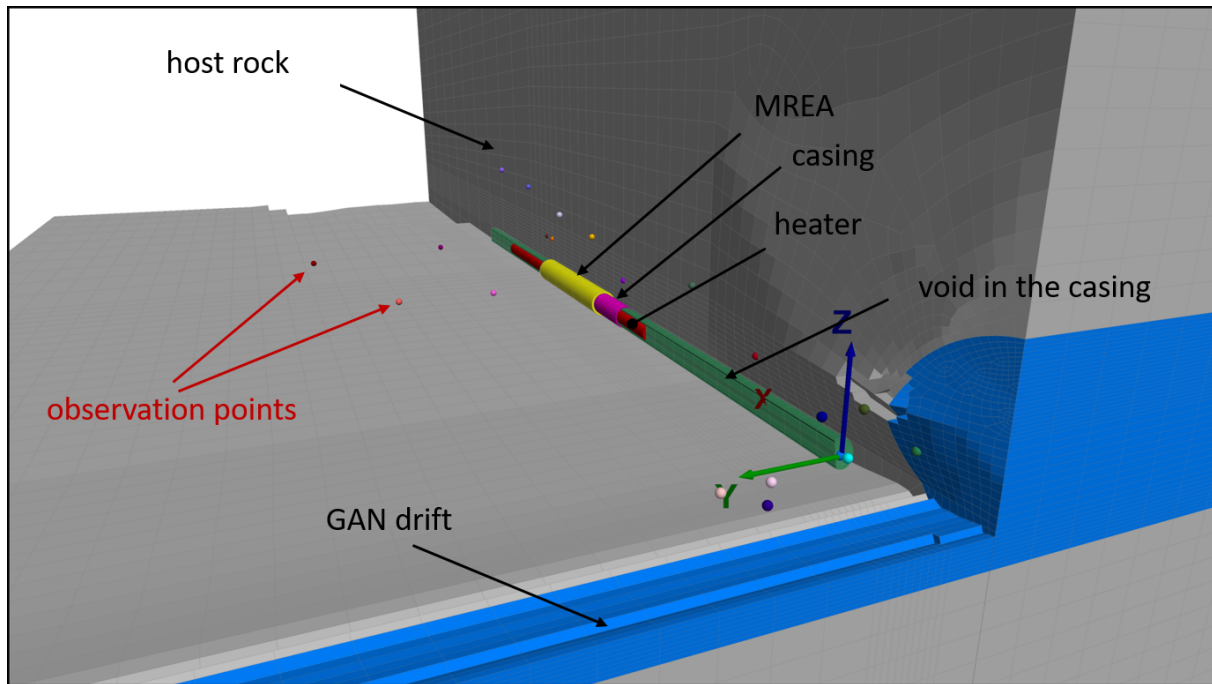
Figure 7.19: Numerical model for the simulation of the ALC1605 experiment by BGE

The numerical model is comprised of 195,545 linear hexahedral elements and 205,984 nodes. To accurately capture the thin materials, such as the 5 cm-thick casing, the mesh is finely detailed within the ALC1605 borehole. The analytical domain spans 60 m in the x-direction, 50 m in both y and z directions.

Initial conditions for the numerical model stipulated an anisotropic total stress state: 12.4 MPa as the minimum horizontal stress in the x-direction, 16 MPa as the maximum horizontal stress in the y-direction, and 12.1 MPa for the vertical lithostatic stress in the z-direction. Zero normal displacements were set for all model faces.

An initial liquid pressure, gauged at 4.7 MPa at the underground research laboratory's depth, was assigned both as an initial condition throughout the domain and as a boundary condition at the top, bottom, and rear boundaries. The front boundary corresponds with the vertical symmetry of the GAN drift. The model's remaining three boundaries function as symmetry planes, where zero fluxes are dictated.

Thermal conditions begin at 21 °C at the model's top and increase linearly to 23 °C at its base. All boundaries maintain thermal adiabatic conditions. The boundaries of the model are far enough so that no thermal reflection due to the adiabatic conditions are expected during the simulation period of few years. Simulations were executed using OpenGeoSys (Wang et al., 2021a,b).

The entire chronology of the ALC1605 experiment, from the commencement of the GAN drift excavation to the onset of heating, has been incorporated into the numerical simulation. Excavation of the GAN drift was carried out in three stages between December 2013 and June 2018, which included the creation of

EURAD (Deliverable n° 7.6) – Modelling report on the effect of temperature on clay host rocks behaviour
Dissemination level: PU
Date of issue of this report: 06/06/2024

Page 191

drift parts GAN5, GAN6, and GAN7. Notably, periods of several years elapsed between each excavation phase. The drilling of the ALC1605 borehole was completed on November 14-15, 2018, swiftly followed by the injection of the MREA cement later that month. A preliminary heating phase commenced in early 2020, operating at a reduced heat power of 33 W/m. By June 2020, the primary heating phase was underway with a power output of 200 W/m, as illustrated in Figure 7.20.

To ensure an accurate representation of the experiment's history, we utilized a novel excavation function within OpenGeoSys, designed to replicate the procedures of a mechanized tunnelling. This feature enables precise modelling of the excavation process, factoring in variables such as excavation speed, excavation direction, and the resulting thermo-hydromechanical conditions in the post-excavation domain. With the utilisation of this function, the excavation history of both the GAN drift and the ALC1605 borehole was effectively simulated, taking into account the waiting periods between excavation phases. The outcome of this sequence is depicted in Figure 7.21, showcasing the pore pressure evolution within the host rock. For the purpose of this simulation, post-excavation pore pressure at the excavation contour is presumed to drop to atmospheric levels (i.e., 0.1 MPa). After the installation of the impermeable liner, an increase of pore pressure is expected. As illustrated in Figure 7.21, the waiting periods substantially influence the pore pressure distribution around the GAN drift and, to some extent, within the ALC1605 borehole. Notably, the GAN5 drift experiences a more pronounced pore pressure redistribution than the GAN7 drift, which was excavated four years later. This results in asymmetric pore pressure distribution along the GAN drift. The results show the significance of accounting for the rock's hydromechanical history before modelling the heating phase.

Figure 7.20: Modelling sequence of events for the ALC1605 experiment

EURAD (Deliverable n° 7.6) – Modelling report on the effect of temperature on clay host rocks behaviour
Dissemination level: PU
Date of issue of this report: 06/06/2024

Page 192
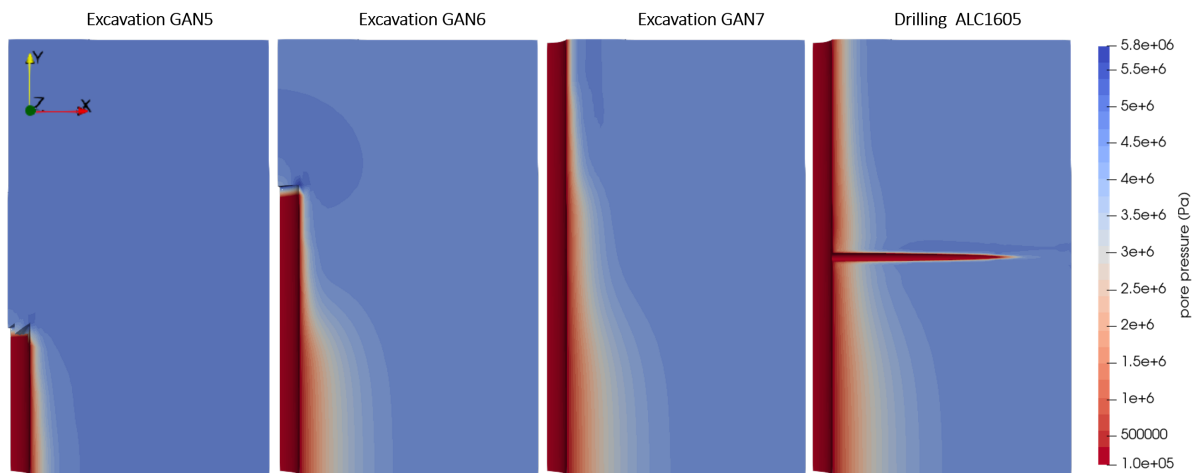
Figure 7.21: Simulation of the excavation process in OGS according to the chronology of events from the excavation of the GAN drift to the drilling of the ALC1605 borehole

7.1.3.2. Blind prediction modelling

The modelling of the ALC1605 experiment was divided into two distinct tasks. The first task entailed a blind prediction where the modelling team was tasked with simulating the experiment without prior knowledge of the actual in-situ results. For the second task, the in-situ experimental outcomes were disclosed to the modelling teams. Armed with this data, the teams then refined their modelling approaches to better align with the experimental findings.

For the blind prediction, we made several assumptions based on the description of the experiment provided by ANDRA. On the mechanical side, the host rock is considered linear elastic orthotropic. The elastic parameters used by Tourchi et al. (2021) in the modelling of the ALC1604 experiment located also in the GAN drift were considered instead of the given values in Table 2.6. The simplification of the mechanical behaviour by considering only elasticity is mainly due to some difficulties encountered when using the excavation function with plastic models. Further numerical developments are needed to increase the numerical stability for the modelling of excavation problems under consideration of plasticity in OpenGeoSys. Since elasticity is assumed, strains are reversible if backfilling is considered. For this reason, the simulation were carried out without mechanical backfilling after the excavation. We thus keep the strains developed during the excavation for the simulation of the heating phase. On the hydraulic side, the hydraulic parameters of the material in the borehole were considered after the excavation. Thus, the steel casing and the materials within the casing (heater and void) are assumed to be impermeable with a very low permeability of $10^{-25}\,\mathrm{m}^2$. For the MREA cement, we assign the same parameters as for the Cox. The permeability of the Cox used in the generic benchmark exercises was also considered here, see Table 2.6. On the thermal side, a high conductivity were assigned for the void in the casing instead of thermal parameters of air. In the void, thermal convection and thermal radiation are occurring and help to transport the heat away from the heater. Since these two phenomena are not considered in the simulation, a higher conductivity is assumed to take them into account. The thermal parameters of the Cox are taken from Table 2.6. The heat power is applied in the heater in two steps: $33\,\mathrm{W\,m^{-1}}$ in the test phase of heating, then $200\,\mathrm{W\,m^{-1}}$ during the main phase of heating. The parameters used in the simulation are summarized in Table 7.8.

The results of the blind prediction simulation are first qualitatively analysed in term of temperature and pore pressure evolution in Figure 7.22 after 2000 days of heating. The temperature distribution in the model clearly highlights the heat propagation from the heater into the rock. The maximum temperature in the rock in contact to the heater is about $77\,^{\circ}\mathrm{C}$. The region affected by a temperature increase (over $3\,\mathrm{K}$ of

EURAD (Deliverable n° 7.6) – Modelling report on the effect of temperature on clay host rocks behaviour
Dissemination level: PU
Date of issue of this report: 06/06/2024

Page 193

Table 7.8: Anisotropic thermo-hydro-mechanical parameters for the materials present in the ALC1605 experiment

			Casing/Heater	Cox/MREA	Void
Intrinsic permeability parallel to bedding	[m^2]	$k_\parallel$	1E−25	3.9E−20	1E−25
Intrinsic permeability normal to bedding	[m^2]	$k_\perp$	1E−25	1.3E−20	1E−25
Young's modulus parallel to bedding	[MPa]	$E_\parallel$	–	5200	–
Young's modulus normal to bedding	[MPa]	$E_\perp$	–	4000	–
Poisson's ratio parallel to bedding	[–]	$\nu_{\parallel\parallel}$	–	0.25	–
Poisson's ratio normal to bedding	[–]	$\nu_{\parallel\perp}$	–	0.35	–
Shear modulus parallel to bedding	[MPa]	$G_\parallel$	–	2080	–
Shear modulus normal to bedding	[MPa]	$G_\perp$	–	1481.5	–
Thermal conductivity parallel to bedding	[W/m/K]	$\lambda_\parallel$	54	1.88	20
Thermal conductivity normal to bedding	[W/m/K]	$\lambda_\perp$	54	1.25	20
Specific heat	[J/kg/K]	c_p	480	790	1
Density	[kg/m^3]	ρ	7850	2690	1
Thermal expansivity	[1/K]	α	–	1.25E−5	–
Biot coefficient	[–]	β	–	0.8	–
Porosity	[–]	n	0	0.18	0

temperature increase) reaches 16.5 m in horizontal direction and 13.7 m in vertical direction. The effect of the heating is replicated in the pore pressure distribution where a maximum overpressure of up to 7.9 MPa is observed near the borehole. This pore pressure decreases along with the temperature with distance to the heater. The region affected by the overpressurization (about 0.5 MPa above the initial pressure conditions) reaches 20 m in horizontal direction and 18.4 m in vertical direction. 2000 days after the start of heating, the pressure redistribution due to the GAN drift excavation and waiting time of over six years does not affect the pore pore pressure evolution due to heating around the borehole. Two distinct domains of pore pressure distribution can be observed around the drift and around the borehole. It is to be expected that the draining in the GAN drift will affect the pore pressure evolution in the experiment in the long run. This will cause a dissipation of the overpressure in the model. This is to be verified by further analyses.
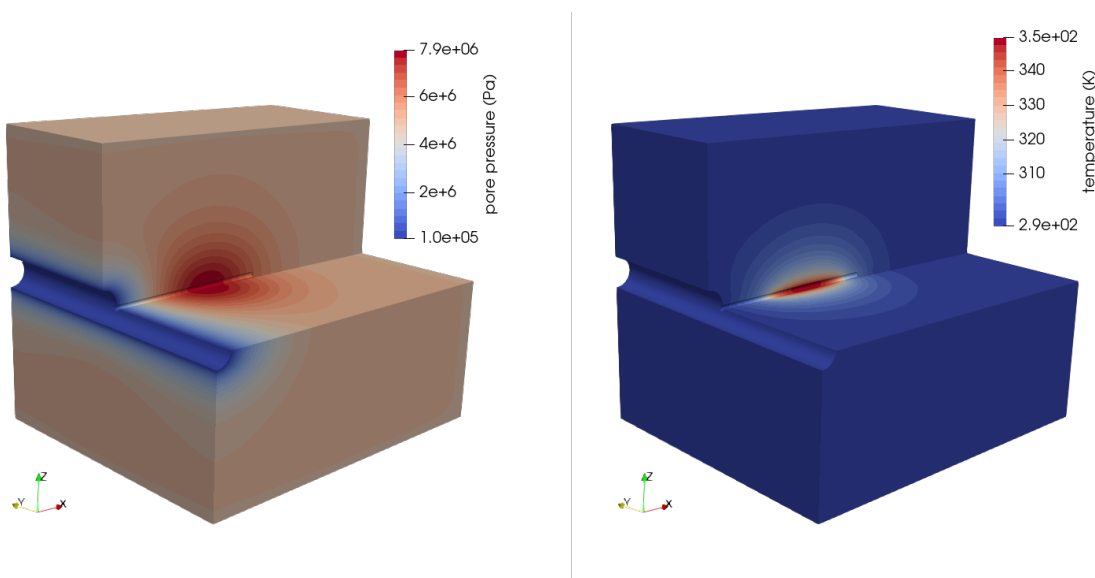
Figure 7.22: Pore pressure and temperature distribution in the model 2000 days after the beginning of heating

EURAD (Deliverable n˚ 7.6) – Modelling report on the effect of temperature on clay host rocks behaviour
Dissemination level: PU
Date of issue of this report: 06/06/2024

Page 194

The quantitative results of the simulation and comparison with experimental data across multiple sensors are presented in Figure 7.23 and Figure 7.24. The obtained temperature evolution from the simulation at the sensors located in horizontal direction shows that the numerical results overpredict the temperature of about $3\,°C$ for most of the sensors. A better agreement with experimental data is observed at sensors ALC1629-03 and ALC1627-03 located approximately $7\,m$ away from the borehole in horizontal and in vertical direction. It is also worth mentioning that the experimental and numerical temperature evolution shows a similar trend, so that better results can be obtained through calibration of the thermal parameter employed in the simulation.
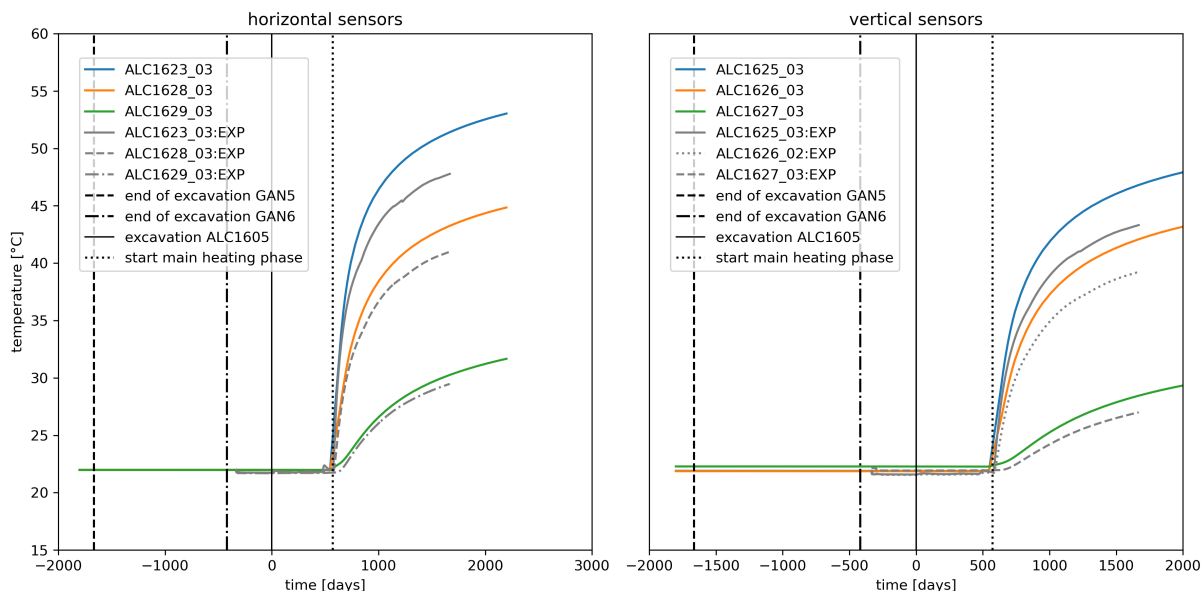
Figure 7.23: Temperature evolution for the blind prediction: numerical vs. experimental results across multiple sensors

As for the pore pressure, the model is not able to reproduce the peak of pore pressure occurring during the excavation of the ALC1605 followed by a significant decrease in horizontal direction (Figure 7.24). In vertical direction, the sudden drop of pore pressure that occurred cannot be predicted by the model neither. This phenomenon already described in section 5.1.4.2 necessitates the use of plastic models to be properly reproduced numerically. In the heating phase, it can be observed that the numerical results significantly over predict the pore pressure of up to $2\,MPa$. At the sensors located away from the borehole like ALC1629-03 and ALC1627-03, the numerical results are much closer to the experimental ones. These observations are in line with those already discussed for the temperature evolution comparison. Thus, an improvement in the temperature evolution results will also improve the pore pressure evolution. Further improvements can be realised by increasing the permeability to lower the pore pressure level. This will be further investigated in the interpretative modelling.

EURAD (Deliverable n° 7.6) – Modelling report on the effect of temperature on clay host rocks behaviour
Dissemination level: PU
Date of issue of this report: 06/06/2024

Page 195
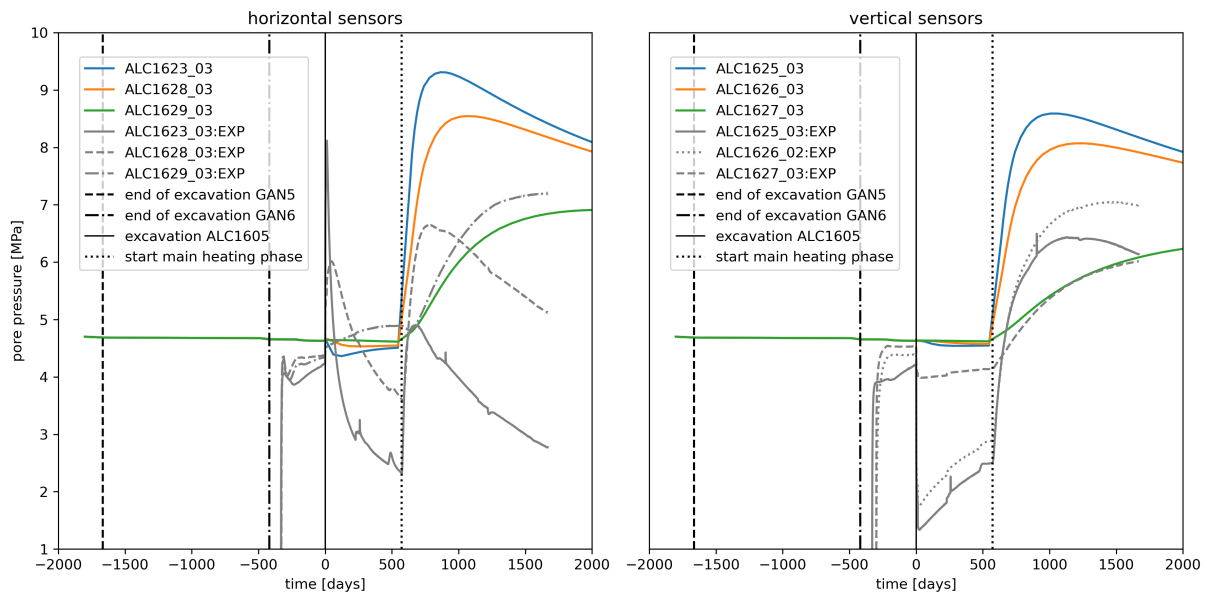
Figure 7.24: Pore pressure evolution for the blind prediction: numerical vs. experimental results across multiple sensors

7.1.3.3. Interpretative modelling

To enhance the outcomes from the predictive modelling, we pursued two approaches. First, we conducted sensitivity analyses to calibrate the thermal parameters, aligning them more closely with experimental results. Subsequently, we integrated a function to modify permeability based on elastic strains, aiming to achieve a more precise control over the pore pressure evolution. Consideration of the elastic strains allows only to capture the behaviour of microfissures in the rock. Pore pressure dissipation due to plasticity are not considered yet.

To enhance the accuracy of the thermal results, we introduced an assumption: the void in the casing is treated as a heat source. This accounts for the heat loss in the casing resulting from both thermal conduction and radiation. Consequently, the total applied heat power is split into two components: one attributed to the heater, representing thermal conduction, and another designated for the void, capturing effects of convection and radiation. The proportion between these components was one of the parameters to optimise. In addition to this ratio, the sensitivity analysis also considered the thermal parameters of the Cox and the void within the casing.

The sensitivity analyses were carried out by computing the euclidean norm of the difference between the experimental and numerical temperature evolution curve at each sensors. The analyses were based on seven sensors. Thus the criterion for optimisation was the sum of the euclidean norms computed at the seven sensors. The objective of the analyses was to minimise the defined criterion in order to obtain the best possible fit between experimental and numerical results. The sensitivity analyses were carried out with the sensitivity software ANSYS OptiSLang (Ansys, 2022) in which 100 designs were generated using the advanced latin hypercupe sampling method. Each design was computed with OpenGeoSys and post processed with python. The resulting temperature evolution curves were further analysed by OptiSLang where the criterion was evaluated. The best designs were then narrowed and the one with the lowest heat loss in the heater was selected for the analyses. Figure 7.25 shows the results of the sensitivity analyses. The temperature curves of the 100 designs for six sensors of the 7 above mentioned are displayed with the experimental one in green and the best design selected in red. For this design, the ratio between the heat power in the heater and in the void accounts for 85.5%, meaning that 14.5% of the heat energy

EURAD (Deliverable n° 7.6) – Modelling report on the effect of temperature on clay host rocks behaviour
Dissemination level: PU
Date of issue of this report: 06/06/2024

Page 196

is dissipated before entering the rock mass. Heat transport by convection and radiation in the casing may explain this loss. The optimised conductivity values for Cox are 2.365 W/m/K in horizontal direction and 1.3975 W/m/K in vertical direction. Those values are in line with those found in the literature. For instance, Tourchi et al. (2021) estimated based on back analysis calculation values of 2.05 W/m/K and 1.33 W/m/K respectively for the horizontal and vertical direction. The conductivity estimated for the void is 26.8 W/m/K with the specific heat of the void being a non sensitive parameter. With the optimised parameters, a good agreement is obtained for the temperature evolution obtained from the THM analysis at the seven sensors, see Figure 7.26.
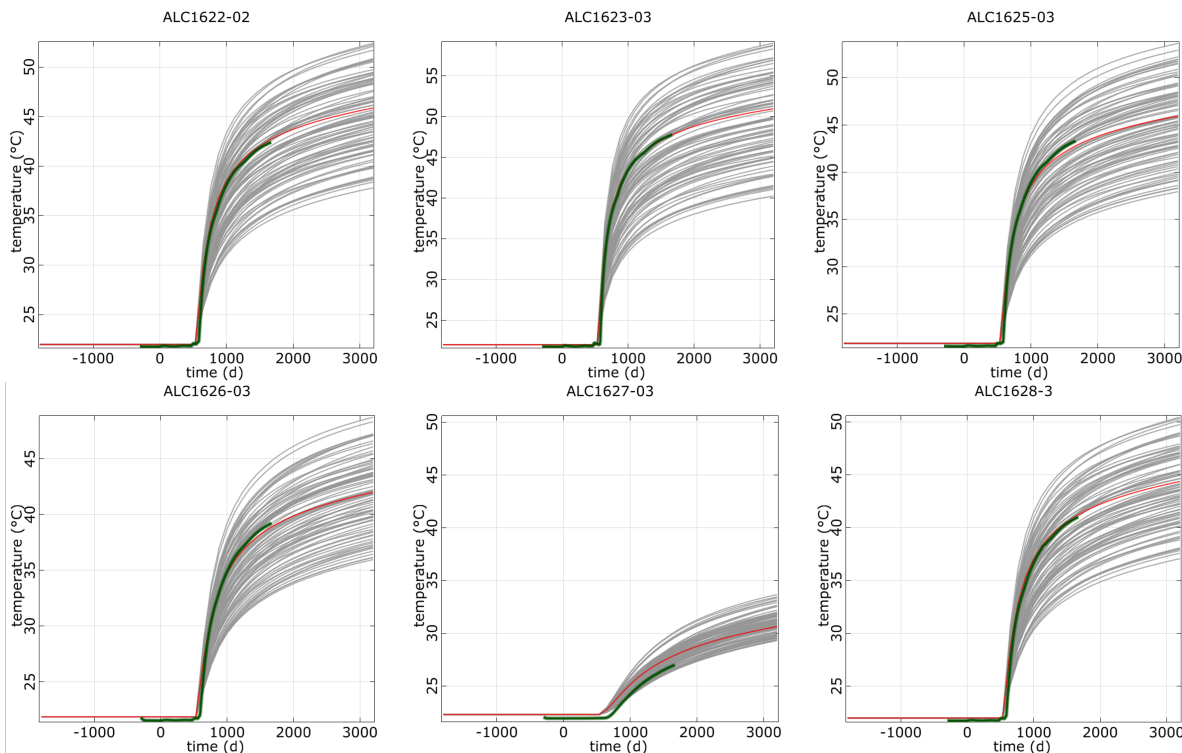
Figure 7.25: Calibration of thermal Parameters for enhanced temperature evolution prediction

EURAD (Deliverable n˚ 7.6) – Modelling report on the effect of temperature on clay host rocks behaviour
Dissemination level: PU
Date of issue of this report: 06/06/2024

Page 197
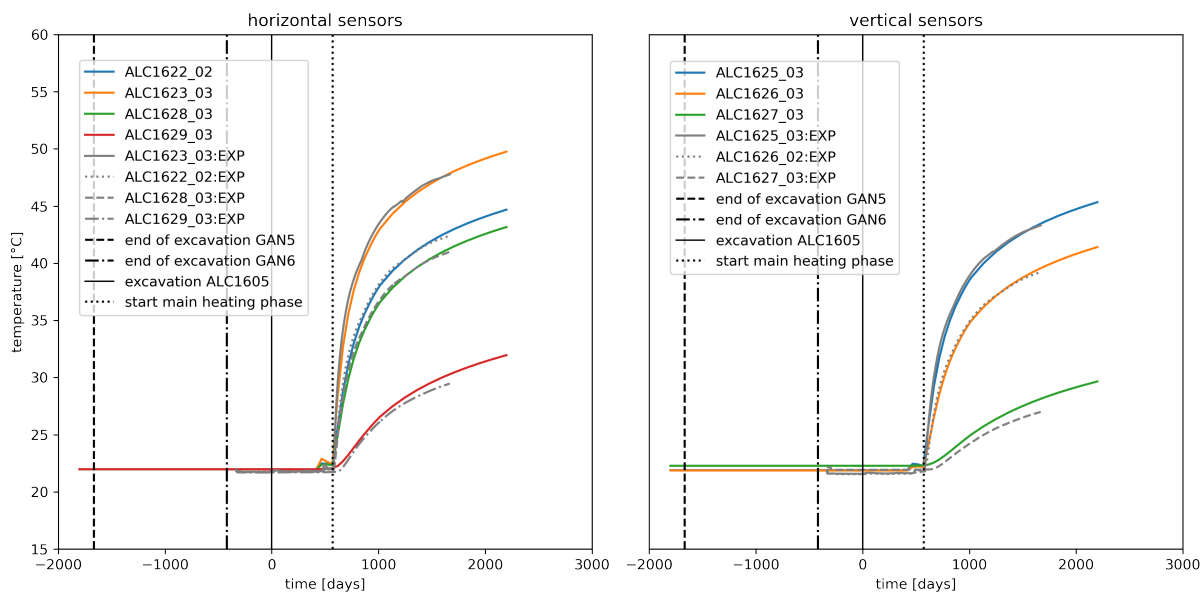
Figure 7.26: Temperature evolution for the interpretative modelling: numerical vs. experimental results across multiple sensors

To improve the pore pressure results, we introduced a strain dependent permeability model instead of a constant one as employed in the blind prediction simulation. This approach relies on the fact that when strains increase, the permeability should also increase. We used for that an exponential function defined as follow:

$$k = k_0 \cdot \exp(a \cdot \epsilon_v)$$

with k_0: the intrinsic permeability in m^2 and ϵ_v: the elastic volumetric strain (dimensionless). $a = 4605.17$ is a fitting parameter that allows to increase the permeability in three orders of magnitude when the volumetric strain exceeds a threshold value of 1×10^{-3}. Below this threshold , one recovers the constant permeability values as given in Table 7.8.

The results obtained using this function are presented in Figure 7.27. The figure shows that the numerical results are much closer to the experimental ones, qualitatively and quantitatively. Only at sensor ALC1623_03 a higher discrepancy remains. At the other sensors a better agreement is reached. Even using this approach the post excavation pore pressure redistribution cannot be captured numerically. The use of elastoplastic models can help to further reduce the remaining discrepancies between the numerical and experimental results. This will be the subject of further studies.

EURAD (Deliverable n° 7.6) – Modelling report on the effect of temperature on clay host rocks behaviour
Dissemination level: PU
Date of issue of this report: 06/06/2024

Page 198
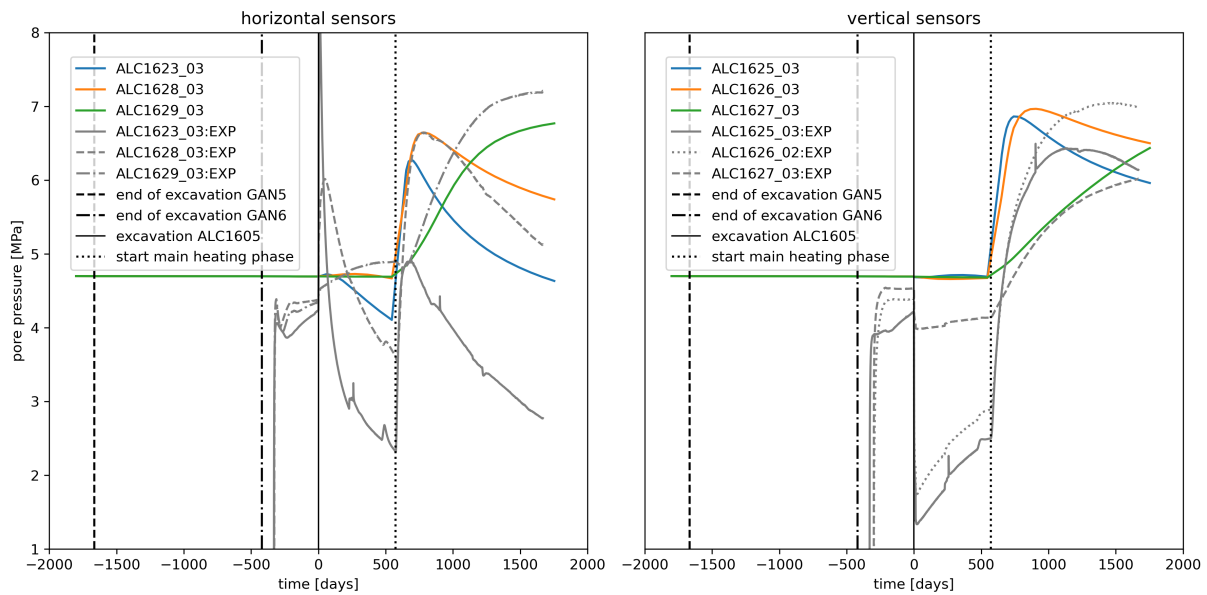
Figure 7.27: Pore pressure evolution for the interpretative modelling: numerical vs. experimental results across multiple sensors

7.1.4. EDF

7.1.4.1. Modelling concept

The aim of this task is to study the behavior of a HLW micro-tunnel ALC1605 which is under thermal load. This exercise was divided into two steps. Step 1 consists in a predictive modelling of the ALC1605 experiment, using for the rock mass parameters the reference values provided previously in the near and far-field modelling exercises. The discrepancies between the results of the model obtained for this prediction will be analyzed. Step 2 consists in an interpretative modelling of the ALC1605 experiment.

The different sub-phases that the ALC1605 micro-tunnel encountered from 2013 till the present were given in the in-situ report provided by the host of sub-task 2.3 (ANDRA). Those sub-phases consisted principally in the excavation phases of the GAN drift (gallery perpendicular to the ALC micro-tunnel), the excavation of the ALC1605 micro-tunnel, the injection of an MREA (Materiau de remplissage de l'Extrados des Alvéoles) cement and a steel casing on the ALC1605 micro-tunnel, the excavation of neighbouring micro-tunnels (AHA1605 and HAE1602) and finally the heating phase of the ALC micro-tunnel under two flows: an intermediate value of 33 W/m and a bigger flow of 220 W/m.

For this in-situ modelling exercise, EDF chose to represent a 3D geometry while using code_aster. In the predictive step, a preliminary modelling was done while using 4 meshes to account for 4 sub-phases: sub-phase 1/ the excavation of the GAN drift ; sub-phases 2 to 4/ the excavation of each of the three tunnels (ALC1605, AHA1605 and HAE1602). The MREA and the steel casing were also represented in the different meshes. The heating of the ALC1605 occurs in sub-phase 3, after the excavation of the neighbouring micro-tunnel AHA1605.

The resulting fields (displacement, stress, internal variables) of a given anterior sub-phase were projected on the mesh of the posterior sub-phase and are considered as its initial fields: for example the resulting fields of sub-phase 1 representing the excavation of the GAN drift were projected on the mesh where the ALC1605 micro-tunnel is excavated and are considered as the initial fields of sub-phase 2. An example of the mesh used for sub-phases 1 and 2 is given in figure 7.28.

EURAD (Deliverable n° 7.6) – Modelling report on the effect of temperature on clay host rocks behaviour
Dissemination level: PU
Date of issue of this report: 06/06/2024

Page 199
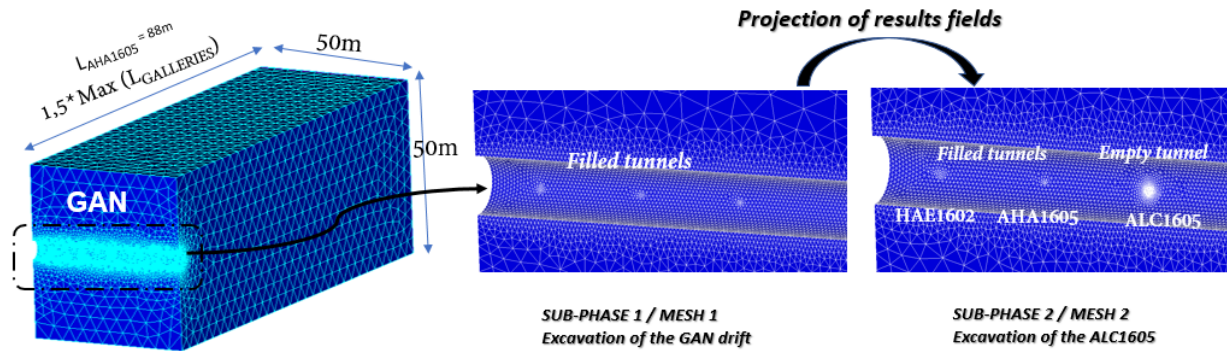
Figure 7.28: Preliminary meshes - sub-phases 1 and 2

This preliminary method of meshing and modelling appeared to be very complicated and caused numerical problems due to the number of necessary projections. In consequence, a simplified method for modelling and meshing was instead used. The later method consisted on using **one type of mesh for all the sub-phases**. We model **only 3 sub-phases**: sub-phase 1/ the excavation of the GAN drift, sub-phase 2/ the excavation of the ALC1605 micro-tunnel and sub-phase 3/ the heating phase of ALC1605. During the excavation and the heating of the ALC1605 , the meshes inside the micro-tunnel are not considered in the model. An example of this simplified mesh is given in figure 7.29.
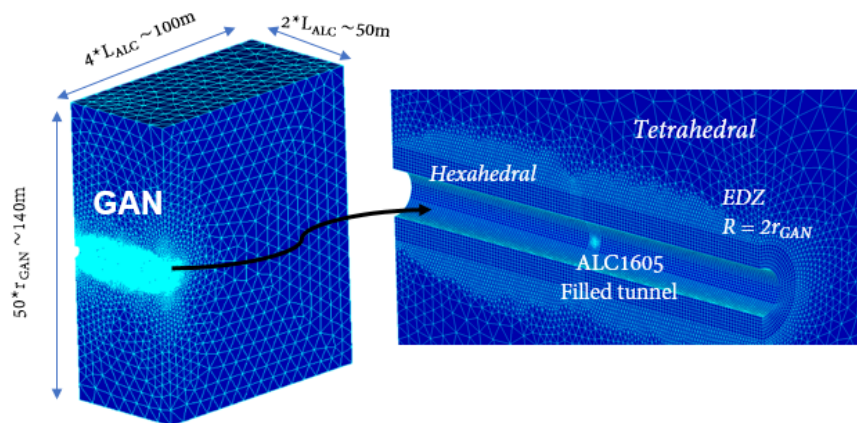
Figure 7.29: Simplified mesh - 180000 Nodes / 776000 Elements

This mesh contains **180000 Nodes (776000 elements)**. An **EDZ (Excavation Damaged Zone)** is represented in this mesh around the GAN drift with a radius equal to 2 times the radius of the drift. The mesh consists of **tetrahedral elements** far from the EDZ and **hexahedral elements** in the EDZ region. For a more simplified mesh, and as first approach, we do not represent the MREA and the steel casing around the ALC1605 micro-tunnel. Moreover, no neighbouring micro-tunnels are taken into account in this mesh. It is important to note that while taking into account a height along Z of 50m, we observed displacements in the arch region of the GAN drift that are bigger than those on its raft. Consequently, the height along Z was increased in order to reduce this observation and was finally taken equal to 50 times the radius of the GAN drift.

The sub-phases that were considered with their respective dates are:

- **Sub-phase 1 - The excavation of the GAN drift** starting 09/12/2013 til 19/06/2018 followed by a

EURAD (Deliverable n˚ 7.6) – Modelling report on the effect of temperature on clay host rocks behaviour
Dissemination level: PU
Date of issue of this report: 06/06/2024

Page 200

waiting phase from 19/06/2018 til 14/11/2018.

- **Sub-phase 2 - The excavation of the ALC1605 micro-tunnel** starting 14/11/2018 til 15/11/2018 followed by a waiting phase from 15/11/2018 til 25/02/2020.

- **Sub-phase 3 - The heating phase of the ALC1605 micro-tunnel**: a low-heating stage under 33W/m from 25/02/2020 until 12/03/2020 followed by a waiting phase until 08/06/2020 when the main-Heating stage under 220 W/m starts and is supposed to continue until 08/03/2023.

Regarding the boundary conditions that were used, we considered those defined in the in-situ report with some minor modifications:

- Instead of considering **DY=0** on the left face and a stress condition on the right face, we considered DY = 0 on the left and right faces and that's because unrealistic displacements on the right face were observed when a stress condition was applied on it (compression negative displacements observed on the right face while tension positive displacements are observed along the GAN drift).

- The **initial temperature profile** is considered to increase linearly with depth from T=21 °C on the top face and reaching T=23 °C on the bottom face (as given in the report). This is because the measurements given (on the OHZ1694 sensor, period between 2017 and 2018) during the excavation phase of the GAN drift showed temperatures higher than 23 °C (i.e. the boundary condition defined on the bottom face).

- During the excavation phases of the GAN drift and the ALC micro-tunnel, we consider a **pore water pressure** that reduces linearly to Patm (0.1 MPa) and a **stress reduction** to 0 % of the initial in-situ stress.

7.1.4.2. Blind prediction modelling

Predictive modelling phase results: in the following sections, we show and describe some of the main results for the predictive modelling phase. More generally, a comparison of those results with the other participants results are shown in section 7.1.7.1.

First, we start by comparing the **initial modelled pore pressure evolution** along the ALC1605 micro-tunnel, **at the beginning of sub-phase 2**, with the measurements given in the in-situ report by the ALC1623 borehole sensor. This comparison is given by figure 7.30-a for the case when the permeability of the EDZ is considered equal to that of the Cox host rock and figure 7.30-b for the case when the permeability of the EDZ is considered 1000 times bigger than that of the Cox host rock, in order to account for the fractures that exists in this EDZ region. We can eventually observe that more coherence is observed when we increase the permeability of the EDZ. In the later case, we are capturing the right slope for the variation of the pore pressure with respect to the distance along the tunnel and only a very slight difference (0,5MPa) in pore pressure between numerical and measured values is observed at the beginning of sub-phase 2 (the excavation of the ALC1605). This result is considered satisfying and as a consequence, we consider $K_{edz} = 1000.K_{cox}$ for all the sub-phases in the predictive modelling phase.

EURAD (Deliverable n° 7.6) – Modelling report on the effect of temperature on clay host rocks behaviour
Dissemination level: PU
Date of issue of this report: 06/06/2024

Page 201
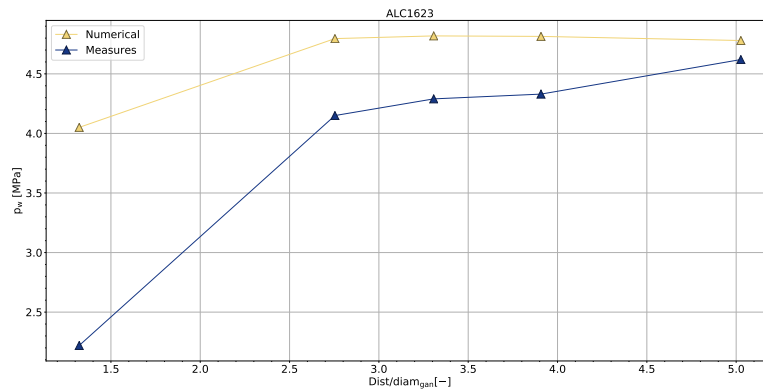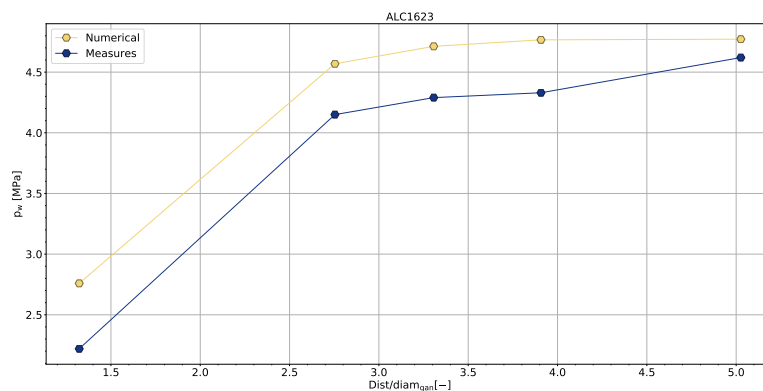
(a) $K_{edz} = K_{cox}$

(b) $K_{edz} = 1000.K_{cox}$

Figure 7.30: Pore pressure evolution on the ALC1605 micro-tunnel at the beginning of sub-phase 2 : model vs measurements for the case when / $K_{edz} = K_{cox}$ and b/ $K_{edz} = 1000.K_{cox}$

As a second step, we compare the modelled pore pressure evolution at the location of two sensors for which the measurements were provided during the predictive phase: the ALC1623 horizontal sensor with 3 measurements locations (1,3,5) and the ALC1625 vertical sensor with 3 measurements locations (1,3,5). The comparison results are given in figure 7.31. In this figure, we can observe that, for the period prior to heating (June 2020):

- **In the Horizontal direction :** the numerical values are close to the measurements prior to heating (06/2020). The pore pressure increase at the end of the excavation of the ALC1605 (15/11/2018) is not well captured.

- **In the Vertical direction :** the pore pressure increase after the excavation of micro-tunnel (after 15/11/2018) is not well captured. We capture instead a decrease of the pore pressure.

- **In both directions :** the model is capturing an increase of pore pressure due to the low heating stage (33 W/m) occurring on between 25/02/2020 and 12/03/2020.

EURAD (Deliverable n˚ 7.6) – Modelling report on the effect of temperature on clay host rocks behaviour
Dissemination level: PU
Date of issue of this report: 06/06/2024

Page 202
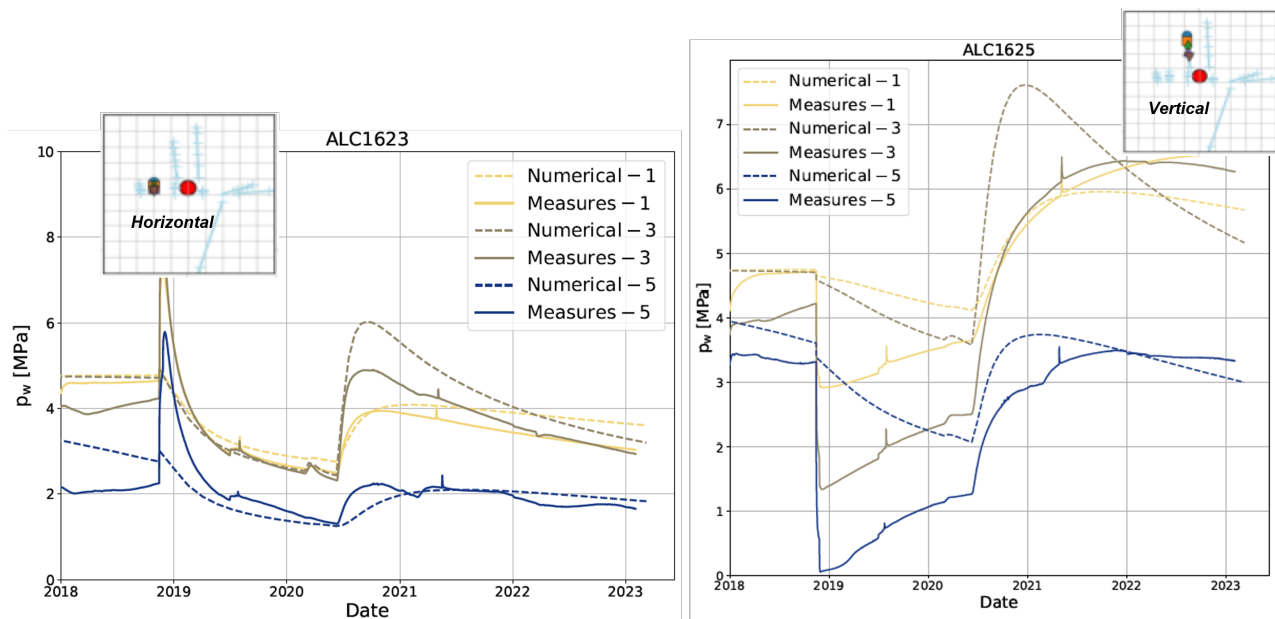
Figure 7.31: Comparison of the pore pressure evolution with horizontal and vertical sensors measurements in the Cox

For the period posterior to the beginning of the heating of the ALC1605 (June 2020), we observe in figure 7.31 that:

- **In the Horizontal direction :** the pore pressure increase, due to heating (beginning in june 2020), is captured : numerical values are close to the measurements ; the modelled pore pressures are slightly overestimated, especially near the heater area (sensor 3).

- **In the Vertical direction :** the pore pressure increase, due to heating, is captured: the modelled pore pressures are overestimated near the heater area (sensor 3), but also near the Gan drift (sensor 1).

- **Other comparisons were done** for sensors ALC1622 – ALC1627- ALC127 - ALC1628 and ALC1629. The same tendencies were observed for each of them.

Finally, we compared the numerical temperatures with the temperature measured in the Cox and on the casing of the ALC1605 micro-tunnel. As for the comparison with the temperature of the Cox (shown in figure 7.32), we can observe that in general, **numerical temperatures are overestimated** near the heater area (sensor 3) in both directions. This result is considered to be conservative towards the real behaviour of the Cox. For the temperature on the casing (figure 7.33), we compared temperature measurements given by 3 sensor (TEM004, TEM006, TEM007) situated along the micro-tunnel with the numerical modelled temperature. We observe a slight underestimation of temperature during the beginning of heating and in general an overestimation of the temperature at the end (tending towards maximum values of 80-90°C). One of the possible explanation of this observation is an applied numerical flow (220 W/m) that might be bigger than the real experimental flow that might have been reduced by the placing of a steel plate at the cell head (in order to reduce convection phenomena). An attempt to calibrate this value of flow is pursued in the interpretative phase.

EURAD (Deliverable n˚ 7.6) – Modelling report on the effect of temperature on clay host rocks behaviour
Dissemination level: PU
Date of issue of this report: 06/06/2024

Page 203
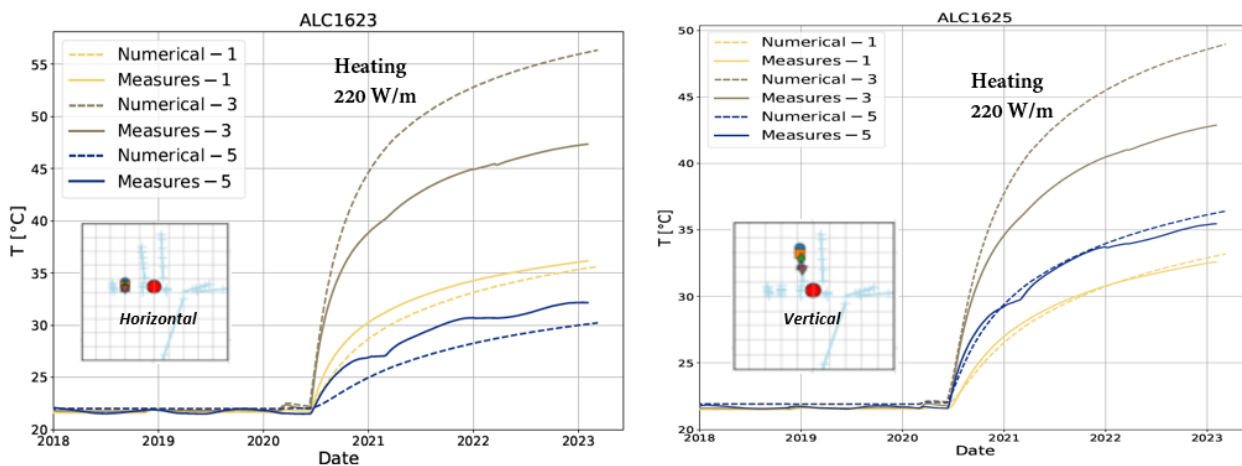
Figure 7.32: Comparison of the temperature evolution with horizontal and vertical sensors measurements in the Cox
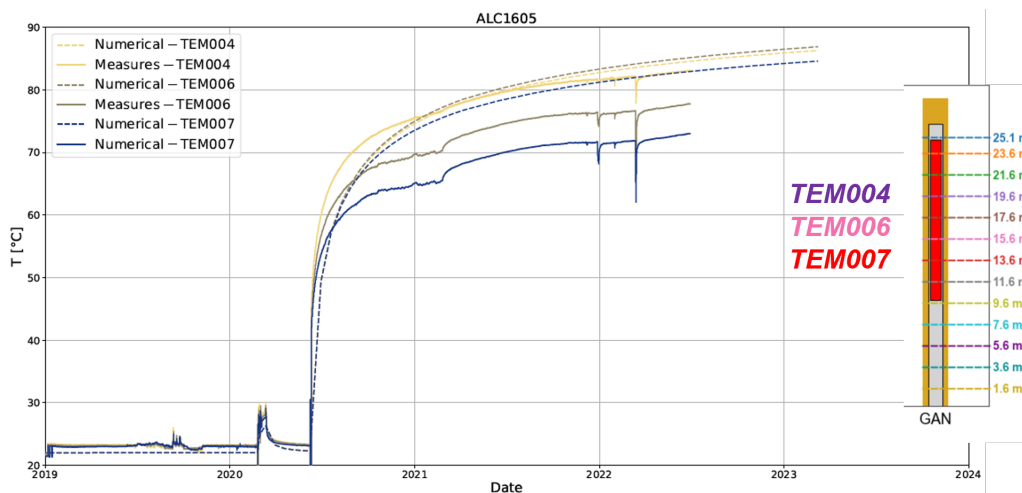
Figure 7.33: Comparison of the temperature evolution on the casing of the ALC1605 micro-tunnel

The pressure, temperature, displacements and stresses results comparisons with other models (participants) results are shown in section 7.1.7.1.

7.1.4.3. Interpretative modelling

In the interpretative modelling phase, some optimization attempts have been tested that consisted in:

- **Reducing the value of the applied heat flow (220 W/m)** in order to better catch the measured temperature evolutions.

- **Modifying the Cox material properties**, in the **EDZ** area and further away from it in order to try better representing the pore pressure evolution's

- **Changing some minor modelling parameters** such as adding more time steps during the heating phase in order to better refine the results.

We start by showing some tests done on the **reduction of the heat flow value** during the heating phase:

EURAD (Deliverable n° 7.6) – Modelling report on the effect of temperature on clay host rocks behaviour
Dissemination level: PU
Date of issue of this report: 06/06/2024

Page 204

instead of considering a value of **F=220 W/m**, we consider a reduced value of **90%F = 198 W/m** applied during the main heating phase in order to consider the effect of the convection phenomena. The results of this modelling case are shown in figure 7.34.

(a) Cox temperatures

(b) ALC1605 casing temperatures
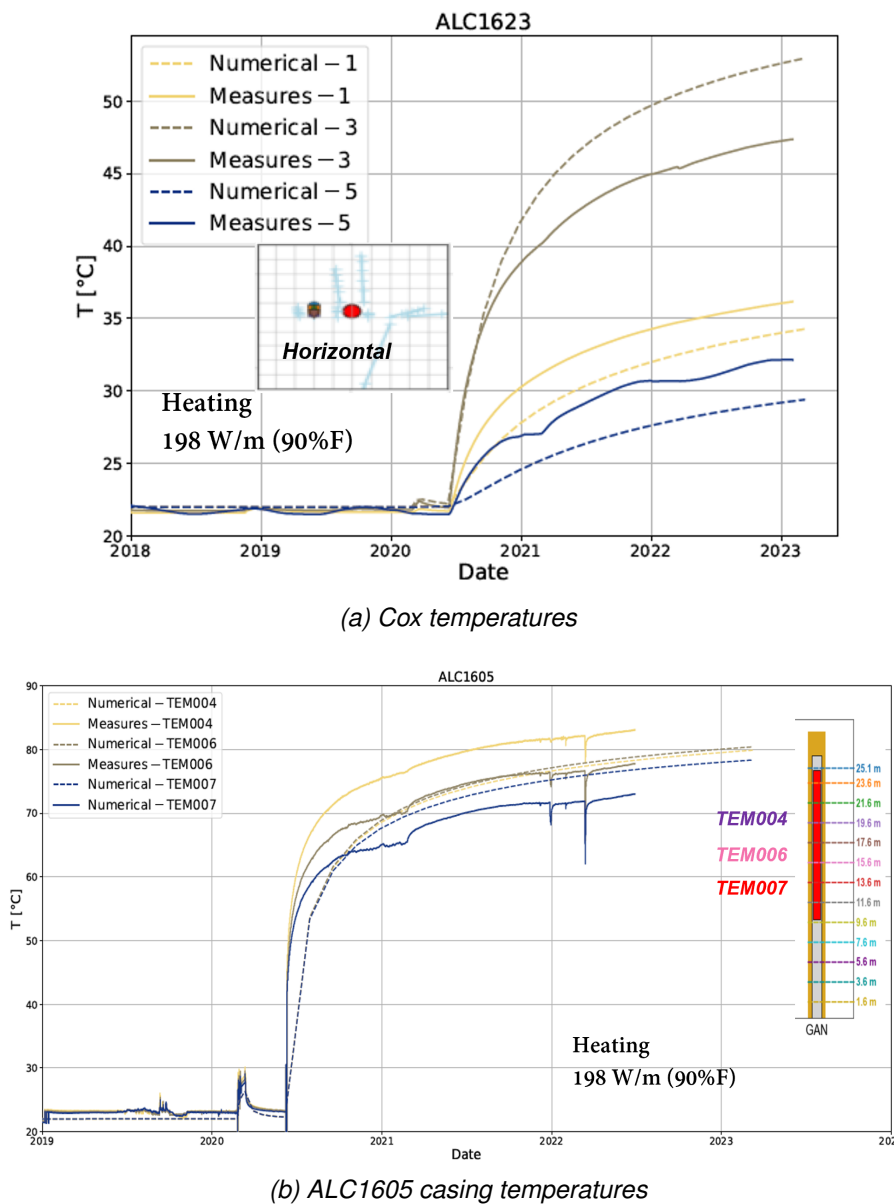
Figure 7.34: Comparison of the temperature evolution for the case of 90%F = 198 W/m: (a) with horizontal sensors measurements in the Cox (b) with measurements on the casing of the ALC micro-tunnel

By comparing figure 7.34-a with figure 7.32 and figure 7.34-b with figure 7.33, we can observe that in the Cox (measured by ALC1623) we have a slightly better described temperature evolution near the heater area (sensor ALC1623-3) for the case when the flow is of 90%F = 198 W/m. However faraway from the heater area (sensors ALC1623-5 & ALC1623-1), the temperatures are better represented by a flow of F = 220 W/m. As for the temperatures on the ALC1605 micro-tunnel casing, it is observed that with a flow of 198 W/m, the temperature is better represented for some sensors (TEM006 & TEM007) , but not for others (TEM004). Intermediate flows of 92%F, 95%F have been also tested and the same tendencies have been observed. In terms of pore pressure evolution's, having a flow of 90%F = 198 W/m resulted in underestimated pressures in the Cox far from the heater area and in a better described pore pressure near the heater area.

EURAD (Deliverable n˚ 7.6) – Modelling report on the effect of temperature on clay host rocks behaviour
Dissemination level: PU
Date of issue of this report: 06/06/2024

Page 205

As a second attempt, we tried **modifying/calibrating the Cox material properties** in the EDZ area and further away from it. We considered:

- in the EDZ, an elastic Young's Modulus of $E_{edz-perp}$ = 3GPa in the direction perpendicular to the bedding and $E_{edz-//}$ = 6GPa in the direction parallel to the bedding. Those values were considered previously, in the predictive modelling phase, equal to the same values in the Cox : 5GPa and 8GPa respectively in the perpendicular and parallel directions. Those later values were chosen according to the values given in the near and far-field modelling sub-tasks for the Cox.

- in the Cox, a water permeability equal to $K_{cox-perp}$ = $7e^{-21}m^2$ in the direction perpendicular to the bedding and $K_{cox-//}$ = $2e^{-20}m^2$ in the direction parallel to the bedding. Those values were considered previously, in the predictive modelling phase, equal to $K_{cox-perp}$ = $1.3e^{-20}m^2$ and $K_{cox-//}$ = $3.9e^{-20}m^2$.

- in the EDZ, we consider that the values of the permeabilities are equal to 10000 the values in the Cox: $K_{edz-perp}$ = $7e^{-17}m^2$ and $K_{edz-//}$ = $2e^{-16}m^2$. Previously (in the predictive phase) those values were considered of 1000 the values in the Cox: $K_{edz-perp}$ = $1.3e^{-17}m^2$ and $K_{edz-//}$ = $3.9e^{-17}m^2$.

This results in considering an **EDZ material** near the gallery of the GAN that is **more permeable to water and less stiff** than that considered in the predictive modelling phase and a less permeable material further away from the EDZ. Moreover, we consider for this modelling case a flow equal to **92% = 202 W/m** applied during the heating area. The numerical pore pressure evolution's comparison in the Cox with measurements in the horizontal and vertical directions is given in figure 7.35.
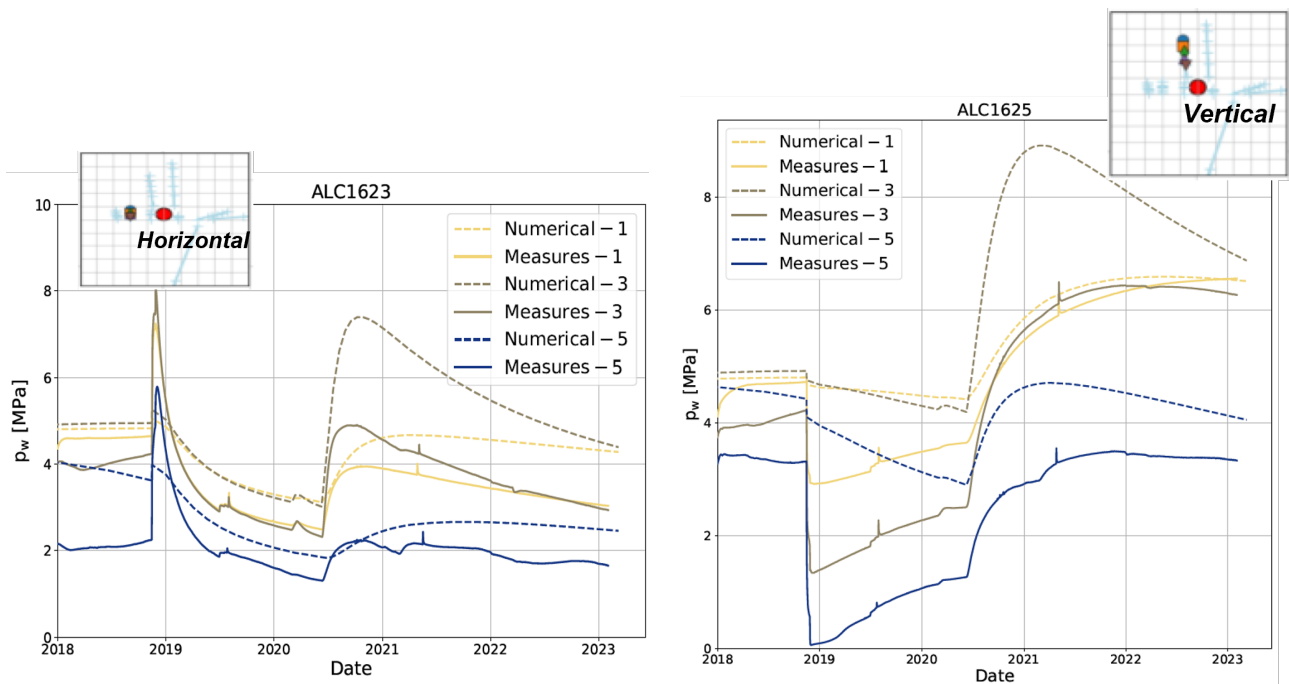
Figure 7.35: Comparison of the pore pressure evolution for the case of modified Cox parameters and 92%F = 200 W/m: (left) with horizontal sensors measurements in the Cox (right) with vertical sensors measurements in the Cox

We can observe that :

- **In the horizontal direction:** the pore pressure increase during the excavation of the ALC1605 micro-tunnel (on 15/11/2018) is closer to the measurements in figure 7.35 than in figure 7.31 (pre-

EURAD (Deliverable n° 7.6) – Modelling report on the effect of temperature on clay host rocks behaviour
Dissemination level: PU
Date of issue of this report: 06/06/2024

Page 206

dictive modelling phase). This is because in the interpretative modelling phase (figure 7.35), we are departing from higher pore pressures just before the excavation of the ALC1605 micro-tunnel (on 14/11/2018). This is due to the fact, that in the interpretative phase, the permeabilities to water in the Cox were taken lower than those considered in the predictive phase. However, during the heating phase (after 06/2020), the pore pressures in the interpretative modelling phase (figure 7.35) are further away from the measurements (more overestimated) than in the case of figure 7.31.

- **In the vertical direction:** with the modified values of the Cox parameters, figure 7.35 is showing a reduced decrease of the pore pressure after the excavation of the ALC1605 micro-tunnel (after 15/11/2018) with respect to the decrease observed with the initial values of the Cox parameters considered in figure 7.31 (predictive modelling phase). However, during the heating phase (after 06/2020), the pore pressures in the interpretative modelling phase (figure 7.35) are further away from the measurements (more overestimated) than in the case of figure 7.31. This is because lower permeabilites for the Cox were considered in the interpretative modelling phase.

Finally, the modification attempts done in the interpretative phase of modelling lead us to conclude that by accounting for a heating flow value reduced with respect to the initial value of 220 W/m, the numerical temperatures and pore pressures evolutions can get closer to the measurements for some sensors but not for others. On another aspect, the modification of the Cox parameters as aimed in our interpretative modelling has improved some of the results as the increase of the horizontal pore pressure during the excavation of the ALC1605 micro-tunnel and the lower decrease of vertical pore pressure after the excavation of the latter. However, the inital pore pressure (before the excavation of the micro-tunnel) were observed to be further away from the measurements and the pore pressures in the heating phase became more overestimated with respect to measurements.

As for the final results of this interpretative phase used for the comparisons to be done with other models (with other participants) in section 7.1.7.2, we chose to re-consider the initial values of the Cox properties and of the heating flow (those considered in the predictive phase) with only some minor changes (refinements) of the simulations time steps. As a matter of fact, even though the results of the predictive phase don't exactly match the experimental curves, but the modelling results (in terms of pressure, temperature, displacements) are quite satisfactory in view of what is being done internationally and are generally representative of the Cox real behaviour. The results presented earlier, particularly regarding pressure and temperature, occasionally show some overestimation of the experimental measures. This tendency is considered to lead to a more conservative modelling approach. Future work offers potential avenues for further refinement, aiming to mitigate this conservatism

7.1.5. LEI

7.1.5.1. Modelling approaches

For modelling in-situ experiment AL1605 LEI proposed 50 m x 50 m 2D model. Model considers ALC1605 and AHA1605 micro tunnels, which location and dimensions were specified according to specification (HITEC Subtask 2.3, 2022). For the modelling of ALC1605 in-situ experiment LEI decided to relate simulation beginning to the end of excavation of GAN drift. Therefore, according to the dates provided in the specification, the excavation of ALC1605 started after 149 days from the beginning of simulation. Excavation took 1 day. Excavation was described as reduction of initial stress to zero stress on ALC1605 tunnel boundary over 1 day. Then after 11 days MREA filling was installed between steel casing and Cox. In the model MREA installation was modelled as instant activation of material. Later excavation of AHA1605 tunnel took part and was represented in the model with the same stress reduction approach, but it took over 3 days. The void space in this tunnel was assumed to be MREA filling and represented in the model by activation of this type of material. After 617 days from simulation beginning the first heating phase

EURAD (Deliverable n˚ 7.6) – Modelling report on the effect of temperature on clay host rocks behaviour
Dissemination level: PU
Date of issue of this report: 06/06/2024

Page 207

began and it ran for 16 days. The main heating phase started when more than 88 days passed. For the predictive modelling the total simulation time was 1500 days. End of simulations would correspond to $\sim 2022/07/27$. For interpretative modelling the total simulation time 1690 days and would correspond to date $\sim 2023/02/02$.

| T0+149 d start of excavation of ALC1605 |

| T0+161 d injection of steel and MREA |

| T0+378 d start of excavation of AHA1605 |

| T0+617 d start of first heating |
| T0+633 d end of first heating |

| T0+721 d start of second heating |
| T0+1500 d end of second heating |
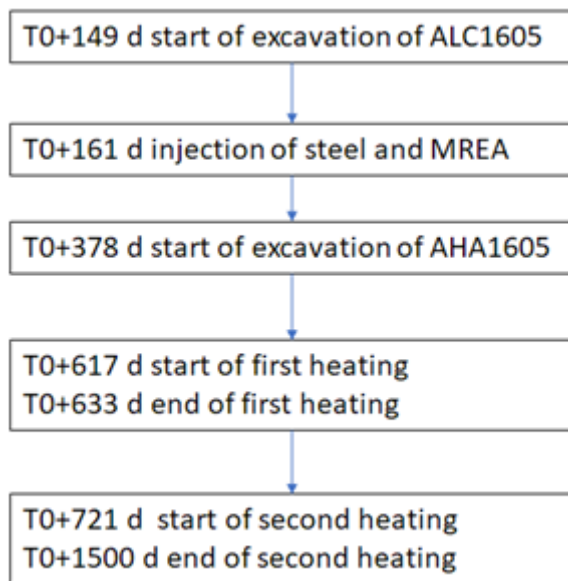
Figure 7.36: Derived timeline for modelling of ALC1605 experiment

7.1.5.2. Predictive modelling

For predictive modelling a thermo-poroelastic model was applied. EDZ was not defined in the model. Gravity was not considered in the model and constant initial stresses were applied. Material properties are summarized in Table 7.1. Cox permeability assumed to be constant. Modelled domain was discretized into 11194 triangular mesh elements, the simulation ran for 37 min, 21 s.
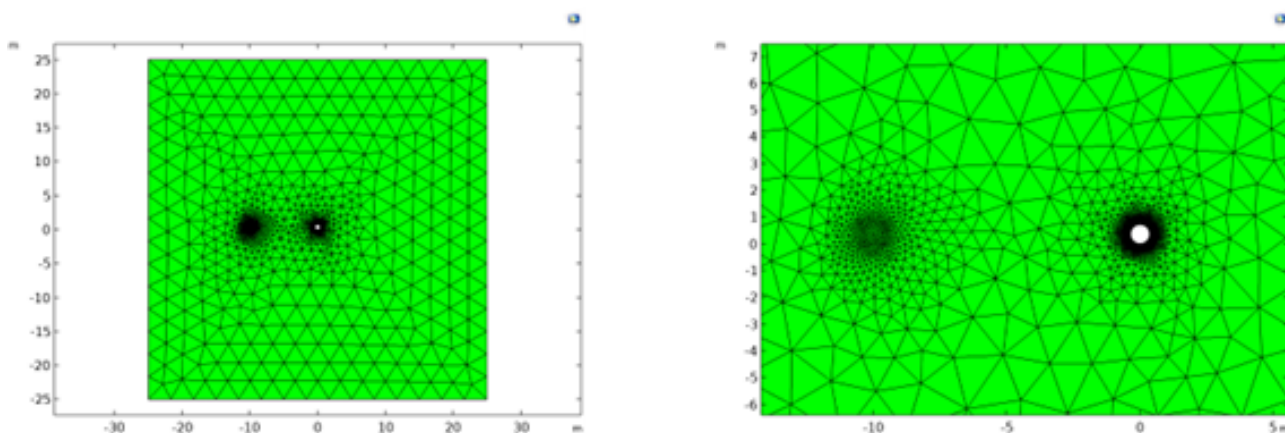
Figure 7.37: Mesh of a) whole model domain, b) mesh close to tunnels

The material properties for steel liner were set exactly according to the specification, the THM related properties of MREA filling (between casing and Cox) were compiled considering the information provided in the specification with some assumptions if not provided. Material properties are presented in Table 7.9. MREA in general described as highly porous and permeable material which do not have mechanical impact on Cox. Its primary purpose is to fill the void between steel casing and Cox to prevent direct contact of oxidising substances and clay-rock.

EURAD (Deliverable n˚ 7.6) – Modelling report on the effect of temperature on clay host rocks behaviour
Dissemination level: PU
Date of issue of this report: 06/06/2024

Page 208

Table 7.9: Main model parameters

Property	Steel	Cox	MREA
Solid density (kg/m^3)	7850	2690	2300
Bulk density (kg/m^3)		2205	345
Porosity (m^3/m^3)	-	0.18	0.85 (fresh)
Permeability (m^2)	-		
K$_{xx}$		3.9e-20	3e-15
K$_{yy}$		1.3e-20	3e-15
Young's modulus (MPa) E$_{iso}$ (Steel, MREA)	210000		20
E$_T$(Cox)		8000	
E$_A$(Cox)		5000	
Poisson's ratio ν_{iso} (Steel, MREA)	0.3		0.1
ν_{xy}		0.56	
ν_{yz}		0.35	
ν_{xz}		0.21	
Biot coefficient		0.8	1
Shear modulus G$_T$ (MPa)		2500	9.09
Thermal conductivity (W/m/K) λ_s (Steel, MREA)	80		0.989
λ_{sxx}(Cox)		1.88	
λ_{syy}(Cox)		1.22	
Linear thermal expansion coefficient α_s (1/K)	1e-5	1.25e-5	1e-5
Solid phase specific heat C$_{ps}$ (J/kg/K)	480	790	101

In this 50 m x 50 m 2D model gravity was not taken into account, thus initial stress and pore pressure were set constant, corresponding to the values at repository level (σh=12.4 MPa, σv=12.1 MPa, σH= 16.4 MPa and P=4.7 MPa). Temperature was set 21 °C on top of domain and increasing with depth considering the gradient 2 °C/50 m resulting in $\sim$ 22 °C at tunnel centre level.

Before the analysis of THM response of Cox at sensors located at difference distance around the ALC1605 micro-tunnel, modelled casing temperature was compared with measured temperature. 2D model geometry intend to represent the middle section of heater (tunnel centre coordinates reflect this taking into consideration tunnel inclination). For the comparison the sensor located in the middle of heating section ALC1605_TEM004 was chosen. Modelling results are presented in Figure 7.38

As could be seen the modelling results overpredict temperature on the casing inner part significantly. In nature heat is transferred in 3 directions thus with 2D geometry the heat flow in third direction is not modelled. Besides in the real system (experiment) there is some heat loss due to convective heat flow in the section between heater and tunnel entrance. Therefore, it was reasonable to assume some heat loss by reduction of heat flux. For subsequent analysis heat flux reduction by 20 percent was assumed. The difference in initial temperature could be related to different sensor location on casing perimeter compared to model point (0.391, 0.36) or unspecified heat flux before heating.

The first comparison of THM modelling results were focused on the nearest sensors located at similar distance from the tunnel (ALC1623_03 located in horizontal direction from micro tunnel and ALC1625_03 located in vertical direction from micro tunnel). The evolution of pore pressure in mentioned sensors is presented in Figure 7.39

As it could be seen from the Figure 7.39 modelled THM response reproduced general trend that the pore pressure is lower after tunnel excavation and did not restore to the in-situ pore pressure before the main

EURAD (Deliverable n˚ 7.6) – Modelling report on the effect of temperature on clay host rocks behaviour
Dissemination level: PU
Date of issue of this report: 06/06/2024

Page 209
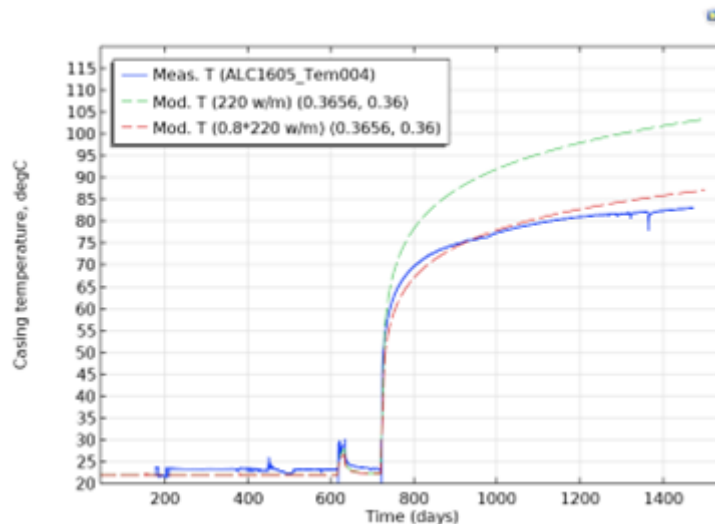
Figure 7.38: Modelled and measured temperature on casing inner wall with 220 W/m power and reduced heat power by 20 %
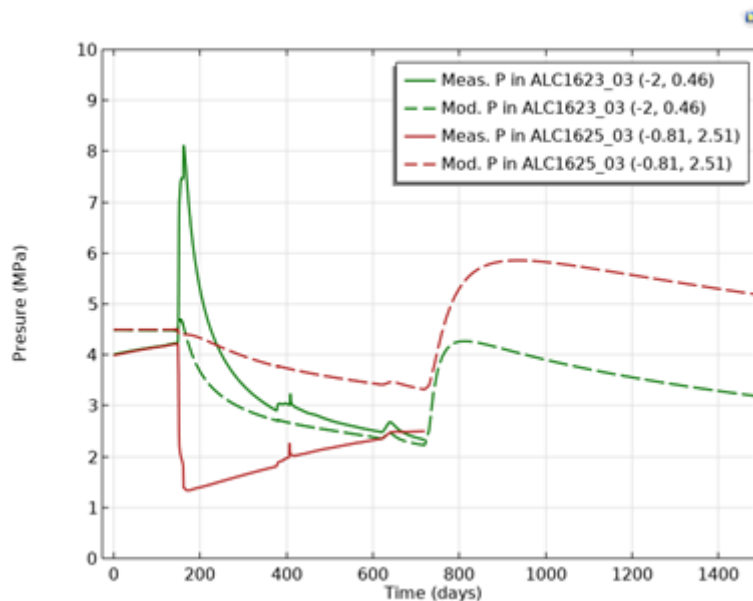
Figure 7.39: Modelled and measured pore pressure in closest sensors to tunnel in vertical (ALC1625_03) and horizontal direction (ALC1623_03)

heating starts. Pore pressure evolution measured by horizontally located sensor was captured well except instant peak of pore pressure shortly after excavation. At the same time pore pressure instant decrease in vertically located sensor was not capture by model. The pore pressure at this sensor point was over predicted by model by <1 MPa by the time heating to start.

7.1.5.3. Interpretative modelling

For interpretative modelling developed thermo-elastoplastic model was applied. Gravity was not considered in the model and constant initial stresses were applied. Parameters for elastoplastic model were taken from laboratory experiment modelling (Young modulus, initial yield stress, hardening parameter and their dependencies on temperature). The parameters derived from experiments with confining Pc=4 and 12 MPa were assigned for Cox clayrock. Strength anisotropy included by assuming that initial yield stress

EURAD (Deliverable n˚ 7.6) – Modelling report on the effect of temperature on clay host rocks behaviour
Dissemination level: PU
Date of issue of this report: 06/06/2024

Page 210

depends on the relative orientation between bedding and principal effective stresses following approach proposed by Manica (Mánica et al. (2022a)). The intrinsic permeability was defined as a function of volumetric and plastic deformations. Material properties are summarized in Table 7.9.

Modelling results of pore pressure evolution in the sensors closest to micro-tunnel are presented in Figure 7.40. As could be seen from the plots, predicted pore pressure evolution in those two sensors did not differ significantly from the results of thermo-poroelastic model. Predicted trends of evolution in time remained similar. Pore pressure evolution in the time period 300-600 days agreed better with measurement in horizontal direction, meanwhile for sensor located vertical direction pressure before main heating was slightly higher than predicted by thermo-poroelastic model, but still overpredicted the measurements.
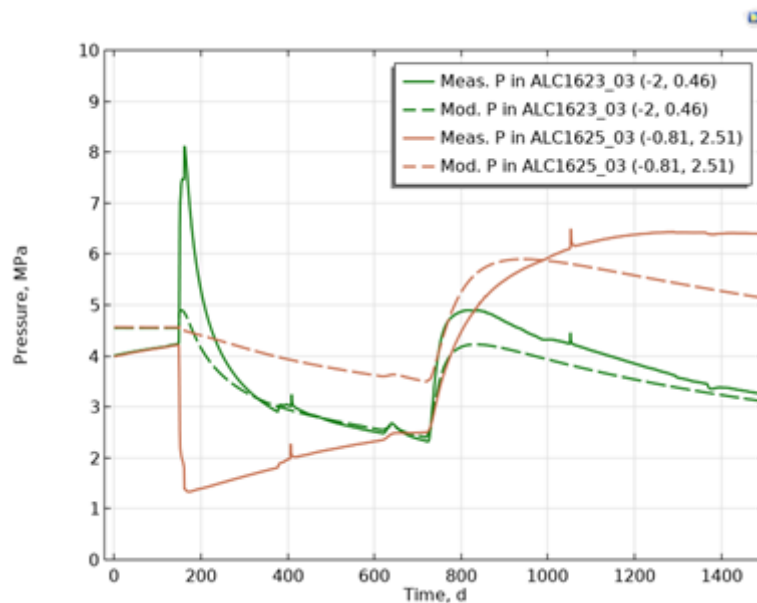
Figure 7.40: Interpretative modelling - Modelled and measured pore pressure in closest sensors to tunnel in vertical (ALC1625_03) and horizontal direction (ALC1623_03)

Therefore, following modifications were done to improve model response. Due to excavation around the micro tunnel mechanically disturbed zone could form. Following Andra information about ZFD zone extension the excavation disturbed zone was defined in the model with dimensions $1.3R_{tunnel}$ (in vertical direction) and $1.8R_{tunnel}$ (in horizontal direction) based on EDZ dimensions in Armand et al. (2014). Model parameter derived from experiment with confining pressure Pc=0 MPa were assigned to EDZ. Another intrinsic permeability was assigned for EDZ and Cox. Thermal conductivity was also assigned a new value based on Tourchi et al. (2021). Modelled domain was discretized into 14773 triangular mesh elements, the simulation run for 1 h 12 min.

Modelled temperature at casing wall (horizontal point) was compared to the sensor located in the middle of heating section (ALC1605_TEM004) (Figure 7.42). As it could be seen the modelled temperature agreed well with measurements initially, but starts to overpredict by the end of simulation. It is believed that this is mainly driven by 2D approximation of heat transfer process occurring in all 3 directions in reality.

Comparison of temperature evolution at the sensors located vertically and horizontally from ALC1605 tunnel confirmed anisotropic temperature distribution. Heat is transferred faster in horizontal direction. However, the maximum temperature value which was achieved by the end of simulation, overpredicted the measured values by ca. 5 °C. The difference was higher for the sensors located closer to the heating section.

EURAD (Deliverable n° 7.6) – Modelling report on the effect of temperature on clay host rocks behaviour
Dissemination level: PU
Date of issue of this report: 06/06/2024

Page 211
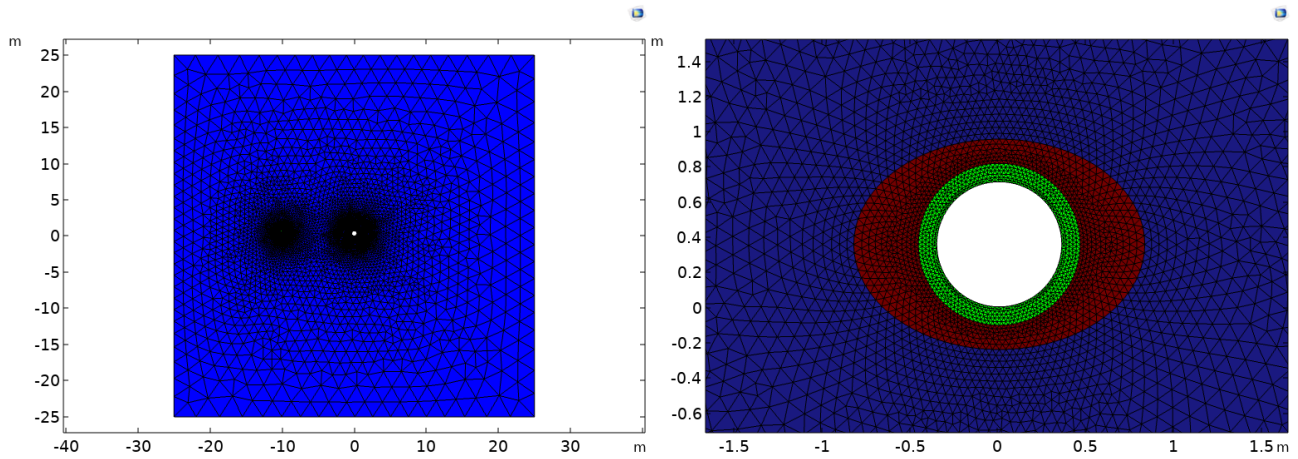
Figure 7.41: Mesh of a) whole model domain, b) mesh close to tunnel ALC1605
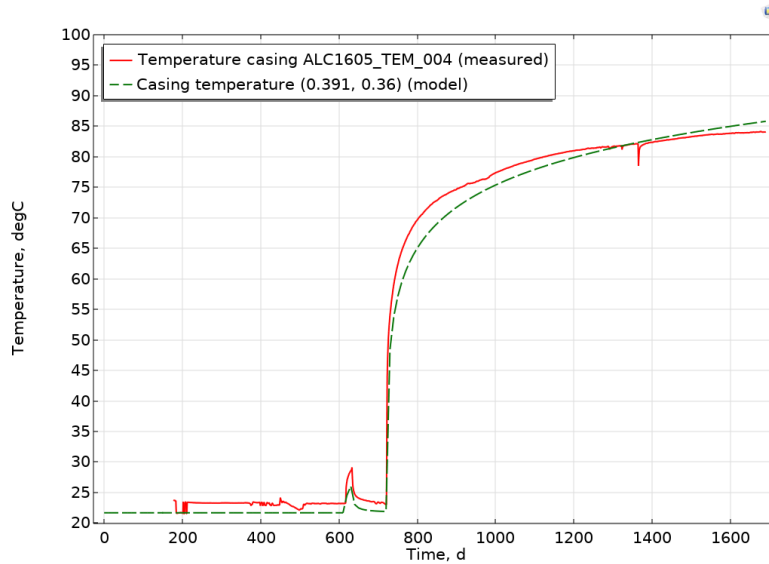
Figure 7.42: Measured and modelled temperature of casing
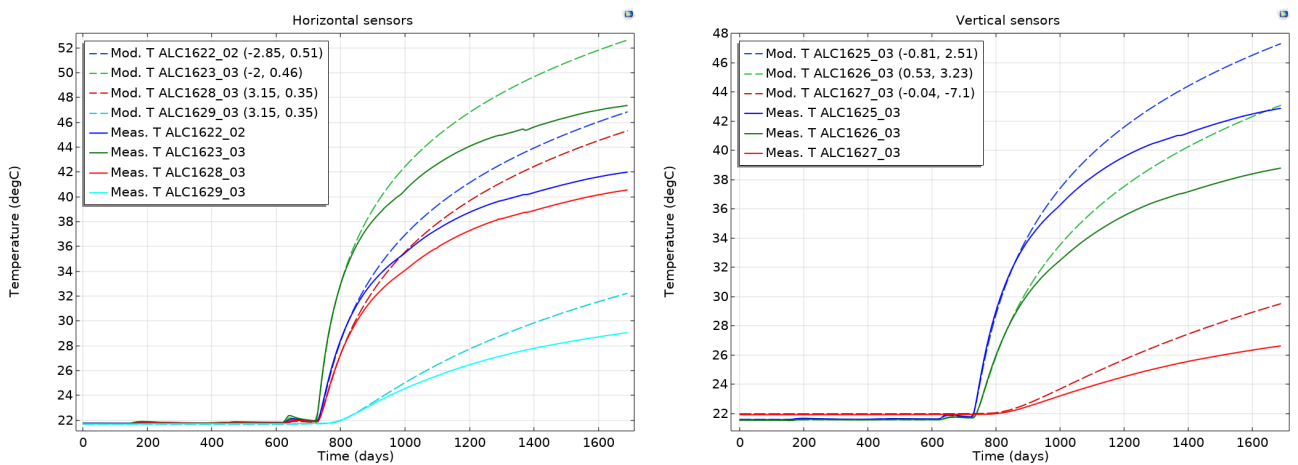
Figure 7.43: Measured and modelled temperature at sensors located at different distance in a) horizontal and b) vertical direction from ALC1605 tunnel

EURAD (Deliverable n˚ 7.6) – Modelling report on the effect of temperature on clay host rocks behaviour
Dissemination level: PU
Date of issue of this report: 06/06/2024

Page 212

Table 7.10: Main model parameters

Property	Steel	Cox	EDZ	MREA
Solid density (kg/m^3)	7850	2690	2690	2300
Bulk density (kg/m^3)		2205	2205	345
Porosity (m^3/m^3)	-	0.18	0.18	0.85 (fresh)
Permeability (m^2)	-			
K_{xx}		3.9e-20	1.7e-20	3e-15
K_{yy}		1.3e-20	0.6e-20	3e-15
Young's modulus (MPa) E_{iso} (Steel, MREA)	210000			20
E_T(Cox)		8864	8864 $\downarrow$ 2579 over 1d	
E_A(Cox)		5619	5619 $\downarrow$ 2386 over 1d	
Poisson's ratio ν_{iso} (Steel, MREA)	0.3		0.1	
ν_{xy}		0.56	0.56	
ν_{yz}		0.35	0.35	
ν_{xz}		0.21	0.21	
Biot coefficient		0.8	0.8	1
Shear modulus G_T (MPa)		2500	2500	9.09
Thermal conductivity (W/m/K) λ_s (Steel, MREA)	80			0.989
λ_{sxx}(Cox)		1.88 (2.05*)	2.05	
λ_{syy}(Cox)		1.22 (1.33*)	1.33	
Linear thermal expansion coefficient α_s (1/K)	1e-5	1.25e-5	1.25e-5	1e-5
Solid phase specific heat C_{ps} (J/kg/K)	480	790	790	101
Parameter for the variation of cohesion with the loading direction Ω_{90}	-	1.3	1.3	-
Parameter for the variation of cohesion with the loading direction Ω_m	-	0.819	0.819	-
Parameter for the variation of cohesion with the loading direction δ_m	-	49.7	49.7	-
Parameter for the variation of cohesion with the loading direction n	-	0.1	0.1	-
Plastic parameters	-	$\beta = 45$, h=f(T), σ_{y0} = const	$\beta = 45$, h=f(T), σ_{y0} = f(T)	-

* Value for simulation with EDZ.

EURAD (Deliverable n° 7.6) – Modelling report on the effect of temperature on clay host rocks behaviour
Dissemination level: PU
Date of issue of this report: 06/06/2024

Page 213

Results presenting pore pressure evolution at sensors are presented in Figure 7.44 and Figure 7.45. As it could be seen from figure, the pore pressure evolution was not isotropic. Modelled pore pressure evolution at horizontally located sensors (ALC1622_02, ALC1623_03 ALC1628_03) reasonably represented decreasing trend in pressure before the main heating phase (except short-term peak after excavation). Slightly higher increase in pore pressure (sensor ALC1623_03) right after excavation was observed with consideration of EDZ, but absolute magnitude of this initial peak still did not match the experimental measurements. Based on the measurements the magnitude of this initial peak was lower for sensors located further away from the tunnel and this trend was captured in model output.

According to measurements during waiting phase the pore pressure was not yet recovered to the initial pressure. The model also showed this trend. During short and the main heating phase the clay-rock response was observed and pore water increase was captured. The following decreasing trend was observed in modelling results too. Decreasing pore pressure profiles also indicates that tunnel is draining as the heating was still ongoing.
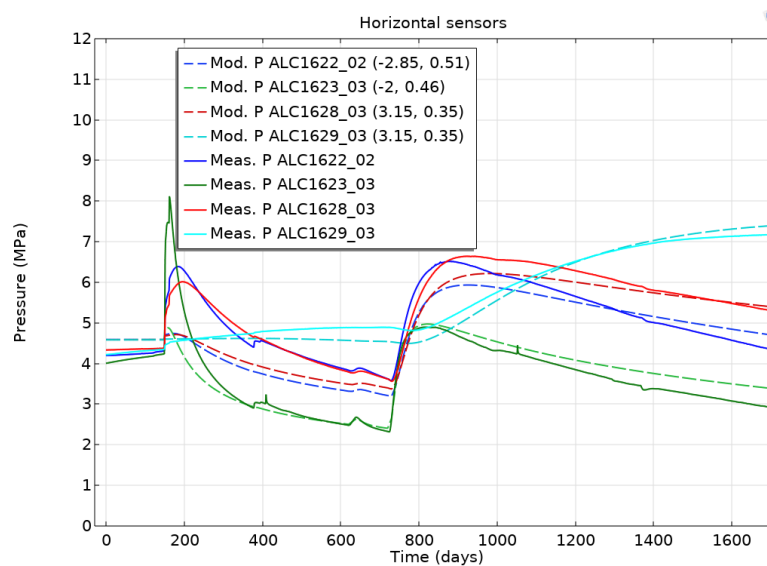
Figure 7.44: Measured and modelled pore pressure at sensors located at different distance in horizontal direction from ALC1605 tunnel

As presented in figure above modelled maximum pore pressure during main heating matched the measured value in sensor ALC1623_03, but in other horizontally located sensors maximum pore pressure is slightly underestimated (by $\sim 0.6 - 0.7$ MPa or $8 - 11\%$). Meanwhile in the longer-term model tend to overestimate the pore pressure in these sensors.

Meanwhile for vertically located sensors modelling results showed maximum pore pressure similar to that of measured in closer sensors (ALC1625_03, ALC1626_03) (difference by ~ 0.4 MPa or $\sim 6 - 7\%$), but more overestimated for further sensor ALC 1627_03 (difference ~ 1.1 MPa or $\sim 18\%$).

After comparison of modelling results and in-situ measurement it was concluded that simulations did not capture well the pore pressure evolution in vertical direction. It could be partly inherited from overestimated temperature, also the assumption of ideally draining conditions on tunnel boundary could had impact on model results.

Taking this into consideration, it could be concluded that current model formulation needs to be improved to represent better THM response in Cox clay-rock.

EURAD (Deliverable n° 7.6) – Modelling report on the effect of temperature on clay host rocks behaviour
Dissemination level: PU
Date of issue of this report: 06/06/2024

Page 214
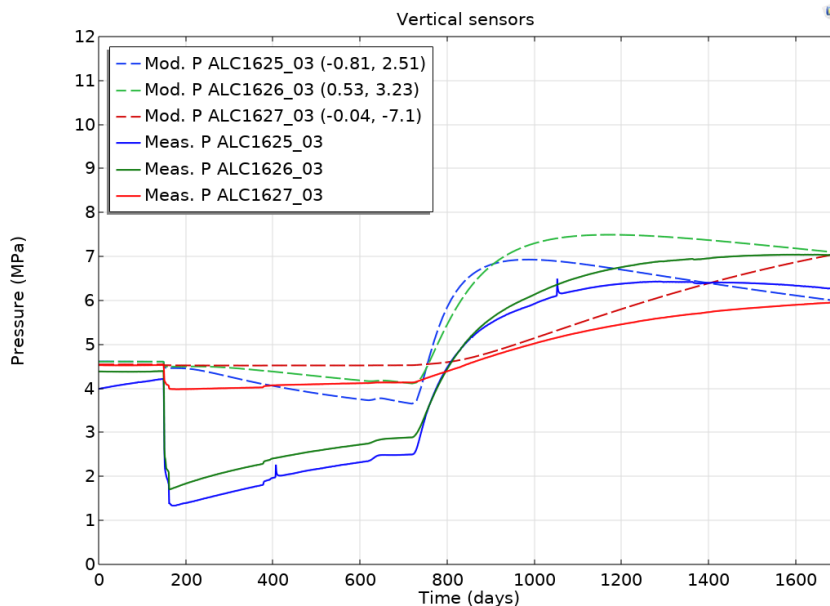
Figure 7.45: Measured and modelled pore pressure at sensors located at different distance in vertical direction from ALC1605 tunnel

7.1.6. ULg

The modelling of ALC1605 test focuses on the thermal effect on the THM behaviour of Cox claystone in the near-field and far-field. It is divided into two phases: predictive modelling and interpretative modelling. A 2D plane strain problem was considered to model the in-situ heater test. To evaluate the impact of two neighboring cells in the experiment due to their relative proximity (AHA1605 and HAE1602), the full cells were taken into account in the predictive modelling. The 2D model is a transversal section located at the mid-plane of the heated zone, the centre of the cell is at (-17.26, 0.01, 0.36) in the local coordinate system. It should extend over 50m in two directions in the plane (see Figure 7.46). The proposed mesh contains 26256 nodes and 8856 elements. The refinement of mesh was considered close to the ALC1605 cell to better reproduce the observation of in-situ measurement.
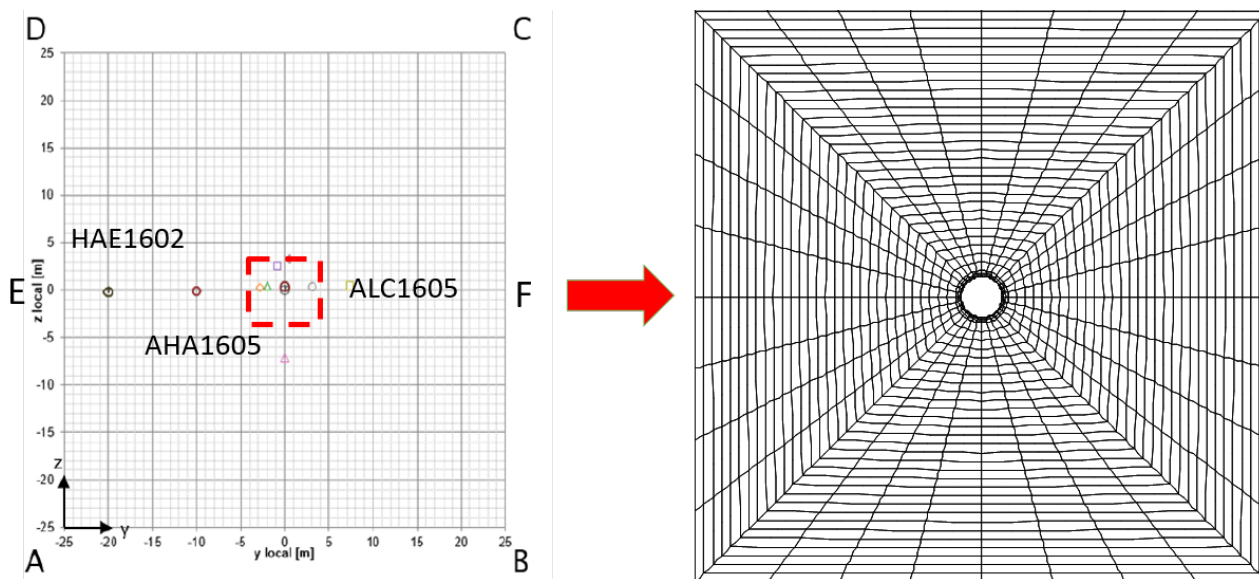
Figure 7.46: Proposed geometry for the ALC1605 2D model

EURAD (Deliverable n˚ 7.6) – Modelling report on the effect of temperature on clay host rocks behaviour
Dissemination level: PU
Date of issue of this report: 06/06/2024

Page 215

A sensitivity analysis was performed with or without two neighboring cells to check their influence on the pore pressure evolution, showing that the impact of the two neighboring cells could be ignored. The other numerical issue is the modelling of the cemented casing. To model the injection of MREA material after the excavation of the cell, a soft material was introduced before the excavation of the cell so as not to limit the convergence of the tunnel. Hence there are four phases defined in the proposed 2D model, each step is modelled by the adaptation of the boundary condition of ALC1605 casing (see in Figure 7.48). In the first step, the excavation of GAN drift is not able to be modeled in 2D. However, the pore pressure redistribution induced by the excavation of GAN drift could be taken into account according to the in-situ measurement of pore pressure. Figure 7.47 gives the Pore pressure profile around the GAN drift before the excavation of ALC1605, in which the pore pressure located at the mid-plane is highlighted in a red rectangle. Therefore the pore pressure decreased linearly from 4.7 MPa at CD and AB to 4.3 MPa at EF in this step, the pore pressure of steel and soft material were fixed with 0 MPa and 0.1 MPa respectively. The excavation of ALC1605 was modelled in the second step. A stress release technique was used to model the excavation of the ALC1605 cell. At the tunnel wall, the in-situ stress decreased linearly from initial value to 0 MPa, and the pore pressure decreased from 4.3 MPa to atmospheric pressure. The pore pressure of steel and soft material kept constant as the first step. In the third step, to model the injection of MREA material, the properties of the soft material were replaced by the properties of MREA. The pore pressure of MREA was released, and a drained boundary was introduced at the extrados of steel. Finally, constant thermal power was imposed at the intrados of steel. The temperature of the full field was released.
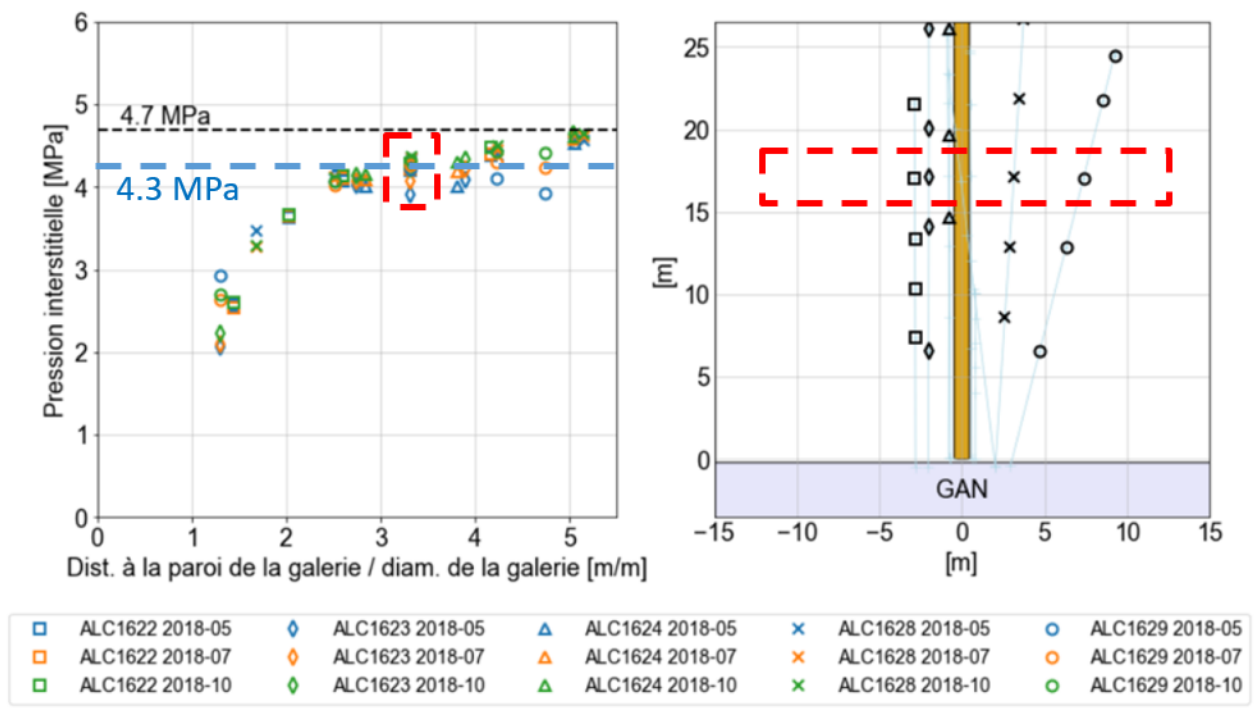
Figure 7.47: Pore pressure profile around the GAN drift before the excavation of ALC1605.

In the predictive modelling, the property of steel is modelled in elasticity, which is defined in Table 7.11. The Cox claystone and MREA injection material were modelled by the elastoplastic consitutive law ORTHOPLA in LAGAMINE code. The parameters for Cox claystone are shown in Table 5.2, and the parameters of MREA is defined in Table 7.12. The start date of the computation is the beginning of the excavation of GAN drift, and the solid and dash lines correspond to the numerical prediction and experimental measurement respectively (same for the following figures). As a first step, the hydraulic boundary condition between the GAN drift and ALC1605 cell (at the extrados of steel) was discussed.

Figure 7.49 shows the temperature and pore pressure evolution with undrained boundary conditions. Both

EURAD (Deliverable n˚ 7.6) – Modelling report on the effect of temperature on clay host rocks behaviour
Dissemination level: PU
Date of issue of this report: 06/06/2024

Page 216
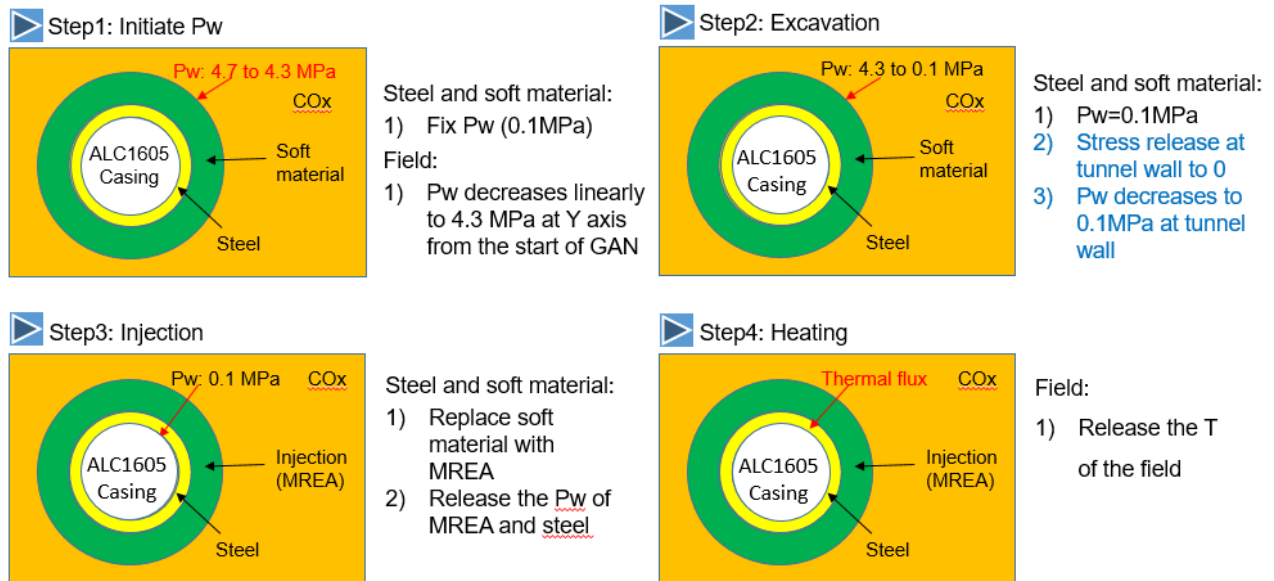
Figure 7.48: The adaptation of the boundary of ALC1605 casing.

Table 7.11: Main parameters for steel

Symbol	Name	Value	Unit
ρ	density	7850	kg/m^3
E	Young's modulus	210	GPa
ν	Poisson's ratio	0.3	-
λ	Thermal conductivity	54	W/m/K
C_p	specific heat	480	J/kg/K
α	thermal dilation	$1E^{-5}$	1/K

the temperature and pore pressure are overestimated. A decrease in temperature and pore pressure was observed from the experimental measurement due to 3D effect, whereas it is unable to be reproduced in our 2D modelling. If a drained boundary is considered in Figure 7.50, the temperature is still overestimated, which is mainly dependent on the intensity of thermal power input and thermal conductivity of the host rock. However, a better agreement of the pore pressure evolution between the numerical prediction and experimental measurement is obtained. In addition, the overpressure at the end of the excavation could not be captured.

EURAD (Deliverable n˚ 7.6) – Modelling report on the effect of temperature on clay host rocks behaviour
Dissemination level: PU
Date of issue of this report: 06/06/2024

Page 217

Table 7.12: Main parameters for MREA

Symbol	Name	Value	Unit
ρ	density	1154	kg/m^3
ϕ	Porosity	0.8	-
E	Young's modulus	50	MPa
ν	Poisson's ratio	0.3	-
k	Permeability	3.32E^{-15}	m^2
λ	Thermal conductivity	0.73	W/m/K
C$_p$	specific heat	2640	J/kg/K
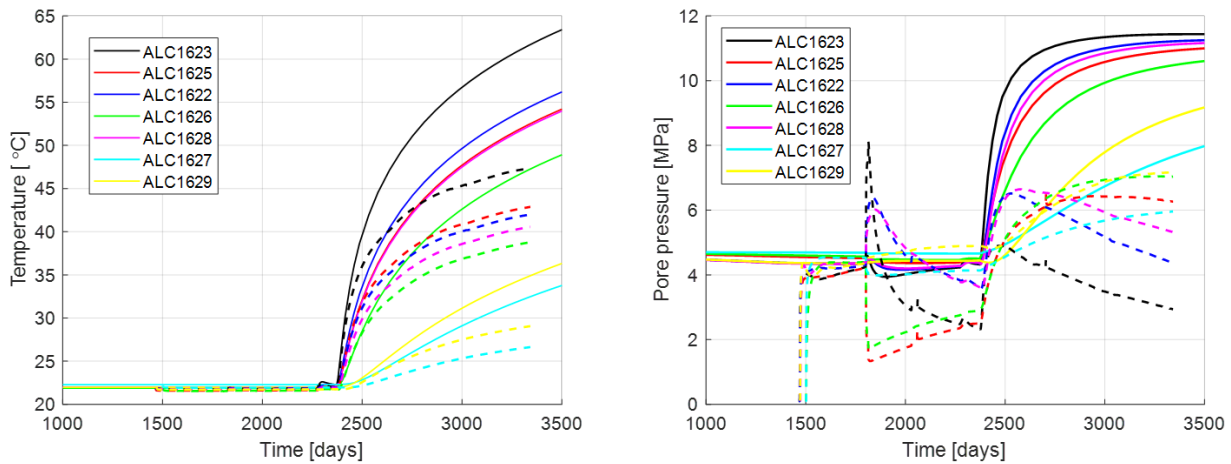
Figure 7.49: Temperature evolution with undrained boundary condition (Solid lines: Numerical; Dash lines: Experimental)
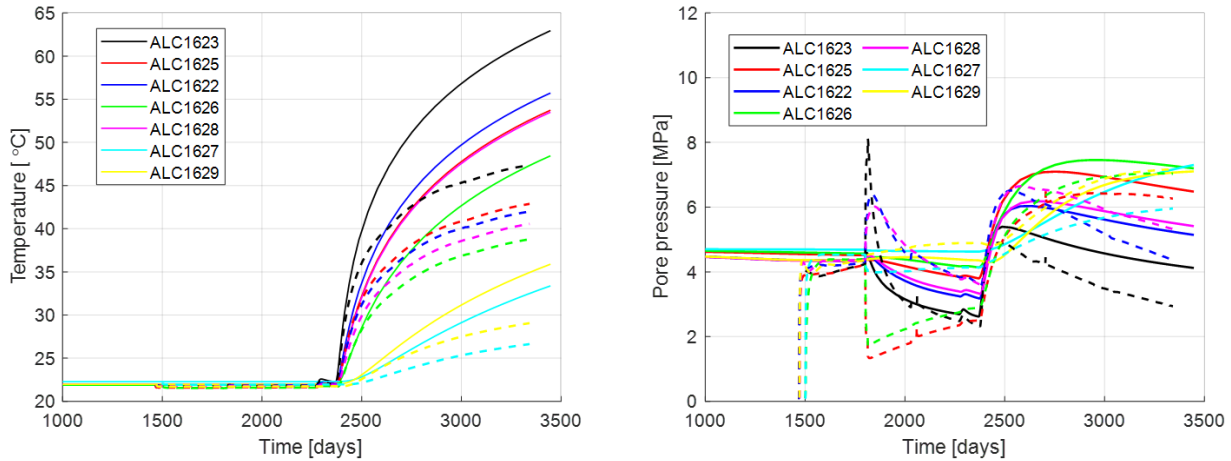
Figure 7.50: Pore pressure evolution with drained boundary condition (Solid lines: Numerical; Dash lines: Experimental)

In interpretative modelling, lower power input under drained boundary condition were taken into account due to the overestimation of temperature in the predictive modelling. The in-situ heater test refers to a 3D problem, hence the power input should be adapted in 2D problem. Considering a higher thermal conductivity value in the direction out of plane, and 10% power loss prescribed in the specification, 2/3 of full power input was introduced in interpretative modelling during the heating. Figure 7.51 shows the temper-

EURAD (Deliverable n˚ 7.6) – Modelling report on the effect of temperature on clay host rocks behaviour
Dissemination level: PU
Date of issue of this report: 06/06/2024

Page 218

ature evolution with 2/3 of power input, a better agreement was observed for most of the measurements. To model the evolution of the temperature, the impact of the thermal conductivity of the host rock was analyzed. Figure 7.52 shows the temperature evolution with different thermal conductivities compared to the values defined in Table 5.2. For 2D problem, it is difficult to perfectly capture the evolution of temperature both at the start and end of the heating phase. Although the dissipation of thermal power in 3D case is challenging for 2D modelling, the initial values of thermal conductivities are sufficient to reproduce the temperature profile of the in-situ measurements. The evolution of pore pressure is drawn in Figure 7.53, in which the pore pressure is well reproduced in some measurements during the heating. The pore pressure in the horizontal direction is better reproduced than in the vertical direction. In fact, the over pressure was not pronounced in the numerical prediction, whether during the heating or at the end of the excavation phase.
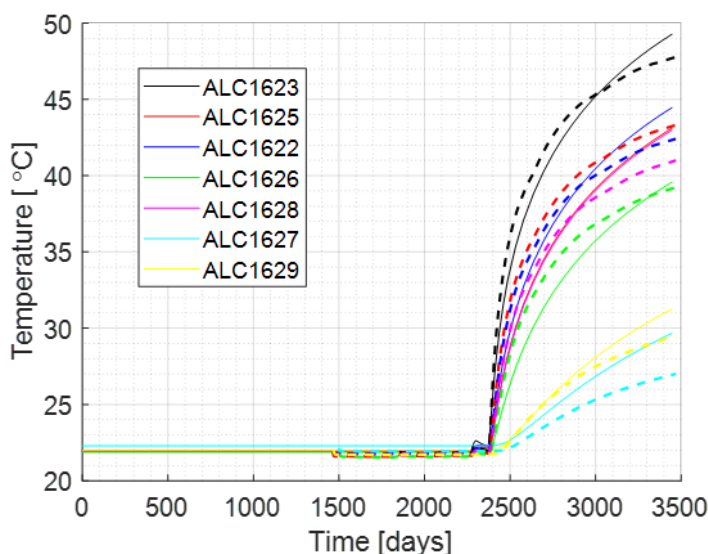
Figure 7.51: Temperature evolution with 2/3 power input under drained boundary condition
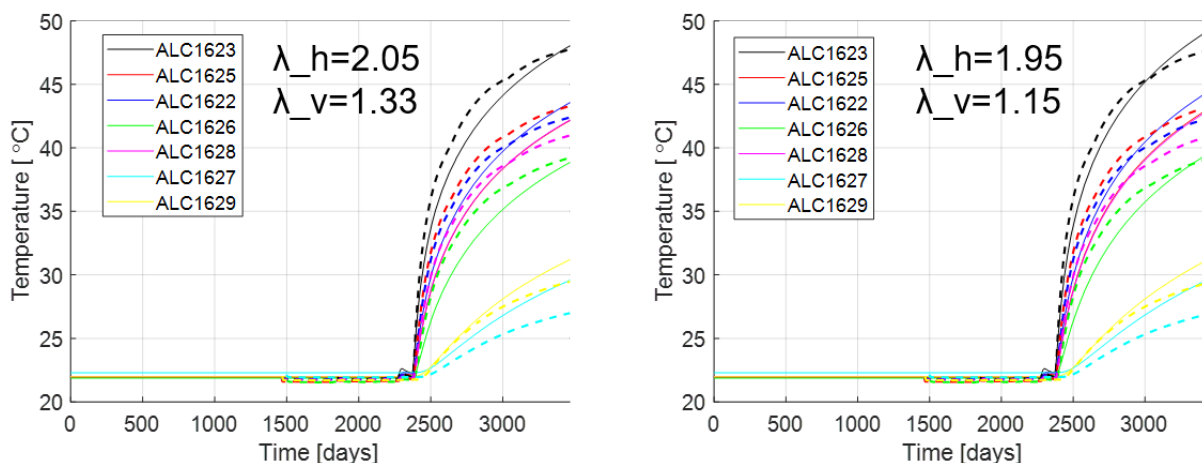
Figure 7.52: Temperature evolution with different thermal conductivities

EURAD (Deliverable n˚ 7.6) – Modelling report on the effect of temperature on clay host rocks behaviour
Dissemination level: PU
Date of issue of this report: 06/06/2024

Page 219
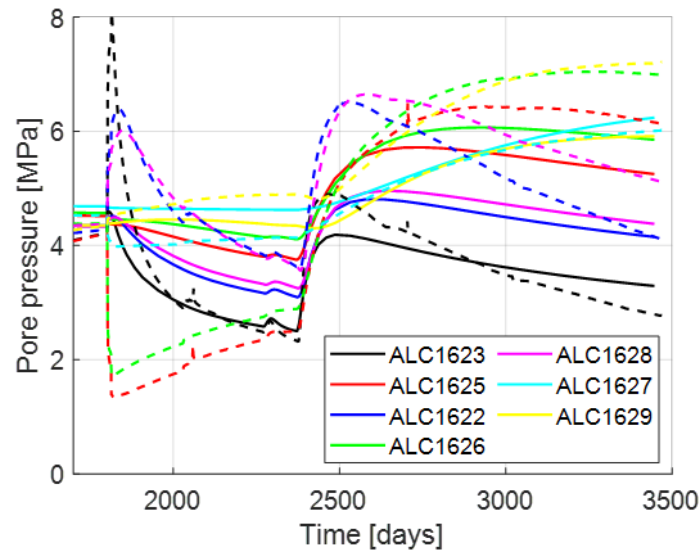
Figure 7.53: Pore pressure evolution with 2/3 power input under drained boundary condition

To reproduce the overpressure observed from the experimental test, an artificial elliptical EDZ with the horizontal radius equals to 1.38 m was introduced in the modelling. The modified properties of the host rock in the EDZ are defined in Table 7.13. The Young's moduli decrease 10 times in the bedding and normal to the bedding, and an increase of 1000 times of intrinsic permeabilities was also introduced in the EDZ. The general idea is to reproduce the over pressure at the boundary of the EDZ induced by the anisotropy.

Table 7.13: Modified properties in the EDZ

Symbol	Name	Value	Unit
$E_\parallel$	Young's modulus parallel to bedding	800	MPa
$E_\perp$	Young's modulus normal to bedding	500	MPa
$k_\parallel$	Intrinsic permeability parallel to bedding	$3.9E^{-17}$	m^2
$k_\perp$	Intrinsic permeability normal to bedding	$1.3E^{-17}$	m^2

Figure 7.54 shows the profile of pore pressure and its distribution after the excavation of the cell. Compared to the simulation without EDZ, the pore pressure of ALC1623 at the end of the excavation increased from 4.3 MPa to 5.5 MPa, which indicated that the introduction of the EDZ was helpful in reproducing the pressurization process. The over pressure zone was highlighted in the horizontal direction, and the maximum value of the pore pressure around the cell is around 6.6 MPa. In fact, to reproduce the over pressure at the measurements is also strongly dependent on the size of the EDZ, and our objective is to make the over pressure zone approach to the measurements numerically. However, much lower pore pressure was observed during the heating phase when there was an EDZ defined, a minimum value of 1.5 MPa was captured at the measurement ALC1623, which should be related to the large permeability close to the drained boundary.

EURAD (Deliverable n˚ 7.6) – Modelling report on the effect of temperature on clay host rocks behaviour
Dissemination level: PU
Date of issue of this report: 06/06/2024

Page 220
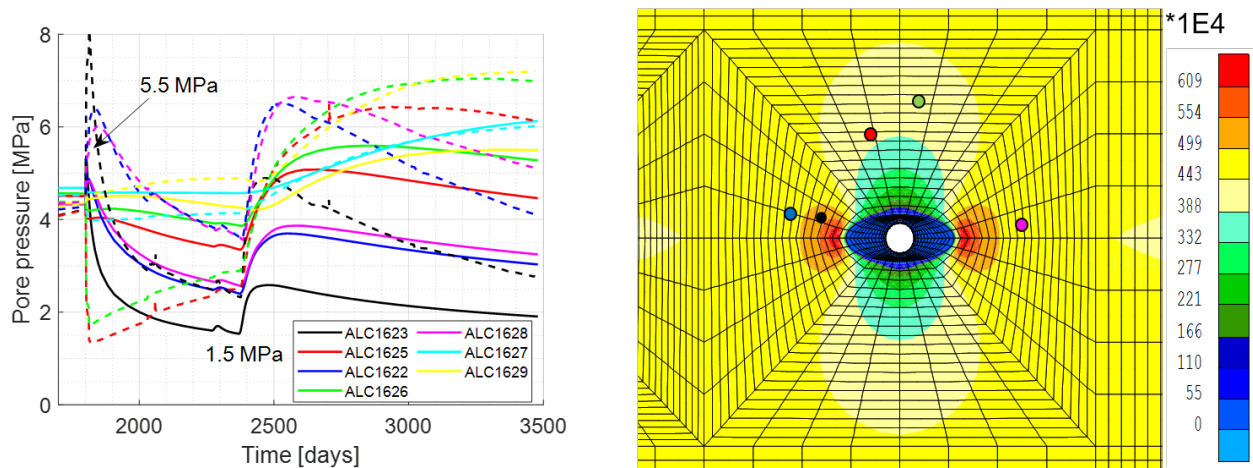
Figure 7.54: Pore pressure evolution and its distribution after the excavation of ALC1605 with an artificial EDZ

In conclusion, the thermal power loss should be taken into account in 2D problem. Although the pore pressure distribution induced by the excavation of GAN drift was considered at the first step of the modelling, the long-term impact from the GAN drift is complicated to model. The introduction of artificial EDZ can help to reproduce the over pressure around the boundary of the EDZ, but the pore pressure is underestimated during the heating phase.

7.1.7. Synthesis of results

Five teams took part in the modelling of the ALC1605 experiment: Andra, BGE, EDF in 3D and LEI and ULg in 2D. In order to compare the output from the different geometries, the responses of the sensors located in the plane at the middle of the heated zone are considered.

7.1.7.1. Predictive modelling

In the predictive modelling step, the teams used the parameters provided in the generic cases, or based on the ALC1604 experience (Tourchi et al., 2021).

The models capture well the anisotropic response of the Cox claystone, with a higher temperature parallel to bedding than perpendicular. However, almost all the teams tend to overestimate the temperature evolution (Figure 7.55). This is expected for the 2D models as plane strain conditions do not allow longitudinal fluid flow and heat flux.

EURAD (Deliverable n˚ 7.6) – Modelling report on the effect of temperature on clay host rocks behaviour
Dissemination level: PU
Date of issue of this report: 06/06/2024

Page 221
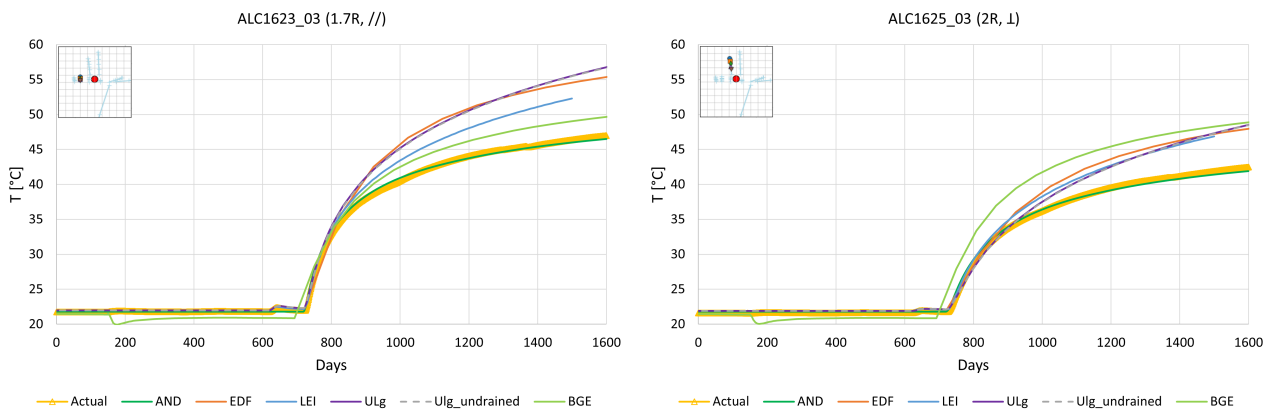
Figure 7.55: Temperature evolution at a distance of 2 cell radii, parallel to bedding (left) and perpendicular to bedding

The models also reproduce the anisotropic pressure response but fail to model the amplitude of the peaks observed in the near-field when excavating the ALC1605 microtunnel (at 162 days): at 2 radii distance from the tunnel, a pressure increase up to 8.1 MPa was recorded by the sensor located parallel to bedding and a pressure drop down to 1.4 MPa was seen perpendicular to bedding (Figure 7.56).
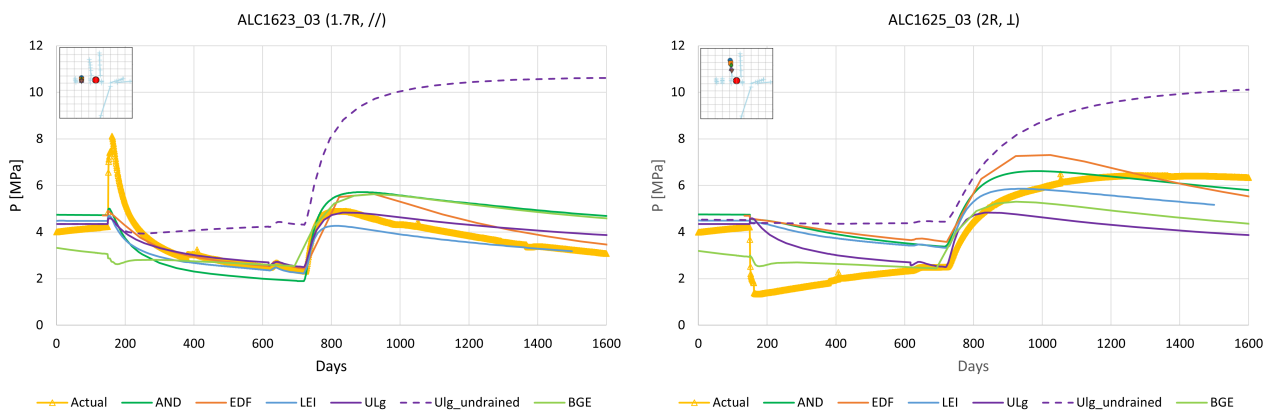
Figure 7.56: Pressure evolution at a distance of 2 cell radii, parallel to bedding (left) and perpendicular to bedding

The sensitivity study performed by ULg clearly shows that a better match is achieved if a drained boundary condition is considered (the undrained case is shown with the dashed purple lines on Figure 7.56).

7.1.7.2. Interpretative modelling

At the end the blind prediction step, the modellings teams got access to the temperature and pressure data at different distances from the cell.

After adjusting the mechanical and flow properties in the Cox and in the EDZ, most teams were able to get a better match on the temperature evolution in both direction. On Figure 7.57, comparison is made with the blind prediction results, shown with dashed lines.

EURAD (Deliverable n° 7.6) – Modelling report on the effect of temperature on clay host rocks behaviour
Dissemination level: PU
Date of issue of this report: 06/06/2024

Page 222
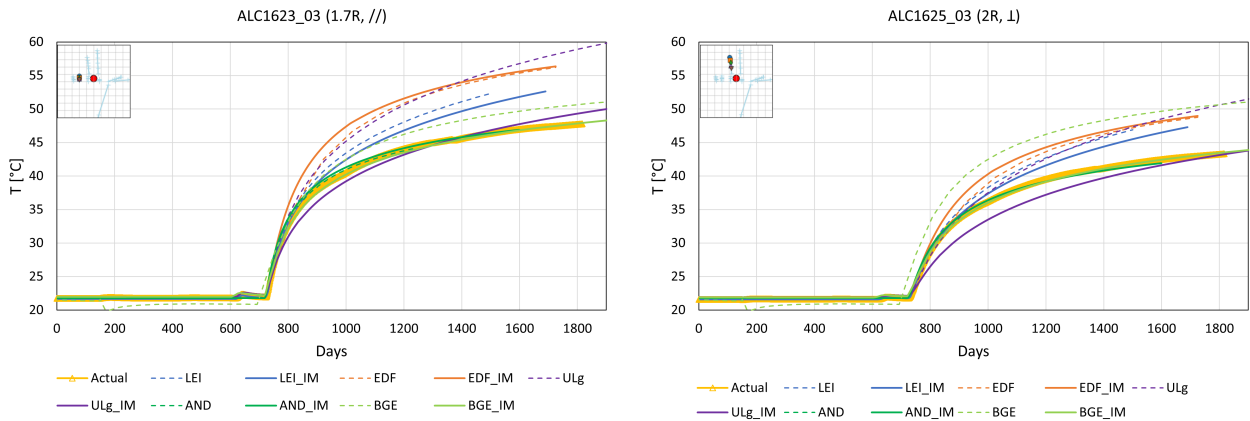
Figure 7.57: Interpretative modelling - Temperature evolution at a distance of 2 cell radii, parallel to bedding (left) and perpendicular to bedding (right). Blind prediction curves are displayed as dashed lines

For the pore pressure, however, no team still manages to properly model the evolution after the excavation, especially perpendicular to bedding (Figure 7.58, right).
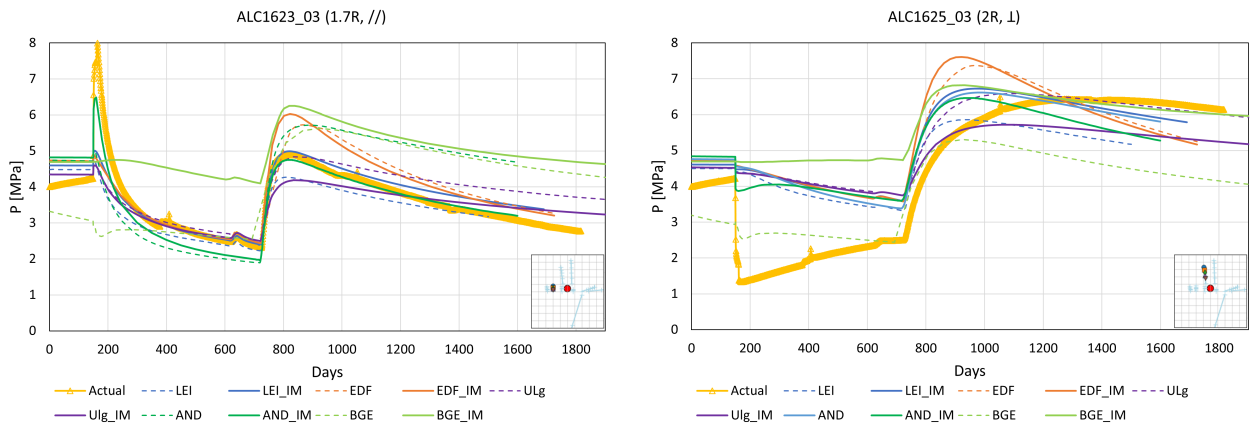
Figure 7.58: Interpretative modelling -Pressure evolution at a distance of 2 cell radii, parallel to bedding (left) and perpendicular to bedding (right). Blind prediction curves are displayed as dashed lines

This exercise actually confirms that the simple poro-elastic approach cannot model the behaviour of the Cox in the near-field. An elasto-visco-plastic approach may be necessary to take into account the presence of the EDZ and the evolution of permeability around the borehole with time. When looking at the evolution of temperature (Figure 7.59) further away from the borehole (7.5 radii away from the cell), all models match better the actual data.

EURAD (Deliverable n° 7.6) – Modelling report on the effect of temperature on clay host rocks behaviour
Dissemination level: PU
Date of issue of this report: 06/06/2024

Page 223
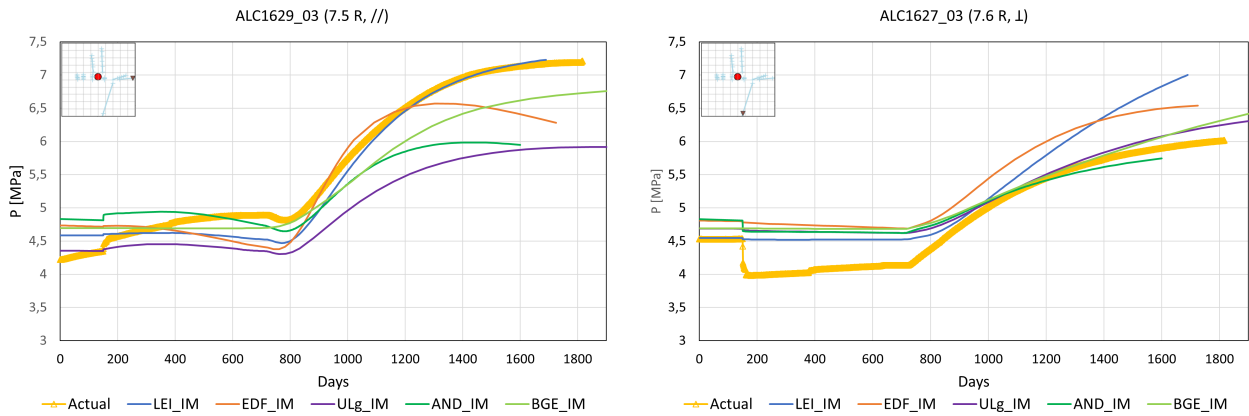
Figure 7.59: Temperature evolution at a distance of 7.5 cell radii, parallel to bedding (left) and perpendicular to bedding (right)

For the pore pressure, none of the models display the sharp pressure drop perpendicular to bedding after the excavation of the microtunnel and the slow increase in both direction during the waiting phase, from 150 days to the start of the heating period around 750 days (Figure 7.60).
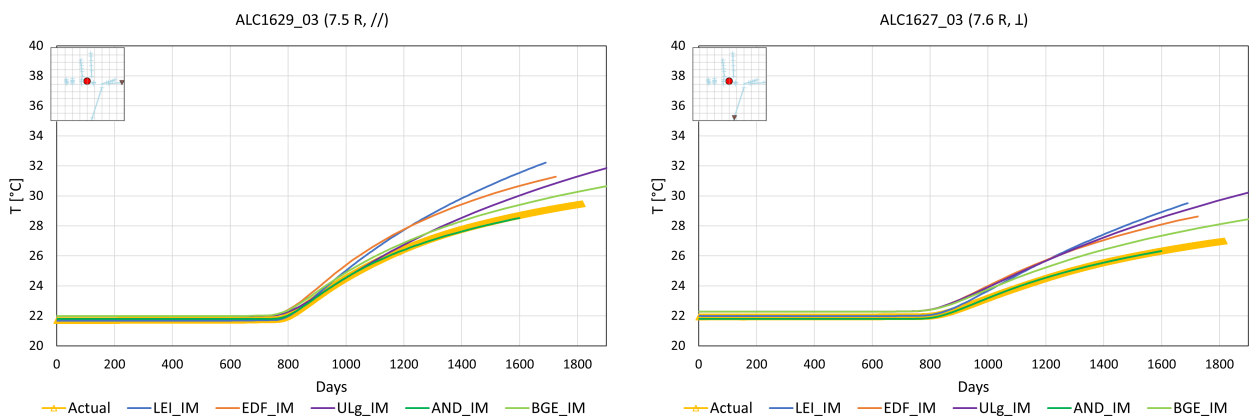
Figure 7.60: Pressure evolution at a distance of 7.5 cell radii, parallel to bedding (left) and perpendicular to bedding (right)

The thermal pressurisation plots on Figure 7.61 focus on the heating phase as the induced pressure variation is plotted against the temperature increase. One sees on the left plot that at a distance of 2 cell radii from the borehole wall, the results are very scattered, but a closer match is achieved at a distance of 7.5 radii (right plot). At this distance, all the models consistently underestimate the pressurisation in the perpendicular direction (dashed line), but most are close to reality in the parallel orientation.

EURAD (Deliverable n° 7.6) – Modelling report on the effect of temperature on clay host rocks behaviour
Dissemination level: PU
Date of issue of this report: 06/06/2024

Page 224
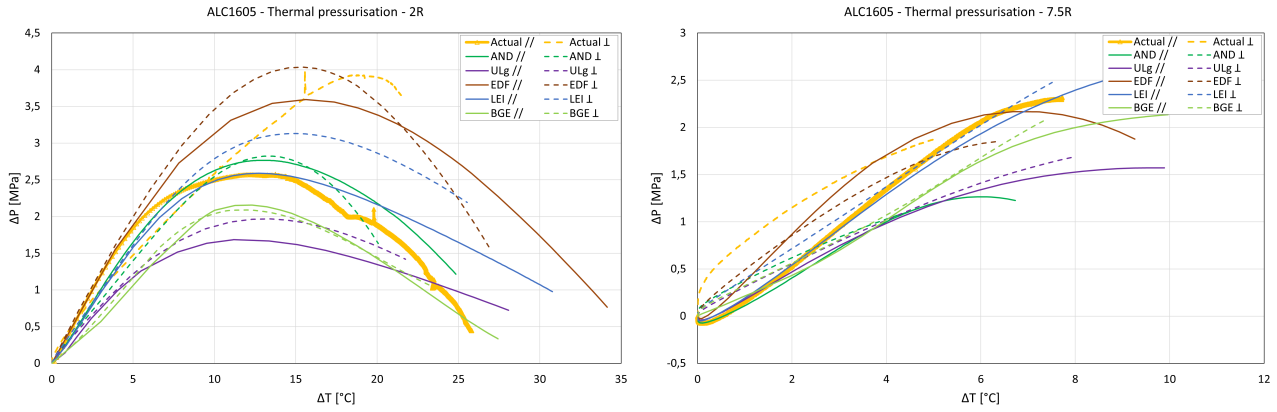
Figure 7.61: Pressure vs Temperature evolution during the heating phase at a distance of 2 cell radii (left) and 7 cell radii (right)

7.1.7.3. Conclusion

This exercise showed that the simple poroelastic approach cannot account for the complex processes occuring in the near-field when excavating the micro-tunnels. All the teams underestimated the anisotropic impact of the cell excavation on the pore pressure. A better match is however achieved in the sensors located further away from the boreholes.

Plane strain conditions do not allow longitudinal fluid flow and heat flux for the teams using 2D models. As a result, these teams overestimated the temperature and pore pressure evolution when heating. The 3D models give generally a better response, especially in the far field.

EURAD (Deliverable n˚ 7.6) – Modelling report on the effect of temperature on clay host rocks behaviour
Dissemination level: PU
Date of issue of this report: 06/06/2024

Page 225

7.2. Large scale in situ PRACLAY Heater test

7.2.1. Introduction to the large scale in situ Heater test

In the frame of RD&D on the geological disposal of radioactive waste in Belgium, the large-scale PRACLAY Heater test is being carried out in the HADES underground research laboratory (URL) in Mol (Belgium) by the ESV EURIDICE GIE. The large-scale PRACLAY Heater test aims at examining, at a scale and in conditions that are representative for a real repository, the combined impact of hydro-mechanical disturbances caused by the gallery construction and a large-scale thermal load on the Boom Clay due to the disposal of heat emitting high-level waste in deep clay formation. The large-scale heater test will confirm or deny that the clay can sustain elevation of temperature in the near-field, or in the excavation damaged zone, and in the far field without any loss of its favourable properties for the geological disposal of radioactive waste.

The HADES underground research laboratory was built at a depth of approximately 225 m in the Boom Clay Formation which is one of the potential host formation studied for the disposal of nuclear waste in deep geological formation. This sedimentary clay formation characterised as poorly indurated clay presents favourable properties such as a very low permeability, self-sealing properties and a high retention capacity of radionuclides. The construction of the laboratory started beginning the eighties and after several stages of extension, the PRACLAY gallery, hosting the large scale heater test, was excavated in 2007 (Figure 7.62).
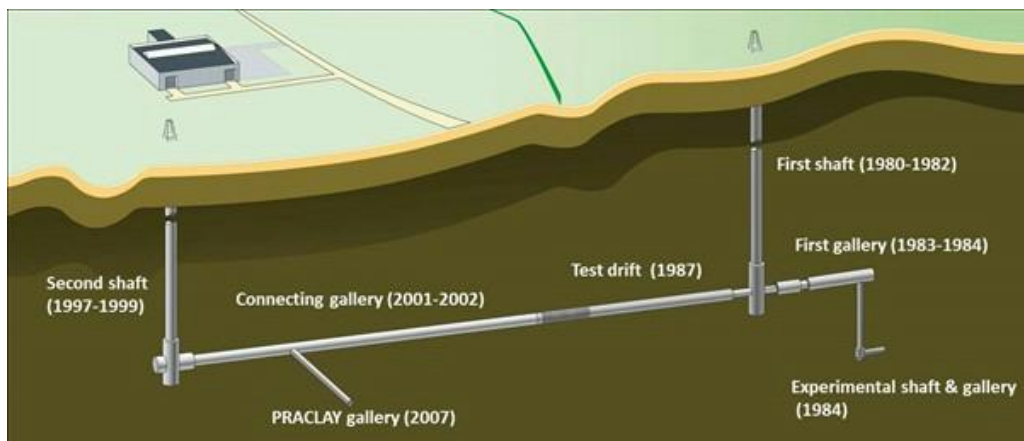
Figure 7.62: Layout of the underground laboratory at Mol, Belgium (EURIDICE website, 2018)

This section describes the benchmark exercise in the framework of the EURAD WP HITEC. After the presentation of the main stages of the PRACLAY Heater tests a set of modelling is described. Two main modelling cases are proposed in this exercise. The first one consists in an "academic version" of the PRACLAY Heater test while the second case corresponds to a free case where the modelling team is free to choose the constitutive law. In all cases, it is proposed to model the experiment from the beginning of the excavation to the on-going running heater test.

7.2.2. Experimental set-up and main steps of the PRACLAY Heater test

The PRACLAY gallery was constructed perpendicular to the existing Connecting gallery from October 4, 2007 to November 6, 2007. Figure 7.63 shows the general layout of the test setup of the PRACLAY heater test, and a brief introduction about the geometry and materials of the test setup is here presented. More information can be found at Van Marcke, P., Li, X.L., Bastiaens, W., Verstricht, J., Chen, G., Leysen, J., and Rypens, J. (2013). The gallery is 45 m long with an external diameter of 2.5m. The gallery is supported by 81 concrete lining rings (Ring 1-Ring 81) with a thickness of 0.3m and a length of 0.5 m. Most of the rings

EURAD (Deliverable n° 7.6) – Modelling report on the effect of temperature on clay host rocks behaviour
Dissemination level: PU
Date of issue of this report: 06/06/2024

Page 226

have a concrete grade of C80/95. Each ring mainly consists of 8 normal segments (S1-S8) and one key segment S9. At the end of the PRACLAY gallery, C30/37 concrete was poured over a length of 2m to form the end-plug. The diameter of this plug is slightly larger than the rest of the gallery. The steel structure of the tunneling shield, made in carbon steel, was left in place to support the 2.5 m-long gallery between the concrete lining Ring 81 and the end plug.
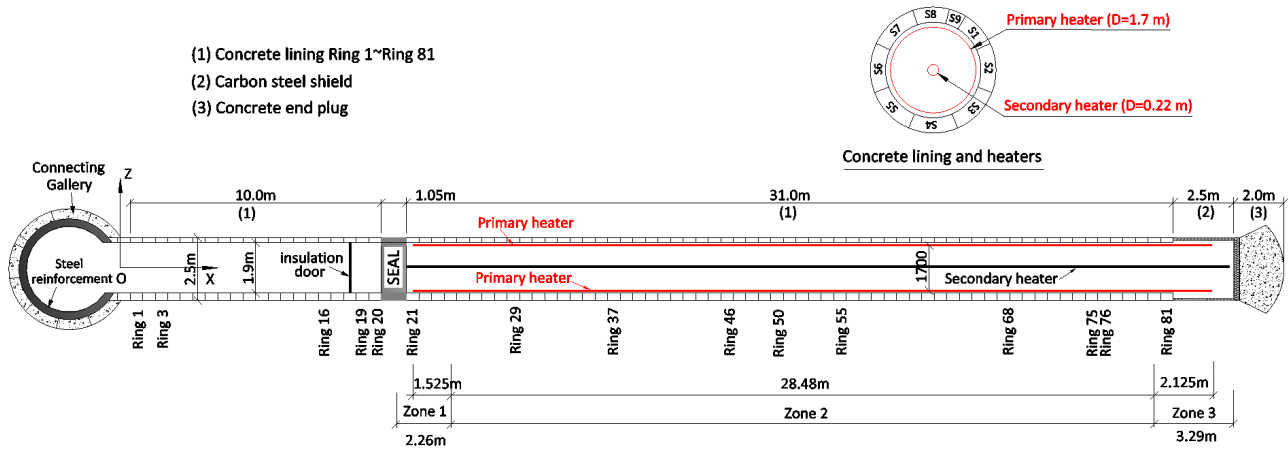
Figure 7.63: General layout of the PRACLAY gallery and test setup

A 1.05 m-long hydraulic bentonite-based seal was fitted between Ring 20 and Ring 21 to separate the heated section of the PRACLAY Gallery from the non-heated section. It was installed from January 18, 2010 to February 11, 2010. The hydraulic seal cut off hydraulically the preferential pathway through the gallery and the excavation damaged zone around the gallery by closing off the heated part of the PRACLAY gallery. In other words, the main role of the hydraulic seal is to create an undrained boundary at the intersection between the non-heated and the heated section. The hydraulic seal consists of a massive stainless steel structure (downstream flange, upstream flange, steel cylinder, closing steel frame) and an external annular rings of compacted MX-80 bentonite blocks placed against the Boom Clay.

The heater system is composed of two main systems. The first one, the primary heater consists of electrical cables placed 100mm from the gallery intrados. The second one, which is a back-up one, was placed at the centre of the gallery and will work only if the primary system failed.

To achieve the expected boundary conditions and to efficiently transfer the heat from the heater elements to the concrete lining, the heated section of PRACLAY gallery was backfilled with M34 Mol sand in 2011. This operation was realized by blowing it in a dry state into the gallery and was then artificially pressurized. A total volume of about $43m^3$ was injected into this part of the gallery between January and May 2012 and the pore water pressure increased artificially in five steps as seen in Figure 7.64. Saturation of the backfilled gallery was then naturally completed with the water flowing from the surrounding Boom Clay into the gallery. At the commencement of heating experiment, the pore water pressure pointed to 1MPa. During the heating phase of the experiment, the pressure evolves naturally without any human intervention (adding or subtracting an amount of water).

EURAD (Deliverable n˚ 7.6) – Modelling report on the effect of temperature on clay host rocks behaviour
Dissemination level: PU
Date of issue of this report: 06/06/2024

Page 227
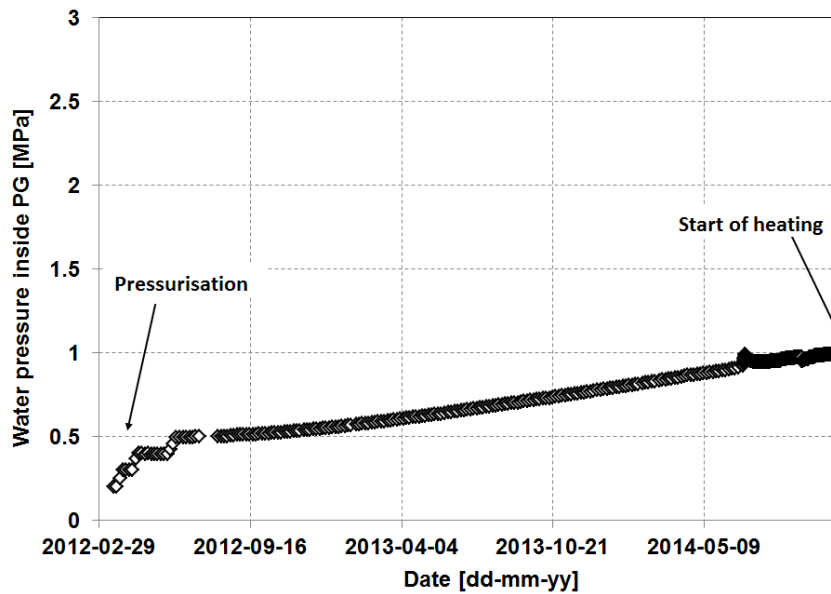
Figure 7.64: Evolution of the pore water pressure inside the backfilled part of the PRACLAY Gallery before the switch-on of the heater

On November 3, 2014, the primary heater was switched on, the heater power was stepwise increased until the temperature at the lining extrados pointed to 80°C. This heating phase is named the start-up heating phase. Thereafter, the heater power was decreased step by step to maintain the temperature at the lining extrados at 80°C for 10 years, this phase is called the stationary heating phase (Dizier, A., Chen, G.J., Li, X.L., Leysen, J., Verstricht, J., Troullinos, I., and Rypens, J. (2016)) (Table 7.14) . In March 2015, an insulation door was installed in front of the seal to limit as much as possible the dissipation of the heat through the non-heated section.

Table 7.14: Main test phases of the PRACLAY Heater test

Test phases	Date
Excavation of the PRACLAY gallery	From 2007-10-04 to 2007-11-06
Installation of seal (bentonite steel structure)	From 2010-01-18 to 2010-02-11
Saturation, and pressurization in the backfilled gallery	From 2011-12-22 to 2014-11-03
First heating step : 250 W/m	From 2014-11-03 to 2015-01-07
Second heating step : 350 W/m	From 2015-01-07 to 2015-03-03
Third heating step : 450 W/m	From 2015-03-03 to 2015-08-17
Stationary heating phase (80°C constant)	From 2015-08-17 to 2025-08-17

A large instrumentation network with about 1100 sensors was set up around the PRACLAY gallery to monitor and follow up the responses in the test setup and the host Boom Clay from the gallery excavation till the end of the heater test. Boreholes drilled from Connecting gallery (CG boreholes) and PRACLAY Gallery (PG boreholes) were instrumented with multi-filter piezometers complemented with thermocouples (Figure 7.65).

EURAD (Deliverable n˚ 7.6) – Modelling report on the effect of temperature on clay host rocks behaviour
Dissemination level: PU
Date of issue of this report: 06/06/2024

Page 228
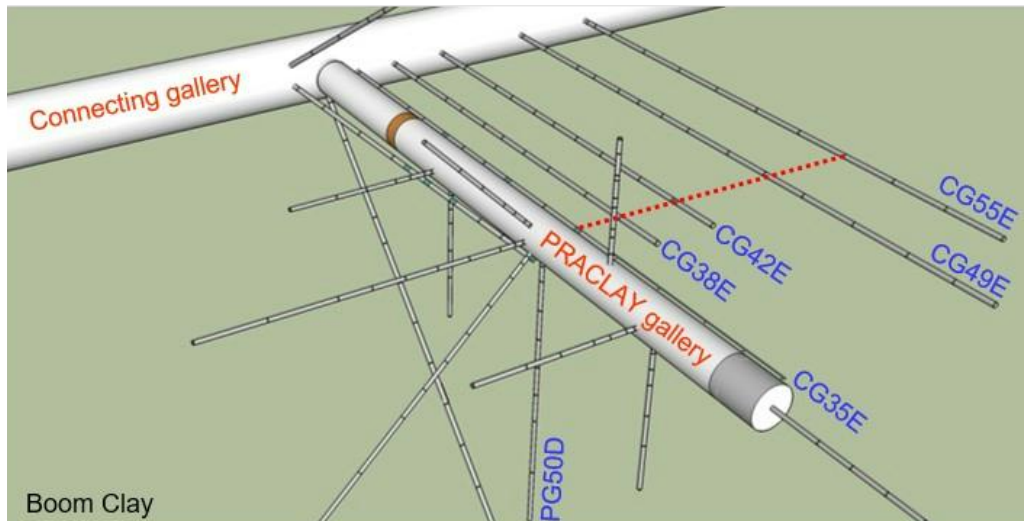
Figure 7.65: Layout of the monitoring boreholes around the PRACLAY gallery

7.2.3. Modelling the large scale in situ PRACLAY Heater test

This benchmark proposes to model the large scale PRACLAY Heater test with fully coupled thermo-hydro-mechanical finite elements. Two cases were proposed, the first case corresponds to an academic version of the PRACLAY experiment with assumptions and simplifications of the constitutive models. The second one corresponds to a modelling exercise where the constitutive models are let free to be chosen by the modelling team. Both cases are 2D plane strain models. It is worth noting that the backfilled sand is not considered in any modelling for simplification. In all this document, the sign convention of the soil mechanics is used with the compressive stress and strain defined as positive.

7.2.3.1. Geometry and materials

The geometry of this model is a cross section of the backfilled PRACLAY gallery and host Boom Clay perpendicular to the PRACLAY gallery axis. This model is representative of the mid-plane of the PRACLAY heater test (around Ring 50). By considering the symmetric nature of the problem, only a quarter of the full cross section is modelled, and the simulated region measures 100m in both directions (Figure 7.66). Two materials are included in this figure: Boom Clay and the concrete lining. The segmental concrete lining is modelled though a monolithic ring where the joints are not represented. The inner radius and outer radius of the concrete lining are respectively 0.95m and 1.25m. An over-excavation of 6 cm is assumed and the excavation radius is estimated to be 1.31m. The modelling of the experiment can be done without the concrete lining with an adaptation of the boundary conditions.

EURAD (Deliverable n° 7.6) – Modelling report on the effect of temperature on clay host rocks behaviour
Dissemination level: PU
Date of issue of this report: 06/06/2024

Page 229
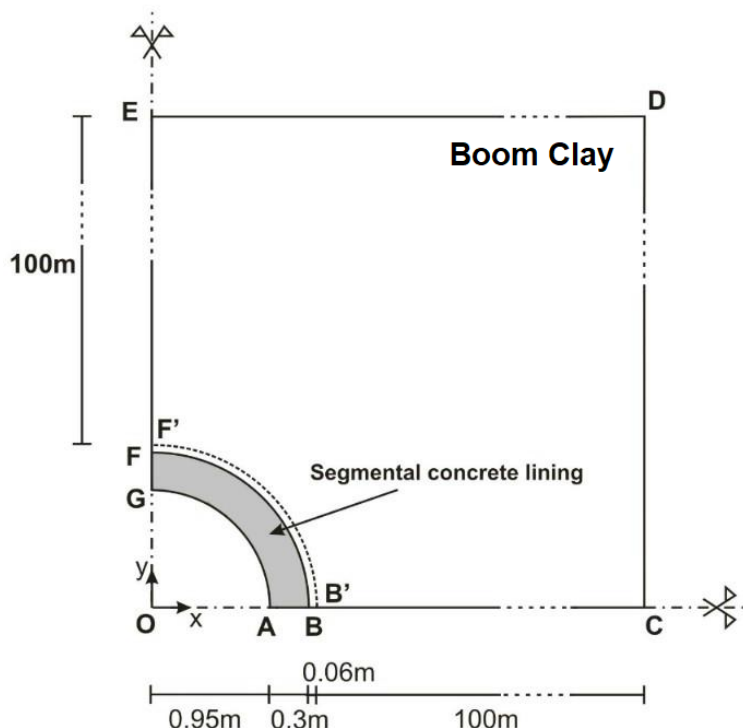
Figure 7.66: Geometry (not at scale) and materials in the two dimensional plane strain coupled THM model (2D-PS THM) for the PRACLAY heater test

7.2.3.2. Initial conditions

The initial temperature and pore pressure in the materials are presented in Table 7.15. A constant initial temperature of 16.5°C is assumed for all the three materials. The initial pore pressure in the Boom Clay is 2.25MPa, and a constant initial pore pressure of 0.1MPa is assumed in the concrete. The initial stresses in the lining are assumed to be 0.1MPa in all directions. The initial vertical stress in the Boom Clay perpendicular to the bedding plane is 4.5MPa, and the initial horizontal stress in the Boom Clay parallel to the bedding plane is 3.825MPa.

Table 7.15: Initial conditions for Boom Clay

Parameters		Components	Boom Clay
		σ_{yy}	4.5
Total stress	MPa	σ_{xx}	3.825
		σ_{zz}	3.825
Pore pressure	MPa	P_0	2.25
Temperature	°C	T_0	16.5

7.2.3.3. Main material parameters

This section presents the main thermo-hydro-mechanical material parameters used to model the PRA-CLAY Heater test. The Drucker-Prager model (Drucker and Prager (1952)) which is used to model the mechanical behavior of the clay is briefly described.

EURAD (Deliverable n° 7.6) – Modelling report on the effect of temperature on clay host rocks behaviour
Dissemination level: PU
Date of issue of this report: 06/06/2024

Page 230

7.2.3.4. Boom Clay thermo-hydro-mechanical characteristics

The Boom Clay is assumed to be fully saturated, and the basic physical properties of the Boom Clay used in this benchmark are presented in Table 7.16 (Bernier et al. (2017); Charlier et al. (2010)). The Boom Clay is a cross-anisotropic material, and its thermo-hydro-mechanical parameters parallel to the bedding plane are higher than those perpendicular to the bedding plane. Based on numerical interpretations of the temperatures/pore pressures measured from a small-scale ATLAS III heating test, the principal components of the thermal conductivity/intrinsic permeability tensor (two parallel components, λ_h and k_h, and two perpendicular component, λ_v and k_v, were obtained from Chen et al. (2011).

Table 7.16: Main physical, thermo-hydraulic parameters for the Boom Clay

Name	Symbol	Value	Unit
Solid phase density	ρ_s	2639	kg/m^3
Bulk density	ρ'	2000	kg/m^3
Porosity	n	0.39	
Isotropic intrinsic permeability	k	2.83×10^{-19}	m^2
Vertical intrinsic permeability	k_v	2×10^{-19}	m^2
Horizontal intrinsic permeability	k_h	4×10^{-19}	m^2
Isotropic thermal conductivity	λ	1.47	W/mK
Vertical thermal conductivity	λ_v	1.31	W/mK
Horizontal thermal conductivity	λ_h	1.65	W/mK
Linear thermal expansion coefficient	α_s	1×10^{-5}	$^\circ C^{-1}$
Solid phase specific heat	C_p	769	J/(kgK)

7.2.3.5. Mechanical characteristics of Boom Clay

A friction angle criterion such as a Drucker-Prager model (Drucker and Prager (1952)) is proposed for the Boom Clay. The elastic deformation is calculated by elastic modulus, E and Poisson's ratio ν. The following yield criterion was adopted to define the onset of yielding which can be written adopting the notation of Desai and Siriwardane (1984):

$$f \equiv \sqrt{J_{2D}} - \frac{2\sin\phi'}{\sqrt{3}\,(3 - \sin\phi')}\left(J_1 + \frac{3c'}{\tan\phi'}\right) = 0$$

where :

- J_1 is the first invariant of the stress tensor defined by $J_1 = \sigma_{ii}$;

- J_{2D} is the second invariant of the deviatoric stress tensor defined by $J_{2D} = \frac{1}{2}\hat{\sigma}_{ij}\hat{\sigma}_{ij}$ with $\hat{\sigma}_{ij} = \sigma_{ij} - \frac{J_1}{3}\delta_{ij}$;

- ϕ' is the effective internal friction angle;

- c' is the effective internal cohesion.

A non-associated plastic flow rule is assumed with the plastic potential function g taking the form

$$g \equiv \sqrt{J_{2D}} - \frac{2\sin\psi'}{\sqrt{3}\,(3 - \sin\psi')}\left(J_1 + \frac{3c'}{\tan\psi'}\right) = 0$$

EURAD (Deliverable n˚ 7.6) – Modelling report on the effect of temperature on clay host rocks behaviour
Dissemination level: PU
Date of issue of this report: 06/06/2024

Page 231

where ψ' is the effective dilation angle.

In this formulation, the plastic flow is assumed to induce hardening of the yield surface, which is introduced via a hyperbolic variation of the friction angle, ϕ', as a function of the Von Mises equivalent plastic strain ϵ_{eq}^{p} (Barnichon (1998)):

$$\phi' = \phi'_0 + \frac{\left(\phi'_f - \phi'_0\right)\epsilon_{eq}^{p}}{\beta_\phi + \epsilon_{eq}^{p}}$$

where ϕ'_0 is the initial friction angle, ϕ'_f is the final friction angle, the Von Mises equivalent plastic strain ϵ_{eq}^{p} is obtained by integration of the Von Mises equivalent plastic strain rate $\dot{\epsilon}_{eq}^{p}$:

$$\epsilon_{eq}^{p} = \int_0^t \dot{\epsilon}_{eq}^{p} dt$$

$$\dot{\epsilon}_{eq}^{p} = \sqrt{\frac{2}{3}\dot{\epsilon}_{eq}^{p}\dot{\epsilon}_{eq}^{p}}$$

where

- $\dot{\epsilon}_{eq}^{p}$ is the deviatoric plastic strain rate tensor;

- β_ϕ is the hardening parameter representing the value of equivalent plastic strain for which half of the hardening is achieved.

The elasto-plastic Drucker-Prager model parameters for the Boom Clay are given in Table 7.17 with isotropic parameters.

Table 7.17: Boom Clay elasto-plastic parameters

Name	Symbol	Value	Unit
Isotropic elastic modulus	E	300	MPa
Poisson's ratio	ν	0.125	–
Effective cohesion	c′	0.3	MPa
Initial effective friction angle	$\phi'_{c,0}$	5	°
Final effective friction angle	$\phi'_{c,f}$	18	°
Hardening parameter	B_ϕ	0.01	–
Dilation angle	Ψ	5	°

Table 7.18 presents the anisotropic elastic properties for Boom Clay.

EURAD (Deliverable n° 7.6) – Modelling report on the effect of temperature on clay host rocks behaviour
Dissemination level: PU
Date of issue of this report: 06/06/2024

Page 232

Table 7.18: Boom Clay anisotropic elastic parameters

Name	Symbol	Value	Unit
Young's modulus parallel to bedding	$E_{\parallel}$	400	MPa
Young's modulus perpendicular to bedding	$E_{\perp}$	200	MPa
Poisson's ratio parallel to bedding	$\nu_{\parallel}$	0.25	–
Poisson's ratio perpendicular to bedding	$\nu_{\perp}$	0.125	–
Shear modulus normal to bedding plane	$G_{\perp}$	80	MPa

7.2.3.6. Concrete lining parameters

The concrete of the segmental lining is mainly made of C80/95 concrete. The concrete is modelled via an elastic law. As the ring is modelled without taking into account the existence of the joints (longitudinal and circumferential) between the concrete segments, a permeability higher than that of the Boom Clay is chosen as seen in Table 7.19.

Table 7.19: Concrete main properties

Name	Symbol	Value	Unit
Solid phase density	ρ_s	2650	kg/m^3
Bulk density	ρ'	2420	kg/m^3
Porosity	n	0.1	
Young's modulus	E	42	GPa
Poisson's ratio	ν	0.2	–
Intrinsic permeability	k	4.5×10^{-18}	m^2
Thermal conductivity	λ	2.86	W/mK
Linear thermal expansion coefficient	α_s	1×10^{-5}	$°C^{-1}$
Solid phase specific heat	C_p	800	J/(kgK)

7.2.4. Boundary conditions

The boundary conditions used are defined as follows.

7.2.4.1. Mechanical boundary conditions

The following mechanical boundary conditions are set in the 2D-PS model (Figure 7.67):

- The boundaries DE and CD are respectively subjected to a vertical and a horizontal total stress;

- The boundaries GF and FE is horizontally fixed (no horizontal displacement);

- The boundaries AB and BC is vertically fixed (no vertical displacement);

- The modelling of the excavation is let free to the team. It can be done by a stress release technique (the total stresses are reduced to 0.1MPa) combined with contact elements or by imposing a radial displacement of 6cm. In any case, the excavation is assumed to happen in 24 hours (t_0+1 day). If the concrete lining is not modelled, it is proposed to fix the radial displacements at the wall after the excavation phase.

EURAD (Deliverable n° 7.6) – Modelling report on the effect of temperature on clay host rocks behaviour
Dissemination level: PU
Date of issue of this report: 06/06/2024

Page 233
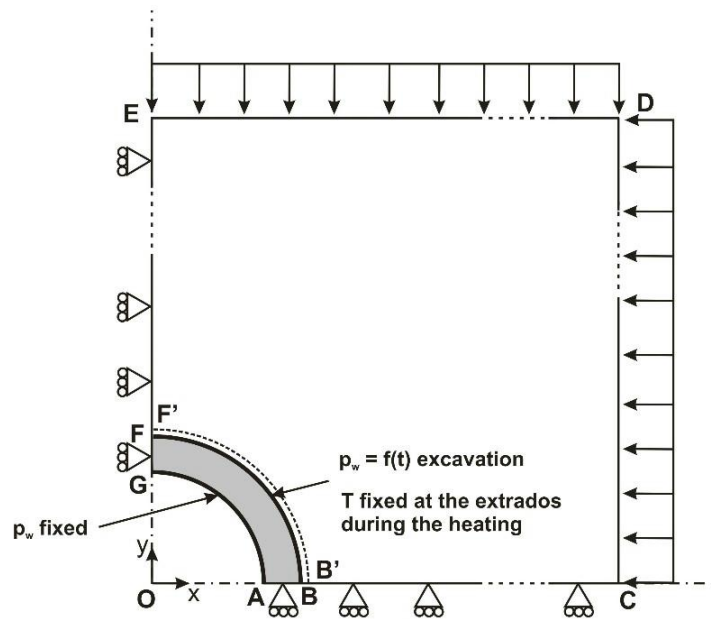
Figure 7.67: Illustration of the boundary conditions

7.2.4.2. Hydraulic boundary conditions

The following hydraulic boundary conditions are set in the 2D-PS model (Figure 7.67):

- The pore pressure at the boundaries CD, DE are constant with a value of 2.25MPa;

- The boundaries GF, FE, AB and BC are impervious;

- During the excavation, the pore pressure at the wall decreases from 2.25MPa to the atmospheric pressure (i.e. 0.1MPa) in 24 hours (t_0+1 day);

- After the excavation and before the artificial pressurization in the backfill sand, the pore pressure in the gallery is equal to the atmospheric pressure (at boundary GA) (between t_0+1 day and t_0+1609 days);

- From the start of the artificial injection (t_0+1609 days) up to the commencement of the heating phase (t_0+2582 days), the pore water pressure is imposed at GA according to Figure 7.68;

- During the heating phase (t_0+2582 days), as the backfilled part of the PG is not modelled, it is proposed to impose the pore water pressure at the intrados at the boundary GA as in Figure 7.68. If the lining is not modelled, the pore pressure will be imposed at the wall of the clay (boundary FB) with the assumption that the pore pressure is the same between the intrados and the extrados. In a second step, the modelling team is free to apply an undrained boundary conditions during the heating at the boundary GA to model the thermal pressurization of the clay.

EURAD (Deliverable n˚ 7.6) – Modelling report on the effect of temperature on clay host rocks behaviour
Dissemination level: PU
Date of issue of this report: 06/06/2024

Page 234
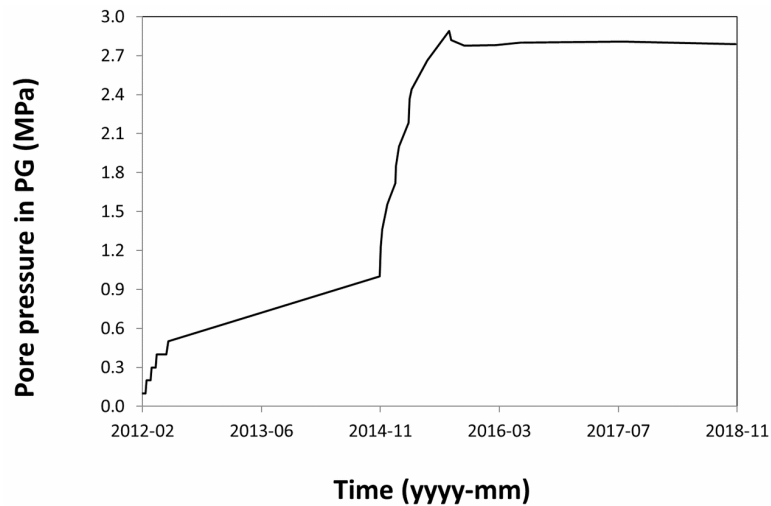
Figure 7.68: Pore pressure boundary condition in the PG after pressurization used in the 2D-PS model for the PRACLAY Heater test

7.2.4.3. Thermal boundary conditions

The following thermal boundary conditions are set in the 2D-PS model (Figure 7.67):

- The pore pressure at the boundaries CD, DE are constant with a value of 2.25 MPa;

- The temperature at the boundaries CD, DE is constant with a value of 16.5 °C;

- The boundaries AB, BC, GF and FE are adiabatic;

- Based on the measured temperature at the lining extrados, a temperature boundary condition is set at the lining extrados, as seen in Figure 7.69. The heater was switched on on November 3, 2014 (t_0+2582 days), and the temperature at the lining extrados reached 80°C on August 17, 2015 (t_0+2829 days); a constant temperature of 80°C will be maintained at the lining extrados for 10 years till August 17, 2025 (t_0+6522 days).
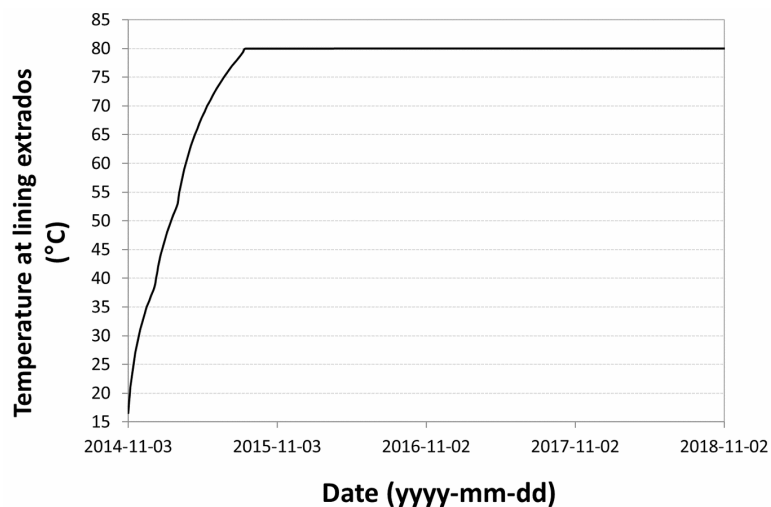
Figure 7.69: Temperature boundary condition at the lining extrados

EURAD (Deliverable n˚ 7.6) – Modelling report on the effect of temperature on clay host rocks behaviour
Dissemination level: PU
Date of issue of this report: 06/06/2024

Page 235

7.2.5. Proposed modelling cases to model the large scale in situ PRACLAY Heater test

The two cases using 2D Plane strain coupled thermo-hydro-mechanical model are presented in this section.

7.2.5.1. Case1

Case 1 is defined as an "academic" version of the PRACLAY Heater test. The main goal of this case is to do a cross-validation between the participants and the used finite element code. Different sub-cases can be associated with Case 1 with a gradual increase of the complexity such as in the three following sub-cases:

1. Anisotropic initial stress conditions and the Boom Clay is considered as elastic;

2. Anisotropic initial stress conditions and the elasto-plastic Drucker-Prager model without hardening of the friction angle is used to model the Boom Clay;

3. Anisotropic initial stress conditions and the elasto-plastic Drucker-Prager model with hardening of the friction angle is used to model the Boom Clay.

In the first sub-case considering the elastic properties, the lining does not have to be modelled as the convergence of the clay will not be sufficient to reach the contact with the concrete lining. In this case, it is thus proposed to fix the radial displacements at the wall after excavation. Sub-case 1 and sub-case 2 are optional but sub-case 3 is mandatory.

7.2.5.2. Case2

For Case 2, the choice of mechanical model is let free to the modelling teams. The boundary conditions remained the same as described above. The main goal of this case is to first perform a comparison between the mechanical models and second to make a comparison with experimental data.

7.2.6. Results and comparisons between the modelling teams

This section presents the comparisons between the results obtained by the modelling teams with the academic cases of the modelling of the large scale in situ PRACLAY Heater test. Four teams contributed to this benchmark, i.e. UPC, ULiège, BGE and EURIDICE/ SCK CEN. Table 7.20 summarises what cases were realised by the involved modelling teams and with which finite element codes. Case 1.1, case 1.2 and case 1.3 are the academic cases where the boundary conditions, the parameters and properties are fixed. For the case 1.2, two elastic models were considered, one with isotropic elasticity (BGE and EURIDICE/ SCK CEN) and another one with anisotropic elasticity (UPC and EURIDICE/ SCK CEN). Case 2 is a free case where the modelling teams are free to choose their constitutive models. This case are presented by the each involved modelling teams in another section.

EURAD (Deliverable n˚ 7.6) – Modelling report on the effect of temperature on clay host rocks behaviour
Dissemination level: PU
Date of issue of this report: 06/06/2024

Page 236

Table 7.20: Modelling teams contributing to the PRACLAY benchmark exercise

Teams	Finite element code	Case 1.1	Case 1.2	Case 1.3	Case 2
UPC	Code Bright	X	X	X	X
BGE	OpenGeoSys	X	X		
ULiège	LAGAMINE	X		X	X
EURIDICE/SCK CEN	COMSOL	X	X	X	

7.2.6.1. Case1.1 - elastic case

Case 1.1 deals with the modelling of the large scale in situ PRACLAY Heater test with an elastic constitutive law. Four teams (BGE, ULiège, UPC and EURIDICE/ SCK CEN) participated to this case. Figure 7.70 and Figure 7.71 show the comparisons between the teams for points in the horizontal and vertical direction for the temperature and pore water pressure evolution. It can be seen that for this elastic case, the four modelling teams have similar results in terms of temperature and pore water pressure evolution in both horizontal and vertical directions. During the excavation phase, differences can be observed between BGE and the three other teams but these disappear during the modelling of the heating phase.

(a) Temperature evolution

(b) Pore water pressure evolution

Figure 7.70: Numerical results (elastic case) of temperature (a) and pore water pressure (b) evolution in the horizontal direction for BGE, ULiège, UPC and EURIDICE / SCK CEN.

EURAD (Deliverable n° 7.6) – Modelling report on the effect of temperature on clay host rocks behaviour
Dissemination level: PU
Date of issue of this report: 06/06/2024

Page 237

(a) Temperature evolution

(b) Pore water pressure evolution

Figure 7.71: Numerical results (elastic case) of temperature (a) and pore water pressure (b) evolution in the vertical direction for BGE, ULiège, UPC and EURIDICE / SCK CEN.

7.2.6.2. Case 1.2 – perfect plasticity with anisotropic elasticity

Two modelling teams, UPC and EURIDICE/ SCK CEN, contributed to the case 1.2 which is the perfect elasto-plastic case. In this modelling, the elasticity is assumed be cross-anisotropic as in the elastic case. Figure 7.72 and Figure 7.73 showing the numerical evolution of the temperature and of the pore water pressure for selected points in the horizontal and vertical directions. It can be observed a good agreement between the modelling teams for the temperature and pore water pressure evolution. Differences can be observed during the heating phase but there are minor.

(a) Temperature evolution

(b) Pore water pressure evolution
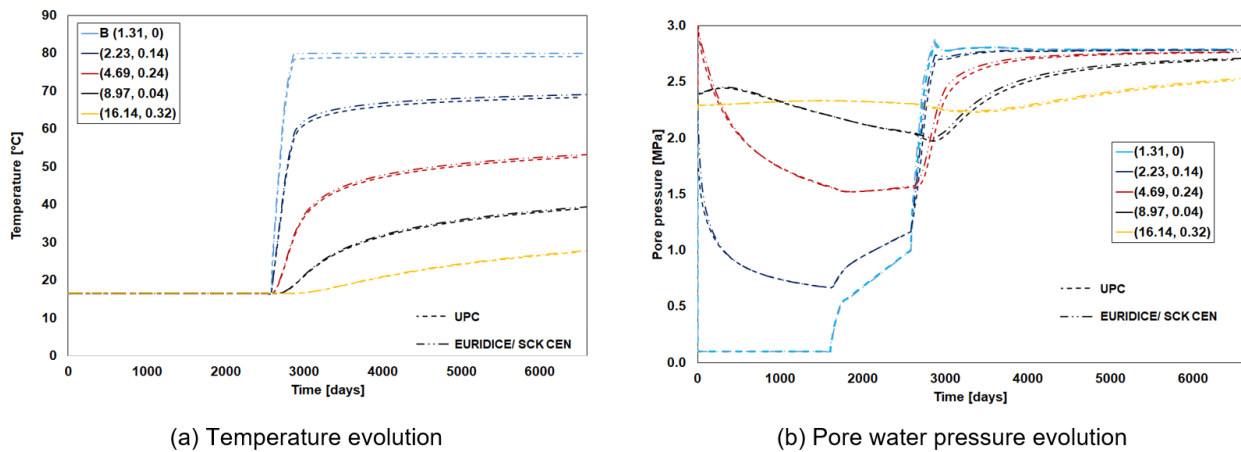
Figure 7.72: Numerical results (perfect elasto-plasticity) of temperature (a) and pore water pressure (b) evolution in the horizontal direction for UPC and EURIDICE/ SCK CEN.

EURAD (Deliverable n° 7.6) – Modelling report on the effect of temperature on clay host rocks behaviour
Dissemination level: PU
Date of issue of this report: 06/06/2024

Page 238
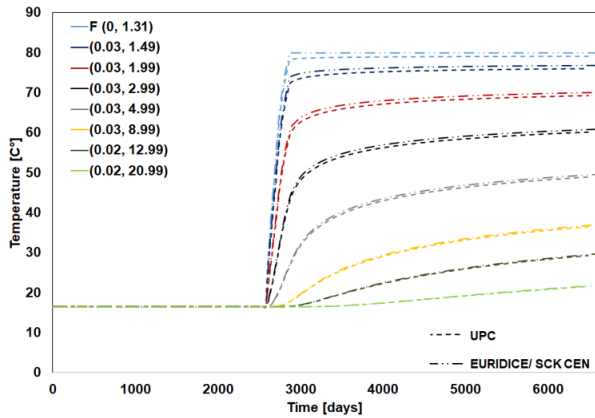
(a) Temperature evolution
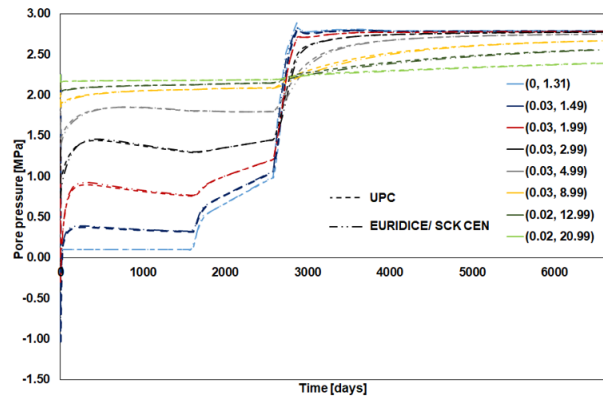
(b) Pore water pressure evolution

Figure 7.73: Numerical results (perfect elasto-plasticity)of temperature (a) and pore water pressure (b) evolution in the vertical direction for UPC and EURIDICE/ SCK CEN.

7.2.6.3. Subcase 1.2 perfect plasticity with isotropic elasticity

BGE and EURIDICE/SCK CEN also modelled this case with isotropic elasticity. The comparison between them can be observed in Figure 7.74 and Figure 7.75 for the temperature and pore water pressure evolution in the horizontal and vertical directions respectively. It can be observed similar results during the heating phase for both modelling teams. A difference appears at the early beginning of the simulation, during the modelling of the excavation. It is attributed to a difference in the way to consider the boundary conditions during this phase.
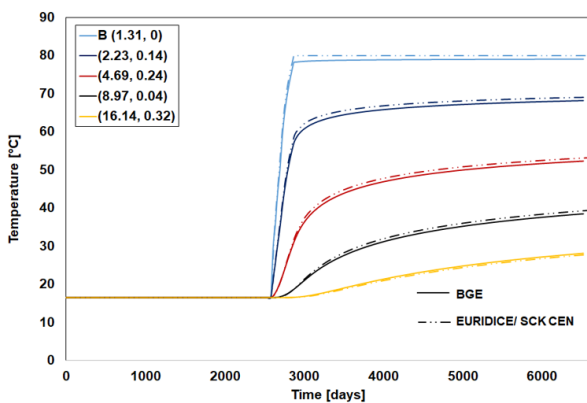
(a) Temperature evolution
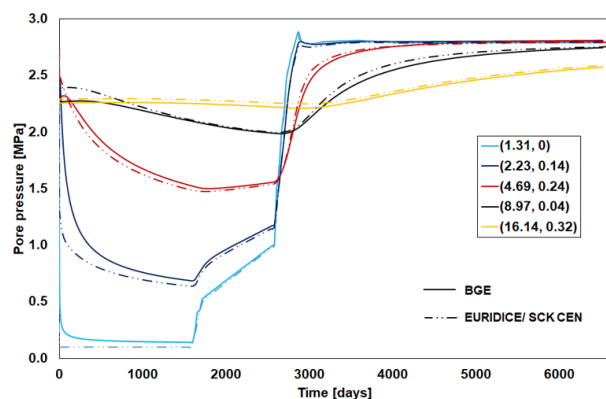
(b) Pore water pressure evolution

Figure 7.74: Numerical results of temperature (a) and pore water pressure (b) evolution in the horizontal direction for BGE and EURIDICE/ SCK CEN (case 1.2 with isotropic elasticity).

EURAD (Deliverable n° 7.6) – Modelling report on the effect of temperature on clay host rocks behaviour
Dissemination level: PU
Date of issue of this report: 06/06/2024

Page 239

(a) Temperature evolution

(b) Pore water pressure evolution
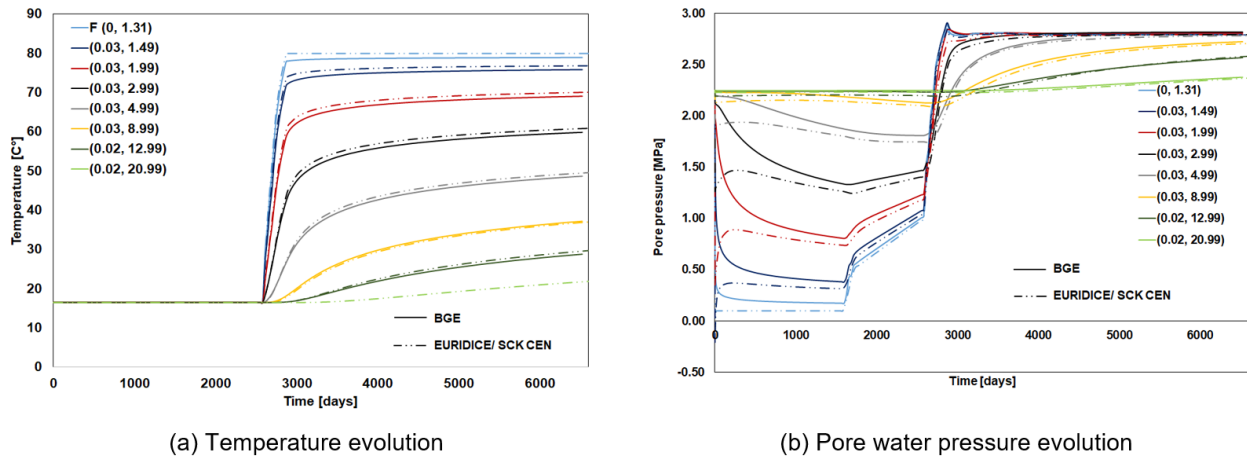
Figure 7.75: Numerical results of temperature (a) and pore water pressure (b) evolution in the vertical direction for BGE and EURIDICE/ SCK CEN (case 1.2 with isotropic elasticity).

7.2.6.4. Case 1.3 – elasto-plasticity with the hardening of the friction angle

Case 1.3 corresponds to an elasto-plastic model considering the hardening of the friction angle. ULiège, UPC and EURIDICE /SCK CEN modelled this case. Figure 7.76 and Figure 7.77 show the results of the comparison between the three modelling teams for the evolution of the temperature and pore water pressure evolution in the horizontal and vertical directions respectively. Results are similar between these three modelling teams for both the temperature and pore water pressure evolution.

(a) Temperature evolution

(b) Pore water pressure evolution
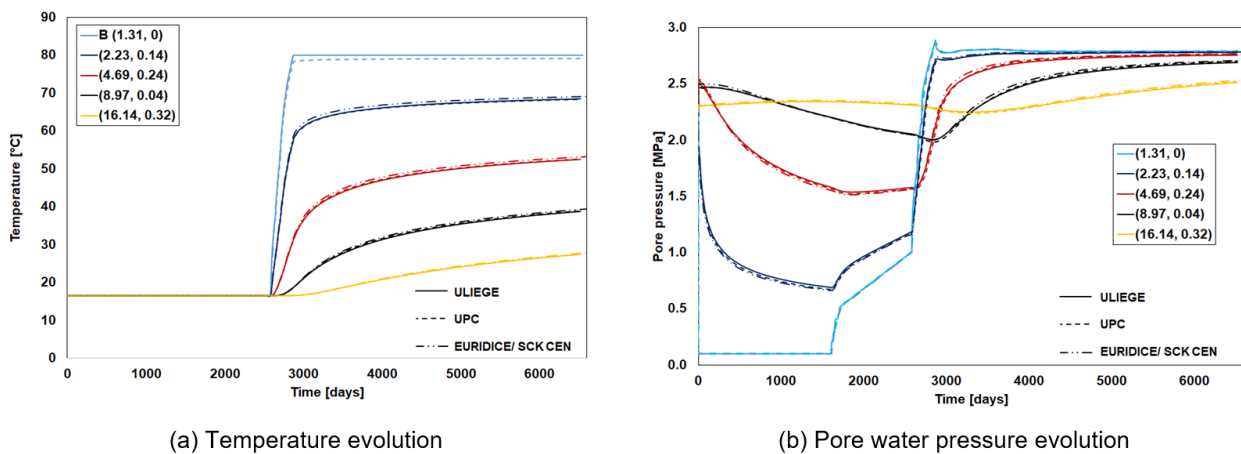
Figure 7.76: Numerical results of temperature (a) and pore water pressure (b) evolution in the vertical direction for ULiège, UPC and EURIDICE / SCK CEN (case 1.3).

EURAD (Deliverable n° 7.6) – Modelling report on the effect of temperature on clay host rocks behaviour
Dissemination level: PU
Date of issue of this report: 06/06/2024
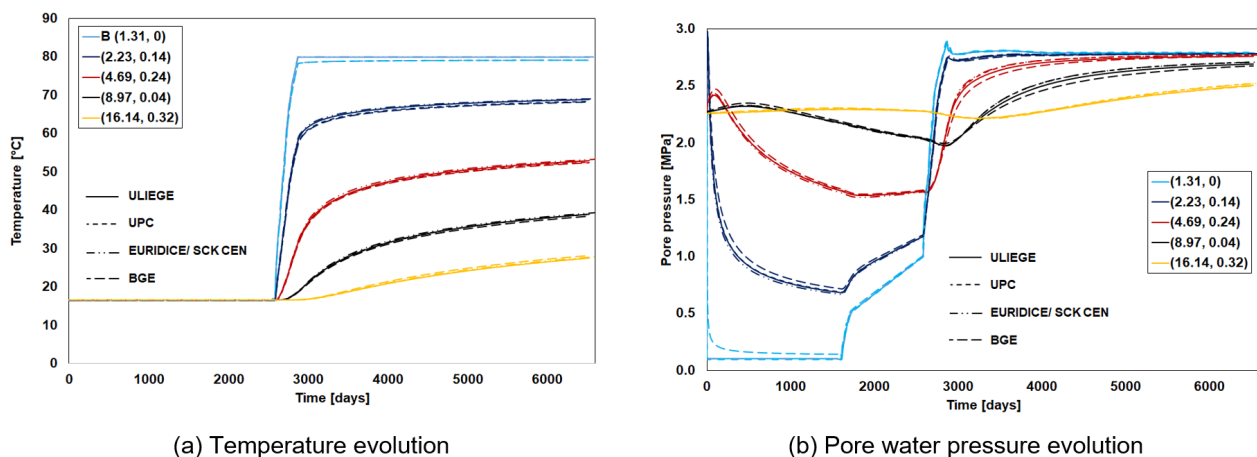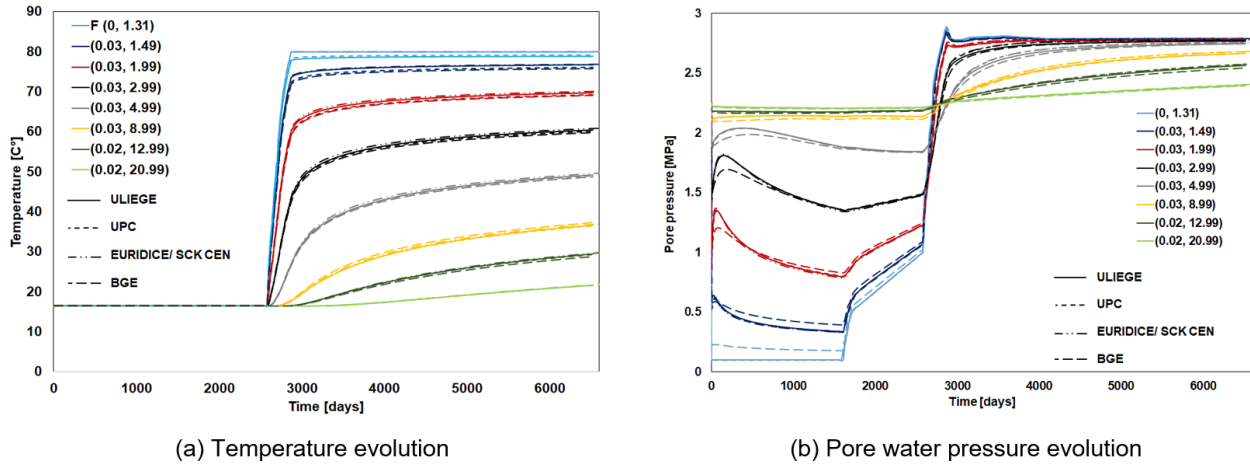
Page 240

(a) Temperature evolution

(b) Pore water pressure evolution
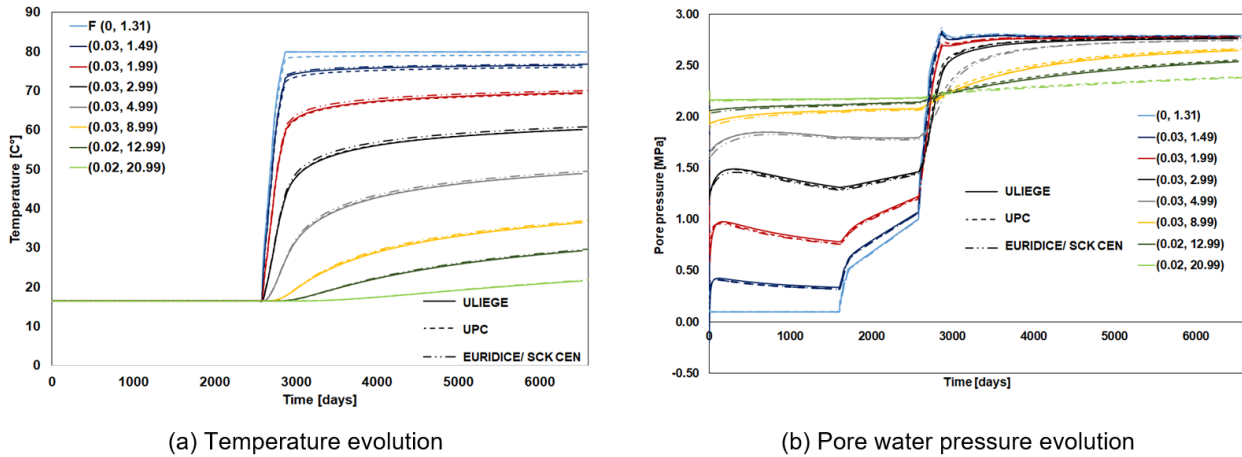
Figure 7.77: Numerical results of temperature (a) and pore water pressure (b) evolution in the vertical direction for ULiège, UPC and EURIDICE / SCK CEN (case 1.3).

7.2.7. Free version: ULiège

In order to better reproduce the experimental observations from the in situ test, a free version was carried out. The geometry and boundary conditions are already detailed in the benchmark descriptions. The constitutive model used in the free version is the ORTHOPLA with isotropic hardening/softening and anisotropic cohesion variation. In this section, the focus is put on the reproduction of the in-situ measurements of temperature and pore pressure. The locations of monitoring boreholes around the PRACLAY gallery are shown in Figure 7.65. The elastoplastic parameters for the Boom Clay are defined in Table 7.21.

Table 7.21: Elastoplastic parameters for the Boom Clay

Symbol	Name	Value	Unit
$\psi_c = \psi_E$	Dilatancy angles	0	°
$\phi_{c,0} = \phi_{E,0}$	Initial compression friction angle	5	°
$\phi_{c,f} = \phi_{E,f}$	Final compression friction angle	18	°
B_ϕ	Friction angle hardening coefficient	0.01	-
B_c	Cohesion softening coefficient	0.01	-
$\bar{c}$	Cohesion for isotropic loading	0.258	MPa
$A_\parallel$	Cohesion parameter	0.187	-
b_1	Cohesion parameter	2.580	-
c_f	Ratio of cohesion softening	3	-

Figure 7.78 shows the evolution of the temperature of the monitoring boreholes around the PRACLAY gallery. To reproduce the evolution of temperature, the thermal conductivity of the host rock plays a significant role. The thermal conductivity in the horizontal direction was underestimated, while it was overestimated in the vertical direction. The reproduction of the temperature profile was almost perfect in the current modelling. Figure 7.79 presents the evolution of pore pressure in the horizontal and vertical directions. The pore pressure was generally overestimated during the waiting phase, while it was globally underestimated during the heating phase. Some strategies need to be applied to optimize the numerical prediction for the pore pressure evolution. There are many options to choose from. The intrinsic permeability leads to a direct impact on the pore pressure. The stiffness of the host rock could also largely affect the pore pressure (Chen et al., 2023), like the modification of the Poisson ratio and Young's modulus. From

EURAD (Deliverable n° 7.6) – Modelling report on the effect of temperature on clay host rocks behaviour
Dissemination level: PU
Date of issue of this report: 06/06/2024

Page 241
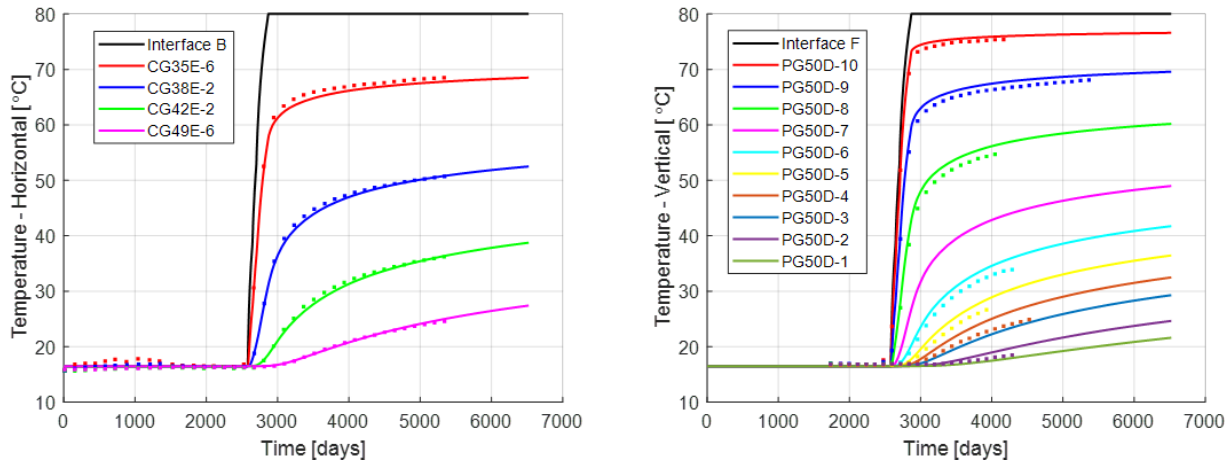
Figure 7.78: Temperature evolution in the horizontal and vertical directions
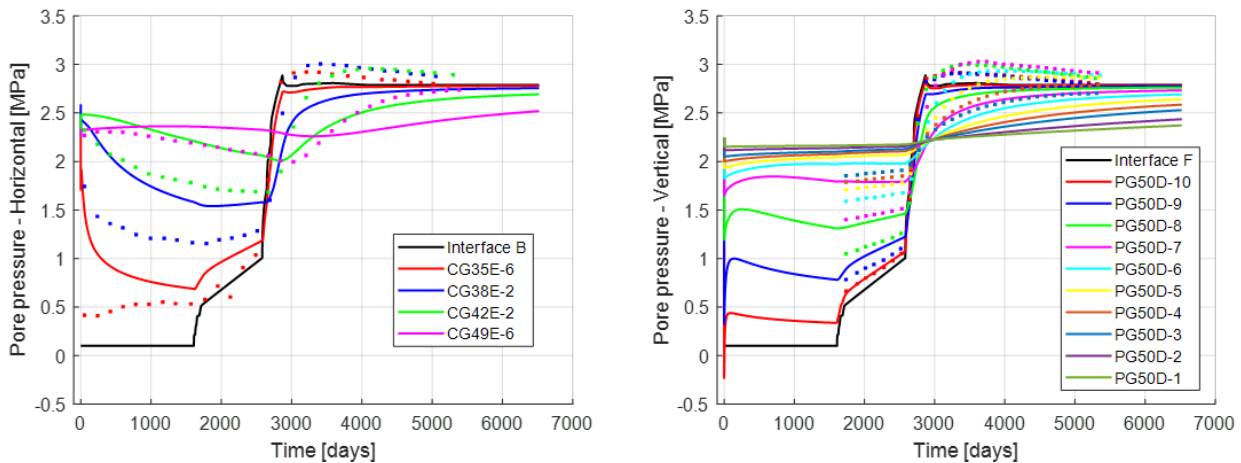
Figure 7.79: Pore pressure evolution in the horizontal and vertical directions

the previous results, for the monitoring borehole very close to the wall, the overestimation of pore pressure should be related to the permeability of the rock mass. The underestimation of pore pressure could be improved by the increase in stiffness of the host rock. However, the adaptation of each parameter should be reasonable. Imagine the permeability in the EDZ is larger than the measured value from the laboratory due to the potential fracture or cracks, and the inherent stiffness of rock material is higher than the measured value because of the inevitable disturbance when making the samples. Hence the optimization of the permeability and stiffness is essential for the improvement of the numerical prediction.

To reproduce the evolution of pore pressure, an artificial EDZ with a radius of 6.45 m was first introduced in the modelling, and the sound layers corresponding to the EDZ own higher stiffness. The proposed values of permeability and Young's modulus are described in Table 7.22. In the EDZ, an increase of 1.5 times of permeability was introduced. In the sound layers, an increase of Young's modulus was considered, while the Poisson's ratio was kept constant. Figure 7.80 presents the pore pressure profile in the horizontal and vertical directions. Globally, a good agreement was reached between the experimental measurement and numerical prediction during the waiting phase, especially for the monitoring boreholes located close to the gallery. The thermal pressurization was successfully reproduced during the heating phase, where the thermo-hydro-mechanical coupling effects were highly pronounced.

EURAD (Deliverable n˚ 7.6) – Modelling report on the effect of temperature on clay host rocks behaviour
Dissemination level: PU
Date of issue of this report: 06/06/2024

Page 242

Table 7.22: Modified properties in the EDZ and sound layers

	Symbol	Name	Value	Unit
EDZ	$k_{\parallel}$	Intrinsic permeability parallel to bedding	$6E^{-19}$	m^2
	$k_{\perp}$	Intrinsic permeability normal to bedding	$3E^{-19}$	m^2
Sound layers	$E_{\parallel}$	Young's modulus parallel to bedding	1400	MPa
	$E_{\perp}$	Young's modulus normal to bedding	700	MPa
	$G_{\parallel}$	Shear modulus parallel to bedding	580	MPa
	$G_{\perp}$	Shear modulus normal to bedding	280	MPa
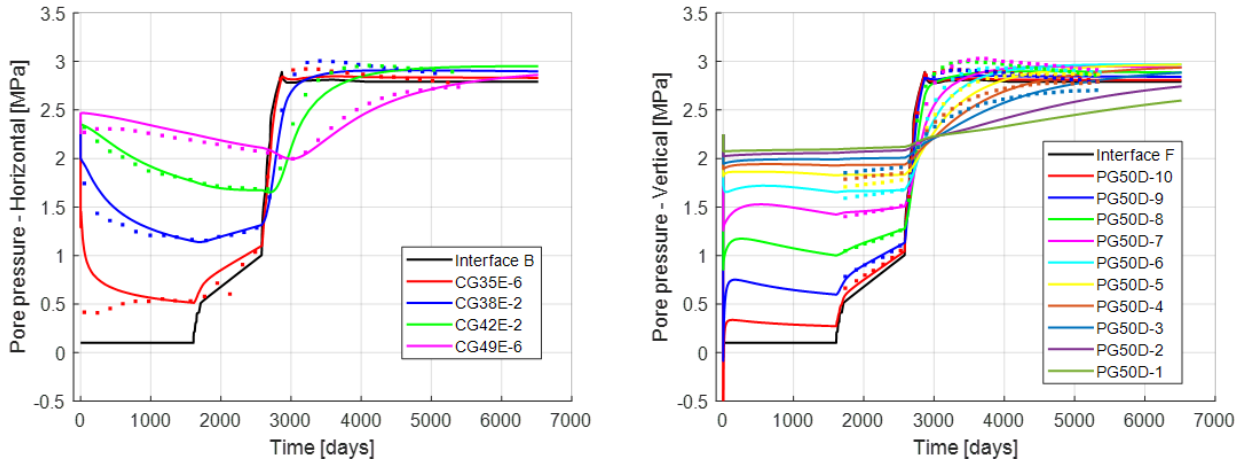
Figure 7.80: Pore pressure evolution with an artificial EDZ and sound layers

The introduction of an artificial EDZ and sound layers is sufficient to reproduce the pore pressure from the in-situ measurement. However, there is no clear prescribed border between the EDZ and sound layers in the real case, and the property of the host rock should change in a more reasonable way. Thus the dependency of the permeability and stiffness on the deformation were taken into account. A strain-dependent isotropic evolution of the hydraulic permeability tensor is taken into account based on a power (cubic) formulation (Pardoen (2015)):

$$k_{w,ij} = k_{w,ij,0} \left(1 + \beta_{per}\langle YI - YI^{thr}\rangle \hat{\varepsilon}^3_{eq}\right) \tag{7.1}$$

Where $k_{w,ij,0}$ is the initial intrinsic water permeability tensor, β_{per} is an evolution parameter, $\hat{\varepsilon}^p_{eq}$ is taken as the Von Mises' equivalent deviatoric plastic strain to consider the plastic deformation in the permeability evolution, YI is the yield index and YI^{thr} is a threshold value below which there is no intrinsic permeability variation. With YI < 1 if the current state of the material is elastic and YI = 1 for the plastic state (on the yield surface). In addition, it is to mention that permeability increases are assumed irreversible.

To introduce the dependency between the deformation and the stiffness of geomaterials, a stiffness degradation curve is typically used to explain the shear stiffness for a wide range of shear strains. Atkinson and Sallfors (1991) divided the strain levels into three categories: the very small strain level, where the stiffness modulus is constant in the elastic range; the small strain level, where the stiffness modulus varies non-linearly with strain; and the large strain level, where the soil is very close to failing and the soil stiffness is relatively low. According to Atkinson and Sallfors (1991) and Mair (1993), this hypothesis was demonstrated using the normalized stiffness degradation curve by contrasting it with the ground response from geotechnical construction and the measurement accuracy from the laboratory study in Figure 7.81.

EURAD (Deliverable n˚ 7.6) – Modelling report on the effect of temperature on clay host rocks behaviour
Dissemination level: PU
Date of issue of this report: 06/06/2024

Page 243
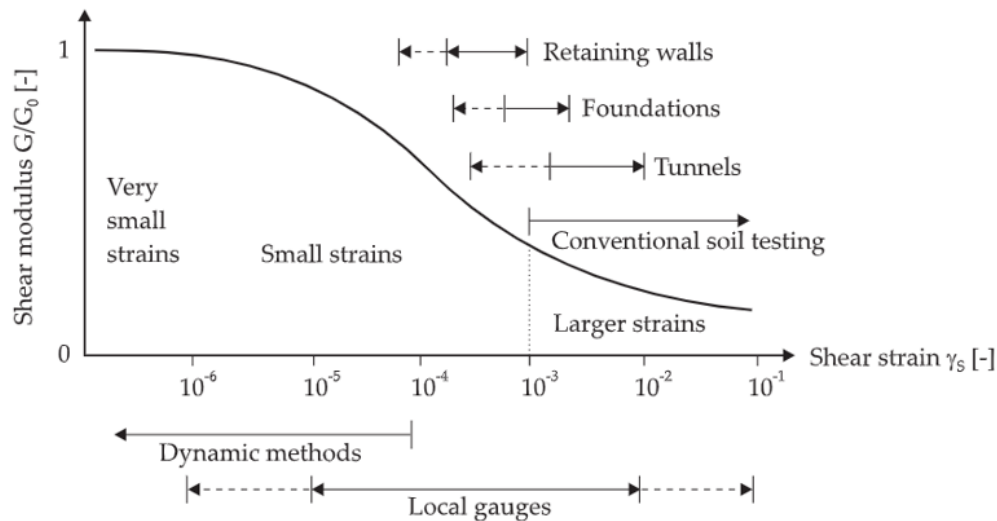
Figure 7.81: Typical stiffness degradation curve.

The HSsmall model was considered here to represent the high stiffness at small strain levels, which is extended with an elastic overlay model on the basis of the Plaxis Hardening Soil model. The model was initially implemented in the finite element program Plaxis (version 8.4). The additional details required for the small-strain stiffness formulation are obtained from modulus reduction curves where the shear modulus, G, is expressed as a logarithmic function of the shear strain, γ, varying from extremely low strain levels to high strain levels (vibrations). In the HSsmall model the reduction curve is described by the small-strain shear modulus, G_0, and the shear strain at which the secant shear modulus has reduced to 0.7 times G_0 ($\gamma_{0.7}$). An empirical equation for secant shear modulus depending on the shear strain is defined as:

$$G_s = \frac{G_0}{1 + a\gamma/\gamma_{0.7}} \tag{7.2}$$

The constant a is defined as 0.385 to reach the best fit. It should be mentioned that this equation presents the secant shear modulus, not the tangent shear modulus. Taking the derivative with respect to the shear strain, the tangent shear modulus is given:

$$G_t = \frac{G_0}{\left(1 + a\gamma/\gamma_{0.7}\right)^2} \tag{7.3}$$

It should be noted that Poisson's ratio keeps constant, hence the evolution of Young's modulus is consistent with the shear modulus. In LAGAMINE code, the initial and minimum values of Young's modulus were implemented. With the increase of shear strain, Young's modulus decreases up to the minimum value. A cut-off of Young's modulus was defined in the code in case of too small stiffness.

The parameters in the current modelling referred to (Chen et al., 2023) defined in Table 7.23. Figure 7.82 showed the pore pressure evolution depending on the modification of permeability and stiffness with respect to the shear strain. Compared to the results with artificial EDZ and sound layers, the pore pressure evolution remained consistent during the waiting phase, and a better agreement was obtained during the heating phase, especially where the rock mass was far from the wall.

In conclusion, the thermal pressurization due to the discrepancy of thermal dilation between solid and fluid phases is well predicted in the EDZ. The sensitive analysis of the THM parameters on the evolution of temperature and pore pressure has been carried out. The introduction of hydraulic permeability and stiffness dependent on the shear strain is sufficient to reproduce the pore pressure evolution in a more practical way. A good agreement is obtained between the in-situ measurement and the numerical results.

EURAD (Deliverable n˚ 7.6) – Modelling report on the effect of temperature on clay host rocks behaviour
Dissemination level: PU
Date of issue of this report: 06/06/2024

Page 244

Table 7.23: Parameters for the hydraulic permeability and small strain stiffness

Symbol	Name	Value	Unit
$k_{\parallel}$	Intrinsic permeability parallel to bedding	4E−19	m^2
$k_{\perp}$	Intrinsic permeability normal to bedding	2E−19	m^2
β_{per}	Evolution parameter	1.5E5	–
YI^{thr}	threshold yield index	0.95	–
$\hat{\varepsilon}^3_{eq}$	Von Mises' equivalent deviatoric plastic strain	0.04	–
$E_{int_{\parallel}}$	Initial Young's modulus parallel to bedding	1600	MPa
$E_{int_{\perp}}$	Initial Young's modulus normal to bedding	800	MPa
$E_{min_{\parallel}}$	Minimum Young's modulus parallel to bedding	320	MPa
$E_{min_{\perp}}$	Minimum Young's modulus normal to bedding	160	MPa
$\gamma_{0.7}$	Evolution parameter	0.032	–
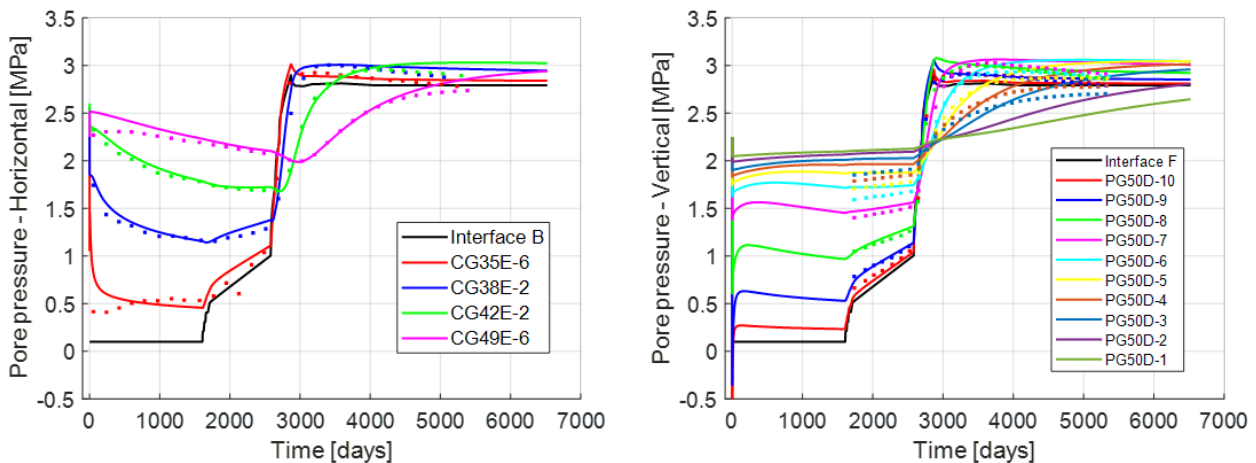
Figure 7.82: Pore pressure evolution depending on the permeability and stiffness modification

EURAD (Deliverable n˚ 7.6) – Modelling report on the effect of temperature on clay host rocks behaviour
Dissemination level: PU
Date of issue of this report: 06/06/2024

Page 245

7.2.8. Free version: UPC

This section contains an account of the work performed by UPC to analyse the large-scale PRACLAY heater test. The mechanical constitutive model used to represent the mechanical behaviour of Boom Clay in the analyses reported in this section is the advanced Hyperbolic Mohr-Coulomb (HMC) model with hardening-softening and nonlocal formulation (see Section 4.7). A concrete lining has been installed in the PRACLAY gallery and an isotropic thermo-elastic model is used to represent its behaviour. In additon, a bi-lienar elastic constitutive model is adopted to represent the properties of air gap element.

Air gap approach to simulate over-excavation According to specifications, gallery over-excavation needs to be considered. For that purpose, a bi-linear elastic model that uses two different elastic moduli has been employed: the open gap uses a very small elastic modulus (E_{open}^{gap}) whereas the closed gap is modelled with a much larger elastic modulus (E_{closed}^{gap}), as shown in Figure 7.83. A volumetric strain (ε^v) is set as the threshold between the open gap and closed gap, as:

$$E^{gap} = \begin{cases} E_{open}^{gap}, & \varepsilon^v < \varepsilon_{limit}^v \\ E_{closed}^{gap}, & \varepsilon^v \geq \varepsilon_{limit}^v \end{cases}$$

During the excavation stage, the deformations of the gallery wall increase until the gallery contacts the concrete lining when the gallery deformation reaches the width of the air gap. Afterwards, the gallery wall and concrete lining deform together, and the support forces will be provided by the interaction between the host rock and the concrete lining. To represent this occurrence, ε_{limit}^v should be theoretically set at 1.0, however, in the current simulations, ε_{limit}^v is set as 0.99 to avoid numerical difficulties.
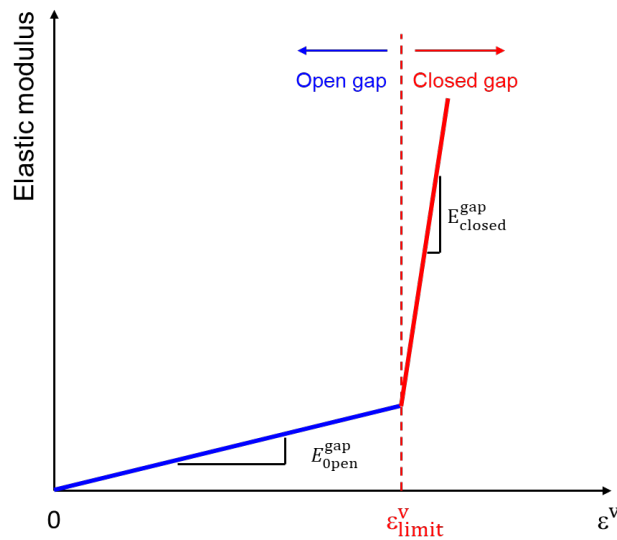
Figure 7.83: The Bi-linear constitutive model.

From the hydraulic point of view, the gap permeability is higher by several orders of magnitude compared to the other materials. A high porosity, close to 1.0, should be considered. In this study, however, the initial porosity is set as 0.8 to suppress numerical problems. The intrinsic permeability varies with the evolution of porosity:

$$k = k_0 \frac{\phi^3}{(1-\phi)^2} \frac{(1-\phi_0)^2}{\phi_0^3}$$

where ϕ_0 is reference porosity and k_0 is intrinsic permeability for a porosity ϕ_0.

EURAD (Deliverable n˚ 7.6) – Modelling report on the effect of temperature on clay host rocks behaviour
Dissemination level: PU
Date of issue of this report: 06/06/2024

Page 246

For the water retention curve and the relative permeability law, the well-known Van-Genuchten model is adopted:

$$k_{rl} = \sqrt{S_e} \left[1 - \left(1 - S_e^{1/\lambda\,\lambda} \right) \right]^2 \tag{7.4}$$

$$S_e = \frac{S_l - S_{lr}}{S_{ls} - S_{lr}} = \left[1 + \left(\frac{S_u}{P} \right)^{\frac{1}{1-\lambda}} \right]^{-\lambda} \tag{7.5}$$

S_e is the effective liquid saturation. S_l is the degree of saturation; S_{lr} is the residual degree of saturation; S_{ls} is the degree of saturation in saturated conditions; P and λ are the model parameter. In this study, a very low value of the reference air entry pressure is considered, which means that the saturation occurs suddenly when capillary pressure vanishes (Tourchi, 2020; Tourchi et al., 2021).

Regarding heat flow, Fourier's law is used to describe the thermal properties of the air gap element. The variation of the thermal conductivity can be shown in:

$$\lambda = \lambda_{sat} S_l + \lambda_{dry} \left(1 - S_l \right) \tag{7.6}$$

where λ is the thermal conductivity; λ_{sat} and λ_{dry} are the thermal conductivity of the water-saturated and dry porous medium, respectively. Table 7.24 lists the input parameters of the air gap element.

Due to over-excavation, the contact is supposed to occur during the gallery excavation as the host rock converges towards the support producing a contact pressure on the interface between host rocks and support. Salehnia et al. (2015) and Salehnia (2014) developed hydro-mechanical interface elements and implemented them in the finite element software LAGAMINE. Moreover, they applied the developed interface elements to the hydro-mechanical simulation of the large-scale gallery excavation in Boom Clay to analyse the evolutions of pore pressure and displacements (Salehnia et al., 2015).

As a verification step, numerical simulations of hydro-mechanical excavation problems have been carried out in CODE_BRIGHT, using the air gap element to represent the contact between the host rock and the concrete lining. The two-dimensional plane strain numerical model in CODE_BRIGHT is consistent with the one shown by Salehnia et al. (2015). The gallery has a total excavated radius of 2.49 m taking into account 40 cm of the concrete lining and a 9 cm gap (over-excavation) between the rock and the lining. The constitutive model parameters in CODE_BRIGHT are the same ones as in LAGAMINE, except for the anisotropy of cohesion (anisotropic cohesion is adopted in LAGAMINE, but isotropy in CODE_BRIGHT).

The initial pore pressure (2.25 MPa) and initial stresses (σ_{xx} = 3.8475 MPa, σ_{yy} = 4.5 MPa) are applied in the whole model. Two modelling stages have been considered, the excavation stage (0–6 days) and the waiting stage (6–500 days); the corresponding boundary conditions can be found in Figure 7.84(a) and Figure 7.84(b). Figure 7.84(c) show the utilized mesh consisting of 1276 quadrilateral elements.

EURAD (Deliverable n˚ 7.6) – Modelling report on the effect of temperature on clay host rocks behaviour
Dissemination level: PU
Date of issue of this report: 06/06/2024

Page 247
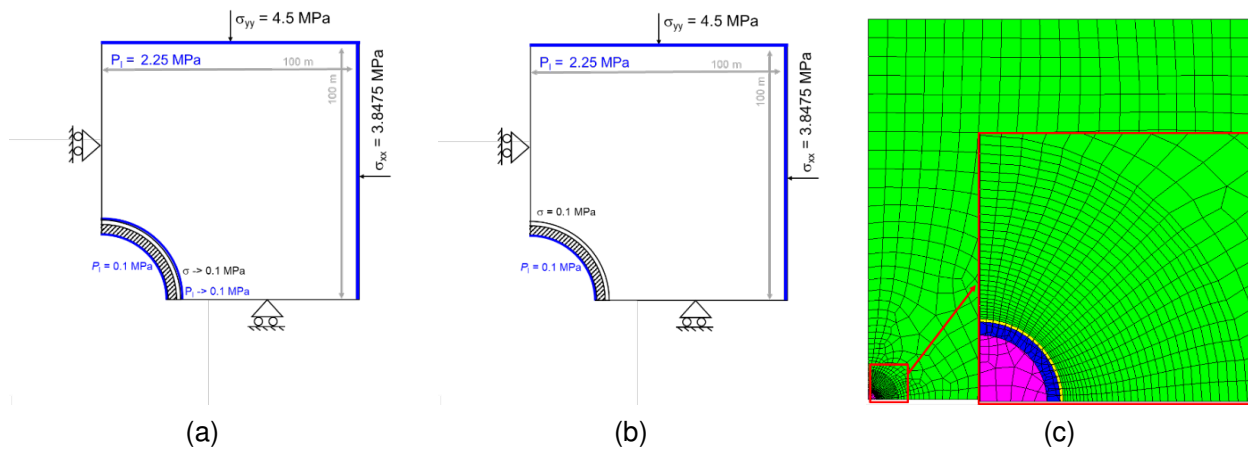
Figure 7.84: Conceptual model showing (a) the excavation stage, 0–6 days, (b) the waiting stage, 6 days–500 days, and (c) the utilized mesh (1276 quadrilateral elements).

Table 7.24: Input parameters of the air gap element.

Properties	Parameter			Value
Thermal	Thermal conductivity	λ_{dry}	[W/m/K]	0.035
	Thermal conductivity	λ_{sat}	[W/m/K]	0.6
	Linear thermal expansion coefficient	α_s	[°C^{-1}]	1.4×10^{-5}
Hydraulic	Intrinsic permeability	k_0	[m^2]	1×10^{-16}
	Porosity	ϕ	[–]	0.8
	Van Genuchten model parameter	P_0	[MPa]	10
	Van Genuchten model parameter	σ_0	[N m^{-1}]	0.001
	Van Genuchten model parameter	λ		0.5
	Van Genuchten model parameter	S_{rl}		7×10^{-3}
	Van Genuchten model parameter	a		10
Mechanical	Young's modulus	E_{open}^{gap}	[MPa]	1
	Young's modulus	E_{closed}^{gap}	[MPa]	100
	Poisson's ratio	ν	[–]	0.3
	Strain limit	ε_{limit}^v	[–]	0.99
Physical	Solid phase density	ρ_s	[kg/m^3]	1
	Solid phase specific heat	C_s	[J/(kgK)]	1000

Comparisons of Hydro-Mechanical (HM) responses between LAGAMINE (using the contact element) and CODE_BRIGHT (using the air gap approach) are presented in Figure 7.85. Figure 7.85(a) shows the comparison of displacements in the excavation stage. Since the convergence of the host rock due to the excavation takes place mostly during the excavation phase and, therefore, contact between host rock and lining occurs then. It can be observed that the evolution of displacements in CODE_BRIGHT are consistent with those in LAGAMINE. There is a little bit of discrepancy in deformations between both CODE_BRIGHT and LAGAMINE, and this discrepancy might be caused by different utilized mechanical constitutive models (i.e., different anisotropy of cohesion). Furthermore, Figure 7.85(b) and Figure 7.85(c) show the pore pressure profiles at time t = 6 days and t = 500 days, and both CODE_BRIGHT and LAGAMINE are consistent. Such a good agreement of HM responses verify the adopted air gap approach in analysing the over-excavation problems.

EURAD (Deliverable n° 7.6) – Modelling report on the effect of temperature on clay host rocks behaviour
Dissemination level: PU
Date of issue of this report: 06/06/2024

Page 248
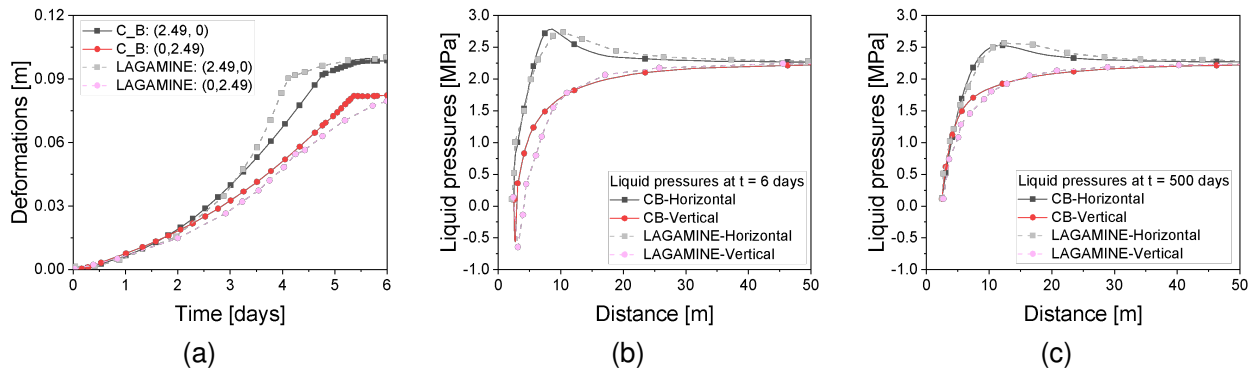
Figure 7.85: Comparisons between CODE_BRIGHT (C_B) results and LAGAMINE results for (a) the evolutions of displacements at two different points, (b) liquid pressure profiles at time t = 6 days*, and (c) liquid pressure profiles at time* t = 500 days*.*

Figure 7.86(a) and Figure 7.86(b) respectively show the deformed geometry and the volumetric strains at time t = 4.825 days (during the excavation stage) in the CODE_BRIGHT analysis. In Figure 7.86(a), the host rocks contact the concrete lining at the right hand corner point, however, there are still some spaces at the top corner point. Correspondingly, as shown in Figure 7.86(b), the volumetric strain at the right corner is close to 1.0 (i.e., the air gap is at a closed condition) and the air gap elements where close to the top corner are still at the open condition.
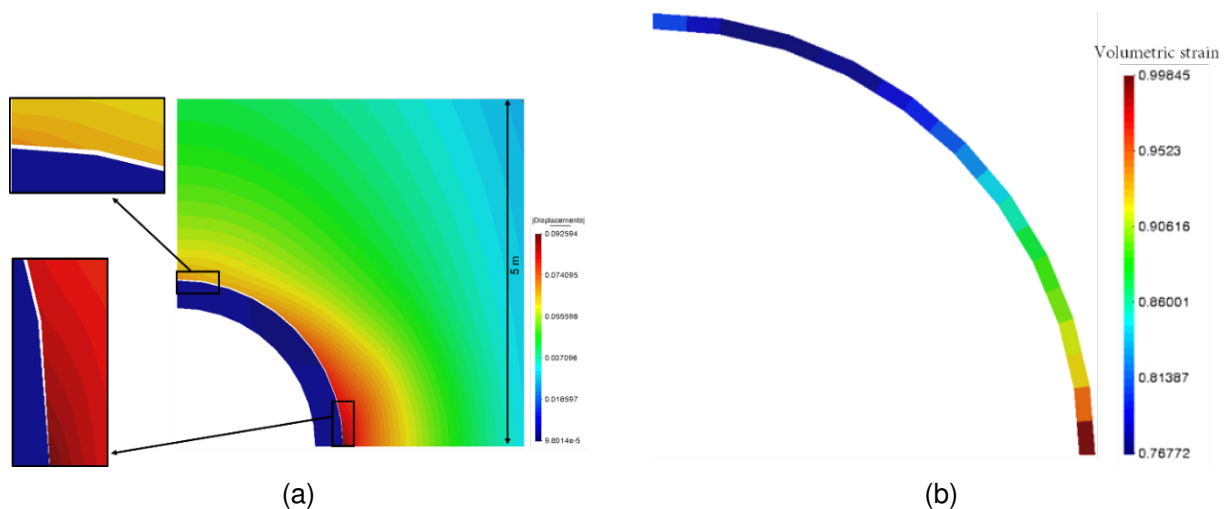
Figure 7.86: (a) Deformed geometry, and (b) th volumetric strains at time t = 4.825 days*.*

Additionally, numerical models without air gap and without lining have been carried out using CODE_BRIGHT, to examine the effect of both structures on the deformations of the host rock. Figure 7.87 shows the comparison of deformations between results obtained from (1) the numerical model with air gap and lining, and (2) the numerical model without air gap and without lining. It can be observed that at the beginning of the excavation, both results are the same; however, for the case with air gap elements and lining, contact occurs as the host rock converges towards the lining, whereas, for the cases without air gap and without lining, the deformations continue to increase. In conclusion, the presented air gap approach can reasonably characterise the contact problems between host rocks and the concrete lining, which can be used in analysing the over-excavation effects.

EURAD (Deliverable n° 7.6) – Modelling report on the effect of temperature on clay host rocks behaviour
Dissemination level: PU
Date of issue of this report: 06/06/2024

Page 249
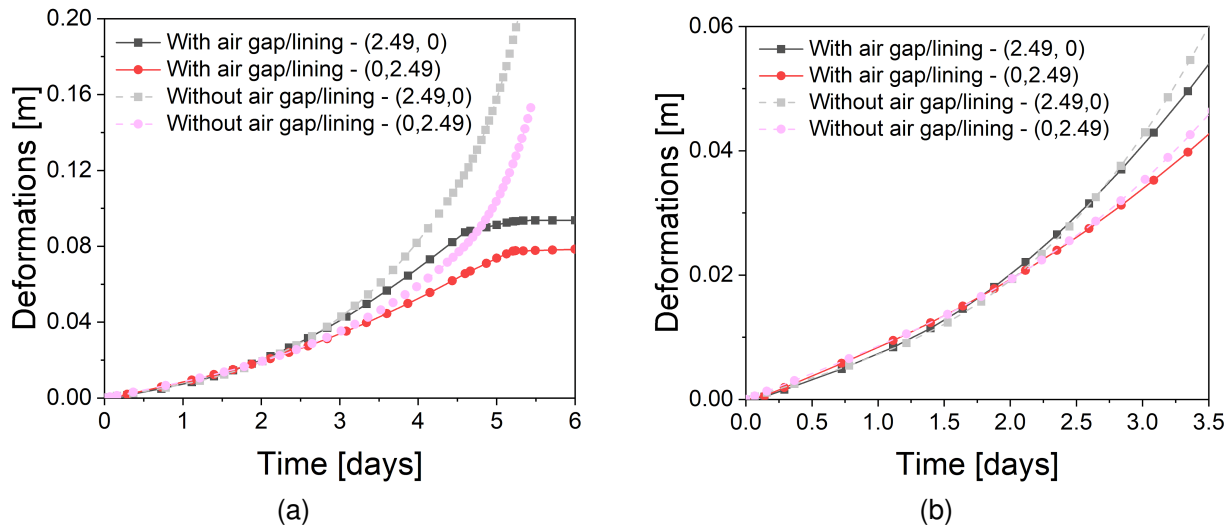
Figure 7.87: Comparison of deformations with and without air gap elements/lining in CODE_BRIGHT simulations: (a) in the period of 0–6 days, (b) in the period of 0–3.5 days.

7.2.8.1. PRACLAY numerical model

In accordance with specifications, the numerical model represents the mid-plane of the PRACLAY Heater test (around Ring 50). Only a quarter of the cross-section is considered due to the symmetric nature of the problem. The calculation domain measures 100 m in the x- and y- directions. An over-excavation of 6 cm is assumed and the excavation radius is estimated to be 1.31 m. The inner and outer radii of the concrete lining are 0.95 m and 1.25 m, respectively. Table 7.24 lists input parameters of the air gap element. Table 7.25 lists the initial conditions of the numerical model, Table 7.26 contains the input parameters for the mechanical model of Boom Clay, and Table 7.27 lists the main physical properties of Boom Clay and concrete lining. The Young's modulus and Poisson's ratio of the concrete lining used are 42 000 MPa and 0.2, respectively.

Regarding the modelling stages, four different stages have been considered, as shown in Figure 7.88. In each modelling stage, the boundary conditions at the gallery wall are as follows:

- **The excavation stage** (04-Oct-2007 to 06-Nov-2007). During excavation, the host rock freely deforms until contacting the outer boundary of the concrete lining. The smoothed excavation method (Song et al., 2021a) has been utilized; after that the boundary conditions at the wall are provided by the interaction between the host rock and the concrete lining. The pore pressure at the gallery is assumed to decrease from 2.25 MPa to atmospheric pressure (0.1 MPa).

- **The waiting stage** (from 06-Nov-2007 to 05-Mar-2012). The pore pressure in the inner boundary of the concrete lining is maintained at 0.1 MPa.

- **The artificial injection stage** (from 05-Mar-2012 to 13-Nov-2014). The pore pressure is prescribed at the inner boundary of the concrete lining according to Figure 7.89(a).

- **The heating stage** (from 03-Nov-2014 to 17-Aug-2025). Based on the measured temperature at the lining extrados, a temperature boundary condition is set at the lining extrados, as shown in Figure 7.89(b). In addition, a no-flow B.C. is applied to during the heating stage, as specified.

EURAD (Deliverable n° 7.6) – Modelling report on the effect of temperature on clay host rocks behaviour
Dissemination level: PU
Date of issue of this report: 06/06/2024

Page 250
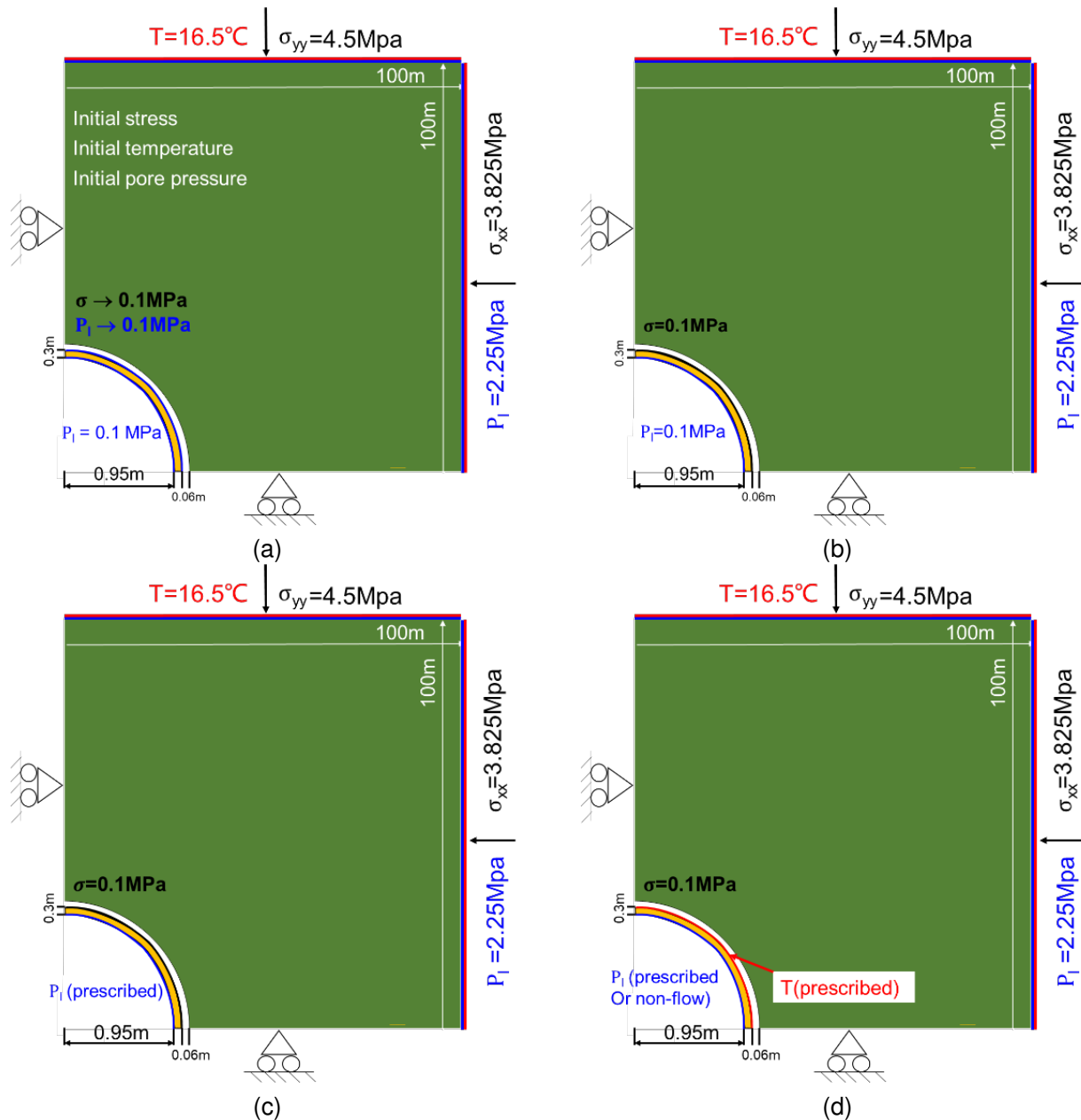
Figure 7.88: Boundary conditions at different modelling stages: (a) the excavation stage, (b) the waiting stage, (c) the artificial injection stage, and (d) the heating stage.

Constant boundary conditions (temperature, pore pressure and total stresses) are applied at the far boundaries in all stages. In both the bottom and the left boundaries, the normal displacements are restrained and no-flow hydraulic boundary conditions are prescribed. Figure 7.90 shows the mesh used comprising 5043 quadrilateral elements.

EURAD (Deliverable n° 7.6) – Modelling report on the effect of temperature on clay host rocks behaviour
Dissemination level: PU
Date of issue of this report: 06/06/2024

Page 251
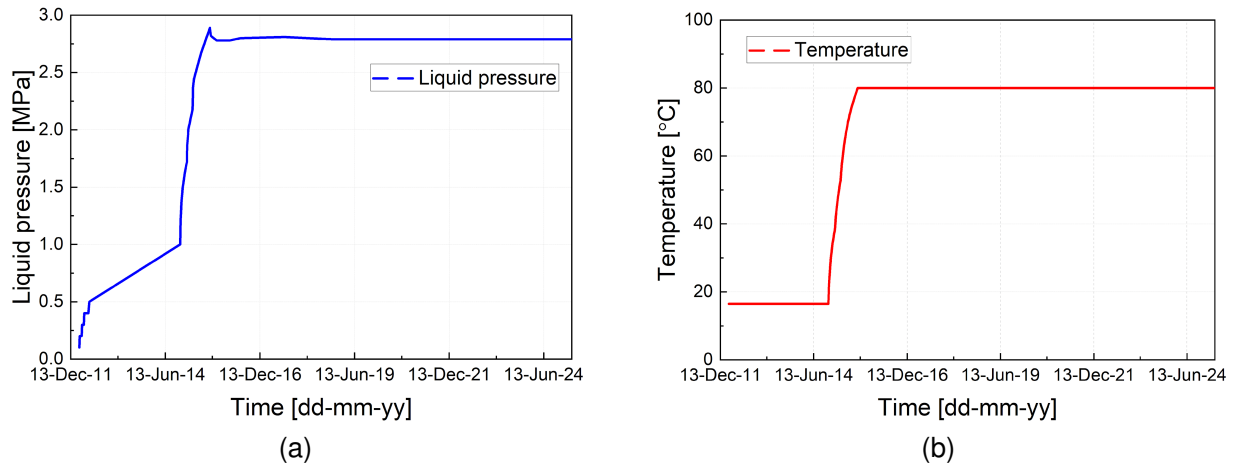
Figure 7.89: (a) Pore pressure boundary condition at the inner boundary of concrete lining in the artificial injection stage, and (b) temperature boundary condition at the lining extrados.
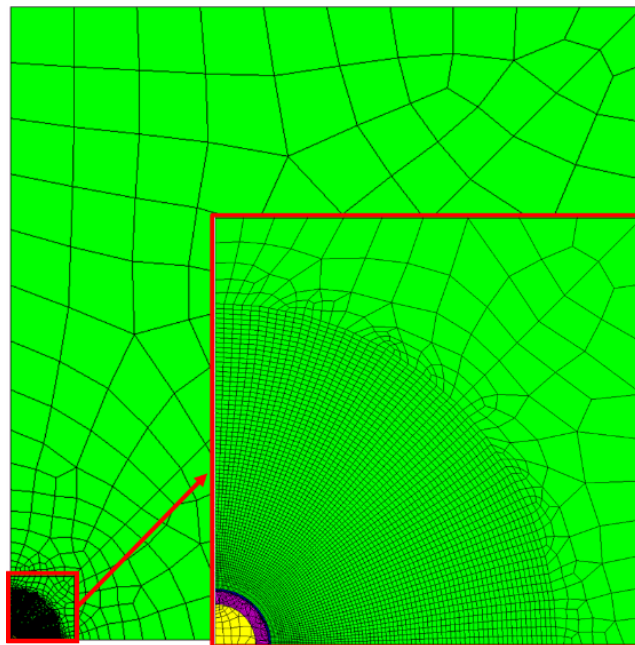
Figure 7.90: Mesh used in the numerical model (5043 quadrilateral elements).

Table 7.25: Initial conditions.

		Boom Clay	Concrete	Air gap
Total stresses	[MPa]	$\sigma_{xx} = \sigma_{zz} = -3.825; \sigma_{yy} = -4.5$	$\sigma_{xx} = \sigma_{yy} = \sigma_{zz} = -0.1$	$\sigma_{xx} = \sigma_{yy} = \sigma_{zz} = -0.1$
Pore pressures	[MPa]	2.25	0.1	0.1
Temperature	[°C]	16.5	16.5	16.5
Initial porosity	[–]	0.39	0.1	0.8

EURAD (Deliverable n° 7.6) – Modelling report on the effect of temperature on clay host rocks behaviour
Dissemination level: PU
Date of issue of this report: 06/06/2024

Page 252

Table 7.26: Input mechanical parameters for Boom Clay (free version).

Elastic	Elastic moduli	E_1 = 400 MPa, E_2 = 200 MPa
	Poisson's ratio	ν_1 = 0.25, ν_2 = 0.125
	Shear modulus	G = 80 MPa
Plastic	Peak strength	ϕ_{ini} = 8 deg, ϕ_{peak} = 18 deg, c_0 = 0.3 MPa, P_{t0} = 0.1 MPa
	Post-rupture	b_{post} = 160, b_{res} = 1.5
	Hardening	ξ = 0.005, a_{hard} = 0.002
	Residual strength	r_{post} = 0.1, ϕ_{res} = 10 deg
	Flow rule	ω = 0.1
Viscoplastic	$\eta_{perzyna}$	1×10^5 MPa s
	Stress power	1.0
Strength anisotropy	Ω_{90} = 1.29, Ω_m = 0.94, δ_m = 45 deg, n = 0.1	
Internal length	l_s	0.08

Table 7.27: Main physical, thermo-hydraulic parameters for Boom Clay and Concrete.

Material parameters		Boom Clay	Concrete
Solid phase density	[kg/m^3]	2639	2650
Porosity	[–]	0.39	0.1
Horizontal intrinsic permeability	[m^2]	4×10^{-19}	4.5×10^{-18}
Vertical intrinsic permeability	[m^2]	2×10^{-19}	4.5×10^{-18}
Horizontal thermal conductivity	[W/mK]	1.65	2.86
Vertical thermal conductivity	[W/mK]	1.31	2.86
Linear thermal expansion coefficient	[°C^{-1}]	1×10^{-5}	1×10^{-5}
Solid phase specific heat	[J/(kgK)]	769	800

Numerical results of the free version. In this section, numerical studies of the free version case will be carried out. As specified, the choice of mechanical model is let free to the modelling teams, and UPC decided to adopt the advanced Hyperbolic Mohr-Coulomb (HMC) model with hardening-softening and non-local formulation. In this section, the overpressure mechanism is first analysed. Subsequently, parametric analyses are carried out to analyse the sensitivity of temperature, pore pressure and plastic strains to THM properties. In addition, the effect of hydraulic boundary conditions will be examined: the specified pore pressure and the no-flow boundary conditions will be used in the heating stage. In addition, comparisons of temperatures and pore pressures between numerical predictions and experimental observations will be presented.

To better understand the overpressure mechanism, the pore pressure variation can be expressed as:

$$\mathrm{d}p = \Pi\,\mathrm{d}\sigma + \Lambda\,\mathrm{d}T \tag{7.7}$$

showing that the pore pressure variations on the changes of applied stresses and changes of temperatures. Π is the Skempton's coefficient, and Λ is the thermal pressurization coefficient. For the isotropic

EURAD (Deliverable n° 7.6) – Modelling report on the effect of temperature on clay host rocks behaviour
Dissemination level: PU
Date of issue of this report: 06/06/2024

Page 253

poroelastic case (Braun, 2019b; Vu et al., 2020):

$$\Pi_{\mathsf{iso}} = \frac{-\dfrac{b}{K}}{\dfrac{b^2}{K} + \dfrac{b - \phi}{K_S} + \dfrac{\phi}{K_w}} \tag{7.8}$$

$$\Lambda_{\mathsf{iso}} = \frac{3\phi(\alpha_w - \alpha)}{\dfrac{b^2}{K} + \dfrac{b - \phi}{K_S} + \dfrac{\phi}{K_w}} \tag{7.9}$$

$$K_{\mathsf{iso}} = \frac{E}{3(1 - 2\nu)} \tag{7.10}$$

For the anisotropic case (Vu et al., 2020):

$$\Pi_{\mathsf{aniso}} = \frac{1}{\mathbf{B} : \mathbf{C_e}\mathbf{B} + \dfrac{1}{3K_S}(\mathbf{B} - \phi\mathbf{I}) : \mathbf{I} + \dfrac{\phi}{K_w}} \mathbf{B} : \mathbf{C_e} \tag{7.11}$$

$$\Lambda_{\mathsf{aniso}} = \frac{(3\alpha_S - \mathbf{I} : \boldsymbol{\alpha}) + 3\phi(\alpha_l - \alpha_S)}{\mathbf{B} : \mathbf{C_e}\mathbf{B} + \dfrac{1}{3K_S}(\mathbf{B} - \phi\mathbf{I}) : \mathbf{I} + \dfrac{\phi}{K_w}} \tag{7.12}$$

$$K_{\mathsf{aniso}} = \frac{2E_1(1 + 2\nu_2) + E_2(1 - \nu_1)}{9\left(1 - \nu_1 - 2\nu_2^2 \dfrac{E_1}{E_2}\right)} \tag{7.13}$$

The subscripts of 'iso' and 'aniso' represent the isotropic and anisotropic cases, respectively. K_w is the bulk modulus of water. α_l and α_s are the linear thermal expansion coefficient of the liquid and solid phases, respectively. From the analytical solutions, the overpressure is mainly controlled by Biot's coefficient b, solid compressibility K_s, and water compressibility K_w. In the current analyses, the Biot coefficient, b, is equal to 1.0 and, therefore $K_s \rightarrow \infty$. In that case, the overpressure is mainly controlled by the drained bulk modulus K.

The expressions above show that the stiffness parameters (E_1, E_2, ν_1 and ν_2) play a crucial role in the pore pressure evolution. Therefore, in the following, the sensitivity of the THM responses to the stiffness parameters is first studied. Afterwards, parametric analyses are performed to discuss the effect of thermal conductivity, intrinsic permeability and HM coupling parameters on the THM response. Finally, the effect of hydraulic boundary conditions and mesh sizes will be explored.

(a). Sensitivity analyses of the THM response to Young's moduli. In this section, three different groups of parameters (see Table 7.28) are used: in Case A.1, the specified information of stiffness parameters is employed, while, in Case A.3, the stiffness properties presented in Chen et al. (2011) are adopted. For Case A.2, intermediate stuffness parameters have ben employed. The plastic parameters are derived from the plastic properties presented in Salehnia et al. (2015) for Boom Clay.

EURAD (Deliverable n˚ 7.6) – Modelling report on the effect of temperature on clay host rocks behaviour
Dissemination level: PU
Date of issue of this report: 06/06/2024

Page 254

Table 7.28: Input parameters for Cases A1, A2 and A3 (with different stiffness parameters).

	A.1*	A.2	A.3
Description	Specified stiffness		After Chen et al. (2011)
Stiffness	E_1 = 400 MPa E_2 = 200 MPa ν_1 = 0.25 ν_2 = 0.125 G = 80 MPa	E_1 = 1000 MPa E_2 = 500 MPa ν_1 = 0.25 ν_2 = 0.125 G = 250 MPa	E_1 = 1400 MPa E_2 = 700 MPa ν_1 = 0.25 ν_2 = 0.125 G = 280 MPa
Calculated K	K = 185.86 MPa	K = 464.65 MPa	K = 650.51 MPa
Intrinsic permeability	$K_\parallel = 4 \times 10^{-19}\,\mathrm{m}^2$ $K_\perp = 2 \times 10^{-19}\,\mathrm{m}^2$	$K_\parallel = 4 \times 10^{-19}\,\mathrm{m}^2$ $K_\perp = 2 \times 10^{-19}\,\mathrm{m}^2$	$K_\parallel = 4 \times 10^{-19}\,\mathrm{m}^2$ $K_\perp = 2 \times 10^{-19}\,\mathrm{m}^2$
H-M coupling parameter	$\beta^s = 5 \times 10^3$	$\beta^s = 5 \times 10^3$	$\beta^s = 5 \times 10^3$
Strength	ϕ_{ini} = 8°, ϕ_{peak} = 18°, c_0 = 0.3 MPa, P_{t0} = 0.1 MPa, b_{post} = 160, b_{res} = 1.5, ξ = 0.005, a_{hard} = 0.002, r_{post} = 0.1, ϕ_{res} = 10°, ω = 0.1, $\eta_{perzyna}$ = 1 × 10^5 MPa s, m = 1.0, Ω_{90} = 1.29, Ω_m = 0.94, δ_m = 45°, n = 0.1, l_s = 0.07		
Water retention curve	P_0 = 7 MPa, λ^r = 0.47		
Thermal conductivity	$\lambda_\parallel$ = 1.65 W/mK, $\lambda_\perp$ = 1.31 W/mK		

Figure 7.91 shows the comparisons of temperature and pore pressure between experimental data and numerical predictions (Case A.1). The numerical predictions of temperatures are generally consistent with experimental data, although a limited overestimate can be observed in the vertical study points. However, the numerical results of pore pressure are far from experimental observations: numerical predictions overestimate the experimental observations in the waiting stage, but underestimate the experimental data in the heating stage.

Figure 7.92 and Figure 7.93 show the comparisons of temperature and pore pressure results between experimental observations and numerical results from Case A.2 and Case A.3, respectively. There is no difference in temperature between Case A.1, Case A.2 and Case A.3, because the same thermal conductivity and the same thermal capacity of Boom Clay are considered. On the other hand, when increasing stiffness, the numerical results of pore pressure decrease in the waiting stage, while increasing in the heating stage. For Case A.2, the numerical predictions of pore pressure match well with experimental observations. However, in Case A.3, pore pressures are overestimated in the heating stage.

Figure 7.94 shows the developed EDZ for the three cases A.1, A.2 and A.3 at the end of the simulations (time t = 6522 days). It can observed that different stiffness properties result in different contours of EDZ, however, there is no significant difference in the size of the EDZ zones (or, plastic zones) between different cases.

EURAD (Deliverable n° 7.6) – Modelling report on the effect of temperature on clay host rocks behaviour
Dissemination level: PU
Date of issue of this report: 06/06/2024

Page 255

Figure 7.91: Comparison of temperature and pore pressure between numerical simulations and field observations: (a) temperature at the points in the horizontal direction, (b) temperature at the points in the vetical direction, (c) pore pressure at the points in the horizontal direction, and (d) pore pressure at the points in the vertical direction. Case A.1.

EURAD (Deliverable n˚ 7.6) – Modelling report on the effect of temperature on clay host rocks behaviour
Dissemination level: PU
Date of issue of this report: 06/06/2024

Page 256

Figure 7.92: Comparison of temperature and pore pressure between numerical simulations and field observations: (a) temperature at the points in the horizontal direction, (b) temperature at the points in the vetical direction, (c) pore pressure at the points in the horizontal direction, and (d) pore pressure at the points in the vertical direction. Case A.2.

EURAD (Deliverable n˚ 7.6) – Modelling report on the effect of temperature on clay host rocks behaviour
Dissemination level: PU
Date of issue of this report: 06/06/2024

Page 257

(a)

(b)

(c)

(d)

Figure 7.93: Comparison of temperature and pore pressure between numerical simulations and field observations: (a) temperature at the points in the horizontal direction, (b) temperature at the points in the vetical direction, (c) pore pressure at the points in the horizontal direction, and (d) pore pressure at the points in the vertical direction. Case A.3.

(a)

(b)

(c)
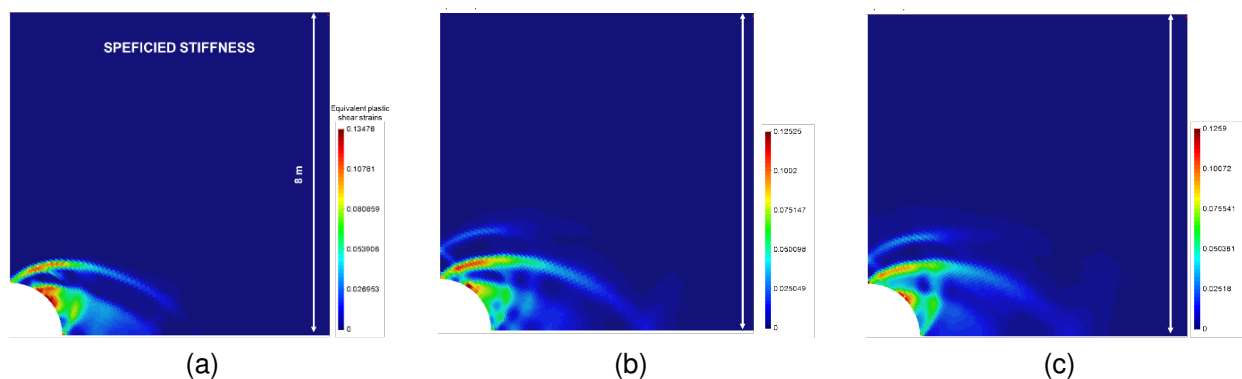
Figure 7.94: Developed EDZ at the end of simulations (17th August 2025): (a) Case A.1, (b) Case A.2, and (c) Case A.3.

(b). Sensitivity analyses of the THM behaviours to Poisson's ratio ν_1. In this section, to analyse the effect of Poisson's ratio ν_1 on the THM responses, two different cases of ν_1 have been considered: $\nu_1 = 0.35$ and $\nu_1 = 0.45$. Table 7.29 lists the input parameters of Case B.2 and Case B.3. Figure 7.95 and Figure 7.96 show the temperatures and pore pressures for Case B.2 and Case B.3, respectively. As expected, there is no difference in temperatures when using different values of ν_1. It can be noted that there is no significant difference in the pore pressure evolutions for different values of ν_1. In addition, it can

EURAD (Deliverable n˚ 7.6) – Modelling report on the effect of temperature on clay host rocks behaviour
Dissemination level: PU
Date of issue of this report: 06/06/2024

Page 258

be concluded from Figure 7.97 that, there is no significant difference of resulting EDZ between different cases. In summary, it can stated that temperature and pore pressure are independent of ν_1.

Table 7.29: Input parameters for Cases B2 and B3 (with different Possions ratios of ν_1).

	B.2	B.3
Stiffness	$E_1 = 400\,\text{MPa}$ $E_2 = 200\,\text{MPa}$ $\nu_1 = 0.35$ $\nu_2 = 0.125$ $G = 91\,\text{MPa}$	$E_1 = 400\,\text{MPa}$ $E_2 = 200\,\text{MPa}$ $\nu_1 = 0.45$ $\nu_2 = 0.125$ $G = 83\,\text{MPa}$
Calculated K	$K = 213.7\,\text{MPa}$	$K = 252.99\,\text{MPa}$
Intrinsic permeability	$K_\| = 4 \times 10^{-19}\,\text{m}^2$ $K_\perp = 2 \times 10^{-19}\,\text{m}^2$	$K_\| = 4 \times 10^{-19}\,\text{m}^2$ $K_\perp = 2 \times 10^{-19}\,\text{m}^2$
H-M coupling parameter	$\beta^s = 5 \times 10^3$	$\beta^s = 5 \times 10^3$
Strength	$\phi_{ini} = 8°$, $\phi_{peak} = 18°$, $c_0 = 0.3\,\text{MPa}$, $P_{t0} = 0.1\,\text{MPa}$, $b_{post} = 160$, $b_{res} = 1.5$, $\xi = 0.005$, $a_{hard} = 0.002$, $r_{post} = 0.1$, $\phi_{res} = 10°$, $\omega = 0.1$, $\eta_{perzyna} = 1 \times 10^5\,\text{MPa s}$, $m = 1.0$, $\Omega_{90} = 1.29$, $\Omega_m = 0.94$, $\delta_m = 45°$, $n = 0.1$, $l_s = 0.07$	
Water retention curve	$P_0 = 7\,\text{MPa}$, $\lambda_r = 0.47$	
Thermal conductivity	$\lambda_\| = 1.65\,\text{W/mK}$, $\lambda_\perp = 1.31\,\text{W/mK}$	

EURAD (Deliverable n˚ 7.6) – Modelling report on the effect of temperature on clay host rocks behaviour
Dissemination level: PU
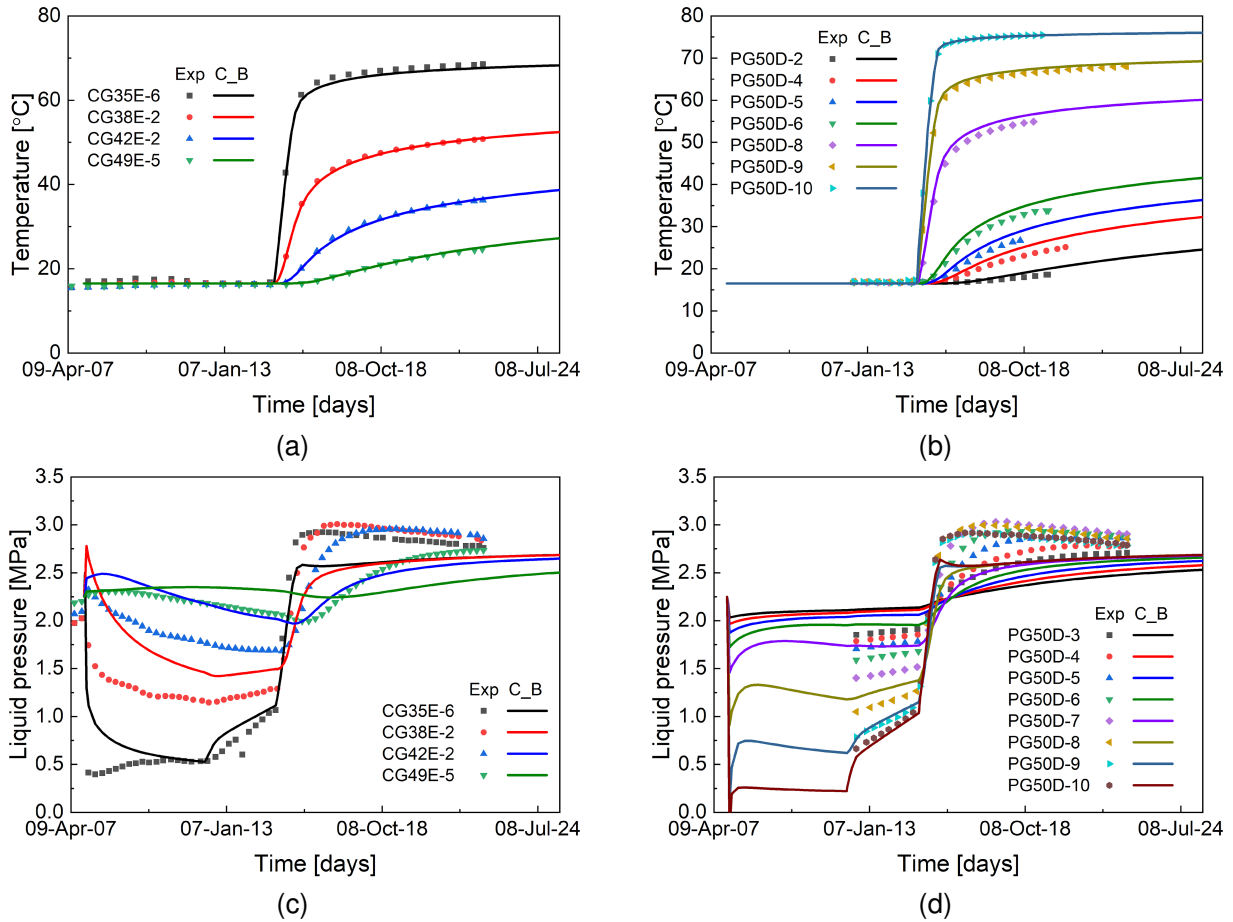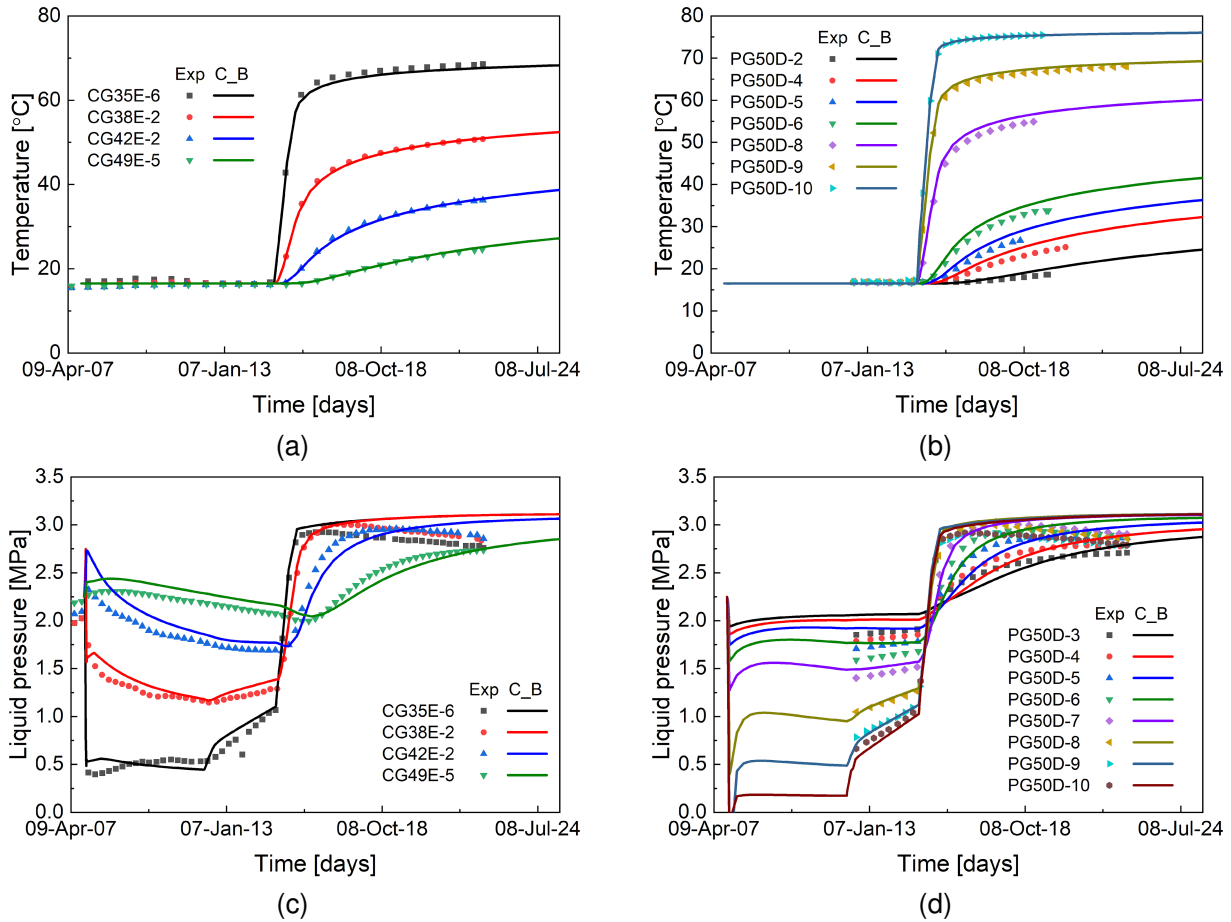Date of issue of this report: 06/06/2024

Page 259

Figure 7.95: Comparison of temperature and pore pressure between numerical simulations and field observations: (a) temperature at the points in the horizontal direction, (b) temperature at the points in the vetical direction, (c) pore pressure at the points in the horizontal direction, and (d) pore pressure at the points in the vertical direction. Case B.2.

EURAD (Deliverable n° 7.6) – Modelling report on the effect of temperature on clay host rocks behaviour
Dissemination level: PU
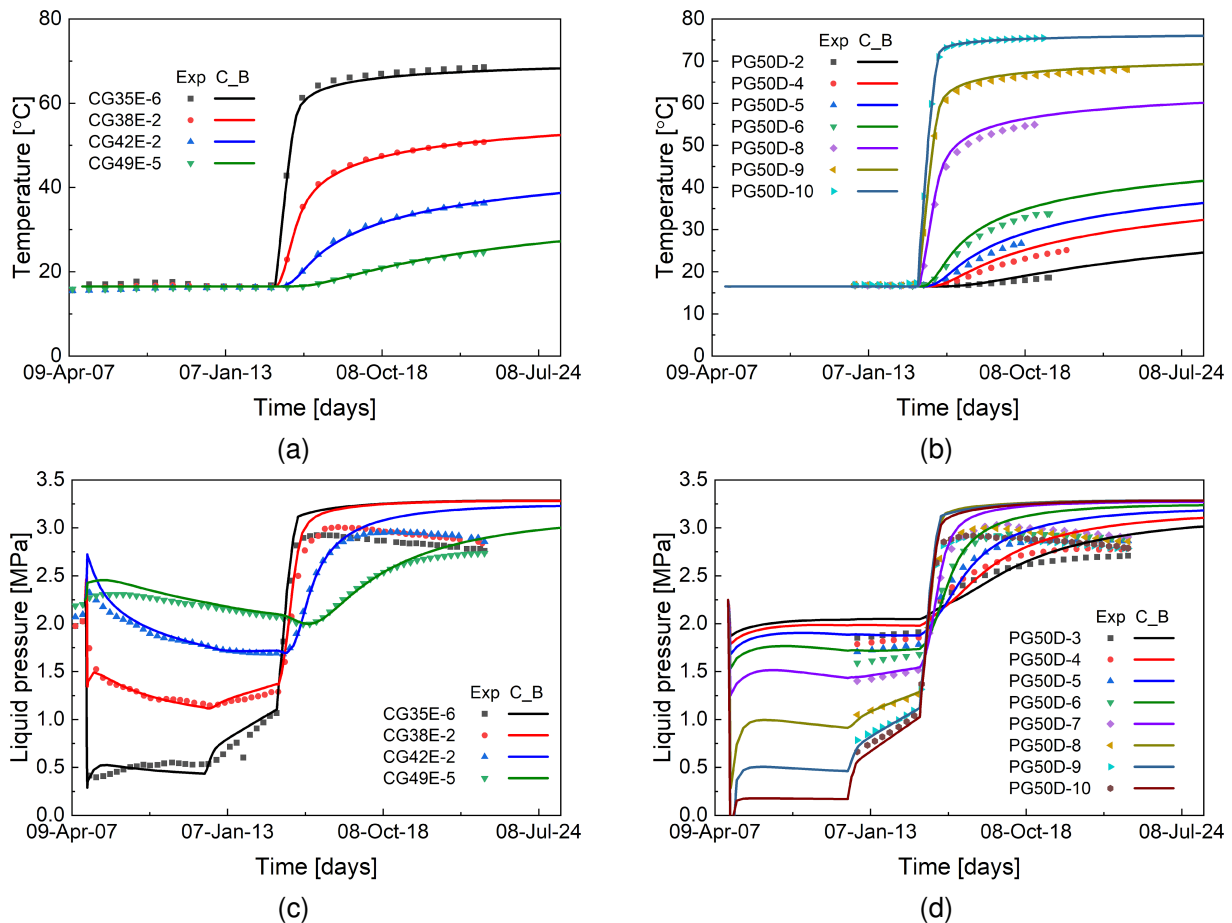Date of issue of this report: 06/06/2024

Page 260

Figure 7.96: Comparison of temperature and pore pressure between numerical simulations and field observations: (a) temperature at the points in the horizontal direction, (b) temperature at the points in the vetical direction, (c) pore pressure at the points in the horizontal direction, and (d) pore pressure at the points in the vertical direction. Case B.3.

EURAD (Deliverable n˚ 7.6) – Modelling report on the effect of temperature on clay host rocks behaviour
Dissemination level: PU
Date of issue of this report: 06/06/2024

Page 261

(a)   (b)   (c)

Figure 7.97: Developed EDZ at the end of simulations (17th August 2025): (a) Case A.1, (b) Case B.2, and (c) Case B.3.

(c). Sensitivity analyses of the THM response to Poisson's ratio ν_2. Sensitivity analyses of the THM responses to Poisson's ratio ν_2 are reported in this section. As indicated in Table 7.30, the bulk modulus K is very sensitive to the values of ν_2; changing ν_2 from 0.25 to 0.4 can result in variations of bulk modulus from 300 MPa to 1604.1 MPa. Accordingly, the pore pressure would be significantly changed, because bulk modulus is a critical parameter controlling the overpressure.

Figure 7.98 and Figure 7.99 show the evolution of temperatures and pore pressures for Case C.2 and Case C.3, respectively. By comparing the results in Figure 7.91 (for the case of $\nu_2 = 0.125$) and Figure 7.98 (for the case of $\nu_2 = 0.25$), the pore pressure results have been improved when using $\nu_2 = 0.25$, however, the pore pressures are still underestimated in the heating stage. In contrast, it can be observed in Figure 7.99 that pore pressures are overestimated for Case C.3. Figure 7.100 shows the contours of EDZ (plastic deviatoric strains) at the end of the simulation (17th August 2025). There is a significant difference in EDZ between Case C.3 and the other two cases (Case A.1, specified stiffness, and Case C.2), and the differences are caused by the different overpressures that were developed in different cases.

EURAD (Deliverable n° 7.6) – Modelling report on the effect of temperature on clay host rocks behaviour
Dissemination level: PU
Date of issue of this report: 06/06/2024

Page 262

Table 7.30: Input parameters for Cases C2 and C3 (with different Possions ratios ν_2). After Chen et al. (2011).

	C.2	C.3
Stiffness	E_1 = 400 MPa E_2 = 200 MPa ν_1 = 0.25 ν_2 = 0.25 G = 100 MPa	E_1 = 400 MPa E_2 = 200 MPa ν_1 = 0.25 ν_2 = 0.4 G = 100 MPa
Calculated K	K = 300 MPa	K = 1606.1 MPa
Intrinsic permeability	$K_\parallel = 4 \times 10^{-19}\,\text{m}^2$ $K_\perp = 2 \times 10^{-19}\,\text{m}^2$	$K_\parallel = 4 \times 10^{-19}\,\text{m}^2$ $K_\perp = 2 \times 10^{-19}\,\text{m}^2$
H-M coupling parameter	$\beta^s = 5 \times 10^3$	$\beta^s = 5 \times 10^3$
Strength	ϕ_{ini} = 8°, ϕ_{peak} = 18°, c_0 = 0.3 MPa, P_{t0} = 0.1 MPa, b_{post} = 160, b_{res} = 1.5, ξ = 0.005, a_{hard} = 0.002, r_{post} = 0.1, ϕ_{res} = 10°, ω = 0.1, $\eta_{\text{perzyna}} = 1 \times 10^5$ MPa s, m = 1.0, Ω_{90} = 1.29, Ω_m = 0.94, δ_m = 45°, n = 0.1, l_s = 0.07	
Water retention curve	P_0 = 7 MPa, λ_r = 0.47	
Thermal conductivity	$\lambda_\parallel$ = 1.65 W/mK, $\lambda_\perp$ = 1.31 W/mK	

EURAD (Deliverable n˚ 7.6) – Modelling report on the effect of temperature on clay host rocks behaviour
Dissemination level: PU
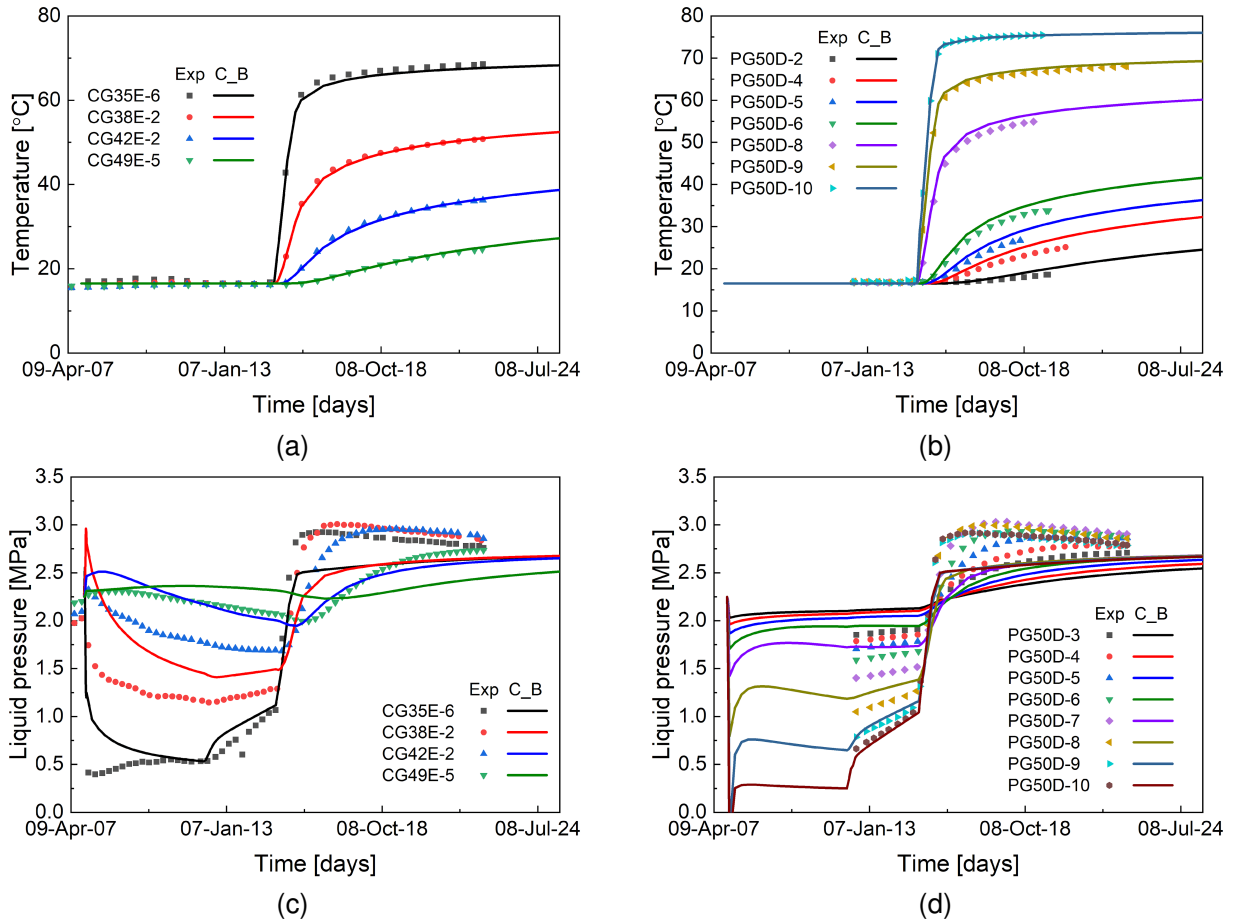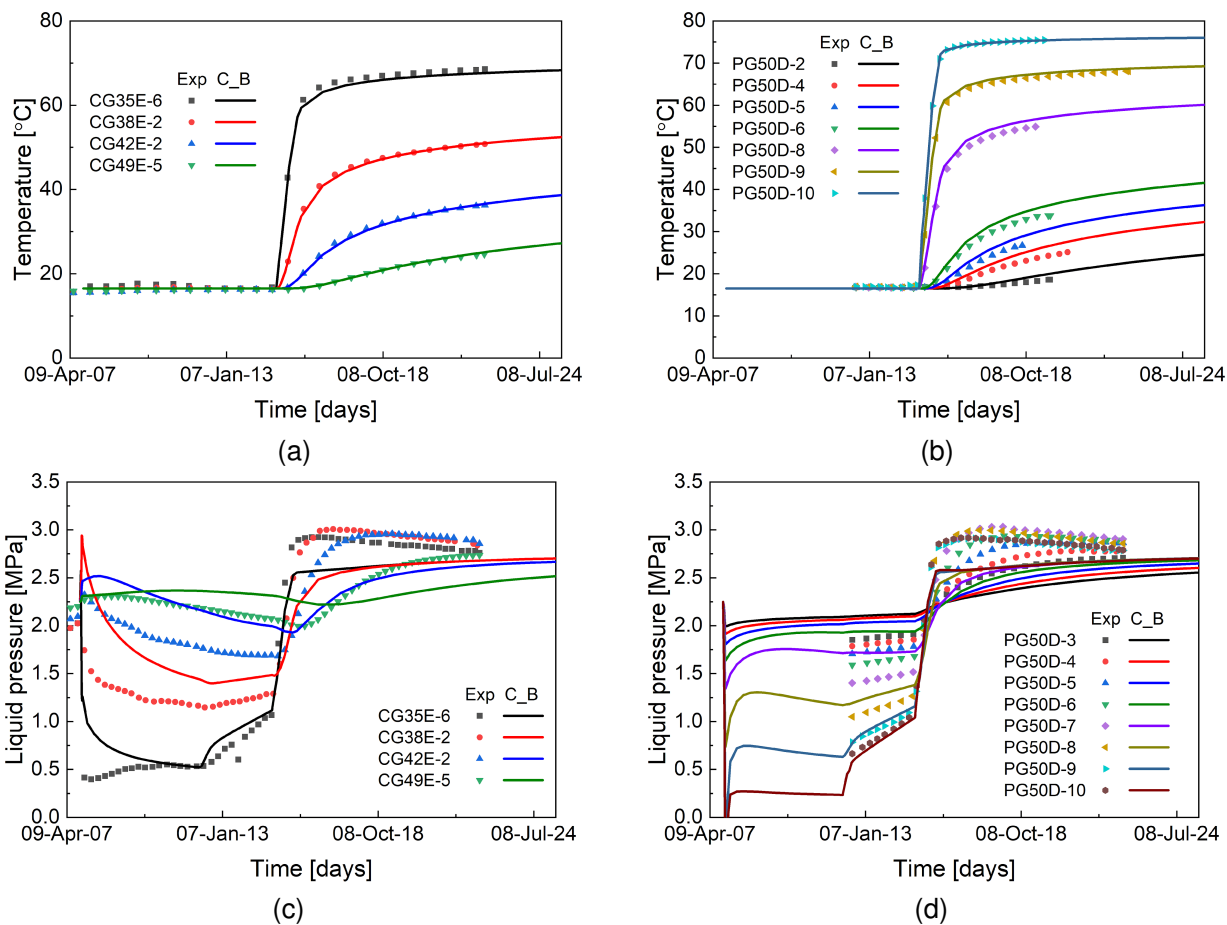Date of issue of this report: 06/06/2024

Page 263

Figure 7.98: Comparison of temperature and pore pressure between numerical simulations and field observations: (a) temperature at the points in the horizontal direction, (b) temperature at the points in the vetical direction, (c) pore pressure at the points in the horizontal direction, and (d) pore pressure at the points in the vertical direction. Case C.2.
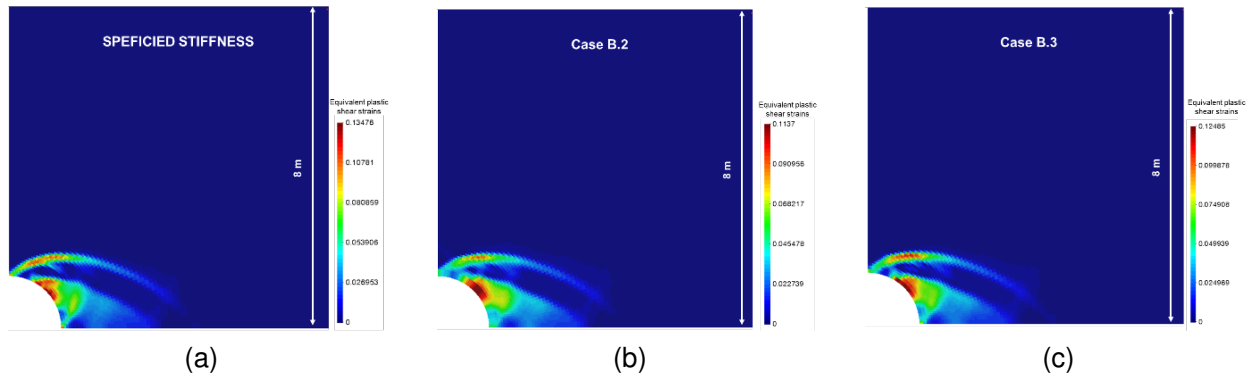
EURAD (Deliverable n˚ 7.6) – Modelling report on the effect of temperature on clay host rocks behaviour
Dissemination level: PU
Date of issue of this report: 06/06/2024

Page 264

(a)

(b)

(c)

(d)

Figure 7.99: Comparison of temperature and pore pressure between numerical simulations and field observations: (a) temperature at the points in the horizontal direction, (b) temperature at the points in the vetical direction, (c) pore pressure at the points in the horizontal direction, and (d) pore pressure at the points in the vertical direction. Case C.3.

(a)

(b)

(c)

Figure 7.100: Developed EDZ at the end of simulations (17th August 2025): (a) Case A.1, (b) Case C.2, and (c) Case C.3.

(d). Sensitivity analyses of the THM response to thermal conductivity. Based on the updated information from Chen et al. (2023), input parameters of thermal conductivity can be changed to $\lambda_{\parallel}$ = 1.9 W/mK, $\lambda_{\perp}$ = 1.2 W/mK. Consequently, Case D.2 has been analysed using those updated thermal conductivity parameters. The rest of the parameters are the same as in case A.1.

Comparing the results of Case A.1 (Figure 7.91) and Case D.2 (Figure 7.101), it can be noted that the

EURAD (Deliverable n˚ 7.6) – Modelling report on the effect of temperature on clay host rocks behaviour
Dissemination level: PU
Date of issue of this report: 06/06/2024

Page 265

temperature results have been significantly improved when using the updated information on thermal conductivity ($\lambda_\parallel$ = 1.9 W/mK, $\lambda_\perp$ = 1.2 W/mK). In contrast, there is no significant difference in pore pressure evolutions between Case A.1 (Figure 7.91) and Case D.2 (Figure 7.101).
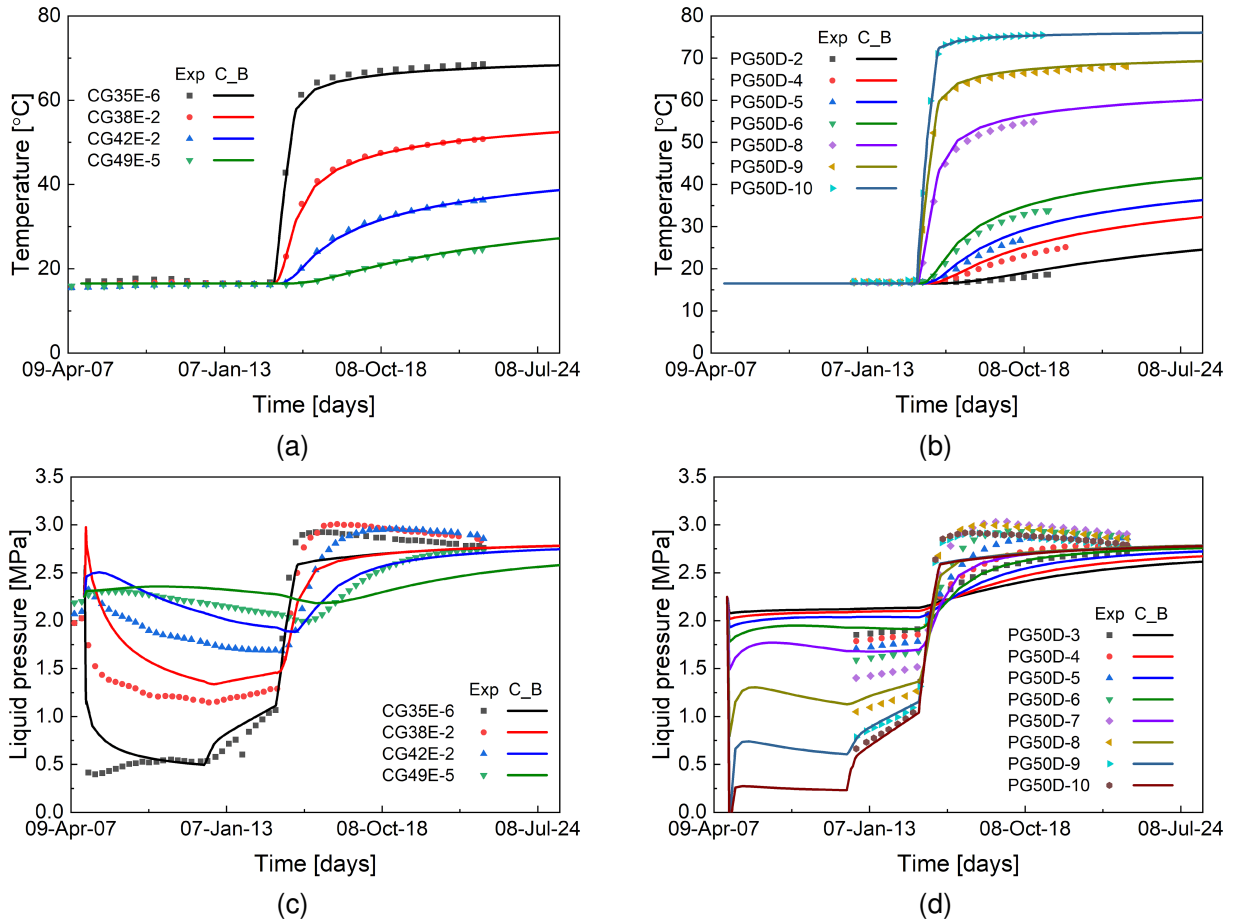

Figure 7.101: Comparison of temperature and pore pressure between numerical simulations and field observations: (a) temperature at the points in the horizontal direction, (b) temperature at the points in the vetical direction, (c) pore pressure at the points in the horizontal direction, and (d) pore pressure at the points in the vertical direction. Case D.2.
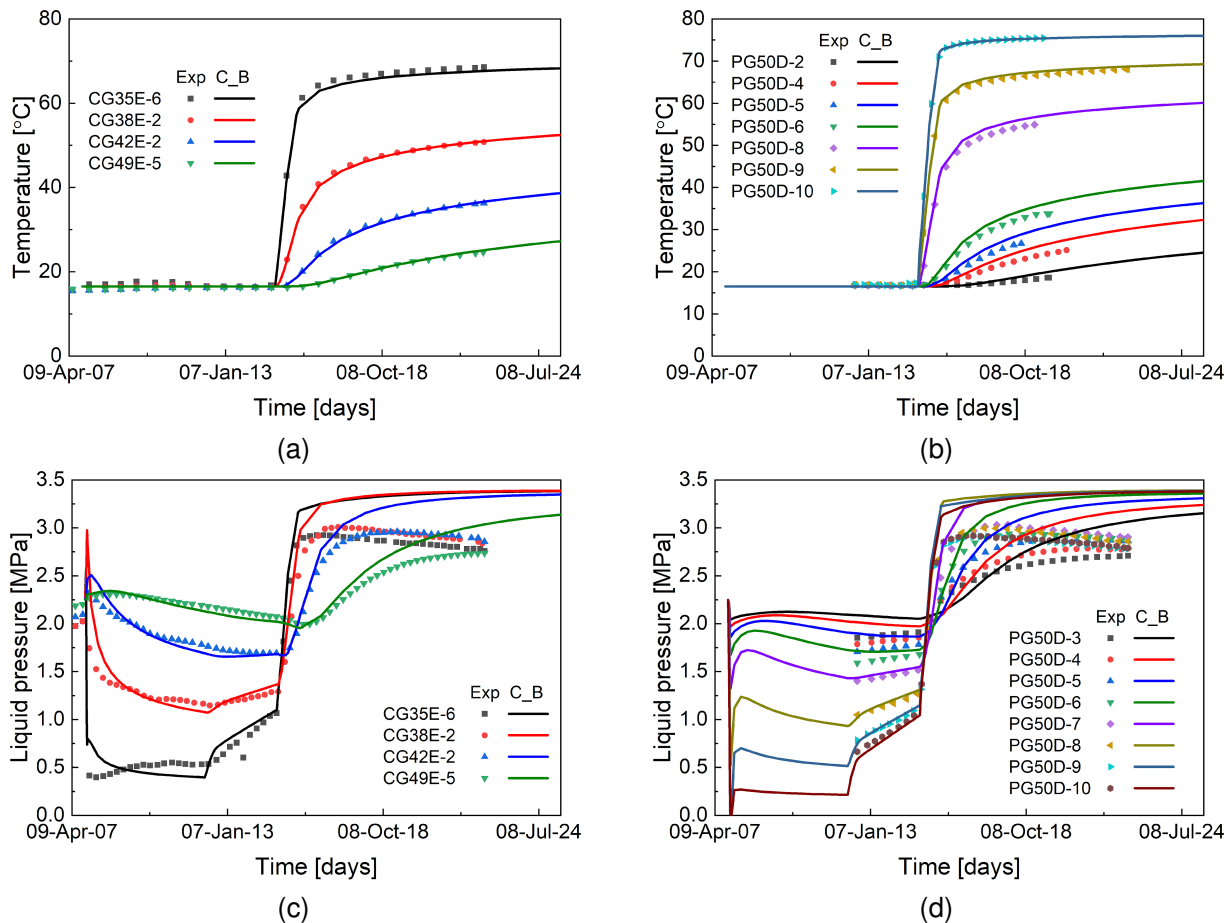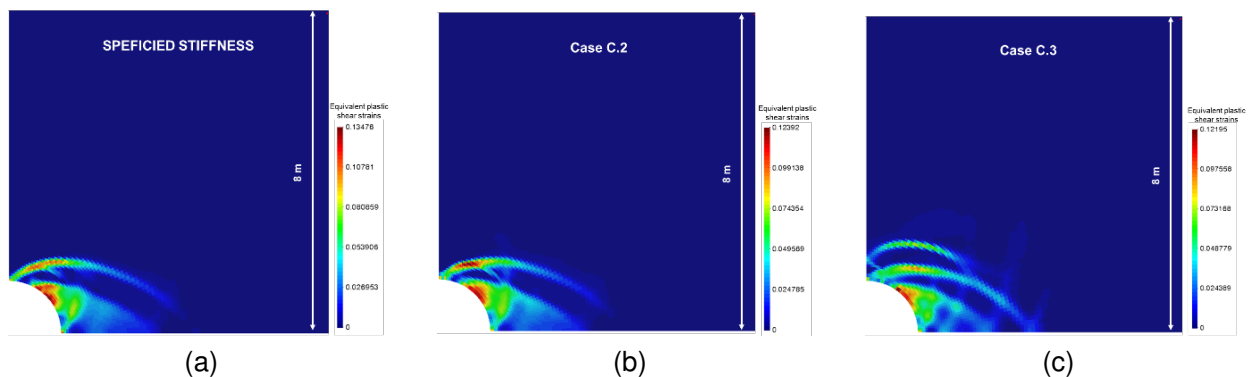
(e). Sensitivity analyses of the THM response to intrinsic permeability. Based on the sensitivity analyses presented above, it was decided to use the stiffness of Case A.2 (E_1 = 1000 MPa, E_2 = 500 MPa, ν_1 = 0.25, ν_2 = 0.125, G = 250 MPa), the thermal conductivity of Case D.2 ($\lambda_\parallel$ = 1.9 W/mK, $\lambda_\perp$ = 1.2 W/mK), while the rest of input parameters are listed in Table 7.31.

Liquid dissipation depends strongly on the intrinsic permeability ($K_\parallel$, $K_\perp$) and, therefore, in this study, two different cases of intrinsic permeability have been considered:the specified intrinsic permeability: $K_\parallel$ = 4×10^{-19} m^2, $K_\perp$ = 2×10^{-19} m^2, and those from Salehnia et al. (2015): $K_\parallel$ = 5.06×10^{-19} m^2, $K_\perp$ = 3×10^{-19} m^2. Figure 7.102 and Figure 7.103 show that the numerical predictions of temperature agree well with experimental observations when using the updated thermal conductivity ($\lambda_\parallel$ = 1.9 W/mK, $\lambda_\perp$ = 1.2 W/mK).

The obtained pore pressures are very sensitive to the input values of intrinsic permeability. In Case E.1, the numerical results of pore pressure overestimate the experimental data in the waiting stage. However, in Case E.2, the numerical predictions of pore pressure match well with experimental observations. In addition, there is nearly no difference in the obtained strain localizations between Case E.1 and Case E.2.

EURAD (Deliverable n˚ 7.6) – Modelling report on the effect of temperature on clay host rocks behaviour
Dissemination level: PU
Date of issue of this report: 06/06/2024

Page 266

Table 7.31: Input parameters for Cases E1 and E2 (with different intrinsic permeability).

	E.1	E.2
Stiffness	E_1 = 1000 MPa, E_2 = 500 MPa, ν_1 = 0.25, ν_2 = 0.125, G = 250 MPa	
Intrinsic permeability	$K_\parallel$ = 4 × 10^{-19} m^2 $K_\perp$ = 2 × 10^{-19} m^2	$K_\parallel$ = 5.06 × 10^{-19} m^2 $K_\perp$ = 2.3 × 10^{-19} m^2
H-M coupling parameter	β^s = 5 × 10^3	β^s = 5 × 10^3
Strength	ϕ_{ini} = 8°, ϕ_{peak} = 18°, c_0 = 0.3 MPa, P_{t0} = 0.1 MPa, b_{post} = 160, b_{res} = 1.5, ξ = 0.005, a_{hard} = 0.002, r_{post} = 0.1, ϕ_{res} = 10°, ω = 0.1, $\eta_{perzyna}$ = 1 × 10^5 MPa s, m = 1.0, Ω_{90} = 1.29, Ω_m = 0.94, δ_m = 45°, n = 0.1, l_s = 0.07	
Water retention curve	P_0 = 7 MPa, λ_r = 0.47	
Thermal conductivity	$\lambda_\parallel$ = 1.9 W/mK, $\lambda_\perp$ = 1.2 W/mK	

EURAD (Deliverable n˚ 7.6) – Modelling report on the effect of temperature on clay host rocks behaviour
Dissemination level: PU
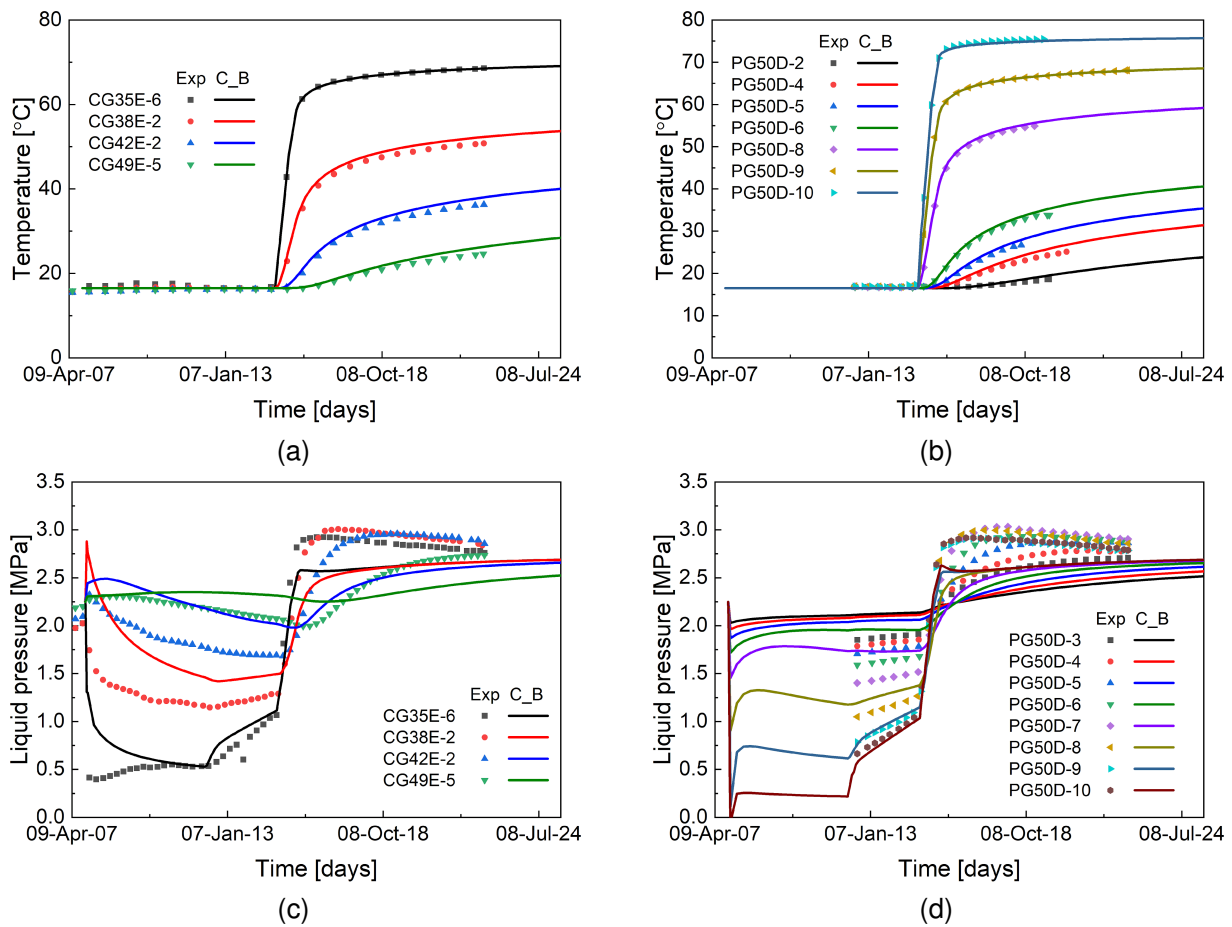Date of issue of this report: 06/06/2024

Page 267

Figure 7.102: Comparison of temperature and pore pressure between numerical simulations and field observations: (a) temperature at the points in the horizontal direction, (b) temperature at the points in the vetical direction, (c) pore pressure at the points in the horizontal direction, and (d) pore pressure at the points in the vertical direction and (e) plastic shear strains at the end of simulations (17th August 2025). Case E.1.

EURAD (Deliverable n˚ 7.6) – Modelling report on the effect of temperature on clay host rocks behaviour
Dissemination level: PU
Date of issue of this report: 06/06/2024

Page 268

Figure 7.103: Comparison of temperature and pore pressure between numerical simulations and field observations: (a) temperature at the points in the horizontal direction, (b) temperature at the points in the vetical direction, (c) pore pressure at the points in the horizontal direction, and (d) pore pressure at the points in the vertical direction and (e) plastic shear strains at the end of simulations (17th August 2025). Case E.2.

EURAD (Deliverable n° 7.6) – Modelling report on the effect of temperature on clay host rocks behaviour
Dissemination level: PU
Date of issue of this report: 06/06/2024

Page 269

(f). Sensitivity analyses of the THM response to the HM coupling parameter β^k. This section presents the analysis of the effect of β^k on the THM response. The only difference between Case E.1 and the current simulation (Case F.1) is the input values of β^k: $\beta^k = 5 \times 10^3$ in Case E.1, and $\beta^k = 5 \times 10^7$ in Case F.1. It can be observed in Figure 7.104(a) and Figure 7.104(b) that the numerical predictions of temperatures are again consistent with experimental observations, as expected.

However, β^k plays a crucial role in the evolution of pore pressures. As shown in Figure 7.104(c) and Figure 7.104(d), liquid dissipation would be very fast in Case F.1, due to the large values of β^k considered, and pore pressures are significantly underestimated. On the other hand, in the field tests, it was observed that there is almost no change in intrinsic permeability in the heating stage (Li et al., 2023) and, therefore, it would be more reasonable to use a relatively small value of β^k in the numerical simulations.

EURAD (Deliverable n° 7.6) – Modelling report on the effect of temperature on clay host rocks behaviour
Dissemination level: PU
Date of issue of this report: 06/06/2024

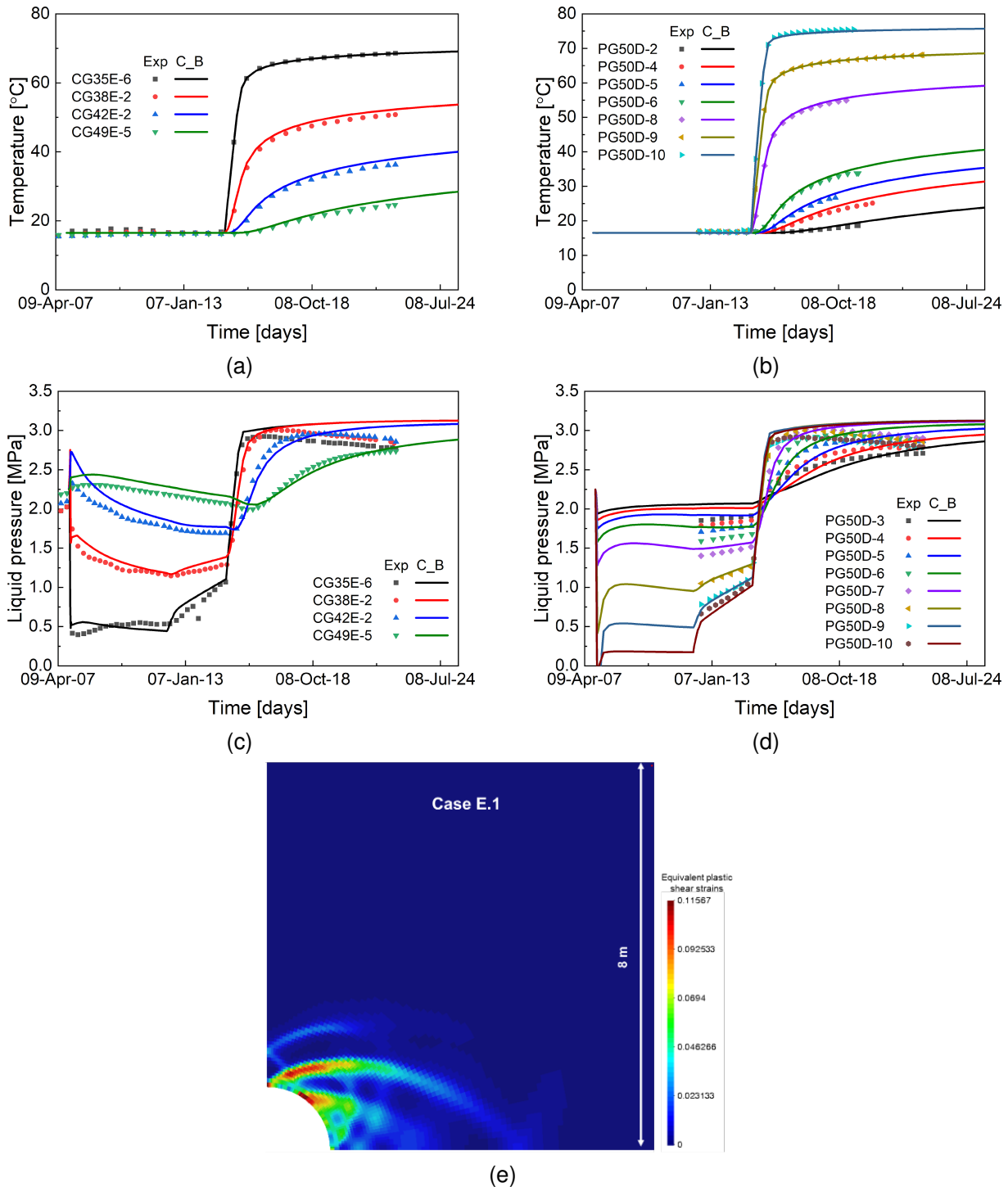Page 270

(a)

(b)

(c)

(d)

(e)

Figure 7.104: Comparison of temperature and pore pressure between numerical simulations and field observations: (a) temperature at the points in the horizontal direction, (b) temperature at the points in the vetical direction, (c) pore pressure at the points in the horizontal direction, and (d) pore pressure at the points in the vertical direction and (e) plastic shear strains at the end of simulations (17th August 2025). Case F.1.

EURAD (Deliverable n˚ 7.6) – Modelling report on the effect of temperature on clay host rocks behaviour
Dissemination level: PU
Date of issue of this report: 06/06/2024

Page 271

(g). Sensitivity analyses of the THM response to the hydraulic boundary conditions. In this section, the effect of hydraulic boundary conditions is examined. Now, the specified liquid pressure boundary condition is applied to the inner boundary of the concrete lining during the heating stage. Input parameters of material properties of the current model (Case G.1) are the same as in Case E.2. Comparing the THM results of Case G.1 and Case E.2, it can be observed that the numerical predictions of temperatures in both models agree well with experimental data. However, when using the specified liquid pressure B.C., numerical results of pore pressure underestimate the experimental observations. Finally, Figure 7.105(e) shows the strain localization close to the gallery wall, and there is no significant difference in plastic strains between Case G.1 and Case E.2.

EURAD (Deliverable n° 7.6) – Modelling report on the effect of temperature on clay host rocks behaviour
Dissemination level: PU
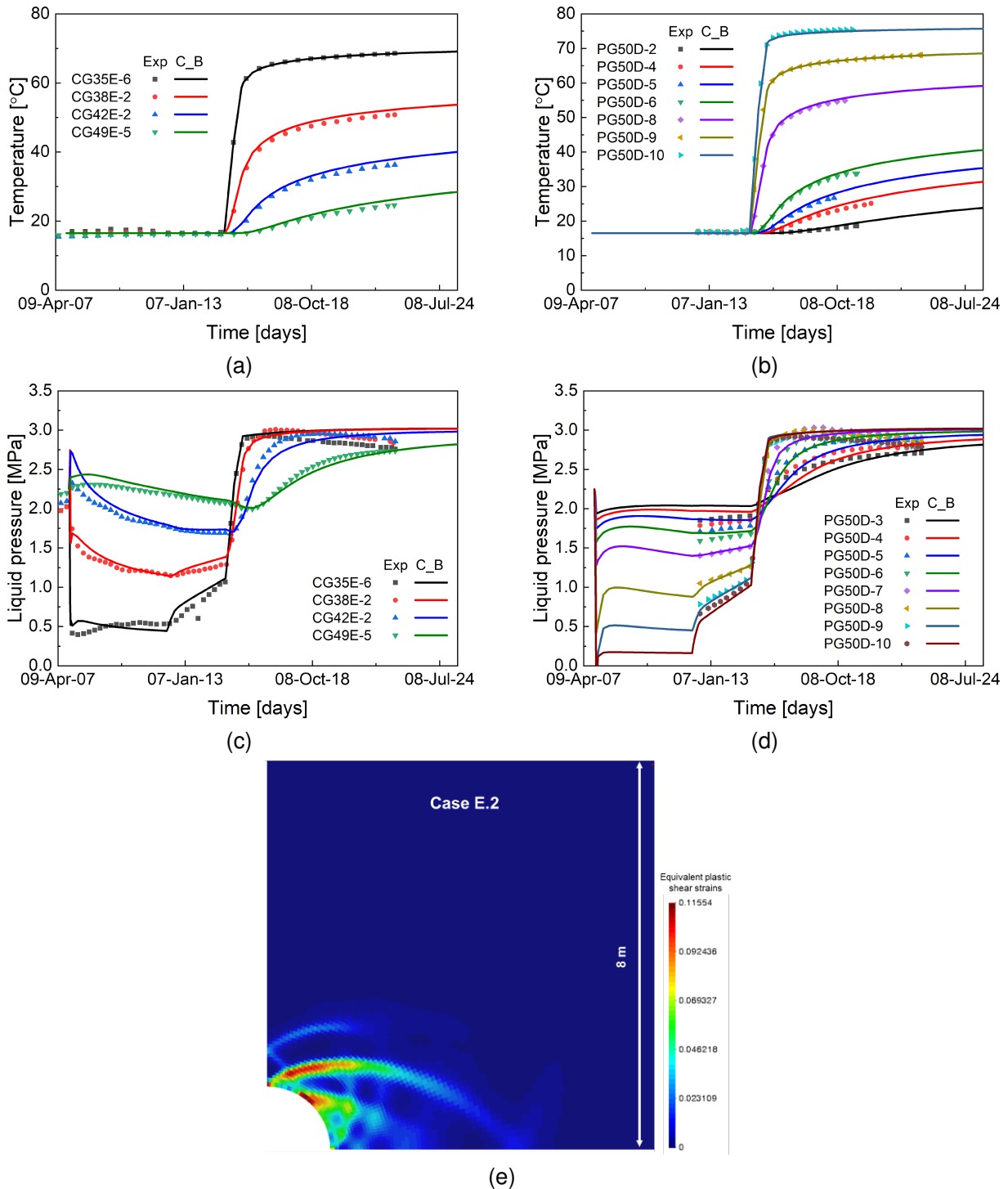Date of issue of this report: 06/06/2024

Page 272

Figure 7.105: Comparison of temperature and pore pressure between numerical simulations and field observations: (a) temperature at the points in the horizontal direction, (b) temperature at the points in the vetical direction, (c) pore pressure at the points in the horizontal direction, and (d) pore pressure at the points in the vertical direction and (e) plastic shear strains at the end of simulations (17th August 2025). Case G.1.

EURAD (Deliverable n° 7.6) – Modelling report on the effect of temperature on clay host rocks behaviour
Dissemination level: PU
Date of issue of this report: 06/06/2024

Page 273

(h). Sensitivity analyses of the THM response to mesh discretization. The nonlocal approach is introduced in the advanced Hyperbolic Mohr-Coulomb (HMC) constitutive model; a length scale is selected to ensure that there are enough elements near any integration point. Once this length value is set, the results will not depend on the degree of further refinement of the mesh. To analyse the sensitivity of THM response to the employed mesh, another numerical model with finer mesh has been analysed in this section. The only difference between the current simulation (Case H.1) and Case E.2 is the mesh: 9614 quadrilateral elements are used in Case H.1. Figure 7.106 shows the mesh of the numerical model; smaller mesh sizes are adopted in the zone close to the gallery wall.

Figure 7.107(a)–(d) show the results of temperatures and pore pressures. It can be noted that the numerical predictions of temperatures, and pore pressures agree well with experimental observations. Figure 7.107(e) shows the contours of plastic shear strains at the end of simulations (17th August 2025). Comparing the results of Case E.2 (see Figure 7.103) and Case H.1 (Figure 7.107), it can be observed that there is nearly no difference in THM responses between both models, verifying the mesh independency of the current simulations.
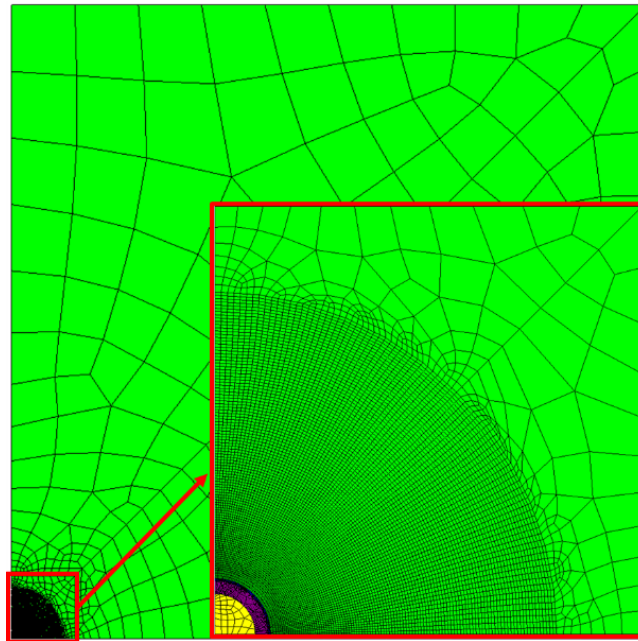
Figure 7.106: The mesh size of the numerical model with Case H.1. 9614 quadrilateral elements are used.

EURAD (Deliverable n˚ 7.6) – Modelling report on the effect of temperature on clay host rocks behaviour
Dissemination level: PU
Date of issue of this report: 06/06/2024
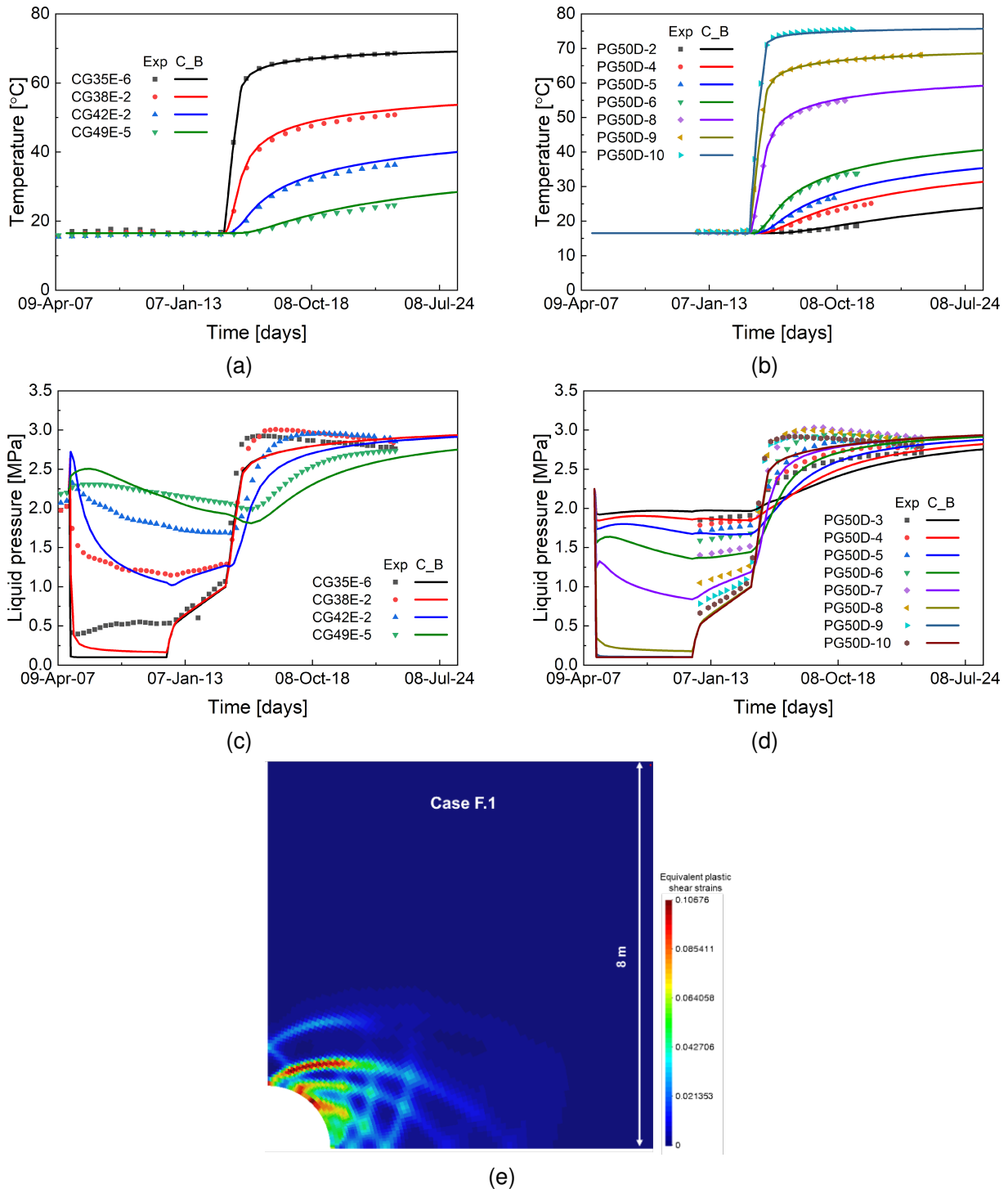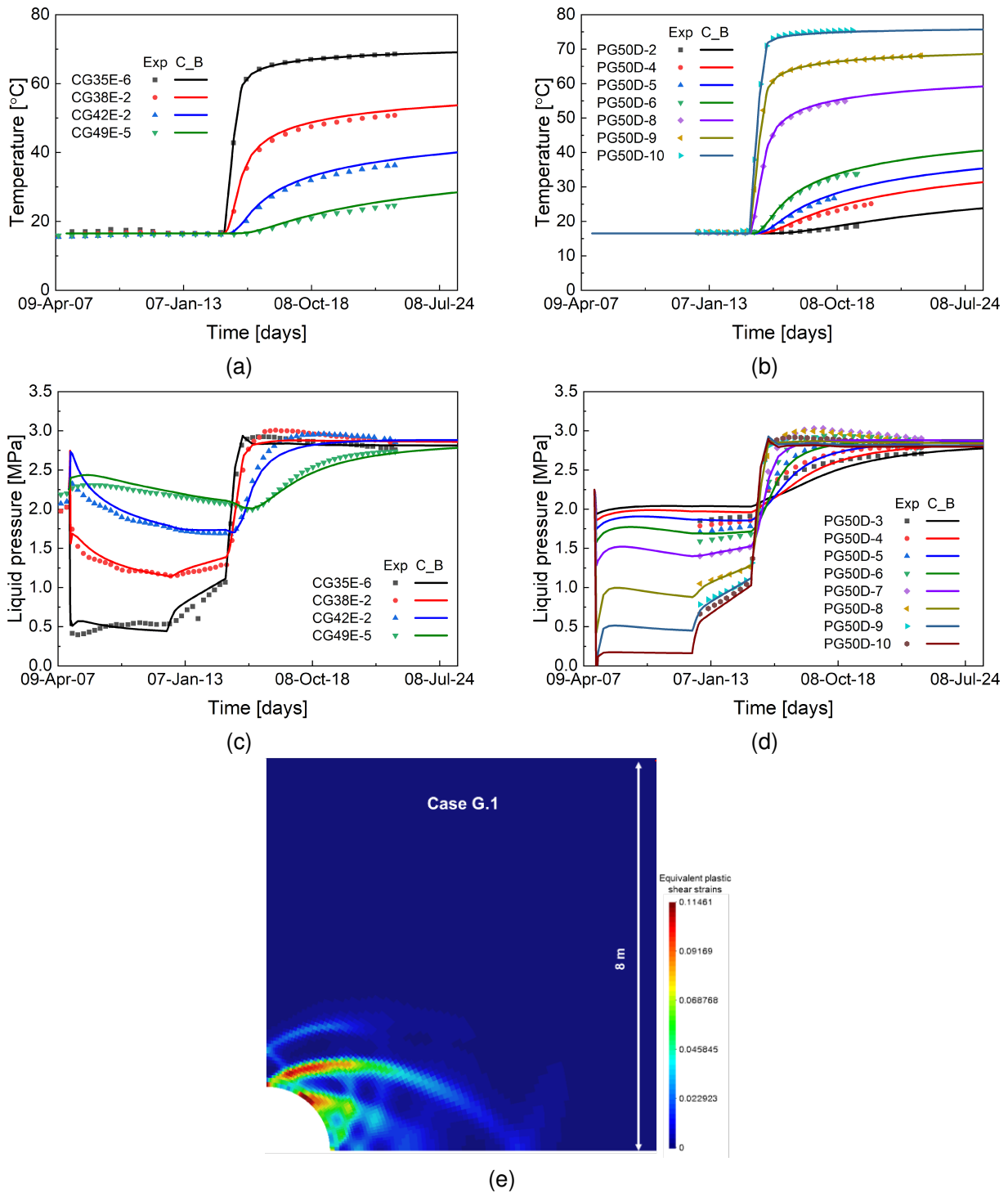
Page 274
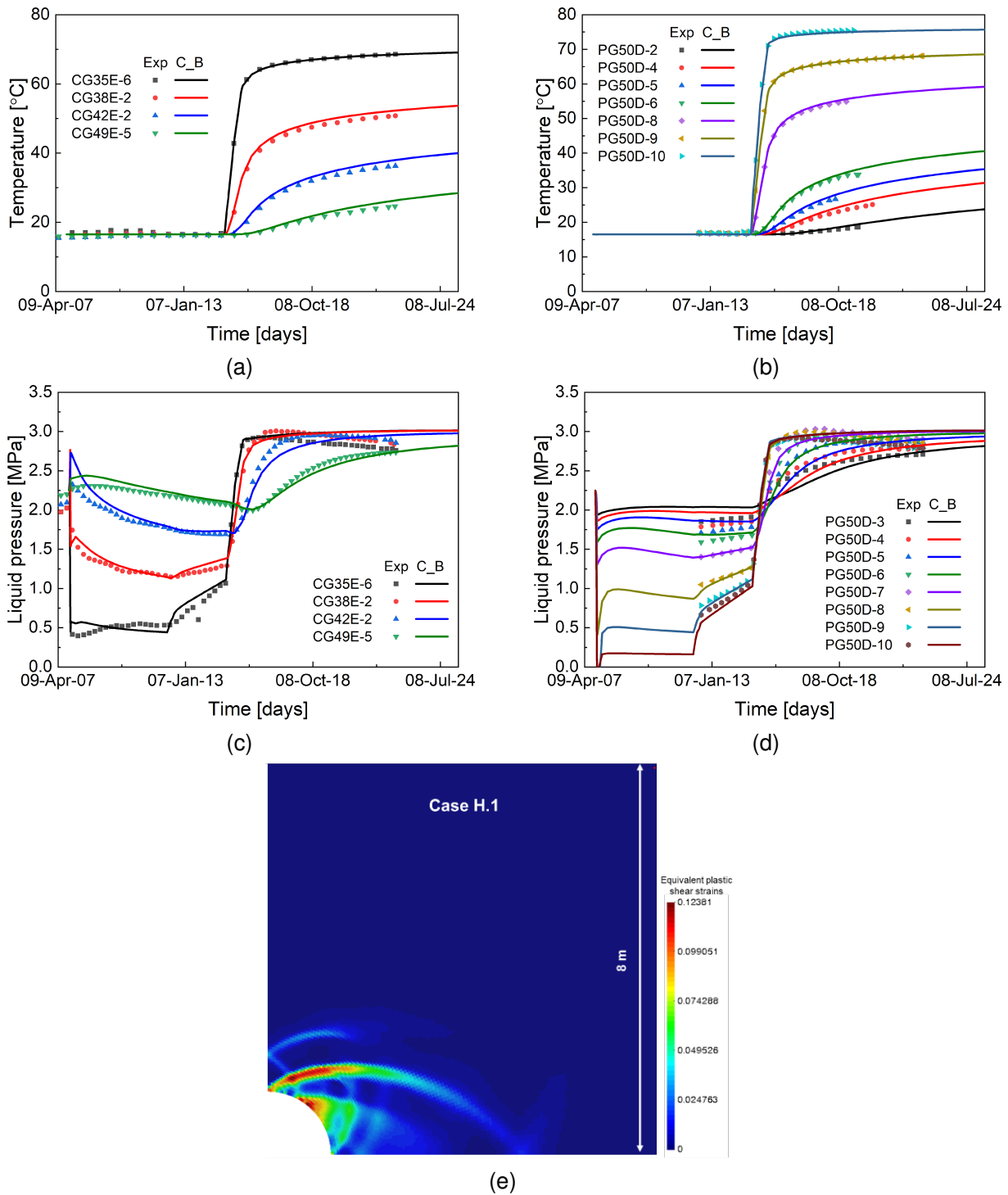
Figure 7.107: Comparison of temperature and pore pressure between numerical simulations and field observations: (a) temperature at the points in the horizontal direction, (b) temperature at the points in the vetical direction, (c) pore pressure at the points in the horizontal direction, and (d) pore pressure at the points in the vertical direction and (e) plastic shear strains at the end of simulations (17th August 2025). Case H.1.

EURAD (Deliverable n° 7.6) – Modelling report on the effect of temperature on clay host rocks behaviour
Dissemination level: PU
Date of issue of this report: 06/06/2024

Page 275

7.2.8.2. Final results of the free version

After assessing the ensemble the results obtained, it has been decided to adopt the results of Case H.1 as the final results to be analysed in more detail. As discussed in Figure 7.107, results of temperatures and pore pressures in agreement with observations have been obtained. In this section, the results of the model in terms of time evolutions and THM profiles are presented and discussed. Figure 7.108 shows the evolutions of temperature and pore pressure for the specified points, while, Figure 7.109 shows the temperature, pore pressure and the plastic multiplier on the horizontal and vertical lines for some specific times (t = 1, 1609, 2582, 2647, 2702, 2869, 6522 days).

As shown in Figure 7.108(a) and (b), in the heating stage, temperatures increase with time and the maximum temperature is around $80\,°C$ located at the gallery wall. Temperatures decrease with increased distance to the tunnel wall. As shown in Figure 7.108(c) and (d), pore pressures increase in the artificial injection stage due to the liquid injection, and increase in the heating stage due to thermal pressurization. Anisotropy of liquid pressure distribution is apparent: the liquid dissipation is faster in the horizontal direction than in the vertical direction (see Figure 7.110).

Figure 7.109 shows the temperature and pore pressure along the horizontal and vertical directions at several different times. As time increases, the thermal effect zone enlarges. Regarding the pore pressure profiles, the pore pressure close to the gallery wall increases significantly during the heating stage due to thermal pressurization. The contours of the plastic shear strains are shown in Figure 7.111: the plastic shear strains are mainly developed during the excavation stage; in the artificial injection and the heating stages, the plastic strains continue to develop, but at a smaller rate.
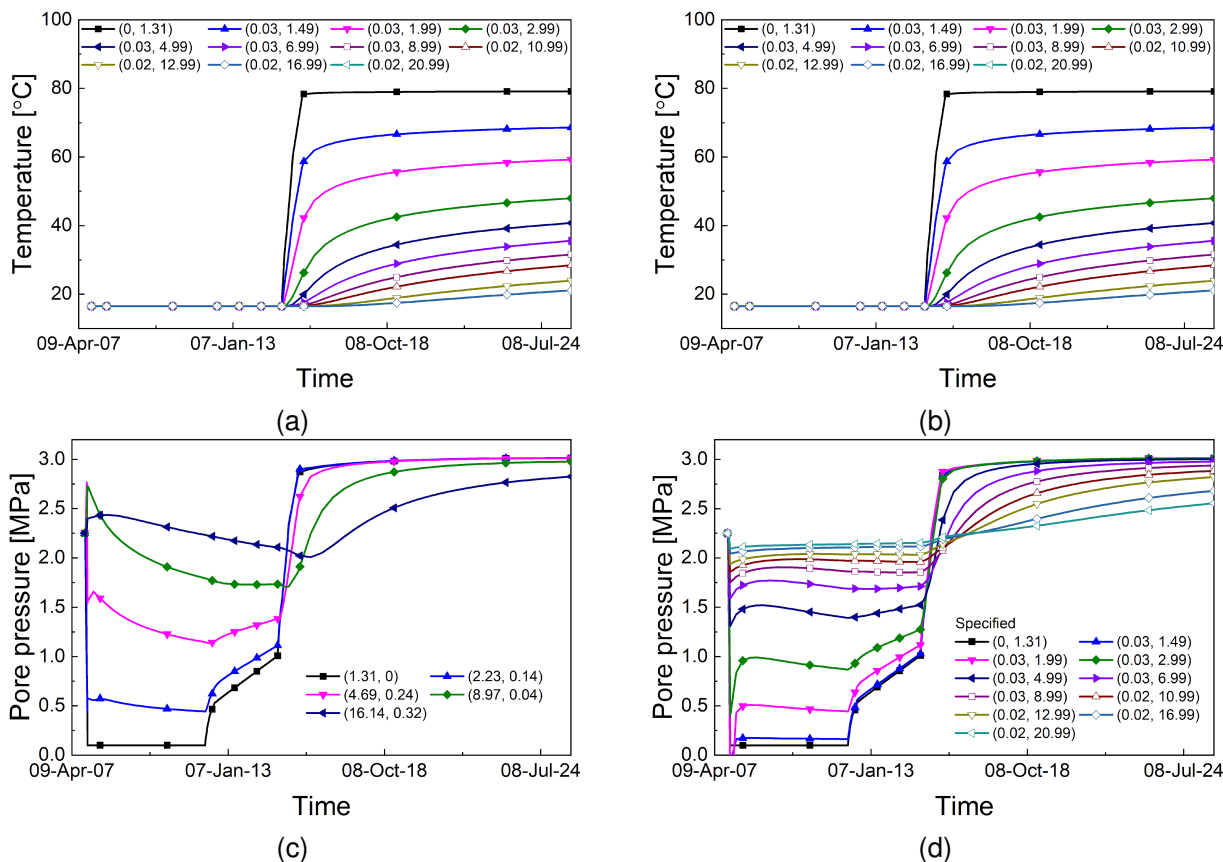
Figure 7.108: Evolutions of (a) temperature at the points in the horizontal direction, (b) temperature at the points in the vertical direction, (c) pore pressure at the points in the horizontal direction, and (d) pore pressure at the points in the vertical direction. Free version.

EURAD (Deliverable n° 7.6) – Modelling report on the effect of temperature on clay host rocks behaviour
Dissemination level: PU
Date of issue of this report: 06/06/2024

Page 276
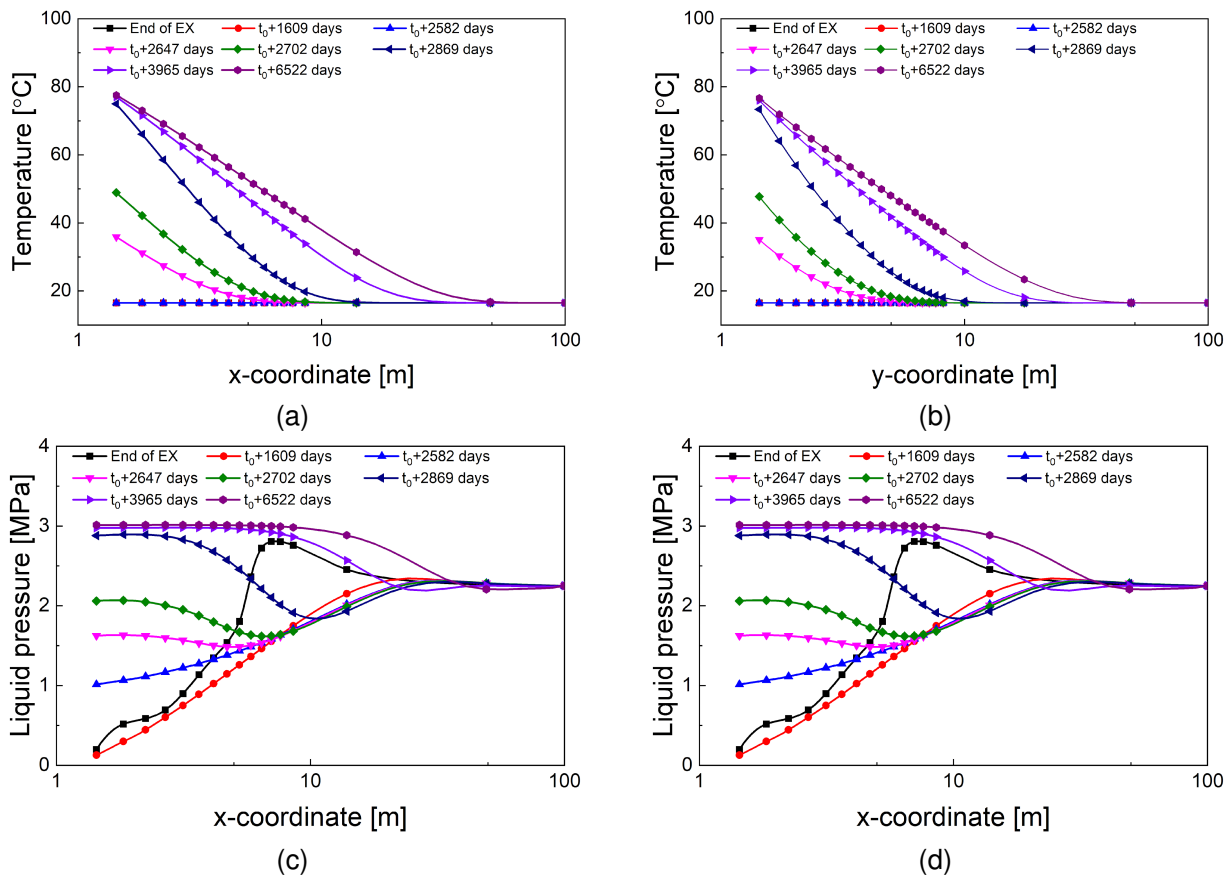
Figure 7.109: Distributions of (a) temperature on the horizontal line, (b) temperature on the vertical line, (c) pore pressure on the horizontal line, and (d) pore pressure on the vertical line. Free version.

EURAD (Deliverable n° 7.6) – Modelling report on the effect of temperature on clay host rocks behaviour
Dissemination level: PU
Date of issue of this report: 06/06/2024

Page 277
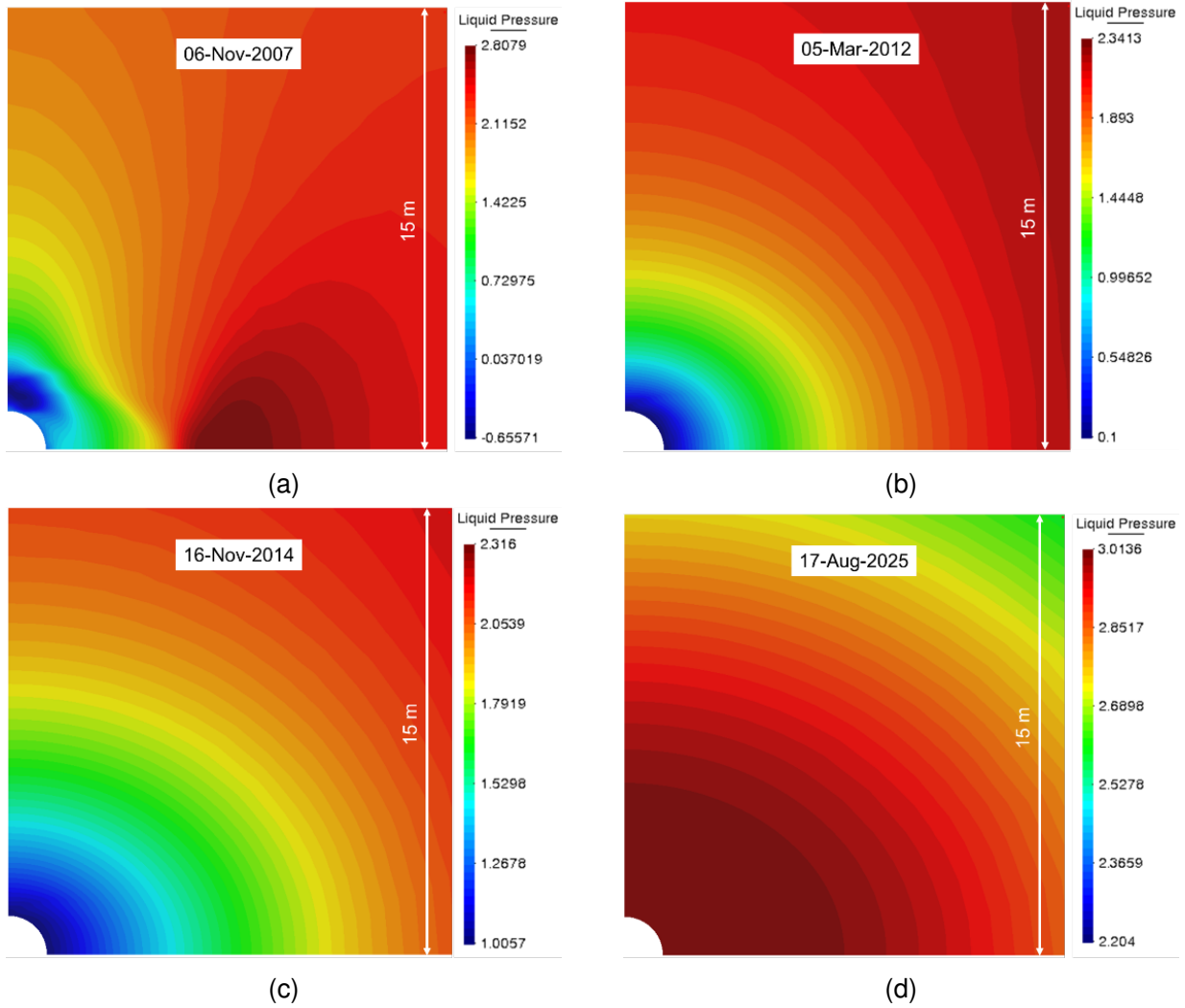
Figure 7.110: Contours of pore pressure in the vicinity of the gallery at: (a) 06-Nov-2007, (b) 05-Mar-2012, (c) 13-Nov-2014, and (d) 17-Aug-2025. Free version.

EURAD (Deliverable n˚ 7.6) – Modelling report on the effect of temperature on clay host rocks behaviour
Dissemination level: PU
Date of issue of this report: 06/06/2024

Page 278
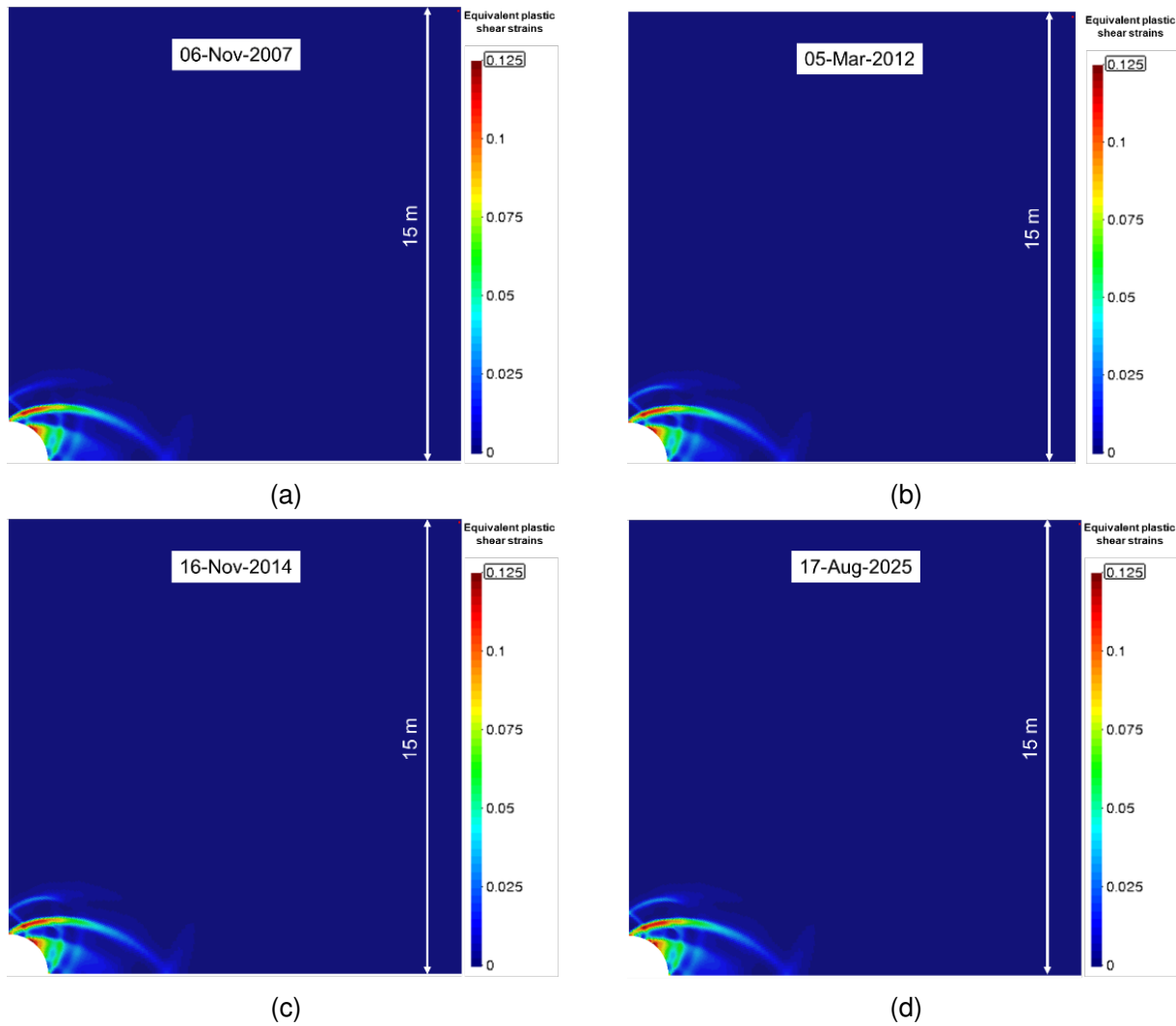
Figure 7.111: Contours of equivalent plastic shear strains in the vicinity of the gallery at: (a) 06-Nov-2007, (b) 05-Mar-2012, (c) 13-Nov-2014, and (d) 17-Aug-2025. Free version.

7.2.8.3. Conclusions

In this study, numerical simulations have been performed to analyse the large-scale PRACLAY heater test in the HADES URL. The air gap approach is proposed to represent the contact between the host clay and the concrete lining. Regarding the mechanical constitutive model of Boom Clay, the advanced Hyperbolic Mohr-Coulomb (HMC) model with hardening-softening and nonlocal formulation has been used. In addition, the overpressure mechanism has been properly characterised using both analytical and numerical approaches.

Sensitivity analyses have been performed, to analyse the effect of THM properties on the THM responses. According to the analyses performed, pore pressures depend strongly on stiffness parameters: thermal pressurization is larger when the drained bulk increases. Intrinsic permeability plays a significant role in the liquid dissipation and, therefore, changing the intrinsic permeability can significantly modify the pore pressure evolution. In both field tests and numerical simulations, the intrinsic permeability remains almost constant with increasing temperature.

Experimental data from the large scale PRACLAY experiment have been used to validate the numerical results. A good agreement between numerical and experimental results has been obtained in terms of both

EURAD (Deliverable n˚ 7.6) – Modelling report on the effect of temperature on clay host rocks behaviour
Dissemination level: PU
Date of issue of this report: 06/06/2024

Page 279

temperature and pore pressures. From the numerical model, the evolutions of temperature, pore pressure and equivalent plastic shear strains have been established. In the future, three-dimensional simulations would be performed to analyse further the coupled thermal-hydro-mechanical behaviour of the PRACLAY heater test.

7.2.9. Synthesis of results

Four cases were proposed to model the large scale in situ PRACLAY Heater test. Three academic versions of the experiment and a free one. Four teams contributed to this benchmark exercise; BGE, ULiège, UPC and EURIDICE/SCK CEN. The results of the benchmark with academic version of the PRACLAY experiment showed a good agreement between the involved modelling teams when modelling the experiment with elastic and elasto-plastic constitutive laws. In all cases, the anisotropy of the clay is taken into account with anisotropic intrinsic permeability and anisotropic thermal conductivity, and the elastic behaviour is model with cross-elasticity.

In addition, two teams , ULiège and UPC, modelled the large scale in situ PRACLAY Heater test with the free version. By using two different approaches, they were able to reproduce the experimental variation of the temperature and the thermal pressurization of the pore water.

To achieve this result, ULiège used an isotropic hardening/softening Drucker-Prager model with variation of the cohesion with the direction to model the anisotropic behaviour of the clay. They also introduced a strain-dependent isotropic evolution of the hydraulic permeability tensor and the shear strain depending on the shear strain reproducing the stiffness degradation curve. With these elements, they were able to reproduce the evolution of the temperature and the pore water in both horizontal and vertical directions.

UPC modelled the experiment with the air gap approach to represent the contact between the host clay and the concrete lining. The mechanical constitutive model used was the advanced Hyperbolic Mohr-Coulomb (HMC) model with hardening-softening and nonlocal formulation. With this approach, they were able to reproduce properly the overpressure mechanism using both analytical and numerical approaches.

From both analysis performed by ULiège and UPC, it can be seen that pore pressures depend strongly on stiffness parameters and the thermal pressurization is larger when the drained bulk increases. They also showed that intrinsic permeability plays a significant role in the liquid dissipation and, therefore, changing the intrinsic permeability can significantly modify the pore pressure evolution.

EURAD (Deliverable n˚ 7.6) – Modelling report on the effect of temperature on clay host rocks behaviour
Dissemination level: PU
Date of issue of this report: 06/06/2024

Page 280

8. Conclusion/synthesis

A series of benchmarking exercises were proposed to eight European modelling teams. Six codes were tested, five based on finite element method and one on the finite difference method.

In the first benchmark, focusing on the effect of heating in the near-field, very consistent results were obtained in the elastic isotropic case. More variations were observed on the pressure and stress predictions in the anisotropic case, especially on the Cox and Opalinus clay rocks. They were most likely due to differences in the THM formulations and assumptions made in the different codes and to some mesh dependency. The models were able to represent the development of the EDZ. Some variations appeared on the extent of the EDZ, but all models indicate a limited effect of heating on its development.

Because of some issues with the Opalinus clay input data, the far-field benchmark was run only on a Cox case. As for the near-field case, the responses vary near the tunnel, but very consistent results are obtained at mid-distance between two cells. An anisotropic poro-elastic behaviour is known to provide a good prediction of the evolution of both temperature and pore pressure. These results increase therefore the confidence one can have in this type of model and show the robustness of the modelling approach used to design some of the repositories. In addition, these exercises showed that when a case is correctly set, different finite-element codes can get consistent results when modelling the elastic behaviour of clay rocks, both in the near-field and in the far-field. Thanks to this benchmarking exercises, all these codes can therefore be considered verified and validated. Finally, this project gave an opportunity to improve some of the codes (Song et al., 2023) or to validate some recent developments (Souley et al., 2023a). A novel double-scale approach was also developed by CNRS-3SR but came too late to be tested on the benchmark cases.

The triaxial compression tests performed by ULorraine on heated Cox samples were modelled by several teams. This exercise showed the importance of defining correctly the boundary conditions. In some cases, the overpressure generated by the fast heating rate may have induced some damage in the samples. Some models were updated to take into account the strength decrease with temperature. This decrease should however be taken cautiously as the post-mortem analysis of samples heated to very high temperatures in some in-situ heating experiments did no show any impact on the strength. The effect may therefore be temporary, or due to some damage on the clay samples when extracting the cores or when preparing the samples.

The last step of this exercise consisted in modelling two large-scale in-situ heating experiments: ALC1605 in the Cox claystone and the PRACLAY Heater Test in the Boom clay. In both cases, the teams successfully managed to reproduce the anisotropic response of the clay host rocks to excavation and heating. In particular, the evolution of temperature and pore pressure was well modelled in the far-field with a poro-elastic approach. More advanced models are needed to take into account the processes occurring around the tunnels (EDZ, convergence). The parameters that played a significant role to match the measurements were the stiffness of the sound clay rock and of the damaged clay, and the permeabilities in both zones.

Bibliography

Abelev, A. V. and Lade, P. V. (2004). Characterization of failure in cross-anisotropic soils. *Journal of Engineering Mechanics*, 130(5):599–606.

Amadei, B. (2012). *Rock anisotropy and the theory of stress measurements*, volume 2. Springer Science & Business Media.

Ansys (2022). Ansys optiSLang - software for sensitivity analysis and optimization. Version 7.5.2.

Armand, G., Conil, N., Talandier, J., and Seyedi, D. M. (2017). Fundamental aspects of the hydrome-chanical behaviour of Callovo-Oxfordian claystone: From experimental studies to model calibration and validation. *Computers and Geotechnics*, 85:277–286.

Armand, G., Leveau, F., Nussbaum, C., de La Vaissiere, R., Noiret, A., Jaeggi, D., Landrein, P., and Righini, C. (2014). Geometry and properties of the excavation-induced fractures at the meuse/haute-marne url drifts. *Rock mechanics and rock engineering*, 47(1):21–41.

Atkinson, J. and Sallfors, G. (1991). Experimental determination of soil properties. general report to session 1. In *Proc. 10th ECSMFE, Florence*, volume 3, pages 915–956.

Barnichon, J.-D. (1998). *Finite element modelling in structural and petroleum geology*. PhD thesis, Universite de Liege.

Bentley Systems (2020). PLAXIS CONNECT Edition 20.04.

Bergman, T., Incropera, F., DeWitt, D., and Lavine, A. (2011). *Fundamentals of heat and mass transfer*. John Wiley & Sons.

Bernier, F., Li, X., and Bastiaens, W. (2017). Twenty-five years' geotechnical observation and testing in the Tertiary Boom Clay formation. *Géotechnique*, 52(2):229–237.

Biot, M. (1973). Nonlinear and semilinear rheology of porous solids.

Braun, P. (2019a). *Comportement thermo-hydro-mécanique de l'argilite du Callovo-Oxfordien: Effets des chemins de contrainte et des variations de température*. PhD thesis, Paris Est.

Braun, P. (2019b). *Thermo-hydro-mechanical behavior of the Callovo-Oxfordian claystone: Effects of stress paths and temperature changes*. PhD thesis, Université Paris-Est.

Buchwald, J., Kaiser, S., Kolditz, O., and Nagel, T. (2021). Improved predictions of thermal fluid pres-surization in hydro-thermal models based on consistent incorporation of thermo-mechanical effects in anisotropic porous media. *International Journal of Heat and Mass Transfer*, 172:121127.

Bumbieler, F., Plúa, C., Tourchi, S., Vu, M.-N., Vaunat, J., Gens, A., and Armand, G. (2020). Feasibility of constructing a full-scale radioactive high-level waste disposal cell and characterization of its thermo-hydro-mechanical behavior. *International Journal of Rock Mechanics and Mining Sciences*.

Campanella, R. G. and Mitchell, J. K. (1968). Influence of temperature variations on soil behavior. *Journal of the Soil Mechanics and Foundations Division*, 94(3):709–734.

CEA and EDF (2023). MTest: unit mechanical behaviour testing.

Chaboche, J. L. (2008). A review of some plasticity and viscoplasticity constitutive theories. *International Journal of Plasticity*, 24(10):1642–1693.

Chambon, R., Caillerie, D., and El Hassan, N. (1998). One-dimensional localisation studied with a second grade model. *European Journal of Mechanics-A/Solids*, 17(4):637–656.

Charlier, R., Chambon, R., and Collin, F. e. a. (2010). Deliverable D13 - Simulation of lab and in-situ test. Technical report, TIMODAZ project, contract number F16W-CT-2007-036449.

Chaudhry, A. A., Buchwald, J., Kolditz, O., and Nagel, T. (2019). Consolidation around a point heat source (correction and verification). *International Journal for Numerical and Analytical Methods in Geomechanics*, 43(18):2743–2751.

Chen, G., Li, X., Dizier, A., Verstricht, J., Sillen, X., and Levasseur, S. (2023). Characterization of boom clay anisotropic thm behaviour based on two heating tests at different scales in the hades url. *Geological Society, London, Special Publications*, 536(1):SP536–2022.

Chen, G., Sillen, X., Verstricht, J., and Li, X. (2011). ATLAS III in situ heating test in boom clay: Field data, observation and interpretation. *Computers and Geotechnics*, 38(5):683–696.

Chen, L., Shao, J.-F., and Huang, H. (2010). Coupled elastoplastic damage modeling of anisotropic rocks. *Computers and Geotechnics*, 37(1-2):187–194.

Cheng, A.-D. (1997). Material coefficients of anisotropic poroelasticity. *International journal of rock mechanics and mining sciences*, 34(2):199–205.

Collin, F., Chambon, R., and Charlier, R. (2006). A finite element method for poro mechanical modelling of geotechnical problems using local second gradient models. *International journal for numerical methods in engineering*, 65(11):1749–1772.

Collin, F., Levasseur, S., and Chambon, R. (2009). Numerical post failure methods in multiphysical problems. *European journal of environmental and civil engineering*, 13(7-8):983–1004.

Collin, F., Li, X.-L., Radu, J.-P., and Charlier, R. (2002). Thermo-hydro-mechanical coupling in clay barriers. *Engineering Geology*, 64(2-3):179–193.

Cosenza, P., Fauchille, A.-L., Prêt, D., Hedan, S., and Giraud, A. (2019). Statistical representative elementary area of shale inferred by micromechanics. *Int. J. Eng. Sci.*, 142:53–73.

Cosenza, P., Prêt, D., Giraud, A., and Hedan, S. (2015a). Effect of the local clay distribution on the effective elastic properties of shales. *Mech. Mater.*, 84:55–74.

Cosenza, P., Prêt, D., and Zamora, M. (2015b). Effect of the local clay distribution on the effective electrical conductivity of clay rocks. *J. Geophys. Res. Solid Earth*, 120:145–168.

Coussy (2004). Poromechanics.

de Souza Neto, E. A., Perić, D., and Owen, D. R. J. (2008). *Computational methods for plasticity*. John Wiley & Sons Ltd, Chichester.

Delage, P., Sultan, N., and Cui, Y. J. (2000). On the thermal consolidation of Boom Clay. *Canadian Geotechnical Journal*, 37(2):343–354.

Desai, C. and Siriwardane, H. (1984). *Constitutive laws for engineering materials: With emphasis on geologic materials*. Prentice-Hall, Inc., New Jersey.

Desbois, G., Höhne, N., Urai, J. L., Bésuelle, P., and Viggiani, G. (2017). Deformation in cemented mudrock (Callovo-Oxfordian Clay) by microcracking, granular flow and phyllosilicate plasticity: insights from triaxial deformation, broad ion beam polishing and scanning electron microscopy. *Solid Earth*, 8(2):291–305.

EURAD (Deliverable n˚ 7.6) – Modelling report on the effect of temperature on clay host rocks behaviour
Dissemination level: PU
Date of issue of this report: 06/06/2024

Page 283

Dizier, A., Chen, G.J., Li, X.L., Leysen, J., Verstricht, J., Troullinos, I., and Rypens, J. (2016). *The Start-up Phase of the PRACLAY Heater Test.* EURIDICE report, EUR_PH_16_025, Mol, Belgium.

Drucker, D. and Prager, W. (1952). Soil mechanics and plasticity analysis or limit design. *Quarterly Applied Mathematics*, 10(2):157–165.

EDF (1989-2022). Finite element code_aster, analysis of structures and thermomechanics for studies and research.

EDF (2017). *Code_Aster Documentation R7.01.40: Model of behavior LKR.* Électricité de France (EDF).

François, B., Labiouse, V., Dizier, A., Marinelli, F., Charlier, R., and Collin, F. (2014). Hollow cylinder tests on boom clay: modelling of strain localization in the anisotropic excavation damaged zone. *Rock mechanics and rock engineering*, 47(1):71–86.

Frey, J., Chambon, R., and Dascalu, C. (2013). A two-scale poromechanical model for cohesive rocks. *Acta Geotechnics*, 8:107–124.

Galavi, V. and Schweiger, H. (2010). Nonlocal Multilaminate Model for Strain Softening Analysis. *International Journal of Geomechanics*, 10.

Gbewade, C., Grgic, D., Giraud, A., and Schoumacker, L. (2023). Experimental study of the effect of temperature on the mechanical properties of the Callovo-Oxfordian Claystone. *Rock Mechanics and Rock Engineering*.

Gens, A., Vaunat, J., Garitte, B., and Wileveau, Y. (2007). In situ behaviour of a stiff layered clay subject to thermal loading: Observations and interpretation. *Stiff Sedimentary Clays: Genesis and Engineering Behaviour - Geotechnique Symposium in Print 2007*, 57(2):207–228.

Gramegna, L., Bernachy-Barbe, F., Collin, F., Talandier, J., and Charlier, R. (2022). Pore size distribution evolution in pellets based bentonite hydration: Comparison between experimental and numerical results. *Engineering Geology*, page 106700.

Grunwald, N., Lehmann, C., Maßmann, J., Naumov, D., Kolditz, O., and Nagel, T. (2022). Non-isothermal two-phase flow in deformable porous media: systematic open-source implementation and verification procedure. *Geomechanics and Geophysics for Geo-Energy and Geo-Resources*, 8(3).

Günther, R.-M., Salzer, K., Popp, T., and Lüdeling, C. (2015). Steady-state creep of rock salt: improved approaches for lab determination and modelling. *Rock mechanics and rock engineering*, 48:2603–2613.

Helfer, T., Bleyer, J., Frondelius, T., Nagel, T., and Naumov, D. (2020). The MFrontGenericInterfaceSupport project. *The journal of open source software*, 5(48).

Hoek, E. and Brown, E. T. (1980). Empirical strength criterion for rock masses. *Journal of the geotechnical engineering division*, 106(9):1013–1035.

Horai, K.-i. (1971). Thermal conductivity of rock-forming minerals. *Journal of Geophysical Research (1896-1977)*, 76(5):1278–1308.

Itasca, C. G. I. (2019). *FLAC3D, Fast Lagrangian Analysis of Continua, Fluid Mechanical Interaction.* Itasca, Minneapolis; Minnesota.

Jaeger, J. (1960). Shear failure of anistropic rocks. *Geological magazine*, 97(1):65–72.

Kell, G. S. (1975). Density, thermal expansivity, and compressibility of liquid water from 0. deg. to 150. deg.. Correlations and tables for atmospheric pressure and saturation reviewed and expressed on 1968 temperature scale. *Journal of Chemical and Engineering data*, 20(1):97–105.

EURAD (Deliverable n˚ 7.6) – Modelling report on the effect of temperature on clay host rocks behaviour
Dissemination level: PU
Date of issue of this report: 06/06/2024

Page 284

Ken-Ichi, K. (1984). Distribution of directional data and fabric tensors. *International journal of engineering science*, 22(2):149–164.

Kleine, A. (2007). *Modélisation Numérique du Comportement des Ouvrages Souterrains par une Approche Viscoplastique.* PhD thesis, .

Lade, P. V. (2007). Modeling failure in cross-anisotropic frictional materials. *International Journal of Solids and Structures*, 44(16):5146–5162.

Laigle, F. (2004). *Modèle Conceptuel pour le Développement de Lois de Comportement adaptées à la Conception des Ouvrages Souterrains.* PhD thesis, .

Lekhnitskii, S. G., Fern, P., Brandstatter, J. J., and Dill, E. (1964). Theory of elasticity of an anisotropic elastic body.

Li, X., Dizier, A., Chen, G., Verstricht, J., and Levasseur, S. (2023). Forty years of investigation into the thermo-hydromechanical behaviour of boom clay in the hades url. *Geological Society, London, Special Publications*, 536(1):SP536–2022.

Mair, R. (1993). Unwin memorial lecture 1992. developments in geotechnical engineering research: Application to tunnels and deep excavations. delivered at the ice on 17 march 1992.(abridged).(winner of 1994 geotechnical research medal). In *Proceedings of the institution of civil engineers-civil engineering*, volume 97, pages 27–41. Thomas Telford-ICE Virtual Library.

Mánica, M. (2018). *Analysis of underground excavations in argillaceous hard soils - weak rocks*. PhD thesis, Technical University of Catalonia.

Mánica, M. A., Ciantia, M. O., and Gens, A. (2020). On the stability of underground caves in calcareous rocks due to long-term weathering. *Rock Mechanics and Rock Engineering*, 53:3885–3901.

Mánica, M. A., Gens, A., Vaunat, J., Armand, G., and Vu, M. N. (2022a). Numerical simulation of underground excavations in an indurated clay using non-local regularisation. Part 1: formulation and base case. *Geotechnique*, 72(12):1092–1112.

Mánica, M. A., Gens, A., Vaunat, J., Armand, G., and Vu, M. N. (2022b). Numerical simulation of underground excavations in an indurated clay using non-local regularisation. Part 2: sensitivity analysis. *Géotechnique*, 72(12):1113–1128.

Mánica, M. A., Gens, A., Vaunat, J., and Ruiz, D. F. (2018). Nonlocal plasticity modelling of strain localisation in stiff clays. *Computers and Geotechnics*, 103:138–150.

Menaceur, H., Delage, P., Tang, A., and Talandier, J. (2016). The status of water in swelling shales: an insight from the water retention properties of the callovo-oxfordian claystone. *Rock Mechanics and Rock Engineering*, 49(12):4571–4586.

Mindlin, R. D. (1965). Second gradient of strain and surface-tension in linear elasticity. *International Journal of Solids and Structures*, 1(4):417–438.

Nagel, T., Parisio, F., Naumov, D., Lehmann, C., and Kolditz, O. (2019). MFront and OpenGeoSys - Connecting two open-source initiatives for simulations in environmental geosciences andenergy geotechnics. In *MFront User Meeting*, Paris.

Nguyen T.S., L. A. (2015). Simultaneous gas and water flow in a damage-susceptible bedded argillaceous rock. *Can. Geotech. J.*, 52:18–32.

Olivella, S., Gens, A., Ramírez, J., and Alonso, E. (1995). Numerical formulation for a simulator (CODE_BRIGHT) for the coupled analysis of saline media. *coupled analyses of saline media*.

EURAD (Deliverable n˚ 7.6) – Modelling report on the effect of temperature on clay host rocks behaviour
Dissemination level: PU
Date of issue of this report: 06/06/2024

Page 285

Olivella, S., Vaunat, J., and Rodriguez-Dono, A. (2022). *CODE_BRIGHT USER'S GUIDE*. Department of Civil and Environmental Engineering, Polytechnic University of Catalonia (UPC), Barcelona, Spain.

Ovando, E. and Mánica, M. A. (2021). Implementation of a material model for the mechanical, thermal, and hydraulic behaviour of claystone. Task 1: Implementation of the local version. Technical report, UNAM Institute of Engineering, Geotechnics department, Mexico City, Mexico.

Özdemir, I., Brekelmans, W., and Geers, M. (2008). FE^2 computational homogenization for the thermo-mechanical analysis of heterogeneous solids. *Computer Methods in Applied Mechanics and Engineering*, 198(3-4):602–613.

Pardoen, B. (2015). *Hydro-mechanical analysis of the fracturing induced by the excavation of nuclear waste repository galleries using shear banding*. PhD thesis, ULiège-Université de Liège.

Pardoen, B., Bésuelle, P., Dal Pont, S., Cosenza, P., and Desrues, J. (2020). Accounting for small-scale heterogeneity and variability of clay rock in homogenised numerical micromechanical response and microcracking. *Rock Mech Rock Eng*, 53:2727–2746.

Pardoen, B., Levasseur, S., and Collin, F. (2015a). Using local second gradient model and shear strain localisation to model the excavation damaged zone in unsaturated claystone. *Rock Mechanics and Rock Engineering*, 48(2):691–714.

Pardoen, B., Seyedi, D., and Collin, F. (2015b). Shear banding modelling in cross-anisotropic rocks. *International Journal of Solids and Structures*, 72:63–87.

Perzyna, P. (1966). Fundamental problems in viscoplasticity. *Advances in Applied Mechanics*, 9:243–377.

Pietruszczak, S. (2010). *Fundamentals of plasticity in geomechanics*. Crc Press Boca Raton, FL.

Pietruszczak, S., Lydzba, D., and Shao, J.-F. (2002). Modelling of inherent anisotropy in sedimentary rocks. *International Journal of Solids and Structures*, 39(3):637–648.

Pietruszczak, S. and Mroz, Z. (1981). Finite element analysis of deformation of strain-softening materials. *International Journal for Numerical Methods in Engineering*, 17(3):327–334.

Pietruszczak, S. and Mroz, Z. (2000). Formulation of anisotropic failure criteria incorporating a microstructure tensor. *Computers and Geotechnics*, 26(2):105–112.

Pietruszczak, S. and Mroz, Z. (2001). On failure criteria for anisotropic cohesive-frictional materials. *International journal for numerical and analytical methods in geomechanics*, 25(5):509–524.

Plúa, C., Vu, M., Armand, G., Rutqvist, J., Birkholzer, J., Xu, H., Guo, R., Thatcher, K., Bond, A., Wang, W., Nagel, T., Shao, H., and Kolditz, O. (2021). A reliable numerical analysis for large-scale modelling of a high-level radioactive waste repository in the Callovo-Oxfordian claystone. *International Journal of Rock Mechanics and Mining Sciences*, 140(December 2020):104574.

R7.01.10 (2014). Modélisations THHM. Généralités et algorithmes, Documentation officielle Code_Aster.

Raude, S. (2015). *Prise en compte des solicitations thermiques sur les comportements instantané et différé des géomatériaux*. PhD thesis, Université de Lorraine Géoressources.

Resende, L. and Martin, J. B. (1985). Formulation of Drucker-Prager cap model. *Journal of Engineering Mechanics*, 111(7):855–881.

Robinet, J.-C., Sardini, P., Coelho, D., Parneix, J.-C., Prêt, D., Sammartino, S., Boller, E., and Altmann, S. (2012). Effects of mineral distribution at mesoscopic scale on solute diffusion in a clay-rich rock: Example of the Callovo-Oxfordian mudstone (Bure, France). *Water Resour. Res.*, 48(5).

EURAD (Deliverable n° 7.6) – Modelling report on the effect of temperature on clay host rocks behaviour
Dissemination level: PU
Date of issue of this report: 06/06/2024

Page 286

Rumble, J. (2019). CRC handbook of chemistry and physics (100th ed.). Boca Rotan, FL.

Salehnia, F. (2014). Hydro-mechanical behavior of boom clay around the connecting gallery. Technical report, ULg-Université de Liège, Liège, Belgium.

Salehnia, F., Collin, F., Li, X. L., Dizier, A., Sillen, X., and Charlier, R. (2015). Coupled modeling of excavation damaged zone in boom clay: Strain localization in rock and distribution of contact pressure on the gallery's lining. *Computers and Geotechnics*, 69:396–410.

Seyedi, D., Armand, G., and Noiret, A. (2017). "Transverse Action" – A model benchmark exercise for numerical analysis of the Callovo-Oxfordian claystone hydromechanical response to excavation operations. *Computers and Geotechnics*, 85:287–305.

Seyedi, D., Plúa, C., Vitel, M., Armand, G., Rutqvist, J., Birkholzer, J., Xu, H., Guo, R., Thatcher, K., Bond, A., Wang, W., Nagel, T., Shao, H., and Kolditz, O. (2021). Upscaling THM modeling from small-scale to full-scale in-situ experiments in the Callovo-Oxfordian claystone. *International Journal of Rock Mechanics and Mining Sciences*.

Simo, J. C., Kennedy, J. G., and Govindjee, S. (1988). Non-smooth multisurface plasticity and viscoplasticity. Loading/unloading conditions and numerical algorithms. *International Journal for Numerical Methods in Engineering*, 26(10):2161–2185.

Song, F. (2021). *Modelling time-dependent plastic behaviour of geomaterials*. PhD thesis, Universitat Politècnica de Catalunya.

Song, F., Collico, S., and Gens, A. (2022). Coupled THM responses of callovo-oxfordian claystone subject to thermal loading. In *2022 Workshop of CODE_BRIGHT USERS*, Barcelona, Spain.

Song, F., Rodriguez-Dono, A., and Olivella, S. (2021a). Hydro-mechanical modelling and analysis of multi-stage tunnel excavations using a smoothed excavation method. *Computers and Geotechnics*, 135:104150.

Song, F., Rodriguez-Dono, A., Olivella, S., and Gens, A. (2021b). Coupled solid-fluid response of deep tunnels excavated in saturated rock masses with a time-dependent plastic behaviour. *Applied Mathematical Modelling*, page 508–535.

Song, H., Corman, G., and Collin, F. (2023). Thermal Impact on the Excavation Damage Zone Around a Supported Drift Using the 2nd Gradient Model. *Rock Mech Rock Eng*, 56:7575–7598.

Souley, M., Armand, G., and Kazmierczak, J.-B. (2017). Hydro-elasto-viscoplastic modeling of a drift at the Meuse/Haute-Marne underground research laboratory (URL). *Comput Geotech*, page 306–320.

Souley, M., Coarita-Tintaya, E., Vu, M., Armand, G., Golfier, F., M. Laviña, M., and Idiart, A. (2023a). A Regularised Anisotropic Elastoplastic Damage and Viscoplastic Model and Its Hydromechanical Application to a Meuse/Haute-Marne URL Drift. *Rock Mechanics and Rock Engineering*.

Souley, M., Vu, M., , de Lesquen, C., and Armand, G. (2023b). Effect of mechanical non-linearities on the thermal-hydraulic-mechanical response of a geological repository. In *Proc. 3. Int. Conf. on Coupled Processes in Fractured Geological Media: Observation, Modeling, and Application (CouFrac 2022), Berkeley*.

Summersgill, F. C., Kontoe, S., and Potts, D. M. (2017). Critical assessment of nonlocal strain-softening methods in biaxial compression. *International Journal of Geomechanics*, 17(7):1–14.

Tan, X. and Konietzky, H. (2014). Numerical study of variation in Biot's coefficient with respect to microstructure of rocks. *Tectonophysics*, 610:159–171.

EURAD (Deliverable n˚ 7.6) – Modelling report on the effect of temperature on clay host rocks behaviour
Dissemination level: PU
Date of issue of this report: 06/06/2024

Page 287

Tidfors, M. and Sällfors, G. (1989). Temperature effect on preconsolidation pressure. *Geotechnical Testing Journal*, 12(1):93–97.

Tourchi, S. (2020). *THM analysis of argillaceous rocks with application to nuclear waste underground storage*. PhD thesis, Universitat Politècnica de Catalunya.

Tourchi, S., Mánica, M. A., Gens, A., Vaunat, J., Vu, M.-N., and Armand, G. (2023). A thermomechanical model for argillaceous hard soils-weak rocks: application to THM simulation of deep excavations in clayston. *Géotechnique*.

Tourchi, S., Vaunat, J., Gens, A., Bumbieler, F., Vu, M.-N., and Armand, G. (2021). A full-scale in situ heating test in callovo-oxfordian claystone: observations, analysis and interpretation. *Computers and Geotechnics*, 133:104045.

Van den Eijnden, A., Bésuelle, P., Chambon, R., and Collin, F. (2016). A FE^2 modelling approach to hydromechanical coupling in cracking-induced localization problems. *International Journal of Solids and Structures*, 97-98:475–488.

Van den Eijnden, A., Bésuelle, P., Collin, F., Chambon, R., and Desrues, J. (2017). Modeling the strain localization around an underground gallery with a hydro-mechanical double scale model; effect of anisotropy. *Computers and Geotechnics*, 85:384–400.

Van Eekelen, H. (1980). Isotropic yield surfaces in three dimensions for use in soil mechanics. *International Journal for Numerical and Analytical Methods in Geomechanics*, 4(1):89–101.

van Genuchten, M. T. (1980). A closed-form equation for predicting the hydraulic conductivity of unsaturated soils. *Soil Science Society of America Journal*, 44(5):892–898.

Van Marcke, P., Li, X.L., Bastiaens, W., Verstricht, J., Chen, G., Leysen, J., and Rypens, J. (2013). *The design and installation of the PRACLAY in-situ experiment*. EURIDICE report 13-129, Mol, Belgium.

Vu, M.-N., Armand, G., and Plua, C. (2020). Thermal pressurization coefficient of anisotropic elastic porous media. *Rock Mechanics and Rock Engineering*, 53(4):2027–2031.

Wang, W., Shao, H., Nagel, T., and Kolditz, O. (2021a). Analysis of coupled thermal-hydro-mechanical processes during small scale in situ heater experiment in callovo-oxfordian clay rock introducing a failure-index permeability model. *International Journal of Rock Mechanics and Mining Sciences*, 142.

Wang, W., Shao, H., Rink, K., Fischer, T., Kolditz, O., and Nagel, T. (2021b). Analysis of coupled thermal-hydro-mechanical processes in callovo-oxfordian clay rock: From full-scale experiments to the repository scale. *Engineering Geology*, 293.

Wu, S. and Wang, X. (2010). Mesh dependence and nonlocal regularization of one-dimensional strain softening plasticity. *Journal of engineering mechanics*, 136(11):1354–1365.

Yven, B., Sammartino, S., Geraud, Y., Homand, F., and Villieras, F. (2007). Mineralogy, texture and porosity of Callovo-Oxfordian argillites of the Meuse/Haute-Marne region (eastern Paris Basin). *Mém. Soc. géol. France*, 178:73–90.

Zervos, A., Papanastasiou, P., and Vardoulakis, I. (2001a). A finite element displacement formulation for gradient elastoplasticity. *International Journal for Numerical Methods in Engineering*, 50(6):1369–1388.

Zervos, A., Papanastasiou, P., and Vardoulakis, I. (2001b). Modelling of localisation and scale effect in thick-walled cylinders with gradient elastoplasticity. *International Journal of Solids and Structures*, 38(30-31):5081–5095.

Zreid, I, K. M. (2016). An implicit gradient formulation for microplane drucker-prager plasticity. *International Journal of Plasticity*, 83:252–272.

EURAD (Deliverable n˚ 7.6) – Modelling report on the effect of temperature on clay host rocks behaviour
Dissemination level: PU
Date of issue of this report: 06/06/2024

Page 288